

THIS WEEK

EDITORIALS

MOTION Tiny beads flock together to go with the crowd flow **p.6**

WORLD VIEW On Lady Macbeth and her damned spot **p.7**



FLIGHT Crashing bees reveal key to happy landings **p.8**

Head start

Europe's mega-project to simulate the human brain has much to offer neuroscience research — whether or not it delivers on its central promise.

From supercomputing to imaging, technologies have developed far enough that it is now possible for us to imagine a day when we will understand the murky workings of our most complex organ: the brain.

True, that day remains distant, but scientists are no longer considered crazy if they report a glimpse of it on the horizon. This turning point has been marked by the independent launches this year of two major brain projects: US President Barack Obama's Brain Research Through Advancing Innovative Neurotechnologies (BRAIN) Initiative and the European Commission's Human Brain Project. Even if they fail to achieve the ambitions the research community sets for them, they are signals of a new confidence.

Right now, the two projects are not equal. The BRAIN Initiative is in an early phase of development, and has so far been promised little new money. The impetus behind it was a brash proposal by a group of neuroscientists for a billion-dollar project to measure the activity of every neuron in the human brain. That ambition was lost on the starting block when peers, justifiably, deemed it scientifically inappropriate — but is yet to be replaced by a single goal of equivalently Apollo-program proportions (see page 26). This may make it hard to maintain the political support large projects always need.

Conversely, the Human Brain Project — headquartered in Switzerland, where it will soon relocate from Lausanne to its new base in Geneva — has 135 partner institutes and is blessed with a plenitude of money and planning. And it has a romantic Moon-landing-level goal: to simulate the human brain in a computer within ten years, and provide it to scientists as a research resource. Programme leaders have committed €72 million (US\$97 million) to the 30-month ramp-up stage; those monies started to flow into labs after the project's launch last month. The project has a detailed ten-year road map, laden with explicit milestones.

UPS AND DOWNS

But will the Human Brain Project realize its pioneers' greatest ambition? Many have raised doubts, arguing that we understand too little about how the brain works to make the ambition feasible. However, the project's scope has matured since the idea was first mooted in 2010, in ways some believe may increase its chances. Initially, it was conceived as a programme whereby bottom-up experimental data — electrophysiological, anatomical or cellular — would feed into a supercomputer without preconceived ideas of how the simulated neuronal circuitry might organize itself. A top-down element has now been introduced.

The bottom-up data feed — mostly from research on mice — remains a core component, but how it is processed in the brain simulator will be guided by the findings of one of the Human Brain Project's 15 subprojects, on high-level human cognitive architecture. This will generate data for both animals and humans, describing how cognitive tasks, such as those involving

space, time and numbers, are processed in the brain. For example, in one major research project, around ten people will be selected for repeated study during the decade-long project. Their 'reference brains' will be measured using a range of non-invasive techniques such as functional magnetic resonance imaging and electroencephalography to work out how the relevant neurocircuitry is organized during specific tasks. The detailed bottom-up data will have to align with this broad architecture.

Another subproject, on neurorobotics, will build or simulate robots to provide 'bodies' in which to test whether simulated brain models

really do elicit the behaviours anticipated.

"Major breakthroughs will continue to emerge from individual investigators."

Supercomputing has proved too slow for real-time brain simulation, so other subprojects will focus on developing faster supercomputers, as well as neuromorphic computing, which can theoretically simulate brain activity orders of magnitude faster than occurs in a real brain (see page 22). Neuroinformatics, medical informatics and ethical challenges are all in there too.

The Human Brain Project may still fail to deliver on its central promise, at least at the desired degree of sophistication. It remains a high-risk initiative, and keeping the unwieldy, multidisciplinary consortium on track may also prove difficult. But the risks are spread over the subprojects, some of which will inevitably add significantly to our sum neuroscience knowledge.

And some will inevitably achieve the European Commission's original goal for the project — it is often forgotten that it was not specifically about the brain at all. In 2010, the commission launched a call for proposals for billion-euro, ten-year flagship projects that would push the development of information and communication technologies while offering a benefit to society. The Human Brain Project, with its relevance to brain disorders in an ageing society, was one of two winners. This heritage, which may turn out to be its greatest strength, explains its unusual interdisciplinarity.

The project will absorb more than €1 billion in the next ten years, half of which will come from the European Commission and half of which will be raised by participants, including a large chunk from Switzerland. But it is much more international than this implies. Although most of the partner institutes are in Europe, some are further afield, in countries including Israel, Japan and the United States. The battle for the brain could be won faster with a global effort, and many will be attracted by the Human Brain Project's systematic approach.

But before getting too starry-eyed about mega-projects, let's remember that major breakthroughs in understanding the brain will continue to emerge from the labs of individual investigators. The journey towards a full understanding of the brain will be long and uncertain, and there will be ample opportunity for individual contributions to help point the way. ■



NEW ANGLES ON THE BRAIN
A Nature special issue
www.nature.com/neuroscience2013

Historic work

Governments need to strengthen support for scientists who preserve our cultural heritage.

In Ireland, parts of England and other areas of Europe there are thousands of artworks that were fashioned from rocks during the Neolithic period and the Bronze Age. Threatened by degradation, such cultural heritage attracts scientists and volunteer citizens to ensure its preservation.

The tools that researchers have devised to help in this task are themselves creative. In one project, biogeochemists and geomorphologists have developed non-invasive methods that enable researchers and citizens to monitor and mitigate decay. Scientists interested in protecting historic collections are determining how climate change will affect the rates of chemical degradation of paper and silk, pest damage and mould growth. Then there is optical coherence tomography, which uses reflections of laser light to provide three-dimensional analyses of structures that are micrometres beneath opaque surfaces. Extensions in the spectral range of this technique are revealing features that are valuable for the conservation and historical analysis of works of art.

Such research diversity and much more, practised in many countries, is devoted to the preservation and restoration of humankind's historical and cultural heritage. Who could question the value of such research? Who would doubt the impact of studies that help to protect heritage tourism, a major contribution to many economies? Who could underestimate the benefit to young people and their teachers in science and history? No one does. In fact, government ministers in various nations along with research-funding agencies, the European Commission, regional authorities and the United Nations Educational, Scientific and Cultural Organization all support such science in one way or another.

And yet these heritage researchers struggle. Many have been particularly hard hit by cutbacks in national and regional funding. But more important is their lack of visibility and influence for attracting long-term support; in that sense, the diversity of their techniques and subject matter undermines them. They also lack research prestige, as judged by the conventional standards of scientific assessment — their

work is published in low-profile journals, in museum reports and in other 'grey' literature. And so bright young researchers see too few career prospects, and leave the field. What a waste.

Last week saw a notable gathering of heritage scientists at a conference in London — notable because of the variety exemplified above, but also because one can speak of them as a community, and one that is much more coherent than in the past. This is thanks to a sequence

"What is most important is to build long-lasting capacity in heritage research."

of events in the United Kingdom that many countries would do well to emulate.

A scientific committee of the House of Lords, the upper house of Britain's parliament, recognized in 2006 that such research was important and neglected. As a result of that analysis, the national Science and Heritage Programme was established in 2007, jointly funded by the Arts and Humanities Research Council and the Engineering and Physical Sciences Research Council. The programme has funded nearly 50 projects involving 200 researchers.

Yet funding is only half the story. It is also crucial for the community to be coherent in its actions and in improving its visibility. Here progress has been made, but much more needs to be done. There has been too much dependence on championship of the field by highly committed individuals. More collective approaches are being established, such as the National Heritage Science Forum in Britain and a global forum developed by the International Centre for the Study of the Preservation and Restoration of Cultural Property in Rome. An agenda of engagement for increasing the influence of UK heritage research was aptly described at last week's conference by heritage scientist May Cassar of University College London (see go.nature.com/bxndif). And a European Commission project initiated the Heritage Portal website (www.heritageportal.eu), which has the potential to highlight the field's achievements. But such forums have a way to go in establishing themselves as forces of influence, and the Heritage Portal is seriously under strength.

What is most important is to build long-lasting capacity in heritage research: a combination of multidisciplinary centres of excellence and, above all, a need for science ministers and universities to ensure that new permanent academic posts are established. These are essential to strengthen the backbone of heritage science, and so secure the future of our common past. ■

Follow the crowd

The behaviour of millions of minuscule beads reveals some secrets of collective motion.

Their claimed wisdom is disputed, but no one should doubt the ability of crowds to make collective decisions. Flocks of starlings twist in unison like smoke swirls in a summer sky, and shoals of fish tack and veer as if in response to electric shocks. Locusts swarm and herds of humans can head in very unwise directions indeed. Even simple bacteria show collective behaviour.

Individuals in each of these systems have very different abilities to communicate with each other, to actively pass on information about their intended actions, so why does collective behaviour across all scales look so similar? Is there some unknown sensation that allows the individuals that comprise such seemingly intelligent crowds to steer; some distant wisdom? Although such behaviour is easy to observe, it has proved hard to capture in simple physical models. If we could master it, the information that this might yield could help engineers to develop swarming robots and design safer crowd-control measures.

On page 95 of this issue, researchers in France report that they

have induced collective motion in millions of tiny plastic beads. The miniature spheres, they say, can sense the orientation of their rolling neighbours and adjust their own actions accordingly. In this way, the scientists can encourage the beads to follow the crowd, simply by pouring more of them into the system.

The scientists — Denis Bartolo and his colleagues — squeezed a conducting liquid suspension of the beads into a miniature racetrack sandwiched between two glass plates, and watched what happened when they applied an electric field. An electrohydrodynamic curiosity called Quincke rotation causes the beads to twitch and then start to roll. At first, they head off at constant speed but in all directions. Then, as more beads are added and their number passes a critical point, the individuals form a crowd and their individual motion coalesces into coherent movement in a unified direction — just like that of a flock of birds. This happens, the scientists say, because the rolling spheres can sense the orientation of their neighbours through simple hydrodynamic and electrostatic interactions.

From plastic balls to intelligent dust: there could be interesting implications here for work that aims to harness self-propelled and swarming microparticles, for example, to diagnose disease or improve communications. The writer Mark Twain said: "Whenever you find yourself on the side of the majority, it is time to pause and reflect." But sometimes, the majority really does rule. ■

NATURE.COM
To comment online,
click on Editorials at:
go.nature.com/xhunjv

TOM RACHMAN



Cleaning damned spots from the obsessive mind

Exposure therapy helps some people affected by compulsive washing, but often the contaminant is intangible, says Stanley Rachman.

“Will these hands ne’er be clean?” In Shakespeare’s play *Macbeth*, Lady Macbeth helps to plot the brutal murder of King Duncan. Afterwards she feels tainted by Duncan’s blood and insists that “all the perfumes of Arabia” could not sweeten her polluted hands. Baffled by her compulsive washing, her doctor is forced to admit: “This disease is beyond my practise.”

In the 400 years since *Macbeth* was first performed, other doctors, psychiatrists, neuroscientists and clinical psychologists — myself included — have also found the problem beyond the reach of their own expertise. We see compulsive washing a lot, mostly as a symptom of obsessive-compulsive disorder (OCD), but also in people who have suffered a physical or emotional trauma, for example in women who have suffered sexual assault. The events trigger a deep-seated psychological, and ultimately biological, response.

We know that the driving force of compulsive washing is a fear of contamination by dirt and germs. An obsessive fear of contact with sexual fluids, for example, can drive compulsive washing in OCD and force people to restrict sexual activity to a specific room in the house. Compulsive washing fails to relieve the anxiety. Most patients with OCD continue to feel contaminated despite vigorous attempts to clean themselves. Why does repeated washing fail?

There is much debate at present about the direction that psychiatric medicine and research should take. We should not underestimate what we can continue to learn from the careful observation of patients. Such observations have led my colleagues and me to diagnose a new cause of OCD and other types of compulsive washing: mental contamination.

Lady Macbeth could be an example of someone suffering from this psychological problem. Mental contamination can be evoked without contact with a tangible contaminant. It is a feeling of internal dirtiness caused by a psychological or physical violation. The source of the pollution is not an external contaminant such as blood or dirt, but human interaction. The affected person develops strong feelings of contamination that are evoked by direct contact with the violator or indirect contacts such as memories, images or reminders of the violation.

Commonly, these patients are unwilling or unable even to speak the name of the violator. Milder forms of this mechanism are prevalent in society — in the course of a bitter divorce, for example. The emotional violations that can cause mental contamination include degradation, humiliation, painful criticism and betrayal. There is a moral element in most cases of mental contamination. Separate psychometric research has confirmed mental contamination as a coherent and measurable concept.

This discovery has large and immediate implications for clinical



NEW ANGLES ON THE BRAIN

A Nature special issue

www.nature.com/neuroscience2013

the patient to repeatedly touch the contaminating object or substance — rubbish, for example — and encourages them not to wash or clean as they then want to. The therapy aims to untangle the psychological ‘conditioned’ association between fear and the source of the fear.

Exposure and response prevention is a feature of cognitive behavioural therapy for OCD and other mental disorders across the world. Yet it is a demanding treatment. Up to one-quarter of patients drop out or refuse it, and up to three in ten of those who remain fail to improve. Over the past decade or so, it has become clear that one reason that these people are not helped by exposure therapy is that the source of their problematic contamination is not physical but mental. Feelings of mental contamination are diffuse, mainly internal and not accessible. In these cases, therefore, repeated hand-washing is misdirected.

And so, crucially, is exposure therapy based on physical contact.

In an early study of 50 young women who had experienced a sexual assault, we found abundant evidence of contact contamination and also mental contamination. After the assault they felt polluted, and understandably engaged in vigorous washing. However, a substantial minority of the women continued to feel polluted for many months after the event.

Mental contamination is essentially a cognitive disorder. The patient’s memories, thoughts and images are the root of the problem. They need a cognitive approach, and my colleagues

and I have developed an effective cognitive treatment for mental contamination. We unravel the circumstances of the violation and why the patients believe that they remain under threat. After working with many patients, we carried out a recent (non-blind) study with 12 people with severe OCD, most of whom had not been helped by traditional cognitive behavioural therapy (A. E. Coughtrey *et al.* *Cogn. Behav. Prac.* **20**, 221–231; 2013). Using the notion of mental contamination, and treating it accordingly, we managed to reduce the symptoms significantly for nine of them. We now plan to conduct a full-scale randomized controlled trial. If the effects of the therapy are confirmed, it would have a major impact. We would at last be able to treat the many patients who are currently, like Lady Macbeth, beyond our help. ■

Stanley Rachman is emeritus professor at the Institute of Psychiatry in London, UK, and the University of British Columbia, Canada, and author of *The Fear of Contamination*.
e-mail: rachman@mail.ubc.ca

THE SOURCE
OF THEIR
PROBLEMATIC
CONTAMINATION IS
NOT PHYSICAL BUT
MENTAL.

RESEARCH HIGHLIGHTS

Selections from the
scientific literature

CHEMISTRY

Micromotors detox chemical weapons

Synthetic micromotors might provide a faster, better way to decontaminate nerve agents.

Converting harmful organophosphate chemicals, such as sarin, into innocuous substances requires high concentrations of hydrogen peroxide and constant stirring over long periods. Such conditions are challenging when eliminating chemical-weapons stockpiles in remote or hostile locations.

Joseph Wang at the University of California, San Diego, and his team overcame these requirements using micromotors made of polymers tipped with platinum. These zip around the contaminated fluid, propelled by bubbles that are produced as platinum reacts with peroxide. In small-volume lab tests, this micromixing neutralized nerve agents at low peroxide concentrations and without external stirring.

Two out of three nerve agents tested with micromotors were almost completely detoxified within 40 minutes. The strategy could provide a general method to accelerate reactions, the authors say.

Angew. Chem. Int. Ed.
<http://doi.org/f2ndgr> (2013)



BOTANY

Two routes to huge blooms

The world's largest flowers develop in two distinct ways.

The plants *Rafflesia* and *Sapria* are two groups within the same family (*Rafflesia keithii* pictured). Their gigantic flowers look similar, smell like rotting meat and form large chambers to lure carrion flies as pollinators.

But when researchers led by Charles Davis of Harvard University in Cambridge, Massachusetts, examined gene-expression patterns and physical structures of developing

flowers, they found that the chambers of the two plant groups come from different tissues. This suggests that the groups evolved their most characteristic features independently.

The study might also help to explain how the flowers of some *Rafflesia* species can get as big as one metre across — the largest of all single blossoms — without collapsing. The flower chambers are derived from the petal whorl, which could provide structural reinforcement.

Proc. Natl Acad. Sci. USA <http://doi.org/pq9> (2013)

ZOOLOGY

Seasonal shift for reindeer eyes

As the seasons change, Arctic reindeer (*Rangifer tarandus*; pictured) alter the colours at the backs of their eyes.

In cats and some other mammals, a reflective surface called the tapetum lucidum reflects light through the retina a second time and improves sight in dim light. Glen Jeffery of University College London and his colleagues studied this structure in reindeer captured within two weeks of the

summer and winter solstices.

The tapetum lucideum changed from golden in summer to deep blue in winter. The winter colour seems to scatter more light across the retina.

Proc. R. Soc. B 280, 20132451 (2013)

VISION

How bees see a steady landing

Lacking stereoscopic vision, bees have evolved another technique to ensure that they land safely.

Emily Baird of Lund

University in Sweden and her colleagues discovered that honeybees (*Apis mellifera ligustica*; pictured) alight safely by controlling the rate at which their landing zone expands in their field of vision. Keeping this 'optic flow' constant means that bees slow down as they near their targets.

Baird's team discovered this technique by studying bees as they landed on vertical discs with a rotating spiral pattern. Optical illusions that slowed down or sped up the apparent optic flow caused bees to change their flight speeds accordingly. Rather than landing, many bees would

FRANS LANTING/CORBIS

KIA HANSEN

EMILY BAIRD/LUND UNIV.

FRANCESCO BALDINI/FLAMINIA CATTERUCCIA

either crash into the spiral or hover in front of it.

This simple method of adjusting speed for landings could be widespread among animals and might even be useful in flying robots in the future, the authors suggest. *Proc. Natl Acad. Sci. USA* <http://doi.org/psp> (2013)

GENETICS

More risk genes for Alzheimer's

The largest genetics study so far of late-onset Alzheimer's disease has identified 11 new genome regions that alter the risk of the disease.

A team of some 200 scientists in the International Genomics of Alzheimer's Project carried out meta-analyses of four separate genome-wide association studies, profiling 17,008 people with Alzheimer's and 37,154 people who did not have the disease. The researchers reproduced their findings by genotyping an independent group of 8,572 Alzheimer's cases and 11,312 controls.

Their results confirmed nine out of ten known Alzheimer's risk genes. Eleven newly identified regions may give more clues about the biology of the disease, for which there are still no effective treatments. *Nature Genet.* <http://doi.org/ppm> (2013)

PALAEOCLIMATOLOGY

Deep ocean is a heat sink

A long-term reconstruction of temperatures in the Pacific Ocean reveals how its heat content has changed since the last glacial era — findings that could augment climate models.

Yair Rosenthal at Rutgers University in New Brunswick, New Jersey, and his colleagues analysed sediment cores in Indonesia's Makassar Strait, and used the mineral composition of tiny sea creatures' shells to calculate past water temperatures.

This showed that, at depths of 500–900 metres, temperatures in the Pacific Ocean were typically higher over the past several thousand years than at present. Over millennia, the waters have undergone prolonged cooling and temperatures are now increasing faster than at any time in the past 10,000 years.

The results support other studies suggesting that the ocean is currently taking up more heat, temporarily slowing the rise in average global air temperatures.

Science 342, 617–621 (2013)

ASTRONOMY

Explosions in the young Universe

The biggest ever thermonuclear blasts happened in the early Universe, when primordial gas clumps collapsed and created the seeds of supermassive black holes.

Arising even before many stars and galaxies had time to form, the origins of big black holes have been a puzzle. Daniel Whalen of Los Alamos National Laboratory in New Mexico and his colleagues used computer simulations to reveal how gas in early galaxies could have cooled rapidly, forming stars that then exploded. The stars quickly collapsed back on themselves, generating turbulence that caused nearby gas clumps to form baby black holes.

In related work, the same team ran other analyses predicting whether light from those supernova blasts would be visible to upcoming space missions. The James Webb Space Telescope, due

COMMUNITY CHOICE

The most viewed papers in science

NEUROSCIENCE

Cells grow in sleeping brains



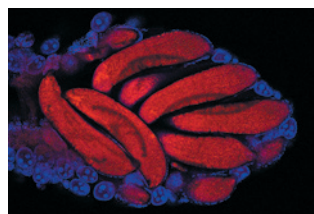
Sleep seems to wake up a type of brain cell that maintains healthy neuron signalling.

Chiara Cirelli and her colleagues at the University of Wisconsin-Madison analysed support cells called oligodendrocytes that wrap around neurons and protect them with a specialized sheath that helps their signals to travel faster.

They collected oligodendrocytes and their precursor cells from mice after the animals had experienced a few hours of sleep or wakefulness and then profiled the expression of newly transcribed genes. Genes that were most active during wakefulness were involved in cell differentiation and death. By contrast, genes that were expressed during sleep promoted cell growth and the production of protective sheaths.

Further experiments showed that the rate of growth of oligodendrocyte precursor cells doubles during sleep, and that cell production increased when mice spent more time in the stage of sleep associated with dreaming.

J. Neurosci. 33, 14288–14300 (2013)



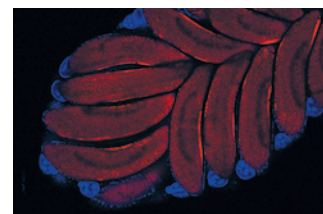
for launch in 2018, should be able to detect these stellar explosions, the authors find. *Astrophys. J.* 777, 99; 110 (2013)

ENTOMOLOGY

Male mosquito boosts egg-making

Male mosquitos deliver more than sperm when they copulate with females: they also provide a hormone that spurs egg development.

A team led by Flaminia Catteruccia at the Harvard School of Public Health in Boston, Massachusetts, studied the malaria-spreading mosquito *Anopheles gambiae*, focusing on a protein that is more abundant in females after mating. Tests using mosquito ovaries showed that this protein helps to direct nutrients into developing eggs (pictured,



red shapes): when the protein was silenced, fewer eggs were produced (left) than when it was expressed (right).

Further work showed that a molecule in male mating secretions binds to this female protein and boosts its expression, which in turn increases egg production.

This is the first demonstration in insects of an interaction between a male hormone and a female protein that changes female reproductive success, the authors say. Interfering with it, perhaps by creating males that lack the hormone, might help to control populations of disease-carrying mosquitoes. *PLoS Biol.* 11, e1001695 (2013)

➔ **NATURE.COM**

For the latest research published by Nature visit:

www.nature.com/latestresearch

SEVEN DAYS

The news in brief

POLICY

Chemical weapons

Syria has destroyed all equipment essential for the production and mixing of chemical weapons, an international team of inspectors announced on 31 October. The news, issued jointly by the United Nations and the Organisation for the Prohibition of Chemical Weapons (OPCW) in The Hague, the Netherlands, came one day before the deadline set by the OPCW. By 15 November, the OPCW Executive Council must approve a plan submitted by Syria to destroy its chemical weapons stockpile.

Flu fights

The Dutch university at which virologist Ron Fouchier and his colleagues created mammalian-transmissible strains of the H5N1 avian influenza virus has appealed against a court ruling obliging it to seek an export permit to publish such research. The Erasmus Medical Center in Rotterdam, the Netherlands, obtained a permit for a paper Fouchier published last year (S. Herfst *et al. Science* **336**, 1534–1541; 2012), but filed a legal challenge that sought to classify such work under

NUMBER CRUNCH

29%

Studies that remain unpublished from 585 large clinical trials registered with ClinicalTrials.gov and completed before 2009. See go.nature.com/sknhdp for more.

Source: C. W. Jones *et al. Br. Med. J.* **347**, f6104 (2013)



GUIDO PARRA

New dolphin species reported

A previously unknown species of humpback dolphin has been found off the coast of Australia. Researchers led by Martin Mendez of the Wildlife Conservation Society in New York identified the as-yet-unnamed species (pictured) from an analysis of 180 skulls and 235 tissue samples of humpback dolphins from around the world (M. Mendez *et al. Mol. Ecol.* <http://doi.org/pp6>; 2013). The team proposes

that humpback dolphins in the Pacific and Indian oceans should be reclassified as three species instead of two: *Sousa plumbea* and *Sousa chinensis*. The humpback dolphin family — which has a characteristic hump just below the dorsal fin — includes at least one other species in the Atlantic Ocean. The discovery could affect conservation policies for the dolphins, which are threatened by habitat loss and fishing.

a regulatory exemption for basic research. The challenge was struck down in a court in September. See go.nature.com/uhtxy3 and page 19 for more.

Grant freeze ends

Officials in Texas have lifted a 10-month freeze on grant funding at the state-supported Cancer Prevention and Research Institute of Texas (CPRIT) in Austin. A moratorium was placed on CPRIT after concerns about its grant-making process prompted a criminal investigation of the agency. See go.nature.com/xsloah for more.

Marine reserves

The Commission for the Conservation of Antarctic Marine Living Resources has failed to agree on a proposal to ban fishing in 1.25 million

square kilometres of the Ross Sea. The plan, discussed at a meeting in Hobart, Australia, that ended on 1 November, would have set up the world's largest marine reserve in what some researchers say is the most endangered area of the polar region. The commission, made up of representatives from 24 countries and the European Union, has failed twice before to agree on similar proposals. See go.nature.com/133el5 for more.

FUNDING

Genomic research

Mexican billionaire Carlos Slim Helú, the world's second-richest man, has donated US\$74 million to the Broad Institute in Cambridge, Massachusetts, for genomic research. The gift from the

Carlos Slim Health Institute will fund collaborations with Mexican scientists to find genetic variants that affect the risk of diseases such as certain cancers, type 2 diabetes and kidney disease in Latin Americans, and follows a previous gift of \$65 million to the Broad made by Slim's foundation in 2010.

FACILITIES

Brain Project move

The European Union's Human Brain Project, launched last month, has unexpectedly scrapped plans to build a dedicated facility in Lausanne, Switzerland. On 29 October, officials at the Swiss Federal Institute of Technology Lausanne (EPFL) announced that the prestigious, billion-euro project will instead

move close to Geneva. The programme will shift into the former Swiss headquarters of the pharma giant Merck Serono, now leased to EPFL and Geneva University.

RESEARCH

Dark matter

The world's most sensitive dark-matter experiment announced its first results on 30 October, reporting no sign of the elusive substance. Astronomical observations point to the presence of dark matter in space, but attempts to detect it directly passing through Earth have produced conflicting results. The findings from a 110-day search at the Large Underground Xenon experiment in Lead, South Dakota, did not confirm three earlier experiments that had reported hints of dark-matter particles. See go.nature.com/lhcojd for more.

EVENTS

Hybrid eclipse

A rare hybrid solar eclipse took place on 3 November (pictured in northern Uganda), as the path of totality moved across the North Atlantic Ocean and Africa. The relative positions of Earth, the Moon and the Sun allowed observers in Africa to see a total eclipse. In parts of the Atlantic, where Earth's curvature placed its surface a



little farther from the Moon, observers saw an annular, or 'ring of fire', eclipse, with the Moon only partially blocking the Sun. This type of eclipse has not occurred since 1854 and will not recur until 2172.

Mars launch

India has launched a spacecraft to Mars. The Mars Orbiter Mission (informally called Mangalyaan) lifted off on 5 November, aiming to reach orbit around the red planet in September 2014. The 4.5-billion-rupee (US\$73-million) mission is the country's first interplanetary probe.

BUSINESS

False drug claims

US regulators announced on 4 November that Janssen Pharmaceuticals has pleaded guilty to making false claims about its schizophrenia drug Risperdal (risperidone). Janssen, based in Titusville, New Jersey, has agreed to pay more than US\$1.6 billion.

The US Food and Drug Administration approved Risperdal for schizophrenia and acute mania, but Janssen also marketed the drug for some elderly patients with dementia, despite the increased risk of stroke in older patients taking the drug.

Prenatal testing

A US court has invalidated a patent at the heart of a territory war in the booming industry of non-invasive prenatal testing. On 30 October, a California federal judge issued the ruling on a patent licensed to Sequenom of San Diego. Sequenom had attempted to invoke its patent in order to block other companies from selling their own non-invasive prenatal tests — a move that could have led to an industry monopoly (see *Nature* **486**, 454; 2012). Sequenom says that it will appeal against the ruling.

PEOPLE

Alcohol agency

Neurobiologist George Koob of the Scripps Research Institute in La Jolla, California, has been appointed to head the US National Institute on Alcohol Abuse and Alcoholism (NIAAA). In January 2014, he will replace interim director Kenneth Warren, whose five-year stint saw the National Institutes of Health consider, and later scrap, a plan to merge

COMING UP

9–13 NOVEMBER

The Society for Neuroscience meets in San Diego, California. Major brain initiatives in the United States and Europe are among the highlighted topics.

go.nature.com/eubkfx

12 NOVEMBER

The International Energy Agency releases its *World Energy Outlook 2013*, which looks at oil resources and demand, and energy efficiency to 2035.

go.nature.com/7j3jw1

the NIAAA and the National Institute on Drug Abuse (see *Nature* **467**, 643; 2010).

AWARDS

Maddox Prize

Pharmacologist David Nutt was awarded the John Maddox Prize for Standing up for Science on 4 November. The prize honours people who, in spite of challenges, promote science in the public interest. Based at Imperial College London, Nutt was fired from his post as the United Kingdom's chief drugs adviser in 2009, after criticizing the government's drugs policy. The award is named after a former editor of *Nature*, and it is jointly awarded by *Nature*, the Kohn Foundation in London and the UK campaign group Sense About Science.

CLARIFICATION

The item 'Data dash' (*Nature* **502**, 598; 2013) may have implied that NASA's rapid data transmission was the result of faster laser beams. In fact, the record was set thanks to greater bandwidth.

NATURE.COM

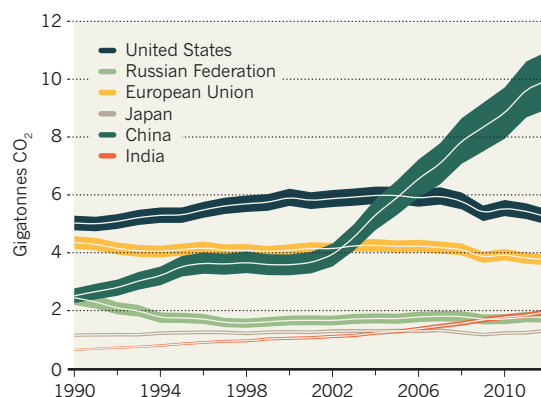
For daily news updates see:
www.nature.com/news

TREND WATCH

Global carbon dioxide emissions increased by just 1.1% in 2012, compared with an annual average of 2.9% since 2000, according to a report released on 31 October by the Netherlands Environmental Assessment Agency. After growing by roughly 10% a year for a decade, Chinese emissions increased by just 3% in 2012, owing to slower economic growth and more low-carbon energy. Emissions from the United States and the European Union fell by 4% and 1.6%, respectively (see chart).

SLOWING GLOBAL EMISSIONS

Recent CO₂ trends may reflect gains in energy efficiency, renewable energies and less-carbon-intensive fossil fuels.

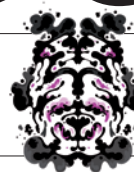


NEWS IN FOCUS

GEOSCIENCE Tremor sensors trundle towards the frozen Alaskan tundra **p.16**

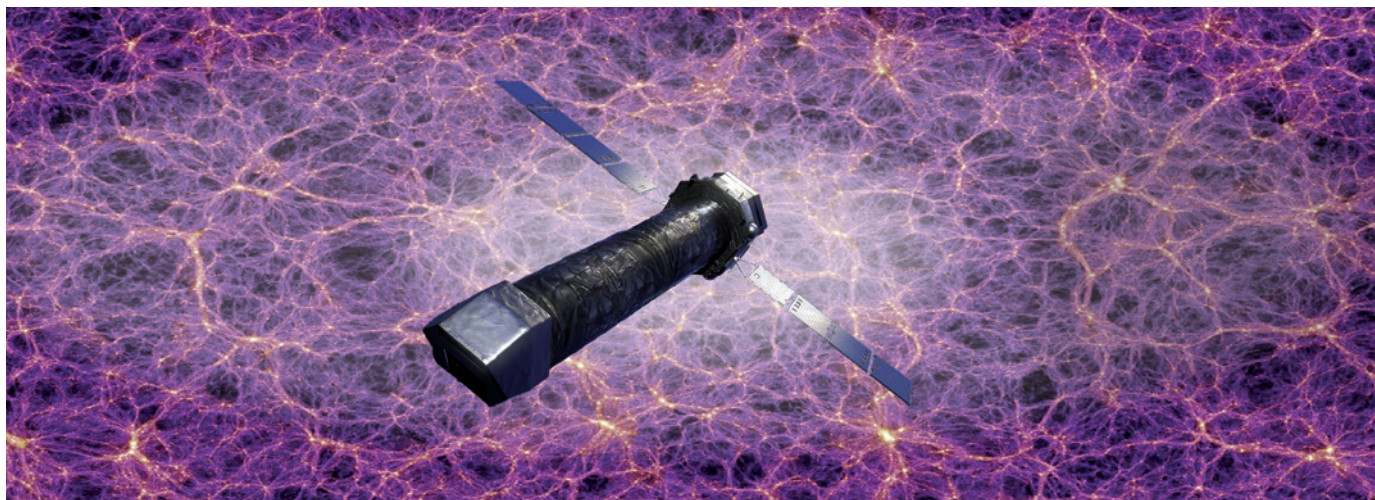
MOLECULAR BIOLOGY Carl Linnaeus had his elephants all mixed up **p.18**

PATHOGENS Virologists challenge rules on export licences **p.19**



NEUROSCIENCE Studies of the brain gain fresh momentum **p.21**

JAVIER GARCIA NOMBELA-ART-ERES.NET/VOLKER SPRINGEL(MPA)/IRAP



Athena+, a planned X-ray observatory that would be the most powerful ever flown, is likely to be launched in 2028.

ASTRONOMY

X-rays top space agenda

European agency selects mission themes, with X-ray telescope the biggest winner.

BY ELIZABETH GIBNEY

An X-ray space telescope has taken pole position ahead of a gravitational-wave observatory in the race to be Europe's next major space-science mission.

On 31 October, European Space Agency (ESA) director of science and robotic exploration, Alvaro Giménez, put forward the “hot and energetic Universe” and the “gravitational Universe” as the two themes that will shape the agency's next large (L-class) projects — the €1-billion (US\$1.4-billion) L2 and L3 missions, scheduled for launch in 2028 and 2034, respectively. ESA's Science Programme Committee, composed of member-state representatives, will consider the recommendation and announce a decision at a meeting on 28–29 November. It would be rare for the committee not to endorse the science director's advice.

The first of the themes is good news for Athena+ (the Advanced Telescope for High Energy Astrophysics), an X-ray observatory that would be the front runner in a formal call — planned for next year — for mission

proposals to probe the hot and energetic aspects of the Universe. The observatory, which will carry a telescope and instruments to measure the energy of X-ray sources and image them with unprecedented precision, would study how hot gas evolves into galaxy clusters and how black holes grow. Luigi Piro, a member of the Athena+ instrument and optics working group at Italy's National Institute for Astrophysics in Rome, says that half of all visible matter is in this ‘hot phase’, but is poorly understood. “We will now be able to tackle questions about how the Universe is actually working and what is the role of hot plasma and black holes in shaping the Universe,” he explains.

The second theme would focus on gravitational-wave astronomy, a field never before studied in space. The planned space-based mission eLISA (evolved Laser Interferometer Space Antenna) would detect the low-frequency gravitational waves that are thought to stretch the fabric of space-time. Gravitational waves have not been directly detected at ground-based observatories. eLISA would bounce lasers between three spacecraft at least one million kilometres apart, and

spot a passing wave when it alters the precise positioning of one of the spacecraft.

eLISA would detect the signals from colliding supermassive black holes and be able to trace the evolution of galaxies, says Karsten Danzmann, director of the Max Planck Institute for Gravitational Physics in Hannover, Germany. Because gravitational ripples can pass undisturbed through matter that affects electromagnetic waves, eLISA will enable scientists to ‘see’ further back in time, to the earliest days of the Universe. It is also hoped that eLISA will tackle questions in fundamental physics, such as whether general relativity holds at the edges of black holes.

For proponents of eLISA, a launch date of 2034 is frustrating, because a pathfinder mission to test the necessary technology is set to fly in 2015 after several years of delays. Danzmann says that the proposal that the X-ray observatory should be the first to launch reflects a desire to concentrate on the “slightly less risky” of the two projects.

But Randall Smith, an X-ray astronomer at the Harvard-Smithsonian Center for Astrophysics in Cambridge, Massachusetts, ►

► admits that he was surprised that his field was picked ahead of gravitational-wave astronomy, given that in previous competitions, including the US Decadal Survey, which decides future NASA missions, the latter had been given the edge.

Many astrophysicists think that the ideal situation would be to go for both projects in parallel, because the two observatories would be looking at some of the same targets, such as black holes, albeit through very different eyes. Bringing the gravitational mission forward would require a cash injection. But Danzmann says that China has already expressed an interest in getting involved with a space-based gravitational-wave detector. And NASA, which pulled out of a similar joint mission in 2011, might be able to reconsider contributing after the launch of the James Webb Space Telescope in 2018, he suggests.

ESA's science programme schedules three missions of this scale every 20 years (see 'X-ray

X-RAY SPECS

The European Space Agency is very close to finalizing the following line-up of large (L-class) missions.

Mission	Name	Launch date	Study targets
L1	JUICE	2022	The magnetic field of Jupiter's moon Ganymede
L2	Athena+	2028	Black holes and galaxy clusters.
L3	eLISA	2034	Gravitational ripples from black-hole mergers.

specs'). In May last year, the Jupiter Icy Moons Explorer (JUICE) was approved as the first of three missions under ESA's Cosmic Vision programme, intended for the L1 launch opportunity in 2022. At that time, previous incarnations of Athena+ and eLISA missed out on selection. The L2 and L3 science themes were based on recommendations from ESA's independent Senior Survey Committee, chaired by astronomer Catherine Cesarsky, a former director-general of the European Southern Observatory.

The current two winners were selected from 32 proposals presented at a meeting in

September. Other options considered were a γ -ray telescope, a mission to explore interstellar space and a host of proposals to explore moons and planets in the Solar System.

Although disappointed that no planetary missions have been put forward, Colin Wilson, a planetary physicist at the University of Oxford, UK, says that his field will still be busy in the coming decade, through planned ESA missions to Mercury, Mars and Jupiter.

But, he adds, exploring the farthest realms of the Solar System, beyond Saturn, will be a real challenge in the coming decades. ■

NEUROSCIENCE

Precision gene editing paves way for transgenic monkeys

Despite political challenges, engineered primates could be better disease models than mice.

BY HELEN SHEN

Anthony Chan spent two years creating the first five monkeys in the world to be genetically engineered with human mutations — in this case, for Huntington's disease. But three of the five monkeys, reported in 2008, developed severe symptoms of Huntington's much more quickly than anticipated, and had to be killed within a month of birth¹. Viruses used to introduce the relevant gene had inserted extra copies randomly, intensifying the symptoms — and highlighting the method's limitations in creating animal disease models.

Chan, a geneticist at Emory University in Atlanta, Georgia, and other scientists around the world are now eyeing precision genome-editing techniques that solve such problems by using enzymes and RNA instead of viruses. Many have high hopes that transgenic monkeys will mimic human genetic conditions more faithfully than mice — and thus permit better drug-development tests. Many also say



Marmosets are among the primates that may soon be engineered with custom genetic-editing methods.

that the primates will accelerate basic research in neuroscience, permitting researchers to map and test complex neural circuits underlying behaviours that do not exist in simpler organisms. "We weren't even able to think about this before," says Chan.

Work is already under way in a few labs. Erika Sasaki, a geneticist at Keio University in Tokyo, was part of the team that used viruses

to produce the first transgenic marmoset to pass on an engineered gene to its offspring². On 11 November, at the annual meeting of the Society for Neuroscience in San Diego, California, Sasaki and her colleagues will present efforts to model autistic behaviour in marmosets using mutations produced with zinc-finger nucleases — a class of DNA-cutting enzyme. Next month, the Salk Institute for



NEW ANGLES ON THE BRAIN

A Nature special issue

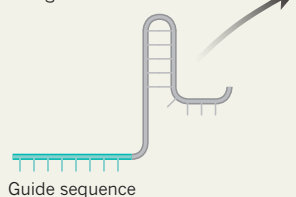
www.nature.com/neuroscience2013

SOURCE: FENG ZHANG/MIT

CRISPR CUTS

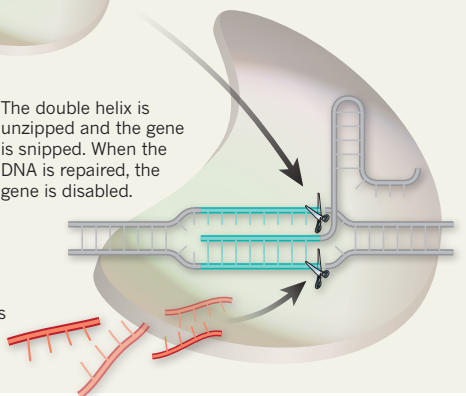
Scientists have developed a precise way to disable genes.

1 Engineer a section of RNA to target a specific region of DNA.



2 The RNA sequence, linked to a DNA-cutting enzyme, finds the right spot on the genome.

3 The double helix is unzipped and the gene is snipped. When the DNA is repaired, the gene is disabled.



4 While the DNA is broken, it is vulnerable to strategic insertions of small amounts of engineered DNA that could alter the gene.

Biological Studies in La Jolla, California, is hosting a workshop to bring together molecular biologists, bioengineers and neuroscientists to work on challenges in the field. "This is something with tremendous potential," says Terrence Sejnowski, head of the computational neurobiology laboratory at the Salk Institute.

Neuroscientists have long wanted transgenic monkeys. Disorders such as autism, schizophrenia and Alzheimer's disease cannot be fully replicated in mice, which lack the complex cognitive and social abilities of primates. Moreover, many neuroactive drugs that showed early promise in mice have failed in human trials.

But researchers have persisted in working with mice, mainly because there is a targeted gene-editing strategy that works in the animals. It relies on extremely rare, spontaneous DNA-swapping events to alter or disable certain genes. The method requires several arduous steps: designing the desired mutation and introducing it to embryonic stem cells; detecting it in the tiny fraction of stem cells that incorporate it; integrating those stem cells into a developing mouse embryo; and then hoping that when the 'patchwork' animal matures, its sperm or eggs will carry the mutation, allowing the creation of transgenic offspring.

The approach is feasible only because mouse stem cells are relatively cheap to maintain and screen, and because mice reach sexual maturity within weeks and produce large litters.

"You don't have that luxury with monkeys," says Edward Callaway, a neuroscientist at the Salk Institute. Marmosets, for example, take 15 months to mature sexually, carry babies for 5 months and often give birth to only 2 young. Macaques take even longer — 3 years to reach sexual maturity, and they typically produce a single baby after a 5.5-month gestation.

But custom monkeys have become a possibility thanks to efficient gene-editing techniques that can support a method in which embryos are manipulated one at a time. In one method, zinc-finger nucleases home in on specific genomic regions, and cut genes open to disrupt their function or allow researchers to substitute in external DNA. In another, called CRISPR, a customizable RNA fragment is used to guide a DNA-cutting enzyme to the right spot (see 'CRISPR cuts'). Feng Zhang, a synthetic biologist at the Massachusetts Institute of Technology (MIT) in Cambridge, showed in May that CRISPR could be used to make precise mutations in multiple genes in mouse embryos³. That, he says, could pave the way for monkey models of human brain disorders that involve more than one gene.

"We now have, for the first time, the possibility of trying some of the treatments for genetic-based diseases in primates," says Robert Desimone, director of the McGovern Institute for Brain Research at MIT.

MIT researchers are now testing CRISPR on

fertilized monkey eggs, in collaboration with researchers from the Oregon National Primate Research Center in Beaverton. They will start by disabling genes. MIT neuroscientist Guoping Feng, one of Zhang's collaborators, wants to disrupt a gene called *SHANK3*, which has been implicated in some human cases of autism. More sophisticated changes, such as swapping in a different version of a gene, will require more work and engineering, says Zhang.

Eventually, he adds, CRISPR might be used to label specific monkey neuron types or control them with light — just as is currently possible with mouse neurons. Basic neuroscientists are especially keen to see those applications succeed. Anthony Movshon, a monkey-vision researcher at New York University, has watched over the past decade as scientists have used genetic tools to stimulate, inhibit and record neural activity in mice and flies. But for many important areas of neuroscience — cognition, attention, memory and decision-making — those animals are "not that interesting," he says.

All of this excitement comes at a time when monkey research has become increasingly difficult. In January, following years of pressure by animal-rights activists, United Airlines announced that it would stop transporting research monkeys — eliminating the last North American air carrier available to primate researchers (see *Nature* **483**, 381–382; 2012). And in April, the New England Primate Research Center in Southborough, Massachusetts — one of eight such centres supported by the US National Institutes of Health — announced that it would close after gradually transferring its animals to other facilities.

Despite the controversies, some researchers say that using transgenic monkeys may be the best way to search for treatments for brain diseases and to investigate how networks of neurons create consciousness. "You want to match the model system to the question you're asking," says Movshon. "It's just as unethical to use a mouse for an experiment for which it's not suited." ■

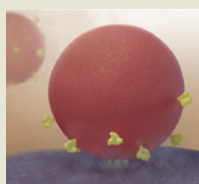
1. Yang, S.-H. *et al.* *Nature* **453**, 921–924 (2008).
2. Sasaki, E. *et al.* *Nature* **459**, 523–527 (2009).
3. Wang, H. *et al.* *Cell* **153**, 910–918 (2013).

"We now have, for the first time, the possibility of trying some of the treatments for genetic-based diseases in primates."

animal-rights activists, United Airlines announced that it would stop transporting research monkeys — eliminating the last North American air carrier available to primate researchers (see *Nature* **483**,

MORE ONLINE

TOP STORY



Rift widens over structure of HIV's molecular model
go.nature.com/iftotec

MORE NEWS

- Most dinosaurs may still have been growing when they died go.nature.com/acca8j
- US to approve two drugs for hepatitis C go.nature.com/qh8z9d
- US tallgrass prairie was hotspot of microbial diversity go.nature.com/ozes2j

NATURE PODCAST



Eye contact in infants predicts autism; a fresh take on Parkinson's; and real science in schools nature.com/nature/podcast



IRIS

Scientists tested rugged new equipment for the Transportable Array near Toolik Lake, Alaska, in 2011.

GEOSCIENCE

US seismic array eyes its final frontier

Moveable sensor grid will begin monitoring Alaska next summer.

BY ALEXANDRA WITZE

On Maine's rugged coast, just north of the tourist town of Boothbay, an underground seismometer is listening for earthquakes. Engineers activated it on 26 September, completing the US\$90-million Transportable Array, an ambitious effort to blanket the contiguous United States with a moveable grid of seismic monitors (see 'On the march').

Since 2004, the set of 400 seismometers, loaded on trucks, has marched gradually eastwards across the continent, from the Pacific coast across the Rocky Mountains and the Great Plains to reach the eastern seaboard. At each spot, technicians dig holes to bury the instruments in plastic tanks underground. The process has drawn the best picture yet of the North American part of Earth's mantle, reaching hundreds of kilometres beneath the surface. The array has illuminated how slow-motion earthquakes shimmy along the coast of the Pacific Northwest, and how molten rock rises in the hot spot deep beneath Yellowstone National Park in Wyoming.

"As the array has moved, the whole picture of what's under North America has gotten much sharper," says Andy Frassetto, a seismologist at the Incorporated Research Institutions

for Seismology (IRIS) in Washington DC, which operates the stations.

Now, the Transportable Array's operators are looking to the far north, in what may be its toughest challenge yet. Having almost finished the job in the lower 48 states, the seismometers will start to be relocated next spring to Alaska — by far the most seismically active US state, and not thoroughly monitored yet. The project's seasoned engineers will have to fly many of the instruments to remote locations by helicopter, then drill into frozen ground and install the seismometers with battery packs to keep them working through the long northern winter. (A few additional stations will be installed across the Canadian border, in the Yukon Territory.)

The Transportable Array, along with other permanent and temporary seismic stations, is one of three cornerstones making up the larger EarthScope initiative. EarthScope was conceived as a way to combine different geophysical views of the deep Earth to provide data on a grand scale for researchers working across North America on all aspects of geoscience. EarthScope's second component comes in the form of Global Positioning System instruments that detect tiny changes in ground movement, such as those that occur along geological faults. The initiative's third component was a

3.2-kilometre-deep hole drilled into California's San Andreas fault, although the effort was marred when instruments lowered down the hole stopped working after just days (see *Nature* **459**, 20–21; 2009).

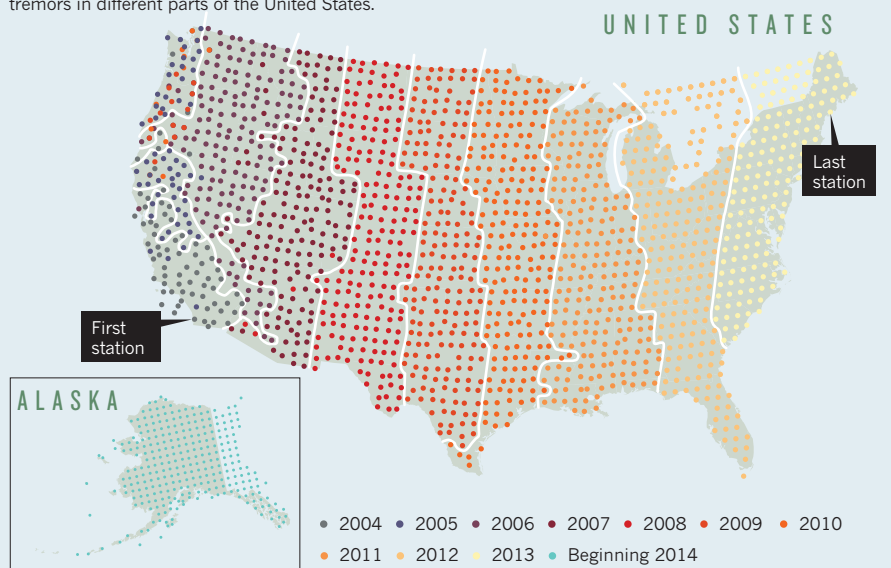
But the first two parts of EarthScope are yielding plenty of insights. "We've learned a lot more by integrating things together than we would have by doing them separately," says Robert Smith, a geophysicist at the University of Utah in Salt Lake City, and an early leader of EarthScope.

When the Transportable Array was initiated in 2004, with funding from the US National Science Foundation, it was just a single station outside San Diego, California. Now, its 400 stations are arranged at 70-kilometre intervals in a regular grid. Each stays in the ground for roughly two years before being dug up and redeployed to the array's leading edge. The stations capture seismic waves travelling through the ground from earthquakes near and far — information that geoscientists can use to probe deeper into Earth, and with greater regularity, than with other, smaller arrays.

Among other things, the EarthScope seismic data have allowed researchers to construct images of the deep Earth, rather like a geological computerized-tomography scan (Y. Yang

ON THE MARCH

Since 2004, 400 moveable seismometers have measured tremors in different parts of the United States.



J. Geophys. Res. **113**, B12310; 2008), and to trace shaking from great earthquakes, such as Japan's Tohoku quake in March 2011, to calculate how a fault ruptured half a world away (M. Ishii *Earth Planets Space* **63**, 609–614; 2011).

Some seismologists worried that things might get boring as the array trundled across the United States, leaving the seismically exciting west for the flatter east. But that did not happen; in fact, the latest data show that the upper part of Earth's mantle east of the Rocky Mountains is just as complex as that in the west, says Suzan van der Lee, a geophysicist at Northwestern University in Evanston, Illinois, who presented the work on 30 October at the annual meeting of the Geological Society of America in Denver, Colorado. The array also captured the surprising magnitude-5.8 earthquake in Virginia in August 2011, and the seismic shaking caused by Hurricane Sandy as it swept the eastern seaboard in October 2012.

Array deployments went so well that the project had money remaining and was able to add 60 previously unplanned Canadian stations in southern Ontario and Quebec, to study a zone of seismicity along the St Lawrence seaway. Other dreams didn't transpire; some scientists wanted to ramp up from taking 40 observations per second to 100. Such a change would have overloaded the data-storage and delivery systems, says the array's manager, Robert Busby of IRIS.

Now, as the array prepares to leave the east coast, project managers are tackling the logistics of the five-year, \$40-million move to Alaska as soon as the snow melts there next spring. About 160 of the 400 stations currently

in the east will remain behind, as part of a plan drawn up by four federal agencies to fill in seismic monitoring gaps in heavily populated areas and near nuclear power plants.

EarthScope managers will use the money saved to buy more durable equipment for Alaska, where the conditions are notoriously tough on outdoor gear. Busby's team is acquiring high-capacity lithium-ion batteries that can be charged by solar panels in the summer and survive all winter. Engineers are also developing methods to relay data by satellite phone, because the mobile-phone network in Alaska covers only a fraction of the state.

And instead of burying seismometers in plastic containers, which could break as the ground thaws and freezes, the team plans to install them deep in permanently frozen ground or solid rock. They have developed a lightweight drill rig that can be carried easily by helicopter, because many of the seismic sites have no road access.

Logistical problems are one reason that the stations will be spaced less densely in Alaska than in the 48 contiguous states — every 85 kilometres instead of every 70. Even so, they will provide a sharper and deeper view of what is happening beneath Alaska than ever before. "It'll make such a difference in so many ways," says Peter Haeussler, a geologist with the US Geological Survey (USGS) in Anchorage, Alaska. "There will be seismometers in the parts of the state that have never had them."

Alaska also has some of the most complex geology in North America, with the Pacific crustal plate slamming into and diving under the continent. Yet little has been done to probe the underlying crust and mantle, mainly because instrumenting the entire state is so expensive. "We have sort of a 'zeroth' order of understanding," says Rick Saltus, a USGS geophysicist in Denver. Now, he says, "we'll get the first order". ■

"There will be seismometers in the parts of the state that have never had them."



The fetus used by Carl Linnaeus as the type specimen of the Asian elephant.

PROTEOMICS

Proteins help solve taxonomy riddle

Proteomic technique proves that 300-year-old Linnaean elephant was wrongly classified.

BY EWEN CALLAWAY

A 300-year-old pickled fetus that was classified by Carl Linnaeus as the type specimen of the Asian elephant has been proved to be an African elephant — by the use of the emerging technology of ancient proteomics.

Evolutionary geneticist Tom Gilbert, whose

University of Copenhagen lab owns one of the world's most advanced DNA sequencing machines, had failed to identify the species from a DNA sample seven years ago because it was too degraded. To sidestep this problem, he and his colleague Enrico Cappellini decided to run an advanced protein analysis using a sample from the oesophagus of the fetus, held in the National Museum of Natural History in

Stockholm. "Clearly it's got protein, because the damn thing still exists," Gilbert says.

The team sequenced several proteins in the specimen that were known to vary between elephant species, and each pointed to an African origin for the fetus (see go.nature.com/ivzyzm). Linnaeus assigned the elephant fetus as the type specimen of the Asian elephant (*Elephas maximus*), but zoologists had long suspected that it was in fact an African elephant (now called *Loxodonta africana*).

The work demonstrates the power of studying ancient proteins. Proteins are more resistant to degradation than DNA and could push the molecular fossil record back millions of years, as well as revealing biological insights that cannot be gleaned from genetic material alone, say scientists who study such remains.

Ancient protein analysis is not a new pursuit, says Matthew Collins, a biogeochemist at the University of York, UK. As long ago as 1954, amino acids were detected in trilobite and dinosaur fossils.

But the field took off in 2000, when Peggy Ostrom, a geochemist at Michigan State University in East Lansing, reported protein sequences from ancient bison and walrus bones up to 50,000 years old¹. Her lab was the first to analyse ancient proteins using the technique of mass spectrometry, which ionizes peptide fragments and then measures their mass, enabling identification when compared with reference databases. Mass spectrometry revolutionized the field of proteomics, in which hundreds of proteins from a tissue are analysed at once, and made it possible to sequence fragmented ancient proteins.

Early efforts by Ostrom, Collins and others focused on individual proteins that are abundant in bone remains, such as collagen. "We call it the barcode of death," says Collins, who uses collagen sequencing to quickly and cheaply identify species found at archaeological sites, such as the animals used to make parchment or the horns on Viking helmets. Collagen is also remarkably stable: it has been sequenced from a 3.5-million-year-old fossil of a giant camel from the Arctic².

But collagen differs very little between closely related animal species, making it useless as a marker for evolutionary change. "You cannot tell an ibex from a domestic goat; you cannot tell a human from a Neanderthal," Collins says. So Cappellini began developing methods to identify large numbers of different proteins in long-dead organisms.

In 2012, his team identified 126 proteins from a 43,000-year-old woolly mammoth femur³. Earlier this year they sequenced 73 proteins from a 750,000-year-old horse fossil⁴. Both specimens also yielded DNA, but the protein data could reveal



NATURE.COM
For the full story on Linnaeus's elephant, see: go.nature.com/ivzyzm

the additional information about which genes were expressed in bone tissue.

Like DNA sequencing, however, mass spectrometry of an ancient sample can yield an overwhelming amount of data, says Ostrom. “It can be daunting, you can get hundreds of sequences from just a single sample of a single protein, from one individual,” she says. And, like ancient DNA, ancient proteins suffer from contamination and chemical modification, although less is known about those processes with proteins, Ostrom says. Another drawback is that proteomics relies on databases of protein

sequences to identify the proteins found. Such databases are lacking for most modern animals, let alone their ancient ancestors.

Researchers studying ancient proteins hope to do more than just sort out museum collections, although Gilbert and Cappellini are working on plenty of these. Ancient proteins can indicate which genes were active in particular tissues from old specimens. They can also reveal phylogenetic information from specimens in which the DNA is too degraded to analyse, such as ancient samples from warm climates, where DNA doesn't last long, says Collins.

For instance, the evolutionary relationship between humans and *Homo floresiensis*, a short-statured human fossil from the Indonesian island of Flores, is unclear, and efforts to extract DNA have so far failed. Ancient proteins might finally place this ‘hobbit’ correctly on the human family tree. ■

1. Ostrom, P. H. *et al. Geochim. Cosmochim. Acta* **64**, 1043–1050 (2000).
2. Rybczynski, N. *et al. Nature Commun.* **4**, 1550 (2013).
3. Cappellini, E. *et al. J. Proteome Res.* **11**, 917–926 (2012).
4. Orlando, L. *et al. Nature* **499**, 74–78 (2013).

VIROLOGY

Pathogen–research laws queried

Scientists fear EU biosafety rules could complicate publication of work on infectious diseases.

BY DECLAN BUTLER

Leading virologists have written to the president of the European Commission to urge him to clarify how laws designed to curb the proliferation of biological weapons apply to the publication of research on dangerous pathogens. The move by the European Society for Virology (ESV) comes after a Dutch court in September upheld a government order that scientists who engineered forms of H5N1 avian influenza to make them transmissible between mammals needed to seek an export permit before publishing such work.

The ESV's five-page letter to José Manuel Barroso, dated 16 October, warns that the court ruling sets an unwelcome precedent. H5N1 is just one of more than 100 dangerous human, animal and plant pathogens and toxins that fall under European Union (EU) export-control legislation from 2009. This means, say the virologists, that any EU scientist who works on one of the listed pathogens could be forced to apply for an export permit before publishing their research.

They write that to better inform courts and policy-makers on scientific issues related to biosecurity laws, the European Commission should consider creating an equivalent of the US National Science Advisory Board for Biosecurity — an independent committee in Bethesda, Maryland, that advises on issues of biosecurity and dual-use research (findings that could be adapted for harmful purposes).

The ESV also backs the case of Ron Fouchier, a virologist at the Erasmus Medical Center (EMC) in Rotterdam, the Netherlands, whose team engineered the H5N1 strains. It was Fouchier's attempt to publish this work that led to the export-licence order. He has been fighting it — and on 31 October, the EMC contested the ruling in the Amsterdam Court of Appeal.

The origin of the ESV's letter dates back to 2011, when Fouchier tried to publish a paper in *Science* that describes how he engineered H5N1 strains that could be transmitted through the air between ferrets. This prompted a global outcry over the biosecurity of such ‘gain-of-function’ research — experiments designed to increase the transmissibility or pathogenicity of organisms (see nature.com/mutantflu). The Dutch government subsequently invoked European export-control legislation to oblige Fouchier and the EMC to obtain an export permit before publishing their work. Fouchier initially threatened to defy the government, but conceded and applied for a permit under protest in April last year. The government granted it a few days later.

Fouchier has argued that the EMC should not have needed a permit because the work fell under an exemption of EU export-control laws for ‘basic scientific research’. He also said that the methods described had already been published. But these arguments were rejected by the court, which added in its ruling that the need to prevent the proliferation of biological weapons outweighed any delays in publication caused by government reviews of such papers.

Giorgio Palù, a virologist at the University of Padua in Italy and president of the ESV, finds it particularly unsettling that the court also ruled that it was not up to Fouchier himself to decide whether to apply for an export permit. Palù thinks this could mean that researchers working on any of the listed dangerous pathogens in the Netherlands, and perhaps in the whole of the EU, might automatically have to request export permits if they intend to publish papers on them.

“If the benefits outweigh the risks, the export licence will be granted.”

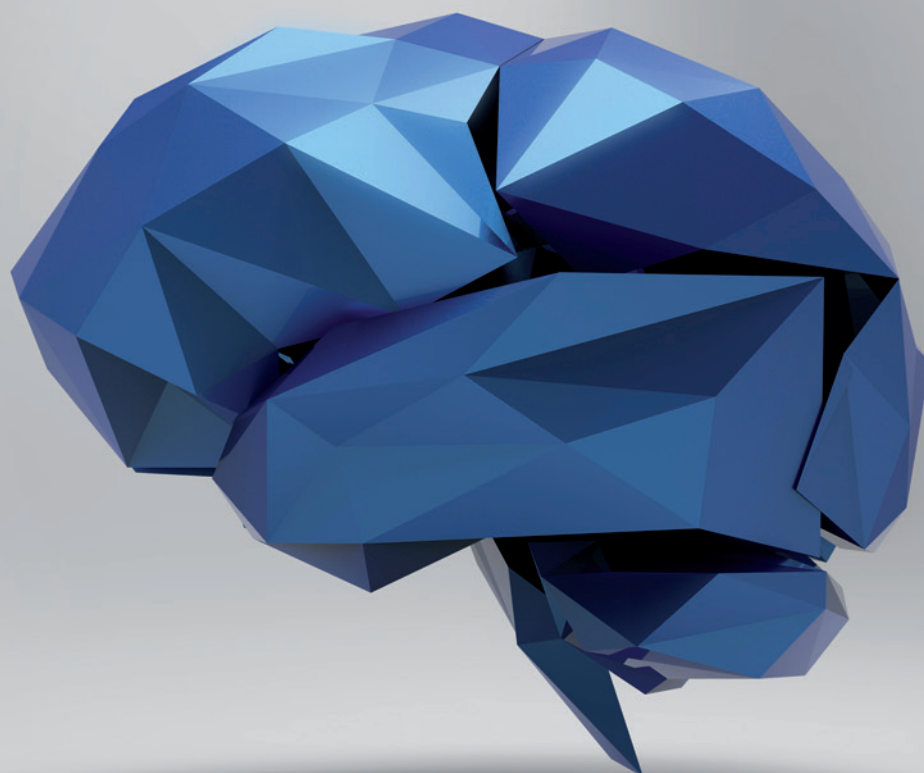
But Thijs van Son, a spokesman for the Dutch foreign-affairs ministry, says that this is not the case. He adds that according to Dutch government policy, the decision on whether to apply for an export permit still lies with the researcher.

“If the researcher is convinced that the export-control legislation is not applicable to his research, he can decide not to apply for an export licence,” says van Son. “However, if he is mistaken, he risks committing an offence and receiving a fine or imprisonment.” Authorities, he adds, are happy to advise researchers on whether they need a permit.

Van Son also says that the ESV letter is correct that the ruling could lead to an increase in the number of papers that Dutch authorities are asked to review. But he says that the export-control law is an essential component of international efforts to halt the proliferation of chemical and biological weapons.

“The licence requirement enables the export-control authorities to assess the proliferation and security risks of, for example, gain-of-function research against the public-health benefits and the freedom to share scientific information,” he says. “If the benefits outweigh the risks, the export licence will be granted. This was the case with the application of Professor Fouchier.”

The Dutch H5N1 case is an unprecedented test of the 2009 EU export laws, and it is not clear how other member states would handle a similar case. Ben Berkhout, a virologist at the University of Amsterdam and a member of the ESV's executive board, says that the ruling has caused uncertainty as to what it covers. “Most work on these pathogens is totally harmless,” he adds. He fears that the ruling will lead to added bureaucracy, and feels that it would be much better for governments to focus on the experiments that carry the greatest risks. ■



NEW ANGLES ON THE BRAIN

Technologies that probe neural circuitry could greatly advance the study of human cognition.

We are entering the golden age of brain science, at least in terms of funding, if not yet understanding. This year, the European Union and United States announced separate long-term programmes to study the human brain that, together, could pour more than US\$2 billion into neuroscience during the next decade (that's more than 2 cents for every neuron in the body's most complex organ). Driving these investments is the sense that researchers are on the verge of making leaps in understanding the brain — advances that could eventually lead to better treatments for mental disorders.

In this special issue, *Nature* taps into this excitement with reporting and opinions on efforts to apply current technologies and invent new ones to grasp how all the grey and white matter in the brain actually works.

Take the design of 'neuromorphic' hardware — computer systems that function according to similar principles as neurons and neural circuits in the brain. After years of development, applications in robotics, mobile electronics and neuroprostheses are finally in sight (see page 22). On the biological side, researchers are applying a broad array of techniques to mapping neural connections in the brain (see page 147). On page 31, neurologist Kenneth Kosik

argues that technologies that can monitor thousands or millions of networked neurons are exactly what are needed to better understand and treat Alzheimer's disease. Meanwhile, researchers with neuroimaging expertise are increasingly in demand, thanks to hopes that the technology will reveal information about everything from the progression of brain diseases to behaviour (see page 153).

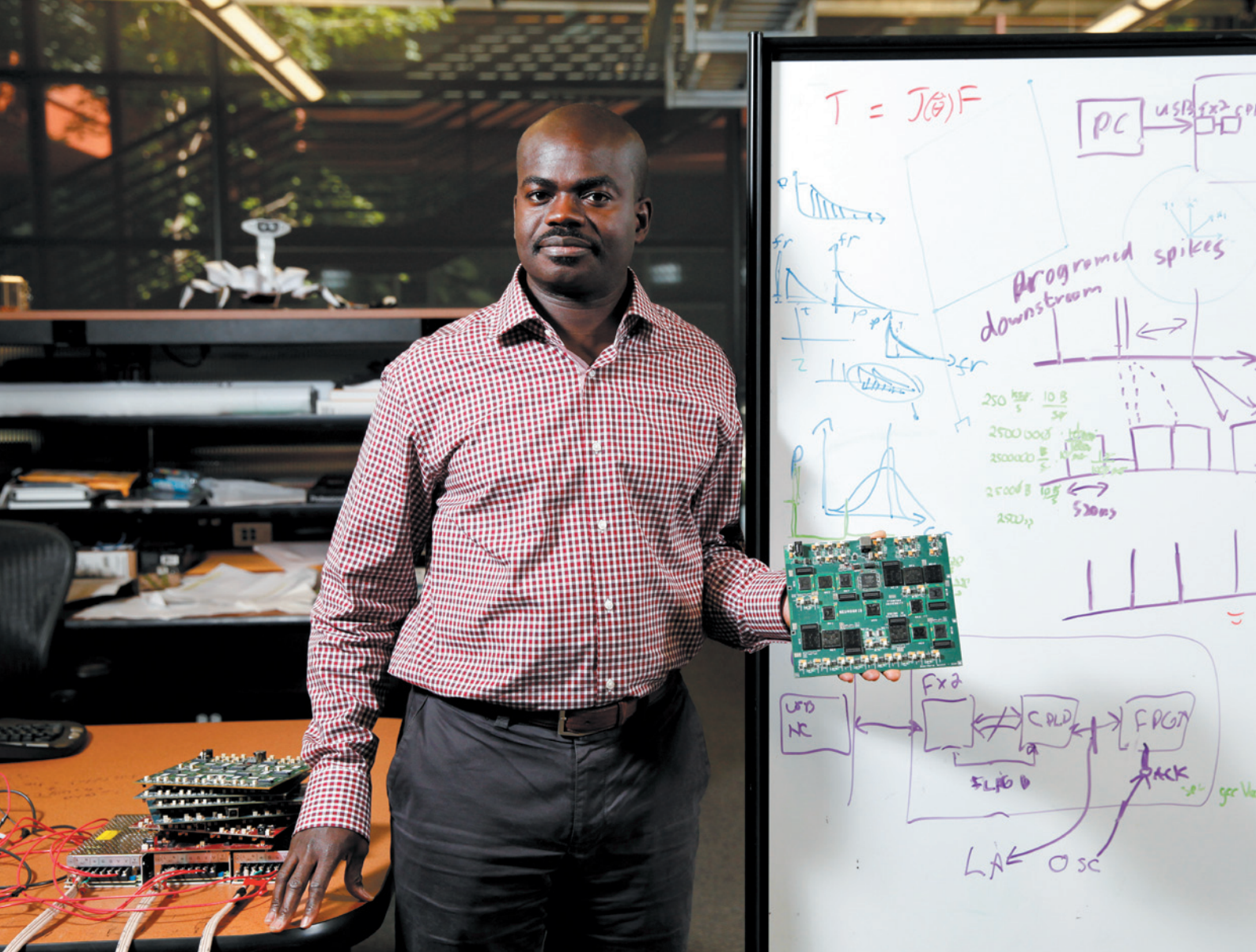
Amid the excitement, there are also significant questions about the major brain projects (see page 5). In the case of the US initiative, neuroscientists are not sure what kind of research it will support, and many in the field have spent much of the year struggling to define the scope of the project (see page 26). However, everyone agrees that the new opportunities presented by technology warrant exploitation. This message comes through especially vividly on page 29, where an anonymous neuroscientist with Parkinson's disease recounts his poignant experience of studying the brain while watching his own begin to fail. ■



NEW ANGLES ON THE BRAIN

A *Nature* special issue

www.nature.com/neuroscience2013



SMART CONNECTIONS

Computer chips inspired by human neurons can do more with less power.

Kwabena Boahen got his first computer in 1982, when he was a teenager living in Accra. “It was a really cool device,” he recalls. He just had to connect up a cassette player for storage and a television set for a monitor, and he could start writing programs.

But Boahen wasn’t so impressed when he found out how the guts of his computer worked. “I learned how the central processing unit is constantly shuffling data back and forth. And I thought to myself, ‘Man! It really has to work like crazy!’” He instinctively felt that computers needed a little more ‘Africa’ in their design, “something more distributed, more fluid and less rigid”.

Today, as a bioengineer at Stanford University in California, Boahen is among a small band of researchers trying to create this kind of

BY M. MITCHELL WALDROP

computing by reverse-engineering the brain.

The brain is remarkably energy efficient and can carry out computations that challenge the world’s largest supercomputers, even though it relies on decidedly imperfect components: neurons that are a slow, variable, organic mess. Comprehending language, conducting abstract reasoning, controlling movement — the brain does all this and more in a package that is smaller than a shoebox, consumes less power than a household light bulb, and contains

nothing remotely like a central processor.

To achieve similar feats in silicon, researchers are building systems of non-digital chips that function as much as possible like networks of real neurons. Just a few years ago, Boahen completed a device called Neurogrid that emulates a million neurons — about as many as there are in a honeybee’s brain. And now, after a quarter-century of development, applications for ‘neuromorphic technology’ are finally in sight. The technique holds promise for anything that needs to be small and run on low power, from smartphones and robots to artificial eyes and ears. That prospect has attracted many investigators to the field during the past five years, along with hundreds of millions of dollars in research funding from agencies in both the United States and Europe.



NEW ANGLES ON THE BRAIN

A Nature special issue

www.nature.com/neuroscience2013

RAMIN RAHIMIAN

Kwabena Boahen holds a 'neuromorphic' circuit board from his Neurogrid device.

Neuromorphic devices are also providing neuroscientists with a powerful research tool, says

Giacomo Indiveri at the Institute of Neuroinformatics (INI) in Zurich, Switzerland. By seeing which models of neural function do or do not work as expected in real physical systems, he says, "you get insight into why the brain is built the way it is".

And, says Boahen, the neuromorphic approach should help to circumvent a looming limitation to Moore's law — the longstanding trend of computer-chip manufacturers managing to double the number of transistors they can fit into a given space every two years or so. This relentless shrinkage will soon lead to the creation of silicon circuits so small and tightly packed that they no longer generate clean signals: electrons will leak through the components, making them as messy as neurons. Some researchers are aiming to solve this problem with software fixes, for example by using statistical error-correction techniques similar to those that help the Internet to run smoothly. But ultimately, argues Boahen, the most effective solution is the same one the brain arrived at millions of years ago.

"My goal is a new computing paradigm," Boahen says, "something that will compute even when the components are too small to be reliable."

SILICON CELLS

The neuromorphic idea goes back to the 1980s and Carver Mead: a world-renowned pioneer in microchip design at the California Institute of Technology in Pasadena. He coined the term and was one of the first to emphasize the brain's huge energy-efficiency advantage. "That's been the fascination for me," he says, "how in the heck can the brain do what it does?"

Mead's strategy for answering that question was to mimic the brain's low-power processing with 'sub-threshold' silicon: circuitry that operates at voltages too small to flip a standard computer bit from a 0 to a 1. At those voltages, there is still a tiny, irregular trickle of electrons running through the transistors — a spontaneous ebb and flow of current that is remarkably similar in size and variability to that carried by ions flowing through a channel in a neuron. With the addition of microscopic capacitors, resistors and other components to control these currents, Mead reasoned, it should be possible to make tiny circuits that exhibit the same electrical behaviour as real neurons. They could be linked up in decentralized networks that function much like real neural circuits in the brain, with communication lines running between components rather than through a central processor^{1,2}.

By the 1990s, Mead and his colleagues had shown it was possible to build a realistic silicon neuron³ (see 'Biological inspiration'). That

device could accept outside electrical input through junctions that performed the role of synapses, the tiny structures through which nerve impulses jump from one neuron to the next. It allowed the incoming signals to build up voltage in the circuit's interior, much as they do in real neurons. And if the accumulating voltage passed a certain threshold, the silicon neuron 'fired', producing a series of voltage spikes that travelled along a wire playing the part of an axon, the neuron's communication cable. Although the spikes were 'digital' in the sense that they were either on or off, the body of the silicon neuron operated — like real neurons — in a non-digital way, meaning that the voltages and currents weren't restricted to a few dis-

"WE ENVISION BUILDING FULLY AUTONOMOUS ROBOTS THAT INTERACT WITH THEIR ENVIRONMENTS IN A MEANINGFUL WAY."

crete values as they are in conventional chips.

That behaviour mimics one key to the brain's low-power usage: just like their biological counterparts, the silicon neurons simply integrated inputs, using very little energy, until they fired. By contrast, a conventional computer needs a constant flow of energy to run an internal clock, whether or not the chips are computing anything.

Mead's group also demonstrated decentralized neural circuits — most notably in a silicon version of the eye's retina. That device captured light using a 50-by-50 grid of detectors. When their activity was displayed on a computer screen, these silicon cells showed much the same response as their real counterparts to light, shadow and motion⁴. Like the brain, this device saves energy by sending only the data that matters: most of the cells in the retina don't fire until the light level changes. This has the effect of highlighting the edges of moving objects, while minimizing the amount of data that has to be transmitted and processed.

CODING CHALLENGE

In those early days, researchers had their hands full mastering single-chip devices such as the silicon retina, says Boahen, who joined Mead's lab in 1990. But by the end of the 1990s, he says, "we wanted to build a brain, and for that we needed large-scale communication". That was a huge challenge: the standard coding algorithms for chip-to-chip communication had been devised for precisely coordinated digital signals, and wouldn't work for the more-random spikes created by neuromorphic systems. Only in the 2000s did Boahen and others devise circuitry and algorithms that would work in this messier system, opening the way for a flurry of development in large-scale neuromorphic systems.

Among the first applications were large-scale emulators to give neuroscientists an easy way

to test models of brain function. In September 2006, for example, Boahen launched the Neurogrid project: an effort to emulate a million neurons. That is only a tiny chunk of the 86 billion neurons in the human brain, but enough to model several of the densely interconnected columns of neurons thought to form the computational units of the human cortex. Neuroscientists can program Neurogrid to emulate almost any model of the cortex, says Boahen. They can then watch their model run at the same speed as the brain — hundreds to thousands of times faster than a conventional digital simulation. Graduate students and researchers have used it to test theoretical models of neural function for processes such as working

memory, decision-making and visual attention.

"In terms of real efficiency, in terms of fidelity to the brain's neuronal networks, Kwabena's Neurogrid is well in advance of other large-scale neuromorphic systems," says Rodney Douglas, co-founder of the INI and co-developer of the silicon neuron.

But no system is perfect, as Boahen himself is quick to point out. One of Neurogrid's biggest shortcomings is that its synapses — of which there is an average of 5,000 per neuron — are simplified connections that cannot be modified individually. This means that the system cannot be used to model learning, which occurs in the brain when synapses are modified by experience. Given the limited space available on the chip, squeezing in the complex circuitry needed to make each synapse behave in a more realistic manner would require circuit elements about a thousand times smaller in area than they are at present — in the realm of nanotechnology. This is currently impossible, although a newly developed class of nanometre-scale memory devices called 'memristors' could someday solve the problem.

Another issue stems from inevitable variations in the fabrication process, which mean that every neuromorphic chip performs slightly differently. "The variability is still much less than what is observed in the brain," says Boahen — but it does mean that programs for Neurogrid have to allow for substantial variations in the silicon neurons' firing rates.

This issue has led some researchers to abandon Mead's original idea of using sub-threshold chips. Instead, they are using more conventional digital systems that are still neuromorphic in the sense that they mimic the electrical behaviour of individual neurons, but are more predictable and much easier to program — at the cost of using more power.

A leading example is the SpiNNaker Project,

BIOLOGICAL INSPIRATION

Neuromorphic technology is based on neurons and neural circuits in the brain. Like the brain, it uses much less power than standard computer chips.

Synapses

Each neuron has about 10,000 of these tiny junctions, which receive signals in the form of voltage spikes coming in from other neurons.

Neuron cell body

In both real neurons and neuromorphic versions, voltages and currents vary smoothly rather than jump in digital fashion from one discrete value to another.

Axon

This fibre, which can be up to 1 metre long, transmits the voltage spikes to other neurons.

Connections

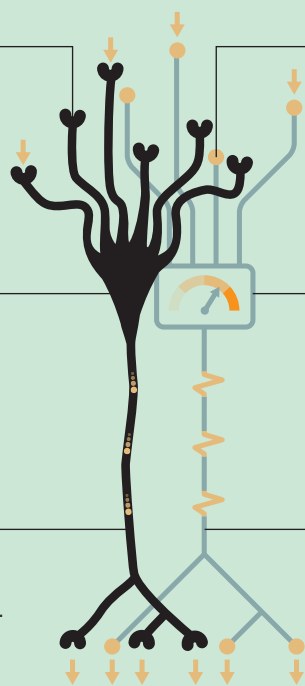
Each emulated neuron receives signals through several thousand of these links, which are often much simpler than biological synapses.

Emulated neuron

Both real and emulated neurons add up, or integrate, incoming signals until they pass a threshold and 'fire', producing an outgoing series of voltage spikes.

Wire

This mimics the axon, and carries the voltage spikes to other emulated neurons.



led since 2005 by computer engineer Steve Furber at the University of Manchester, UK. This system uses a version of the very-low-power digital chips — which Furber helped to develop — that are found in many smartphones. SpiNNaker can currently emulate up to 5 million neurons. These neurons are simpler than those in Neurogrid and burn more power, says Furber, but the system's purpose is similar: "running large-scale brain models in biological real time".

Another effort sticks with neuron-like chips, but boosts their speed. Neurogrid's neurons operate at exactly the same rate as real ones. But the European BrainScaleS project, headed by former accelerator-physicist Karlheinz Meier at Heidelberg University in Germany, is developing a neuromorphic system that currently emulates 400,000 neurons running up to 10,000 times faster than real time. This means it consumes about 10,000 times more energy than equivalent processes in the brain. But the speed is a boon for some neuroscience researchers. "We can simulate a day of neural activity in 10 seconds," Meier says.

Furber and Meier now have the money to push for bigger and better. Together they constitute the neuromorphic arm of the European Union's ten-year, €1-billion (US\$1.3-billion) Human Brain Project, which was officially launched last month. The roughly €100 million devoted to neuromorphic research will allow Furber's group to scale up his system to 500 million digital neurons; Meier's group, meanwhile, is aiming for 4 million.

The success of these research-oriented projects has helped to stoke interest in the idea of using neuromorphic hardware for practical, ultra-low-power applications in devices from phones to robots. Until recently, that hadn't been a priority in the computer industry. Chip designers could usually minimize energy consumption by simplifying circuit design, or splitting computations over multiple processor 'cores' that can run in parallel or shut down when they are not needed.

But these approaches can only achieve so much. Since 2008, the US Defense Advanced Research Projects Agency has spent more than \$100 million on its SyNAPSE project to develop compact, low-power neuromorphic technology. One of the project's main contractors, the cognitive computing group at IBM's research centre in Almaden, California, has used its share of the money to develop digital, 256-neuron chips that can be used as building blocks for larger-scale systems.

BRAIN POWER

Boahen is pursuing his own approach to practical applications — most notably in an as-yet-unnamed initiative he started in April. The project is based on Spaun: a design for a computer model of the brain that includes the parts responsible for vision, movement and decision-making. Spaun relies on a programming language for neural circuitry developed a decade ago by Chris Eliasmith, a theoretical neuroscientist at the University of Waterloo in Ontario, Canada. A user just has to specify

a desired neural function — the generation of instructions to move an arm, for example — and Eliasmith's system will automatically design a network of spiking neurons to carry out that function.

To see if it would work, Eliasmith and his colleagues simulated Spaun on a conventional computer. They showed that, with 2.5 million simulated neurons plus a simulated retina and hand, it could copy handwritten digits, recall the items in a list, work out the next number in a given sequence and carry out several other cognitive tasks⁵. That's an unprecedented range of abilities by neural simulation standards, says Boahen. But the Spaun simulation ran about 9,000 times slower than real time, taking 2.5 hours to simulate 1 second of behaviour.

Boahen contacted Eliasmith with the obvious proposition: build a physical version of Spaun using real-time neuromorphic hardware. "I got very excited," says Eliasmith, for whom the match seemed perfect. "You've got the peanut butter, we've got the chocolate!"

With funding from the US Office of Naval Research, Boahen and Eliasmith have put together a team that plans to build a small-scale prototype in three years and a full-scale system in five. For sensory input they will use neuromorphic retinas and cochleas developed at the INI, says Boahen. For output, they have a robotic arm. But the cognitive hardware will be built from scratch. "This is not a new Neurogrid, but a whole new architecture," he says. It will trade a certain amount of realism for practicality, relying on "very simple, very efficient neurons so that we can scale to the millions".

The system is explicitly designed for real-world applications. On a five-year timescale, says Boahen, "we envision building fully autonomous robots that interact with their environments in a meaningful way, and operate in real-time while [their brains] consume as much electricity as a cell phone". Such devices would be much more flexible and adaptive than today's autonomous robots, and would consume considerably less power.

In the longer term, Boahen adds, the project could pave the way for compact, low-power processors in any computer system, not just robotics. If researchers really have managed to capture the essential ingredients that make the brain so efficient, compact and robust, then it could be the salvation of an industry about to run into a wall as chips get ever smaller.

"But we won't know for sure," Boahen says, "until we try." ■

M. Mitchell Waldrop is a features editor for *Nature* based in Washington DC.

1. Mead, C. *Analog VLSI and Neural Systems* (Addison-Wesley, 1989).
2. Mead, C. *Proc. IEEE* **78**, 1629–1636 (1990).
3. Mahowald, M. & Douglas, R. *Nature* **354**, 515–518 (1991).
4. Mahowald, M. A. & Mead, C. *Sci. Am.* **264**, 76–82 (May 1991).
5. Eliasmith, C. et al. *Science* **338**, 1202–1205 (2012).

BRAIN STORM

Barack Obama announced his BRAIN Initiative on 2 April. Ever since, neuroscientists have been scrambling to work out what it actually is.

BY HELEN SHEN

A mixture of excitement, hope and anxiety made for an electric atmosphere in the crowded hotel ballroom. On a Monday morning in early May, neuroscientists, physicists and engineers packed the room in Arlington, Virginia, to its 150-person capacity, while hundreds more followed by webcast.

Only a month earlier, US President Barack Obama had unveiled the neuroscience equivalent of a Moon shot: a far-reaching programme that could rival Europe's 10-year, €1-billion (US\$1.3-billion) Human Brain Project (see page 5). The US Brain Research Through Advancing Innovative Neurotechnologies (BRAIN) Initiative would develop a host of tools to study brain activity, the president promised, and lead to huge breakthroughs in understanding the mind.

But Obama's vague announcement on 2 April had left out key details, such as what the initiative's specific goals would be and how it would be implemented. So at their first opportunity — a workshop convened on 6 May by the National Science Foundation (NSF) and the Kavli Foundation of Oxnard, California — researchers from across the neuroscience spectrum swarmed to fill in the blanks and advocate for their favourite causes.

The result was chaotic, acknowledges Van Wedeen, a neurobiologist at Harvard Medical School in Boston, Massachusetts, and one of the workshop's organizers. Everyone was afraid of being left out of 'the next big thing' in neuroscience — even though no one knew exactly what that might be. "The belief is we're ready for a leap forward," says Wedeen. "Which leap, and in which direction, is still being debated."

Others describe the BRAIN Initiative as a Rorschach test — an indeterminate entity that invited each researcher to project his or her own hopes and insecurities. But as the initiative has evolved, it has also come to resemble a large-scale sociological experiment, as the sprawling neuroscience community struggles to coalesce around a common research plan under intense public scrutiny and tough financial constraints.

A BIG PICTURE

To the public, Obama's announcement seemed to come from nowhere; the president had never focused much on neuroscience before. In fact, the idea behind it had been spawned some 18 months earlier and almost 6,000 kilometres from the White House. At a meeting in Chicheley, UK, a group of neuroscientists and nanoscientists invited by the Kavli Foundation had developed their vision for the future of neuroscience research: to record electrical

impulses from thousands, or even millions, of neurons at once.

That is the only way in which we might understand how thought emerges from the brain, argues Rafael Yuste, a neuroscientist at

Columbia University in New York City who spearheaded the idea. Current technology can make recordings from only single neurons or small groups of neurons at a time — which, he says, "is like trying to watch a movie on TV by looking at one pixel".

To do better, the architects of the Kavli plan called for a Brain Activity Map (BAM) project: a technology-development programme that would give researchers the tools to start small,

produce detailed maps of neural activity in simple organisms such as the fruitfly, and then move on to larger, more complex mammalian systems such as the mouse retina. They predicted that, within 15 years, BAM would be able to simultaneously record all of the activity in a mouse cortex — and that primates, and even humans, would be next.

BAM was intended to be provocative. "This is not going to happen if we keep waiting on little labs to do little things," declares Yuste. But, for many outsiders, it was ill-conceived — "a complete work of science fiction", says Markus Meister, a neurobiologist at the California Institute of Technology in Pasadena. Critics argued that the effort would take too long, cost too much and, ultimately, run up against the laws of physics, which limit how densely electrodes can be packed inside the brain. Moreover, creating a full activity map covering an organism's entire lifetime could yield a cripplingly large data set, while distracting from what many saw as the real problem: a dearth of computational and theoretical methods with which to interpret the brain's activity. "We just don't understand the data we have," says Mehrdad Jazayeri, a neuroscientist at the Massachusetts Institute of Technology in Cambridge.

But BAM caught the attention of administrators at the White House, who were on the lookout for a bold presidential initiative (see *Nature* **495**, 19; 2013). The first hint of the administration's interest appeared in the president's State of the Union address on 12 February. Few neuroscientists appreciated the significance until five days later, when they were jolted awake by an article on the front page of *The New York Times*, which reported that the White House planned to unveil a ten-year neuroscience initiative

Some describe the initiative as a Rorschach test, inviting each researcher to project his or her own hopes and insecurities.



NEW ANGLES ON THE BRAIN
A *Nature* special issue
www.nature.com/neuroscience2013



by four private institutions, which had committed to a total of \$122 million over varying lengths of time (see 'Obama's BRAIN').

Thus the crush at the NSF's May workshop: after weeks of uncertainty, researchers were hungry for a chance to weigh in. Participants were asked to submit one-page proposals describing a major obstacle to understanding the brain. Then, in a frenetic pitch-fest, authors took the floor for one minute each to argue their cases.

"What I care most about is reconstructing circuits accurately and fast," declared the first speaker, Albert Cardona. A neuroscientist at the Janelia Farm Research Campus near Ashburn, Virginia, he pushed for improved automated techniques to map the brain's anatomy on a super-fine scale. Others called for equally fine-grained recordings from ever-larger numbers of neurons, in the spirit of BAM. Still others championed their favourite model organisms. And some speakers emphasized the importance of big-data storage, as well as the computational and theoretical advances required to make sense of all that information.

BLURRED VISION

To the growing exasperation of audience members, however, there was no convergence towards a coherent agenda for the initiative. No one could even say whether the initiative would be funded with new cash outlays or with money diverted from existing research. By the meeting's end, the hotel lobby had become crowded with restless attendees who had abandoned the talks to check e-mails, make phone calls and run their labs from afar.

Among those who did stay were members of the NIH's BRAIN Initiative advisory committee, a 15-member panel dubbed the 'dream team' — a nickname it has since tried, unsuccessfully, to shake off. Co-chaired by neuroscientists Cornelia Bargmann at the Rockefeller University in New York City and William Newsome of Stanford University in California, the panel's first task was to prepare an interim report outlining the NIH's science goals for the project's first year. Then, once that report had been delivered to the NIH in September, the team would start to develop a long-term implementation plan, due in June 2014.

Shortly after the NSF meeting, the NIH team started on its first order of business: convening a series of four workshops to gather input from the neuroscience community. These covered molecular techniques; large-scale recording technologies; computational and theoretical neuroscience; and human brain studies. The difference in tone was striking. The NSF event had been like a cacophonous town hall meeting, whereas the NIH workshops felt more like an honorary lecture series. Each one began with public presentations by a dozen or so invited speakers, and the proceedings were carefully controlled. Once the open session

based on the Kavli idea. The article suggested that the initiative might receive federal funding on par with the \$3.8 billion spent on the Human Genome Project, and would produce a comprehensive, detailed map of neural activity in the human brain within a decade.

The news alarmed many neuroscientists, who worried that few of them had been consulted, that the money would be made available at the expense of existing programmes and that failure to meet a seemingly impossible goal would undermine public trust in science. "This was a very narrow agenda of a small group of people," recalls Partha Mitra, a neuroscientist at Cold Spring Harbor Laboratory in New York and a vocal critic of BAM.

But the administration was already taking a different tack. By the time of the official announcement on 2 April, the project had been rebranded the BRAIN Initiative and carried a comparatively modest price tag: only \$110 million in federal funding for the 2014 fiscal year. It no longer had a specific lifetime

— although the White House implied that the project could last ten years or longer.

And, unlike BAM, it had no clearly defined goal. Rather than promising to record from any particular number of neurons at once, Obama said simply that new tools were needed to help neuroscientists to develop better pictures of brain circuits in action — and that such technologies could pave the way to treatments for neurological disorders such as epilepsy, autism, Alzheimer's disease and schizophrenia (see *Nature* **499**, 272–274; 2013).

Many neuroscientists found the announcement reassuring — at least the BRAIN Initiative wasn't BAM — but puzzlingly vague. All they knew was that the details would be left up to three government agencies: the Defense Advanced Research Projects Agency (DARPA), which would contribute \$50 million in the first year; the National Institutes of Health (NIH), which would pitch in \$40 million; and the NSF, which would add \$20 million. The initiative would be further supported

OBAMA'S BRAIN

The White House has set lofty objectives for its BRAIN Initiative. Now it is up to the participants (purple) to develop a strategy for the programme.

PRIVATE RESEARCH

- The Allen Institute for Brain Science
\$60 million annually
- Howard Hughes Medical Institute
\$30 million annually
- Kavli Foundation
\$4 million annually for 10 years
- Salk Institute for Biological Studies
\$28 million

FEDERAL AGENCIES

(First year funding)

- Defense Advanced Research Projects Agency
\$50 million
- National Institutes of Health
\$40 million
- National Science Foundation
\$20 million

was over, all of the speakers disappeared into closed discussions with the dream team. One participant likened that experience to being a delegate to the United Nations, with everyone seated around a long oval table behind printed name cards.

Bargmann says that privacy was necessary to allow scientists to speak freely — and sometimes critically — about different experimental approaches. But, in the wider neuroscience community, many felt the selection of invited speakers and topics excluded their interests. The dream team weathered criticism from molecular, cellular and developmental neuroscientists who felt underrepresented, as well as from clinical neuroscientists concerned that there was not enough emphasis on disease research.

Adding to researchers' anxiety was the fact that no one knew whether they would have any involvement in the arms of the project being run by the two other federal agencies. The deputy director of DARPA's defence science office, Geoffrey Ling, said in June that his agency would not be releasing any road maps for its BRAIN Initiative efforts; meanwhile, the NSF's lead on the project, biological sciences chief John Wingfield, said in September that the agency intended to wait for the NIH report before issuing its own plan, to avoid duplication. "There are limits to what we can do," he said, contrasting his agency's roughly \$150-million annual expenditure on neuroscience with the NIH's \$5.5-billion budget.

Meanwhile, almost everyone was worried about where the funding would come from — especially as it became clear that Congress would not set aside any new money for the BRAIN Initiative's first year. A modicum of

OBJECTIVES

- Provide the knowledge for addressing debilitating disorders.
- Develop new imaging technologies and understand how information is stored and processed in neural networks.
- Understand how brain activity leads to perception, decision-making and, ultimately, action.
- Produce a sophisticated understanding of the brain, from individual genes to neuronal circuits to behaviour.

RESEARCH COMMUNITY

- The National Science Foundation convened workshops to solicit ideas.
- The National Institutes of Health set up a 'dream team' of 15 scientists that is producing reports based on community feedback.

new funding should be forthcoming from the NIH: of the \$40 million it agreed to commit, \$10 million will come from the director's discretionary funds. Officials at the NIH and NSF maintained that the initiative would not derail existing programmes. But the dearth of dedicated new funds meant that the three federal agencies would have to begin, at least in part, by packaging together some ongoing projects. The initiative's private partners, likewise, will mostly stick with existing programmes. The Salk Institute for Biological Studies in La Jolla, California, the Allen Institute for Brain Science in Seattle, Washington, and the Howard Hughes Medical Institute in Chevy Chase, Maryland, were all eager to frame the BRAIN Initiative as a continuation of research they already had under way.

SOMETHING FOR EVERYONE

By early September, with the private partners determined to do their own thing and two of the three federal agencies all but silent, interest in the NIH report had reached fever pitch: researchers saw it as the de facto national agenda. On 16 September, the advisory committee at last published its interim report on science priorities. Many had feared that it would fail to be sufficiently inclusive, but the document was instead so staggeringly broad that it seemed to encompass all of circuit-based neuroscience. Cataloguing every cell type in the brain, mapping those cells' full anatomical connections, monitoring and manipulating their signals, modelling and simulation — there was something for everyone. "It would be hard to disagree with this report," said Mitra. "It's written, perhaps, with critics in mind."

NIH director Francis Collins tacitly conceded the report's vastness when he formally accepted it. "These areas of research are expansive, and undoubtedly cover more research than NIH can fund with \$40 million in one year," he said; the more ambitious elements could shape funding requests in years to come. And not just a few years, adds Yuste. "This is something you need 15 years and \$3 billion to do."

Tough choices lie ahead as the committee starts work on the long-term report it must deliver next June. The team will need to rank research priorities as short-, medium- and long-term goals, set timelines, estimate costs and define specific deliverable outcomes for the next few years — altogether a daunting task, says Newsome.

"It's much easier to see a year into the future than ten years into the future," agrees Bargmann.

Already, members of the working group are butting heads over questions such as whether ultra-detailed anatomical maps of the brain — painstakingly obtained with electron microscopy (see page 147) — should take priority over lower-resolution maps that can be completed much more quickly using light microscopy.

And then there is the question of management. Although the three government agencies have kept each other informed of their plans, the White House has so far indicated no intention to coordinate the process more formally. This worries researchers such as Yuste, who is urging the creation of 'brain observatories': multi-agency facilities that, like particle accelerators or giant telescopes, could provide community access to technology too large, costly or specialized for individual labs to maintain. Without higher-level planning, he warns, such efforts will be impossible, and the BRAIN Initiative's investment could end up being squandered on many small grants awarded by the individual agencies. "The whole effort will not be more than the sum of its parts," he warns.

But others, including Bargmann, argue against throwing limited resources behind a monolithic, centralized project. "This is not the time to pick one approach and say this is the right approach," she says. Instead, she hopes to foster the strongest and most creative ideas from individuals and groups of researchers — and see where they lead.

The NIH advisory committee hopes to draw on the creativity of the wider neuroscience community at the upcoming annual meeting of the Society for Neuroscience. On 11 November, hundreds of neuroscientists are expected to pile into room 33C at the San Diego Convention Center in California to weigh in on the NIH's interim recommendations. Armed with only a slightly more defined vision than they had six months ago, they will continue to try to define what the BRAIN Initiative can and should mean for their future. ■

Helen Shen is a reporter for Nature.

SOURCE: THE WHITE HOUSE

COMMENT



NEUROSCIENCE Network studies are needed to understand Alzheimer's **p.31**

EVOLUTION Three books explore what it means to be human **p.34**

PRODUCTIVITY Scientific output of former Soviet states compared **p.39**

OBITUARY Harold Melvin Agnew, Manhattan Project veteran, remembered **p.40**

ILLUSTRATION BY RICHARD WILKINSON



My life with Parkinson's

A neuroscientist reflects on his experience of studying the circuits that control neural activity while his own brain began slowly failing him.

Roughly a year ago, I found myself at an elegant dinner party filled with celebrities and the very wealthy. I am a young professor at a major research university, and my wife and I were invited to mingle and chat with donors to the institution. To any outside observer, my career was ascendant. Having worked intensely and passionately at science for my entire adult life, I had secured my dream job directing an independent neuroscience research laboratory.

I was talking to a businessman who had family members affected by a serious medical condition. He turned to me and said: "You're a neuroscientist. What do you know about Parkinson's disease?"

My gaze darted to catch the eyes of my wife, but she was involved in another conversation. I was on my own, and I paused to gather my thoughts before responding. Because I had a secret.

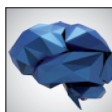
It was a secret that I hadn't yet told any of my colleagues: I have Parkinson's.

I am still at the beginning of my fascinating, frightening and ultimately life-affirming journey as a brain scientist with a disabling disease of the brain. Already it has given me

a new perspective on my work, it has made me appreciate life and it has allowed me to see myself as someone who can make a difference in ways that I never expected. But it took a bit of time to get here.

THE FIRST SIGNS

I remember the first time I noticed that something was wrong. Four years ago, I was filling out a mountain of order forms for new lab equipment. After a few pages, my hand became a quaking lump of flesh and bone, locked uselessly in a tense rigor. A few days later, I noticed my walk was changing: rather than swinging my arm at my side, I held it in front of me rigidly, even grabbing the ▶



NEW ANGLES ON THE BRAIN
A *Nature* special issue
www.nature.com/neuroscience2013

▶ bottom edge of my shirt. I also had an occasional twitch in the last two fingers of my hand.

I was 36 years old and it was the most terrifying time of my life, even without any of these mysterious symptoms. In the span of six months, I found myself in a job that I had spent 20 years preparing for, I became a father for the second time, I moved across the country to a town where we knew no one, and I was working alone in an empty lab wondering who left me in charge. I study the way that neuromodulatory chemicals such as dopamine affect neural activity and behaviour. And now, my own brain chemistry was rebelling against me.

I considered many possibilities. A brain tumour? Dystonia? Motor neurone disease? Huntington's disease? Multiple sclerosis? Was I just stressed out?

My diagnosis came from a young neurology fellow at one of the world's leading centres for the study of movement disorders. He felt more like a peer than an authority figure. He, too, spent a lot of time in the lab doing basic research and published papers in some of the same journals as me; we could have just as easily run into each other at a scientific meeting. As a result, the experience of my diagnosis was oddly collegial.

Right away, I wondered how long I could get away without telling my colleagues. I worried that I would be less likely to get the grants I needed to run my lab if the reviewers were not confident about investing in my future. I wondered whether students and postdocs would be afraid to join my research group. And, perhaps most importantly, how long I would be able to do experiments — the thing that I most love. Stiffness, shaking, fatigue, jerky movements, falls, drooling, laboured speech and the expressionless Parkinsonian mask. These could all be a part of my future.

MIND MATTERS

I was diagnosed with Parkinson's more than two years ago. From that day, I have had a different relationship with the brain — my scientific focus for the past 20 years. I now know what it is like to have a brain disorder and can explore its manifestations first hand. Take the very peculiar symptom known as 'freezing'. Occasionally, when I attempt to lift my hand it well... won't. Notice that I didn't say can't. There is nothing wrong with my arm. It is still strong and capable of moving, but I have to put effort, even focus, into getting it to move — frequently to such a degree that I have to pause whatever else my brain is doing (including talking or thinking). Sometimes, when no one else is around, I use my other hand to move it.

As a neuroscientist, it is simultaneously fascinating and terrifying to be directly confronted with the intersection of the neurophysiological and philosophical constructs

of 'will'. The way my mind and body do battle forces me to reconsider the homunculus, a typically pejorative (among neuroscientists) caricature of a little man pulling levers inside our heads, reading the input and dispatching the output. Virtually all that we know about how the brain is organized belies this image, and yet there is a dualism to my daily experience.

Parkinson's, particularly in young people, is primarily a disorder of motor control, not of cognition. Still, my experience, however limited, leads me to speculate about what it is like to be trapped by a brain gone rogue. When one begins to lose the ability to interact with the world, and when one's faculties for clear perception and cognition are stripped away, what remains of the conscious self?

This brings me to one of the main reasons that I have kept my disease secret: the stigma of 'mental illness'. Because most people do not understand Parkinson's, it may be confused with cognitive disorders such as schizophrenia and Alzheimer's disease. I feel as sharp and productive as ever, but I wasn't sure that others would have faith in me at a time when my career is so fragile. So nearly every moment of my life became a performance, in which I tried to hide my symptoms. At work, at the grocery store, in my front yard, even in front of my kids — I am always keenly aware of my movements. And nowhere more so than at scientific conferences, such as at meetings of the Society for Neuroscience (SfN). You may not notice where my hands are, but I do. Often, I am sitting on them.

Does Parkinson's affect the way I do science? It does affect the day-to-day mechanics of experiments for me. The techniques used in my lab require considerable motor skill at times. I have had to modify how I do some things, including taking more time, compensating with my good hand or using a different grip on instruments. Still, it is pretty remarkable how capable I remain at the bench. The lesson in this for me is that 'lab hands' are more about experience, attention to detail and adaptation of methods than they are about raw dexterity. And the low-to-moderate doses of drugs that I take really help, as do sleep and exercise. By all indications, I will be able to continue research for many years, perhaps even indefinitely.

There is also the question of how this diagnosis affects my scientific direction. I am sometimes asked whether I will wholly or partly switch to studying Parkinson's disease. I suppose I might if the right project came along, but in general I remain focused on the questions that I have already set out for myself. I am also sometimes asked

whether my diagnosis makes me impatient with the pace of discovery of cures. Here my answer is very clear. The dual perspectives of my condition and my position as an active researcher actually reinforce my belief in the importance of discovery science. I am keenly aware that those cures are possible only in the wake of decades of basic research. Above all, my diagnosis makes me want to do the best and most exciting science I can, because the privilege could disappear for any of us in the blink of an eye.

TO TELL OR NOT TO TELL

Back at the dinner party, all eyes were on me waiting to hear my thoughts on Parkinson's. I wanted to tell my colleagues what I was going through. I wanted to look at our donor and say: "Funny you should ask that. Not only am I a neuroscientist, but I also have Parkinson's disease." I wanted to launch into an eloquent monologue that put a personal face on the science of neurodegenerative disease. I wanted to conclude by saying, "And that is why basic brain research is so important."

But I didn't.

Instead, I dispassionately described the pathology and characteristic symptoms of Parkinson's. It was an intellectually engaging exchange, but it wasn't the conversation it could have been. This is one of the main reasons I decided to stop hiding.

Earlier this year, I told my department chair. Over the next few days, I told the administration, my lab and many of my colleagues. It took a lot out of me, but it ended up being one of the best decisions I ever made. Everyone at work was so supportive — I felt silly for having spent four years, since the onset of my symptoms, worrying about how they would react. In the subsequent months, it has become a non-issue for me in how I interact at work. Everyone treats me like any other colleague, and it is such a relief not to worry about who knows anymore. It is still uncommon for me to tell someone new, but I do not do anything to hide my condition, just enough to not call attention to it. For anyone reading this who is going through something similar, I am here to tell you that life is too short to run from who you are. Your colleagues might surprise you, and you can still be a great scientist despite a disability.

So why am I writing this piece anonymously? Because I don't want to be known to the scientific community as 'Parkinson's guy' before I am known as a scientist. That said, I'm not hiding any more, so if you care you can dig enough to find out who I am. I'm okay with that. ■

The author is a neuroscience professor at a major US university. He blogs at parklifensci.blogspot.com and tweets at [@Parklifensci](https://twitter.com/Parklifensci). e-mail: parklifensci@gmail.com



Study neuron networks to tackle Alzheimer's

Researchers have generally looked for signs of Alzheimer's disease in the whole brain or at the single-gene level. The biggest clues will come from monitoring collections of neurons, says **Kenneth S. Kosik**.

Twenty years of research and more than US\$1-billion worth of clinical trials have failed to yield an effective drug treatment for Alzheimer's disease. Most neuroscientists, clinicians and drug developers now agree that people at risk of the condition will probably need to receive medication before the onset of any cognitive symptoms. Yet a major stumbling block for early intervention is the absence of tools that can reveal the first expression of the insidious disease.

So far, researchers have tended to focus on macroscopic changes associated with the disease, such as the build up of insoluble plaques of protein in certain areas of the brain, or on individual genes or molecular pathways that seem to be involved in disease progression.

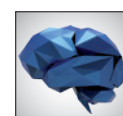
I contend that detecting the first disruptions to brain circuitry, and tracking the anatomical and physiological damage underlying the steady cognitive decline that is symptomatic of Alzheimer's, will require tools that operate at the 'mesoscopic' scale: techniques that probe the activity of thousands or millions of networked neurons. Although such tools are yet to be realized, several existing technologies indicate that they are within reach.

CHARTED TERRITORY

All the current approaches that are used to diagnose Alzheimer's are crude and unreliable. Take the classic biomarkers of the disease: a build up of plaques of the protein β -amyloid in a person's cerebral cortex, for instance, or elevated levels of the tau protein and dampened levels of β -amyloid in their cerebrospinal fluid. Although such markers are predictive of the disease, the interval between their appearance and the onset of cognitive problems is hugely variable, ranging from months to decades.

Frequently, people with a high density of plaques or an ominous cerebrospinal fluid reading show no signs of dementia in behavioural tests. Others show the classic symptoms of the disease, such as memory loss, confusion and inability to formulate a simple plan.

More consistently linked to cognitive difficulties are neurofibrillary tangles — aggregates of tau protein commonly found in the hippocampus and amygdala (the parts of the brain involved in memory and emotion) of people with Alzheimer's, and in the cerebral cortex. Yet even this correlation is imperfect. And unlike for amyloid plaques, which can be monitored using a scanning technique known as positron



NEW ANGLES ON THE BRAIN

A *Nature* special issue

www.nature.com/neuroscience2013

emission tomography (PET), no imaging procedure is yet available to detect tangles in living people.

So although all these markers can be harbingers of disease, none of them captures the subtle disruptions to brain circuitry that mark the onset of cognitive decline or enable researchers to track disease progression from week to week and month to month. Nor do they reveal anything about the even shorter-term fluctuations in cognitive capacity frequently observed in people with Alzheimer's. Relatives and carers often report, for instance, that for brief periods, a person with Alzheimer's might behave normally and be able to engage in conversation, and then an hour later be unable to remember what just transpired.

Aside from biomarkers, clinicians use reams of neuropsychological tests to diagnose Alzheimer's disease. These test a person's memory, emotional responses, language skills, and ability to solve problems or count. However, such tests fail to capture the subtleties of the cognitive deficits at every stage of the disease. For example, asking someone to recall a recently viewed list of items will not reveal how well they are able to pull together memory fragments to make appropriate decisions and predictions. Similarly, being able to join up sequentially numbered dots (a standard test of executive function) is a far cry from mentally mapping out the steps needed to achieve some purpose in daily life, such as food shopping.

IMAGING ISSUES

One of the various types of brain imaging commonly used to probe and diagnose Alzheimer's is functional magnetic resonance imaging (fMRI). This tracks changes to blood oxygenation in the brain while a person is resting or doing certain cognitive tasks. The aim is to reveal faulty wiring or differences in regional brain activity from what is usually observed. However, standard fMRI is limited to scanning the 86 billion human brain neurons and several thousand times more synapses with fewer than 20,000 voxels (volumetric pixels). With this technique, each voxel corresponds to an arbitrary volume of tissue rather than to a specific brain network that mediates cognitive processes. PET, which assesses blood flow and metabolism, as well as the location and density of amyloid plaques, has an even lower spatial resolution.

Furthermore, the current tools used to diagnose Alzheimer's disease and track its progression do not account for innate or acquired individual differences in brain structure that can drastically alter people's tolerance of brain pathology.

Numerous studies have suggested, for instance, that education and higher intellectual achievement, such as greater proficiency

in languages, writing and speaking, can protect people from clinical Alzheimer's disease (with which people show severe cognitive deficits in behavioural tests). For example, a long-running study of nuns, which began in 1986, found that those diagnosed with the disease through post-mortem examinations had, decades before their death, displayed inferior language skills in application letters sent to convents compared with those without the disease¹. This may help to explain why people with similar amyloid burdens in their cerebral cortex can show such dramatic differences in cognitive performance². It also highlights why researchers should avoid evaluating the efficacy of a drug on its ability to break down amyloid plaques alone.

UNCHARTED TERRITORY

Several lines of evidence suggest that networks of neurons in the brain operate as local processing units, with few long-range connections between them — an organizational pattern known as small world³. This evidence includes partial wiring diagrams of the fly and mammalian brain obtained from anatomical tracings, circuit physiology and by reconstructing nanometre-thick slices of brain tissue. Optical-imaging techniques used to track neural activity across the entire brain in organisms such as zebrafish larvae also support this idea⁴.

I believe that tools to analyse how neuron networks operate in the human brain will be crucial to probing the changes to brain circuitry underlying cognitive impairment in Alzheimer's disease. One possibility is using minimally invasive 'nanosensors' that can travel to the brain through blood vessels and communicate neural activity⁵. Diamond-based materials are currently being developed to track the movements of single electrons across nerve membranes.

Even now, several techniques could offer preliminary insights about the collective workings of different regions of the human brain. For example, particularly powerful MRI systems can scan the entire living human brain at a resolution of about 0.7 cubic millimetres (most are limited to 1-mm³ resolution)⁶.

Meanwhile, researchers have used another imaging technique known as magnetoencephalography (MEG) — which maps neural activity by recording the magnetic fields produced by electrical currents in the brain — to predict the development of preclinical Alzheimer's disease, known as mild cognitive impairment, in 5 out of 15 people⁷. People with this condition

experience difficulties that are noticeable to them and to others but that are not severe enough to interfere with daily life. MEG has a poorer spatial resolution than MRI, but records responses in milliseconds rather than in seconds or minutes, capturing more of the numerous intermediary cognitive steps involved in mediating a person's response to a picture, word or task.

Likewise, molecular analyses could shed light on brain activity at the mesoscopic scale. Sequencing the RNA molecules expressed in different regions of the brain, in tissues taken from people who have died, has revealed co-regulated networks of genes associated with late-onset Alzheimer's⁸. Of enormous value would be detailed maps showing the genes expressed, where they are expressed and how they relate to neural networks — as have been obtained for the sea urchin⁹.

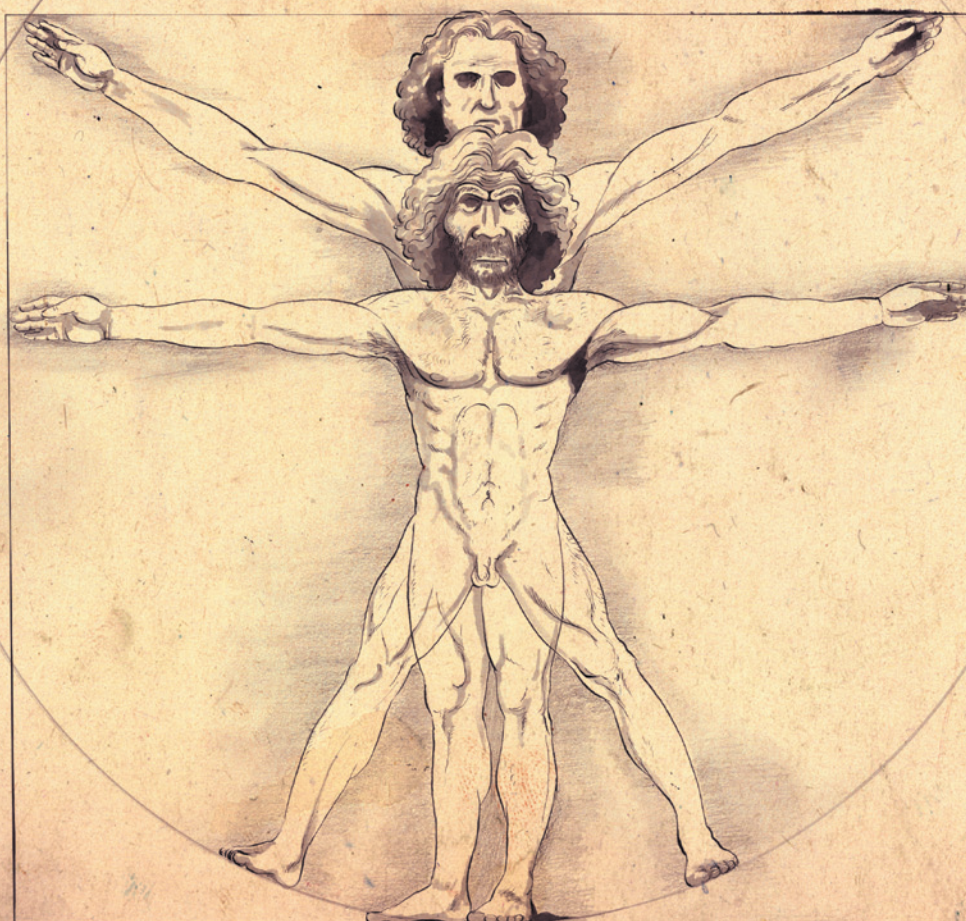
LOOKING AHEAD

Such mesoscopic-scale analyses are precisely what the US BRAIN (Brain Research through Advancing Innovative Neurotechnologies) Initiative is about. Announced by US President Barack Obama in April, the aim of this project is to map and monitor the neural connections in the entire brains of experimental animals, and ultimately in the human cerebral cortex.

Several influential neuroscientists have questioned whether an understanding of consciousness, perception, imagination, emotion and abstraction will emerge from measuring brain activity at the mesoscopic scale. I am similarly sceptical of such lofty claims. Yet I applaud the BRAIN Initiative for its potential to advance Alzheimer's disease research. Monitoring neuron networks is exactly what neuroscientists need to better understand, and ultimately to treat, a disease that is now costing the United States alone upwards of \$200 billion every year. ■

Kenneth S. Kosik is at the Neuroscience Research Institute, and professor in the Department of Cellular, Molecular and Developmental Biology at the University of California, Santa Barbara, California 93106, USA.
e-mail: kenneth.kosik@lifesci.ucsb.edu

1. Iacono, D. et al. *Neurology* **73**, 665–673 (2009).
2. Rowe, C. C. et al. *Neurobiol. Aging* **31**, 1275–1283 (2010).
3. Bullmore, E. & Sporns, O. *Nature Rev. Neurosci.* **13**, 336–349 (2012).
4. Ahrens, M. B. et al. *Nature* **485**, 471–477 (2012).
5. Seo, D., Carmenta, J. M., Rabaey, J. M., Alon, E. & Maharbiz, M. M. Preprint available at <http://arxiv.org/abs/1307.2196> (2013).
6. van Rooden, S. et al. *Alzheimers Dement.* <http://dx.doi.org/10.1016/j.jalz.2013.02.002> (2013).
7. Zamrini, E. et al. *Int. J. Alzheimers Dis.* **2011**, 280289 (2011).
8. Lambert, J.-C. et al. *Nature Genet.* <http://dx.doi.org/10.1038/ng.2802> (2013).
9. Peter, I. S., Faure, E. & Davidson, E. H. *Proc. Natl Acad. Sci. USA* **109**, 16434–16442 (2012).



Phil Disley 2013

ILLUSTRATIONS BY PHIL DISLEY

HUMAN EVOLUTION

Us and them

Tim Radford contemplates three fascinating studies on what it means to be human.

“The proper study of mankind is man”, sang the poet Alexander Pope. Of course, he knew nothing about tool-using chimpanzees, language-manipulating gorillas, self-recognizing orang-utans or problem-solving New Caledonian crows. Nor had he heard of extinct hominins, hunter-gatherer energy budgets, Palaeolithic artefacts, the significance of sweat glands or the evolutionary rewards of cooking, bipedalism and long-distance running.

Still, when he wrote in his 1732 *Essay on Man* about a being “placed on this isthmus of a middle state, a being darkly wise, and rudely great”, he demonstrated what Thomas Suddendorf, author of *The Gap*, calls the “two foundational capacities” (think of

The Gap: The Science of What Separates Us from Other Animals

THOMAS SUDDENDORF

Basic Books: 2013.

The Story of the Human Body: Evolution, Health and Disease

DANIEL E. LIEBERMAN

Pantheon: 2013.

The Accidental Species: Misunderstandings of Human Evolution

HENRY GEE

University of Chicago Press: 2013.

them as legs) that help us to stride the divide between ape and human minds. Humans share the capacity to compose scenarios and nest them within each other, and the

urge to communicate. Other social animals co-operate, deliver alarm calls and trade information. But none seems to match the human drive to link minds, to travel mentally in time, to tell stories, stir emotions, ask questions, compose poems or write books about what it means to be human.

This certainly looks to be the reason why *Homo sapiens* now constitutes eight times the biomass of all other wild terrestrial vertebrates combined. And it also sheds light on why one species, initially formed by the blind forces of natural selection acting upon random mutation, might be about to step

NATURE.COM

See *Nature's* essay series on being human at:

go.nature.com/kkdmk9

off the evolutionary treadmill altogether, and take control of its own future. That three authors — Suddendorf, Henry Gee and Daniel Lieberman — can take the same theme, address the same research and cite the same authorities to deliver three very different, complementary and equally enjoyable books is a measure of the fascination of the topic, complexity of the arguments and the fragility of the evidence so far.

Each author has made a scholarly career in the business of asking how we got here, and each approaches the question from a different perspective. Bipedalism has traditionally been seen as the starting point of humankind's long journey from prey to predator, and from Africa's Rift Valley to world domination. But for the psychologist Suddendorf it is something that can be disposed of in a couple of pages. As he tells us, bipedalism freed the hands to grip and throw, but it came with serious side effects, "including back problems and hemorrhoids".

For Gee, gate-keeper of the palaeontological papers in this journal, bipedalism is just one change among many — one peculiar posture adopted by a group of animals. He notes in *The Accidental Species* that the posture is seen nowhere else, "but one could say the same for knuckle walking in chimps and gorillas, brachiation in gibbons, and the four-handed swing of orangutans".

For the evolutionary biologist and barefoot runner Lieberman, however, bipedalism was a "monumental and consequential" shift. The two-legs-good, four-legs-bad effect is discussed on at least 40 pages of *The Story of the Human Body*; running, too, gets a good show. We are what we are because our bodies could do what they did. The legs of *Homo erectus* were 10–20% longer than those of the hominin *Australopithecus*, which meant the first humans could cover great distances at a lower energy cost. But longer legs make arboreal life difficult, so once humans got moving, they had to stay on the road. Lieberman argues that it is "not just incorrect but also dangerous to view modern human evolution as solely a triumph of brains over brawn". It

was the hunter-gatherer physique that got us to where we are now. And today's burgeoning human ills — obesity, cardiovascular disease, cancer, sleep apnoea, terrible teeth, osteoporosis and so on — occur because we eat more generously than hunter-gatherers but work considerably less.

All three authors mention brain size, but Suddendorf points out that, when it comes to relative brain size, humans don't top the charts. There are mice and shrews in which the brain makes up an extraordinary 10% of overall body weight (the human proportion is 2%). So if brain capacity is what makes the difference, there should be some other scale that puts humans at the top. Suddendorf and Andrew Whiten have proposed one: an excess of absolute brain mass over and above that predicted by body size. Meanwhile, Gee points out that crows demonstrate a kind of calculation and craftiness that humans recognize. Because the common ancestor of birds and primates lived more than 250 million years ago, this "shoots a huge hole" in the idea that modern humans are very clever just because previous hominins were quite clever, and the ones before them only relatively so.

We can't ask the earlier hominins. *H. sapiens* once shared the planet with *H. erectus*, Neanderthals, Denisovans and the little Hobbit of Flores. They have all gone. The last man standing must now compose answers on the basis of only the slight, capricious and often ambiguous evidence that remains. Gee calls this "the Beowulf effect": Old English verse survives mainly in just four manuscripts, and one of them, which includes *Beowulf*, almost perished in a blaze in 1731. What if it had burned, uncopied? What then would we know about the song and story of the past?

Lieberman builds up a picture of vanished society by examining humankind as it is now. He looks at Tanzanian hunter-gatherers and

the Kalahari Bushmen, and works backwards to shape an increasingly speculative story of how things might have been as foraging, scavenging, hunting and resourceful humans colonized even the most inhospitable habitats. Suddendorf is more concerned with the things we can learn from other surviving primates. Yes, apes cooperate, communicate, use tools, share knowledge, solve problems, demonstrate self-awareness and display emotions. But he carefully leaves open the big question: how much can you conclude from each case study? Gee, meanwhile, gazes into both past and future, and sees the idea of evolutionary upward mobility (or as Pope had it, "upward will he soar, and little less than angel, would be more") a profound misreading of Darwin.

Both Suddendorf and Lieberman directly address the question of natural selection in a world in which humans have seemingly taken control of nature, and ensured the survival of the not-so-fit. Puzzlingly, says Suddendorf, "the rich, successful, powerful, beautiful, and well-educated people seem to breed less, not more, than most of the rest of us". But he suspects humans could find more dramatic ways of cutting short their own success story, with a little help from war and famine. Lieberman would have us get up off our chairs, set down our books and chew tough fibrous stuff: our bodies may not be the best of all possible bodies, but they are the only ones we have, and we should look after them.

All three books would make marvellous gifts. *The Gap* is ideal for someone who already has a decent collection about human evolution. *The Story of the Human Body* is a readable introduction to the whole field and great on the making of our physicality. *The Accidental Species* is discursive, rich in good stories and terrible jokes, and a salutary reminder of how little we know. I shall hang on to all three. ■

Tim Radford is a former science editor of *The Guardian* and author of *The Address Book: Our Place in the Scheme of Things*. e-mail: radford.tim@gmail.com

"Each author has made a scholarly career in the business of asking how we got here."



A paved paradise

Mike Davis explores a vision of car-free, socially networked urban environments.

Happy City opens with a joyful adrenaline rush. Charles Montgomery is sweating at the pedals in a mountain-bike dash through the streets of Bogotá with the city's charismatic "Mayor of Happiness", Enrique Peñalosa. "Then he was off," Montgomery marvels, "jumping curbs ... and barking into his cell phone while his pin-striped trousers flapped in the breeze."

The image of hyperkinetic populist Peñalosa — who was mayor from 1998 to 2001 — rushing through barrios and urging his citizens to stop using cars and organize fiestas, may be romanticized. But he did divert the highway budget into building bike paths, pedestrian plazas and Bogotá's first rapid-transit system. In Montgomery's view, Peñalosa had "redesigned the experience of city living for millions of people".

The example of Bogotá provides an irresistible introduction to Montgomery's thesis that a growing global rebellion against private cars, exclusionary zoning and sprawl could be the dawn of a new urban world. From Milwaukee in Wisconsin to Seoul, Montgomery argues, the "battle for the shape and soul of cities ... is finally reaching a critical mass". After decades of ferment, neighbourhood activism is rapidly evolving from protest against individual grievances to an alternative politics of urban design. Montgomery exuberantly lists the changes: for example, shopping malls reclaimed as 'mini-villages'; towns recast for children's needs; and fenceless neighbourhoods. As he puts it, visionary urban designers and politicians "are reorganizing the systems that hold cities together and rewriting the rules that dictate the shapes and functions of our buildings".

None of this chimes with my own daily experience of southern California life as an 'ultra-commuter' (my job is 160 kilometres from home). Nor does it give me hope that some miracle will reverse the United States' national indifference, much of it ominously racial in origin, that tolerates the death of Detroit, Michigan. Once the centre of car manufacture and the Motown music industry, Detroit is now a bankrupt shell with barely 40% of its 1950 population.

But Montgomery has no time for pessimists, writing that if Bogotá or Athens can be "reconfigured to boost happiness", these principles can heal richer cities around the world.

The 'happy city' thesis is a tough one to lift off the ground, and early parts of the book simply do not fly. For example, Montgomery sets up a contrast between the good city and the bad suburb that fails to sample anything like the average reality of metropolitan life. To illustrate urban happiness, he has a huge home-court advantage: he lives in Vancouver, Canada, the most well-planned and prosperous big city in North America. At the other extreme, he takes a bizarre bus trip with home bargain-hunters through a foreclosed and semi-abandoned suburb near Stockton, California — ground zero of the 2008 US mortgage apocalypse.

Most of Montgomery's critique of the emotional emptiness and environmental costs of suburban life is familiar sociological boilerplate that dates back to the 1950s. He understandably hurries through this to arrive at a more interesting subject: environmental psychology's view of human responses to the built environment. Numerous studies, such as the global World Values Survey, show that people are happier in densely social, architecturally complex, pedestrian-oriented, park-rich and culturally stimulating environments. When efficient alternatives are available, they will even cut the umbilical cords to their cars.

But Montgomery also cites uncomfortable research from sources including Harvard University in Cambridge, Massachusetts, and the University of Zurich in Switzerland. This shows that too many North Americans and Germans are socially programmed to choose status symbols such as supersized suburban homes at the end of nowhere over a connection with other people or a walk in a park.

None of this is Earth-shaking news. Bookshelves groan with glossy catalogues of urban invention and 'smart growth' — a genre that, too often, is simply a celebration of gentrification or an advertisement to move to Canada or Scandinavia. What redeems

Montgomery's book from his own miscast exhilaration is the surprising richness and critical acuity of his case studies. Although



Happy City:
Transforming Our
Lives Through
Urban Design

CHARLES
MONTGOMERY
Farrar, Straus and
Giroux: 2013.

cherry-picked from such privileged laboratories as Vancouver and Copenhagen, he focuses on the wider applicability of urban-design innovations to generic places, even the suburban badlands of California and Texas.

A fascinating example is the reform of zoning restrictions in Vancouver's older 'streetcar' suburbs.

Most planners define

the essence of 'Vancouverism' as its downtown peninsula — a utopian mini-Manhattan with quiet high-rise neighbourhoods and almost no traffic congestion. Montgomery, however, rightly sees a more revolutionary step in the city's legalization of the conversion of alley garages into cottages and basements into apartments. This simple zoning reform has enabled "one of the biggest urban infill projects on the continent", allowing thousands of residents to find affordable housing in inner suburbs. Hopefully, planners and housing advocates in Los Angeles and other North American cities with shortages of affordable housing will recognize the ingenuity of this initiative and the part that decent mass transit plays in making it work. Montgomery offers other compelling examples showing the power of community imagination, or simply its common sense, when unleashed.

But it would be folly to ignore the special conditions that make the innovation of urban happiness possible in Montgomery's case-study cities. Without exception, these locations have had strong social-democratic or progressive governance. It is hard to imagine that market forces in sunbelt cities such as Phoenix, Arizona, would ever allow such communitarian design principles to sink deep roots. And, for most of the world's present and future urban population, from Lagos in Nigeria to Chengdu in China, the conversation first needs to take place at the more fundamental level of basic needs and human rights. ■

Mike Davis is a writer and urban historian based in San Diego, California.
e-mail: michael.davis@ucr.edu

➔NATURE.COM
Mike Davis analyses
'instant' copycat
cities at:
go.nature.com/6kzsod



Q&A Jad Abumrad

Airwave trailblazer

Jad Abumrad co-hosts Radiolab, the science-heavy, nationally syndicated US public-radio show. As it enters its tenth year, he takes time out from a 21-city North American tour with co-host Robert Krulwich to talk about crafting high-speed science stories on radio.

How did you get into science and radio?

I grew up in Tennessee in the 1980s, an Arab kid in a Southern Baptist landscape. My mother is a molecular biologist and my father is a surgeon, and as a kid I'd be stuck in their labs after school, bored out of my skull and playing with the rats. I gravitated to music, and as a teen I would stay in my room composing scores for imaginary films. After studying writing and music in college, I started volunteering in public radio and eventually secured a late-night slot to air forgotten documentaries on WNYC — New York Public Radio. Two days before the show aired, I asked my boss who the host would be. He said, "You."

How did the show evolve?

In the early days, the station mercifully treated me with benign neglect. I didn't know what I was doing. Most of the show was old material, borrowed and rehashed. Inevitably there would be a hole in the programme, and in a panic I would throw together a little segment on the politics of Zimbabwe or I'd ask listeners to scream on my voicemail. In 2003, I met science broadcaster Robert Krulwich

and we experimented with combining radio formats such as interviews, documentaries, storytelling and music. We settled on a 'two-guys-talking' format, but with quotes from scientists and surreal soundscapes popping out like thought bubbles. From the beginning, Radiolab had a digital sensibility, a sense of speed and density that some have heralded as the future of public radio and others have complained is too jittery.

Do you ever run up against the limits of radio?

In our episode on colour, when talking about the retina with a biologist, we asked which creature had the most types of colour-receptor cone in its eyes. The answer was the mantis shrimp, which has 16 cones, each receptive to a different wavelength of light. Unable to convey this visually, we gathered a 160-voice choir in a cathedral, divided them up according to colours in the spectrum and asked them to sing us a rainbow as the shrimp would see it.

What happens at your live show?

Apocalyptic tells stories of mass destruction, focusing on the extinction of dinosaurs

at the end of the Cretaceous period 65 million years ago. Some moments, in which you learn bits of chemistry and physics, or the lights dim and we all listen deeply, feel like the on-air show. The rest is strange and new. There is animation and video to reveal the mechanics of violent collapse. There are giant dinosaur puppets made by the Australian theatre company Erth. Musicians create swells of sound that make you feel like the roof is going to fall in. Comedians like Reggie Watts and Patton Oswalt will make you laugh. We're all moving towards our own end, as individuals and as a species, but we hope to leave you with a sense of how extraordinary it is to be alive.

What is the gist of the science in the show?

We present a theory proposed by scientists Jay Melosh, Peter Schultz, Douglas Robertson and Kirk Johnson that draws on ballistic simulations to argue that the Cretaceous extinction may have been much faster than previously thought. The conventional picture is of a global 'nuclear winter' brought on by ash thrown up into the atmosphere by a meteor that killed off the dinosaurs over tens of thousands of years. We argue that the extinction may have taken just a single afternoon.

Is it true that you plan to branch out from science?

Yes and no. Scientific ideas can be irreducibly complex and wrestling with them can be exhausting. But it's no longer acceptable for people not to understand what's happening in science, and I do find science endlessly inspiring even when it's pissing me off. So science reporting will always be a fundamental part of what we do. But in recent months I have thought about getting into legal affairs. I wonder sometimes what it would be like to cover an election. And what about sports?

Have you got things wrong?

Absolutely. For a show about stochasticity, we wanted to demonstrate how hard it is to tell a signal from noise at the molecular level. So we ran a tape of a 99-year-old woman singing through a noise filter, over and over. We felt it was a gorgeous metaphor for how our bodies deal with biological 'noise', the topic of a reported segment by Carl Zimmer. But Carl said that it was not even remotely correct. We had an epiphany: let's just play the incorrect version and then broadcast Carl telling us how wrong it is, followed by a good-faith attempt to correct ourselves. We've never claimed to know what we're talking about, which may explain why no one has come to stick a pitchfork in our foreheads. ■

INTERVIEW BY JASCHA HOFFMAN



Brain tissue affected by Alzheimer's disease prepared for microscope examination.

the aggregation of amyloid interferes with neuronal signalling and causes dementia. Since they formulated their amyloid-cascade hypothesis, this has been the dominant view on the cause of AD.

The need to understand the mechanisms of the disease, and find targets for preventing it, is becoming urgent. With the greying of society, it is predicted that some 66 million people worldwide will have dementia in 2030. Funded by governments and the pharmaceutical industry, studies are being undertaken that are unprecedented in terms of sample size, follow-up and comprehensiveness. By tracking genetics, brain structure and cerebrospinal fluid, almost all the studies aim to localize the pathways and mechanisms proposed by the amyloid-cascade hypothesis. Most assume that this research roller coaster will reveal what causes AD. But will it?

Lock invites readers to look at alternatives to our current path. She delivers key concepts in epidemiology, neuroscience and genetics in a way that is both scholarly and free of unnecessary technical details. Lock's bird's-eye view and mix of diverging sources of information is refreshing. For example, she writes of the astonishing reluctance of individuals screened for biomarkers to change their convictions about their risk of developing AD. Just pages later, she recounts the very similar reluctance of scientists to change their convictions about the mechanism by which the condition develops — even when faced with findings that contradict the amyloid-cascade hypothesis.

Lock calls for a paradigm shift. She hopes that careful investigation of lifestyle and environmental exposure, and their effects on gene expression, will reveal opportunities for intervention. But if we find them, will we be able to implement them? Our ability to change unhealthy behaviours lags far behind our recognition of them as unhealthy, and we have only begun to touch on ways to help people take pleasure in healthy lifestyles. Moreover, restrictive measures on the marketing of temptations may become a major issue for industry and economies. Lock invites us to face such challenges and take responsibility for implementing preventive measures worldwide, irrespective of national and personal incomes. For its wide scope and balanced critical evaluation, *The Alzheimer Conundrum* is an inspiring read for everyone working in the field. ■

Eus Van Someren is a professor of neurophysiology, founder of sleepregistry.org and head of the Sleep & Cognition department of the Netherlands Institute for Neuroscience of the Royal Netherlands Academy of Arts and Sciences, Amsterdam, the Netherlands.
e-mail: e.van.someren@nin.knaw.nl

ANTHROPOLOGY OF MEDICINE

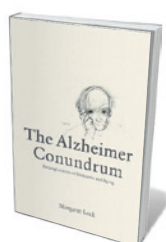
Where we are now with Alzheimer's

Eus Van Someren welcomes a call to critically evaluate progress in research on this form of dementia.

In the Mini Mental State Examination, a questionnaire used worldwide to evaluate the severity of dementia, an early question is "Where are we now?" That is also the primary question of Margaret Lock's *The Alzheimer Conundrum*. This anthropological study peers back at a century of grappling with Alzheimer's disease (AD) and surveys the quest to understand its mechanisms and the scientific enterprise needed to unravel them.

Lock dares to pose big questions, and is well prepared to do so. For ten years, she intensively studied epidemiological and neurobiological research on AD, went to meetings, and interviewed experts, people at risk and carers. The result reads like a travel diary, with a balance between engagement and objectivity. Lock highlights how scientific progress can be both accelerated and impeded by paradigms, the entangled interests of the pharmaceutical industry, the media and personal beliefs. She covers the history of AD, prominent views on its cause, risk factors such as mild cognitive impairment, and biomarkers.

Along the way, Lock dissects three fundamental tensions. The first is between the 'localization' approach that attributes dementia to specific neuropathological changes, and the 'entanglement' approach that includes complex interactions between mind, environment, ageing and life events. The second is between the view that AD is intrinsic to ageing, and the understanding that it is a distinct pathology. The third is between deterministic genomics, and the view that adds epigenetics.



The Alzheimer Conundrum: Entanglements of Dementia and Aging

BY MARGARET LOCK
Princeton University Press: 2013.

techniques for brain tissue made the invisible visible and revealed the amyloid plaques and neurofibrillary tangles that have come to be regarded as key players in dementia.

After decades of dormancy, AD research reappeared on stage in 1966. Psychiatrist Martin Roth and his colleagues reintroduced Alzheimer's idea, describing autopsies of patients diagnosed with dementia that showed not arteriosclerosis — then the primary suspect — but numerous plaques and tangles. In 1992, neuroscientists John Hardy and Gerald Higgins proposed that



NEW ANGLES ON THE BRAIN

A Nature special issue

www.nature.com/neuroscience2013

Correspondence

Discard Soviet doctorate systems

The research performance of most former Soviet states is still low compared with that of many Western countries. In my view, progress will be stifled as long as the archaic academic systems passed down from the former Soviet Union persist.

I have analysed the research performance of several of these nations on the basis of their per capita gross expenditure on research and development (GERD; see go.nature.com/8oclnj) from 1998 to 2010 and their number of research publications from 1998 to 2012 (see www.scimagojr.com).

The Baltic countries — Estonia, Lithuania and Latvia — were notably more productive in 2012 than Russia, Ukraine and Belarus (see 'Research performance in former Soviet nations', left), with Estonia's publication output per 1,000 people approaching that of the United States (1.7 in 2012). Also, the research performance of the Baltic states has progressed markedly since 1998 (see figure, right).

The figure also shows that each country's publication output seems to have improved as research funding has increased. Georgia, however, had no increase in GERD between 1998 and 2005 (no more recent data are available), yet managed to more than triple its number of research publications between 1998 and 2012. Russia and Belarus have given a particularly poor return on investment in terms of research publications.

The success of Georgia and the Baltic states since 1998 may be connected with their adoption of internationally recognized standards for doctorate degrees and academic promotion. These countries now use a Western PhD model dedicated to original research, and career advancement depends on producing peer-reviewed publications — which is not the case in Russia, Ukraine, Belarus

and other former Soviet states.

Those poorly performing countries continue to use the old Soviet split-level doctorate degree. This degree can take more than 20 years to complete and involves only a minimal initial training in research, which may not be original and is not subject to independent peer review. The rest of a student's time is taken up with administrative tasks — for example, preparing reports for committees and government departments.

The poor research performance in most former Soviet states stems partly from weak funding management (data not shown). But there is also an urgent need for fundamental academic reform in those countries.

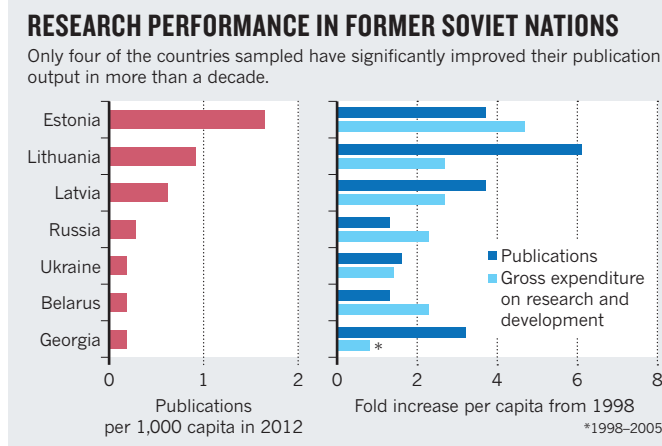
Alexander Gorobets *Sevastopol, Ukraine.*
alex.gorobets@mail.ru

Ranking Brazilian research output

As presidents of the Brazilian Association for the Advancement of Science and the Brazilian Academy of Sciences, we object to your negative perspective on CAPES, our education ministry's agency for the Coordination for the Improvement of Higher Education Personnel (*Nature* **500**, 510–511; 2013).

The impact factor is just one of a long list of indicators used by CAPES since 1976 to rate programmes in 48 fields of research, from social studies to physics. It is important to stress that the agency uses a system of peer review to evaluate and rank Brazil's graduate programmes — not to assess individual curricula vitae. The country's scientific community analyses data on the performance of each programme over the previous three years.

Other indicators that CAPES evaluates include recognition of faculty members' research by the international community; the coherence, consistency



and comprehensiveness of the curriculum and infrastructure for teaching, research and continuing education; students' participation in research; and the contribution of faculty members to the supervision of doctoral students.

There are several ranking systems worldwide that also incorporate journal impact factors and citations into their metrics and are acknowledged by the scientific community. One is the Academic Ranking of World Universities (also known as the Shanghai Ranking), which inspired the Ranking Web (or Webometrics) for universities around the world.

Helena B. Nader *Brazilian Association for the Advancement of Science, São Paulo, Brazil.*
hbnader.bioq@epm.br
Jacob Palis *Brazilian Academy of Sciences, Rio de Janeiro, Brazil.*

Russia embraced Wallace's works

On the centenary of Alfred Russel Wallace's death this week, it is worth recalling the remarkable influence that the naturalist's ideas had in Russia during his lifetime. His major works were translated into Russian, including his books *The Malay Archipelago* (1869), *Darwinism* (1889) and *Man's Place in the Universe* (1903).

Although Wallace was most famous as Charles Darwin's

co-discoverer of evolution by natural selection, the demand among Russian intellectuals was mainly for Wallace's own publications. Many warmed to Wallace's contention that human spiritual faculties cannot be explained by natural selection.

Theologians such as Alexander Gusev (1842–1904) used it to defend Orthodox Christianity against 'non-believers'. Gusev even accused the translators of Wallace's *Contributions to the Theory of Natural Selection* (1870) of censoring 'unscientific' ideas and of distorting Wallace's holistic view of science and religion (G. S. Levit and S. V. Polatayko *Theor. Biosci.* <http://doi.org/pq8>).

Russia's fascination with Wallace's work helped to shape the debate among early evolutionists on alternative versions of Darwinism (see D. Todes *Nature* **462**, 36–37; 2009) and opened up discussion on the uniqueness of the human soul.

Georgy S. Levit *Friedrich Schiller University, Jena, Germany, University of King's College, Halifax, Nova Scotia, Canada, and National Research University ITMO, St Petersburg, Russia.*
Uwe Hossfeld *Friedrich Schiller University, Jena, Germany, and National Research University ITMO, St Petersburg, Russia.*
Lennart Olsson *Friedrich Schiller University, Jena, Germany.*
lennart.olsson@uni-jena.de

Harold Melvin Agnew

(1921–2013)

Physicist and Manhattan Project veteran.

Harold Melvin Agnew, one of the last surviving members of the team that began the nuclear age, died on 29 September. Equipped with only an undergraduate degree, Agnew helped to set in motion the first controlled, self-sustaining nuclear chain reaction, worked on the atomic bomb, and witnessed the bombing of Hiroshima in Japan from inside an aircraft that was part of the strike operation.

A native of Colorado, Agnew studied chemistry at the University of Denver. There, he pitched on a championship softball team and earned a scholarship to pursue graduate studies at Yale University in New Haven, Connecticut. Early in 1942, Agnew accepted a position as a research assistant at the Metallurgical Laboratory at the University of Chicago in Illinois, where the world's first nuclear reactor was taking shape under the stands of an athletic field. On 2 December 1942, he witnessed the first controlled nuclear reaction.

Agnew's next assignment, beginning in early 1943, was to work with a small team to disassemble a particle accelerator at the University of Illinois and to arrange for its transportation to a facility in Los Alamos, New Mexico, the new home of the Manhattan Project to build the first atomic bomb. The team included his wife, Beverly, whom he had met at high school; while Agnew worked on the accelerator, Beverly signed on as a secretary and assistant involved in the management of the new facility.

As work on the atomic bomb neared completion, the physicist Luis Alvarez (who joined Los Alamos in 1944) assembled a team that would accompany the weapon into combat. Agnew, who stated in a later interview that he had "wanted to get in the war", was among the first volunteers.

Starting in late 1944, the team spent six months developing and testing the instrumentation and procedures that would enable them to determine from an aeroplane the power of a nuclear explosion. Rather than trying to measure the level of radiation released after the bomb had exploded, the Alvarez group decided to use a microphone fitted with circuitry that would translate the shock wave of the blast into electrical signals that could be recorded on an aircraft's gun camera.

Agnew and the rest of the team began their journey to war at Wendover Air Force Base in Utah. Outfitted with uniforms and taught how to salute, the scientists were



flown to Tinian in the Northern Mariana Islands, the base from which B-29 aircraft were being sent to burn Japanese cities to the ground.

A B-29 called *Enola Gay* lifted off the Tinian runway for Hiroshima at 2.45 a.m. on 6 August 1945, with the uranium bomb aboard. A second B-29, *The Great Artiste*, took off two minutes later. As well as a crew of ten men, the second aeroplane carried three scientific observers: Alvarez, Lawrence Johnson and Agnew. At 8.15 a.m., bombardier Kermit Beahan opened the bay doors and dropped three parachute-equipped blast gauges designed to transmit the magnitude and duration of the bomb's blast wave to a receiver on the plane. Each of the three scientists manned a receiver tuned to the frequency of one of the detecting probes. When the bomb was dropped, Alvarez could not locate his frequency, and Agnew and Johnson provided all the data on the shock waves reverberating from the explosion.

With his primary task accomplished, Agnew pulled out his personal 16-millimetre motion-picture camera and filmed the mushroom cloud. A plane trailing five kilometres behind *The Great Artiste* was equipped with a high-speed still camera, but Agnew's 'unofficial' film was the only motion-picture footage of the Hiroshima explosion. Three days later, Agnew equipped the tail gunners of the aeroplanes on the Nagasaki mission with film cameras, thereby

ensuring a motion-picture record of the second atomic strike.

Agnew ended up giving his footage to the Hoover Institution on War, Revolution and Peace at Stanford University in California. "I should have held them until today," he remarked later, "sold them on eBay and become a millionaire".

With the war over, Agnew earned a PhD in 1949 working under nuclear physicist Enrico Fermi at the University of Chicago. Returning to Los Alamos, he then joined a project to develop hydrogen and thermonuclear weapons, served as project manager for a bomb test on Bikini Atoll in 1954 and became director of the Los Alamos National Laboratory in 1970.

Retiring from the post in 1979, Agnew was president and chief executive of General Atomics, a firm developing innovative nuclear reactors, headquartered in San Diego, California, until 1985. He served as scientific adviser to the Supreme Allied Commander Europe (one of NATO's two highest-ranking military commanders) in the early 1960s and as a White House science councillor for much of the 1980s. He also chaired and served on several military advisory boards, was a member of the US National Academy of Sciences and the National Academy of Engineering, and received various awards.

A scientific 'cold warrior', Agnew never expressed regret about his involvement in the Manhattan Project. "My feeling towards Hiroshima and the Japanese was, they bloody well deserved it," he remarked in 1984. He favoured the use of tactical nuclear weapons in Vietnam, and argued successfully against a comprehensive nuclear-test-ban treaty, although he did once say that he would require every world leader to witness an atomic blast while standing in his underwear, "so he feels the heat and understands just what he's screwing around with".

Towards the end of his life, Agnew summed up the achievements of his generation with pride. "We brought a quick end to a devastating war and maintained the peace and eventually saw democracy prevail. That's something you can hang your hat on." ■

Tom Crouch is senior curator of aeronautics at the Smithsonian Institution's National Air and Space Museum in Washington DC.
e-mail: croucht@si.edu

LOS ALAMOS NAT'L LABORATORY

Sculpting neuronal connectivity

It emerges that a transcription program differentially regulates inhibitory inputs in distinct neuronal compartments — an unexpected coordinated switch for achieving experience-dependent ‘plasticity’ in neural circuits. [SEE LETTER P.121](#)

EMILY SYLWESTRAK & PETER SCHEIFFELE

Experiences trigger long-lasting changes in memory and behaviour. Although manifested at the organismal level, such changes arise from modifications of individual synaptic connections between neurons. Specifically, new sensory experiences alter a neuron's activity (its output of action potentials) by modulating the strength of the synaptic connections that it receives¹. On page 121 of this issue, Bloodgood *et al.*² demonstrate that a transcriptional program drives highly localized changes in synaptic connections between neurons. The authors' results thus offer a refined molecular explanation for experience-dependent learning processes.

When an animal explores an uncharted environment, neural activity originating from its sensory organs propagates into the brain, where neurons receive a barrage of concurrent excitatory and inhibitory inputs. The net activity signal that each neuron receives is determined by a delicate balance of these two competing forces. In some neurons, excitation prevails and the cells produce an action-potential spike; in others, inhibition overrides excitation and the cells remain silent.

The cellular location of an inhibitory input — that is, whether it impinges on a neuron's cell body (soma) or dendritic projections — as well as its strength govern how effectively excitatory inputs sum up. Somatic inhibitory synapses, which lie close to the spike-initiation machinery, can effectively cancel excitation³. Farther away along the dendrite, an inhibitory input can merely dampen an excitatory signal. Separate regulation of somatic and dendritic synapses allows a neuron to both ‘gate’ its spiking activity and control the dendritic integration of excitatory inputs. Nonetheless, little is known about the molecular mechanisms that selectively regulate these inhibitory inputs at a subcellular level.

A leading hypothesis has been that neuronal activity triggers specific gene-expression programs downstream, with the resulting gene products modulating transmission at synapses⁴. Because these gene products would be synthesized in the soma, they have been implicated in rather non-selective, cell-wide changes in total synapse number or strength⁵.

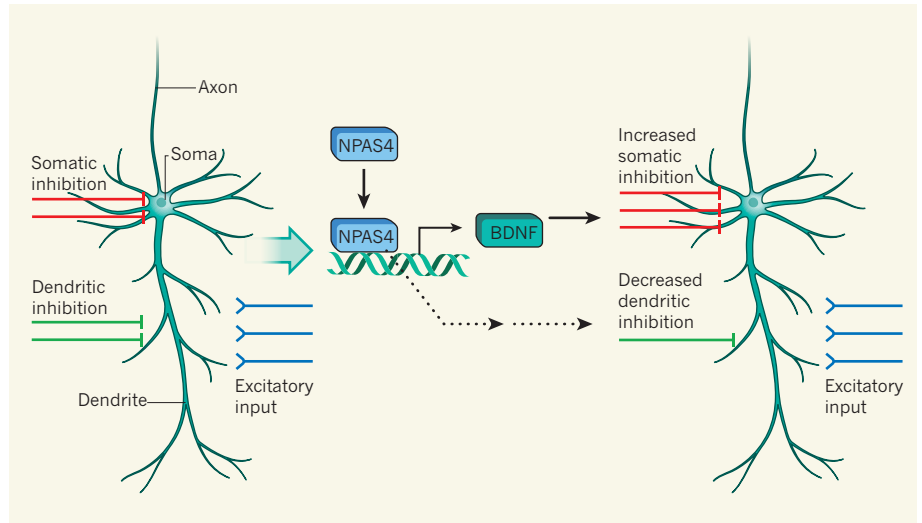


Figure 1 | Subcellular-specific regulation of neuronal activity. When an animal explores a new environment, its hippocampal neurons receive excitatory inputs conveying spatial information. This excitation is balanced by inhibitory inputs that impinge on the cells' soma and dendrites. Bloodgood *et al.*² show that increases in neuronal activity drive an NPAS4-dependent transcriptional program, a key target of which is the gene encoding BDNF. The latter protein selectively stimulates the formation of somatic inhibitory synapses and, through parallel, unknown pathways, reduces the number of dendritic inhibitory synapses. Thus, the NPAS4 transcriptional program independently controls at least two distinct classes of inhibitory synapse.

The transcription factor NPAS4 is one such activity-regulated gene product, which itself initiates a gene-expression program that modulates the total number of inhibitory synapses *in vitro*⁶. But whether activity-regulated gene products can act on a spatially restricted set of synapses to provide more-refined control of neuronal function has remained unclear.

To address this question, Bloodgood and colleagues housed mice either in standard cages or in enriched environments containing running wheels and novel objects to stimulate activity in the hippocampus — a brain structure that is crucial for spatial navigation and memory. Exposure to the enriched environment resulted in a marked increase in NPAS4 levels in hippocampal neurons. Moreover, this transcription factor changed the number of inhibitory synaptic connections made with pyramidal cells, the main excitatory cell type in the hippocampus. Most notably, NPAS4 triggered an increase in somatic inhibitory synapses, with a simultaneous reduction in dendritic inhibitory synapses (Fig. 1).

NPAS4 can control the expression of many

genes, one or more of which might mediate the observed differential effects on the number of somatic versus dendritic inhibitory synapses. To identify the genes responsible, Bloodgood *et al.* performed a comprehensive screen involving three search criteria: for genes that are directly regulated by NPAS4; those that are strongly upregulated by neuronal activity; and those that control the number of inhibitory synapses. The gene encoding brain-derived neurotrophic factor (BDNF) satisfied all three requirements. (Intriguingly, BDNF has also been shown^{7,8} to be regulated independently in different cellular compartments.)

The authors' further analyses confirmed that NPAS4 promotes BDNF production during bouts of increased neuronal activity. Furthermore, using mice lacking BDNF, they showed that this factor is necessary for the increase in the number of somatic inhibitory synapses. However, the reduction in dendritic-synapse number persisted in these mutants, indicating that different NPAS4 target genes regulate this aspect of NPAS4-dependent synapse remodelling.

Bloodgood and colleagues' characterization of the NPAS4-mediated control of specific sets of inhibitory synapses is a significant step forward in our understanding of how activity can exert long-lasting changes in synapse number. Nonetheless, some questions about the implications of these findings remain.

The hippocampus contains several types of inhibitory interneuron cell, and these vary in their activity, synaptic function and subcellular targeting of pyramidal cells⁹. Whereas Bloodgood and co-workers' experimental set-up was designed to separate somatic and dendritic inputs through spatially restricted stimulation, it would be beneficial to extend this study to investigate the specific cell types at play. Various mouse lines that allow distinct interneuron subpopulations to be accessed¹⁰ could be useful for this purpose. Knowing precisely which cell groups are involved will be instructive in further refinement of hypotheses for how activity-induced changes in inhibition affect hippocampal processing and behaviour.

Another question is how the effects of BDNF become confined to specific subcellular compartments. Neurons transcribe several different messenger RNAs of BDNF, and it could be that activity-induced BDNF mRNAs are preferentially trafficked to somatic synapses, where they are translated locally. Another possibility is that newly synthesized BDNF protein is selectively released near somatic synapses. Alternatively, specificity might arise from the axonal processes of other neurons that make contact, such that inhibitory axons targeting the soma are more responsive to BDNF than their dendrite-targeting counterparts.

More broadly, the ability of NPAS4 to coordinately and bi-directionally modulate somatic versus dendritic inhibition has implications for synaptic plasticity (the processes by which synapses grow stronger or weaker depending on their activity level), which relates to learning. To induce plasticity at excitatory synapses, the net excitatory-inhibitory input must trigger the entry of calcium ions into the dendrite¹¹. Nearby dendritic inhibition normally dampens the efficacy of synaptic input. NPAS4 activation would relieve this inhibition, making individual synapses more likely to undergo the lasting changes associated with learning and memory. At the same time, increased somatic inhibition would tighten the time window in which combined synaptic input can produce a spike. The consequences of both actions are that fewer excitatory synapses would be needed to cause the cell to spike, but that those inputs must be more temporally coincident.

Bloodgood and colleagues' data unify several previous observations concerning the activity dependence and synapse-forming potential of NPAS4 and BDNF. Moreover, they characterize synapse-specific rules governing the effects of NPAS4 activation, and thereby highlight an extra layer of adaptability

of neural circuits and a mechanism by which sensory input can produce long-lasting changes in synaptic connectivity. ■

Emily Sylwestrak and Peter Scheiffele are in Biozentrum, University of Basel, CH-4056 Basel, Switzerland. E.S. is also at F. Hoffmann-La Roche, pRED, Pharma Research and Early Development, DTA Neuroscience, Basel.
e-mail: peter.scheiffele@unibas.ch

1. Turrigiano, G. G. *Cell* **135**, 422–435 (2008).
2. Bloodgood, B. L., Sharma, N., Browne, H. A.,

- Trepman, A. Z. & Greenberg, M. E. *Nature* **503**, 121–125 (2013).
3. Pouille, F. & Scanziani, M. *Science* **293**, 1159–1163 (2001).
4. West, A. E., Griffith, E. C. & Greenberg, M. E. *Nature Rev. Neurosci.* **3**, 921–931 (2002).
5. Turrigiano, G. *Cold Spring Harb. Perspect. Biol.* **4**, a005736 (2012).
6. Lin, Y. et al. *Nature* **455**, 1198–1204 (2008).
7. Dieni, S. et al. *J. Cell Biol.* **196**, 775–788 (2012).
8. Matsuda, N. et al. *J. Neurosci.* **29**, 14185–14198 (2009).
9. Freund, T. F. & Buzsáki, G. *Hippocampus* **6**, 347–470 (1996).
10. Taniguchi, H. et al. *Neuron* **71**, 995–1013 (2011).
11. Bear, M. F. & Malenka, R. C. *Curr. Opin. Neurobiol.* **4**, 389–399 (1994).

APPLIED PHYSICS

On a roll

Populations of rolling particles have been shown to display unidirectional collective motion in a racetrack enclosure. Theoretical modelling suggests that hydrodynamic and electrostatic effects promote such behaviour. SEE LETTER P.95

MICHAEL SHELLEY

In a study published in 1896, the German physicist Georg Quincke demonstrated that, when suspended in an electrically conducting fluid, an insulating sphere will rotate if a sufficiently strong electric field is applied¹. On page 95 of this issue, Bricard *et al.*² use this little-known effect — now called Quincke rotation — as the energy-transfer mechanism, or motor, to drive populations of millions of microspheres to spontaneously form rolling herds (Fig. 1). In a racetrack-shaped enclosure, these 'Quincke roller' herds merge into a unidirectional swarm that circles the track (see Fig. 2 of the paper), and increase in size with increasing roller concentration. The authors interpret and rationalize their results using mathematical modelling to show that, at short distances, Quincke rollers interact mainly through two pairwise effects: a hydrodynamic interaction that promotes 'polar' alignment of rolling directions (that is, the movement of rollers in the same direction) and a repulsive electrostatic interaction.

Herds of Quincke rollers are a new example of active matter. This is the subject of a field spanning many disciplines that originated through researchers' desire to understand self-organized structures in biology, such as bird flocks and bacterial swarms, and the cellular cytoskeleton³. Although active matter lacks a simple definition, we tend to think of active-matter systems as those composed of many, possibly identical, interacting particles that each use a local energy source to execute a change in shape, orientation or position. Roller herds are akin to microswimmer suspensions, such as bacterial baths⁴, whose members also

interact with each other hydrodynamically. But, unlike such free swimmers, Quincke rollers move through an applied net torque, which results in a very different hydrodynamic coupling between them.

Other synthetic active-matter systems have been devised and powered by chemical reactions⁵, mechanical vibration⁶, hydrolysis of the cellular energy molecule ATP⁷, and light⁸, magnetic⁹ and electric fields (as for Quincke rollers). The interactions between the constituent particles of an active-matter system can be mediated by several effects: induced flows in the surrounding fluid; spatially distributed fields such as a chemical concentration or an electric field; direct mechanical coupling; and collisions. The set of observed collective

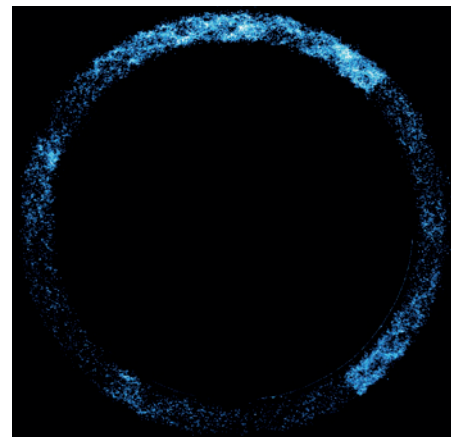


Figure 1 | Roller herds. Bricard *et al.*² show how populations of rolling microspheres confined to a track spontaneously form moving herds. Particle size is 5 micrometres; the length of the track is 31.5 millimetres.

behaviours is also large — the formation of vortices, jets, aggregates, crystals, asters, swarms, strange suspension rheologies, defect dynamics and persistent turbulent-like motions. Active matter is obviously rich in phenomena.

The strengths of the present study include the novelty of the system's energy-transfer mechanism, the relative simplicity of the system's behaviours (at least under the geometric constraints of the racetrack) and the apparent completeness of the explanatory theory. Another strength is that the theory can be related to phenomenological models of flocking¹⁰, the parameters of which are generally unmoored from specific physics or behavioural responses. The authors' experimental videos of Quincke roller herds forming, travelling and merging are well worth watching (see go.nature.com/tqlqsp); especially striking is the footage showing the rollers' decidedly un-herd-like behaviour when confined to a square enclosure.

I do have two slight quibbles. One of the roller swarm's features is its statistical uniformity, or lack of large density fluctuations, at high concentrations (see Fig. 4c of the paper²). The authors say that large density fluctuations have, until now, been considered a hallmark of active-matter systems such as theirs. This seems a straw-man argument; although large density fluctuations are certainly a feature of many such systems, their appearance is more a matter of scientific interest than of definition. A counterpoint example is suspensions of self-propelled 'puller' particles, which are powered from the front. Theoretical studies have shown that such puller suspensions, unlike 'pushers' and despite hydrodynamic interactions, also maintain near-statistical uniformity, although they show no propensity at all towards swimmer alignment¹¹ (the generously minded might consider this a peculiar form of collective behaviour). In addition, although Bricard *et al.* put their nonlinear theory to good use in calculating the transitions and stability of the theory's steady states, I find it a little disappointing when studies do not take the extra step of simulating the full dynamics and seeking greater exposure of a theory to experimental observations.

What might further studies of Quincke rollers or related systems explore? The present study shows that the geometry of the enclosure is one of the main determinants of how a Quincke-roller suspension behaves. Given that a single continuous travelling swarm appears at high concentrations in the racetrack geometry, it would be interesting to see what dynamics emerge in a figure-of-eight enclosure in which collisions seem inevitable. Because the authors conjecture that active-matter systems could have applications in understanding social phenomena, let me mention one. Pedestrians in New York show both local alignment and repulsion while moving around the city, and when two opposing masses intersect at

a crossing, I have observed the spontaneous formation of interwoven lanes that facilitated the (mostly) collision-free and efficient displacement of New Yorkers from one side of the street to the other. I suspect that tourist masses, often less accustomed to dense city life, move around the city in a less orderly way. I seriously wonder whether a related physical system — perhaps one inducing apolar alignment — might be concocted that would reproduce this observation. I wonder, too, whether Quincke rollers might be constrained along a wall, perhaps by placing them in depressions, so as to make a microfluidic pump.

Lastly, I believe that a true understanding of flocking by birds and fish remains out of the reach of small-scale systems such as the Quincke rollers described here. This is because we still lack an understanding of how large, inertially dominated, swimming or flying organisms interact with each other, constructively or destructively, through their vortical fields. ■

Michael Shelley is in the Courant Institute, New York University, New York, New York 10012, USA.

e-mail: shelley@cims.nyu.edu

1. Quincke, G. *Ann. Phys.* **295**, 417–486 (1896).
2. Bricard, A., Caussin, J.-B., Desreumaux, N., Dauchot, O. & Bartolo, D. *Nature* **503**, 95–98 (2013).
3. Ramaswamy, S. *Annu. Rev. Cond. Mat. Phys.* **1**, 323–345 (2010).
4. Dombrowski, C., Cisneros, L., Chatkaew, S., Goldstein, R. E. & Kessler, J. O. *Phys. Rev. Lett.* **93**, 098103 (2004).
5. Paxton, W. F. *et al.* *J. Am. Chem. Soc.* **126**, 13424–13431 (2004).
6. Kudrolli, A., Lumay, G., Volfson, D. & Tsimring, L. S. *Phys. Rev. Lett.* **100**, 058001 (2008).
7. Sanchez, T., Chen, D. T. N., DeCamp, S. J., Heymann, M. & Dogic, Z. *Nature* **491**, 431–434 (2012).
8. Palacci, J., Sacanna, S., Steinberg, A. P., Pine, D. J. & Chaikin, P. M. *Science* **339**, 936–940 (2013).
9. Snezhko, A., Belkin, M., Aranson, I. S. & Kwok, W.-K. *Phys. Rev. Lett.* **102**, 118103 (2009).
10. Toner, J., Tu, Y. & Ramaswamy, S. *Ann. Phys.* **318**, 170–244 (2005).
11. Saintillan, D. & Shelley, M. J. *J. R. Sci. Interf.* **9**, 571–585 (2012).

EVOLUTIONARY ECOLOGY

Novelty makes the heart grow fonder

Research on guppies provides the most definitive evidence yet for the rare-male effect — a long-standing hypothesis to explain the perplexing maintenance of variation in traits that are subject to strong mate choice. SEE LETTER P.108

**JEFFREY S. MCKINNON
& MARIA R. SERVEDIO**

The little fish commonly known as guppies are almost as popular among evolutionary biologists as they are among home aquarists, because they provide a tantalizing opportunity to explore how genetic variation is maintained in natural populations. The males of this species (*Poecilia reticulata*) present a dazzling display of colour variation, and it is known that female guppies show strong mating preferences on the basis of male colour patterns. But the maintenance of this colour variation presents an evolutionary mystery, because sexual selection for a specific form of a trait should erode variation in that trait¹. The discovery² that, in a natural setting, male guppies with rare colour patterns survive better than more common types, presumably because they are less often targeted by predators, was an important advance in explaining guppy colour diversity. Now, on page 108 of this issue, members of the same research group (Hughes *et al.*³) show that wild guppy males with rare traits obtain more matings and leave more offspring. Thus, it seems that the diverse coloration in this species is promoted

by both natural and sexual selection.

Negative frequency-dependent selection — which in the case of sexual selection is sometimes called the rare-male effect — is a process in which the evolutionary fitness of a trait goes up as its relative abundance goes down. The literature on this effect goes back a long way and is substantial, but has at times been heavily criticized^{4,5}. Some of the best available evidence has come from investigations of guppies in the laboratory, in which preferences for both unfamiliar and rare traits (phenotypes) have been documented^{6,7}. But the relevance of such laboratory results to natural populations has been open to question because of a lack of studies in natural settings^{7,8}.

Hughes and colleagues' study is noteworthy in large part because it involves naturally occurring male colour phenotypes in natural pools located along streams in Trinidad. To perturb these stream systems from a possible evolutionary equilibrium in the abundance of different colour patterns, and to enhance the power to detect negative frequency-dependent selection, the authors experimentally adjusted the frequencies of different types of males (Fig. 1). For balance, they made the same phenotypes rare in some pools and common

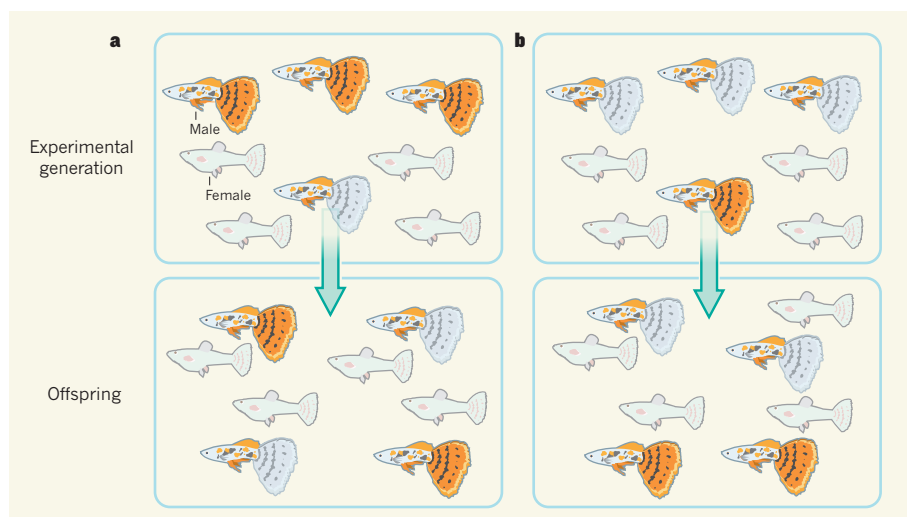


Figure 1 | The rare-male effect in a natural population. Hughes *et al.*³ adjusted the frequency of male guppies in stream pools such that males with coloured tails were common and males with uncoloured tails were uncommon (a), or the reverse (b). The frequency of females was kept constant. In both types of pool, the authors found that the rare males obtained more matings with females and, as a result, contributed proportionally more offspring to the next generation.

in others. Then, to evaluate the reproductive success of the males, they undertook the daunting task of genotyping more than 1,400 offspring of pregnant females collected from the pools at the end of the experiment. Working across three stream systems and with an impressive level of replication, the researchers observed a strong pattern of elevated mating and reproductive success for whichever male type was rare.

Although this is an important study, it is not without limitations. One potential issue stems from the fact that, in guppies, fertilization is internal, and females can store sperm for weeks or months. When Hughes *et al.* collected females from their experimental pools and allowed the fish to give birth in the lab, they found strong evidence for a rare-male effect among the fathers of the first round of offspring. But when the females were obliged to use stored sperm for a second brood, the rare-male effect among the fathers of those offspring was not statistically significant. The authors argue that, in nature, female guppies mate frequently and rarely rely on stored sperm, so that all natural broods are essentially equivalent to the first broods in their experiment. However, the data reviewed by Hughes and colleagues in support of this claim are not extensive, and more work on this point would be helpful.

There was also a technical limitation in the genotyping technique used by the authors: relying on variable genomic regions known as microsatellites, they could confidently assign paternity to only a minority of individual offspring. Although there is no reason to expect this to create any bias in the data, it might be worthwhile revisiting the samples as more powerful methods for assigning paternity become available.

Hughes and colleagues' evidence for the

rare-male effect in nature raises intriguing questions. The most obvious is, why do female guppies prefer males with uncommon colour patterns? Here we have more hypotheses than data sets. One theoretical analysis suggests that greater survival of rare male types, which has been found in guppies², might contribute to the evolution of such a preference, even if it is costly⁹. Interestingly, the same analysis points out that the negative feedback inherent in sexual selection for rarity (such selection causes rare types to become common) can ultimately prevent preferences for rare males from becoming ubiquitous. It remains to be determined whether preference for rarity varies among guppy females in experimental populations such as those used in this study. Hughes *et al.* point out that the rare-male effect might also emerge if females avoid mating with males

that share the colour patterns of their previous mates, to increase the genetic diversity of their offspring. Alternatively, preferences for rarity could have evolved because they lead to lower rates of inbreeding if populations are small and intermittently isolated. It has even been suggested¹⁰ that mating preferences for rare types provide no benefit for females and may be a manifestation of a preference for novelty that has evolved in other contexts.

The clever manipulations of natural populations used by Hughes *et al.* may, as the authors suggest, be a promising avenue for exploring the maintenance of variation by frequency-dependent selection in other systems. It might well be the case that, when put to the test, preferences for rarity might themselves not prove to be so rare. ■

Jeffrey S. McKinnon is in the Department of Biology and Center for Biodiversity, East Carolina University, Greenville, North Carolina 27858, USA. **Maria R. Servedio** is in the Department of Biology, University of North Carolina Chapel Hill, Chapel Hill, North Carolina 27599, USA. e-mails: mckinnonj@ecu.edu; servedio@email.unc.edu

1. Kotiaho, J. S., LeBas, N. R., Puurtinen, M. & Tomkins, J. L. *Trends Ecol. Evol.* **23**, 1–3 (2008).
2. Olendorf, R. *et al. Nature* **441**, 633–636 (2006).
3. Hughes, K. A., Houde, A. E., Price, A. C. & Rodd, F. H. *Nature* **503**, 108–110 (2013).
4. Partridge, L. *Phil. Trans. R. Soc. Lond. B* **319**, 525–539 (1988).
5. Ajuria Ibarra, H. & Reader, T. J. *Zool.* **290**, 81–95 (2013).
6. Gray, S. M. & McKinnon, J. S. *Trends Ecol. Evol.* **22**, 71–79 (2007).
7. Mariette, M. M., Zajitschek, S. R. K., Garcia, C. M. & Brooks, R. C. J. *Evol. Biol.* **23**, 1772–1782 (2010).
8. Bleay, C., Comendant, T. & Sinervo, B. *Proc. R. Soc. B* **274**, 2019–2025 (2007).
9. Kokko, H., Jennions, M. D. & Houde, A. *Proc. R. Soc. B* **274**, 1317–1324 (2007).
10. Hughes, K. A., Du, L., Rodd, F. H. & Reznick, D. N. *Anim. Behav.* **58**, 907–916 (1999).

This article was published online on 30 October 2013.

NEUROSCIENCE

What to do and how

Decisions can differ depending on the context that surrounds them. Analyses of the prefrontal cortex region of the monkey brain indicate that a dynamical process at the neuronal population level controls this behaviour. [SEE ARTICLE P.78](#)

JEFFREY C. ERLICH & CARLOS D. BRODY

Neurons typically receive inputs from many thousands of others. This dense connectivity suggests that brain functions such as perception, cognition and motor control result from the concerted activity of populations of neurons, rather than from single-cell activity. Nevertheless, neuroscientists have

long made discoveries by recording from, and thinking about, one neuron at a time. But more-recent developments in electrophysiological recording¹ and imaging² of the dynamics of hundreds of neurons simultaneously, alongside advances in data-analytic and theoretical tools^{3,4}, highlight the importance of understanding the relationship between the dynamics of large neural populations and the computations

those dynamics embody^{5–11}. In a tour de force reported on page 78 of this issue, Mante *et al.*¹² use electrophysiology together with sophisticated behavioural and neural modelling to add a population-dynamics view of the computations underlying flexible, context-dependent behaviour.

How you respond to a glance up a busy street should be very different depending on whether you intend to cross the road or hail a taxi. In the first case, you should pay attention to the motion of the cars, in the second case to their colour. Such stimulus-feature selection is an example of cognitive control¹³ — our brains' ability to flexibly adapt how we process information from moment to moment, depending on current goals. Mante and colleagues wanted to know how the brain decides which aspect of a stimulus should guide a behaviour.

The authors designed an elegant task to explore this flexibility (Fig. 1a). They trained monkeys to look at a screen showing randomly moving dots, each dot randomly coloured either red or green. In trials in the colour context, the monkeys had to decide whether there were more red dots or more green dots, regardless of the dots' direction of motion. In the motion context, the animals decided whether most of the dots were moving left or right, regardless of the dots' colour. In both contexts, the same set of stimuli, containing motion and colour signals, was used.

The team then recorded from the monkeys' prefrontal cortex (PFC), a brain region thought to be crucial for flexible, context-dependent behaviour and which also controls the motor activity that animals use to report their decisions. Consistent with previous work^{14,15}, the activity of individual PFC neurons depended in complex, time-varying ways on multiple

aspects of the task, including the motion and colour signals in the stimulus, the context and the monkey's decision. In what initially seemed a bewildering array of responses, these dependencies varied greatly across neurons.

To look at the data from a population viewpoint, the authors put together all the individual recordings for a given stimulus, and defined the neural population's response as the dynamical trajectory followed in a high-dimensional space in which each dimension represents the activity of one of the recorded neurons. They then used linear regression to find the axes (corresponding to a direction) in this space that best represented responses to the motion and the colour in the stimulus, and the monkeys' decision (Fig. 1b). They could therefore estimate separately how each signal's representation in the PFC developed over time, and how it depended on the context.

Which features of the data explained the context dependence of the behaviour? Not changes in the decision axis, which pointed in the same direction in both contexts. Nor could the behaviour be explained by irrelevant inputs being blocked from reaching the PFC, or by the inputs being changed in some context-dependent way, because the stimulus axes and the stimulus signals (motion and colour) on those axes remained remarkably constant across the two contexts. Yet, somehow, the decision signal was driven by the motion signal in the motion context, and by the colour signal in the colour context.

To investigate how the switch in response to the different contexts came about, Mante *et al.* used modelling. They took model neurons with nonlinear input–output functions, and densely connected them in a recurrent network. They provided the network with inputs

representing the motion and colour signals and, separately, the current context signal. The activity of one of the model neurons was used to indicate the decision of the network.

The team then 'trained' the network by finding the strengths of the neuronal connections required to produce the appropriate, context-dependent decision in each trial. Starting the training from different initial random connection strengths led to different connection patterns that solved the problem. But cutting-edge analyses of how the model networks were solving the problem revealed that all the solutions shared two dynamical principles.

First, a line of closely spaced, stable, fixed points lay along the decision axis, with the two possible outcomes at opposite ends of the line. During each trial, stimulus-driven evidence for or against a decision accumulated along that line by gradually nudging the system from one fixed point to the next. Second, in dynamical systems, some inputs can cause a long-lasting perturbation in the system's trajectory, whereas other inputs can be short-lived, and rapidly decay away. In Mante and co-workers' model networks, the critical feature that depended on context was which of the inputs was short-lived. In the colour context, for example, signals from the irrelevant input (motion) were rapidly quenched and had no lasting impact on the neural trajectory, whereas colour signals persisted to drive the decision (Fig. 1c).

In other words, the context dependence was not achieved by controlling or gating the flow of information from one neuronal population to another. Instead, it was achieved within a single, densely interconnected cell population by controlling the directions along which the population dynamics quenched the neural activity. This dynamical principle can only be

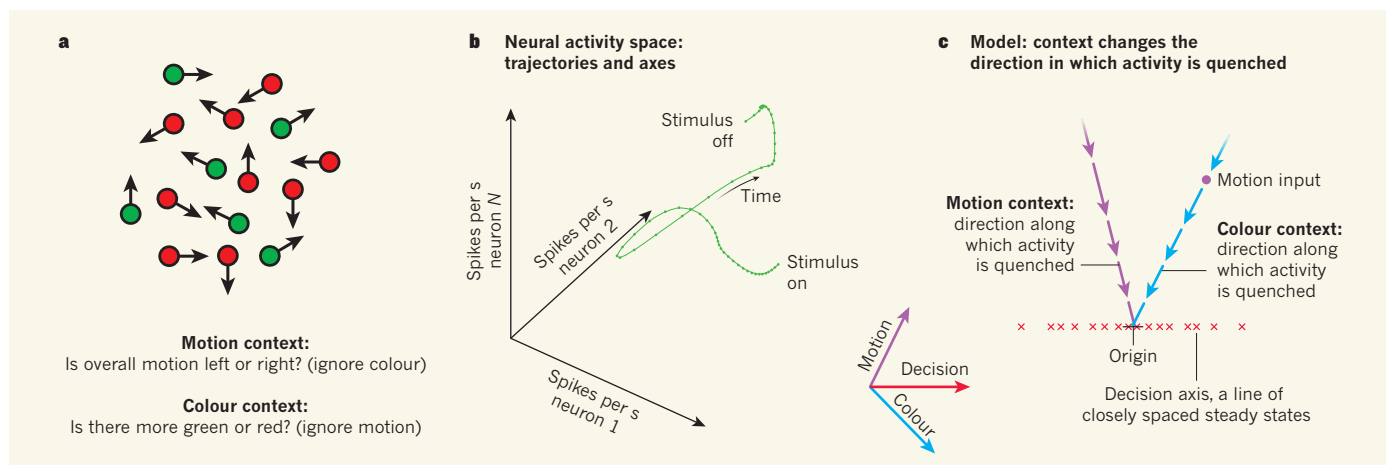


Figure 1 | The experiment and its results. **a**, Schematic view of the visual stimulus used by Mante *et al.*¹² in their study and the context-dependent decision their subjects had to make on each trial. **b**, In the neural activity space, each dimension corresponds to the activity of one recorded neuron. Together they give rise to the dynamical trajectory followed by the neuronal population in response to a particular stimulus (green). The thick coloured arrows illustrate the motion, colour and decision axes. **c**, Dynamical principle for context-dependent feature selection. In the colour context,

one of the directions in neural space along which activity is quenched points in the same direction as the motion-input axis. Motion signals therefore decay rapidly in the colour context. In the motion context, the rapidly quenched direction points elsewhere, allowing the motion input to nudge the system from one fixed point to the next along the decision axis (red crosses), driving the decision. Neither the stimulus inputs nor the decision axes change across the two contexts; only the quenching direction changes.

understood — in fact, only exists — at the population level. And because the neural trajectories in the model closely resembled the neural trajectories in the data, Mante *et al.* propose this principle as the neural basis of flexible, context-dependent processing.

This fascinating study raises some intriguing questions. First, how do we go beyond correlations and causally test the authors' proposed principle? With existing perturbation methods, we cannot align manipulations with the critical axes that define the population's dynamical behaviour. Second, is the region of PFC that the authors recorded from even necessary for the context-dependent behaviour investigated here? The behavioural task used is new, so this question has never been addressed. Third, the conclusions on the behaviour of neural populations are based on data from many separate single-neuron recordings. Will the same principles hold when multi-neuron recordings are used to directly see the population neural trajectories in single trials? Finally, what is the specific mechanism that the network uses to change its quenching directions? These questions aside, Mante *et al.* have led the field with novel and deep ideas that should drive much discussion and thinking. ■

Jeffrey C. Erlich and Carlos D. Brody are at the Princeton Neuroscience Institute and Department of Molecular Biology, Princeton University, Princeton, New Jersey 08544, USA. C.D.B. is also at the Howard Hughes Medical Institute.
e-mail: brody@princeton.edu

1. Pfeiffer, B. E. & Foster, D. J. *Nature* **497**, 74–79 (2013).
2. Dombeck, D. A., Khabbazi, A. N., Collman, F., Adelman, T. L. & Tank, D. W. *Neuron* **56**, 43–57 (2007).
3. Yu, B. M. *et al.* *J. Neurophysiol.* **102**, 614–635 (2009).
4. Goldman, M. S. *Neuron* **61**, 621–634 (2009).
5. Laurent, G. *Nature Rev. Neurosci.* **3**, 884–895 (2002).
6. Briggman, K. L., Abarbanel, H. D. I. & Kristan, W. B. Jr *Science* **307**, 896–901 (2005).
7. Machens, C. K., Romo, R. & Brody, C. D. *J. Neurosci.* **30**, 350–360 (2010).
8. Harvey, C. D., Coen, P. & Tank, D. W. *Nature* **484**, 62–68 (2012).
9. Churchland, M. M. *et al.* *Nature* **487**, 51–56 (2012).
10. Shenoy, K. V., Sahani, M. & Churchland, M. M. *Annu. Rev. Neurosci.* **36**, 337–359 (2013).
11. Rigotti, M. *et al.* *Nature* **497**, 585–590 (2013).
12. Mante, V., Sussillo, D., Shenoy, K. V. & Newsome, W. T. *Nature* **503**, 78–84 (2013).
13. Miller, E. K. & Cohen, J. D. *Annu. Rev. Neurosci.* **24**, 167–202 (2001).
14. Roy, J. E., Riesenhuber, M., Poggio, T. & Miller, E. K. *J. Neurosci.* **30**, 8519–8528 (2010).
15. Clark, K. L., Noudoost, B. & Moore, T. J. *J. Neurosci.* **32**, 10907–10914 (2012).

CLIMATE SCIENCE

Uncertain then, irrelevant now

Uncertainty in estimates of the effects of aerosols on climate stems from poor knowledge of the past, pristine atmosphere — so getting a better understanding of these effects might not be as useful as was thought. [SEE ARTICLE P.67](#)

BJORN STEVENS

Aerosol particles in the atmosphere have long been feared to be the joker in the climate system's pack of cards. Even before the greenhouse effect became a household word, scientists had begun to consider the possibility that increasing concentrations of particles in the atmosphere's lowest layer (the troposphere) were acting to cool the planet, and thus masking what would otherwise be much larger temperature changes caused by rising concentrations of atmospheric carbon dioxide¹. Reporting on page 67 of this issue, Carslaw *et al.*² use an innovative approach to demonstrate that most of the uncertainty in estimates of aerosol forcing — the aerosol perturbation caused by humans that induces a global surface-temperature change — that is associated with cloud-affecting aerosols can be attributed to uncertainty in the emission rate of aerosol precursors from natural sources.

Their work suggests that, if there is an aerosol joker, it was probably played a century ago, and has become irrelevant to understanding present and future changes in global climate.

The aerosol, like the Earth system itself, is fascinatingly complex. How it interacts with clouds and radiation depends not only on its composition and concentration, but also on how these properties are distributed across particles of different sizes. All of these factors depend on uncertain microphysical processes and poorly understood aerosol sources, which in turn are integrated by the vagaries of the wind. Consequently, estimates of the strength of aerosol forcing derived from models that attempt to represent these poorly understood factors are controversial³. Carslaw *et al.* had the brilliant insight to recognize that something could be learned from this uncertainty.

Using a comprehensive model of global aerosols to train a simple statistical model, the researchers characterized the 28-dimensional

uncertainty landscape of the comprehensive model. By exploring this landscape, they find that poorly constrained natural sources determine the state of the pristine atmosphere, and thus dominate uncertainty in estimates of radiative forcing associated with aerosol–cloud interactions. Their findings aid the interpretation of earlier studies in which seemingly large differences in aerosol forcing have been found to be associated with relatively small changes in rather arbitrary parameters — such as the minimum number of cloud droplets permitted in a model of a cloud⁴. Carslaw and colleagues' work suggests that these parameters essentially act as a proxy for the state of the pristine atmosphere.

The disproportionate sensitivity of aerosol forcing to the background state of the pristine atmosphere suggests that the present, far-from-pristine atmosphere should be quite well buffered against further changes in sources of tropospheric aerosols. Consistent with this line of thinking, the authors used their model to show that the aerosol forcing from an important class of aerosol–cloud interaction has not changed for more than 30 years, a period that has witnessed a massive increase in the footprint of human influence on Earth and its atmosphere. Aerosol forcing is thus so well buffered that it has probably ceased to be relevant for present and future global climate changes.

Because aerosol forcing tends to plateau as aerosol concentrations rise, climate sensitivity — the change in the globally averaged temperature that accompanies a doubling of atmospheric CO₂ concentration — is better constrained from observations of the more recent past (for which changes in CO₂ forcing dominate; Fig. 1) than by referencing a distant, pre-industrial era whose atmospheric aerosol burden, Carslaw *et al.* argue, might well be unknowable. An analysis⁵ of observations over this more recent past, which discounts past uncertainty in aerosol forcing and exploits our better understanding of other elements of Earth's energy budget, such as average ocean heating rates, suggests that a surprisingly large climate sensitivity is not being masked by a large effect of aerosols, as was initially feared¹.

Because changes in tropospheric aerosols are localized near their sources, the above arguments do not rule out the possibility that anthropogenic emissions cause large regional effects. But if one follows the logic of Carslaw and co-workers' findings, such effects will also have been most evident in the more distant past — particularly for a scenario in which natural emissions of aerosol

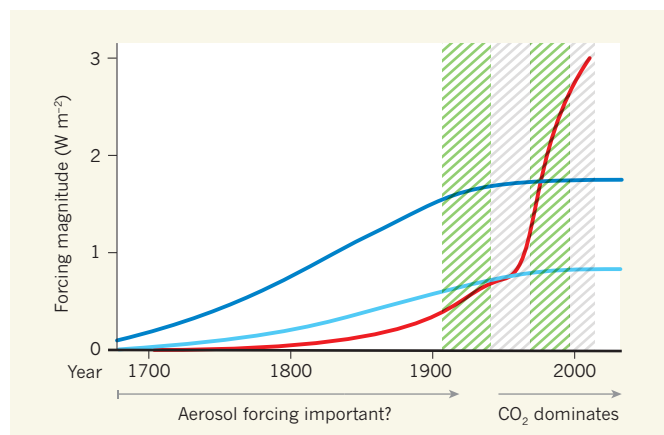


Figure 1 | Climate forcing by tropospheric aerosols and carbon dioxide.

The dark blue line represents the magnitude of the cooling effect from a tropospheric aerosol-forcing scenario in which a pristine natural atmosphere is strongly susceptible to perturbation by anthropogenic aerosol sources produced before the twentieth century. The light blue line depicts a scenario in which stronger natural sources of aerosols render the atmosphere less susceptible to human perturbations. The red line indicates the magnitude of the warming effect from forcing caused by changes in CO₂ and other long-lived greenhouse-gas levels. Shaded bands represent the more complex pattern of global warming over the past century (green, strong warming; grey, modest warming). Carslaw *et al.*² report that aerosol forcing has hardly changed since 1980, and so forcing has been dominated by CO₂ changes over the past 33 years. (Curves adapted from data in refs 2 and 5.)

precursors are low, thus making the pristine atmosphere especially susceptible to perturbations in aerosols and their precursors (Fig. 1). In fact, there is surprisingly little evidence of changing weather patterns attributable to large alterations in regional air quality over North America and Europe in the past. But more effort should be devoted to identifying a smoking gun for regional effects of aerosols in historical records, for instance through a systematic study of temperature changes in the twentieth century. In the absence of a

clear signal from the past, it seems reasonable to assume that the climatic effect of future changes in aerosol emissions, even on a regional scale, will not be large.

But the ultimate lesson to be drawn from Carslaw and colleagues' research, and from other studies^{6–10} published this year, is that a lack of understanding of basic processes — such as how patterns of cloudiness and large-scale atmospheric, or oceanic, circulation respond to warming — is limiting progress in quantifying present and future changes in Earth's climate. Only by refocusing research on these basic processes does climate science stand a chance of remaining relevant to a public that is grappling to understand the pace and pattern of climate change. ■

Bjorn Stevens is at the Max Planck Institute for Meteorology, KlimaCampus, Hamburg 20146, Germany.
e-mail: bjorn.stevens@mpimet.mpg.de

1. Charlson, R. J. *et al.* *Science* **255**, 423–430 (1992).
2. Carslaw, K. S. *et al.* *Nature* **503**, 67–71 (2013).
3. Stevens, B. & Boucher, O. *Nature* **490**, 40–41 (2012).
4. Hoose, C. *et al.* *Geophys. Res. Lett.* **36**, L12807 (2009).
5. Bengtsson, L. & Schwartz, S. E. *Tellus B* **65**, 21533 (2013).
6. Bony, S. *et al.* *Nature Geosci.* **6**, 447–451 (2013).
7. Kosaka, Y. & Xie, S.-P. *Nature* **501**, 403–407 (2013).
8. Stevens, B. & Bony, S. *Science* **340**, 1053–1054 (2013).
9. Zhang, R. *et al.* *J. Atmos. Sci.* **70**, 1135–1144 (2013).
10. Meehl, G. A., Hu, A., Arblaster, J. M., Fasullo, J. & Trenberth, K. E. *J. Clim.* **26**, 7298–7310 (2013).

PSYCHOLOGY

Good and bad news on the adolescent brain

In response to bad news about risk, young adolescents alter estimates of their own vulnerability to adverse events less accurately than older people. The finding has implications for managing risk-taking behaviour in young people.

VALERIE F. REYNA

Winston Churchill once referred to Russia as “a riddle wrapped in a mystery inside an enigma”. Adolescence could be described in the same way. Adolescents are at the peak of physical robustness, yet they are also at an elevated risk of death, injury and disease. Much of this

increased mortality and morbidity has been blamed on risky decision-making processes performed by a still-maturing brain¹. Massive public-health campaigns and educational efforts have been aimed at reducing unhealthy risk taking, and have generally focused on exposing adolescents to information about the adverse health consequences of risky behaviours. Writing in *Proceedings of the National*

Academy of Sciences, Moutsiana *et al.*² present a study that raises questions about how effective all of this 'bad news' is in teaching adolescents to update their risk estimates.

Previous research has shown that adults are more likely to incorporate good news than bad news into their beliefs. For example, news that a genetic mutation places them at lower risk of cancer than they thought is more likely to alter an adult's belief about his or her cancer risk than is news of a mutation that puts them at higher risk. Moutsiana and colleagues have now examined this process of belief updating in response to good and bad news in individuals aged from 9 to 26 years, a period during which the brain is maturing. The participants were presented with 40 adverse events and asked for their estimates of personal risk — how likely (as a percentage) the event was to happen to them in the future. Then, the actual likelihood was presented and, in a second session a few moments later, they re-estimated their personal risk of the same events (Fig. 1).

The researchers found that updating beliefs about risk did not change significantly with age for good news (when participants were at a lower risk of an adverse event than they thought). But information about being at a higher risk — bad news — was correlated with age, such that beliefs were not sufficiently updated in younger participants. The gap between learning from good versus bad news narrowed with age. The authors controlled statistically for a host of alternative explanations for these age differences, including prior beliefs and past experience with the events. They also ensured that the youngest respondents understood the concept of percentages and that none of the respondents was depressed, which could have produced differences in responses to negative events.

In the brain, dopaminergic neurons are activated in response to outcomes such as rewards; in particular, they signal the discrepancy between expected and actual rewards — referred to as prediction-error signals. Moutsiana *et al.* argue that the good–bad differences they document originate in an asymmetry in the development of dopaminergic responses to prediction-error signals. In fact, hyper-responses to rewards in the striatum region of the brain (a rewards area) peak during adolescence³, although some research suggests⁴ that adolescents are hyporesponsive to rewards. By contrast, activity in the brain's prefrontal cortex region (a cognitive-control area), specifically the inferior frontal gyrus, is associated with updating beliefs to negative errors in this estimation task.

Moutsiana *et al.* also recorded an important developmental difference in individuals' memories of the presented risk information, assessed by asking the participants the presented actual probability at the end of the sessions. They found that misremembering



Figure 1 | Adverse events. Moutsiana *et al.*² studied how adolescents' estimates of their own risk of experiencing an adverse event, such as a broken bone, changed in response to information about their actual risk.

was related to age for both good and bad news, with younger participants remembering less accurately. Furthermore, memory for risks correlated with updating of risk estimates across the age range. Nevertheless, although such memory differences influence risk perception and behaviour⁵, they do not explain the good–bad differences observed in this study.

Much of the research on adolescent risk taking, including this study, is steeped in theories of neo-Freudian dualism, in which the prefrontal cortex (Sigmund Freud's 'super-ego') suppresses the urges of an instinctual limbic system (the 'id'). But this latest work highlights the often-neglected issue of learning. In an earlier generation of research, learning was the centrepiece of psychology — generally speaking, to be a psychologist was to be a learning theorist. Learning also offered the hope of change, by definition, because learning involves an alteration in knowledge or beliefs.

Current theories of the adolescent brain rightly emphasize socio-emotional development⁶, but one lesson from Moutsiana and colleagues' study is that cognitive and motivational changes from childhood to adulthood are intertwined. Learning, which is a cognitive faculty, occurs for positive and negative information, but it occurs differently depending on motivational salience (people are more motivated to believe good news than bad news).

This work opens the door to many questions about risk perceptions and their effect on behaviour. Like many others in the field of risky decision-making, this study extracts numerical risk estimates from participants and provides them with other such estimates. How do we know that a person understands his or her personal risk? We ask them to parrot a probability. Although there are advantages to this method (for example, it permits intriguing analyses of calibration and updating), it

ignores a basic psychological truth about risk estimates: that the estimates used by people in the real world to guide their behaviour are mentally represented not as precise quantities but as qualitative gists, such as 'a really high risk'⁷. Researchers in medical decision-making and public health have come to realize that simply remembering and repeating a number verbatim does not capture how most people represent risk in their minds and brains^{8–10}.

Moutsiana and colleagues' exciting findings highlight the related concept of the emotional gist of risk information, which is likely to colour intuitions about risk differently across the lifespan¹¹. The riddle of adolescent risk taking may not be solved any time soon, but we are seeing a great leap in scientific knowledge about this topic, with broad implications for enhancing public health and well-being. ■

Valerie F. Reyna is at the Human Neuroscience Institute, Cornell University, Ithaca, New York 14850, USA.
e-mail: vr53@cornell.edu

1. Reyna, V. F. *et al.* *J. Exp. Psychol. Learn.* **37**, 1125–1142 (2011).
2. Moutsiana, C. *et al.* *Proc. Natl Acad. Sci. USA* **110**, 16396–16401 (2013).
3. Casey, B. J. *et al.* *Proc. Natl Acad. Sci. USA* **108**, 14998–15003 (2011).
4. Bjork, J. M. *et al.* *J. Neurosci.* **24**, 1793–1802 (2004).
5. Mills, B., Reyna, V. F. & Estrada, S. *Psychol. Sci.* **19**, 429–433 (2008).
6. Strang, N. M., Chein, J. M. & Steinberg, L. *Front. Hum. Neurosci.* **7**, 223 (2013).
7. Reyna, V. F. *Med. Decis. Making* **28**, 850–865 (2008).
8. Peters, E. *Curr. Dir. Psychol. Sci.* **21**, 31–35 (2012).
9. Reyna, V. F. & Huettel, S. A. in *The Neuroscience of Risky Decision Making* (eds Reyna, V. F. & Zayas, V.) 11–42 (Am. Psychol. Assoc., in the press).
10. Zikmund-Fisher, B. J. *Med. Care Res. Rev.* **70**, 37S–49S (2013).
11. Tymula, A. *et al.* *Proc. Natl Acad. Sci. USA* **109**, 17135–17140 (2012).

This article was published online on 30 October 2013.

Cortical connectivity and sensory coding

Kenneth D. Harris^{1,2} & Thomas D. Mrsic-Flogel^{2,3}

The sensory cortex contains a wide array of neuronal types, which are connected together into complex but partially stereotyped circuits. Sensory stimuli trigger cascades of electrical activity through these circuits, causing specific features of sensory scenes to be encoded in the firing patterns of cortical populations. Recent research is beginning to reveal how the connectivity of individual neurons relates to the sensory features they encode, how differences in the connectivity patterns of different cortical cell classes enable them to encode information using different strategies, and how feedback connections from higher-order cortex allow sensory information to be integrated with behavioural context.

Our senses are constantly bombarded with a vast amount of information. To guide behaviour, the brain must extract and amplify a relatively small number of features from this massive input; for example, features corresponding to the nature and location of objects in the world. In mammals, the cerebral cortex has a central role in this process. The cortex contains multiple hierarchically arranged areas devoted to each modality. Neuronal populations in these areas extract features of sensory scenes and integrate them with non-sensory cognitive and behavioural variables, in a progressively abstract manner¹. Each sensory stimulus causes a complex pattern of activity in the neuronal populations of multiple cortical areas. The relationship between sensory stimuli, and the firing patterns they evoke, defines the ‘neural code’ of the corresponding populations.

Each cortical area contains a richly interconnected array of diverse cell types, whose patterns of connectivity underlie the cortex’s ability to extract sensory features. The circuits of different cortical regions and species share striking commonalities in their constituent cell types, their intrinsic properties, and the incidence and properties of synaptic connections between them^{2,3}. Connections between cortex and other brain structures, and connections between cortical regions, also show a largely preserved relationship to cortical cell classes. These similarities suggest that there may be a set of general principles linking the common characteristics of cortical circuitry to the nature of cortical processing in multiple areas.

If such common principles exist, they are unlikely to describe which sensory features are encoded in particular cortical areas, but rather how these features are encoded. Cortical neurons detect complex and non-linear features from sensory scenes, whose precise character will obviously differ between sensory modalities. Nevertheless, there are notable commonalities in the strategies with which populations of different cortical areas encode diverse types of information, and in how these strategies differ between neuronal subtypes. An understanding of these strategies in turn enables us to consider why cortex might be organized in this way; for example, why the coding strategies used by each cell class are appropriate to their particular role in the circuit and their particular synaptic targets.

In recent years there has been a great acceleration in progress towards answering these questions, enabled by a number of newly developed experimental techniques. Advances in mouse genetics have provided tools to classify, identify and manipulate different classes of cortical neuron^{4–6}. Optical and electrical techniques now allow scientists to simultaneously record the activity of large numbers of neurons in the living brain^{7,8}. Advances in circuit mapping techniques allow neuronal

connections to be reliably identified^{9–11}. Optogenetic techniques allow scientists to control neuronal activity with high temporal resolution using light-gated proteins¹². Most importantly, recent studies have begun to apply these techniques in combination, directly relating cortical circuitry to sensory coding. Here we review some of the insights recently made with these techniques, with a specific focus on the visual, auditory and somatosensory cortices of rodents.

The organization of cortical connectivity

Cortical neurons divide into two major classes. Principal cells are neurons that use the excitatory neurotransmitter glutamate. Usually pyramidal in shape, these cells respond selectively to specific features of sensory stimuli, and contact local and distant targets through extensive axonal projections. Principal cells comprise approximately 80% of cortical neurons in rodents, and fall into multiple classes distributed across and within cortical layers (Box 1). The remaining approximately 20% are interneurons that release the inhibitory neurotransmitter GABA and make mostly local connections (Box 2). Both principal cells and interneurons comprise multiple subclasses, whose classification is an active area of research.

The probability of connection between two neurons, and the physiological properties of the corresponding synapses, depends on the pre- and postsynaptic cell types (Boxes 1 and 2). Connectivity within a single cell class is also highly structured. Analysis of connections between principal cells reveals an overrepresentation of bidirectional connections between pairs, and of mutual interconnection motifs in larger sets of neurons^{13,14} (although this was not seen in ref. 15). Such non-uniform connectivity occurs both within and between layers, with principal cells more likely to exhibit reciprocal connections if they receive common intra- or inter-laminar input^{16,17}. These data suggest that each cortical area contains multiple interdigitated subnetworks of highly interconnected principal cells (Fig. 1). Note that although motifs such as bidirectional connections can occur several times more frequently than expected by chance, they do not occur with a probability of 1. This suggests that the subnetworks are not discrete: not every pair of neurons within a subnetwork is connected, and each principal cell can belong to multiple subnetworks. Unlike principal cell–principal cell connectivity, connectivity between principal cells and at least some interneuron classes seems to be nonspecific. Although interneurons can show precise targeting of connections to specific cell classes and subcellular locations, their connection probability to neighbouring principal cells is close to 100%, at least for parvalbumin- and somatostatin-expressing interneurons^{18,19}.

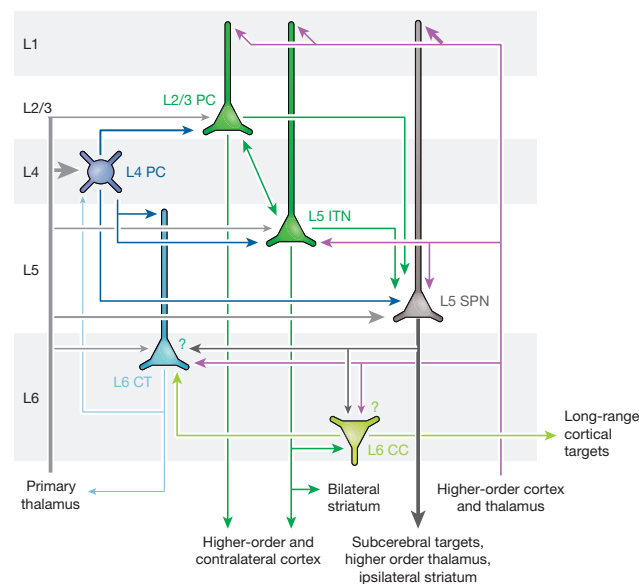
¹UCL Institute of Neurology, Queen Square, London WC1N 3BG, UK. ²UCL Department of Neuroscience, Physiology and Pharmacology, 21 University Street, London WC1E 6DE, UK. ³Biozentrum, University of Basel, Klingelbergstrasse 50/70, CH - 4056 Basel, Switzerland.

BOX 1

Canonical connectivity of cortical principal cells

Sensory information arrives from primary thalamus into all cortical layers, but most densely into L4 and the L5–L6 border^{9,54,95}. Contextual inputs from higher-order cortex and thalamus most densely target L1, L5 and L6, but avoid L4 (refs 2, 9). These inputs are integrated by a diverse array of cortical cell types. The figure shows a current understanding of the connectivity between the major principal cell classes of sensory cortex. Line thickness represents the strength of a pathway; question marks indicate connections that appear likely but have not yet been directly demonstrated.

L4 principal cells comprise two morphological classes, pyramidal and spiny stellate cells, whose intrinsic properties and coding strategies appear largely similar⁹⁶. The architecture of L4 varies between species and modalities, which may reflect its developmental shaping by thalamic innervation and activity^{97,98} in which the L4-specific gene *Rorb* has been implicated⁹⁹. L4 principal cells project to all layers, but most strongly L2/3. However they receive little intracolumnar input in return, as evidenced both by paired recording



studies^{2,15}, and the fact that optogenetic stimulation of L2/3 has little effect on L4 (ref. 46).

L2/3 principal cells are often considered homogeneous, but comprise as-yet incompletely classified subtypes, with different patterns of axonal targets, gene expression, and *in vivo* firing patterns^{100,101}. Their major outputs are to higher order and contralateral cortices, as well as locally to L5.

L5 principal cells comprise two broad subclasses, whose fate is developmentally determined by suppressive interactions between the genes *Satb2*, *Fezf2* and *Ctip2* (ref. 102). 'Intratelencephalic neurons' (ITNs) are often found in upper L5 (ref. 103), and fire adapting spike trains at moderate rates. They project locally upward to L2/3 and distally to the ipsi- and contralateral cortex and striatum, but not to targets outside the telencephalon. 'Subcerebral projection neurons' (SPNs) are larger cells with prominent dendritic tufts in L1 and a periodic spatial organization¹⁰⁴. SPNs show little spike train adaptation, and under some—but not all—conditions fire in bursts¹⁰⁵. SPNs receive prolific inputs from multiple cortical cell classes, whose development depends on Shh signalling¹⁰⁶. However, they give little local output in return⁵², therefore exhibiting the inverse connectivity pattern to L4 principal cells. SPNs of even primary sensory cortices project to subcerebral motor centres, and can directly drive movements¹⁰⁷. Their axons send collaterals to ipsilateral striatum and higher-order thalamus with large, strong 'driver' synapses^{108,109}. Together, these characteristics define a class of neuron that accumulates information from an entire cortical column, and broadcasts sustained, powerful outputs to distant targets.

L6 principal cells comprise at least two subclasses with distinct molecular identities and projection targets¹¹⁰, whose fate is partially determined by the gene *Tbr1* (ref. 102). Corticocortical cells (CCs) have small dendritic trees, long-range horizontal axons, and occasionally bizarre morphologies such as inverted somata¹¹¹. Corticothalamic cells (CTs) send projections to thalamus which, unlike those of L5 SPNs, are weak, target the reticular and primary sensory thalamic nuclei¹⁰⁸, and travel through slowly conducting fibres (as low as 0.5 m s⁻¹ in rabbit)⁵⁰. Corticothalamic cells also project to cortical layer 4, where they strongly target interneurons¹¹¹, as well as hyperpolarizing principal cells via group II mGluRs¹¹². Consistent with this connectivity, optogenetic stimulation of L6 *in vivo* suppresses cortical activity, suggesting a role of this layer in gain control or translaminar inhibition¹¹³.

Functional specificity of excitatory subnetworks

Synaptically connected principal cells tend to process similar types of information. In mouse visual cortex, the connection probability between nearby superficial principal cells is higher for neurons that respond to similar visual features²⁰. Connection probability is elevated for neurons sharing the same orientation preference, but is higher still for neurons responding similarly to natural movies. This suggests that connection probability mirrors similarities in the complex and as-yet poorly understood feature combinations extracted by visual cortical neurons. The relationship between connectivity and sensory tuning is preferential but not exclusive: not all neurons that respond to similar features are connected, and not all connected neurons respond to identical features. This indicates that the neuronal populations that respond to different sensory features are not discrete and disconnected from each other, but interconnected and overlapping. Consistent with functionally specific recurrent connectivity, whole-cell recordings *in vivo* indicate that the excitation principal cells receive from their cortical neighbours is tuned similarly to their direct thalamic input, at least with regard to simple features such as visual orientation and sound frequency^{21–24}. Functionally

specific principal cell connectivity may be a general feature of at least visual cortex, as long-range horizontal excitatory projections in carnivores are also biased towards neurons with similar stimulus preferences²⁵. In contrast to principal cells, local excitatory connections onto interneurons (at least, onto parvalbumin-expressing interneurons) seem unrelated to feature preference^{10,26}.

These data suggest that the interconnected subnetworks postulated in the previous section consist of neurons that are largely, but not exclusively, tuned for similar sensory features. This organization may provide several benefits. First, recurrent excitation amplifies cortical responses^{21–24,27}. By reinforcing thalamic inputs, recurrent excitation can increase the spiking probability of individual neurons, and increase the number of neurons responding to a given stimulus. This will reduce susceptibility to noise and boost the efficiency with which they can drive downstream targets. Second, recurrent excitation prolongs sensory responses^{21–24}. This will again boost the efficacy of sensory responses, and may allow responses to brief stimuli to be maintained for long enough to interact with subsequent sensory inputs as well as later-arriving feedback from higher-order regions. Third, recurrent excitation may allow for

BOX 2

Classes of inhibitory interneuron

The cortex contains three major families of interneuron, each of which divides into multiple subclasses. The figure shows a current understanding of the synaptic targets of five classes of cortical interneuron, with the green neuron representing a principal cell. Question marks indicate connections that appear likely but have not yet been directly demonstrated.

Parvalbumin-expressing interneurons (PVs) are capable of firing rapidly and with high temporal precision. They consist of two main subgroups: basket cells (BCs) that target the soma and proximal dendrites of principal cells, and chandelier cells (ChCs) that target the axon initial segment. PV cells receive strong excitatory inputs from thalamus and cortex¹¹⁴, as well as inhibition from other PVs¹¹⁵. A key role of these cells is to stabilize the activity of cortical networks: their absence leads to epileptiform activity, whereas more moderate chronic dysfunction of these cells has been implicated in diseases such as schizophrenia¹¹⁶.

Somatostatin-expressing interneurons (SOMs) consist largely, but not exclusively, of Martinotti cells that target the tuft dendrites of principal cells, as well as inhibiting other interneurons^{115,117}. Consistent with their targeting of dendritic tufts, these cells have been implicated in behaviour-dependent control of dendritic integration^{88,118}, as well as in more general lateral inhibition⁴⁷. Connections from principal cells to SOMs show facilitating synapses^{119,120}, whose establishment depends on postsynaptic expression of the cell-surface protein Elnf1 (ref. 121). In contrast to PVs, SOMs receive the majority of their input from local principal cells but little inhibition or thalamic drive^{47,115,117}.

5HT3A-receptor-expressing interneurons are the most numerous interneuron of the superficial layers¹²². Although the classification of these neurons is still incomplete, they contain two prominent subgroups: neurogliaform cells (NGs), which are thought to release GABA by volume transmission¹²³; and cells that express vasoactive intestinal peptide (VIP) and preferentially target SOMs^{89,115}. Putative 5HT3A-receptor-expressing cells have been implicated in learning¹²⁴ and control of cortical circuits by higher-order cortex and thalamus^{89,125}.

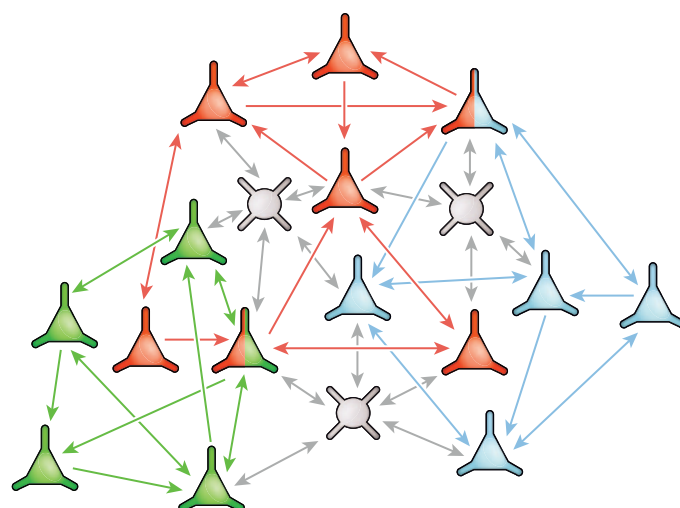
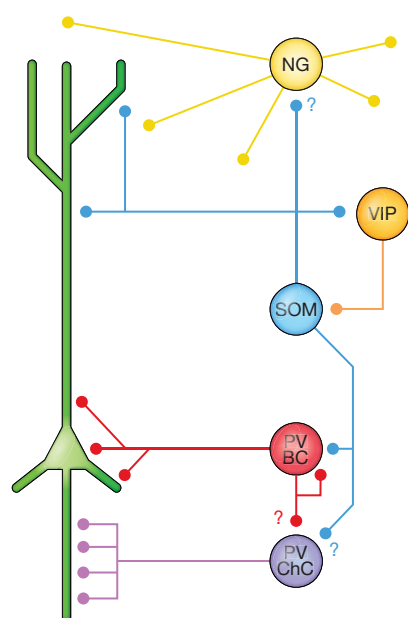


Figure 1 | Proposed fine structure of neocortical connections. Connectivity analyses suggest that cortical circuits contain multiple interdigitated subnetworks of highly interconnected principal cells. Red, blue and green triangles represent principal cells in three subnetworks; arrows of the corresponding colour represent synaptic connections within each subnetwork. Not all cells within a subnetwork are connected, and any cell can belong to more than one subnetwork (striped triangles). Unlike principal cells, parvalbumin-expressing interneurons (grey circles) connect nonspecifically to principal cells in their local area.

more complex feature integration in sensory scenes. Although connection probabilities are elevated between neurons of the same feature preference, substantial connectivity also exists among neurons with different feature preference. If these connections link neurons driven by features whose combination is of particular behavioural relevance (for example, features forming extended visual contours or spectrally complex sounds), recurrent connectivity may allow the subnetwork to specifically amplify responses to these combinations.

Establishment of cortical connectivity patterns

Cortical circuits are wired by a combination of molecular cues and activity-dependent synaptic plasticity. Recent research is beginning to reveal the molecular signals governing the incidence and synaptic properties of connections between specific cell classes (Box 1). However, a key question is what determines the non-uniform connectivity patterns within a principal cell class. The first possibility is that interconnected subnetworks reflect still-undiscovered neuronal subtypes. For example, connection probabilities within the apparently uniform class of callosally projecting layer 5 (L5) principal cells could be predicted by similarity of physiological characteristics¹⁷, suggesting preferential connectivity between cryptic subclasses. Recent work suggests that clonal sister neurons (that is, neurons arising from divisions of a common progenitor cell) are more likely to be synaptically connected and share orientation preference than unrelated cells²⁸. A single progenitor can give rise to preferentially connected principal cells of multiple subclasses, suggesting that early developmental processes beyond subclass specification contribute to wiring intracortical circuits. Transient electrical synapses between clonal sisters before eye opening have been implicated in this process²⁹.

These early developmental processes, however, seem to simply provide a starting point for activity-dependent refinement of cortical circuitry after the onset of sensory experience. Indeed, studies in superficial visual cortex suggest the relationship between principal cell connectivity and visual feature preference is weak at eye-opening, only becoming strong after visual experience, which suggests that sensory input leads to the formation of functionally specific subnetworks³⁰. An intuitive argument suggests that Hebbian plasticity—strengthening of connections between principal cells that fire together—should lead to interconnected subnetworks of cells tuned to similar or commonly co-occurring features;

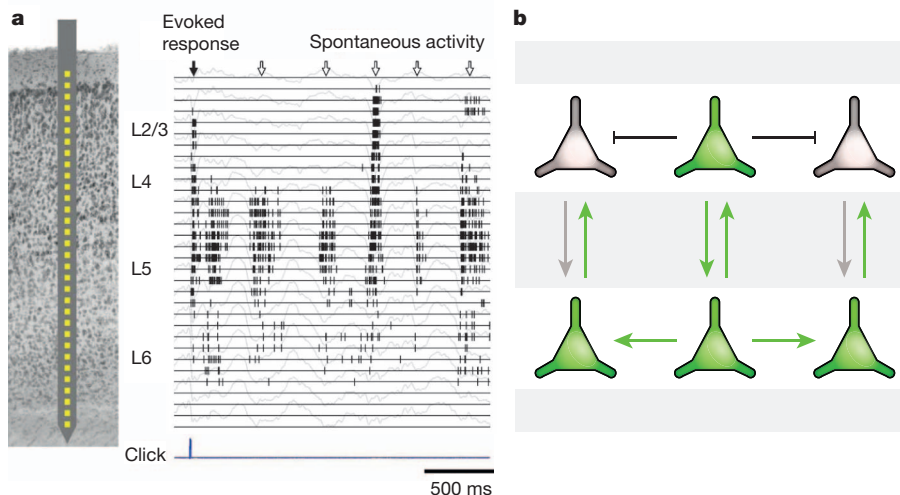


Figure 2 | Coding strategies of different cortical layers. **a**, Cortical activity is sparse in superficial layers but dense in deep layers. Left, inferred location of a multisite electrode in rat auditory cortex, with recording sites indicated by yellow squares. Right, raster plot of activity, with tick marks indicating spike times of simultaneously recorded neurons at the corresponding cortical depths. **b**, Cell-type-specific coding may result from stronger inhibition in superficial and stronger excitation in deep layers. Green-filled triangles represent active neurons; empty triangles represent silent neurons. Arrows represent net excitation, thick black lines represent net inhibition. Part **a** is adapted from ref. 40.

indeed, this is the essence of Hebb's original 'cell assembly' hypothesis³¹. Understanding how more complex cortical plasticity processes sculpt cortical networks to detect salient sensory features, is an important topic of research in computational and experimental neuroscience^{30,32–35}.

Coding strategies differ between cell classes

Different cortical cell classes encode information differently. The major difference is not in what information is encoded (for example, preference for a particular sensory feature), but in the manner in which it is encoded. The best-understood difference in coding strategy between cell classes is in their 'sparseness'. For neuronal classes employing a 'sparse code', information is encoded at any instant by the spiking of a small subset of cells within the population. At the other end of the spectrum (a 'dense code'), most neurons are active at any moment, with information encoded by variations in their firing rates. Sparse coding is typically associated with low mean firing rates and high selectivity of individual neurons for sensory features, although in principle this association is not absolute³⁶. Sparse codes are considered efficient, because they are able to transfer information with fewer spikes³⁷. In addition, sparse codes may also increase information storage capacity at the level of neuronal populations, because of a smaller overlap in representations for different stimuli³⁸. However, sparse coding imposes a different type of cost, as the large number of neurons required to support sparse codes must occupy a significant spatial volume. This cost would be particularly acute for physically larger neurons, such as those that must support long-range axonal projections.

Principal cells

Recordings in multiple modalities indicate that L2/3 principal cells encode information sparsely (Fig. 2a). L2/3 principal cells have low spontaneous and evoked firing rates (usually <1 spike per s in rodents), and respond selectively only to a narrow range of stimulus features^{39–42}. This sparseness is likely to result from a combination of strong, unselective inhibitory connections, and functionally specific excitation. L2/3 contains large numbers of densely connected interneurons⁴³, which provide powerful synaptic inhibition, particularly in awake animals⁴⁴. Both *in vitro* and *in vivo*, optogenetic stimulation of L2/3 principal cells causes predominant inhibition rather than excitation in other L2/3 principal cells^{45–48} (Fig. 2b). Consistent with strong lateral inhibition, recent work suggests that at least in auditory cortex, superficial layer activity *in vivo* is sparse and patchy at a spatial scale of <200 μm ^{40,49}.

In contrast, L5 principal cells—in particular subcerebral projection neurons (SPNs; see Box 1)—encode information densely, firing at relatively high rates (5–15 spikes per s) and responding to a broad range of stimuli in a graded manner^{39–42,50} (Fig. 2a). This firing pattern again mirrors their connectivity, as L5 SPNs integrate thalamic and intracortical

excitatory input from diverse principal cell classes and subnetworks, while receiving weaker inhibition^{9,51–55}. Again consistent with this connectivity, *in vivo* estimates of synaptic currents suggest putative SPNs receive broadly tuned excitatory drive, compared both to the excitation received by other cell classes and to the inhibition they themselves receive^{21,46}. Furthermore, optogenetic stimulation of L5 *in vivo*—unlike stimulation of L2/3—causes self-sustaining activity, consistent with strong recurrent excitation in L5 circuits^{48,56} (Fig. 2b).

By using different coding strategies in different populations, the cortex may have found a way to balance the benefits and costs of sparse coding. We propose that sparse coding in a large number of physically smaller, intracortically projecting neurons (L2/3 principal cells) may allow efficient information storage in local synapses; the use of dense coding in a smaller number of large, long-range projection cells (L5 SPNs) may allow efficient broadcast of the results of cortical computations to distant structures, without requiring excessive physical volume. Thus, the differential coding schemes of L2/3 and L5 principal cells appear tailored for the targets their axons innervate.

Interneurons

The way information is encoded in the cortex's multiple interneuron classes is a topic of active research and some controversy^{26,57–60}. Interneuron activity can be strongly and diversely modulated by non-sensory factors such as ongoing behaviour (see below), but interneurons are also driven by sensory input. Unlike principal cells, interneurons (at least, parvalbumin-expressing interneurons) receive functionally unspecific inputs from nearly every principal cell in the local area^{10,26}. Consistent with this broad connectivity, interneuron sensory tuning seems to approximate the average of the principal cells in their local neighbourhood⁵⁷. As a consequence, even superficial interneurons seem to use a dense coding strategy more similar to deep principal cells than to their superficial principal cell neighbours⁴⁰. However, this coding strategy is intimately related to the way activity is organized across the cortical surface, as discussed below.

Connectivity, coding and cortical maps

One of the most prominent differences in cortical organization between modalities and species is in the spatial mapping of information on the cortical surface. Often, the cortical surface maps the organization of primary receptor surfaces in the sense organs (such as the retinotopic, cochleotopic and somatotopic mapping of visual, auditory and somatosensory cortices). However, when sensory features are mapped in a manner not inherited from the receptor surface, differences between species can be seen. For example, the visual cortices of carnivores and primates, but not rodents, show a functionally organized and periodic arrangement of orientation preference^{61,62} (Fig. 3a). This may be unavoidable in rodents

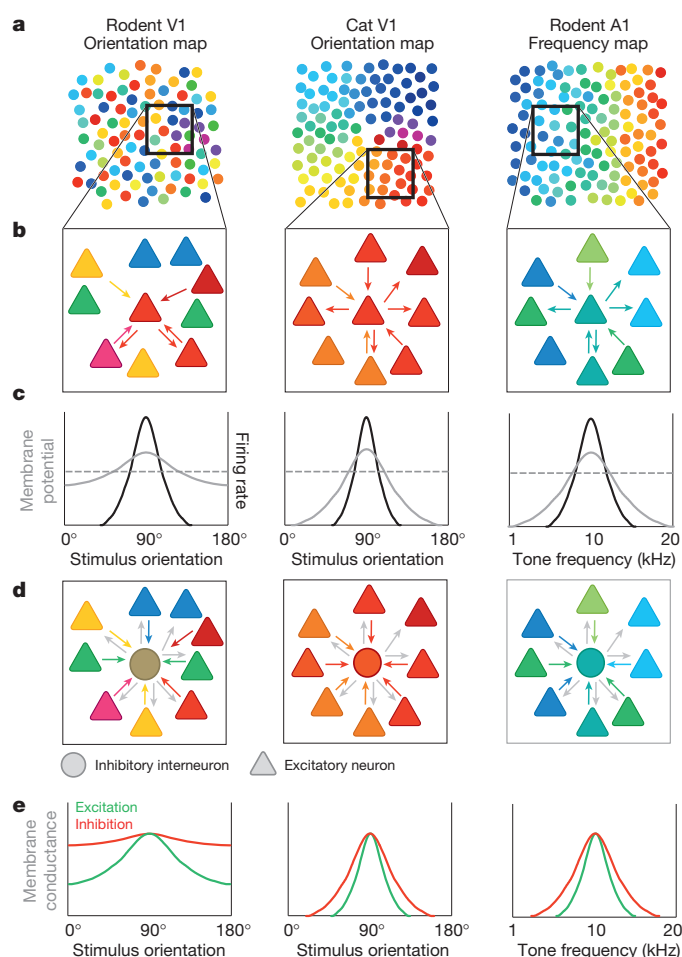


Figure 3 | Proposed relationship between feature mapping and coding in rodent visual cortex, cat visual cortex and rodent auditory cortex. **a**, Non-topographic arrangement of orientation preference in rodent V1 contrasts with spatially contiguous arrangement of orientation preference in cat V1 and of frequency preference in rodent A1. **b**, In all cases, principal cells receive inputs preferentially from neurons with similar feature preference. **c**, Incomplete functional specificity of connections for non-mapped features such as orientation in rodent V1 leads to broader subthreshold tuning. This is converted to sharp tuning of firing output by nonlinear neuronal amplification and synaptic inhibition. **d**, Inhibitory interneurons receive dense and unselective input from all neighbouring neurons. **e**, The inhibitory and excitatory synaptic inputs received by a principal cell are both strongest for the same preferred stimulus, but inhibition is more broadly tuned than excitation, leading to sharpened tuning of spiking output.

given the small size of their visual cortex: if mice had orientation columns similar in size to carnivorans, they would be able to see only one orientation in any part of the visual field.

Differences in cortical maps lead to differences in the tuning of synaptic input for sensory features. Although connections in rodent primary visual cortex (V1) are biased to cells of similar orientation preference, this bias is not complete²⁰ (Fig. 3b). Accordingly, whole-cell recordings in individual neurons show substantial subthreshold depolarization also in response to non-preferred orientations^{22,24,62,63} (Fig. 3c). When features are mapped in a more orderly manner across the cortical surface, such as in iso-orientation domains of carnivoran visual cortex and iso-frequency bands in rodent auditory cortex, subthreshold tuning is sharper^{64–66}, consistent with the dominance of local inputs of similar feature preference (Fig. 3b, c). In carnivoran V1, subthreshold tuning is also broader at ‘pinwheel centres’ (where neighbouring neurons exhibit a diverse range of orientation preferences) than in iso-orientation domains⁶⁴, again reflecting the importance of functional map organization in determining subthreshold tuning.

Despite broad subthreshold tuning, the spiking output of principal cells can still be highly selective for non-mapped features^{62–64}. This seems to reflect a combination of nonlinear neuronal integration, which can convert subtle differences in membrane potential to large differences in spiking⁶⁷, and synaptic inhibition. Consistent with their nonspecific local connectivity, parvalbumin-expressing interneurons are selective for smoothly mapped features such as orientation in cat visual cortex⁶⁸, tone frequency in rodent auditory cortex⁶⁵ and spatial position in rodent visual cortex⁵⁹, but are unselective or broadly tuned for unmapped features such as orientation in mouse V1 (refs 26, 57–59) (Fig. 3d, e). *In vivo* patch-clamp experiments and models suggest that broadly tuned synaptic inhibition has an important role in producing sharp output selectivity for orientation in mouse V1 and in pinwheel centres of carnivoran V1 (refs 64, 69). Thus, selective tuning of excitatory neurons can occur irrespective of whether a stimulus feature is mapped smoothly on the cortical surface, due to functional biases in connectivity, nonlinear neuronal integration, and appropriately tuned inhibition.

These data suggest two hypotheses regarding the relationship between connectivity and coding across areas and species. First, certain features of cortical connectivity appear to be preserved across multiple systems: principal cells receive functionally selective excitatory inputs both locally and from distant regions, while the connectivity of many interneurons is local but nonspecific. Second, although the selectivity of subthreshold responses of principal cells and spiking responses of local interneurons will depend on how a particular stimulus parameter is mapped across the cortical surface, the firing of principal cells—the cortex’s final output—is highly selective even without feature mapping. Indeed, unmapped orientation is found in even highly visual rodents such as squirrels⁶², suggesting mapping is not essential for accurate sensory function.

Redundant coding in cortical populations

Current experimental techniques allow recordings of up to a few hundred neurons simultaneously. One of the most notable findings from these experiments is that cortical population codes are redundant. The firing pattern of a neuronal population can be summarized (to a first approximation) by the subset of neurons that are active at any moment. In principle, the number of potential subsets of even a moderately-sized neural population is vast. In practice however, only a much smaller number of firing patterns can actually occur. The existence of preserved constraints on population activity indicates that cortical coding is redundant, as the firing of any one neuron can be partially inferred from the activity of its peers^{39,49,70}. Redundant coding is found in many other domains: written language is redundant, for example, because only a small fraction of potential letter combinations spell actual words. This redundancy allows words to still be understood if letters are missing or misprinted.

The nature of cortical redundancy can be studied by considering patterns of neuronal correlation. The firing of neighbouring neurons is often correlated, and the structure of correlations in a population is broadly similar when considering the mean responses to different stimuli (‘signal correlations’), the variability of responses to multiple presentations of a single stimulus (‘noise correlations’), as well as activity occurring without sensory stimulation (‘spontaneous correlations’)^{26,70,71}. This preservation of correlation structure suggests that cortical redundancy arises from constraints imposed by cortical wiring. Although individual pairwise correlations are typically weak (approximately <0.1), even weak pairwise correlations indicate strong constraints on the subsets of neurons that may be co-active at the population level⁷².

A natural hypothesis is that the restricted subsets of neurons that can in practice fire together correspond to the interconnected subnetworks suggested by connectivity analyses. Although at present this remains conjecture, several pieces of evidence suggest it may be the case. Correlations are stronger between synaptically connected principal cells²⁰, at least in visual L2/3. These correlations do not reflect the direct driving of one cell by the other, as synaptic connections between principal cells are typically weak (approximately <1 mV)^{15,20}; rather, they indicate that synaptically connected neurons frequently fire together as part of larger

neuronal subsets that provide correlated input to both. Both noise and signal correlations are higher between connected neurons, suggesting a direct relationship between connectivity and the constraints on co-active neuronal subsets²⁰. Finally, the structure of correlations matches that of connectivity patterns across layers and cell classes. For L2/3 principal cells, correlations are typically weak and fall off steeply with anatomical distance^{26,40,49}, consistent with their local and functionally-specific connectivity profiles. Correlations among pairs of fast spiking interneurons and pairs of L5 principal cells are stronger and persist over larger distances^{26,40}, consistent with denser and more widespread connectivity^{26,55}, and therefore larger fractions of shared input.

Another important question is why the cortex might employ redundant coding. Redundant codes are inefficient, in that they require more neurons, more spikes, and thus more energy. Patterns of raw sensory input are redundant: much of the variance in natural image scenes, for example, reflects simple changes of luminance. Eliminating this redundancy seems to be a major function of the early sensory systems^{73,74}, begging the question of why redundancy would be reintroduced in cortex. We suggest two reasons. First, redundant codes are robust. Neuronal activity is noisy; furthermore, long-range neuronal connections are divergent, implying that distal targets receive inputs from only a fraction of the neurons in any given cortical area. Redundant coding allows the noisy output of a small fraction of cells to convey a message close to that encoded by the whole population. Second, cortical redundancy may reflect selective amplification of important sensory features. One might expect the number of neurons used to encode a given feature to match the relevance of that feature for later neuronal processing. The retina might remove redundancy imposed by luminance changes because luminance is not usually behaviourally important; cortex may create new redundancy by allocating large subnetworks to subtle but important sensory features, which thereby gain greater potential control of the animal's behaviour.

Top-down connections and contextual modulation

In the natural environment, animals must combine sensory and non-sensory information in diverse and novel ways according to changing behavioural demands. Neurons of even primary sensory cortex do not just encode sensory input, but integrate it with contextual information such as reward⁷⁵, expectation^{76,77}, attention⁷⁸ and motor action^{79–81}.

Most inputs to primary sensory cortical areas come not from primary thalamus, but from higher-order structures. These 'top-down' inputs can carry detailed information about diverse behavioural and cognitive variables⁸². Top-down inputs project heavily to L1, where they synapse on interneurons, and on the apical tuft dendrites of principal cells. Although distal inputs may not alone drive principal cells to fire, they enable dendritic calcium spikes that increase the gain of a cell's responses to proximal synapses carrying sensory information^{83,84}. By targeting subnetworks encoding sensory features of particular contextual relevance, top-down connections may thus amplify their sensory responses, and enhance contextually-appropriate behavioural outcomes. Consistent with top-down selection of subnetworks, experiments in primate area V4 show that attention to specific locations or features amplifies population responses to corresponding stimuli^{78,85}. Furthermore, both the behavioural and neural correlates of spatial attention can be mimicked by electrical stimulation of a topographically-aligned area of the frontal eye fields^{86,87}, consistent with a role for top-down inputs in this amplification.

Recent evidence from rodent cortex suggests that active behaviour can change the operating mode of sensory cortex in diverse ways, by modulating the activity of different interneuron classes. For example, active whisking hyperpolarizes somatostatin-expressing cells in superficial layers of barrel cortex⁸⁸; this results from their inhibition by VIP-expressing interneurons, which are in turn excited by top-down afferents from motor cortex⁸⁹. In visual cortex, by contrast, locomotion increases the activity of somatostatin-expressing cells⁹⁰. As somatostatin-expressing cells inhibit apical tuft dendrites, these changes are in turn likely to differentially

impact the integration of top-down glutamergic input by principal cells. Understanding the way different active behaviours affect different neuronal classes in different cortical areas is an important topic of current research.

Outlook

Recent progress has suggested how the coding strategies employed by several cortical cell classes may arise from their specific connectivity patterns. We end this review by outlining some of the major questions to be addressed in the near future, which will be aided by the development of emerging techniques.

First, despite extensive research, we still have only a rudimentary understanding of the diverse classes of cortical excitatory and inhibitory neurons. The answer is likely to be complex, with developmental and epigenetic factors defining a hierarchy of ever more subtly differing subclasses. An unbiased classification of cortical cells may be provided not only by rapid progress in developmental neuroscience, but also by new technologies such as single-cell transcriptome sequencing.

Second, the generic input–output connectivity profile of each cell class must be established. In addition to current methods such as multiple patch-clamp recordings *in vitro*, emerging techniques such as viral retrograde tracing⁹¹, large-volume electron microscopic reconstruction^{10,11}, mGrasp⁹², and CLARITY⁹³ will help this endeavour. *In vivo* recordings of identified cells will allow each class's connectivity to be related to the coding strategy that it uses.

Third, although it is now established that activity correlations are higher between synaptically connected neurons²⁰, the relationship between larger-scale population codes and circuit connectivity is still unclear. One question is whether co-active principal cell subsets⁷⁰ really correspond to the interconnected subnetworks suggested by connectivity analyses^{13,14}. Answering this question will require large-scale connectomic analysis of populations whose activity has been previously recorded *in vivo*¹⁰.

A fourth question is how the top-down connectivity of a cell class, and of an individual neuron, relates to its encoding of nonsensory variables. To answer this question will require large-scale recordings in behaving animals, together with anatomical and functional characterization of top-down inputs, for example, by post-hoc tracing, or imaging of axons⁸² and individual synaptic inputs^{8,63}.

Finally, it is important to consider how cortical connections and codes are shaped by experience and learning. The recent availability of genetically encoded Ca²⁺ indicators for long-term imaging now makes it possible to relate changes in an individual neuron's sensory responses to changes in its synapses as animals learn new information⁹⁴. This technique, in combination with techniques to genetically manipulate synaptic plasticity, should provide a powerful tool to study how connectivity and coding develop into a form appropriate for an animal's experience.

Received 20 May; accepted 11 September 2013.

1. Quian Quiroga, R. & Panzeri, S. *Principles of Neural Coding*. (CRC Press, 2013).
 2. Thomson, A. M. & Lamy, C. Functional maps of neocortical local circuitry. *Front Neurosci* **1**, 19–42 (2007).
 3. Douglas, R. J. & Martin, K. A. Neuronal circuits of the neocortex. *Annu. Rev. Neurosci.* **27**, 419–451 (2004).
 4. Gong, S. *et al.* A gene expression atlas of the central nervous system based on bacterial artificial chromosomes. *Nature* **425**, 917–925 (2003).
 5. Madisen, L. *et al.* A robust and high-throughput Cre reporting and characterization system for the whole mouse brain. *Nature Neurosci.* **13**, 133–140 (2010).
 6. Taniguchi, H. *et al.* A resource of Cre driver lines for genetic targeting of GABAergic neurons in cerebral cortex. *Neuron* **71**, 995–1013 (2011); erratum **72**, 1091 (2011).
 7. Buzsáki, G. Large-scale recording of neuronal ensembles. *Nature Neurosci.* **7**, 446–451 (2004).
 8. Chen, T. W. *et al.* Ultrasensitive fluorescent proteins for imaging neuronal activity. *Nature* **499**, 295–300 (2013).
 9. Petreanu, L., Mao, T., Sternson, S. M. & Svoboda, K. The subcellular organization of neocortical excitatory connections. *Nature* **457**, 1142–1145 (2009).
 10. Bock, D. D. *et al.* Network anatomy and *in vivo* physiology of visual cortical neurons. *Nature* **471**, 177–182 (2011).
- Together with ref. 26, this paper shows that synaptic connections from principal cells to interneurons are nonspecific with respect to sensory tuning.

11. Briggman, K. L., Helmstaedter, M. & Denk, W. Wiring specificity in the direction-selectivity circuit of the retina. *Nature* **471**, 183–188 (2011).
12. Fenno, L., Yizhar, O. & Deisseroth, K. The development and application of optogenetics. *Annu. Rev. Neurosci.* **34**, 389–412 (2011).
13. Song, S., Sjostrom, P. J., Reigl, M., Nelson, S. & Chklovskii, D. B. Highly nonrandom features of synaptic connectivity in local cortical circuits. *PLoS Biol.* **3**, e68 (2005).
14. Perin, R., Berger, T. K. & Markram, H. A synaptic organizing principle for cortical neuronal groups. *Proc. Natl Acad. Sci. USA* **108**, 5419–5424 (2011).
15. Lefort, S., Tómm, C., Floyd Sarria, J. C. & Petersen, C. C. The excitatory neuronal network of the C2 barrel column in mouse primary somatosensory cortex. *Neuron* **61**, 301–316 (2009).
16. Yoshimura, Y., Dantzker, J. L. & Callaway, E. M. Excitatory cortical neurons form fine-scale functional networks. *Nature* **433**, 868–873 (2005).
17. Otsuka, T. & Kawaguchi, Y. Cell diversity and connection specificity between callosal projection neurons in the frontal cortex. *J. Neurosci.* **31**, 3862–3870 (2011).
18. Packer, A. M. & Yuste, R. Dense, unspecific connectivity of neocortical parvalbumin-positive interneurons: a canonical microcircuit for inhibition? *J. Neurosci.* **31**, 13260–13271 (2011).
19. Fino, E. & Yuste, R. Dense inhibitory connectivity in neocortex. *Neuron* **69**, 1188–1203 (2011).
20. Ko, H. et al. Functional specificity of local synaptic connections in neocortical networks. *Nature* **473**, 87–91 (2011).
- This paper shows that receptive field similarity and neuronal correlations are higher for connected than unconnected pairs of principal cells in superficial mouse visual cortex.**
21. Sun, Y. J., Kim, Y. J., Ibrahim, L. A., Tao, H. W. & Zhang, L. I. Synaptic mechanisms underlying functional dichotomy between intrinsic-bursting and regular-spiking neurons in auditory cortical layer 5. *J. Neurosci.* **33**, 5326–5339 (2013).
22. Lien, A. D. & Scanziani, M. Tuned thalamic excitation is amplified by visual cortical circuits. *Nature Neurosci.* **16**, 1315–1323 (2013).
23. Li, L. Y., Li, Y. T., Zhou, M., Tao, H. W. & Zhang, L. I. Intracortical multiplication of thalamocortical signals in mouse auditory cortex. *Nature Neurosci.* **16**, 1179–1181 (2013).
24. Li, Y. T., Ibrahim, L. A., Liu, B. H., Zhang, L. I. & Tao, H. W. Linear transformation of thalamocortical input by intracortical excitation. *Nature Neurosci.* **16**, 1324–1330 (2013).
- References 21–24 show that the thalamic and intracortical excitatory inputs a principal cell receives are similarly tuned.**
25. Gilbert, C. D. & Wiesel, T. N. Columnar specificity of intrinsic horizontal and corticocortical connections in cat visual cortex. *J. Neurosci.* **9**, 2432–2442 (1989).
26. Hofer, S. B. et al. Differential connectivity and response dynamics of excitatory and inhibitory neurons in visual cortex. *Nature Neurosci.* **14**, 1045–1052 (2011).
27. Douglas, R. J., Koch, C., Mahowald, M., Martin, K. A. & Suarez, H. H. Recurrent excitation in neocortical circuits. *Science* **269**, 981–985 (1995).
28. Gao, P., Sultan, K. T., Zhang, X. J. & Shi, S. H. Lineage-dependent circuit assembly in the neocortex. *Development* **140**, 2645–2655 (2013).
29. Yu, Y. C. et al. Preferential electrical coupling regulates neocortical lineage-dependent microcircuit assembly. *Nature* **486**, 113–117 (2012).
30. Ko, H. et al. The emergence of functional microcircuits in visual cortex. *Nature* **496**, 96–100 (2013).
- This paper shows that the relationship between sensory tuning and synaptic connectivity is weak at eye opening but grows stronger after visual experience.**
31. Hebb, D. O. *The Organization of Behavior*. (Wiley, 1949).
32. Feldman, D. E. Synaptic mechanisms for plasticity in neocortex. *Annu. Rev. Neurosci.* **32**, 33–55 (2009).
33. Yger, P. & Harris, K. D. The Convallis rule for unsupervised learning in cortical networks. *PLoS Comput. Biol.* (in the press).
34. Harris, K. D. Stability of the fittest: organizing learning through retroaxonal signals. *Trends Neurosci.* **31**, 130–136 (2008).
35. Clopath, C., Busing, L., Vasilaki, E. & Gerstner, W. Connectivity reflects coding: a model of voltage-based STDP with homeostasis. *Nature Neurosci.* **13**, 344–352 (2010).
36. Willmore, B. & Tolhurst, D. J. Characterizing the sparseness of neural codes. *Network* **12**, 255–270 (2001).
37. Olshausen, B. A. & Field, D. J. Sparse coding of sensory inputs. *Curr. Opin. Neurobiol.* **14**, 481–487 (2004).
38. Gardner-Medwin, A. R. The recall of events through the learning of associations between their parts. *Proc. R. Soc. Lond. B Biol. Sci.* **194**, 375–402 (1976).
39. O'Connor, D. H., Peron, S. P., Huber, D. & Svoboda, K. Neural activity in barrel cortex underlying vibrissa-based object localization in mice. *Neuron* **67**, 1048–1061 (2010).
40. Sakata, S. & Harris, K. D. Laminar structure of spontaneous and sensory-evoked population activity in auditory cortex. *Neuron* **64**, 404–418 (2009).
41. de Kock, C. P., Bruno, R. M., Spors, H. & Sakmann, B. Layer- and cell-type-specific suprathreshold stimulus representation in rat primary somatosensory cortex. *J. Physiol. (Lond.)* **581**, 139–154 (2007).
42. Niell, C. M. & Stryker, M. P. Highly selective receptive fields in mouse visual cortex. *J. Neurosci.* **28**, 7520–7536 (2008).
- References 39–42 show that in rodent auditory, somatosensory and visual cortex, superficial principal cells fire sparsely and selectively, whereas deep SPNs and putative interneurons of all layers fire densely and with broad sensory tuning.**
43. Meyer, H. S. et al. Inhibitory interneurons in a cortical column form hot zones of inhibition in layers 2 and 5A. *Proc. Natl Acad. Sci. USA* **108**, 16807–16812 (2011).
44. Haider, B., Hausser, M. & Carandini, M. Inhibition dominates sensory responses in the awake cortex. *Nature* **493**, 97–100 (2013).
45. Mateo, C. et al. In vivo optogenetic stimulation of neocortical excitatory neurons drives brain-state-dependent inhibition. *Curr. Biol.* **21**, 1593–1602 (2011).
46. Adesnik, H. & Scanziani, M. Lateral competition for cortical space by layer-specific horizontal circuits. *Nature* **464**, 1155–1160 (2010).
47. Adesnik, H., Bruns, W., Taniguchi, H., Huang, Z. J. & Scanziani, M. A neural circuit for spatial summation in visual cortex. *Nature* **490**, 226–231 (2012).
48. Beltramo, R. et al. Layer-specific excitatory circuits differentially control recurrent network dynamics in the neocortex. *Nature Neurosci.* **16**, 227–234 (2013).
- References 45–48 show that optogenetic stimulation of superficial layer principal cells causes predominant inhibition in neighbouring neurons, whereas stimulation of deep layer principal cells causes predominant excitation.**
49. Bathellier, B., Ushakova, L. & Rumpel, S. Discrete neocortical dynamics predict behavioral categorization of sounds. *Neuron* **76**, 435–449 (2012).
50. Swadlow, H. A. Efferent neurons and suspected interneurons in S-1 vibrissa cortex of the awake rabbit: receptive fields and axonal properties. *J. Neurophysiol.* **62**, 288–308 (1989).
51. Hefti, B. J. & Smith, P. H. Anatomy, physiology, and synaptic responses of rat layer V auditory cortical cells and effects of intracellular GABA(A) blockade. *J. Neurophysiol.* **83**, 2626–2638 (2000).
52. Brown, S. P. & Hestrin, S. Intracortical circuits of pyramidal neurons reflect their long-range axonal targets. *Nature* **457**, 1133–1136 (2009).
53. Kampa, B. M., Letzkus, J. J. & Stuart, G. J. Cortical feed-forward networks for binding different streams of sensory information. *Nature Neurosci.* **9**, 1472–1473 (2006).
54. Constantinople, C. M. & Bruno, R. M. Deep cortical layers are activated directly by thalamus. *Science* **340**, 1591–1594 (2013).
55. Schubert, D., Kotter, R. & Staiger, J. F. Mapping functional connectivity in barrel-related columns reveals layer- and cell type-specific microcircuits. *Brain Struct. Funct.* **212**, 107–119 (2007).
56. Stroh, A. et al. Making waves: initiation and propagation of corticothalamic Ca²⁺ waves in vivo. *Neuron* **77**, 1136–1150 (2013).
57. Kerlin, A. M., Andermann, M. L., Berezovskii, V. K. & Reid, R. C. Broadly tuned response properties of diverse inhibitory neuron subtypes in mouse visual cortex. *Neuron* **67**, 858–871 (2010).
- This paper shows that in mouse superficial visual cortex, the sensory tuning of parvalbumin-, somatostatin- and vasoactive-intestinal-peptide-expressing interneurons approximates the average tuning of neighbouring principal cells.**
58. Sohya, K., Kameyama, K., Yanagawa, Y., Obata, K. & Tsumoto, T. GABAergic neurons are less selective to stimulus orientation than excitatory neurons in layer II/III of visual cortex, as revealed by in vivo functional Ca²⁺ imaging in transgenic mice. *J. Neurosci.* **27**, 2145–2149 (2007).
59. Liu, B. H. et al. Visual receptive field structure of cortical inhibitory neurons revealed by two-photon imaging guided recording. *J. Neurosci.* **29**, 10520–10532 (2009).
60. Runyan, C. A. & Sur, M. Response selectivity is correlated to dendritic structure in parvalbumin-expressing inhibitory neurons in visual cortex. *J. Neurosci.* **33**, 11724–11733 (2013).
61. Ohki, K., Chung, S., Ch'ng, Y. H., Kara, P. & Reid, R. C. Functional imaging with cellular resolution reveals precise micro-architecture in visual cortex. *Nature* **433**, 597–603 (2005).
62. Van Hooser, S. D., Heimel, J. A., Chung, S. & Nelson, S. B. Lack of patchy horizontal connectivity in primary visual cortex of a mammal without orientation maps. *J. Neurosci.* **26**, 7680–7692 (2006).
63. Jia, H., Rochefort, N. L., Chen, X. & Konnerth, A. Dendritic organization of sensory input to cortical neurons in vivo. *Nature* **464**, 1307–1312 (2010).
64. Mariño, J. et al. Invariant computations in local cortical networks with balanced excitation and inhibition. *Nature Neurosci.* **8**, 194–201 (2005).
65. Wu, G. K., Arbuckle, R., Liu, B. H., Tao, H. W. & Zhang, L. I. Lateral sharpening of cortical frequency tuning by approximately balanced inhibition. *Neuron* **58**, 132–143 (2008).
66. Tan, A. Y., Brown, B. D., Scholl, B., Mohanty, D. & Priebe, N. J. Orientation selectivity of synaptic input to neurons in mouse and cat primary visual cortex. *J. Neurosci.* **31**, 12339–12350 (2011).
67. Carandini, M. & Ferster, D. Membrane potential and firing rate in cat primary visual cortex. *J. Neurosci.* **20**, 470–484 (2000).
68. Cardin, J. A., Palmer, L. A. & Contreras, D. Stimulus feature selectivity in excitatory and inhibitory neurons in primary visual cortex. *J. Neurosci.* **27**, 10333–10344 (2007).
69. Liu, B. H. et al. Broad inhibition sharpens orientation selectivity by expanding input dynamic range in mouse simple cells. *Neuron* **71**, 542–554 (2011).
70. Luczak, A., Bartho, P. & Harris, K. D. Spontaneous events outline the realm of possible sensory responses in neocortical populations. *Neuron* **62**, 413–425 (2009).
- This paper shows that the firing patterns a cortical population can produce are subject to preserved constraints on the timing and combinations of neurons that may be active together.**
71. Smith, M. A. & Kohn, A. Spatial and temporal scales of neuronal correlation in primary visual cortex. *J. Neurosci.* **28**, 12591–12603 (2008).
72. Schneidman, E., Berry, M. J. II, Segev, R. & Bialek, W. Weak pairwise correlations imply strongly correlated network states in a neural population. *Nature* **440**, 1007–1012 (2006).

73. Barlow, H. Redundancy reduction revisited. *Network* **12**, 241–253 (2001).
74. Chechik, G. *et al.* Reduction of information redundancy in the ascending auditory pathway. *Neuron* **51**, 359–368 (2006).
75. Shuler, M. G. & Bear, M. F. Reward timing in the primary visual cortex. *Science* **311**, 1606–1609 (2006).
76. Keller, G. B., Bonhoeffer, T. & Hubener, M. Sensorimotor mismatch signals in primary visual cortex of the behaving mouse. *Neuron* **74**, 809–815 (2012).
77. Jaramillo, S. & Zador, A. M. The auditory cortex mediates the perceptual effects of acoustic temporal expectation. *Nature Neurosci.* **14**, 246–251 (2011).
78. Reynolds, J. H. & Heeger, D. J. The normalization model of attention. *Neuron* **61**, 168–185 (2009).
79. Saleem, A. B., Ayaz, A., Jeffery, K., Harris, K. D. & Carandini, M. Integration of visual motion and locomotion in mouse visual cortex *Nature Neurosci.* (in the press).
80. Poulet, J. F. & Petersen, C. C. Internal brain state regulates membrane potential synchrony in barrel cortex of behaving mice. *Nature* **454**, 881–885 (2008).
81. Niell, C. M. & Stryker, M. P. Modulation of visual responses by behavioral state in mouse visual cortex. *Neuron* **65**, 472–479 (2010).
82. Petreanu, L. *et al.* Activity in motor-sensory projections reveals distributed coding in somatosensation. *Nature* **489**, 299–303 (2012).
83. Larkum, M. E., Zhu, J. J. & Sakmann, B. A new cellular mechanism for coupling inputs arriving at different cortical layers. *Nature* **398**, 338–341 (1999).
84. Larkum, M. E., Senn, W. & Lüscher, H. R. Top-down dendritic input increases the gain of layer 5 pyramidal neurons. *Cereb. Cortex* **14**, 1059–1070 (2004).
85. Cohen, M. R. & Maunsell, J. H. Using neuronal populations to study the mechanisms underlying spatial and feature attention. *Neuron* **70**, 1192–1204 (2011).
86. Moore, T. & Armstrong, K. M. Selective gating of visual signals by microstimulation of frontal cortex. *Nature* **421**, 370–373 (2003).
87. Moore, T. & Fallah, M. Control of eye movements and spatial attention. *Proc. Natl Acad. Sci. USA* **98**, 1273–1276 (2001).
88. Gentet, L. J. *et al.* Unique functional properties of somatostatin-expressing GABAergic neurons in mouse barrel cortex. *Nature Neurosci.* **15**, 607–612 (2012).
89. Lee, S., Kruglikov, I., Huang, Z. J., Fishell, G. & Rudy, B. A disinhibitory circuit mediates motor integration in the somatosensory cortex. *Nature Neurosci.* (in the press).
90. Polack, P. O., Friedman, J. & Golshani, P. Cellular mechanisms of brain state-dependent gain modulation in visual cortex. *Nature Neurosci.* **16**, 1331–1339 (2013).
91. Wickersham, I. R., Finke, S., Conzelmann, K. K. & Callaway, E. M. Retrograde neuronal tracing with a deletion-mutant rabies virus. *Nature Methods* **4**, 47–49 (2007).
92. Kim, J. *et al.* mGRASP enables mapping mammalian synaptic connectivity with light microscopy. *Nature Methods* **9**, 96–102 (2012).
93. Chung, K. *et al.* Structural and molecular interrogation of intact biological systems. *Nature* **497**, 332–337 (2013).
94. Huber, D. *et al.* Multiple dynamic representations in the motor cortex during sensorimotor learning. *Nature* **484**, 473–478 (2012).
95. Smith, P. H., Uhlrich, D. J., Manning, K. A. & Banks, M. I. Thalamocortical projections to rat auditory cortex from the ventral and dorsal divisions of the medial geniculate nucleus. *J. Comp. Neurol.* **520**, 34–51 (2012).
96. Brecht, M. & Sakmann, B. Dynamic representation of whisker deflection by synaptic potentials in spiny stellate and pyramidal cells in the barrels and septa of layer 4 rat somatosensory cortex. *J. Physiol. (Lond.)* **543**, 49–70 (2002).
97. Callaway, E. M. & Borrell, V. Developmental sculpting of dendritic morphology of layer 4 neurons in visual cortex: influence of retinal input. *J. Neurosci.* **31**, 7456–7470 (2011).
98. Narboux-Nême, N. *et al.* Neurotransmitter release at the thalamocortical synapse instructs barrel formation but not axon patterning in the somatosensory cortex. *J. Neurosci.* **32**, 6183–6196 (2012).
99. Jabaudon, D., Shnider, S. J., Tischfield, D. J., Galazo, M. J. & Macklis, J. D. RORbeta induces barrel-like neuronal clusters in the developing neocortex. *Cereb. Cortex* **22**, 996–1006 (2012).
100. Molyneaux, B. J. *et al.* Novel subtype-specific genes identify distinct subpopulations of callosal projection neurons. *J. Neurosci.* **29**, 12343–12354 (2009).
101. Chen, J. L., Carta, S., Soldado-Magraner, J., Schneider, B. L. & Helmchen, F. Behaviour-dependent recruitment of long-range projection neurons in somatosensory cortex. *Nature* **499**, 336–340 (2013).
102. Srinivasan, K. *et al.* A network of genetic repression and derepression specifies projection fates in the developing neocortex. *Proc. Natl Acad. Sci. USA* **109**, 19071–19078 (2012).
103. Groh, A. *et al.* Cell-type specific properties of pyramidal neurons in neocortex underlying a layout that is modifiable depending on the cortical area. *Cereb. Cortex* **20**, 826–836 (2010).
104. Maruoka, H., Kubota, K., Kurokawa, R., Tsuruno, S. & Hosoya, T. Periodic organization of a major subtype of pyramidal neurons in neocortical layer V. *J. Neurosci.* **31**, 18522–18542 (2011).
105. Christophe, E. *et al.* Two populations of layer V pyramidal cells of the mouse neocortex: development and sensitivity to anesthetics. *J. Neurophysiol.* **94**, 3357–3367 (2005).
106. Harwell, C. C. *et al.* Sonic hedgehog expression in corticofugal projection neurons directs cortical microcircuit formation. *Neuron* **73**, 1116–1126 (2012).
107. Matyas, F. *et al.* Motor control by sensory cortex. *Science* **330**, 1240–1243 (2010).
108. Sherman, S. M. Thalamocortical interactions. *Curr. Opin. Neurobiol.* **22**, 575–579 (2012).
109. Reiner, A., Hart, N. M., Lei, W. & Deng, Y. Corticostriatal projection neurons - dichotomous types and dichotomous functions. *Front. Neuroanat.* **4**, 142 (2010).
110. Watakabe, A. *et al.* Area-specific substratification of deep layer neurons in the rat cortex. *J. Comp. Neurol.* **520**, 3553–3573 (2012).
111. Thomson, A. M. Neocortical layer 6, a review. *Front. Neuroanat.* **4**, 13 (2010).
112. Lee, C. C. & Sherman, S. M. Glutamatergic inhibition in sensory neocortex. *Cereb. Cortex* **19**, 2281–2289 (2009).
113. Olsen, S. R., Bortone, D. S., Adesnik, H. & Scanziani, M. Gain control by layer six in cortical circuits of vision. *Nature* **483**, 47–52 (2012).
114. Cruikshank, S. J., Lewis, T. J. & Connors, B. W. Synaptic basis for intense thalamocortical activation of feedforward inhibitory cells in neocortex. *Nature Neurosci.* **10**, 462–468 (2007).
115. Pfeffer, C. K., Xue, M., He, M., Huang, Z. J. & Scanziani, M. Inhibition of inhibition in visual cortex: the logic of connections between molecularly distinct interneurons. *Nature Neurosci.* **16**, 1068–1076 (2013).
116. Lewis, D. A., Hashimoto, T. & Volk, D. W. Cortical inhibitory neurons and schizophrenia. *Nature Rev. Neurosci.* **6**, 312–324 (2005).
117. Xu, H., Jeong, H. Y., Tremblay, R. & Rudy, B. Neocortical somatostatin-expressing GABAergic interneurons disinhibit the thalamorecipient layer 4. *Neuron* **77**, 155–167 (2013).
118. Murayama, M. *et al.* Dendritic encoding of sensory stimuli controlled by deep cortical interneurons. *Nature* **457**, 1137–1141 (2009).
119. Kapfer, C., Glickfeld, L. L., Atallah, B. V. & Scanziani, M. Supralinear increase of recurrent inhibition during sparse activity in the somatosensory cortex. *Nature Neurosci.* **10**, 743–753 (2007).
120. Silberberg, G. & Markram, H. Disynaptic inhibition between neocortical pyramidal cells mediated by Martinotti cells. *Neuron* **53**, 735–746 (2007).
121. Sylwestrak, E. L. & Ghosh, A. Elfn1 regulates target-specific release probability at CA1-interneuron synapses. *Science* **338**, 536–540 (2012).
122. Rudy, B., Fishell, G., Lee, S. & Hjerling-Leffler, J. Three groups of interneurons account for nearly 100% of neocortical GABAergic neurons. *Dev. Neurobiol.* **71**, 45–61 (2011).
123. Oláh, S. *et al.* Regulation of cortical microcircuits by unitary GABA-mediated volume transmission. *Nature* **461**, 1278–1281 (2009).
124. Letzkus, J. J. *et al.* A disinhibitory microcircuit for associative fear learning in the auditory cortex. *Nature* **480**, 331–335 (2011).
125. Jiang, X., Wang, G., Lee, A. J., Stornetta, R. L. & Zhu, J. J. The organization of two new cortical interneuronal circuits. *Nature Neurosci.* **16**, 210–218 (2013).

Acknowledgements We thank B. Rudy, G. Buzsaki, M. Haussler, B. Haider, S. Hofer, R. Bruno and M. Carandini for comments on the manuscript. K.D.H. is supported by the Wellcome Trust, Engineering and Physical Sciences Research Council and US National Institutes of Health. T.M.-F. is supported by the Wellcome Trust and European Research Council.

Author Contributions K.D.H. and T.M.-F. wrote the manuscript.

Author Information Reprints and permissions information is available at www.nature.com/reprints. The authors declare no competing financial interests. Readers are welcome to comment on the online version of the paper. Correspondence should be addressed to K.D.H. (kenneth.harris@ucl.ac.uk) or T.M.-F. (thomas.mrsic-flogel@unibas.ch).

Cooperation between brain and islet in glucose homeostasis and diabetes

Michael W. Schwartz¹, Randy J. Seeley², Matthias H. Tschöp³, Stephen C. Woods⁴, Gregory J. Morton¹, Martin G. Myers⁵ & David D'Alessio²

Although a prominent role for the brain in glucose homeostasis was proposed by scientists in the nineteenth century, research throughout most of the twentieth century focused on evidence that the function of pancreatic islets is both necessary and sufficient to explain glucose homeostasis, and that diabetes results from defects of insulin secretion, action or both. However, insulin-independent mechanisms, referred to as 'glucose effectiveness', account for roughly 50% of overall glucose disposal, and reduced glucose effectiveness also contributes importantly to diabetes pathogenesis. Although mechanisms underlying glucose effectiveness are poorly understood, growing evidence suggests that the brain can dynamically regulate this process in ways that improve or even normalize glycaemia in rodent models of diabetes. Here we present evidence of a brain-centred glucoregulatory system (BCGS) that can lower blood glucose levels via both insulin-dependent and -independent mechanisms, and propose a model in which complex and highly coordinated interactions between the BCGS and pancreatic islets promote normal glucose homeostasis. Because activation of either regulatory system can compensate for failure of the other, defects in both may be required for diabetes to develop. Consequently, therapies that target the BCGS in addition to conventional approaches based on enhancing insulin effects may have the potential to induce diabetes remission, whereas targeting just one typically does not.

The escalating epidemic of obesity, metabolic syndrome and type 2 diabetes (T2D) represents one of the most pressing and costly biomedical challenges confronting modern society^{1,2}. However, much about the pathogenesis of these disorders remains unknown. In this article, we review recent evidence for a BCGS that works in tandem with pancreatic islets to regulate blood glucose levels. Glucose lowering induced by BCGS activation can involve a variety of mechanisms, some of which depend on insulin whereas others are altogether independent of islet hormones. Although islet- and brain-centred systems are distinct entities, evidence suggests that they work cooperatively to maintain stable blood glucose levels across a range of homeostatic challenges. Moreover, each system seems to have the potential to compensate, at least partially, for the failure of the other. Consequently, defects in both systems may be required for diabetes to develop and/or progress. This redundancy of islet- and brain-centred glucoregulatory systems presumably ensures tight regulation of circulating glucose, the body's principal metabolic currency.

Historical perspective

On the basis of his observation in 1854 that diabetes could be induced in rabbits by puncturing the floor of the fourth-cerebral ventricle ('piqure diabetique')³, the renowned physiologist Claude Bernard proposed a role for the brain in both glucose homeostasis and diabetes pathogenesis. This notion remained popular until the discovery of insulin in 1921, and the subsequent identification of liver, muscle and adipose tissue as principal targets of the powerful effects of insulin on glucose metabolism. Combined with evidence linking diabetes pathogenesis to defective insulin secretion and action⁴, the pancreatic islet quickly came to overshadow the brain as the focal point for understanding this disease (Box 1).

Current diabetes treatment options reflect this islet-centred view, consisting principally of recombinant human insulin preparations, insulin secretagogues (some of which also inhibit glucagon secretion), and drugs that increase insulin sensitivity. These drugs enjoy wide use and are

effective in controlling hyperglycaemia, the hallmark of T2D, but they address the consequences of diabetes more than the underlying causes, and thus control rather than cure the disease.

Although insulin-independent mechanisms contribute nearly as much to glucose disposal as insulin does, little is known about how this type of glucose lowering works or what its therapeutic potential might be. Recent work indicates that BCGS activation can markedly improve glucose homeostasis in rodent models of diabetes via largely insulin-independent mechanisms⁵, and the possibility has been raised that a similar mechanism contributes to diabetes remission^{6,7} induced by bariatric surgical procedures such as Roux-en-Y gastric bypass^{8–11}. Reconsideration of how glucose homeostasis is achieved by the body and the respective roles played by islet and brain in this process therefore seems justified.

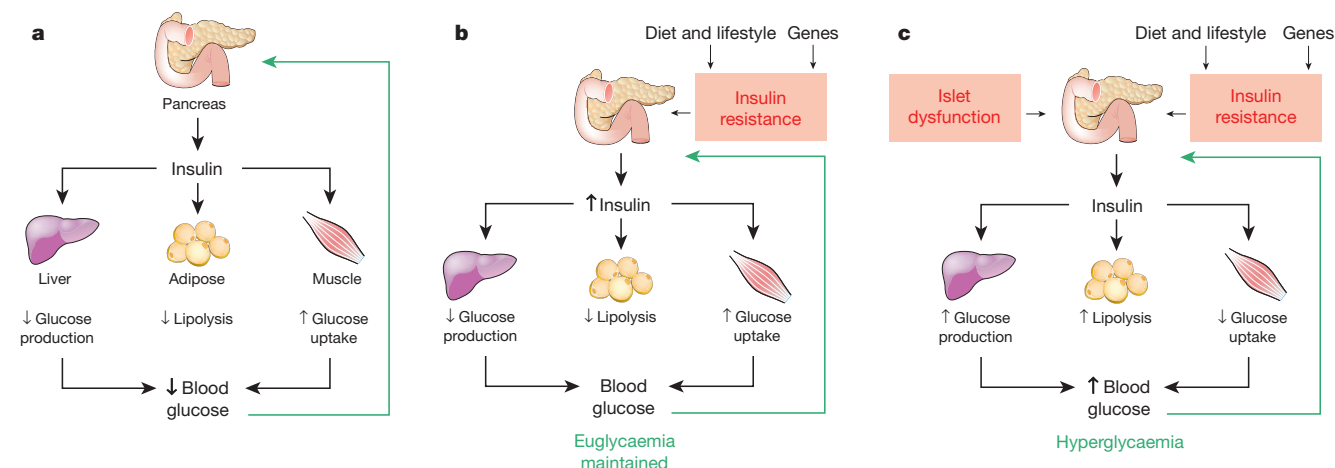
Brain control of glucose homeostasis

A large literature documents glucoregulatory effects of pharmacological or genetic interventions targeting neurons in any of several areas of the hypothalamus (arcuate, ventromedial and paraventricular hypothalamic nuclei) and brainstem. Although uncertainty surrounds both the molecular identity and the role in glucose homeostasis played by many of these neuronal groups^{12–14}, injection of insulin or glucose into discrete hypothalamic areas can lower blood glucose levels and increase liver insulin sensitivity^{15,16}, and similar effects are achieved by restoring functional leptin receptors to specific hypothalamic nuclei of animals that otherwise lack them^{17,18}. Conversely, deletion of receptors for either insulin or leptin (or their downstream signalling intermediates) from defined hypothalamic neurons causes glucose intolerance and systemic insulin resistance, indicating a physiological role for these neurons in the control of glucose metabolism^{19,20}. These and many other observations highlight how the brain can influence glucose homeostasis in response to afferent input from peripheral signals, but they have yet to establish the extent to

¹Diabetes and Obesity Center of Excellence, Department of Medicine, University of Washington, Seattle, Washington 98109, USA. ²Department of Medicine, University of Cincinnati, Cincinnati, Ohio 45237, USA. ³Institute of Diabetes and Obesity, Helmholtz Zentrum München & Division of Metabolic Diseases, Department of Medicine, Technische Universität München, Munich 85764, Germany. ⁴Department of Psychiatry, University of Cincinnati, Cincinnati, Ohio 45237, USA. ⁵Department of Physiology, University of Michigan, Ann Arbor, Michigan 48105, USA.

BOX 1

Traditional glucose homeostasis model



Box 1 Figure | The traditional, islet-centred model of normal and abnormal glucose homeostasis. **a**, Under normal conditions, the islet-centred model proposes that glucose homeostasis is controlled primarily by the effect of rising blood glucose levels to stimulate insulin secretion. Insulin then acts on peripheral tissues such as the liver to suppress hepatic glucose production (HGP), and adipose tissue and muscle to stimulate glucose uptake. Not shown is the effect of the islet hormone glucagon, secretion of which is inhibited by rising glucose levels, and which acts to stimulate HGP. Thus, glucose has opposing actions on the secretion of insulin and glucagon, hormones that in turn have opposing effects on HGP. When blood glucose levels increase (for example, during a meal), therefore, the islet response effectively returns it to baseline. **b**, When individuals with normal islet function become insulin-resistant (for example, in association with dietary and/or genetic factors that cause obesity), the islet-centred model proposes that glucose homeostasis is preserved by the capacity of the islet to increase insulin secretion in a compensatory manner. **c**, If islet dysfunction precludes the increase of insulin secretion needed to overcome insulin resistance, glucose intolerance results. As islet dysfunction progresses, increased HGP and reduced tissue glucose uptake eventually cause overt hyperglycaemia and diabetes.

which such responses participate in the physiological control of circulating glucose levels.

Indirect control of hepatic glucose production

Although there is little doubt that insulin regulates hepatic glucose production (HGP) through a direct action on hepatocytes, insulin has also been proposed to regulate HGP via an indirect mechanism involving insulin action at a remote site²¹. As aberrant control of HGP is fundamental to diabetic hyperglycaemia^{21,22}, its regulation has important clinical implications. The direct action of insulin on hepatocytes and other cell types involves its binding to insulin receptors and activation of signal transduction cascades that regulate a wide range of cellular processes. Of particular relevance to glycaemic control is the canonical insulin receptor substrate-phosphatidylinositol-3-OH kinase (IRS-PI(3)K) pathway (Fig. 1), which mediates insulin inhibition of both glycogenolysis and gluconeogenesis, the two primary determinants of HGP²¹.

In the fasted state, when the intestine is not absorbing nutrients and insulin levels are low, the liver is the primary source of circulating glucose and the rate of HGP is high. After a meal, nutrient-induced insulin secretion and subsequent activation of hepatic IRS-PI(3)K signalling inhibits HGP. The cellular basis for this effect involves PI(3)K-mediated activation of Akt, a serine-threonine kinase that, among other actions, inhibits the transcription factor FOXO1. FOXO1 stimulates gluconeogenesis in hepatocytes, and its inhibition is mandatory for insulin suppression of HGP²¹. Insulin activation of the canonical IRS-PI(3)K pathway in hepatocytes is implicated in the control of HGP by insulin under physiological conditions, and previous studies²³ offer clear evidence in support of this hypothesis.

The concept that HGP can also be controlled by insulin action at a remote site was first proposed more than 15 years ago²⁴ and received compelling support in a recent study²⁵ of 'TLKO' mice with hepatocytes unresponsive to insulin owing to liver-specific deletion of key signal

transduction molecules (the two Akt isoforms as well as FOXO1). In these animals, insulin cannot directly regulate HGP via the Akt-FOXO1 pathway. However, rather than exhibiting the expected loss of regulation,

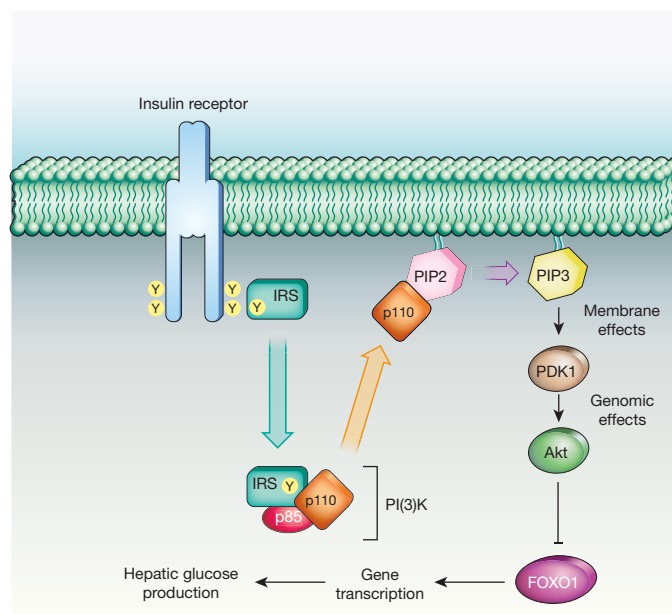


Figure 1 | Insulin signal transduction. In hepatocytes, insulin regulates HGP by activating the IRS-PI(3)K pathway, which inhibits the transcription factor FOXO1. FOXO1 activation increases gluconeogenesis, leading to increased hepatic glucose production (HGP). PIP2, phosphatidylinositol-4,5-bisphosphate; PIP3, phosphatidylinositol-3,4,5-triphosphate.

both HGP and systemic glucose homeostasis are controlled normally in these mice, even in response to exogenous insulin.

These data are among several observations²¹ that point to the existence of an indirect pathway through which insulin and nutrients can regulate HGP even when hepatocytes themselves are insensitive to direct insulin action. An intriguing question is what mechanism mediates the indirect control of HGP by insulin. Although other explanations are possible^{26,27}, the BCGS is both activated by insulin and capable of regulating HGP in humans²⁸ as well as rodent models^{19,20}.

Comparison of the phenotypes of the previously reported TLKO mice²⁵ with liver-specific insulin receptor knockout (LIRKO) mice, in which the liver is also unable to respond to insulin²⁹, is informative. Unlike TLKO mice that have generally normal glycaemic regulation, LIRKO mice are severely glucose intolerant and insulin resistant. This is because LIRKO mice have unrestrained and unregulated HGP because FOXO1 is constitutively active in the absence of insulin-stimulated Akt activation. In LIRKO mice, therefore, increased HGP results from excessive FOXO1 activity, removal of which enables normal control of HGP via the indirect pathway. From this conclusion we infer that although inhibition of HGP by the indirect insulin pathway involves a FOXO1-independent mechanism, it can be blocked by excessive FOXO1 signalling.

Insulin-independent glucose disposal by the BCGS

Although a large literature has established the brain's capacity to affect glucose homeostasis, it has become clear only recently that this can involve mechanisms that are independent of insulin. Studies in which leptin was infused directly into brain ventricles—at doses too low to have any effect outside the brain—of rats and mice with insulin-deficient diabetes clearly demonstrate the ability of central leptin action to normalize markedly increased blood glucose levels^{30,31} despite persistent, severe insulin deficiency. This surprising outcome is incompatible with a strictly islet-centric model of glucose homeostasis. Similar findings have been reported in other rodent models of insulin-deficient diabetes using systemic (rather than central) administration of leptin at supra-physiological doses^{32,33}.

Normal glucose tolerance, the ability to clear glucose from the bloodstream after a systemic glucose load, is believed to involve wide-ranging and highly coordinated effects of insulin across many different tissues. Thus, it seems surprising that in addition to normalizing fasting plasma glucose levels, intracerebroventricular (ICV) leptin infusion also restores glucose tolerance to nearly normal levels in rats with uncontrolled insulin-deficient diabetes³⁰. Leptin action in the brain can therefore orchestrate complex and interconnected processes across several tissues to lower blood glucose despite the absence of insulin signalling. Although mechanisms mediating this effect are still under investigation, normalization of HGP, along with increased glucose uptake in tissues such as skeletal muscle, heart and brown adipose tissue, have a role³⁰.

If activation of the BCGS by exogenous leptin is sufficient to correct diabetes without the need for insulin, why does severe insulin deficiency cause uncontrolled diabetes if the BCGS is left undamaged? The answer may lie in the extensive overlap between peripheral and central glucoregulatory systems. Insulin is required for the proper functioning of many cells and organ systems, including adipose tissue, and states of severe insulin deficiency undermine the ability of adipocytes both to store calories as fat and to secrete leptin. Consequently, severe insulin deficiency begets severe leptin deficiency³⁴, depriving the BCGS of two key inputs and thereby undermining its function. Importantly, this defect is reversible by activating leptin receptors exclusively in the brain, as evidenced by the ability of central leptin infusion to restore normal glucose homeostasis to animals with uncontrolled, insulin-deficient diabetes³⁰. Of course, uncontrolled diabetes can also be reversed by systemic insulin treatment, but this normalizes plasma levels of leptin as well as insulin³⁴. Restoring normal leptin levels is important, because in the absence of a leptin signal (for example, in lipodystrophy or other leptin-deficient conditions), control of hyperglycaemia is much more difficult than in other forms of diabetes³⁵.

Although physiological leptin replacement blocks or attenuates many neuroendocrine responses induced by insulin-deficient diabetes, it does not normalize hyperglycaemia³⁶. This finding suggests that in the absence of insulin, supraphysiological activation of the BCGS is necessary to restore euglycaemia, and delivery of leptin to the brain in supra-physiological amounts achieves this effect. Thus, just as compensation for leptin deficiency requires insulin concentrations well above the normal physiological range (for example, in lipodystrophy or *ob/ob* mice, in which diabetes develops despite profound hyperinsulinaemia), high leptin levels are required to compensate for severe insulin deficiency. Stated differently, although islet- and brain-centred control systems are each able to compensate for the failure of each other, the activity of either system must be amplified for full compensation to occur. Unfortunately, islet failure does not trigger compensatory BCGS activation, but rather has the opposite effect, leading to a vicious cycle that ends in hyperglycaemia.

The use of the term 'insulin independent' to refer to actions mediated by the BCGS that become dysfunctional in the face of islet failure is a potential source of confusion. This is because if we accept that normal operation of the BCGS (including production of leptin by adipocytes) depends on insulin, one can argue that the entirety of glucose homeostasis is 'insulin dependent', even those effects mediated by the BCGS that do not involve a direct effect of insulin to stimulate glucose uptake. To avoid this confusion, we use 'insulin independent' hereafter to refer to effects on tissue glucose metabolism that do not involve direct, insulin-mediated signal transduction.

Recent evidence indicates that hormones other than leptin can also act in the brain to promote insulin-independent glucose lowering. Like insulin, the gastrointestinal hormone FGF19 (or its rodent homologue, FGF15) is secreted in response to meals, and, when given at pharmacological doses, exerts potent anti-diabetic effects³⁷. Glucose-lowering by FGF19 involves actions in liver and adipose tissue, but the brain is also implicated, as ICV administration of FGF19 improves glucose tolerance in obese rats³⁸. To investigate the mechanism underlying centrally mediated glucose lowering by FGF19, a study was recently performed in genetically obese, leptin-deficient *ob/ob* mice⁵. Within 2 h of a single ICV injection of FGF19 (at a dose causing no glucose lowering when given peripherally), *ob/ob* mice displayed markedly improved glucose tolerance, despite no change in insulin secretion or sensitivity⁵. Instead, the glucose-lowering effect of ICV FGF19 resulted from a selective, threefold increase in the insulin-independent component of glucose disposal. In response to diverse hormonal stimuli, therefore, the brain has the inherent capacity to remedy diabetic hyperglycaemia and glucose intolerance via potent, insulin-independent mechanisms⁵, as well as through enhanced insulin sensitivity^{12–20}.

Glucose effectiveness

The term glucose effectiveness (GE) refers to the effect of an increased concentration of glucose to promote its own disposal, independent of insulin action³⁹. Insulin-independent glucose disposal also occurs at basal glucose levels, but our understanding of the underlying mechanisms is insufficiently advanced to know whether the same or distinct processes contribute when plasma glucose levels are high versus in the basal state. In accord with convention, therefore, we use the term 'insulin-independent glucose disposal' to refer to the overall process, including those that operate at basal glucose levels, and reserve the use of 'GE' to refer to insulin-independent glucose disposal when blood glucose levels are increased.

A key point is that insulin-independent glucose disposal makes a large contribution to overall glucose homeostasis, roughly comparable to that of insulin³⁹. Combined with the fact that reduced GE is both a major contributor to obesity-associated glucose intolerance^{39,40} and a strong risk factor for the future development of T2D (ref. 40), it is surprising how little is known about it. Unlike the dynamic and physiologically important regulation that characterizes insulin secretion and action, insulin-independent glucose disposal has traditionally been viewed as the fixed and unregulated process through which insulin-independent tissues obtain glucose to meet their needs^{39,41}. The mechanism typically

invoked to explain insulin-independent glucose disposal involves the passive effect of an increased glucose level to drive its movement down a concentration gradient and into cells (termed glucose mass action), but it is now clear that other mechanisms also exist—mechanisms that are subject to rapid regulation and can profoundly affect glucose homeostasis.

Perhaps the best-documented and most obvious example of rapid regulation of insulin-independent glucose disposal is in response to physical exercise, with the heightened metabolic demands of exercising muscle stimulating glucose uptake in the presence of stable ambient insulin and glucose levels. In addition to exercise, rapid regulation of GE has been reported in response to hormonal stimulation, for example, during intravenous infusion of glucagon-like-peptide-1 (GLP-1). Although GLP-1 improves glucose tolerance by enhancing insulin secretion, it also increases GE via mechanisms that have yet to be studied⁴². Interestingly, GLP-1 action in the hypothalamic arcuate nucleus also improves glucose tolerance⁴³, raising the untested possibility that its effects on GE (like those of leptin and FGF19) are centrally mediated.

Extending this reasoning, it is noteworthy that, by definition, GE increases in response to rising blood glucose levels, and that glucose action on arcuate nucleus neurons has a rapid glucose-lowering effect¹⁶. Collectively, these observations support a model in which, by increasing plasma concentrations of insulin, GLP-1, FGF19 and glucose, consuming a meal generates diverse signals that activate the BCGS. This BCGS activation then contributes to glucose disposal via stimulation of both insulin-dependent and -independent mechanisms that, together with islet responses, are essential for proper glucose handling by the body (Fig. 2).

If insulin-independent glucose disposal is subject to rapid and potent regulation by the brain, it is not clear why neural control of GE has not been detected previously. One explanation may be that previous studies have relied on methods that are not optimized to detect GE. Chief among these is the euglycaemic–hyperinsulinaemic clamp method, considered by

many to be the gold standard for quantitative, *in vivo* assessment of glucose metabolism. With this method, insulin sensitivity is measured as the amount of exogenous glucose that must be infused to maintain stable (or ‘clamped’) blood glucose concentrations when insulin levels are raised. Consequently, experimental interventions that change the amount of glucose required during the clamp are interpreted as having changed insulin sensitivity, despite the fact that some of the infused glucose could have been disposed of by insulin-independent mechanisms. Thus, one cannot know with certainty the extent to which observations based on the clamp method are due to changes in insulin-independent glucose disposal instead of, or in addition to, changes of insulin sensitivity. This limitation can be addressed using a complementary approach based on minimal model analysis of glucose and insulin kinetics during an intravenous glucose tolerance test. This method has seen broad use in clinical research^{39,42,44} and was recently used to reveal the potent stimulatory effect of centrally infused FGF19 on GE in *ob/ob* mice⁵.

A physiological role for the BCGS

Although there is little question that the brain participates in the glucoregulatory response to emergent or stressful conditions (for example, hypoglycaemia), the notion that the BCGS acts together with the islet to control glucose homeostasis under physiological conditions has yet to gain broad acceptance. A common and appropriate criticism is that although brain-directed interventions can affect glucose homeostasis, this should not be taken as evidence that the brain has a physiological role. Although the question of whether the BCGS is vital for normal, day-to-day control of blood glucose levels remains unanswered, several recent observations—that an indirect pathway controlling HGP exists and that this pathway can support normal glucose homeostasis even when the liver cannot respond to insulin directly²⁵, that BCGS activation can be rapidly and potentially engaged to increase insulin-independent

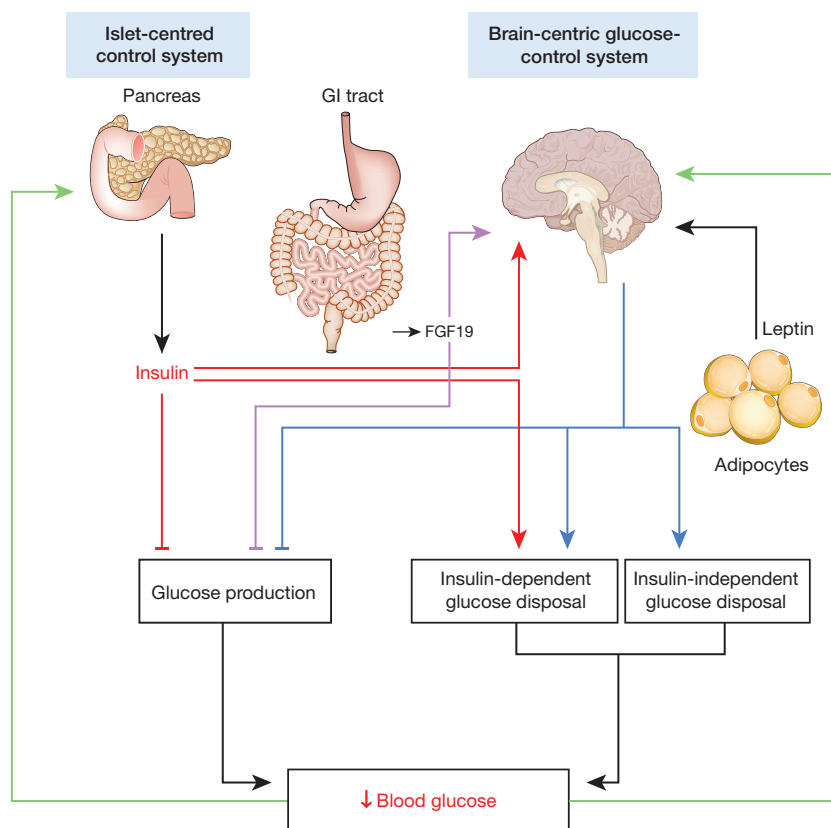


Figure 2 | Schematic illustrations of brain- and islet-centred glucoregulatory systems. The BCGS is proposed to regulate tissue glucose metabolism and plasma glucose levels via mechanisms that are both insulin dependent (for example, by regulating tissue insulin sensitivity) and insulin

independent. Because of extensive redundancy between islet- and brain-centred pathways, dysfunction of both may be required for T2D to develop, and diabetes remission may be possible with therapies that target both pathways.

glucose disposal, and that doing so has the potential to treat diabetic hyperglycaemia—justify reconsideration of this hypothesis and call for studies that offer a definitive test.

Among factors that engender scepticism of the part played by the BCGS is the notion that an islet-centred model (Box 1) is sufficient to explain the physiological control of glucose homeostasis under usual circumstances, because the capacity of the islet to secrete insulin in response to rising glucose levels often compensates for centrally mediated effects. For example, although even subtle disruption of the BCGS (for example, deletion of insulin receptors from a distinct subset of hypothalamic neurons in mice^{19,20}) can reduce liver insulin sensitivity, the effect on glucose homeostasis is minimal because the tendency for blood glucose levels to rise is offset by a compensatory increase of insulin secretion. However, the logic of this argument weakens if BCGS dysfunction is more advanced. As an example, leptin-deficient states such as lipodystrophy increase both HGP and blood glucose levels despite marked hyperinsulinaemia⁴⁵. Thus, impairments of both BCGS and islet function exist along a spectrum that ranges from mild to severe and, although the capacity of the islet to compensate for BCGS impairment is substantial, it has its limits. Normal BCGS function can therefore be seen as being permissive for normal glucose homeostasis, with islet compensation limiting the effect of BCGS dysfunction when it is mild, but not when it is more advanced.

A paucity of mechanistic information is another factor that has limited acceptance of a physiological role for the BCGS in glucose homeostasis. Whereas a great deal is known about how cellular insulin action affects glucose metabolism in hepatocytes (Fig. 1), for example, much less is known about how the brain controls HGP. Although a role for hepatic vagal innervation has been suggested^{12–14}, it is premature to invoke the vagus nerve as the predominant mediator of this effect⁴¹. Another mechanism that may be relevant involves the islet hormone glucagon, which stimulates hepatic gluconeogenesis and glycogenolysis and hence raises HGP. Increased glucagon levels are implicated in the hyperglycaemia of uncontrolled, insulin-deficient diabetes, because both HGP and plasma glucagon levels are raised in this setting.

In this context, the interaction between leptin and glucagon is of interest. First, because leptin normalizes both HGP and increased glucagon levels in rodents with uncontrolled diabetes³⁰, leptin-mediated inhibition of HGP may involve normalization of increased glucagon levels. Interestingly, leptin-mediated inhibition of glucagon secretion seems to be centrally mediated, because the effect is observed regardless of whether leptin is given systemically (at a high dose) or by ICV injection (at a low dose)^{30,33}. Furthermore, the effect of uncontrolled diabetes to increase both glucagon secretion and HGP seems to be triggered, at least in part, by leptin deficiency, because both are reversed by leptin treatment^{30,32,33}. However, increased plasma glucagon levels were normalized by systemic administration of a physiological dose of leptin to rats with streptozotocin-induced diabetes mellitus, and yet hyperglycaemia did not substantially improve³⁶. Thus, the extent to which leptin-mediated normalization of circulating glucagon levels mediates its glucose-lowering effects in this setting awaits further study.

Further insight into the physiological role the BCGS has in glucose homeostasis can be gleaned from the hepatic response to a nutrient challenge. After a meal (or in response to a glucose load), the liver switches from being a net producer to a net consumer of glucose, and a surprisingly large fraction of the glucose absorbed during a meal is taken up into the liver⁴¹. This response is triggered by rising glucose concentrations in the hepatic portal vein (the vessel into which ingested nutrients enter before gaining access to the systemic circulation), which seems to be sensed by the BCGS⁴¹. Activation of the BCGS in turn strongly enhances liver glucose uptake via a mechanism that is augmented by insulin action in the brain²⁷.

Several key questions remain to be addressed. One is whether the regulated component of insulin-independent glucose disposal is required for normal glucose homeostasis (a possibility that seems likely, given its considerable involvement), and if so, another is whether intact BCGS function is required for normal GE. Affirmative answers to both questions

would constitute indisputable evidence that the brain has a physiological role in glucose homeostasis—perhaps comparable to that played by the islet, which itself is subject to regulation by the brain^{12–20,46}.

Two-system control of glucose homeostasis

On the basis of the above reasoning, we propose that in response to a meal, both islet- and brain-centred systems are engaged and have important roles to restore homeostasis (Box 2). As ingested nutrients are absorbed into the circulation, increased insulin secretion and its canonical action on muscle, fat and liver both promote glucose disposal and inhibit its endogenous production. At the same time, the recruitment of insulin-independent mechanisms, in part through BCGS activation, makes a contribution to the overall process comparable to that of insulin. Like the action of insulin, these insulin-independent effects serve to both enhance glucose disposal (for example, through increased liver glucose uptake) and inhibit glucose production.

After a meal, the contributions made by insulin-dependent and -independent mechanisms to the overall process are roughly equal, reflecting a partnership between direct, peripheral tissue effects of insulin and BCGS activation that ensures the efficient return of increased plasma glucose levels to basal values (Fig. 2). This two-system model incorporates interactions between the BCGS and islet-based systems into physiological glucose homeostasis via coordinate regulation of insulin-dependent and -independent mechanisms.

Is diabetes a failure of two systems?

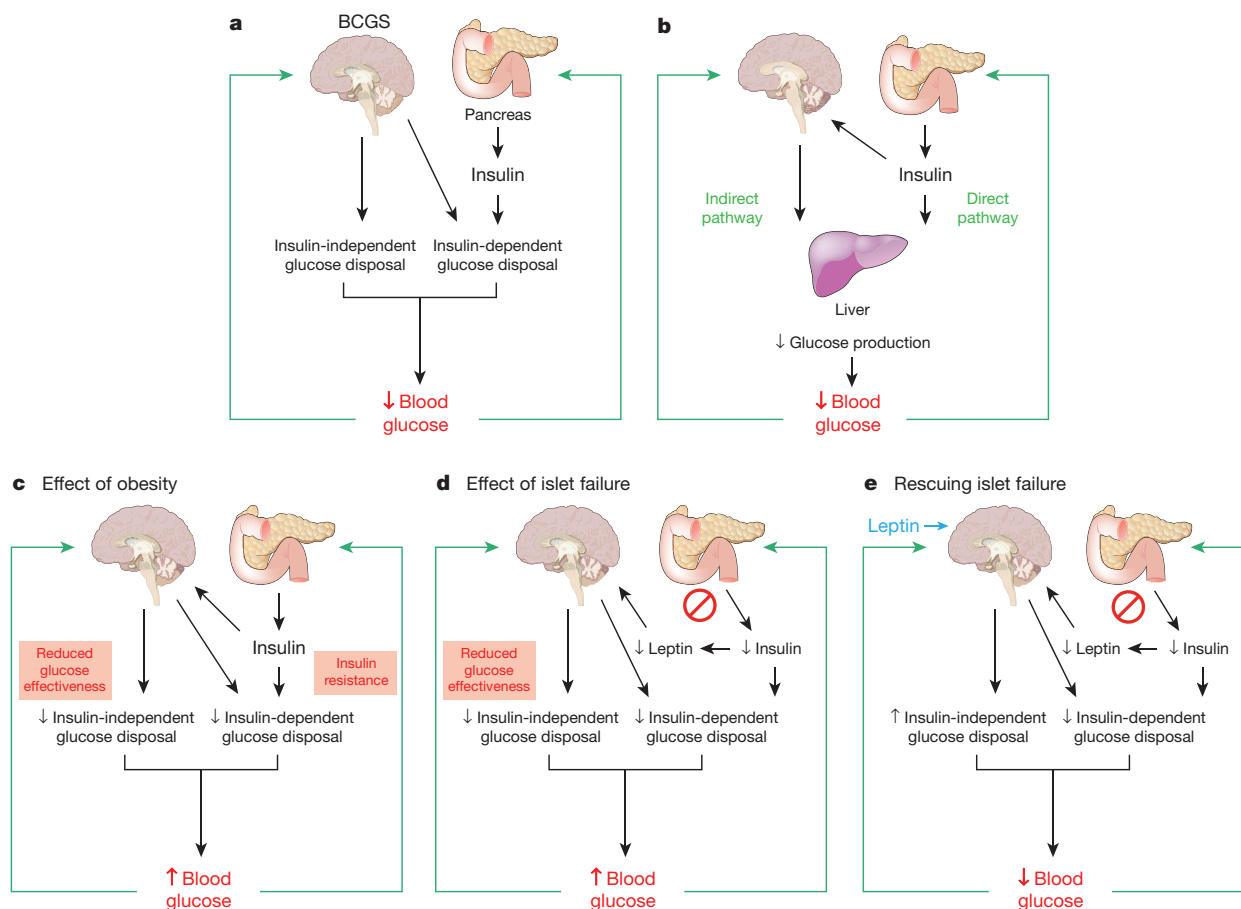
In addition to establishing that the brain can potentially increase GE, the observation that ICV leptin administration normalizes hyperglycaemia in rodents with uncontrolled diabetes indicates that BCGS activation can compensate effectively for severe insulin deficiency. This conclusion in turn suggests that disorders of both islet- and brain-centred systems may be necessary for T2D to occur (Fig. 3). This hypothesis is compatible with the observation that loss of canonical insulin action in specific tissues (for example, liver) has little effect on glucose homeostasis²⁴, and that reduced GE contributes importantly to hyperglycaemia in T2D (ref. 39). But what is the evidence that BCGS function is impaired in individuals with diabetes? To our knowledge, there are no established examples in which diabetes occurs in the absence of BCGS dysfunction. Diabetes and BCGS dysfunction are tightly coupled to one another because (1) proper BCGS function depends on normal islet function, relying on inputs from insulin as well as other hormones whose secretion is either dependent on islet function (for example, leptin) or defective in diabetes (for example, GLP-1), and (2) rodent models of obesity and T2D are associated with hypothalamic injury and gliosis, a potentially important cause of BCGS dysfunction^{47–51}. These hypothalamic alterations are proposed to reduce the ability of the BCGS to respond to relevant humoral signals (including insulin as well as leptin), and hence contribute to the associated fall of GE and onset of systemic insulin resistance that places an increased demand on islets in the lead up to T2D (Fig. 3). Whether this form of hypothalamic injury also occurs in human hypothalamus is under investigation, and early data support this possibility^{47,52}. Thus, hypothalamic injury or inflammation offers a plausible mechanism linking impairment of the BCGS to T2D pathogenesis, and studies to test this hypothesis critically are warranted.

Prospects for diabetes remission

Beyond causing weight loss, bariatric surgery induces diabetes remission in a far higher percentage of cases than can be achieved with conventional medical therapy^{6,7,10}. The mechanism underlying metabolic benefit conferred by bariatric procedures is incompletely understood but may involve improvements of both islet- and brain-centred glucoregulatory systems. A previous study in a model of bariatric surgery ('duodenal exclusion') showed that blood glucose levels could be normalized in diabetic rats via insulin-independent activation of a neural circuit that inhibits HGP⁸. Using a similar surgical model, another study⁵³ demonstrated that regulation of HGP after this procedure requires neuronal glucose sensing in

BOX 2

BCGS and islet-centred glucose homeostasis model



Box 2 Figure | Model integrating the BCGS and islet-centred system in normal and abnormal glucose homeostasis. **a**, Under normal conditions, glucose homeostasis is controlled by complex and highly coordinated interactions between brain- and islet-centred systems. Like islets, the BCGS senses a variety of humoral signals, and in response to these inputs, BCGS activation increases glucose disposal by both insulin-dependent (for example, by increasing tissue insulin sensitivity) and insulin-independent (by increasing GE, which accounts for ~50% of overall glucose disposal³⁹) mechanisms. **b**, Although insulin normally inhibits HGP through its direct action on the liver, an indirect pathway also exists through which insulin can preserve normal HGP and blood glucose levels even when hepatocytes cannot respond to insulin directly²⁵. We propose that this is among the effects mediated by the BCGS. **c**, Obesity is associated with reduced GE³⁹ and with insulin resistance, and BCGS dysfunction contributes to both. When BCGS dysfunction is mild, the resulting tendency for blood glucose levels to increase stimulates insulin secretion, such that glucose homeostasis is preserved (at the expense of higher insulin levels). When BCGS dysfunction is more severe, however, even marked hyperinsulinaemia cannot preserve normal glucose homeostasis³⁵, owing in part to the inability of reduced GE to be compensated by increased insulin secretion. Thus, intact BCGS function is required for normal glucose homeostasis. **d**, Islet dysfunction is not compensated by BCGS activation; to the contrary, impaired islet function can itself impair BCGS function (by reducing secretion of leptin as well insulin, when islet damage is severe) creating a vicious cycle that results initially in glucose intolerance. As both BCGS and islet dysfunction progress, overt hyperglycaemia and T2D result. **e**, Islet dysfunction can be compensated for by supraphysiological BCGS activation, which can achieve near-normal glucose homeostasis in rodent models of diabetes via insulin-independent mechanisms. Thus, therapeutic interventions targeting the BCGS as well as the traditional islet-based system may achieve diabetes remission, whereas targeting just one system typically does not.

the hepatic portal bed, and recent work indicates that despite having no effect on weight loss, body composition, food intake or energy expenditure⁵⁴, sub-diaphragmatic vagotomy blocked the effect of bariatric surgery to reduce HGP in a rat model of obesity⁹. Furthermore, recent work suggests that insulin signalling in the ventromedial hypothalamus is required for the effect of bariatric surgery to inhibit HGP in an obese rat model⁵⁵. Although mechanisms underlying BCGS activation by bariatric surgery await further study, recent evidence offers a link between enhanced secretion of FGF19, the nervous system and the gastrointestinal tract⁵⁶. The larger point is that, should metabolic benefit arising from

bariatric procedures be shown to involve BCGS activation, this would in turn suggest that diabetes remission may be achievable through interventions that activate both islet- and brain-centred glucoregulatory systems, whereas targeting just one does not. In principle, achieving this goal should not require surgical manipulation of the gastrointestinal tract.

Conclusion

When Claude Bernard proposed a dominant role for the brain in glucose homeostasis and diabetes pathogenesis, it was not the radical notion that it seems to be today. After all, the brain is implicated in the homeostatic

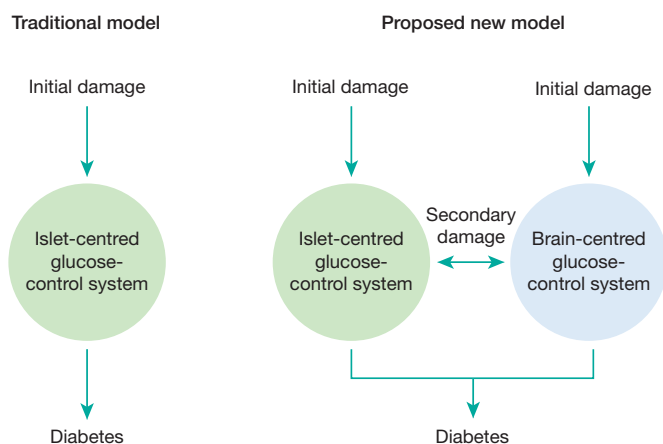


Figure 3 | Proposed contributions of defective brain- and islet-centred glucoregulatory systems to T2D pathogenesis. The traditional view holds that diabetes arises as a consequence of damage to, and ultimately failure of, beta-cell function. We propose a two-component model in which failure of glucose homeostasis can begin after initial impairment of either pancreatic islets or the BCGS. Malfunction of either of the two systems can initiate a cascade that drives the remaining glucoregulatory system into failure over time. Only when both systems are compromised does diabetes develop. Consequently, interventions that target both systems have greater therapeutic potential than those that target just one system.

control of most physiological processes that are essential for survival, ranging from body fuel stores (for example, fat mass) and body temperature to blood pressure and many endocrine systems. From this perspective, it seems surprising that control of glucose homeostasis should be governed entirely by peripheral mechanisms, despite some 90 years of research that has focused more or less exclusively on this view. One wonders how this area of science would have developed if leptin and its ability to normalize glucose levels in uncontrolled diabetes had been discovered in 1921, rather than insulin.

The surprise with which recent demonstrations of brain-mediated, insulin-independent correction of diabetes have been greeted brings into bold relief how, in the years since the discovery of insulin, metabolic research has been focused on only one part of the system governing glucose homeostasis—the part involving pancreatic islets. Despite having a role that may be comparable to that of insulin, insulin-independent glucose disposal has until now been seen as phenomenological and less worthy of study, and the notion that it might be regulated by the brain has not been previously considered.

Looking to the future, there are several important fundamental questions to address. Before the broader scientific community can (or should) be expected to embrace a role for the brain comparable to that of the islet in the day-to-day control of blood glucose levels, studies are needed to determine whether the maintenance of normal GE, which is known to be required for normal glucose tolerance, is dependent on a properly functioning BCGS. A related and equally important question is whether the link between reduced GE and the development of T2D (ref. 40) is explained by BCGS dysfunction. Such a finding would offer direct evidence that failure of both the BCGS and the islet is integral to diabetes pathogenesis.

Lastly, the observation that hormones such as FGF19 can act in the brain to improve glucose homeostasis in animal models of diabetes identifies new avenues for diabetes drug development. To expand on this specific example, the mechanism underlying the central action of FGF19 is proposed to involve a specific FGF receptor subtype, FGFR1c, that is widely expressed in the brain. In principle, there is no reason why synthetic agonists of this receptor should not prove effective for glucose lowering in patients with diabetes. Indeed, the efficacy of such drugs may not rely entirely on their central action, because activating this receptor in peripheral tissues seems to also be beneficial⁵⁷. The larger

point is that drugs that target the BCGS have important potential to synergize with current, islet-based approaches in ways that may fundamentally improve the management of what is among the most common, costly and debilitating diseases afflicting Western society.

Received 22 April; accepted 19 September 2013.

- Ogden, C. L. *et al.* Prevalence of overweight and obesity in the United States, 1999–2004. *J. Am. Med. Assoc.* **295**, 1549–1555 (2006).
- Cowie, C. C. *et al.* Prevalence of diabetes and impaired fasting glucose in adults in the U.S. population: National Health And Nutrition Examination Survey 1999–2002. *Diabetes Care* **29**, 1263–1268 (2006).
- Bernard, C. *Leçons de Physiologie Expérimentale Appliquées à la Médecine* (Paris, J.-B. Baillière, 1854).
- Biddinger, S. B. & Kahn, C. R. From mice to men: insights into the insulin resistance syndromes. *Annu. Rev. Physiol.* **68**, 123–158 (2006).
- Morton, G. J. *et al.* FGF19 action in the brain induces insulin-independent glucose lowering. *J. Clin. Invest.* <http://dx.doi.org/10.1172/JCI70710> (1 October 2013).
- Administration of a low dose of the hormone FGF19 directly into the brain of leptin-deficient *ob/ob* mice ameliorated glucose intolerance by rapidly, potentially and selectively increasing glucose effectiveness.**
- Mingrone, G. *et al.* Bariatric surgery versus conventional medical therapy for type 2 diabetes. *N. Engl. J. Med.* **366**, 1577–1585 (2012).
- Schauer, P. R. *et al.* Bariatric surgery versus intensive medical therapy in obese patients with diabetes. *N. Engl. J. Med.* **366**, 1567–1576 (2012).
- Breen, D. M. *et al.* Jejunal nutrient sensing is required for duodenal–jejunal bypass surgery to rapidly lower glucose concentrations in uncontrolled diabetes. *Nature Med.* **18**, 950–955 (2012).
- Jiao, J. *et al.* Restoration of euglycemia after duodenal bypass surgery is reliant on central and peripheral inputs in Zucker *fa/fa* rats. *Diabetes* **62**, 1074–1083 (2013).
- Cummings, D. E. & Flum, D. R. Gastrointestinal surgery as a treatment for diabetes. *J. Am. Med. Assoc.* **299**, 341–343 (2008).
- Kashyap, S. R. *et al.* Metabolic effects of bariatric surgery in patients with moderate obesity and type 2 diabetes: analysis of a randomized control trial comparing surgery with intensive medical treatment. *Diabetes Care* **36**, 2175–2182 (2013).
- Schwartz, M. W. & Porte, D. Jr. Diabetes, obesity, and the brain. *Science* **307**, 375–379 (2005).
- Sandoval, D., Cota, D. & Seeley, R. J. The integrative role of CNS fuel-sensing mechanisms in energy balance and glucose regulation. *Annu. Rev. Physiol.* **70**, 513–535 (2008).
- Elmquist, J. K., Coppari, R., Balthasar, N., Ichinose, M. & Lowell, B. B. Identifying hypothalamic pathways controlling food intake, body weight, and glucose homeostasis. *J. Comp. Neurol.* **493**, 63–71 (2005).
- Obici, S., Zhang, B. B., Karkanias, G. & Rossetti, L. Hypothalamic insulin signaling is required for inhibition of glucose production. *Nature Med.* **8**, 1376–1382 (2002).
- Lam, T. K., Gutierrez-Juarez, R., Pocai, A. & Rossetti, L. Regulation of blood glucose by hypothalamic pyruvate metabolism. *Science* **309**, 943–947 (2005).
- Coppari, R. *et al.* The hypothalamic arcuate nucleus: a key site for mediating leptin's effects on glucose homeostasis and locomotor activity. *Cell Metab.* **1**, 63–72 (2005).
- Morton, G. J. *et al.* Leptin regulates insulin sensitivity via phosphatidylinositol-3-OH kinase signaling in mediobasal hypothalamic neurons. *Cell Metab.* **2**, 411–420 (2005).
- Jordan, S. D., Konner, A. C. & Bruning, J. C. Sensing the fuels: glucose and lipid signaling in the CNS controlling energy homeostasis. *Cell. Mol. Life Sci.* **67**, 3255–3273 (2010).
- Hill, J. W. *et al.* Direct insulin and leptin action on pro-opiomelanocortin neurons is required for normal glucose homeostasis and fertility. *Cell Metab.* **11**, 286–297 (2010).
- Lin, H. V. & Accili, D. Hormonal regulation of hepatic glucose production in health and disease. *Cell Metab.* **14**, 9–19 (2011).
- DeFronzo, R. A. Banting Lecture. From the triumvirate to the ominous octet: a new paradigm for the treatment of type 2 diabetes mellitus. *Diabetes* **58**, 773–795 (2009).
- Edgerton, D. S. *et al.* Effects of insulin on the metabolic control of hepatic gluconeogenesis *in vivo*. *Diabetes* **58**, 2766–2775 (2009).
- Mittelman, S. D., Fu, Y. Y., Rebrin, K., Steil, G. & Bergman, R. N. Indirect effect of insulin to suppress endogenous glucose production is dominant, even with hyperglucagonemia. *J. Clin. Invest.* **100**, 3121–3130 (1997).
- Lu, M. *et al.* Insulin regulates liver metabolism *in vivo* in the absence of hepatic Akt and Foxo1. *Nature Med.* **18**, 388–395 (2012).
- Systemic insulin administration was shown to suppress HGP effectively in mice with livers that were genetically modified to be unable to respond to the direct effect of insulin, thus establishing the existence of an indirect mechanism for control of HGP.**
- Cheng, Z. & White, M. F. The AKTion in non-canonical insulin signaling. *Nature Med.* **18**, 351–353 (2012).
- Ramnanan, C. J. *et al.* Brain insulin action augments hepatic glycogen synthesis without suppressing glucose production or gluconeogenesis in dogs. *J. Clin. Invest.* **121**, 3713–3723 (2011).
- Kishore, P. *et al.* Activation of K_{ATP} channels suppresses glucose production in humans. *J. Clin. Invest.* **121**, 4916–4920 (2011).
- Michael, M. D. *et al.* Loss of insulin signaling in hepatocytes leads to severe insulin resistance and progressive hepatic dysfunction. *Mol. Cell* **6**, 87–97 (2000).

30. German, J. P. *et al.* Leptin activates a novel CNS mechanism for insulin-independent normalization of severe diabetic hyperglycemia. *Endocrinology* **152**, 394–404 (2011).
Hyperglycaemia was normalized by direct infusion of leptin into the brain of rats with uncontrolled, insulin-deficient diabetes, establishing the inherent capacity of the brain to maintain glucose homeostasis without the need for insulin.
31. Morton, G. J. & Schwartz, M. W. Leptin and the central nervous system control of glucose metabolism. *Physiol. Rev.* **91**, 389–411 (2011).
32. Yu, X., Park, B. H., Wang, M. Y., Wang, Z. V. & Unger, R. H. Making insulin-deficient type 1 diabetic rodents thrive without insulin. *Proc. Natl Acad. Sci. USA* **105**, 14070–14075 (2008).
33. Kruger, A. J. *et al.* Leptin treatment confers clinical benefit at multiple stages of virally induced type 1 diabetes in BB rats. *Autoimmunity* **44**, 137–148 (2011).
34. Havel, P. J. *et al.* Marked and rapid decreases of circulating leptin in streptozotocin diabetic rats: reversal by insulin. *Am. J. Physiol.* **274**, R1482–R1491 (1998).
35. Semple, R. K., Savage, D. B., Cochran, E. K., Gorden, P. & O'Rahilly, S. Genetic syndromes of severe insulin resistance. *Endocr. Rev.* **32**, 498–514 (2011).
36. German, J. P. *et al.* Leptin deficiency causes insulin resistance induced by uncontrolled diabetes. *Diabetes* **59**, 1626–1634 (2010).
37. Schaap, F. G. Role of fibroblast growth factor 19 in the control of glucose homeostasis. *Curr. Opin. Clin. Nutr. Metab. Care* **15**, 386–391 (2012).
38. Ryan, K. K. *et al.* Fibroblast growth factor-19 action in the brain reduces food intake and body weight and improves glucose tolerance in male rats. *Endocrinology* **154**, 9–15 (2013).
39. Best, J. D. *et al.* Role of glucose effectiveness in the determination of glucose tolerance. *Diabetes Care* **19**, 1018–1030 (1996).
A definitive review of glucose effectiveness and its role in both normal glucose homeostasis and diabetes.
40. Martin, B. C. *et al.* Role of glucose and insulin resistance in development of type 2 diabetes mellitus: results of a 25-year follow-up study. *Lancet* **340**, 925–929 (1992).
41. Moore, M. C., Coate, K. C., Winnick, J. J., An, Z. & Cherrington, A. D. Regulation of hepatic glucose uptake and storage *in vivo*. *Adv. Nutr.* **3**, 286–294 (2012).
42. D'Alessio, D. A., Kahn, S. E., Leusner, C. R. & Ensink, J. W. Glucagon-like peptide 1 enhances glucose tolerance both by stimulation of insulin release and by increasing insulin-independent glucose disposal. *J. Clin. Invest.* **93**, 2263–2266 (1994).
43. Sandoval, D. A., Bagnol, D., Woods, S. C., D'Alessio, D. A. & Seeley, R. J. Arcuate glucagon-like peptide 1 receptors regulate glucose homeostasis but not food intake. *Diabetes* **57**, 2046–2054 (2008).
44. Kahn, S. E. *et al.* Treatment with a somatostatin analog decreases pancreatic B-cell and whole body sensitivity to glucose. *J. Clin. Endocrinol. Metab.* **71**, 994–1002 (1990).
45. Petersen, K. F. *et al.* Leptin reverses insulin resistance and hepatic steatosis in patients with severe lipodystrophy. *J. Clin. Invest.* **109**, 1345–1350 (2002).
46. Osundiji, M. A. & Evans, M. L. Brain control of insulin and glucagon secretion. *Endocrinol. Metab. Clin. North Am.* **42**, 1–14 (2013).
47. Thaler, J. P. *et al.* Obesity is associated with hypothalamic injury in rodents and humans. *J. Clin. Invest.* **122**, 153–162 (2012).
48. Cai, D. One step from prediabetes to diabetes: hypothalamic inflammation? *Endocrinology* **153**, 1010–1013 (2012).
49. Posey, K. A. *et al.* Hypothalamic proinflammatory lipid accumulation, inflammation, and insulin resistance in rats fed a high-fat diet. *Am. J. Physiol. Endocrinol. Metab.* **296**, E1003–E1012 (2009).
50. Milanski, M. *et al.* Inhibition of hypothalamic inflammation reverses diet-induced insulin resistance in the liver. *Diabetes* **61**, 1455–1462 (2012).
51. Horvath, T. L. *et al.* Synaptic input organization of the melanocortin system predicts diet-induced hypothalamic reactive gliosis and obesity. *Proc. Natl Acad. Sci. USA* **107**, 14875–14880 (2010).
52. Alkemade, A. *et al.* AgRP and NPY expression in the human hypothalamic infundibular nucleus correlate with body mass index, whereas changes in α MSH are related to type 2 diabetes. *J. Clin. Endocrinol. Metab.* **97**, E925–E933 (2012).
53. Troy, S. *et al.* Intestinal gluconeogenesis is a key factor for early metabolic changes after gastric bypass but not after gastric lap-band in mice. *Cell Metab.* **8**, 201–211 (2008).
54. Shin, A. C., Zheng, H. & Berthoud, H. R. Vagal innervation of the hepatic portal vein and liver is not necessary for Roux-en-Y gastric bypass surgery-induced hypophagia, weight loss, and hypermetabolism. *Ann. Surg.* **255**, 294–301 (2012).
55. Paranjape, S. A. *et al.* Improvement in hepatic insulin sensitivity after Roux-en-Y gastric bypass in a rat model of obesity is partially mediated by hypothalamic insulin action. *Diabetologia* **56**, 2055–2058 (2013).
56. Gerhard, G. S. *et al.* A role for fibroblast growth factor 19 and bile acids in diabetes remission after Roux-en-Y gastric bypass. *Diabetes Care* **36**, 1859–1864 (2013).
57. Ai-Luen, W. *et al.* Amelioration of type 2 diabetes by antibody-mediated activation of fibroblast growth factor receptor 1. *Sci. Transl. Med.* **3**, 113ra26 (2011).

Acknowledgements The authors would like to thank A. G. Bell for inspiration and D. Porte Jr for comments. This work was partly funded by National Institutes of Health (NIH) grants DK083042 (M.W.S.), DK093848 (R.J.S.) and DK089053 (G.J.M.), and the Nutrition Obesity Research Centre and Diabetes Research Centre at the University of Washington, and the Helmholtz Alliance ICeMED (Imaging and Curing Environmental Metabolic Diseases), through the Initiative and Networking Fund of the Helmholtz Association.

Author Contributions All of the authors contributed to the ideas presented in and the writing of this manuscript.

Author Information Reprints and permissions information is available at www.nature.com/reprints. The authors declare no competing financial interests. Readers are welcome to comment on the online version of the paper. Correspondence and requests for materials should be addressed to M.W.S. (mschwart@u.washington.edu).

Large contribution of natural aerosols to uncertainty in indirect forcing

K. S. Carslaw¹, L. A. Lee¹, C. L. Reddington¹, K. J. Pringle¹, A. Rap¹, P. M. Forster¹, G. W. Mann^{1,2}, D. V. Spracklen¹, M. T. Woodhouse^{1,†}, L. A. Regayre¹ & J. R. Pierce³

The effect of anthropogenic aerosols on cloud droplet concentrations and radiative properties is the source of one of the largest uncertainties in the radiative forcing of climate over the industrial period. This uncertainty affects our ability to estimate how sensitive the climate is to greenhouse gas emissions. Here we perform a sensitivity analysis on a global model to quantify the uncertainty in cloud radiative forcing over the industrial period caused by uncertainties in aerosol emissions and processes. Our results show that 45 per cent of the variance of aerosol forcing since about 1750 arises from uncertainties in natural emissions of volcanic sulphur dioxide, marine dimethylsulphide, biogenic volatile organic carbon, biomass burning and sea spray. Only 34 per cent of the variance is associated with anthropogenic emissions. The results point to the importance of understanding pristine pre-industrial-like environments, with natural aerosols only, and suggest that improved measurements and evaluation of simulated aerosols in polluted present-day conditions will not necessarily result in commensurate reductions in the uncertainty of forcing estimates.

The impact of aerosol changes on cloud albedo (called the aerosol first indirect forcing)¹ is estimated² to exert a global mean radiative forcing of climate over the industrial period between -0.4 W m^{-2} and -1.8 W m^{-2} . Other aerosol–cloud interaction effects, involving rapid adjustments, may be of comparable magnitude³ but their radiative effects are even less well understood on a global scale^{3,4}. The uncertainty in the aerosol forcing is much larger than the uncertainty in the well-constrained positive forcing of $1.7 \pm 0.2 \text{ W m}^{-2}$ that is due to carbon dioxide change. The aerosol indirect forcing therefore has a highly uncertain influence on climate change and has the potential to mask a significant portion of greenhouse gas warming⁵.

The magnitude of the forcing caused by aerosol–cloud interactions depends on several poorly modelled aspects of the climate, but is broadly understood to stem from different treatments of aerosols, clouds and radiation^{3,6–8}. Nevertheless, the fundamental driver is the change in aerosols from the pre-industrial period to the present day, which controls the change in cloud droplet concentrations. It is recognized that quantification of aerosol indirect forcing requires an understanding of both the pre-industrial aerosol state^{9–12} and the effect of the substantial anthropogenic perturbation. However, because of the complexity of processes that determine cloud-forming aerosol concentrations¹⁰ and the computational expense of global aerosol models which explicitly simulate their production and loss processes^{13–16}, a comprehensive assessment of the magnitude and leading causes of uncertainty in indirect forcing has not been attempted.

Perturbed parameter simulations

Here we carry out a variance-based sensitivity analysis of a global aerosol model to attribute the uncertainty in the aerosol first indirect forcing to uncertainties in the emissions and processes that control changes in aerosol over the industrial period. We perform an ensemble of perturbed parameter global aerosol microphysical model simulations using present-day (PD) and pre-industrial (PI) emissions (PD is defined as the year 2000 and PI is defined¹⁷ as 1750, with additional PI simulations to test the effect of using alternative reference years of 1850 or 1900). The 168

1-year model simulations in the PI and PD periods cover the full expert-elicited uncertainty space of 28 parameters describing natural and anthropogenic aerosol emissions, aerosol precursor gas emissions, microphysical processes and structures of the aerosol model (see Methods). To characterize fully the magnitude and causes of model uncertainty we use Bayesian emulators conditioned on the ensemble data to generate continuous model output across the parameter space^{18,19}. This approach enables a Monte Carlo sampling of the model uncertainty space²⁰ so that a full variance-based sensitivity analysis of the model outputs can be performed.

Radiative forcing uncertainty

Figure 1 shows the annual mean first indirect radiative forcing and the associated 1σ uncertainty when assuming the 1750 reference state. The global annual mean indirect forcing is -1.16 W m^{-2} ($\sigma = 0.22 \text{ W m}^{-2}$, 95% confidence interval -0.7 W m^{-2} to -1.6 W m^{-2}), compared to the multi-model range reported in ref. 2 of -0.4 W m^{-2} to -1.8 W m^{-2} (best estimate, -0.7 W m^{-2}) and an estimate ($-0.6 \pm 0.4 \text{ W m}^{-2}$) based on assimilated PD aerosol optical depth²¹. Our estimated 95% confidence interval is slightly narrower than the multi-model ensemble range, most probably because the latter includes structural differences in the host model aerosol, cloud and radiation schemes^{2,3,6}. Nevertheless, improved understanding of the aerosol processes and emissions would clearly help to reduce uncertainty in model forcing calculations.

The seasonal variation of global mean forcing and the contributions of different parameters to the uncertainty are shown in Fig. 2a and b (see the Methods and Extended Data Table 3 for the definition and elicited range of each parameter). The eight most important parameters account for 92% of the forcing variance: volcanic SO_2 emissions, anthropogenic SO_2 emissions, dimethyl sulphide (DMS) emissions from marine biota, the width of the accumulation mode, dry deposition of accumulation mode aerosol, sub-grid sulphate particle formation, the width of the Aitken mode, and the diameter of emitted fossil fuel combustion particles. Several parameters that have a large effect on uncertainties in PD concentrations of cloud condensation nuclei (CCN)¹⁸

¹School of Earth and Environment, University of Leeds, Leeds, LS2 9JT, UK. ²National Centre for Atmospheric Science, University of Leeds, Leeds, LS2 9JT, UK. ³Department of Atmospheric Science, Colorado State University, Fort Collins, Colorado 80523, USA. [†]Present address: CSIRO Marine and Atmospheric Research, Aspendale, Victoria 3195, Australia.

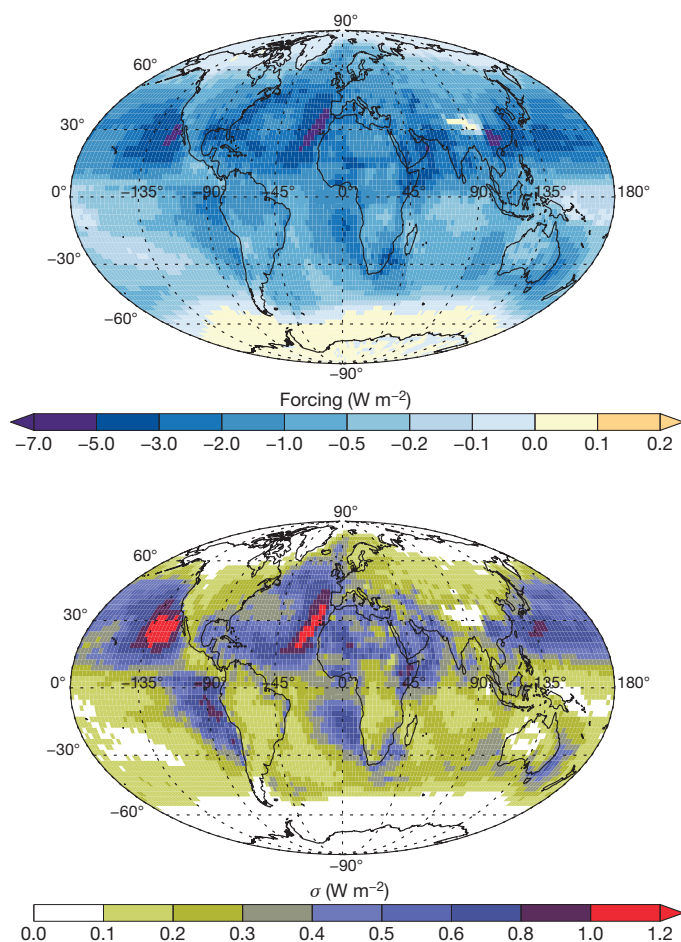


Figure 1 | The global distribution of annual mean aerosol first indirect forcing and associated uncertainty. a, First indirect forcing; b, standard deviation σ of forcing. The maps were computed from a Monte Carlo sampling of an emulator of forcing in each grid cell of the model.

have a small effect on forcing uncertainty, which is related to the way they perturb PI and PD CCN, as we discuss below.

A striking aspect of the results is the large contribution to the global mean forcing uncertainty from emissions of natural aerosol and precursor gases. Together, emissions of volcanic SO_2 , marine DMS, biogenic volatile organic carbon (forming secondary organic aerosol), biomass burning and sea spray account for 45% of the global annual mean forcing variance (Fig. 2b). This compares with 34% of the annual mean forcing variance that is due to the eight parameters associated with anthropogenic fossil fuel, biofuel, SO_2 and sulphate particle emissions. The biomass burning emissions were perturbed as a single parameter and not separated into natural wildfires and anthropogenic biomass burning. However, the annual mean 2% contribution of biomass burning to the forcing variance means that the natural–anthropogenic split is not important to our overall conclusions. Moreover, the seasonality of the uncertainty caused by biomass burning suggests that it can be attributed mostly to northern mid-latitude emissions associated with natural fires (see Methods).

The relative contribution of different parameters to the uncertainty depends on the sampled range in the ensemble (Extended Data Table 3). The range for DMS ($-50\%/+100\%$) is consistent with assessments of multiple emission parameterizations²² and the same range for volcanic SO_2 is plausible given the uncertainty in sources²³. However, our assumed range of $-40\%/+50\%$ for the main anthropogenic aerosol uncertainty (SO_2 emissions) is high compared to the most recent inventories. Thus, it is likely that our estimate of the natural aerosol effect on forcing uncertainty is an underestimate.

It is important to note that most of the natural emissions do not, by themselves, cause a forcing over the industrial period because the emission source strengths were defined to be the same in the PI and PD simulations (except for biomass burning); that is, a high setting of the emissions in the PI simulation was paired with the same high setting in the PD. However, natural emissions affect the uncertainty in the aerosol first indirect forcing because they affect the background aerosol state upon which the forcing is calculated (see below).

Because our variance-based approach considers parameter interactions, we are able to establish that the large contribution of natural aerosol emissions to forcing uncertainty is not strongly dependent on the magnitude of the other parameters. This is important information because, for example, the large sensitivity of forcing to natural sulphur emissions could be overemphasized if particle formation rates due to sulphuric-acid-driven nucleation were too high in the model. However, such parameter interactions can be quantified as the difference between the sum of the main effect variances (coloured bars in Fig. 2b) and the total variance (100% in Fig. 2b); see the Methods. Interactions generally account for less than 10% of the total forcing variance, demonstrating that the ranked uncertainty results are robust to uncertainties in the model set-up.

The effect of some parameters on forcing uncertainty could be underestimated if the parameter varied in an unknown way between the PI and PD eras, which we have not accounted for here. For example, if DMS or volcanic emissions were at the low end of the uncertainty range in the PI and at the higher end in the PD then the resulting increase in sulphate aerosol over this period would constitute an additional uncertainty in the forcing²³. It is plausible that natural emissions change over time, implying that the uncertainty attributable to these parameters could be underestimated. Whether other parameters behave in this way depends on the extent to which the model processes represent an absolute understanding or whether they have been inadvertently tuned to conditions in the PD atmosphere.

Alternative reference years

The contribution of natural emissions to the forcing uncertainty will depend on the reference year that is used. The 1750 reference, used here, is commonly assumed to represent a pristine PI state, whereas early industrial decades from the 1850s onwards have also been used²⁴. To test the effect of using alternative years for forcing, we repeated our calculations for the periods 1850–2000, 1850–1980 and 1900–2000 (limited to June to reduce computational cost). For the alternative reference years we used the same natural emissions as in 1750, but different anthropogenic emissions (see Methods). As expected, the indirect forcing is lower when a slightly polluted reference year is used (a June mean of -1.30 W m^{-2} for 1850 and -0.96 W m^{-2} for 1900, versus -1.42 W m^{-2} for 1750). The uncertainty analysis shows that the standard deviation of forcing is slightly larger when the reference year is 1850 ($\sigma = 21\%$ of mean) than for 1750 ($\sigma = 19\%$ of mean); see Extended Data Table 4. However, the uncertainties in 1850 emissions are likely to be larger than for the year 2000, which we have not attempted to account for, so we expect our estimate of 1850–2000 forcing uncertainty to be an underestimate. The contribution of anthropogenic emissions to the forcing uncertainty is also greater using an 1850 reference (46% of variance, versus 38% using 1750). This change compared to 1750 is mainly caused by the increased contribution from fossil fuel and sulphate particle emissions. These results show that natural emissions remain a substantial part of the forcing uncertainty even when slightly polluted reference years are used. They also confirm that the uncertainty in forcing is strongly sensitive to the assumed PI emissions, whether natural or anthropogenic: the large absolute change in anthropogenic emissions between 1980 and 2000 causes hardly any change in the contribution of anthropogenic emissions to the uncertainty in forcing referenced to 1850 (47% versus 46% of variance; see Extended Data Table 4), but the small absolute change in emissions

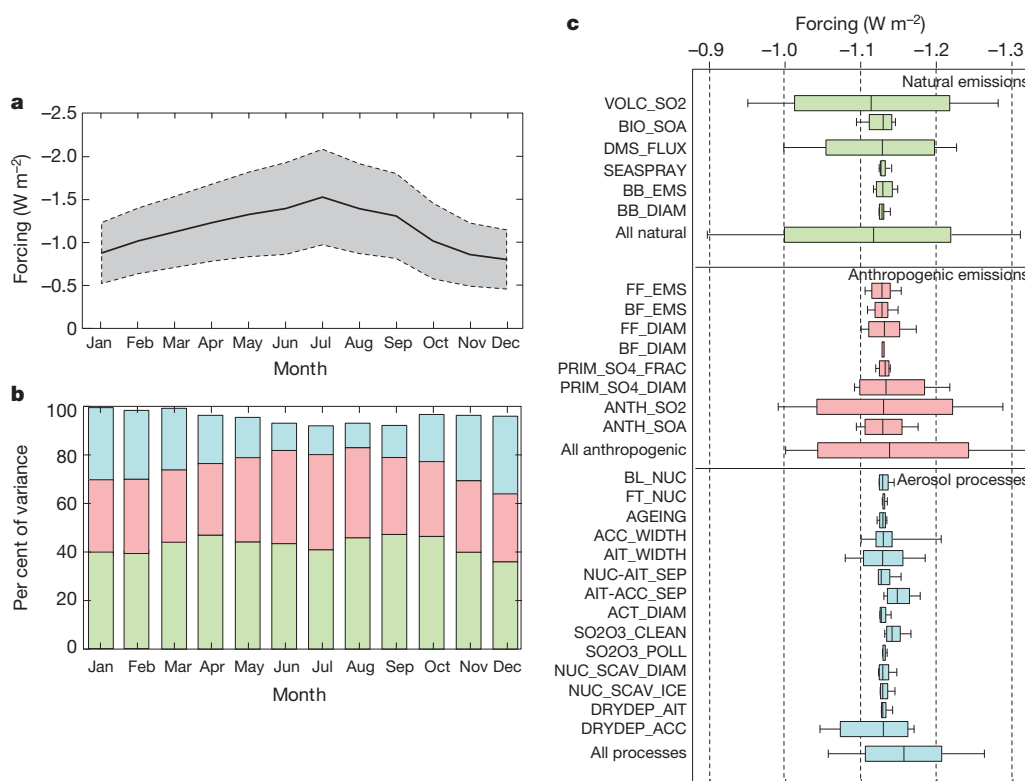


Figure 2 | Magnitude and sources of uncertainty in global mean aerosol first indirect forcing. **a**, Global mean forcing and two-standard-deviation uncertainty range. **b**, Seasonal cycle of the contribution of different groups of parameters to global monthly mean forcing variance (green, natural emissions; pink, anthropogenic emissions; blue, aerosol processes). The difference

between 1750 and 1850 causes a large change in the anthropogenic contribution (38% to 46%).

Although not a focus of this work, our results also suggest that most of the aerosol–cloud forcing has probably been realized by 1980 and has changed little between 1980 and 2000 (comparing 1850–1980 and 1850–2000 time periods; see Extended Data Table 4). This, combined with the uncertainty analysis, indicates that it may be possible to place a relatively tight constraint on the aerosol forcing over recent decades (compared to the PI-to-PD period), which would help determine the forcing contribution to the reduction in warming trend.

Importance of natural aerosols

The large contribution of natural aerosol emissions to forcing uncertainty is caused by three factors (Fig. 3a–d). First, the 1σ response of CCN to changing DMS emissions is 44% higher in the PI period than in the PD period ($\sigma = 12.9 \text{ cm}^{-3}$ versus 9.0 cm^{-3}) between 60° S and 60° N in July, caused by the more efficient nucleation of new particles in the cleaner PI atmosphere. Second, cloud droplet number concentrations increase more steeply with CCN when concentrations are low in the PI era. This effect occurs because high droplet concentrations limit the in-cloud supersaturation. Third, cloud albedo sensitivity to changes in cloud droplet concentrations (the susceptibility¹) is higher in the PI era because the dependence of albedo A on droplet number N is approximately $dA/dN = A(1 - A)/3N$. The combined effect of these three factors means that the forcing uncertainty is more strongly affected by natural aerosol (which affects PI cloud albedo in a near-linear way) than PD anthropogenic aerosol (which affects PD albedo in a sub-linear way). For the region of high forcing off the coast of Chile, CCN concentrations rise in our model by a factor of 6.6 (75 cm^{-3} in the PI period to 500 cm^{-3} in the PD). Under these conditions, and with a cloud albedo of 0.5, the sensitivity of albedo to CCN is about 15 times higher in the PI period than in the PD.

between the sum of variances and 100% is accounted for by parameter interactions. **c**, Global annual mean forcing uncertainty range due to specific parameters and groups of parameters. The box shows the interquartile range and the whisker shows the 9%–91% confidence interval. The definition of each parameter is given in Extended Data Table 3.

Although natural aerosol emissions cause only a small uncertainty in PI and PD CCN, they can have a disproportionate effect on forcing uncertainty compared to some process parameters, which we illustrate for typical conditions in Fig. 3e. For example, aerosol deposition processes were identified as a major uncertainty in PD CCN¹⁸. However, uncertainty in such a process causes an uncertainty in CCN that is in proportion to the aerosol abundance (so the absolute error in CCN will be higher in the PD than in the PI). In contrast, the uncertainty in DMS emissions causes approximately the same absolute error in CCN in the PI and PD. As shown in Fig. 3e, the relationship between CCN, cloud droplet concentrations and albedo means that there is some degree of cancellation of errors in the case where the CCN error is proportional to the amount of aerosol. For the illustrative conditions used in Fig. 3e, when PD CCN concentrations are about double the PI levels, the uncertainty in forcing is a factor of ten higher in the absolute case than in the proportional case.

Implications

Our study provides the first assessment of how aerosol processes and emissions affect the uncertainty in indirect forcing between the PI and PD periods and provides quantitative support for previous studies that have highlighted the importance of understanding PI aerosol^{9–12}. There are several implications. First, it will prove difficult to constrain the sources of forcing uncertainty by making observations in the PD atmosphere^{11,21}, because the low sensitivity of PD clouds to these emissions^{18,22} is unrepresentative of the PI atmosphere. We would need to understand the effects of natural emissions on PI-like aerosol. The nearest equivalent we have to PI conditions in the PD atmosphere is in very clean environments⁹, but the spread of perturbed particle concentrations^{10,25} may make it difficult to observe sufficiently pristine environments, except over very remote marine locations²⁶. Second, because the magnitude of the PI emissions themselves (notably volcanic and DMS) are now unmeasurable, some of the forcing uncertainty in

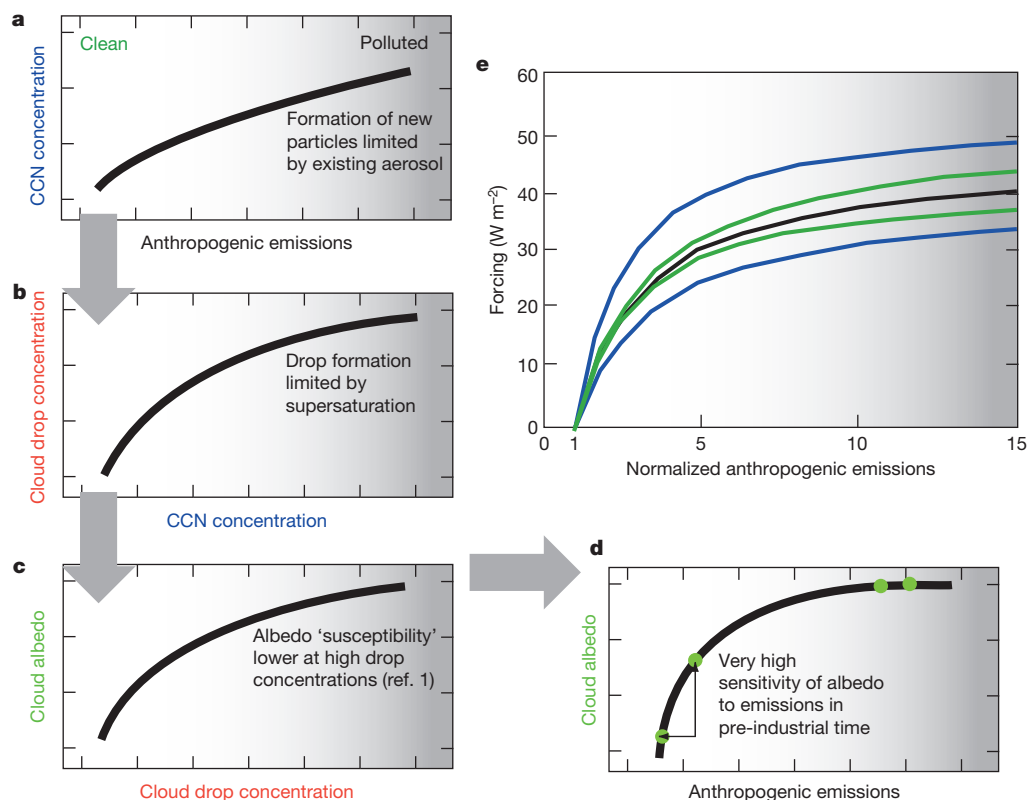


Figure 3 | Schematic explaining the importance of natural emissions for forcing uncertainty. **a**, CCN concentrations are more sensitive to emissions of sulphur precursor gases in the PI era because the condensation sink of the nucleating sulphuric acid vapour onto existing aerosol is lower. **b**, Cloud droplet concentrations are more sensitive to changes in CCN when droplet concentrations are low because higher droplet concentrations suppress in-cloud supersaturation and limit the activation of additional aerosol particles. **c**, Cloud albedo is more susceptible to changes in cloud droplet concentration when concentrations are low¹. **d**, All three effects in **a–c** lead to a much higher sensitivity of albedo to precursor gas emissions in the PI era. **e**, Calculated effect of how the uncertainty in modelled aerosol affects the uncertainty in forcing. In this example, it is assumed that the CCN concentration scales in direct proportion with anthropogenic emissions (horizontal axis), as occurs approximately in the model. Uncertainties are then applied to CCN ($\pm \Delta \text{CCN}$). The green lines show the uncertainty in forcing when ΔCCN is proportional to the CCN concentration and the blue lines show a case where ΔCCN is constant and independent of the anthropogenic emissions. The initial PI CCN concentration is 50 cm^{-3} , rising to a maximum of 750 cm^{-3} in the PD. The cloud droplet number concentration (CDNC) is

calculated as $\text{CDNC} = 375 \times (1 - \exp(-0.0025 \times \text{CCN}))$ (ref. 28). The albedo A of the baseline cloud is assumed to be 0.5 and the albedo versus CDNC is $dA/d\ln(\text{CDNC}) = A(1 - A)/3A$ (ref. 1). The forcing is calculated according to $-F_0 T_a^2 \Delta A$, where ΔA is the change in albedo from the PI value (0.5), T_a is the transmission of the atmosphere (assumed to be 0.75) and F_0 is the radiative flux, assumed to be 340 W m^{-2} . The black line shows the calculated forcing assuming the baseline aerosol number concentration. The green line shows the calculated forcing assuming $\pm 30\%$ uncertainty in CCN ($35\text{--}65 \text{ cm}^{-3}$ in the PI era to $525\text{--}975 \text{ cm}^{-3}$ maximum in the PD). This calculation represents an uncertainty in aerosol concentrations due to a process that affects PI and polluted aerosol concentrations by the same factor, such as dry deposition. The blue line shows the calculated forcing assuming $\pm 15 \text{ cm}^{-3}$ uncertainty in CCN ($35\text{--}65 \text{ cm}^{-3}$ in the PI era, as in the scaled calculation, to a maximum polluted concentration of $735\text{--}765 \text{ cm}^{-3}$). This calculation represents an uncertainty in aerosol concentrations due to a process or emission that affects PI and polluted aerosol by approximately the same absolute amount, such as caused by uncertainty in DMS or volcanic SO_2 emissions. The small absolute change in aerosol has a much larger effect on forcing uncertainty than the scaled aerosol change.

climate simulations may be irreducible²⁷. Therefore, empirical estimates of PI-to-PD forcing based on observations of aerosol and aerosol–cloud relations under PD conditions^{21,28} may not be accurate. Third, efforts to constrain the magnitude of equilibrium climate sensitivity based on net forcing and ocean heat content relative to a PI reference²⁴ will always be hampered by our limited ability to constrain the natural aerosol state. Although it makes sense to define the forcing relative to a PI reference period when the forcing was zero and the Earth was approximately in energy balance, this does not imply zero error contribution from the reference state. We have shown that the uncertainties in PI-to-PD forcing are strongly affected by the PI aerosol. Other reference periods could be considered, but equilibrium climate sensitivity studies would need to account for uncertainties in ocean heat content. A final implication is that the major sources of uncertainty will depend on the period over which forcing is calculated, so future aerosol indirect forcing may be sensitive to a different set of parameters. Therefore, accurate simulation of past forcing, if this could be achieved, may not guarantee accurate future estimates. Furthermore, other aerosol–cloud interaction effects not considered here^{3,4} may also

depend nonlinearly on aerosol between the PI period and the PD, and the uncertainties could be dominated by a different set of parameters.

Future efforts to reduce the uncertainty in simulated aerosol forcing need to combine measurements and models in ways that target sources of uncertainty, rather than relying on good model–observation agreement of PD aerosol as a measure of model fidelity. This means that models need to be based on sound microphysical processes and must not be reliant on tuning to PD aerosol levels. It is also essential for climate models and other models used for long-term simulations to include accurate representations of all natural aerosols, even if they have a small effect on PD aerosol levels in polluted environments. Even as future simulations of aerosol–cloud interaction become increasingly spatially resolved and able to capture more aerosol–cloud interaction processes and associated uncertainties, the uncertainty introduced from a poorly constrained pristine aerosol state will remain.

METHODS SUMMARY

The GLObal Model of Aerosol Processes (GLOMAP)^{15,16} calculates the time-dependent global distribution of size-resolved aerosol particles, including the

microphysical processes of particle nucleation, growth, coagulation, cloud cycling and deposition. The model transport is prescribed in terms of three-dimensional gridded wind speed, temperature and humidity fields from the European Centre for Medium-Range Weather Forecasts analyses. Anthropogenic emissions (from fossil fuel, biofuel and biomass burning) were set to their 1750 (plus alternative 1850 and 1900) values in the PI era and year 2000 values for the PD and were perturbed by a given factor (see Extended Data Tables 1 and 2). The uncertainty range for each parameter was chosen on the basis of expert elicitation¹⁸. The model was run for 168 combinations of parameter settings from among 28 parameters representing aerosol and precursor gas emissions, microphysical processes and aerosol model structures (see Extended Data Table 3).

The radiative forcing between the PI era and the PD was calculated using a radiative transfer model²⁹ and a monthly and geographically varying data set of cloud optical depth³⁰. The diurnal cycle of incoming solar radiation was accounted for, but no diurnal cycle of cloud cover was assumed. Cloud droplet concentrations were calculated from the aerosol size distribution assuming a characteristic updraft speed of 0.15 m s^{-1} over ocean and 0.3 m s^{-1} over land. The albedo change in each grid cell was then calculated in terms of the change in cloud droplet effective radius at constant liquid water path³¹. Global mean forcings were calculated for 1750–2000, 1850–2000, 1900–2000 and 1850–1980 (see Extended Data Table 4).

A Gaussian process emulator was built to describe the monthly and global mean PI-to-PD change in top-of-the-atmosphere radiation across the space of the 28 uncertain parameters¹⁸, and then a Monte Carlo sampling of the emulator was used to generate a probability distribution of global mean forcing. Variance decomposition was used to quantify the fraction of variance attributable to the uncertain parameters. The forcing and uncertainty maps (Fig. 1) were generated by performing a similar analysis on separate emulators for each model grid cell.

Online Content Any additional Methods, Extended Data display items and Source Data are available in the online version of the paper; references unique to these sections appear only in the online paper.

Received 29 March; accepted 16 September 2013.

- Twomey, S. Aerosols, clouds, and radiation. *Atmos. Environ. A* **25**, 2435–2442 (1991).
- Forster, P. *et al.* in *Climate Change 2007: The Physical Science Basis, Contribution of Working Group I to the Fourth Assessment Report of the Intergovernmental Panel on Climate Change* (eds Solomon, S. *et al.*) 129–234 (Cambridge Univ. Press, 2007).
- Lohmann, U. & Feichter, J. Global indirect aerosol effects: a review. *Atmos. Chem. Phys.* **5**, 715–737 (2005).
- Stevens, B. & Feingold, G. Untangling aerosol effects on clouds and precipitation in a buffered system. *Nature* **461**, 607–613 (2009).
- Andreae, M. O., Jones, C. D. & Cox, P. J. Strong present-day aerosol cooling implies a hot future. *Nature* **435**, 1187–1190 (2005).
- Quaas, J. *et al.* Aerosol indirect effects—general circulation model intercomparison and evaluation with satellite data. *Atmos. Chem. Phys.* **9**, 8697–8717 (2009).
- Lohmann, U. & Ferrachat, S. Impact of parametric uncertainties on the present-day climate and on the anthropogenic aerosol effect. *Atmos. Chem. Phys.* **10**, 11373–11383 (2010).
- Pan, W. W., Tatang, M. A., McRae, G. J. & Prinn, R. G. Uncertainty analysis of indirect radiative forcing by anthropogenic sulfate aerosols. *J. Geophys. Res.* **103**, 3815–3823 (1998).
- Andreae, M. O. Aerosols before pollution. *Science* **315**, 50–51 (2007).
- Andreae, M. O. & Rosenfeld, D. Aerosol–cloud–precipitation interactions. Part 1. The nature and sources of cloud-active aerosols. *Earth Sci. Rev.* **89**, 13–41 (2008).
- Penner, J. E., Xu, L. & Wang, M. H. Satellite methods underestimate indirect climate forcing by aerosols. *Proc. Natl Acad. Sci. USA* **108**, 13404–13408 (2011).
- Hoese, C. *et al.* Constraining cloud droplet number concentration in GCMs suppresses the aerosol indirect effect. *Geophys. Res. Lett.* **36**, L12807 (2009).
- Adams, P. J. & Seinfeld, J. H. Predicting global aerosol size distributions in general circulation models. *J. Geophys. Res.* **107**, 4370, doi: 10.1029/2001JD001010 (2002).
- Liu, X., Penner, J. E. & Herzog, M. Global modeling of aerosol dynamics: model description, evaluation, and interactions between sulfate and nonsulfate aerosols. *J. Geophys. Res.* **110**, D18206, doi: 10.1029/2004JD005674 (2005).
- Spracklen, D. V. *et al.* A global off-line model of size-resolved aerosol microphysics. I. Model development and prediction of aerosol properties. *Atmos. Chem. Phys.* **5**, 2227–2252 (2005).
- Mann, G. W. *et al.* Description and evaluation of GLOMAP-mode: a modal global aerosol microphysics model for the UKCA composition-climate model. *Geosci. Model Dev.* **3**, 519–551 (2010).
- Dentener, F. *et al.* Emissions of primary aerosol and precursor gases in the years 2000 and 1750 prescribed data-sets for AeroCom. *Atmos. Chem. Phys.* **6**, 4321–4344 (2006).
- Lee, L. A. *et al.* The magnitude and causes of uncertainty in global model simulations of cloud condensation nuclei. *Atmos. Chem. Phys.* **13**, 8879–8914 (2013).
- Lee, L. A., Carslaw, K. S., Pringle, K. J. & Mann, G. W. Mapping the uncertainty in global CCN using emulation. *Atmos. Chem. Phys.* **12**, 9739–9751 (2012).
- Saltelli, A., Tarantola, S. & Chan, K. P.-S. A quantitative model-independent method for global sensitivity analysis of model output. *Technometrics* **41**, 39–56 (1999).
- Bellouin, N., Quaas, J., Morcrette, J.-J. & Boucher, O. Estimates of aerosol radiative forcing from the MACC re-analysis. *Atmos. Chem. Phys.* **13**, 2045–2062 (2013).
- Woodhouse, M. T. *et al.* Low sensitivity of cloud condensation nuclei to changes in the sea-air flux of dimethyl-sulphide. *Atmos. Chem. Phys.* **10**, 7545–7559 (2010).
- Schmidt, A. *et al.* Importance of tropospheric volcanic aerosol for indirect radiative forcing of climate. *Atmos. Chem. Phys.* **12**, 7321–7339 (2012).
- Otto, A. *et al.* Energy budget constraints on climate response. *Nature Geosci.* **6**, 415–416 (2013).
- Manktelow, P. T., Carslaw, K. S., Mann, G. W. & Spracklen, D. V. Variable CCN formation potential of regional sulfur emissions. *Atmos. Chem. Phys.* **9**, 3253–3259 (2009).
- Penner, J. E., Zhou, C. & Xu, L. Consistent estimates from satellites and models for the first aerosol indirect forcing. *Geophys. Res. Lett.* **39**, L13810 (2012).
- Neelin, J. D., Bracco, A., Luo, H., McWilliams, J. C. & Meyerson, J. E. Considerations for parameter optimization and sensitivity in climate models. *Proc. Natl Acad. Sci. USA* **107**, 21349–21354 (2010).
- Jones, A. *et al.* Indirect sulphate aerosol forcing in a climate model with an interactive sulphur cycle. *J. Geophys. Res.* **106**, 20293–20310 (2001).
- Edwards, J. M. & Slingo, A. Studies with a flexible new radiation code. I. Choosing a configuration for a large scale model. *Q. J. R. Meteorol. Soc.* **122**, 689–719 (1996).
- Rossow, W. B. & Schiffer, R. A. Advances in understanding clouds from ISCCP. *Bull. Am. Meteorol. Soc.* **80**, 2261–2287 (1999).
- Rap, A. *et al.* Natural aerosol direct and indirect radiative effects. *Geophys. Res. Lett.* **40**, 3297–3301 (2013).

Acknowledgements This research has received funding from the Natural Environment Research Council AEROS project (project number NE/G006172/1) and GASSP project (project number NE/J024252/1), the EC Seventh Framework Programme under grant agreement FP7-ENV-2010-265148 (Integrated Project PEGASOS), and the National Centre for Atmospheric Science. K.S.C. and P.M.F. are currently Royal Society Wolfson Merit Award holders.

Author Contributions K.S.C. wrote the manuscript. L.A.L. did the statistical analysis. C.L.R., K.J.P. and G.W.M. performed the aerosol modelling. M.T.W., L.A.R. and K.J.P. prepared the emissions. K.S.C., L.A.L. and C.L.R. did the data interpretation. A.R. and P.M.F. did the forcing calculations. All authors contributed to the editing of the manuscript.

Author Information Reprints and permissions information is available at www.nature.com/reprints. The authors declare no competing financial interests. Readers are welcome to comment on the online version of the paper. Correspondence and requests for materials should be addressed to K.S.C. (k.s.carslaw@leeds.ac.uk).

METHODS

Model description. The GLObal Model of Aerosol Processes (GLOMAP-mode)^{15,16} is a three-dimensional global aerosol microphysics model that simulates the evolution of the particle size distribution and size-resolved chemical composition of aerosol particles on a global three-dimensional grid. The model has previously been evaluated against observations¹⁶ and improved by comparing aerosol simulations against a more detailed version of the model that treats the aerosol size distribution using a sectional approach³². The GLOMAP models have been widely used and evaluated against global measurements of particle number concentrations^{33,34}, CCN^{35,36}, aerosol chemical components^{37–39}, and cloud droplets⁴⁰. The aerosol module is run within the TOMCAT global three-dimensional offline chemistry transport model⁴¹. The aerosol and chemical species are transported by three-dimensional meteorological fields read in from the European Centre for Medium-Range Weather Forecasts (ECMWF) ERA-Interim reanalyses for 2008. Aerosol transport is advanced every 30 min by interpolating between the analyses, which are updated every 6 h and the aerosol microphysical/chemical processes are calculated on a range of shorter time-steps of less than 30 min. Uncoupling the aerosol from the model transport and meteorology in the chemistry transport model (so that aerosol does not affect meteorology) is equivalent to the commonly used “double-call” approach in a climate model⁴² in which the aerosol radiative effects are decoupled from the model physics so that particular radiative forcings can be diagnosed using pairs of model runs. The model was run at a horizontal resolution of $2.8^\circ \times 2.8^\circ$ with 31 vertical levels between the surface and 10 hPa.

The aerosol size distribution is defined by seven log-normal modes: one nucleation mode and soluble and insoluble modes covering the Aitken, accumulation and coarse size ranges. The aerosol chemical components are sulphate, sea salt, black carbon, particulate organic matter and dust. Secondary organic aerosol is produced from the first stage oxidation products of biogenic monoterpenes and anthropogenic volatile-organic-carbon compounds, and is assumed to have zero vapour pressure. It is combined with the particulate-organic-matter component after kinetic condensation on the aerosol. The model includes dust emissions, but we do not perturb them because we focus on the effect on CCN concentrations, which we have previously shown are not strongly affected by dust particles even in intense dust storms⁴³.

The microphysical model resolves the main processes that shape the particle size distribution on a global scale: new particle formation, coagulation, gas-to-particle transfer, cloud processing, and dry and wet deposition. Wet deposition of particles occurs by two processes. In-cloud nucleation scavenging in which activated particles form cloud droplets and are removed in precipitation and below-cloud impaction scavenging by falling raindrops. ECMWF meteorological fields are used to diagnose large-scale frontal precipitation and sub-grid convective precipitation is assumed to occur in 30% of the affected grid box area. Low-level stratiform clouds are read in separately from International Satellite Cloud Climatology Project (ISCCP) D2 data³⁰. In these clouds we assume that aerosol particles are activated and subsequently undergo ‘cloud processing’ in which sulphate mass is added to activated aerosol owing to the aqueous-phase oxidation of sulphur dioxide.

Concentrations of the oxidants OH, O₃, H₂O₂ and NO₃ and HO₂ were specified on the three-dimensional grid using six-hourly monthly mean concentrations from a TOMCAT simulation with detailed tropospheric chemistry⁴⁴. Concentrations of H₂O₂ are depleted through the aqueous-phase reaction with SO₂ and replenished through the reaction HO₂ + HO₂ (ref. 15). A spin-up period of six months was performed (three months of which had parameters set at their median value and formed the basis of a further three-month spin for each of the runs with the changed parameter settings).

Emissions. The emission fluxes were perturbed by scaling baseline values, which are specified in Extended Data Table 1 for the 1750–2000 simulations, and in Extended Data Table 2 for the 1850–2000, 1900–2000 and 1850–1980 simulations. The Aerosol Comparisons between Observations and Models (AeroCom) emissions scenarios used for 1750 and 2000 are not available for the intermediate years. For the three additional time periods we therefore used the emissions prepared for the Atmospheric Chemistry and Climate Model Intercomparison Project (ACCMIP⁴⁵) for 1850, 1900, 1980 and 2000. For the sensitivity runs, we show results for June after two months of spin-up after the perturbations were applied.

Cloud droplet number concentrations. CDNCs were calculated as a post-processing step using an activation parameterization⁴⁶ and the modelled monthly mean aerosol size distribution and composition in each grid cell for each perturbed parameter run. These calculations account for the coupling between the uncertain aerosol particle size distribution (and composition) and the number of particles activated into cloud droplets.

An updraft speed of 0.15 m s^{-1} was used over marine regions and 0.3 m s^{-1} over land, which is typical of cloud-base speeds in low-level stratus and stratocumulus clouds. Because updraft is highly variable in clouds it is normal to report updraft measurements as the standard deviation σ of a probability density function

of updrafts (normally centred on zero). However, it is possible to calculate CDNC using a single characteristic updraft speed (w^*) that gives comparable results to using a probability density function of updrafts⁴⁷. The characteristic speed is given by $w^* = B\sigma$, where B is a conversion factor constrained through closure studies to be in the range 0.65–0.8 (refs 47, 48). Here, we use $w^* = 0.15 \text{ m s}^{-1}$ over marine regions, which equates to $\sigma = 0.19\text{--}0.23 \text{ m s}^{-1}$, and $w^* = 0.3 \text{ m s}^{-1}$ over land, which equates to $\sigma = 0.38\text{--}0.46 \text{ m s}^{-1}$. The updrafts used to calculate CDNC should be representative of cloud base, where activation primarily occurs. Updrafts at cloud base are typically smaller than in-cloud updrafts as the latent heat released by condensation onto cloud droplets fuels higher in-cloud updrafts^{49,50}. For example, in measurements during the Marine Stratus/Stratocumulus Experiment (MASE) experiment⁵¹ the standard deviation rises from 0.3 m s^{-1} at cloud base to 0.6 m s^{-1} at cloud top. Thus, we consider our updraft velocities to be appropriate for cloud base.

To test the effect of higher updraft speeds, we recalculated CDNC for July using $w^* = 0.25 \text{ m s}^{-1}$ over oceans and 0.4 m s^{-1} over land. We then built a new emulator for global annual mean forcing. The global mean forcing changes negligibly at the higher speeds. The fractional contributions to variance change from low to high updraft speed as follows: natural aerosol changes from 45% to 42%, anthropogenic emissions decrease from 34% to 33% and processes rise from 19% to 21%.

Radiative forcing. The forcing was calculated as the difference of top-of-the-atmosphere net short-wave plus long-wave radiative fluxes between the PD and the PI periods. The PD and PI runs were performed using identical meteorological analyses. Each parameter perturbation run in the PI period was paired with its equivalent setting in the PD period. The PI and PD simulations are therefore identical in every respect except for the anthropogenic emissions. The modelled aerosol properties were then used to calculate the CDNC values in the PI and PD periods, from which the forcing was calculated for each two-dimensional grid point of the model.

We used the off-line version of the Edwards and Slingo radiative transfer model²⁹ with six bands in the short-wave and nine bands in the long-wave, with a delta-Eddington two-stream scattering solver at all wavelengths. We used a monthly mean climatology for water vapour, temperature and ozone based on ECMWF reanalysis data, together with surface albedo and cloud optical depth fields from the International Satellite Cloud Climatology Project (ISCCP-D2)³⁰ for the year 2000. The diurnal cycle of incoming solar radiation was accounted for, but no diurnal cycle of cloud cover was assumed. The sensitivity of our forcing estimates to the cloud climatology is very small³¹, according to an extra set of calculations performed using the 1983–2008 multi-annual ISCCP cloud climatology.

The cloud albedo forcing between the PI and PD experiments is quantified by modifying the cloud droplet effective radius r_e for low- and mid-level water clouds up to 600 hPa:

$$r_e^{\text{PI}} = r_e^{\text{PD}} \times \left(\frac{\text{CDNC}^{\text{PD}}}{\text{CDNC}^{\text{PI}}} \right)^{1/3}$$

where CDNC is the monthly mean cloud droplet number concentration in each grid cell. A fixed value for $r_e^{\text{PD}} = 10 \mu\text{m}$ is used in order to ensure consistency with the ISCCP cloud retrievals. This overestimates the strength of the forcing because clouds with more droplets tend, on average, to have less water for reasons that are physically understood⁵². However, our conclusions about the relative sources of uncertainty are not affected.

Perturbed parameters. The ensemble of model runs was designed to enable an emulator to be built. The ensemble consists of 168 combinations of parameter settings from 28 parameters representing aerosol and precursor gas emissions, microphysical processes and aerosol model structures. The uncertainty range for each parameter was chosen based on expert elicitation¹⁸ (see Extended Data Table 3 for a complete list). Parameter combinations within the uncertainty range were defined by a maximin Latin Hypercube sampling of the parameter space. Paired simulations were run for one year for 1750 and 2000 using the AeroCom emissions (336 runs in total) and for one month for 1850, 1900, 1980 and 2000 using the ACCMIP emissions. Each parameter setting in the PI era was paired with the same parameter setting in the PD. Anthropogenic emissions (from fossil fuel, biofuel and biomass burning) were set to their 1750, 1850 or 1900 values in the PI era and the year 1980 and 2000 values for the PD and were perturbed by the same factor.

Parameters 1 to 14 define aerosol microphysical processes and the definition of the size distribution modal parameters, whereas parameters 15 to 28 define the emission of aerosols and precursor gases. Full details about the parameter ranges and the process of expert elicitation are provided in ref. 18. Here we summarize the main aspects of the perturbed parameters.

The boundary-layer nucleation parameterization (P1) assumes a rate $j = A[\text{H}_2\text{SO}_4(\text{g})]$, with A (in units of s^{-1}) being the perturbed parameter. Throughout the atmosphere (but important only in the free troposphere) we use a binary homogeneous $\text{H}_2\text{SO}_4\text{--H}_2\text{O}$ nucleation rate model scaled by an uncertain factor (P2).

Ageing is the process by which freshly emitted carbonaceous particles (for example, from biomass burning) can become increasingly water soluble as they accumulate water-soluble compounds during transport. The controlling parameter, as used in many global models⁵³, is the number of monolayers of soluble material required to convert the particles into water-soluble particles, which can then act as CCN. The lower limit of our assumed ageing means that initially insoluble particles become soluble on the timescale of hours in polluted regions. This process affects the number of aerosol particles able to form cloud droplets in the forcing calculation, and also affects the cloud processing of aerosol during run time of the model.

The activation diameter (P4) defines the dry-equivalent diameter at which particles are able to activate to cloud droplets during run time of the model. A single value of activation diameter is used globally in a given run. The activation diameter controls the formation of cloud droplets in all low-level clouds, and thereby controls which particles undergo cloud processing (sulphate production on the particles due to oxidation of sulphur dioxide) and removal in precipitation, and therefore shapes the particle size distribution. Cloud droplet concentrations from run-time of the model are not used in the forcing calculations (they are only used as a physical process that shapes the particle size distribution). For the forcing (see previous section) cloud droplet concentrations are quantified as a post-processing step based on the uncertain particle size distributions and an assumed updraft speed. In reality, the activation diameter in a given cloud updraft is controlled by the particle size distribution, solubility and updraft speed. The updraft speed was not included as a perturbed parameter because the chemical transport model does not have a parameterization of updrafts in different cloud types and environments. Perturbation of the activation diameter accounts approximately for the uncertainty in updraft speed, but by prescribing a value in each simulation it ignores the way that the diameter is coupled to the properties of the aerosol size distribution in a given grid cell. This approach is likely to overestimate the uncertainty because it allows a larger variation in the number of aerosol particles that can be cloud processed, which would otherwise be damped by the coupling of particle number and activation diameter. Nevertheless, activation diameter makes a small contribution to global forcing uncertainty (Fig. 2c).

The parameters SO2O3_CLEAN and SO2O3_POLL (P5 and P6) control the cloud droplet pH, which affects the production rate of aerosol sulphate from oxidation of sulphur dioxide by ozone. The pH is the perturbed parameter and can cause a change in rate by a factor of 10^5 for pH between 3 and 6. One parameter is used for clean (lower acidity) environments (sulphur dioxide less than 0.5 parts per billion) and one for polluted environments.

The in-cloud scavenging diameter offset (P7) controls the diameter of aerosols that can be removed by in-cloud nucleation scavenging. This allows some particles to be activated but not scavenged, assuming that the largest droplets initiate precipitation. The lower limit of P7 (zero nanometres) assumes all activated particles are subject to removal during precipitation.

The scavenging efficiency in ice-containing clouds (P8) controls the fraction of particles accessible to nucleation scavenging when air is below -10°C . Our previous work has shown this parameter to be important in controlling aerosol transport to the Arctic³⁸. Dry deposition of Aitken and accumulation mode particles (P9 and P10) is scaled for each particle size by a given factor. GLOMAP calculates the wind speed and size-dependent deposition velocity due to Brownian diffusion, impaction and interception. The accumulation and Aitken mode width parameters (P11 and P12) define prescribed, globally constant geometric standard deviations of the log-normal size distribution modes. The mode separation diameters (P13 and P14) define the ranges over which the geometric mean radius can vary while staying in a particular mode.

Fossil fuel, biofuel and biomass burning particle emission flux parameters (P15, P16 and P17) scale the mass emission fluxes in the PI based on the 1750, 1850 or 1900 emissions and in the PD based on the year 2000 emissions. The spatial distribution of emissions is different in the PI and PD. Our perturbation accounts for uncertainty in the monthly mean flux but does not account for uncertainty in the spatial pattern or temporal variability in the emissions. Thus, for wildfires we are not able to separate the effects of more intense fires versus more frequent fires, which might have different effects on forcing uncertainty. The biomass burning from open fires was not separated into natural and anthropogenic emissions, so we cannot apportion the uncertainty. Examination of the variation of uncertainty due to these parameters shows a clear seasonal cycle, with a peak contribution to global mean variance of 5% in July and August, which can be attributed to northern mid-latitude wildfires, versus generally less than 1% at other times. The tropical fires are important for CCN¹⁸ but the uncertainty in forcing is limited by the low sensitivity of cloud albedo at very high CCN concentrations. Because most of the northern mid-latitude emissions can be associated with natural fires⁵⁴, we have associated the biomass burning uncertainties with the natural emissions.

Fossil fuel, biofuel and biomass burning particle emission sizes (P18, P19 and P20) directly control the number of emitted particles for a given mass flux, and therefore directly influence the CCN population. The sub-grid scale sulphate particle production parameters (P21 and P22) define the formation of particles in sub-grid scale power plant plumes^{55,56}. P21 defines the fraction of the emitted sulphur dioxide mass that enters the model grid square as new sulphate particles and P22 defines the dry size of these particles (and hence their number concentration for fixed mass) when emitted into the global grid box.

The sea spray particle mass flux (P23) is scaled by a factor. GLOMAP-mode simulates sea spray particles between 35 nm and 20 μm dry diameter. This parameter conflates multiple sources of uncertainty associated with the wind-speed dependence of the flux such as processes not unaccounted for in the parameterizations (for example, fetch), the wind speed, and the limited spatial resolution of the wind fields in the model.

Anthropogenic sulphur dioxide emissions (P24) are scaled by a factor based on the emissions in 1750, 1850, 1900 and 2000, as described above. Continuously degassing volcanic sulphur dioxide emissions (P25) are scaled based on a global inventory widely used in global models⁵⁷. Time-averaged sporadic emissions are also included. Volcanic emissions are assumed to be the same in the PI and PD simulations.

DMS emissions (P26) are controlled by the sea-water concentration of DMS⁵⁸ and the wind-driven transfer velocity parameterization⁵⁹. We conflate these uncertainties by perturbing the calculated sea-air transfer flux by a given factor. This leads to identical absolute perturbations to the DMS flux in the PI era and the PD. We do not account for uncertainty in the spatial pattern of DMS seawater concentration, which is likely to be an important factor in the overall uncertainty⁶⁰.

The biogenic secondary-organic-aerosol production parameter (P27) conflates the uncertainty in the emissions of the precursor gases (biogenic volatile organic carbons) and the uncertainty in the yield of secondary-organic-aerosol material following oxidation reactions into a single parameter. P27 scales the volatile organic carbon emissions (with fixed chemical yield) such that global annual secondary-organic-aerosol production lies between the values given in the table. There are also uncertainties in the volatility of different compounds that we do not account for here. The range of emissions used here has been shown to span the range of global *in situ* measurements of organic aerosol³⁷.

Anthropogenic secondary organic aerosol production (P28) is treated in a similar way to biogenic secondary organic aerosol, by conflating the uncertainty in emissions and yield into a single emission uncertainty. We used the same approach as in ref. 37 by scaling gridded carbon monoxide emissions over a range known to span the range of observed organic aerosol in the PD atmosphere. The range is then scaled further to account for the changes in carbon monoxide emissions in 1850, 1900 and 1980.

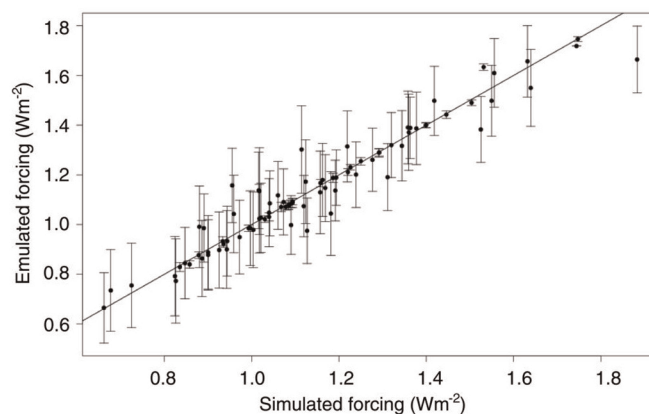
Model emulation. Gaussian process emulation^{18–20} was used to estimate model predictions at untried points throughout the space of the uncertain model parameters. An emulator was built for the monthly mean first indirect radiative forcing for every two-dimensional grid point (to produce Fig. 1 in the main text) and for the global annual mean and monthly mean forcings to generate Fig. 2 in the main text. The emulator was validated in each case using 84 additional model runs (Extended Data Fig. 1) to ensure that the emulator uncertainty around its mean is low compared to the parametric uncertainty. Twenty-eight of the validation runs were designed to lie near the training points and 64 were defined using a separate Latin Hypercube design⁶¹. The coefficient of determination (r^2) of the global annual mean emulator forcing versus simulated forcing is 0.94.

Variance-based sensitivity analysis. Variance-based sensitivity analysis is used to decompose the uncertainty in the model predictions to the uncertainty in the model parameters. The total variance of the forcing was calculated by sampling from the emulator mean function using the extended-FAST method²⁰. We sampled 5,000 points per parameter (140,000 in total) from the emulator to obtain a probability distribution of forcing. Two measures of sensitivity were calculated: the main effect index measures by how much the variance will be reduced if the parameter can be learnt precisely, and the total effect index measures both the individual effect and the interaction effect of each parameter with all others. The two sensitivity measures are compared to assess the sensitivity of the model output to interactions. Figure 2b (see main text) shows that parameter interactions account for generally less than 10% of the monthly global mean forcing variance (shown as the residual white space above each coloured bar). We note that a nonlinear response of the model output to a parameter across the specified range is accounted for in the main effect variance.

Uncertainty results using different reference periods. Extended Data Table 4 presents results for the additional simulations in which alternative reference years were used for the calculation of forcing (1850 and 1900 instead of 1750), as well as for the period 1850–1980.

32. Mann, G. W. *et al.* Intercomparison of modal and sectional aerosol microphysics representations within the same 3-D global chemical transport model. *Atmos. Chem. Phys.* **12**, 4449–4476 (2012).

33. Spracklen, D. V. *et al.* Explaining global surface aerosol number concentrations in terms of primary emissions and particle formation. *Atmos. Chem. Phys.* **10**, 4775–4793 (2010).
34. Reddington, C. L. *et al.* Primary versus secondary contributions to particle number concentrations in the European boundary layer. *Atmos. Chem. Phys.* **11**, 12007–12036 (2011).
35. Korhonen, H. *et al.* Influence of oceanic dimethyl sulfide emissions on cloud condensation nuclei concentrations and seasonality over the remote Southern Hemisphere oceans: a global model study. *J. Geophys. Res.* **113**, D15204 (2008).
36. Spracklen, D. V., Carslaw, K. S., Poschl, U., Rap, A. & Forster, P. M. Global cloud condensation nuclei influenced by carbonaceous combustion aerosol. *Atmos. Chem. Phys.* **11**, 9067–9087 (2011).
37. Spracklen, D. V. *et al.* Aerosol mass spectrometer constraint on the global secondary organic aerosol budget. *Atmos. Chem. Phys.* **11**, 12109–12136 (2011).
38. Browne, J., Carslaw, K. S., Arnold, S. R., Pringle, K. & Boucher, O. The scavenging processes controlling the seasonal cycle in Arctic sulphate and black carbon aerosol. *Atmos. Chem. Phys.* **12**, 6775–6798 (2012).
39. Schmidt, A. *et al.* Excess mortality in Europe following a future Laki-style Icelandic eruption. *Proc. Natl Acad. Sci. USA* **108**, 15710–15715 (2011).
40. Pringle, K. J. *et al.* A multi-model assessment of the impact of sea spray geoengineering on cloud droplet number. *Atmos. Chem. Phys.* **12**, 11647–11663 (2012).
41. Chipperfield, M. P. New version of the TOMCAT/SLIMCAT off-line chemical transport model: intercomparison of stratospheric tracer experiments. *Q. J. R. Meteorol. Soc.* **132**, 1179–1203 (2006).
42. Bellouin, N. *et al.* Impact of the modal aerosol scheme GLOMAP-mode on aerosol forcing in the Hadley Centre Global Environmental Model. *Atmos. Chem. Phys.* **13**, 3027–3044 (2013).
43. Manktelow, P. T., Carslaw, K. S., Mann, G. W. & Spracklen, D. V. The impact of dust on sulfate aerosol, CN and CCN during an East Asian dust storm. *Atmos. Chem. Phys.* **10**, 365–382 (2010).
44. Arnold, S. R., Chipperfield, M. P. & Blitz, M. A. A three-dimensional model study of the effect of new temperature-dependent quantum yields for acetone photolysis. *J. Geophys. Res.* **110**, D22305, doi: 10.1029/2005JD005998 (2005).
45. Lamarque, J.-F. *et al.* Historical (1850–2000) gridded anthropogenic and biomass burning emissions of reactive gases and aerosols: methodology and application. *Atmos. Chem. Phys.* **10**, 7017–7039 (2010).
46. Fountoukis, C. & Nenes, A. Continued development of a cloud droplet formation parameterization for global climate models. *J. Geophys. Res.* **110**, D11212 (2005).
47. Morales, R. & Nenes, A. Characteristic updrafts for computing distribution-averaged cloud droplet number, autoconversion rate and effective radius. *J. Geophys. Res.* **115**, D18220, doi: 10.1029/2009JD013233 (2010).
48. Peng, Y., Lohmann, U. & Leaitch, R. Importance of vertical velocity variations in cloud droplet nucleation process of marine stratus clouds. *J. Geophys. Res. Atmos.* **110**, D21213, doi:10.1029/2004JD004922 (2005).
49. Lu, M. & Seinfeld, J. H. Study of the aerosol indirect effect by large-eddy simulation of marine stratocumulus. *J. Atmos. Sci.* **62**, 3909–3932 (2005).
50. Hill, A. A., Feingold, G. & Jiang, H. The influence of entrainment and mixing assumption on aerosol-cloud interactions in marine stratocumulus. *J. Atmos. Sci.* **66**, 1450–1464 (2009).
51. Guo, H., Liu, Y. & Daum, P. H. Senum, G. I. & Tao, W.-K. Characteristics of vertical velocity in marine stratocumulus: comparison of large eddy simulations with observations. *Environ. Res. Lett.* **3**, 045020 (2008).
52. Ackerman, A. S. *et al.* The impact of humidity above stratiform clouds on indirect climate forcing. *Nature* **432**, 1014–1017 (2004).
53. Wilson, J., Cuvelier, C. & Raes, F. A modeling study of global mixed aerosol fields. *J. Geophys. Res.* **106**, 34081–34092 (2001).
54. Stocks, B. J. *et al.* Large forest fires in Canada, 1959–1997. *J. Geophys. Res.* **107**, 8149, doi: 10.1029/2001JD000484 (2002).
55. Luo, G. & Yu, F. Sensitivity of global cloud condensation nuclei concentrations to primary sulfate emission parameterizations. *Atmos. Chem. Phys.* **11**, 1949–1959 (2011).
56. Stevens, R. G. *et al.* Nucleation and growth of sulfate aerosol in coal-fired power plant plumes: sensitivity to background aerosol and meteorology. *Atmos. Chem. Phys.* **12**, 189–206 (2012).
57. Andres, R. J. & Kasgnoc, A. D. A time-averaged inventory of subaerial volcanic sulfur emissions. *J. Geophys. Res.* **103**, 25251–25262 (1998).
58. Kettle, A. J. & Andreae, M. O. Flux of dimethylsulfide from the oceans: a comparison of updated data sets and flux models. *J. Geophys. Res.* **105**, 26793–26808 (2000).
59. Nightingale, P. D. *et al.* In situ evaluation of air-sea gas exchange parameterizations using novel conservative and volatile tracers. *Glob. Biogeochem. Cycles* **14**, 373–387 (2000).
60. Woodhouse, M. T. *et al.* Sensitivity of cloud condensation nuclei to regional changes in dimethyl-sulphide emissions. *Atmos. Chem. Phys.* **13**, 2723–2733 (2013).
61. Bastos, L. & O'Hagan, A. Diagnostics for Gaussian process emulators. *Technometrics* **4**, 425–438 (2011).
62. Cofala, J., Amann, M., Klimont, Z. & Schopp, W. *Scenarios of World Anthropogenic Emissions of SO₂, NO_x and CO up to 2030*. Internal report of the Transboundary Air Pollution Programme (International Institute for Applied Systems Analysis, Laxenburg, 2005).
63. Bond, T. C. *et al.* A technology-based global inventory of black and organic carbon emissions from combustion. *J. Geophys. Res.* **109**, D14203, doi:10.1029/2003JD003697 (2004).
64. van der Werf, G. R., Randerson, J. T., Collatz, G. J. & Giglio, L. Carbon emissions from fires in tropical and subtropical ecosystems. *Glob. Change Biol.* **9**, 547–562 (2003).
65. Gong, S. A parameterization of sea-salt aerosol source function for sub and super-micron particles. *Glob. Biogeochem. Cycles* **17**, 1097, doi: 10.1029/2003GB002079 (2003).
66. Guenther, A. *et al.* A global model of natural volatile organic compound emissions. *J. Geophys. Res.* **100**, 8873–8892 (1995).



Extended Data Figure 1 | Validation of the global annual mean forcing emulator. The error bars show the emulator 95% uncertainty range around the mean prediction. The 1:1 line is shown.

Extended Data Table 1 | Emissions of aerosols and precursor gases used in the 1750–2000 simulations

Aerosol source	Emitted species	PD (2000) flux	PI (1750) flux	Ref.
Fossil fuel	BC / Tg C per year	3.0	0.0	17
	POM / Tg POM per year	3.2	0.0	17
Power stations	SO ₂ / Tg S per year	24.2	0.0	17, 62
Industrial processes	SO ₂	19.6	0.0	17, 62
Transportation	SO ₂	4.8	0.0	17, 62
Off-road	SO ₂	0.8	0.0	17, 62
Biofuel	BC / Tg C per year	1.6	0.4	17, 63
	POM / Tg POM per year	9.1	1.6	17, 63
Domestic	SO ₂ / Tg S per year	4.8	0.12	17, 63
Wildfires	BC / Tg C per year	3.1	1.03	17, 64
	POM / Tg POM per year	34.7	12.8	17, 64
	SO ₂ / Tg S per year	2.1	1.46	17, 64
Volcanoes	SO ₂ / Tg S per year	12.6	12.6	57
Marine dimethyl sulphide	DMS* / Tg S per year	17.1	17.1	58
Sea spray	Salt	Wind-dependent flux	Wind-dependent flux	65
Biogenic volatile organic carbon	Monoterpenes (α-pinene) / Tg POM produced per year	5–360	5–360	37, 66 (for spatial/temporal variation)
Anthropogenic volatile organic carbon	VOC / Tg POM produced per year	2–112	0.0	37

* The DMS emission flux is a global annual value but emissions are calculated at each time step based on the seawater DMS concentration field⁵⁸ and a sea–air transfer velocity⁵⁹. These baseline emissions were perturbed according to the factors given in Extended Data Table 3, except for the volatile organic carbon emissions, which were perturbed over the absolute range indicated in this table and in Extended Data Table 3. BC, black carbon; POM, particulate organic matter; VOC, volatile organic carbon.

Extended Data Table 2 | Emissions of aerosols and precursor gases used in the 1850–2000, 1900–2000 and 1850–1980 simulations.

Aerosol source	Emitted species	2000 flux	1980 flux	1900 flux	1850 flux	Ref.
Fossil fuel	BC / Tg C per year	3.0	2.1	0.4	0.1	45
	POM / Tg POM per year	5.8	3.5	0.8	0.2	45
Power stations	SO ₂ / Tg S per year	24.8	30.7	1.8	0.0	45
Industrial processes	SO ₂	8.8	11.3	5.6	0.6	45
Transportation	SO ₂	7.7	6.9	0.9	0.0	45
Off-road	SO ₂	5.6	3.6	0.9	0.0	45
Biofuel	BC / Tg C per year	2.2	2.5	2.0	1.0	45
	POM / Tg POM per year	12.1	12.0	8.9	6.4	45
Domestic	SO ₂ / Tg S per year	4.3	6.2	2.6	0.4	45
Wildfires	BC / Tg C per year	1.03	1.03	1.03	1.03	17, 64
	POM / Tg POM per year	12.8	12.8	12.8	12.8	17, 64
	SO ₂ / Tg S per year	1.46	1.46	1.46	1.46	17, 64
Volcanoes	SO ₂ / Tg S per year	12.6	12.6	12.6	12.6	57
Marine dimethyl sulphide	DMS / Tg S per year	17.1	17.1	17.1	17.1	58
Sea spray	Salt	Wind-dependent flux	Wind-dependent flux	Wind-dependent flux	Wind-dependent flux	65
Biogenic volatile organic carbon	Monoterpenes (α -pinene) / Tg POM produced per year	5-360	5-360	5-360	5-360	37, 66
Anthropogenic volatile organic carbon	VOC / Tg POM produced per year	2.7-145.0	2.6-150.0	0.5-26.5	0.3-15.0	37, 45 (CO emissions)

Extended Data Table 3 | Parameters and their maximum ranges used in the model simulations.

Parameter number	Parameter name	Description	Uncertainty range	Effect
Process parameters				
P1	BL_NUC	Boundary layer nucleation rate	$3.2 \times 10^{-7} - 2 \times 10^{-4} \text{ s}^{-1}$	Absolute
P2	FT_NUC	Free troposphere nucleation rate	0.01 – 10	Scaled
P3	AGEING	Ageing 'rate' from insoluble to soluble	0.3 – 5 monolayer	Absolute
P4	ACT_DIAM	Cloud drop activation dry diameter	50 – 100 nm	Absolute
P5	SO2O3_CLEAN	pH of cloud drops (controls SO ₂ + O ₃)	pH 4 – 6.5	Absolute
P6	SO2O3_POLL	pH of cloud drops (SO ₂ + O ₃)	pH 3.5 – 5	Absolute
P7	NUC_SCAV_DIAM	Nucleation scavenging offset dry diameter	0 – 50 nm	Absolute
P8	NUC_SCAV_ICE	Nucleation scavenging fraction (accumulation mode) in mixed and ice clouds (T < −15 °C)	0 – 1	Scaled
P9	DRYDEP_AIT	Dry deposition velocity of Aitken mode aerosol	0.5 – 2	Scaled
P10	DRYDEP_ACC	Dry deposition velocity of accumulation mode aerosol	0.1 – 10	Scaled
P11	ACC_WIDTH	Mode width (accumulation soluble/insoluble mode)	1.2 – 1.8	Absolute
P12	AIT_WIDTH	Mode width (Aitken soluble/insoluble)	1.2 – 1.8	Absolute
P13	NUC-AIT_SEP	Mode separation diameter (nucleation/Aitken)	9 – 18 nm	Absolute
P14	AIT-ACC_SEP	Mode separation diameter (Aitken/accumulation)	0.9 – 2 × ACT_DIAM	Scaled
Aerosol and precursor gas emissions				
P15	FF_EMS	BCOC mass emission rate (fossil fuel)	0.5 – 2	Scaled
P16	BB_EMS	BCOC mass emission rate (biomass burning)	0.25 – 4	Scaled
P17	BF_EMS	BCOC mass emission rate (biofuel)	0.25 – 4	Scaled
P18	FF_DIAM	BCOC emitted number median dry diameter (fossil fuel)	30 – 80 nm	Absolute
P19	BB_DIAM	BCOC emitted number median dry diameter (biomass burning)	50 – 200 nm	Absolute
P20	BF_DIAM	BCOC emitted number median dry diameter (biofuel)	50 – 200 nm	Absolute
P21	PRIM_SO4_FRAC	Mass fraction of SO ₂ converted to new sulphate particles in sub-grid plumes	0 – 1%	Scaled
P22	PRIM_SO4_DIAM	Emitted number median dry diameter of sub-grid sulphate particles	20 – 100 nm	Absolute
P23	SEASPRAY	Sea spray mass flux (coarse/accumulation)	0.2 – 5	Scaled
P24	ANTH_SO2	SO ₂ emission flux (anthropogenic)	0.6 – 1.5	Scaled
P25	VOLC_SO2	SO ₂ emission flux (volcanic)	0.5 – 2	Scaled
P26	DMS_FLUX	DMS emission flux	0.5 – 2	Scaled
P27	BIO_SOA	Biogenic monoterpene production of SOA	5 – 360 Tg POM per year *	Absolute
P28	ANTH_SOA	Anthropogenic VOC production of SOA	2 – 112 Tg POM per year *	Absolute

The Latin Hypercube sampling of parameter combinations was designed to lie within these ranges. In the 'effect' column, for the scaled parameters the magnitude of the parameter was multiplied by a factor lying between the maximum and minimum given in the 'uncertainty range' column and for absolute adjustments, the parameter was set to a value within the range of absolute values in the 'uncertainty range' column. BCOC, black carbon/organic carbon; SOA, secondary organic aerosol. *The values given refer to the mass of POM produced, although the perturbations were actually applied to the emitted VOCs. The POM range refers to year 2000. For other years see Extended Data Table 2. The baseline emissions are given in Extended Data Tables 1 and 2.

Extended Data Table 4 | Results for the different periods.

Period	Emissions	Forcing (W m ⁻²)	Forcing standard deviation (W m ⁻²)	Forcing standard deviation divided by forcing	Percentage of variance due to natural emissions	Percentage of variance due to anthropogenic emissions	Percentage of variance due to aerosol processes
Annual mean values							
1750–2000	AeroCom	−1.16	0.22	0.18	45	34	14
June mean values							
1750–2000	AeroCom	−1.42	0.27	0.19	45	38	13
1850–2000	ACCMIP	−1.30	0.28	0.22	37	46	11
1900–2000	ACCMIP	−0.96	0.20	0.21	37	43	13
1850–1980	ACCMIP	−1.29	0.27	0.21	38	47	11

All numbers refer to global means. The last three columns refer to percentage of variance.

SHANK3 overexpression causes manic-like behaviour with unique pharmacogenetic properties

Kihoon Han^{1,2,3}, J. Lloyd Holder, Jr^{3,4,5}, Christian P. Schaaf^{1,3}, Hui Lu^{1,2,3}, Hongmei Chen^{3,4,6}, Hyojin Kang^{1,3,†}, Jianrong Tang^{3,4}, Zhenyu Wu^{3,4}, Shuang Hao^{3,4}, Sau Wai Cheung^{1,7}, Peng Yu^{1,3}, Hao Sun^{3,4,6}, Amy M. Breman^{1,7}, Ankita Patel^{1,7}, Hui-Chen Lu^{3,4,6,8} & Huda Y. Zoghbi^{1,2,3,4,8}

Mutations in *SHANK3* and large duplications of the region spanning *SHANK3* both cause a spectrum of neuropsychiatric disorders, indicating that proper *SHANK3* dosage is critical for normal brain function. However, *SHANK3* overexpression per se has not been established as a cause of human disorders because 22q13 duplications involve several genes. Here we report that *Shank3* transgenic mice modelling a human *SHANK3* duplication exhibit manic-like behaviour and seizures consistent with synaptic excitatory/inhibitory imbalance. We also identified two patients with hyperkinetic disorders carrying the smallest *SHANK3*-spanning duplications reported so far. These findings indicate that *SHANK3* overexpression causes a hyperkinetic neuropsychiatric disorder. To probe the mechanism underlying the phenotype, we generated a *Shank3* *in vivo* interactome and found that *Shank3* directly interacts with the Arp2/3 complex to increase F-actin levels in *Shank3* transgenic mice. The mood-stabilizing drug valproate, but not lithium, rescues the manic-like behaviour of *Shank3* transgenic mice raising the possibility that this hyperkinetic disorder has a unique pharmacogenetic profile.

An increasing number of neuropsychiatric disorders such as autism spectrum disorder (ASD), intellectual disability, schizophrenia, obsessive-compulsive disorder and bipolar disorder are being classified as 'synaptopathies'^{1–4}, because the genes mutated in these disorders lead to abnormal synaptic development or function. For example, all members of the *SHANK* gene family (*SHANK1*, *SHANK2* and *SHANK3*), which encode for core scaffolding proteins organizing macromolecular complexes at the postsynaptic density (PSD)⁵, have been linked to human synaptopathies^{6–8}. Point mutations in *SHANK3* (also called *ProSAP2*) are seen in non-syndromic autism, intellectual disability and schizophrenia^{8–12}, and deletions of the region containing *SHANK3* cause Phelan-McDermid syndrome (22q13 deletion syndrome)^{13,14}. Furthermore, mice modelling *SHANK3* deletion mirror the human behavioural phenotypes and display synaptic abnormalities^{15–17}.

Interestingly, a few 22q13 duplications spanning *SHANK3* have been reported in patients diagnosed with Asperger syndrome, attention deficit hyperactivity disorder (ADHD) or schizophrenia^{9,10,18}, indicating that increased expression of *SHANK3* could be also deleterious. Because duplication cases involve large genomic regions (>0.8 Mb) with more than 20 genes, however, it is unclear if it is *SHANK3* overexpression that causes a neurological phenotype. Here we describe the generation and characterization of *Shank3*-overexpressing mice and studies on the role of *SHANK3* duplication in hyperkinetic neuropsychiatric disorders in humans. We identify a mechanism that contributes to the neuronal phenotype and report pharmacological therapies that might benefit individuals with *SHANK3* overexpression.

Manic-like behaviour in *Shank3* transgenic mice

We introduced an amino-terminal enhanced green fluorescent protein (EGFP) tag into mouse *Shank3* to generate EGFP-*Shank3* transgenic

mice (Fig. 1a and Extended Data Fig. 1a). Similar to endogenous *Shank3* (ref. 16), EGFP-*Shank3* transcript was detected in cortex, hippocampus and striatum (Fig. 1b). The regional and developmental expression of EGFP-*Shank3* recapitulated those of endogenous *Shank3* (Extended Data Fig. 1b–d). EGFP-*Shank3* was targeted to the dendritic spines and co-localized with excitatory postsynaptic marker PSD-95, but not with inhibitory postsynaptic marker gephyrin (Fig. 1c). Compared to wild-type mice, transgenic mice expressed 1.2-fold to twofold higher levels of each of the three major *Shank3* isoforms (α , β and γ), with ~50% more total *Shank3* protein (Fig. 1d and Extended Data Fig. 1e, f), which parallels expression in human *SHANK3* duplication patients. There was no significant change in levels of other synaptic proteins in the hippocampus and striatum of transgenic mice (Extended Data Fig. 1g, h).

Our *Shank3* transgenic mice showed increased locomotor activity and speed compared with wild-type littermates in the open field test (Fig. 2a, b and Extended Data Fig. 2a). Transgenic mice were also hyperactive in their home cages, indicating that their behaviour in the open field was not due to the novel environment (Extended Data Fig. 2b). Given that one patient carrying a large 22q13 duplication spanning *SHANK3* has been reported to have ADHD¹⁰, we sought to determine whether the hyperactivity in the transgenic mice is related to ADHD by testing whether it could be corrected by amphetamine, a treatment for ADHD. Surprisingly, rather than the expected paradoxical calming effect, an acute injection of amphetamine aggravated the hyperactivity of transgenic mice to a greater degree than wild-type mice (Fig. 2c, d). As increased sensitivity to amphetamine is one characteristic of mania¹⁹—bipolar disorder can be misdiagnosed as ADHD, especially in children due to the overlap in diagnostic criteria²⁰—we pursued behavioural tests to determine if there are abnormalities typically associated with a manic state.

¹Department of Molecular and Human Genetics, Baylor College of Medicine, Houston, Texas 77030, USA. ²Howard Hughes Medical Institute, Baylor College of Medicine, Houston, Texas 77030, USA. ³Jan and Dan Duncan Neurological Research Institute at Texas Children's Hospital, Houston, Texas 77030, USA. ⁴Department of Pediatrics, Baylor College of Medicine, Houston, Texas 77030, USA. ⁵Division of Neurology and Developmental Neuroscience, Baylor College of Medicine, Houston, Texas 77030, USA. ⁶The Cain Foundation Laboratories, Texas Children's Hospital, Houston, Texas 77030, USA. ⁷Medical Genetics Laboratories, Baylor College of Medicine, Houston, Texas 77030, USA. ⁸Program in Developmental Biology and Department of Neuroscience, Baylor College of Medicine, Houston, Texas 77030, USA. [†]Present address: National Institute of Supercomputing and Networking, Korea Institute of Science and Technology Information, Daejeon, South Korea.

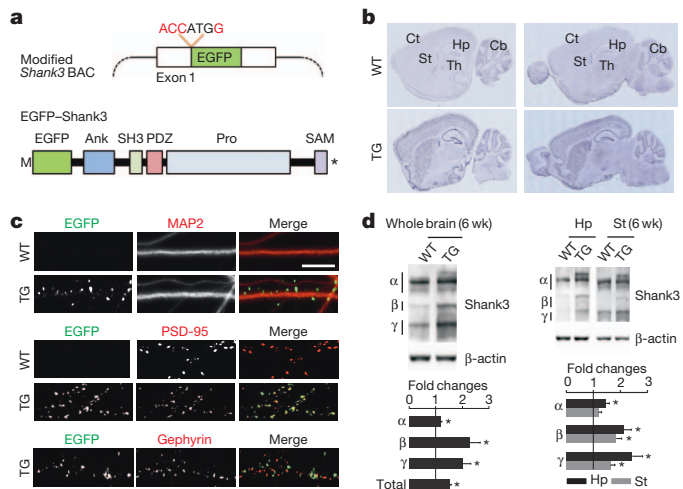


Figure 1 | Characterization of EGFP-Shank3 expression in *Shank3* transgenic mice. **a**, Diagrams show the modified *Shank3* BAC and EGFP-Shank3. Kozak (ACCATGG) and EGFP-coding sequence were integrated into the start codon of *Shank3*. **b**, RNA *in situ* hybridization with a probe against EGFP detected EGFP-Shank3 in the brain. Cb, cerebellum; Ct, cortex; Hp, hippocampus; St, striatum; TG, transgenic; Th, thalamus; WT, wild type. **c**, EGFP-Shank3 localizes to excitatory postsynaptic sites in cultured hippocampal neurons. MAP2 is a dendritic marker. Scale bar, 10 μ m. **d**, Quantification of the fold changes of Shank3 (α , β and γ isoforms) in synaptosomal fraction of whole brain ($n = 4$, biological replicates), hippocampus or striatum ($n = 6$) from 6-week-old mice. All data are presented as mean \pm s.e.m. * $P < 0.05$; unpaired two-tailed Student's t -test.

Immobility during the tail-suspension test has been used as an indicator of despair. Consistent with manic-like behaviour²¹, the duration of immobility in *Shank3* transgenic mice was less than wild-type littermates (Fig. 2e); the transgenic mice also exhibited elevated acoustic

startle response with reduced prepulse inhibition (PPI), abnormal circadian rhythms, and hyperphagia-like behaviour (Fig. 2f–j and Extended Data Fig. 2c, d), all of which are behaviours observed in humans during manic episodes^{22,23}.

We normalized Shank3 levels by crossing the transgenic mice with *Shank3B*^{+/-} mice¹⁶ and found that this reversed hyperactivity, reduced immobility in tail-suspension and reduced PPI (Extended Data Fig. 3). *Shank3* transgenic mice also displayed decreased social interaction (Extended Data Fig. 2e–g), which has also been seen in patients with large 22q13 duplications^{9,18}. Unlike *Shank3* knockout mice^{16,17}, *Shank3* transgenic mice did not exhibit repetitive behaviour (Extended Data Fig. 2h–j), but they made fewer calls during the ultrasonic vocalization test at postnatal day 13 (Extended Data Fig. 2k, l). Together, these results suggest that $\sim 50\%$ increase in Shank3 level causes a hyperkinetic phenotype in mice that resembles mania, and that it is the increased dosage of *SHANK3* in 22q13 duplications that probably contributes to hyperkinesia in humans.

SHANK3 duplications in humans

To confirm unequivocally the role of *SHANK3* dosage in the neuropsychiatric phenotypes, we queried the array Comparative Genomic Hybridization (aCGH) database at the Molecular Genetics Laboratory of Baylor College of Medicine and identified two cases that carry small duplications (Fig. 3a, b and Supplementary Data).

The first individual is an 11-year-old girl diagnosed with ADHD, combined type. The 22q13 duplication includes the entire *SHANK3* and part of the *ACR* gene (Fig. 3a). *ACR* encodes acrosin, a protease expressed in sperm facilitating its penetration into oocytes, with no known expression or function in the brain. This individual has seizures and exhibits hyperactivity, poor attention, auditory overstimulation, hyperphagia and kleptomania. Notably, her hyperactivity is resistant to the paradoxical calming effect of stimulant medications seen in most cases of ADHD. The second individual is a 35-year-old man diagnosed with bipolar disorder and epilepsy who has a duplication encompassing

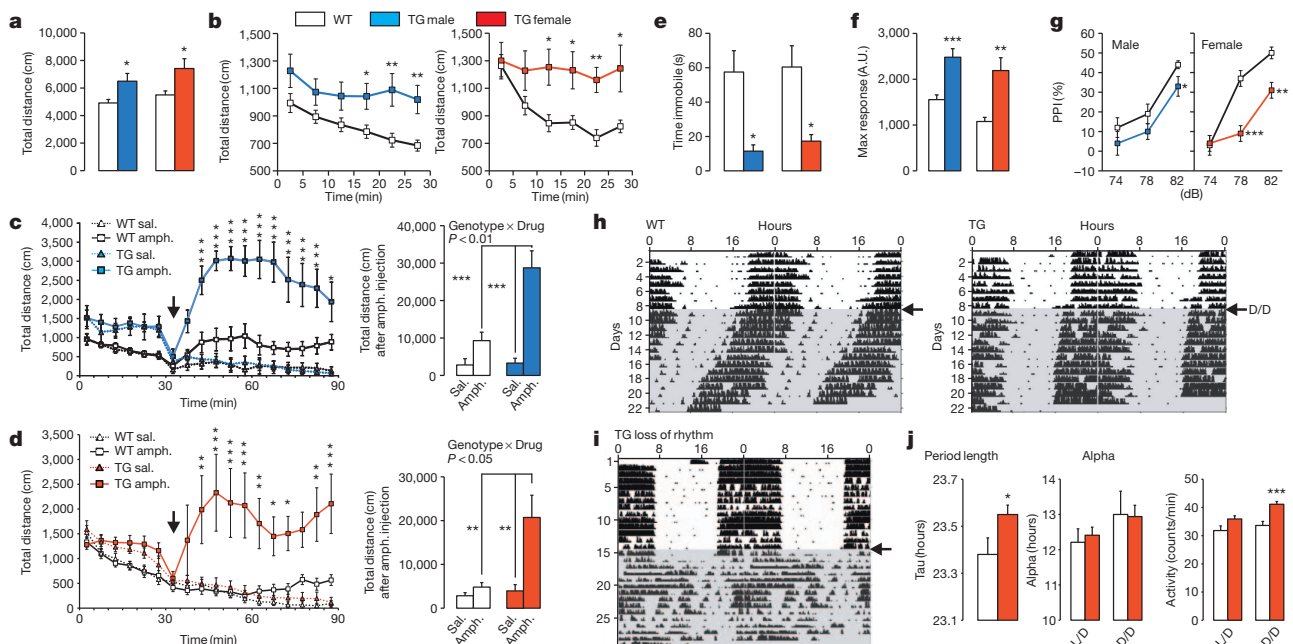


Figure 2 | *Shank3* transgenic mice display manic-like behaviours. **a**, Transgenic mice show increased locomotor activity in the open field test. **b**, Transgenic mice did not habituate during the open field assay. **c**, **d**, Transgenic mice are hypersensitive to amphetamine. After 30 min of basal activity, amphetamine (2 mg per kg) or saline was administered (arrow) and locomotor activity was monitored for 60 min. **e**, Transgenic mice spend less time immobile in the tail-suspension test. **f**, Increased acoustic (120 dB) startle response of transgenic mice. **g**, Abnormal PPI of transgenic mice. **h**, **i**, **j**, Abnormal circadian rhythms of transgenic mice. **h**, Wheel running actograms of wild-type and transgenic female mice. After 8 days of light/dark (L/D) cycle, animals were released into constant darkness (arrow, D/D) for 2 weeks. **i**, Among 20 transgenic mice tested, 3 displayed complete loss of rhythm during D/D. **j**, Transgenic mice showed increased period length and activity count, but normal alpha, compared to wild-type mice. All data are presented as mean \pm s.e.m. * $P < 0.05$; ** $P < 0.01$; *** $P < 0.001$. Statistical analyses for behavioural assays are in Supplementary Table 1.

h–j, Abnormal circadian rhythms of transgenic mice. **h**, Wheel running actograms of wild-type and transgenic female mice. After 8 days of light/dark (L/D) cycle, animals were released into constant darkness (arrow, D/D) for 2 weeks. **i**, Among 20 transgenic mice tested, 3 displayed complete loss of rhythm during D/D. **j**, Transgenic mice showed increased period length and activity count, but normal alpha, compared to wild-type mice. All data are presented as mean \pm s.e.m. * $P < 0.05$; ** $P < 0.01$; *** $P < 0.001$. Statistical analyses for behavioural assays are in Supplementary Table 1.

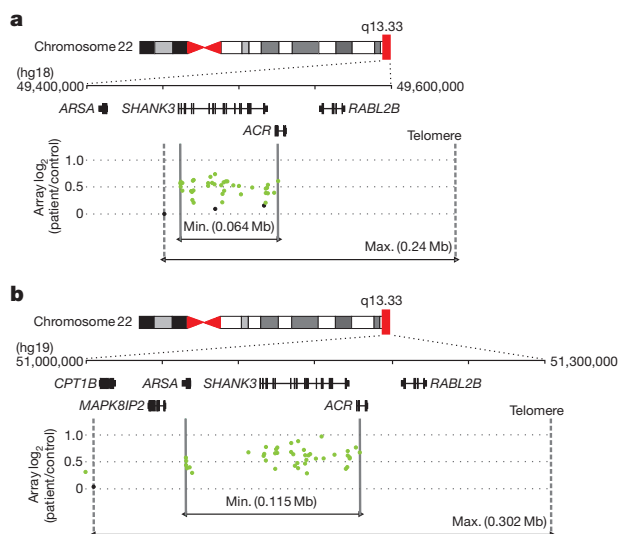


Figure 3 | Individuals with *SHANK3* duplications have hyperkinetic disorders. **a**, Array plot of an exon-targeted chromosome microarray analysis on DNA from an 11-year-old female with ADHD, seizures and aberrant behaviours. Black dots indicate probes with normal copy number and green dots indicate copy number gain. Solid and dotted lines define the minimum and maximum expected boundaries of the duplication, respectively. **b**, Array plot of the 35-year-old male with bipolar disorder and epilepsy.

SHANK3, *ACR* and *ARSA*, the gene encoding arylsulfatase A (Fig. 3b). *ARSA* deficiency causes metachromatic leukodystrophy, and duplications of *ARSA* have not been associated with any neurobehavioural phenotype.

These two individuals carry the smallest 22q13 duplications spanning *SHANK3* reported so far, and their molecular and clinical findings support the notion that *SHANK3* duplications result in hyperkinetic disorders and seizures in humans. More detailed clinical and molecular cytogenetic information about both individuals is provided in the supplementary material.

Synaptic E/I imbalance in *Shank3* transgenic mice

Having found that humans with *SHANK3* duplications have a hyperkinetic disorder and seizures, we evaluated the *Shank3* transgenic mice for seizures and synaptic abnormalities. We observed spontaneous seizures in the *Shank3* transgenic mice, but never in wild-type littermates (Supplementary Video 1). We monitored for electrographic seizures using electroencephalography (EEG). The EEG of transgenic mice showed hyperexcitability discharges accompanied by electrographic seizures (Fig. 4a). As alteration in the neuronal excitatory/inhibitory (E/I) balance is considered to cause seizures²⁴, we examined morphological and functional changes of both excitatory and inhibitory synapses. Cultured hippocampal pyramidal neurons from transgenic mice displayed increased VGLUT1-positive PSD-95 (VGLUT1 is also known as SLC17A7), an excitatory synaptic marker, and decreased VGAT-positive (also known as SLC32A1) gephyrin, an inhibitory synaptic marker, puncta density (Fig. 4b).

We examined functional properties of synapses by whole-cell patch clamping in CA1 pyramidal neurons of acute hippocampal slices. Neuronal density, paired-pulse facilitation ratio, input–output relationship and intrinsic excitability of these neurons were similar in wild-type and transgenic mice, indicating normal basal synaptic transmission at Schaffer collateral-CA1 synapses of transgenic mice (Extended Data Fig. 4a–e). Consistent with decreased density of VGAT-positive gephyrin puncta in cultured hippocampal neurons from transgenic mice, we observed reduction in GABA_A receptor-mediated miniature inhibitory postsynaptic current (mIPSC) frequency, but not in amplitude or decay time (Fig. 4c). AMPA receptor-mediated miniature EPSC (mEPSC) was normal, but amplitude of spontaneous EPSC (sEPSC, without

tetrodotoxin) was increased in transgenic mice (Extended Data Fig. 4f and Fig. 4d). There was no change in the AMPA/NMDA ratio in CA1 pyramidal neurons of transgenic compared to wild-type mice (Fig. 4e). Consistently, NMDA receptor-dependent synaptic plasticity measured by extracellular field recordings at Schaffer collateral-CA1 pyramidal synapses was normal in transgenic mice (Extended Data Fig. 4g, h). The spontaneous seizures of transgenic mice, together with morphological and functional alterations in synapses, indicate that the synaptic E/I balance in transgenic neurons is shifted towards excitation.

Arp2/3 complex mediates F-actin increase

To understand the molecular mechanisms underlying the synaptic alterations of *Shank3* transgenic mice, we set out to identify the *in vivo* interactors of *Shank3*. We used the EGFP-tag of the *Shank3* transgene to isolate *Shank3* protein complexes (Extended Data Fig. 5a). Immunoprecipitation followed by mass-spectrometry analysis identified 273 proteins that bind *Shank3 in vivo* (Supplementary Table 4). There was notable overlap between the proteins on this list, those from our previous yeast two-hybrid screening²⁵, and known mouse or human PSD proteins^{26,27} (Extended Data Fig. 5b). We combined our two *Shank3*-focused experimental lists (previous yeast two-hybrid screening²⁵ and current *in vivo* immunoprecipitation, for a total of 404 proteins called the *Shank3* interactome) for further analysis (Extended Data Fig. 5c, d).

We performed Gene Ontology (GO) and pathway analysis, which suggested that regulation of actin cytoskeleton is a principal role of the *Shank3* interacting proteins (Extended Data Fig. 5e and Supplementary Table 5). Based on this analysis, we proposed that abnormal regulation of the actin cytoskeleton could be one major molecular change in the synapses of transgenic mice. Accordingly, we evaluated the effects of a 50% increase in *Shank3* on F-actin levels. We found that F-actin levels of excitatory synapses were increased by ~30% in cultured hippocampal pyramidal neurons from transgenic mice compared to wild-type mice (Fig. 5a), which was restored by expression of *Shank3* small interfering RNA (siRNA) (Extended Data Fig. 6a, b). Next, we used our *Shank3* interactome to generate a sub-network of actin-related proteins (Fig. 5b) to focus the search on molecular mediators of the elevated F-actin. This network comprises both known and previously unknown *Shank3* interactors, which we confirmed by western blotting (Extended Data Fig. 5f). The most interesting new *Shank3* direct interactors we identified (based on both yeast two-hybrid screening and *in vivo* immunoprecipitation) were two subunits of the Arp2/3 complex (ARPC2 and ARPC5L) (Fig. 5b). Arp2/3 complex consists of seven-subunits and binds directly to the F-actin mother filament to initiate nucleation and branching²⁸. Consistent with the interaction analysis, ARPC2 clusters co-localized with EGFP–*Shank3* and significantly enlarged in transgenic neurons (Extended Data Fig. 5g and Fig. 5c); the latter observation was reversed by *Shank3* siRNA (Extended Data Fig. 6c). To initiate actin polymerization, Arp2/3 complex must be activated by nucleation-promoting factors (NPFs)²⁸. Given that the NPFs WASF1 and cortactin (CTTN) directly interact with *Shank3* (refs 29, 30), *Shank3* could function as a scaffold that brings WASF1, cortactin and Arp2/3 together, facilitating the formation of F-actin structures (Fig. 5d). Consistent with our hypothesis, co-localization of WASF1 and ARPC2 was enhanced in transgenic neurons (Fig. 5e). Furthermore, the density of dendritic spines was increased in transgenic brains compared to wild-type brains (Fig. 5f).

Our analysis indicated that hippocampal pyramidal neurons of transgenic mice have a reduced number of inhibitory synapses (Fig. 4b, c), which was unexpected based on the exclusive localization of EGFP–*Shank3* in excitatory synapses (Fig. 1c). To understand the underlying mechanism, we first investigated inhibitory neurons, changes of which might secondarily affect inhibitory synapses on pyramidal neurons. However, we found that there was no difference in synapse number on the GAD-6-positive inhibitory neurons of transgenic mice, although these neurons express EGFP–*Shank3* (Extended Data Fig. 7).

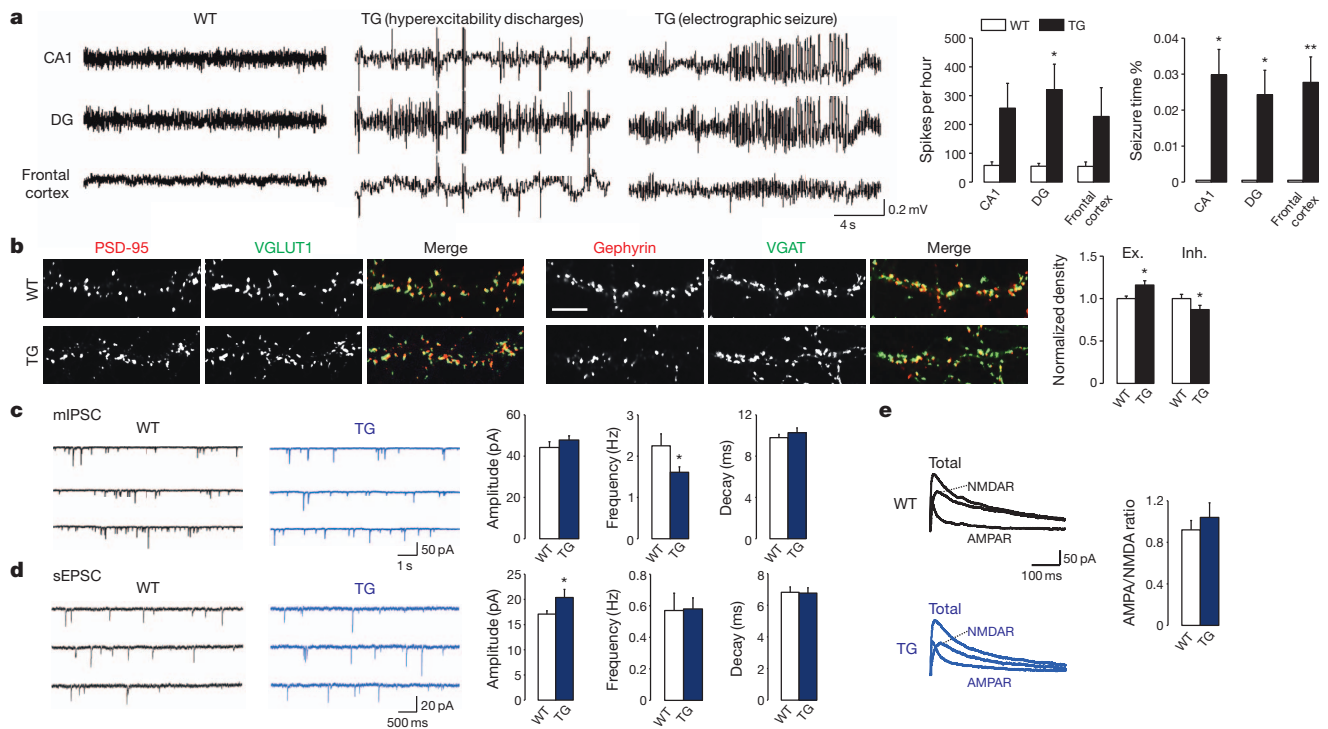


Figure 4 | Abnormal EEG and altered synaptic excitatory/inhibitory balance of *Shank3* transgenic mice. **a**, Representative EEG traces from wild-type ($n = 5$) and transgenic ($n = 10$) mice. Transgenic mice showed prolonged hyperexcitability discharges and electrographic seizure in all recorded regions. The frequency of epileptiform spikes (dentate gyrus) and electrographic seizure were significantly increased in transgenic mice. **b**, Increased VGLUT1-positive PSD-95 ($n = 28$, three independent experiments) and decreased VGAT-positive gephyrin ($n = 25$) puncta density in cultured hippocampal pyramidal

We next explored a possible cell-autonomous relationship between excitatory and inhibitory synapses of transgenic pyramidal neurons. We speculated that increased clustering of actin-related proteins in excitatory synapses might reduce some of those proteins in inhibitory synapses, thereby contributing to the decrease of inhibitory synapse number. We focused on actin-related proteins, because the actin cytoskeleton defines the molecular architecture of both E/I synapses³¹. We picked Mena (also known as Enah) and profilin as candidates for four reasons: they directly interact with gephyrin in inhibitory synapses³²; profilin1 and profilin2 are recruited to excitatory synapses by neuronal activity^{33,34}; profilin2 was also identified in our *Shank3* *in vivo* immunoprecipitation (Supplementary Table 4); and Mena and profilin interact with proteins in the *Shank3* interactome (Extended Data Fig. 8). Both proteins showed decreased localization to inhibitory synapses, and profilin2 showed enhanced localization to excitatory synapses in transgenic neurons (Fig. 5g–i). Together, these results suggest that increased expression of *Shank3* enhances F-actin levels through Arp2/3 complex in excitatory synapses of transgenic neurons. By modulating the synaptic distributions of Mena and profilin2, this contributes, at least in part, to changes in inhibitory synapses.

Shank3 transgenic mice respond to valproate

Having established that *Shank3* overexpression causes mania-like behaviour in mice and a hyperkinetic syndrome in humans, we tested whether mood-stabilizing drugs for human mania could rescue the behavioural abnormalities of transgenic mice. First, we examined the effect of lithium, the first Food and Drug Administration (FDA)-approved treatment for bipolar disorder, which inhibits multiple targets including inositol monophosphatase and glycogen synthase kinase 3 (GSK3)³⁵. The basal activity of GSK3- β in transgenic mouse hippocampus and striatum was similar to that of wild-type mice (Fig. 6a). Mice

were fed with lithium carbonate-containing chow for three weeks, resulting in serum lithium levels (wild type: 0.82 ± 0.04 ; transgenic: $0.91 \pm 0.08 \text{ mmol l}^{-1}$) comparable to those in the therapeutic range for humans ($0.6 \sim 1.2 \text{ mmol l}^{-1}$). Lithium did not mitigate any of the manic-like behaviours of *Shank3* transgenic mice (Fig. 6b and Extended Data Fig. 9).

Given that our mice display seizures in addition to manic-like behaviour, we decided to test valproate, another FDA-approved mood-stabilizing drug used to treat manic or mixed episodes that also acts as an anticonvulsant, increases GABA neurotransmission and inhibits sodium channels, calcium channels and histone deacetylase 1 (ref. 36). We treated the transgenic mice with acute intraperitoneal injections of either valproate (200 mg per kg) or saline and subjected them to behavioural testing. Valproate reversed the baseline hyperactivity, the amphetamine-hypersensitivity (Fig. 6c, d), and the abnormal acoustic startle response and PPI (Fig. 6e–h) in transgenic mice. The behaviour of wild-type mice, except for a decrease in baseline activity and an increase of PPI in male mice, was not significantly affected by valproate treatment (Fig. 6c–h). Valproate also significantly decreased the frequency of epileptiform spikes in transgenic mice as measured by EEG (Fig. 6i). Valproate treatment changed neither the levels of synaptic proteins in hippocampus or striatum of wild-type and transgenic mice, nor F-actin levels in cultured hippocampal neurons of transgenic mice (Extended Data Fig. 10).

Discussion

There are many genomic loci for which both deletions and duplications cause human neuropsychiatric disorders, indicating that proper dosage of some genes is critical for normal brain function^{37,38}. In most cases, however, the genes causing the respective phenotypes are poorly defined, making it hard to understand pathogenesis and to develop

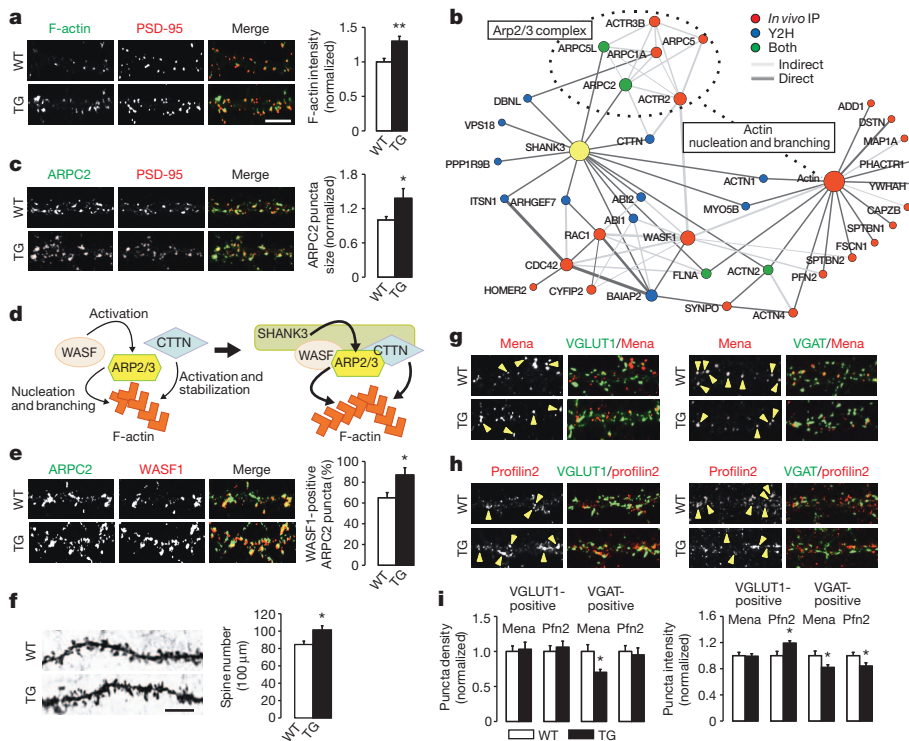


Figure 5 | Shank3 interacts directly with Arp2/3 complex to increase F-actin levels in *Shank3* transgenic mice. **a**, Increased synaptic F-actin in cultured hippocampal pyramidal neurons from transgenic mice ($n = 29$, three independent experiments). Scale bar, 10 μm . **b**, Actin cytoskeleton-related sub-network of Shank3 interactome. Y2H, yeast two-hybrid. **c**, Increased ARPC2 cluster size in transgenic pyramidal neurons ($n = 20$). **d**, Diagram shows the proposed role of Shank3 as a platform for F-actin regulating proteins. **e**, Increased co-localization of ARPC2 and WASF1 in transgenic pyramidal neurons ($n = 22$). **f**, Golgi-staining of CA1 pyramidal neurons shows more dendritic spines in transgenic mice ($n = 40$ neurons from 3 animals per genotype). **g, h**, Excitatory and inhibitory synaptic distributions of Mena (**g**) and profilin2 (**h**) in cultured CA1 pyramidal neurons. Yellow arrowheads indicate protein puncta co-localized with corresponding synaptic markers. **i**, Quantification of (**g**) and (**h**). Density of VGLUT1-positive Mena puncta is decreased in transgenic neurons ($n = 18$). VGLUT1-positive profilin2 puncta intensity is increased in transgenic neurons ($n = 13$), whereas VGAT-positive Mena and profilin2 puncta intensity are decreased in transgenic neurons. All data are presented as mean \pm s.e.m. * $P < 0.05$; ** $P < 0.01$.

targeted therapies. Chromosome 22q13 spanning *SHANK3* is one example. Although *SHANK3* loss has been shown to cause ASD in humans, *SHANK3* overexpression has never been definitively determined to cause neuropsychiatric disease. In this study, we generated *Shank3* transgenic mice that model a human duplication and identified patients with the smallest 22q13 duplications involving *SHANK3*. The remarkable similarity of the neurobehavioural phenotypes between the mouse model and patients with *SHANK3* duplications supports the notion that *SHANK3* overexpression causes a hyperkinetic neuropsychiatric disorder that approximates mania. Indeed, either a 50% reduction or

50% increase in *Shank3* levels results in marked neuropsychiatric phenotypes and a predisposition to epilepsy.

Notably, the manic-like behaviour of *Shank3* transgenic mice was reversed selectively by valproate but not by lithium treatment. It is not uncommon to find human patients with bipolar disorder that are resistant to lithium monotherapy³⁹. Indeed, a subset of individuals with the rapid-cycling form of bipolar disorder is highly resistant to lithium⁴⁰. As GSK3 is considered the major target for lithium's efficacy in the treatment of BPD⁴¹, the lithium-resistance of *Shank3* transgenic mice and their normal GSK-3 β activity are congruent with a mechanism independent of GSK-3 and possibly more dependent upon synaptic alterations, including E/I imbalance.

Synaptic E/I imbalance is likely to underlie the pathogenesis for seizures^{24,42} and a broad spectrum of neuropsychiatric disorders^{1,43}. We found morphological and functional changes in E/I synapses of transgenic neurons favouring excitation, which might account for both seizures and hyperkinetic behaviour. Consistent with this, GABAergic dysfunction in patients with bipolar disorder has been reported⁴⁴, and valproate (which increases GABA neurotransmission and decreases high-frequency action potential firing) rescued the manic-like behaviours of transgenic mice. In contrast, lithium enhances excitatory postsynaptic potentials in CA1 synapses⁴⁵, which might explain the resistance of *Shank3* transgenic mice to lithium treatment. Mechanistically,

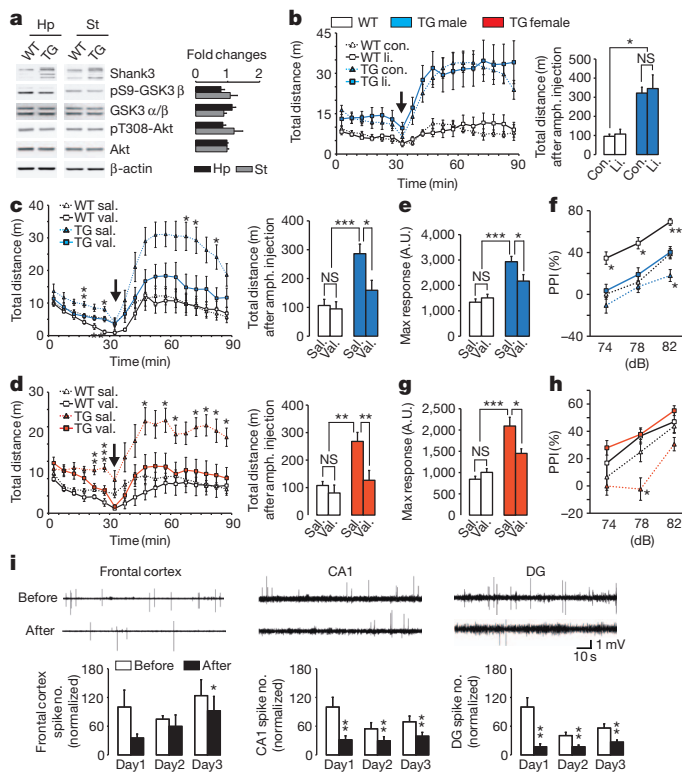


Figure 6 | Valproate, but not lithium, rescues manic-like behaviours of *Shank3* transgenic mice. **a**, Basal activities of GSK-3 β and Akt in the hippocampus and striatum of transgenic mice (10-week-old, $n = 7$) are normal. **b**, Amphetamine-sensitivity of male transgenic mice was not rescued by lithium. NS, not significant. **c, d**, Basal locomotor activity and amphetamine-sensitivity of transgenic mice were rescued by valproate. Basal activity of wild-type male mice was decreased by valproate during one 5-min time bin. **e–h** Acoustic startle response (**e, g**) and PPI (**f, h**) of transgenic mice were rescued by valproate. Valproate increased PPI of wild-type male mice. **i**, Rescue of abnormal EEG in transgenic mice by valproate. During the three consecutive days of tests, EEG was recorded from the three brain regions of transgenic mice ($n = 7$) for one hour before and after valproate injection. Representative EEG traces measured on day 1 are shown. The number of epileptiform spikes was quantified and normalized to the baseline values before treatment of day 1. All data are presented as mean \pm s.e.m. * $P < 0.05$; ** $P < 0.01$; *** $P < 0.001$.

enhanced F-actin polymerization through Arp2/3 complex could be responsible for the synaptic changes of transgenic neurons, but other Shank3-dependent molecular pathways cannot be excluded.

In conclusion, our study advances our understanding of the human diseases associated with *SHANK3* and the mechanisms that can lead to bipolar disorder. We propose two distinct mechanisms leading to bipolar disorder: one is dysfunction of the well-established GSK-3 pathway that is responsive to lithium treatment; the second is a synaptic dysfunction associated with an E/I balance shifted towards excitation, which could result in hyperkinetic behaviours, and which is resistant to lithium but sensitive to valproate. We believe this sort of pharmacogenetic analysis in model organisms could improve treatment strategies for patients with bipolar disorder as the genetic underpinnings of each patient's illness are elucidated.

METHODS SUMMARY

BAC clone (RP23-278D8) containing entire mouse *Shank3* was modified by recombinant techniques. The linearized segment including *EGFP-Shank3* plus ~12 kb in the 5' direction and ~2 kb in the 3' direction was injected into the FVB/N embryos to generate transgenic mice. Behavioural, electrophysiological, biochemical and cell biological characterization of the mice were performed and analysed blind to genotypes. All experimental procedures were reviewed and approved by the Institutional Animal Care and Use Committee for Baylor College of Medicine. The details of experimental procedures, reagents and bioinformatic analyses are described in the Methods.

Online Content Any additional Methods, Extended Data display items and Source Data are available in the online version of the paper; references unique to these sections appear only in the online paper.

Received 20 February; accepted 2 September 2013.

Published online 23 October 2013.

- Südhof, T. C. Neurologins and neuroligins link synaptic function to cognitive disease. *Nature* **455**, 903–911 (2008).
- Zoghbi, H. Y. Postnatal neurodevelopmental disorders: meeting at the synapse? *Science* **302**, 826–830 (2003).
- Bourgeron, T. A synaptic trek to autism. *Curr. Opin. Neurobiol.* **19**, 231–234 (2009).
- Ting, J. T., Peca, J. & Feng, G. Functional consequences of mutations in postsynaptic scaffolding proteins and relevance to psychiatric disorders. *Annu. Rev. Neurosci.* **35**, 49–71 (2012).
- Sheng, M. & Kim, E. The Shank family of scaffold proteins. *J. Cell Sci.* **113**, 1851–1856 (2000).
- Sato, D. *et al.* *SHANK1* Deletions in Males with Autism Spectrum Disorder. *Am. J. Hum. Genet.* **90**, 879–887 (2012).
- Berkel, S. *et al.* Mutations in the *SHANK2* synaptic scaffolding gene in autism spectrum disorder and mental retardation. *Nature Genet.* **42**, 489–491 (2010).
- Grubbs, A. M., Schmeisser, M. J., Schoen, M. & Boeckers, T. M. Postsynaptic ProSAP/Shank scaffolds in the cross-hair of synaptopathies. *Trends Cell Biol.* **21**, 594–603 (2011).
- Durand, C. M. *et al.* Mutations in the gene encoding the synaptic scaffolding protein *SHANK3* are associated with autism spectrum disorders. *Nature Genet.* **39**, 25–27 (2007).
- Moessner, R. *et al.* Contribution of *SHANK3* mutations to autism spectrum disorder. *Am. J. Hum. Genet.* **81**, 1289–1297 (2007).
- Gauthier, J. *et al.* Novel de novo *SHANK3* mutation in autistic patients. *Am. J. Med. Genet. B. Neuropsychiatr. Genet.* **150B**, 421–424 (2009).
- Gauthier, J. *et al.* De novo mutations in the gene encoding the synaptic scaffolding protein *SHANK3* in patients ascertained for schizophrenia. *Proc. Natl Acad. Sci. USA* **107**, 7863–7868 (2010).
- Bonaglia, M. C. *et al.* Disruption of the *ProSAP2* gene in a t(12;22)(q24.1;q13.3) is associated with the 22q13.3 deletion syndrome. *Am. J. Hum. Genet.* **69**, 261–268 (2001).
- Bonaglia, M. C. *et al.* Identification of a recurrent breakpoint within the *SHANK3* gene in the 22q13.3 deletion syndrome. *J. Med. Genet.* **43**, 822–828 (2006).
- Bozdagi, O. *et al.* Haploinsufficiency of the autism-associated *Shank3* gene leads to deficits in synaptic function, social interaction, and social communication. *Mol. Autism* **1**, 15 (2010).
- Peca, J. *et al.* *Shank3* mutant mice display autistic-like behaviours and striatal dysfunction. *Nature* **472**, 437–442 (2011).
- Wang, X. *et al.* Synaptic dysfunction and abnormal behaviors in mice lacking major isoforms of *Shank3*. *Hum. Mol. Genet.* **20**, 3093–3108 (2011).
- Failla, P. *et al.* Schizophrenia in a patient with subtelomeric duplication of chromosome 22q. *Clin. Genet.* **71**, 599–601 (2007).
- Shaltiel, G. *et al.* Evidence for the involvement of the kainate receptor subunit GluR6 (GRIK2) in mediating behavioral displays related to behavioral symptoms of mania. *Mol. Psychiatry* **13**, 858–872 (2008).
- Leibenluft, E. & Rich, B. A. Pediatric bipolar disorder. *Annu. Rev. Clin. Psychol.* **4**, 163–187 (2008).
- Martinowich, K., Schloesser, R. J. & Manji, H. K. Bipolar disorder: from genes to behavior pathways. *J. Clin. Invest.* **119**, 726–736 (2009).
- Perry, W., Minassian, A., Feifel, D. & Braff, D. L. Sensorimotor gating deficits in bipolar disorder patients with acute psychotic mania. *Biol. Psychiatry* **50**, 418–424 (2001).
- Belmaker, R. H. Bipolar disorder. *N. Engl. J. Med.* **351**, 476–486 (2004).
- McCormick, D. A. & Contreras, D. On the cellular and network bases of epileptic seizures. *Annu. Rev. Physiol.* **63**, 815–846 (2001).
- Sakai, Y. *et al.* Protein interactome reveals converging molecular pathways among autism disorders. *Sci. Transl. Med.* **3**, 86ra49 (2011).
- Collins, M. O. *et al.* Molecular characterization and comparison of the components and multiprotein complexes in the postsynaptic proteome. *J. Neurochem.* **97** (Suppl 1), 16–23 (2006).
- Bayés, A. *et al.* Characterization of the proteome, diseases and evolution of the human postsynaptic density. *Nature Neurosci.* **14**, 19–21 (2011).
- Campellone, K. G. & Welch, M. D. A nucleator arms race: cellular control of actin assembly. *Nature Rev. Mol. Cell Biol.* **11**, 237–251 (2010).
- Proepper, C. *et al.* Abelson interacting protein 1 (Abi-1) is essential for dendrite morphogenesis and synapse formation. *EMBO J.* **26**, 1397–1409 (2007).
- Naisbitt, S. *et al.* Shank, a novel family of postsynaptic density proteins that binds to the NMDA receptor/PSD-95/GKAP complex and cortactin. *Neuron* **23**, 569–582 (1999).
- Sheng, M. & Kim, E. The postsynaptic organization of synapses. *Cold Spring Harb. Perspect. Biol.* (<http://dx.doi.org/10.1101/cshperspect.a005678>) (2011).
- Giesemann, T. *et al.* Complex formation between the postsynaptic scaffolding protein gephyrin, profilin, and Mena: a possible link to the microfilament system. *J. Neurosci.* **23**, 8330–8339 (2003).
- Neuhoff, H. *et al.* The actin-binding protein profilin I is localized at synaptic sites in an activity-regulated manner. *Eur. J. Neurosci.* **21**, 15–25 (2005).
- Ackermann, M. & Matus, A. Activity-induced targeting of profilin and stabilization of dendritic spine morphology. *Nature Neurosci.* **6**, 1194–1200 (2003).
- Jope, R. S. Anti-bipolar therapy: mechanism of action of lithium. *Mol. Psychiatry* **4**, 117–128 (1999).
- Rosenberg, G. The mechanisms of action of valproate in neuropsychiatric disorders: can we see the forest for the trees? *Cell. Mol. Life Sci.* **64**, 2090–2103 (2007).
- Ramocki, M. B. & Zoghbi, H. Y. Failure of neuronal homeostasis results in common neuropsychiatric phenotypes. *Nature* **455**, 912–918 (2008).
- Toro, R. *et al.* Key role for gene dosage and synaptic homeostasis in autism spectrum disorders. *Trends Genet.* **26**, 363–372 (2010).
- Gitlin, M. Treatment-resistant bipolar disorder. *Mol. Psychiatry* **11**, 227–240 (2006).
- Dunner, D. L. & Fieve, R. R. Clinical factors in lithium carbonate prophylaxis failure. *Arch. Gen. Psychiatry* **30**, 229–233 (1974).
- Gould, T. D. & Manji, H. K. Glycogen synthase kinase-3: a putative molecular target for lithium mimetic drugs. *Neuropsychopharmacology* **30**, 1223–1237 (2005).
- Maglóczy, Z. & Freund, T. F. Impaired and repaired inhibitory circuits in the epileptic human hippocampus. *Trends Neurosci.* **28**, 334–340 (2005).
- Marin, O. Interneuron dysfunction in psychiatric disorders. *Nature Rev. Neurosci.* **13**, 107–120 (2012).
- Benes, F. M. *et al.* Regulation of the GABA cell phenotype in hippocampus of schizophrenics and bipolars. *Proc. Natl Acad. Sci. USA* **104**, 10164–10169 (2007).
- Schloesser, R. J., Martinowich, K. & Manji, H. K. Mood-stabilizing drugs: mechanisms of action. *Trends Neurosci.* **35**, 36–46 (2012).

Supplementary Information is available in the online version of the paper.

Acknowledgements We are indebted to the patients and families who participated in this study; to J. W. Belmont and N. Miller for contributing patients to this study; G. Feng for sharing *Shank3B* mice; G. Schuster for injection of *Shank3* BAC; and C. Spencer for behavioural assays training. This project was supported by The Howard Hughes Medical Institute (H.Y.Z.), National Institutes of Health (NIH) ARRA grant (1R01NS070302) (H.Y.Z.), the Baylor Intellectual and Developmental Disabilities Research Center (P30HD024064) confocal, electrophysiology and mouse neurobehavioral cores, and the Cancer Prevention and Research Institute of Texas (CPRT) RP110784. J.L.H. was supported by an Early Career Award from the Thrasher Research Fund, NIH 2T32NS043124 and the Ting Tsung and Wei Fong Chao Foundation; C.P.S. was supported by the Joan and Stanford Alexander family, the Ting Tsung and Wei Fong Chao Foundation and the Doris Duke Clinical Scientist Development Award.

Author Contributions K.H., J.L.H., H.L., H.C., J.T., H.-C.L. and H.Y.Z. designed the experiments. K.H., J.L.H., H.L., H.C., J.T., Z.W., S.H. and H.S. performed the research. K.H., J.L.H., C.P.S., H.L., H.C., H.K., J.T., Z.W., S.H., S.W.C., P.Y., A.M.B., A.P., H.-C.L. and H.Y.Z. collected, analysed and interpreted the data. K.H., J.L.H., C.P.S., H.L., H.K., J.T., H.-C.L. and H.Y.Z. wrote and edited the paper.

Author Information Reprints and permissions information is available at www.nature.com/reprints. The authors declare no competing financial interests. Readers are welcome to comment on the online version of the paper. Correspondence and requests for materials should be addressed to H.Y.Z. (hzoghbi@bcm.edu).

METHODS

Generation of *Shank3* transgenic mice. To generate *Shank3* transgenic mice, we used a BAC clone (RP23-278D8) containing a segment of mouse chromosome 15. This BAC clone was modified by recombinering techniques⁴⁶ to insert Kozak sequence (ACCATGG) followed by EGFP sequence (cloned from pEGFP-C1) at the first start codon of *Shank3* gene (exon 1). The modified BAC clone was double digested with NotI/SwaI, and the ~75 kb linearized segment with entire *Shank3* gene plus ~12 kb 5' and ~2 kb 3' was injected into the FVB/N embryos (Extended Data Fig. 1a). The primers used for genotyping were designed against EGFP sequence (forward: 5'-ATGGTGAGCAAGGGCGAGGAG-3', reverse: 5'-GCGGACTTGAAGAAGTCGTGC-3'). All procedures to maintain and use these mice were approved by the Institutional Animal Care and Use Committee for Baylor College of Medicine.

Primary antibodies. Antibodies used for the western blots and/or immunostainings are Akt (Cell Signaling Technology; 4691), phospho-Akt (Thr 308) (Cell Signaling Technology; 2965), ARPC2 (Millipore; 07-227), β -actin (Abcam; ab20272), CYFIP2 (Abcam; ab95969), GABA_A β 3 (NeuroMab; 75-149), GAD-6 (Developmental Studies Hybridoma Bank), Gephyrin (Synaptic Systems; 147 111), GFP (Abcam; ab290, ab13970), GKAP (NeuroMab; 75-156), GluR2 (NeuroMab; 75-002), GSK-3 α/β (Millipore; 05-412), phospho-GSK-3 β (Ser 9) (Cell Signaling Technology; 9336), Homer (Santa Cruz; sc-15321), MAP2 (Sigma; M9942), Mena/Vasp (Millipore; MAB2635), mGluR5 (Millipore; AB5675), NR1 (Millipore; MAB363), Profilin2 (TU-Braunschweig; 4H5), PSD-95 (NeuroMab; 75-028), pan-Shank (3856; (ref. 47)), Shank1 (NeuroMab; 75-064), Shank2 (NeuroMab; 75-088), Shank3 (Santa Cruz; H-160), VGAT (Synaptic Systems; 131 002), VGlut1 (Synaptic Systems; 135 302) and WASF1 (NeuroMab; 75-048).

Preparation of brain lysates and western blot. S2 (soluble fraction) and P2 (crude synaptosomal fraction) subcellular, and PSD fractions (synaptic fraction after one time Triton X-100 washout) were prepared as described⁴⁸. For Akt and GSK3 detection, brains were dissected and homogenized in ice-cold lysis buffer (20 mM Tris-HCl, pH 7.4, 150 mM NaCl, 2 mM EDTA, 1% Triton X-100, 10% glycerol with protease and phosphatase inhibitor (Roche)). Western blot images were acquired by LAS 4000 (GE Healthcare) and quantified by an ImageJ software package.

Hippocampal neuron cultures, transfection and immunostaining. Hippocampal neurons were prepared from postnatal day 0-1 FVB/N mice and plated on poly-D-lysine/mouse laminin coated coverslips (BD Biosciences) in Neurobasal medium supplemented with GlutaMAX-I (Invitrogen), B-27 and 1% FBS. At days *in vitro* (DIV) 7, neurons were transfected with pEGFP-C1 plus either control or *Shank3* siRNA (Ambion, s81603 or s81605). At DIV 14, neurons were fixed with 4% formaldehyde/4% sucrose in PBS, and permeabilized with 0.2% Triton X-100 in PBS. PBS with 0.1% BSA and 3% horse serum was used for blocking and antibody incubation. Alexa-conjugated phalloidin (Invitrogen) was used to visualize F-actin. Z-stack images were acquired by LSM710 (Zeiss) confocal microscope under the same parameter settings and the images were quantified (in a blinded manner) using ImageJ.

RNA *in situ* hybridization. Hybridization probe specific for EGFP sequence was prepared by PCR amplification from the pEGFP-C1 using the following primers (forward: 5'-ATGGTGAGCAAGGGCGAGGAG-3', reverse: 5'-CTGTACAGCTCGTCCATGCC-3'). Riboprobe was generated using DIG RNA labelling mix (Roche).

Golgi staining. Standard Golgi-Cox impregnation using the FD Rapid GolgiStain kit (NeuroTechnologies) was performed with brains from 10-week-old FVB/N male mice. Serial sagittal sections (50 μ m) were collected and images of dendritic spines on the secondary branches (apical dendrites of CA1 pyramidal neurons) were acquired by LSM710 (Zeiss) confocal microscope under differential interference contrast (DIC) mode. The images were quantified (in blinded manner) using ImageJ.

Cresylviolet staining. Brains from 10-week-old FVB/N male mice were cryosectioned (25 μ m) and stained with 0.2% cresyl violet.

Drug treatment. For each experiment, individual was blinded to genotype and littermates were randomly distributed to control and treatment groups as follows; Animal with genotype A was assigned to control, next animal of genotype A to drug, third to control. Same with genotype B. Amphetamine and valproate (Sigma) were dissolved in normal saline to final concentration of 0.2 g l⁻¹ and 20 g l⁻¹, respectively. Mice received intraperitoneal injection of amphetamine (2 mg per kg), valproate (200 mg per kg) or saline in a volume of 10 ml kg⁻¹. Valproate was injected three times before each behavioural assay (10:00 and 17:00 on the day prior to the assay and 9:00 of the day of assay), and assays were performed 30 min after final injection. For lithium treatment, mice were fed either lithium carbonate-containing chow or control chow (Harlan Teklad). The lithium group was initially fed 0.2% lithium carbonate chow for a week followed by 0.4% chow for two more weeks before the behavioural assays.

Water with 0.85% sodium chloride was provided to counteract toxicity of lithium. Lithium concentration in serum was measured using lithium assay kit (Crystal Chem) according to the manufacturer's instruction.

Behavioural assays. All data acquisition and analyses were carried out by an individual blinded to the genotype. For behavioural assays, 2-3-month-old mice (both males and females) of the F1 hybrid (FVB/N \times C57BL/6J) were used to mitigate strain specific effects. A sample size of mice was chosen to mitigate genetic background variance. Before each test, mice were habituated in the test room at least for 30 min. Mice with sign of seizures (before, during or after test) were excluded from the analysis. The summary of statistical analysis for behavioural assays is provided in Supplementary Table 1.

Open field. After habituation in the test room (600 lx, 60 dB white noise), mice were placed in the centre of a clear, open Plexiglass chamber (40 \times 40 \times 30 cm), and the activities were measured by photobeam breaks (Accuscan) for 30 min. To measure amphetamine response, mice received intraperitoneal injection of saline or amphetamine after 30 min test of basal activities, and the activities were measured for additional 60 min.

Home-cage activity. Single-caged mice were habituated in the cage for 12 h, and the activities were measured by photobeam breaks (Accuscan) for 48 h under the light cycle of 07:00-19:00.

Tail suspension. After habituation period in the test room (600 lx, 60 dB white noise), mice were suspended by their tails. Movements were recorded and the immobile time was automatically measured by ANY-maze software (Stoelting). The same parameter setting for the definition of immobility was applied for all the mice tested.

Acoustic startle response and prepulse inhibition. Mice were placed in a test chamber (San Diego Instruments) and habituated for 5 min with 70 dB background white noise. Eight trial types (no stimulus, a 40 ms 120 dB sound as the startle stimulus, and three different prepulse sounds (20 ms 74, 78, 82 dB) either alone or 100 ms before the startle stimulus) were presented in pseudo-random order with six times per each trial type. The interval between each trial type was 10 to 20 s. The maximum startle amplitude during the 65 ms period following the onset of the startle stimulus was used to calculate percentage prepulse inhibition.

Circadian rhythms. Mice were individually housed in cages equipped with a 11.5 cm diameter wheel, and wheel-running activity was recorded by VitalView software (Respironics Mini-Mitter system). Mice were held on a 12:12 light/dark cycle for 8 to 14 days with food, water and temperature at 20 \pm 2 $^{\circ}$ C. Mice were then released into constant dark for 14 days.

Three chamber test. The test was performed as previously described⁴⁹. The three chamber apparatus is a clear Plexiglass box (24.75 \times 16.75 \times 8.75 inches) with removable partitions separating the box into left, centre and right chambers. The age- and gender-matched C57BL/6J mice were used as novel partners. Two days before the test, the novel partner mice were habituated to the wire cages (3 inches diameter by 4 inches in height) for 1 h per day. The wire cage with inanimate novel object inside served as a control. The test mouse was habituated in the chamber for 15 min as described⁴⁹. During the habituation period, neither wild-type nor *Shank3* transgenic mice showed a preference for either side of the chamber (data not shown). After the habituation period, the novel partner mouse was placed into one of the wire cages and located randomly in either the right or left side of chamber. The novel object was placed into the wire cage located in the other side of chamber. The test mouse was allowed to explore the three chamber apparatus for 15 min. The movements were recorded and the total amount of time spent in each chamber was automatically measured by ANY-maze software (Stoelting). The close interaction time, defined by rearing, sniffing or pawing at each wire cage, was measured manually.

Grooming. After habituation period in the test room (600 lx, 60 dB white noise), mice were placed into the centre of a Plexiglass cylinder (20 cm in diameter by 30 cm in height) and videotaped for 10 min. The amount of time spent grooming was measured from the videotape.

Ultrasonic vocalization. Separation-induced ultrasonic vocalizations (USV) were measured on pups of postnatal day 6 to 13. A standard housing cage containing one female and her offspring was transferred to a holding room and allowed to acclimate for 30 min. Following this acclimation period, the cage was transferred to a testing room. Pups were placed into a clean and warm (35 $^{\circ}$ C) cage and allowed to acclimate for 5 min. The mother was removed from the testing room and transferred back to the holding room. After 5 min acclimation period, one pup will be placed individually into a plastic beaker in a testing chamber. A bat detector positioned 10 cm above the beaker transduced ultrasonic signals. USV was quantified for a total testing period of 2 min using sound analysis software (Ultravox, Noldus Information Technology).

EEG measurement. All data acquisition and analyses were carried out blinded to genotype. FVB/N 2-3-month-old male mice were anaesthetized with isoflurane. Under aseptic conditions, each mouse was surgically implanted with tungsten

electrodes (50 μm diameter) aimed at hippocampal CA1 (P2.0R1.2H1.3) and dentate (P2.0R1.8H1.8) regions. The third EEG electrode made of silver wire (127 μm diameter) was implanted in the subdural space of the right frontal cortex area. A reference/grounding electrode was then positioned in the occipital region of the skull. All electrode wires were attached to a miniature connector (Harwin Connector). After 3 to 5 days of post-surgical recovery, EEG activities (filtered between 0.1 Hz and 5 kHz, sampled at 10 kHz) were recorded for 1 h per day over 3 to 5 days. In the experiments evaluating the effects of valproate on EEG activities, adult male *Shank3* transgenic mice with implanted electrode went through recording sessions for 3 consecutive days. On each day, animals received one hour baseline recording before valproate (200 mg per kg, i.p.) followed by another hour of post recording.

EEG data analysis. Electrographic seizure time lasting over 10 s was counted manually and normalized as the percentage of the total recording period. The number of abnormal epileptiform spikes were counted using Clampfit 10 software (Molecular Devices) when the sharp positive deflections exceeding twice the baseline and lasting 25–100 ms⁵⁰. In the pharmacological tests, spike numbers were normalized to the baseline value before drug administration on day 1.

Whole-cell patch-clamp recordings. All data acquisition and analyses were carried out blinded to genotype. Acute fresh hippocampal slices were prepared from FVB/N male mice at the age of 6–8-weeks old as previously described⁵¹. Coronal slices (250- μm thick) containing medial hippocampus were cut with a vibratome (Leica Microsystems) in a chamber filled with chilled (2–5 °C) cutting solution containing (in mM) 110 choline-chloride, 25 NaHCO₃, 25 D-glucose, 11.6 sodium ascorbate, 7 MgSO₄, 3.1 sodium pyruvate, 2.5 KCl, 1.25 NaH₂PO₄ and 0.5 CaCl₂. The slices were then incubated in artificial cerebrospinal fluid (ACSF, in mM) containing 119 NaCl, 26.2 NaHCO₃, 11 D-glucose, 3 KCl, 2 CaCl₂, 1 MgSO₄, 1.25 NaH₂PO₄ at the room temperature. The solutions were bubbled with 95% O₂ and 5% CO₂. Whole-cell recording was made using patchclamp amplifiers (Multiclamp 700B) under infrared-differential interference contrast microscopy (Zeiss). Data acquisition and analysis were performed using digitizers (DigiData 1440A) and analysis software pClamp 10 (Molecular Devices). Signals were filtered at 2 kHz and sampled at 10 kHz. Spontaneous EPSCs (sEPSCs), miniature EPSCs (mEPSCs) and IPSCs (mIPSCs) were recorded from CA1 hippocampal pyramidal neurons at –70 mV in voltage-clamp mode. sEPSCs were recorded in the presence of GABA_A receptor blocker, SR95531 (10 μM). mEPSCs were recorded in the presence of tetrodotoxin (TTX, 0.5 μM) and SR95531 (10 μM). Glass pipettes with a resistance of 2.5–5 M Ω were filled with a solution containing (in mM) 140 potassium gluconate, 5 KCl, 10 HEPES, 0.2 EGTA, 2 MgCl₂, 4 MgATP, 0.3 Na₂GTP and 10 Na₂-phosphocreatine, pH 7.2 (with KOH). For recording mIPSCs, potassium gluconate was replaced with KCl (140 μM) in the pipette solution. Besides TTX (0.5 μM), glutamate receptor antagonists 6-cyano-7-nitroquinoxaline-2,3-dione disodium (CNQX) (10 μM) and D-2-amino-5-phosphonopivalic acid (D-AP-5) (25 μM) were also added to the bath. Series resistance (15–30 M Ω) and input resistance (100–200 M Ω) were monitored throughout the whole-cell recording. Evoked EPSCs were recorded in the presence of SR95531 (10 μM). To stimulate presynaptic inputs, stimulation pulses (50 μs duration at 0.1 Hz) were applied to a bipolar tungsten stimulation electrode (WPI) placed along the Schaffer collaterals. Extracellular stimuli were administered using a stimulator system (Master 8). The stimulating and recording pipettes were placed at the same depth in the slice and the distance between them was kept constant (~300 μm). Data were discarded when the change in the series resistance was >20% during the course of the experiment. The whole-cell recording was performed at 30 \pm 1 °C with the help of an automatic temperature controller (Warner Instruments). For measurements of the AMPA-to-NMDA receptor ratio, the CA1 pyramidal neuron was voltage-clamped at 40 mV. First, a stable baseline recording of total EPSCs was obtained. The NMDA receptor antagonist D-AP-5 (50 mM) was then applied to the bath for 5–10 min to isolate fast AMPA-receptor-mediated EPSCs. Digital subtraction of AMPA-receptor-EPSCs from the total EPSCs from the same neuron yielded NMDA-receptor-EPSCs. An average of 12–20 EPSCs were collected for each type of EPSC. The bath solution contained picrotoxin (100 μM). The intracellular solution contained 140mM CsCH₃SO₃, 10mM HEPES, 1 mM EGTA, 5mM TEA-Cl, 2mM MgCl₂, 2.5mM MgATP and 0.3mM GTP, pH 7.2–7.4 (with CsOH).

Extracellular field recordings. All data acquisition and analyses were carried out blinded to genotype. One- to two-month-old FVB/N male mice were anaesthetized with isoflurane and their brains were removed and immersed immediately in ice-cold cutting solution (in mM): 110 sucrose, 3 KCl, 0.5 CaCl₂, 60 NaCl₂, 7 MgCl₂, 1.25 NaH₂PO₄, 28 NaHCO₃, 5 D-glucose saturated with 95% O₂ and 5% CO₂. 400- μm thick transverse hippocampal slices were prepared with a vibrating microtome Series 1000 (Vibratome) and recovered at 31 \pm 0.5 °C for an hour in an interface chamber. Field excitatory postsynaptic potential (fEPSP) were recorded at 31 \pm 0.5 °C in an interface chamber perfused at 1 ml min^{–1} with artificial

cerebrospinal fluid (ACSF) containing (in mM): 125 NaCl, 2.5 KCl, 2 CaCl₂, 1 MgCl₂, 1.25 NaH₂PO₄, 25 NaHCO₃, and 15 D-glucose. Extracellular stimuli were administered along the Schaffer collaterals using Formvar-insulated, bipolar nichrome electrodes controlled by a stimulus isolator (A-M Systems). An ACSF-filled glass-recording electrode was placed in stratum radiatum to record the field potential changes. Electrophysiological traces were amplified with AC-coupled amplifier (model 1800; A-M Systems), digitized using a Digidata 1320A (Molecular Devices), and acquired with pClamp 10 software (Molecular Devices). To assess baseline synaptic transmission, input–output relationships were examined by measuring the rising slope of the fEPSP evoked by 100- μs pulses over various stimulus intensities (1 V to 10 V). The stimulation intensity that evoked a fEPSP whose slope was 30–40% of the maximum fEPSP slope, determined by the input–output recording experiment, was used for the following recording paradigms. Long-term potentiation (LTP) was induced by two trains of 100 stimuli pulses at 100 Hz that are separated 20 s apart. To monitor LTP development, the fEPSPs were recorded every 20 s for 20 min before and 60 min after induction. The magnitude of potentiation was determined by measuring the changes in the slope of the fEPSP. NMDAR-dependent long-term depression (LTD) formation was induced with 900 paired stimuli with 50 ms inter-stimulus interval at 1 Hz frequency. In all experiments, genotypes were confirmed by PCR with tails cut. All data are shown as mean \pm s.e.m.

In vivo immunoprecipitation and mass spectrometry. Striatum and hippocampus were dissected from 8 animals (5-weeks-old) per each genotype (wild-type and *Shank3* transgenic FVB/N male mice), and crude synaptosomal fraction solubilized with deoxycholic acid (DOC) buffer was prepared as described previously⁴⁷. Then ~10 mg of lysates were incubated with GFP-Trap beads (ChromoTek) for 2 h at 4 °C. The beads were briefly washed with binding/dialysis buffer (50 mM Tris-HCl, pH 7.4, 0.1% Triton X-100) and boiled in with 1 \times NuPAGE LDS sample buffer (Invitrogen) to be loaded on SDS–PAGE (NuPAGE 4–12% Bis-Tris Gel, Invitrogen). The eluted proteins were visualized with Coomassie Brilliant blue stain and excised into 10 gel pieces according to molecular size. The individual gel pieces were destained and subject to in-gel digestion using trypsin. Tryptic peptide was dissolved in 10 μl of loading solution (5% methanol containing 0.1% formic acid) and subjected to nanoflow LC–MS/MS analysis with a nano-LC II (Thermo Scientific) coupled to LTQ Orbitrap Velos (Thermo Scientific) mass spectrometer. The peptides were loaded onto an in-house Reprosil-Pur Basic C18 (3 μm , Dr. Maisch) trap column which was 2 cm \times 75 μm size. Then the trap column was washed with loading solution and switched in-line with an in-house 100 mm \times 75 μm column packed with Reprosil-Pur Basic C18 equilibrated in 0.1% formic acid/water. The peptides were separated with a 75 min discontinuous gradient of 5–28% acetonitrile/0.1% formic acid at a flow rate of 450 nl min^{–1}. Separated peptides were directly electro-sprayed into LTQ Orbitrap Velos mass spectrometer. The LTQ Orbitrap instrument was operated in the data-dependant mode acquiring fragmentation spectra of the top 50 strongest ions and under direct control of Xcalibur software (Thermo Scientific). Obtained MS/MS spectra were searched against target-decoy mouse refseq database in Proteome Discoverer 1.3 interface (Thermo Fisher) with Mascot algorithm (Mascot 2.3, Matrix Science). The precursor mass tolerance was confined within 20 p.p.m. with fragment mass tolerance of 0.5 Da and a maximum of two missed cleavage allowed. Assigned peptides were filtered with 5% false discovery rate (FDR) and subject to manual verifications. Any protein whose peptide was identified from wild-type brain sample was excluded from the further analysis.

Construction of Shank3 interactome network. To build an interaction network with the union set of Shank3 interactors (*in vivo* immunoprecipitation plus yeast two-hybrid screening), protein interactions were adopted from iRefIndex database (<http://irefindex.org>) which provides consolidated protein interactions from the 10 primary interaction databases (BIND, BioGRID, CORUM, DIP, HPRD, IntAct, MINT, MPact, MPPI and OPHID). Only the interactions among human and mouse genes were included. The direct interactions were distinguished from the indirect interactions based on experimental assays. Network graphics were generated with Cytoscape⁵². Nodes and edges were coloured based on the source and interaction type of the proteins, respectively. Thickness of edges for direct interactions correlates with the number of supportive evidences in the interaction database (Fig. 5b). To simplify the network, orphan nodes, defined by the nodes which have interaction only with Shank3, were excluded from the network (Extended Data Fig. 5c).

Network topology analysis of Shank3 interactome. Shortest path length (the number of links of the shortest path travelling from one protein to another protein) was calculated to measure the network topology of Shank3 interactome. To test the significance, we randomly picked the same number of proteins from the mouse PSP²⁶ and calculated shortest path length of the interactome network generated with the proteins. This re-sampling was repeated 10,000 times and the

empirical *P* value (the number of sample networks whose mean path length is smaller than that of Shank3 interactome/10,000) was calculated.

Gene ontology (GO) analysis. The GO analysis was carried out using DAVID software (version 6.7)^{53,54}. The union set of Shank3 interactors from the *in vivo* immunoprecipitation and yeast two-hybrid screening was tested against a customized background gene list in which genes expressed at low levels in mouse brain were excluded.

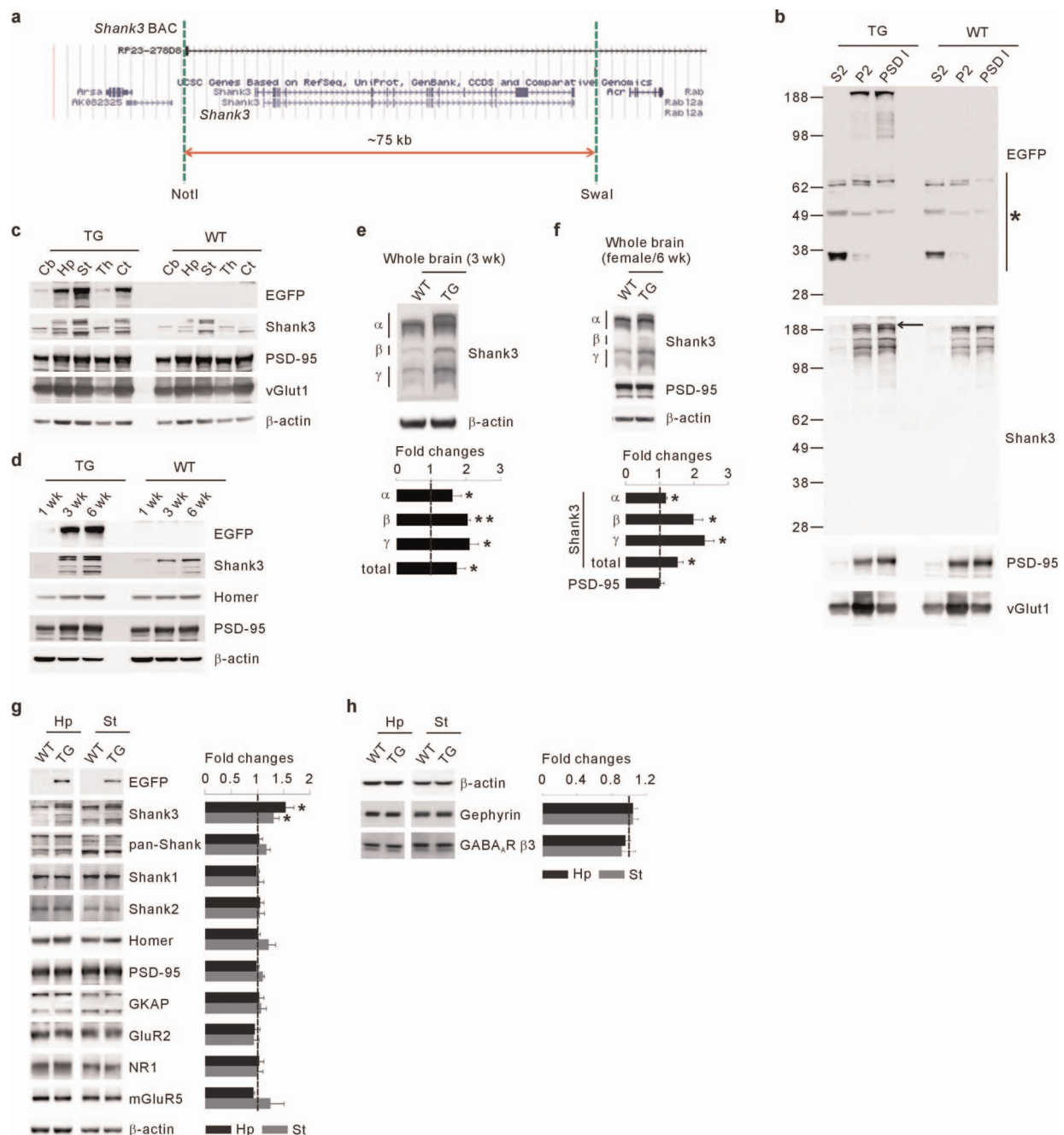
Human subjects. Both individuals were referred to the Medical Genetics Laboratories, Baylor College of Medicine, Houston, USA, for clinical array comparative genomic hybridization (aCGH) analysis. Following informed consent, approved by the Institutional Review Board for Human Subject Research at Baylor College of Medicine, the medical records of the respective individuals were reviewed. Additional clinical information was obtained by phone interview with patient 1's legal guardian and patient 2, respectively.

Array comparative genomic hybridization. Patient DNA, isolated from peripheral whole blood using the Puregene DNA extraction kit (Gentra) following the manufacturer's instructions, was analysed using the Baylor College of Medicine V8 OLIGO clinical genomic microarray, described⁵⁵. Briefly, this is a custom-designed genomic microarray with both genome-wide coverage and supplementary exonic coverage of ~1,700 known or suspected disease genes, including *SHANK3*.

Quantification and statistical analysis. For quantification, values from three independent experiments with at least three biological replicates were used. For behavioural assays, all population values appear normally distributed and the variance is similar between the groups. *P* values were calculated by Student's

t-test or analysis of variance with proper post-hoc tests (GraphPad Prism), as specified in each figure legend or Supplementary Tables 1–3. All data are presented as mean ± s.e.m. **P* < 0.05; ***P* < 0.01; ****P* < 0.001.

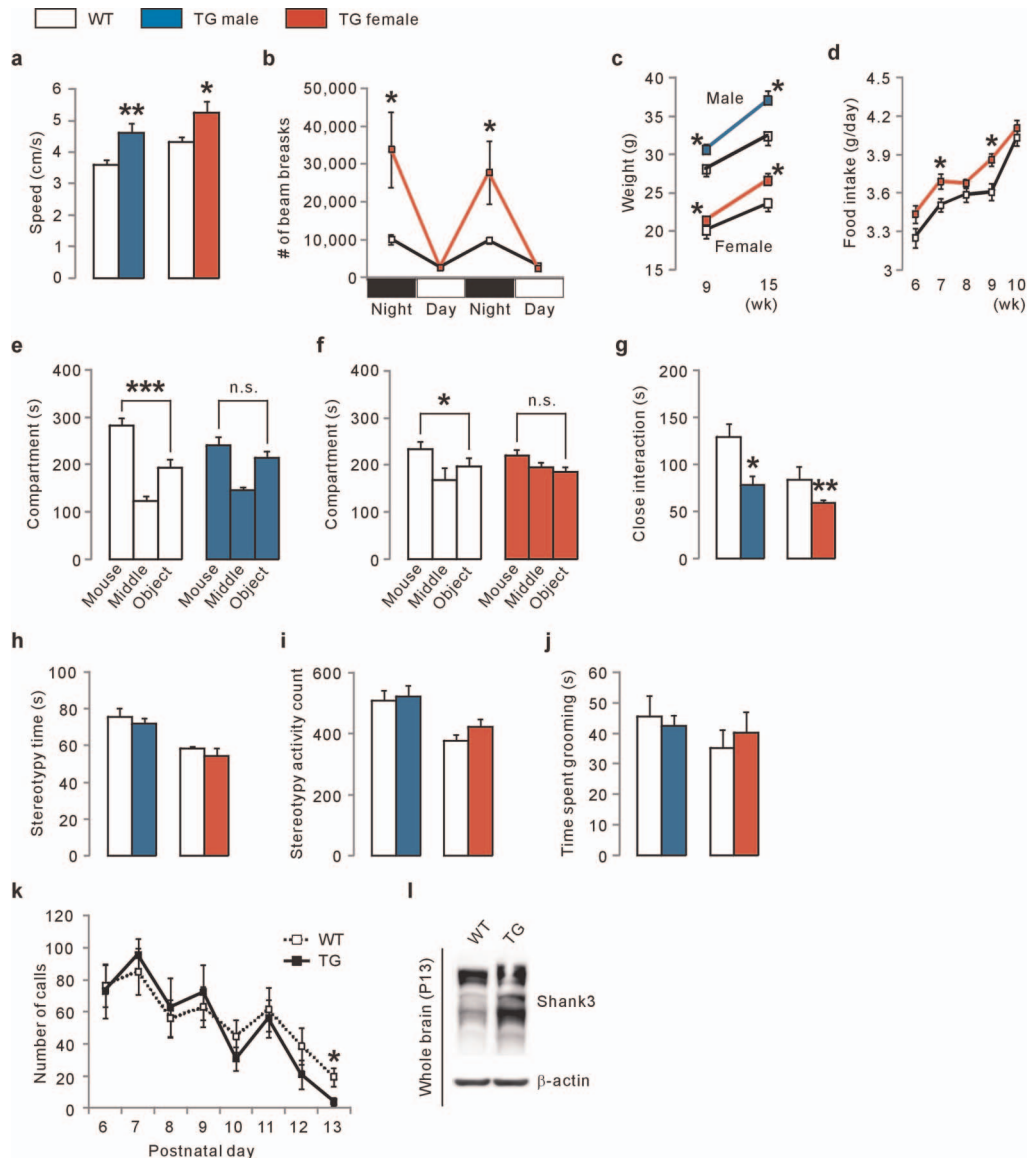
46. Warming, S., Costantino, N., Court, D. L., Jenkins, N. A. & Copeland, N. G. Simple and highly efficient BAC recombineering using galK selection. *Nucleic Acids Res.* **33**, e36 (2005).
47. Choi, J. *et al.* Regulation of dendritic spine morphogenesis by insulin receptor substrate 53, a downstream effector of Rac1 and Cdc42 small GTPases. *J. Neurosci.* **25**, 869–879 (2005).
48. Han, K. *et al.* Regulated RalBP1 binding to RalA and PSD-95 controls AMPA receptor endocytosis and LTD. *PLoS Biol.* **7**, e1000187 (2009).
49. Chao, H. T. *et al.* Dysfunction in GABA signalling mediates autism-like stereotypies and Rett syndrome phenotypes. *Nature* **468**, 263–269 (2010).
50. Roberson, E. D. *et al.* Amyloid-β/Fyn-induced synaptic, network, and cognitive impairments depend on tau levels in multiple mouse models of Alzheimer's disease. *J. Neurosci.* **31**, 700–711 (2011).
51. Lu, H., Lim, B. & Poo, M. M. Cocaine exposure *in utero* alters synaptic plasticity in the medial prefrontal cortex of postnatal rats. *J. Neurosci.* **29**, 12664–12674 (2009).
52. Shannon, P. *et al.* Cytoscape: a software environment for integrated models of biomolecular interaction networks. *Genome Res.* **13**, 2498–2504 (2003).
53. Dennis, G. *et al.* DAVID: database for annotation, visualization, and integrated discovery. *Genome Biol.* **4**, P3 (2003).
54. Huang D. W., Sherman B. T. & Lempicki R. A. Systematic and integrative analysis of large gene lists using DAVID bioinformatics resources. *Nature Protocols* **4**, 44–57 (2009).
55. Boone, P. M. *et al.* Detection of clinically relevant exonic copy-number changes by array CGH. *Hum. Mutat.* **31**, 1326–1342 (2010).



Extended Data Figure 1 | Characterization of expression patterns of EGFP-Shank3 and other synaptic proteins in *Shank3* transgenic mice.

a, Description of the *Shank3* BAC used for transgenic mice generation (image was modified from UCSC genome browser). **b**, Western blot images show expression of EGFP-Shank3 in the synaptic fraction of *Shank3* transgenic brain lysates. EGFP antibody recognized EGFP-Shank3 (~200 kDa) specifically in synaptic fractions of *Shank3* transgenic mice. Asterisk indicates non-specific bands detected by the EGFP antibody. Shank3 antibody detected endogenous Shank3 plus EGFP-Shank3 (arrow) in the transgenic samples. S2, soluble fraction; P2, crude synaptosomal fraction; PSD I, synaptic fraction after one time Triton X-100 washout. **c**, The brain regional expression pattern of

EGFP-Shank3 is similar to that of endogenous Shank3. Cb, cerebellum; Ct, cortex; Hp, hippocampus; St, striatum; Th, thalamus. **d**, The brain developmental expression pattern of EGFP-Shank3 is similar to that of endogenous Shank3. **e**, The fold changes of Shank3 proteins in 3-week-old transgenic mice ($n = 4$) are similar to those of 6-week-old mice (Fig. 1d). **f**, Female transgenic mice ($n = 4$) show similar fold changes of Shank3 proteins to male transgenic mice (Fig. 1d). **g**, **h**, Expression levels of excitatory (**g**) and inhibitory (**h**) synaptic proteins are not significantly altered, except Shank3, in the synaptosomal fraction of 8-week-old transgenic hippocampus and striatum ($n = 6$). All data are presented as mean \pm s.e.m. P values ($*P < 0.05$) were derived from unpaired, two-tailed Student's t -test.

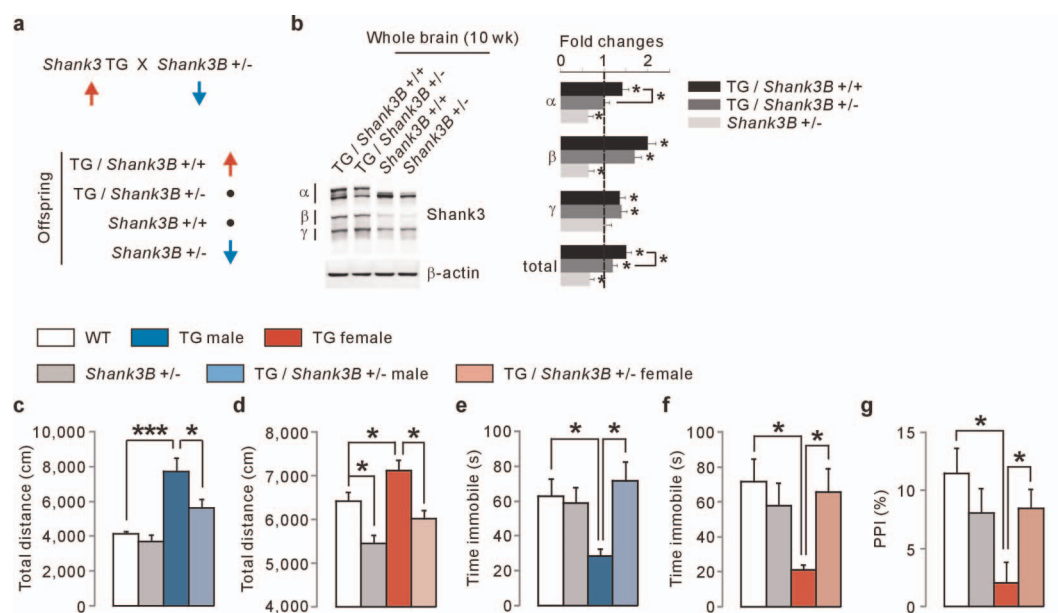


Extended Data Figure 2 | Behavioural characterization of *Shank3* transgenic mice.

a, Transgenic mice showed increased locomotor speed during the 30 min open-field assay. **b**, Female transgenic mice showed increased home-cage activity. **c**, Transgenic mice have increased body weight compared to wild-type mice measured at 9-weeks-old (male wild type: 28.1 ± 0.9 , male transgenic: 30.6 ± 0.7 , female wild type: 20.1 ± 0.3 , female transgenic: 21.4 ± 0.4 , $n = 10-13$; $*P < 0.05$; unpaired two-tailed Student's *t*-test) and 15-weeks-old (male wild type: 32.4 ± 1.2 , male transgenic: 37.0 ± 1.3 , female wild type: 23.6 ± 0.4 , female transgenic: 26.6 ± 0.9 , $n = 10-13$; $*P < 0.05$). **d**, Increased food intake by transgenic mice. Food intake was measured from single-caged female transgenic or wild-type mice from 6- to 10-weeks-old. At 7-weeks-old (wild type: 3.51 ± 0.05 , transgenic: 3.69 ± 0.06 , $n = 9-11$; $*P < 0.05$; unpaired two-tailed Student's *t*-test) and 9-weeks-old (wild type: 3.61 ± 0.07 , transgenic: 3.86 ± 0.05 , $n = 9-11$; $*P < 0.05$), food

intake by transgenic mice was significantly higher than wild-type mice. **e**, **f**, In the 3-chamber assay, male (**e**) and female (**f**) transgenic mice did not show significant preference for novel mice to novel objects. **g**, Transgenic mice spent significantly less time in close interaction with novel social partners.

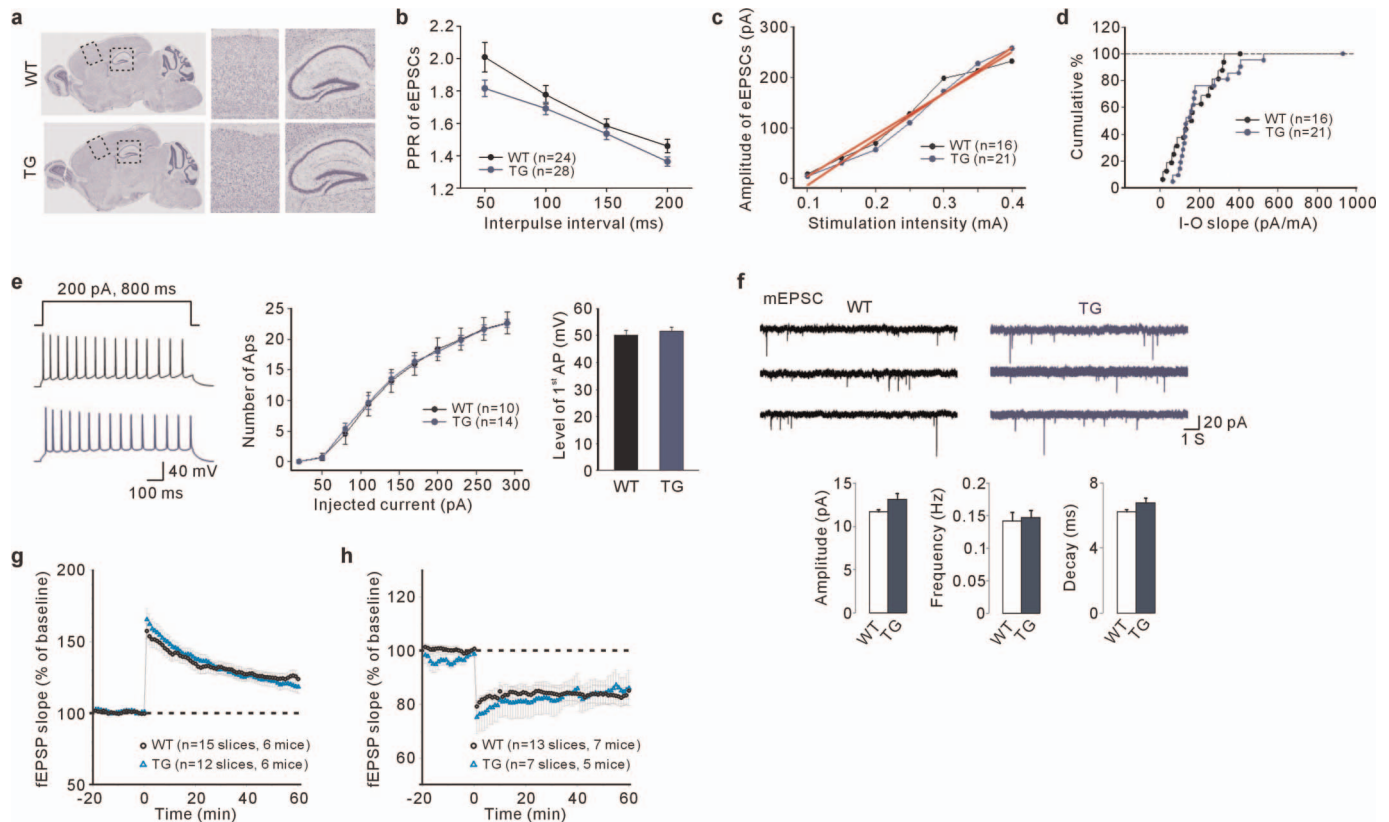
h, **i**, Stereotypy time (**h**) and activity count (**i**) during the 30 min open-field test were normal in transgenic mice. **j**, Time spent in grooming during 10 min monitoring was normal in transgenic mice. **k**, Separation-induced ultrasonic vocalization was measured from wild-type and transgenic mice of postnatal day 6 to 13. Transgenic mice made less calls than wild type at postnatal day 13. **l**, At postnatal day 13, transgenic mice express more Shank3 proteins than wild-type mice. All data are presented as mean \pm s.e.m. $*P < 0.05$, $**P < 0.01$, $***P < 0.001$. The summary of statistical analyses for behavioural assays is provided in Supplementary Table 1.



Extended Data Figure 3 | Behavioural phenotypes of *Shank3* transgenic mice were rescued by crossing with *Shank3B*^{+/-} mice. **a**, Schematic diagram shows possible genotypic combinations and their *Shank3* expression levels (arrow) from the crossing between *Shank3* transgenic mice and *Shank3B*^{+/-} mice. **b**, Quantification of the levels of *Shank3* proteins in each genotype ($n = 4$). The fold changes were compared to the wild-type (*Shank3B*^{+/+}) controls. Crossing of *Shank3* transgenic mice with *Shank3B*^{+/-} mice

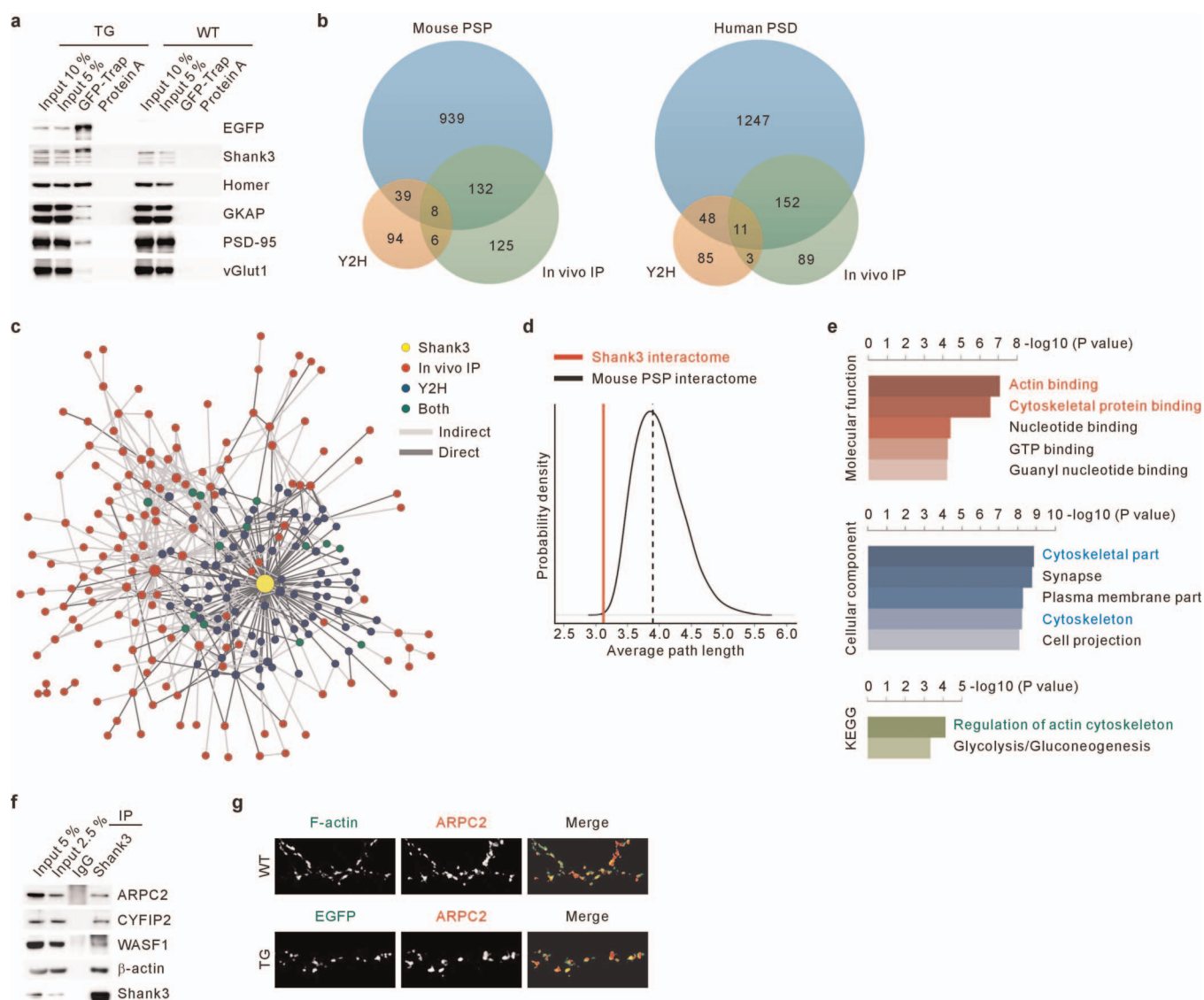
significantly decreased the levels of α isoform and total *Shank3* protein.

c, d, Locomotor activities of male (**c**) and female (**d**) *Shank3* transgenic mice were rescued by crossing with *Shank3B*^{+/-} mice. **e, f**, Immobile time in tail-suspension test of male (**e**) and female (**f**) *Shank3* transgenic mice were rescued by crossing with *Shank3B*^{+/-} mice. **g**, Prepulse inhibition (by 78 dB) of female *Shank3* transgenic mice was rescued by crossing with *Shank3B*^{+/-} mice. All data are presented as mean \pm s.e.m. * $P < 0.05$; *** $P < 0.001$.



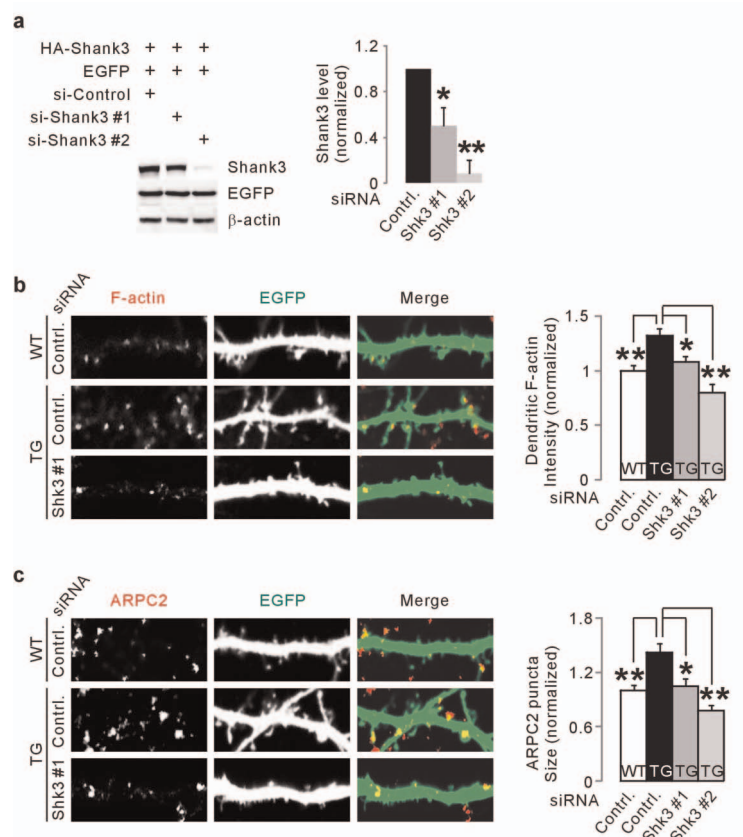
Extended Data Figure 4 | Basal synaptic transmission and NMDA receptor-dependent synaptic plasticity are normal at the hippocampal Schaffer collateral-CA1 synapses of *Shank3* transgenic mice. **a**, Images of cresylviolet staining show normal cytoarchitecture of transgenic brain. **b**, Normal paired-pulse facilitation ratio (PPR) of evoked EPSCs (eEPSCs) at transgenic Schaffer collateral-CA1 synapses. **c**, **d**, Normal synaptic input-output (I-O) relationship at transgenic Schaffer collateral-CA1 synapses. I-O curve (**c**) and cumulative curve of I-O slope (**d**) are shown. Red lines in **c** represent the fitting curves. **e**, Left, sample traces of action potentials triggered by 200 pA current injection

in hippocampal CA1 region of wild-type and transgenic mice. Middle and right, unaltered number of action potentials triggered by the injection of current at different level (middle) and amplitude of the first action potential triggered by 800-ms-long pulse of 200 pA current (right) show normal intrinsic excitability of hippocampal CA1 pyramidal neurons in transgenic mice. **f**, Amplitude, frequency and decay of mEPSC are not altered in CA1 pyramidal neurons of transgenic mice. **g**, **h**, NMDA receptor-dependent long-term potentiation (**g**) and long-term depression (**h**) at Schaffer collateral-CA1 pyramidal synapses are normal in transgenic neurons.



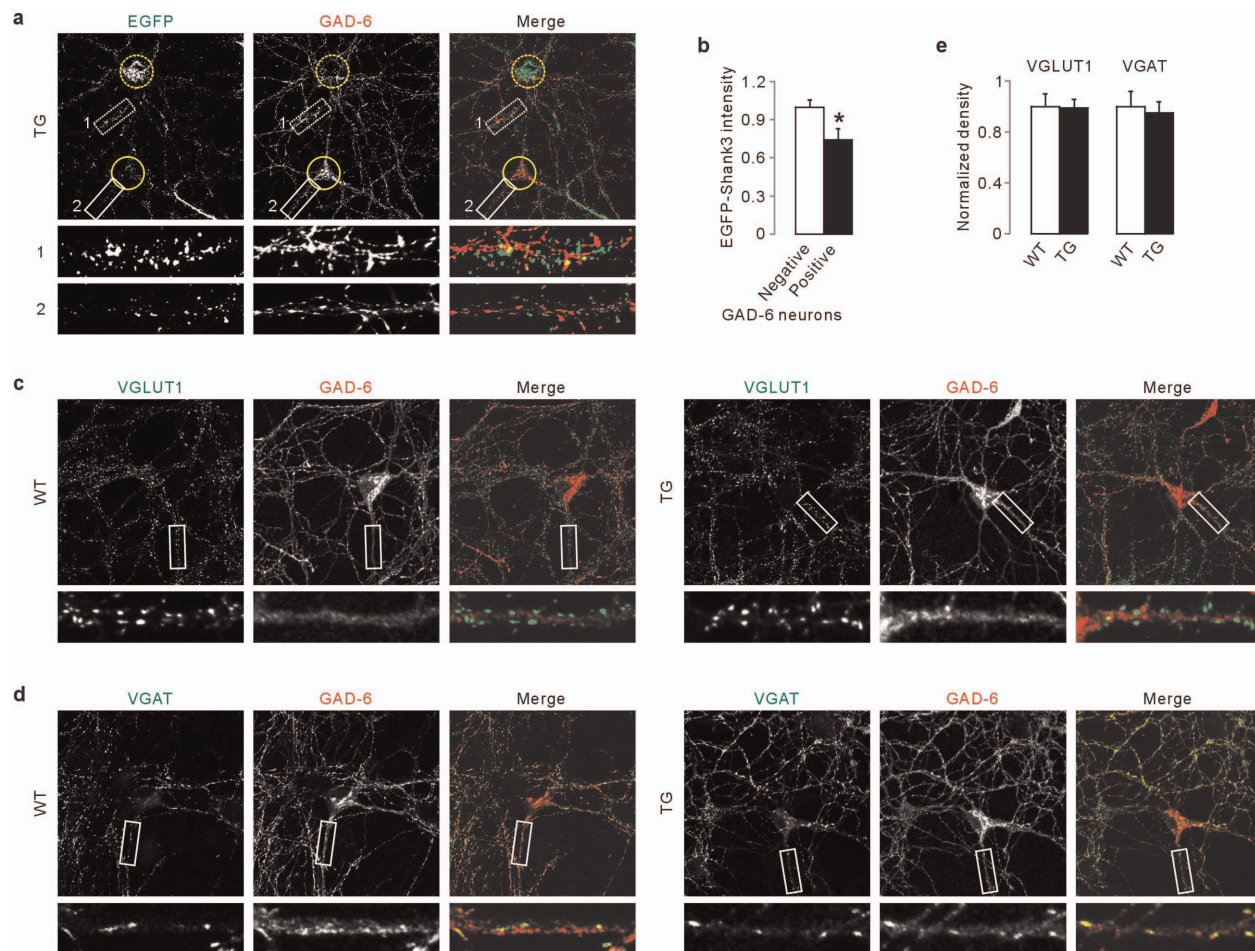
Extended Data Figure 5 | Generation and characterization of Shank3 *in vivo* interactome. **a**, Isolation of EGFP–Shank3 protein and its interactors from synaptosomal fraction of transgenic mice. **b**, Venn diagrams show overlaps among the protein lists from Shank3 *in vivo* immunoprecipitation, Shank3 yeast two-hybrid screening, and either published mouse PSP (postsynaptic proteome) or human PSD. **c**, Shank3 interactome network. **d**, Average path length of Shank3 interactome (3.12, red line) is significantly ($P < 0.0001$) shorter than that of mouse PSP interactome (mean = 3.91, black

line), supporting strong connectivity of Shank3 interactome. **e**, GO and KEGG pathway analysis of Shank3 interactome reveal enrichment of actin cytoskeleton-related function/pathway. The full result of analysis is in Supplementary Table 5. **f**, Confirmation of the *in vivo* interactions between Shank3 and actin-related proteins. **g**, In cultured hippocampal neurons, ARPC2 proteins are co-localized with F-actin (upper panel) and EGFP–Shank3 (lower panel).



Extended Data Figure 6 | *Shank3* siRNA reversed increased F-actin levels and ARPC2 cluster size in cultured hippocampal pyramidal neurons from *Shank3* transgenic mice. **a**, Validation of the two siRNAs against *Shank3*. HEK293T cells were transfected with HA-*Shank3* plus control or *Shank3* siRNA. EGFP plasmid was co-transfected as an internal control. After 48 h, expression levels of HA-*Shank3* were measured by western blot and quantified

($n = 3$). **b**, siRNA targeting *Shank3* (si-*Shank3*) reversed the increased F-actin levels of *Shank3* transgenic neurons. Image for si-*Shank3* #2 is not shown. **c**, si-*Shank3* reversed the increased ARPC2 cluster size of *Shank3* transgenic neurons. All data are presented as mean \pm s.e.m. from 20–30 neurons per condition. P values ($*P < 0.05$, $**P < 0.01$) were derived from one-way ANOVA with post hoc Tukey's multiple comparison.

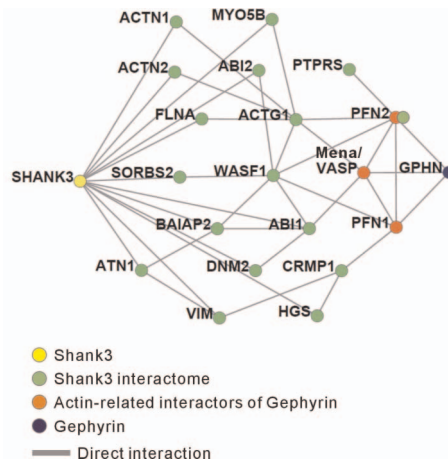


Extended Data Figure 7 | Normal excitatory and inhibitory synapse numbers of GAD-6-positive inhibitory neurons of *Shank3* transgenic mice.

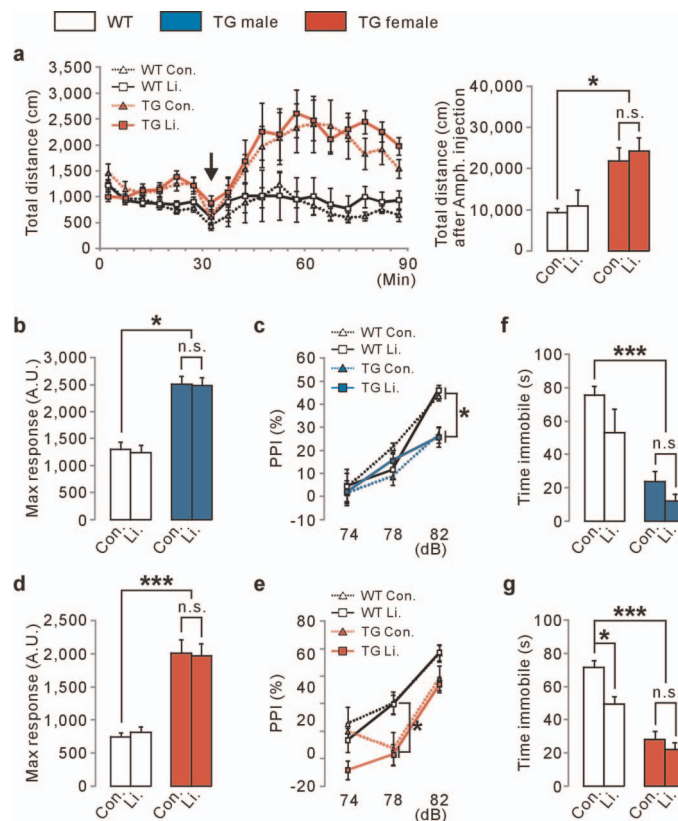
a, Expression of EGFP-Shank3 in GAD-6-positive inhibitory neurons of *Shank3* transgenic mice. The yellow circles of dotted line and solid line indicate neuronal cell bodies of a GAD-6-negative excitatory neuron and a GAD-6-positive inhibitory neuron, respectively. The box 1 shows dendritic segment of the excitatory neuron and the box 2 shows that of the inhibitory neuron.

b, Quantification of dendritic EGFP-Shank3 intensity in excitatory and inhibitory transgenic mice. Inhibitory neurons express less EGFP-Shank3

(excitatory neurons: 1.00 ± 0.06 , inhibitory neurons: 0.74 ± 0.09 , $n = 10$; $*P < 0.05$; unpaired two-tailed Student's *t*-test). **c**, Normal excitatory synapse number of GAD-6-positive inhibitory neurons of *Shank3* transgenic mice. **d**, Normal inhibitory synapse number of GAD-6-positive inhibitory neurons of *Shank3* transgenic mice. **e**, Quantification of (c) (wild type: 1.00 ± 0.10 , transgenic: 0.99 ± 0.07 , $n = 18$; $P > 0.05$; unpaired two-tailed Student's *t*-test) and (d) (wild type: 1.00 ± 0.12 , transgenic: 0.95 ± 0.09 , $n = 20$; $P > 0.05$; unpaired two-tailed Student's *t*-test).

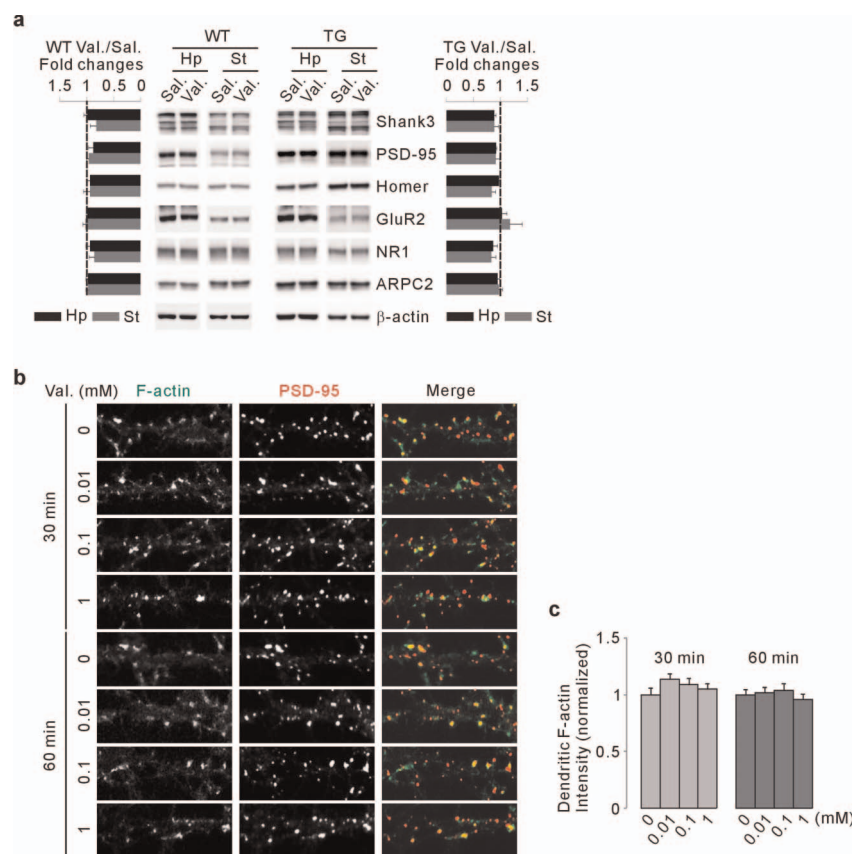


Extended Data Figure 8 | Shank3 interactome is connected with gephyrin-interacting actin-related proteins, Mena, profilin1 and profilin2. Based on a literature search, we selected candidate actin-related proteins (Mena/VASP, profilin1 and profilin2) that directly interact with inhibitory postsynaptic protein gephyrin. To understand potential interactions among these proteins and the Shank3 interactome, we generated interaction network using the information from our yeast two-hybrid screening and IRefIndex PPI database (<http://irefindex.org>). The interaction network shows that Mena/VASP, profilin1 and profilin2 are connected with Shank3 interactome mainly through actin-related proteins. Note that one of the gephyrin-interacting proteins, profilin2, was also identified by our Shank3 *in vivo* immunoprecipitation (Supplementary Table 4).



Extended Data Figure 9 | Mania-like behaviours of *Shank3* transgenic mice are resistant to lithium treatment. a, Basal and amphetamine-induced locomotor activities of female transgenic mice were not affected by lithium treatment. b–e, Abnormal acoustic startle response (b, d) and PPI (c, e) of male and female transgenic mice were not rescued by lithium treatment.

f, g, Immobile time of male (f) and female (g) transgenic mice in tail-suspension test was not rescued by lithium treatment. Wild-type female mice showed decreased immobile time upon lithium treatment, which is an expected response to high dose lithium treatment in wild-type mice. All data are presented as mean \pm s.e.m. * $P < 0.05$; *** $P < 0.001$.



Extended Data Figure 10 | Valproate treatment does not affect synaptic protein and F-actin levels in neurons of *Shank3* transgenic mice. **a**, One hour after final valproate injection (200 mg per kg), synaptosomal fraction was prepared from brains, and indicated proteins were detected by western blotting. Neither wild-type nor transgenic mice showed significant change in the levels of synaptic proteins by valproate treatment ($n = 7$). **b**, Representative confocal

images of *Shank3* transgenic cultured hippocampal pyramidal neurons (DIV 14) treated with different concentrations of valproate (0, 0.01, 0.1 and 1 mM) for 30 or 60 min. **c**, Quantification of (b). There was no significant change in F-actin levels by valproate treatment ($n = 16$ per condition). All data are presented as mean \pm s.e.m.

Context-dependent computation by recurrent dynamics in prefrontal cortex

Valerio Mante^{1,†,*}, David Sussillo^{2,*}, Krishna V. Shenoy^{2,3} & William T. Newsome¹

Prefrontal cortex is thought to have a fundamental role in flexible, context-dependent behaviour, but the exact nature of the computations underlying this role remains largely unknown. In particular, individual prefrontal neurons often generate remarkably complex responses that defy deep understanding of their contribution to behaviour. Here we study prefrontal cortex activity in macaque monkeys trained to flexibly select and integrate noisy sensory inputs towards a choice. We find that the observed complexity and functional roles of single neurons are readily understood in the framework of a dynamical process unfolding at the level of the population. The population dynamics can be reproduced by a trained recurrent neural network, which suggests a previously unknown mechanism for selection and integration of task-relevant inputs. This mechanism indicates that selection and integration are two aspects of a single dynamical process unfolding within the same prefrontal circuits, and potentially provides a novel, general framework for understanding context-dependent computations.

Our interactions with the world are inherently flexible. Identical sensory stimuli, for example, can lead to very different behavioural responses depending on ‘context’, which includes goals, previous expectations about upcoming events, and relevant past experiences^{1,2}. Animals can switch rapidly between behavioural contexts, implying the existence of rapid modulation, or ‘gating’, mechanisms within the brain that select relevant sensory information for decision-making and action. A large attention literature suggests that relevant information is selected by top-down modulation of neural activity in early sensory areas^{3–8}, which may take the form of modulation of firing rates^{3,5–7}, or modulation of response synchrony within or across areas^{4,5,8}. The top-down signals underlying such ‘early’ modulations of sensory activity arise, in part, from prefrontal cortex (PFC)^{2,5}, which is known to contribute to representing and maintaining contextual knowledge, ignoring irrelevant information, and suppressing inappropriate actions^{1,2,9,10}. These observations have led to the hypothesis that early selection may account for the larger effect of relevant as compared to irrelevant sensory information on contextually sensitive behaviour.

Here we test this hypothesis with a task requiring context-dependent selection and integration of visual stimuli. We trained two macaque monkeys (A and F) to perform two different perceptual discriminations on the same set of visual stimuli (Fig. 1). The monkeys were instructed by a contextual cue to either discriminate the direction of motion or the colour of a random-dot display, and to report their choices with a saccade to one of two visual targets (Fig. 1a). While monkeys performed this task, we recorded extracellular responses from neurons in and around the frontal eye field (Extended Data Fig. 1a, f), an area of PFC involved in the selection and execution of saccadic eye movements^{11,12}, the control of visuo-spatial attention¹³, and the integration of information towards visuomotor decisions^{12,14}.

We found no evidence that irrelevant sensory inputs are gated, or filtered out, before the integration stage in PFC, as would be expected from early selection mechanisms^{3–8}. Instead, the relevant input seems to be selected late, by the same PFC circuitry that integrates sensory evidence towards a choice. Selection within PFC without previous

gating is possible because the representations of the inputs, and of the upcoming choice, are separable at the population level, even though they are deeply entwined at the single neuron level. An appropriately trained recurrent neural network model reproduces key physiological observations and suggests a new mechanism of input selection and integration. The mechanism reflects just two learned features of a dynamical system: an approximate line attractor and a ‘selection vector’, which are only defined at the level of the population. The model mechanism is readily scalable to large numbers of inputs, indicating a general solution to the problem of context-dependent computation.

Behaviour and single-unit responses

The monkeys successfully discriminated the relevant sensory evidence in each context, while largely ignoring the irrelevant evidence (Fig. 1c–f, monkey A; Extended Data Fig. 2a–d, monkey F). To vary the difficulty of the discrimination, we changed the strength of the motion and colour signals randomly from trial to trial (Fig. 1b). In the motion context, the choices of the monkeys depended strongly on the direction of motion of the dots (Fig. 1c), whereas the choices depended only weakly on colour in the same trials (Fig. 1d). The opposite pattern was evident in the colour context: the now relevant colour evidence exerted a large effect on choices (Fig. 1f) whereas motion had only a weak effect (Fig. 1e).

As is common in PFC^{1,2,15–18}, the recorded responses of single neurons appeared to represent several different task-related signals at once, including the monkey’s upcoming choice, the context, and the strength of motion and colour evidence (Extended Data Figs 1 and 3). Rather than attempting to understand the neural mechanism underlying selective integration by studying the responses of single PFC neurons, we focussed on analysing the responses of the population as a whole. To construct population responses, we pooled data from both single and multi-unit recordings, which yielded equivalent results. The great majority of units were not recorded simultaneously, but rather in separate sessions. Units at all recording locations seemed to contribute to the task-related signals analysed below (Extended Data Fig. 1) and were thus combined.

¹Howard Hughes Medical Institute and Department of Neurobiology, Stanford University, Stanford, California 94305, USA. ²Department of Electrical Engineering and Neurosciences Program, Stanford University, Stanford, California 94305, USA. ³Departments of Neurobiology and Bioengineering, Stanford University, Stanford, California 94305, USA. [†]Present address: Institute of Neuroinformatics, University of Zurich/ETH Zurich, CH-8057 Zurich, Switzerland.

*These authors contributed equally to this work.

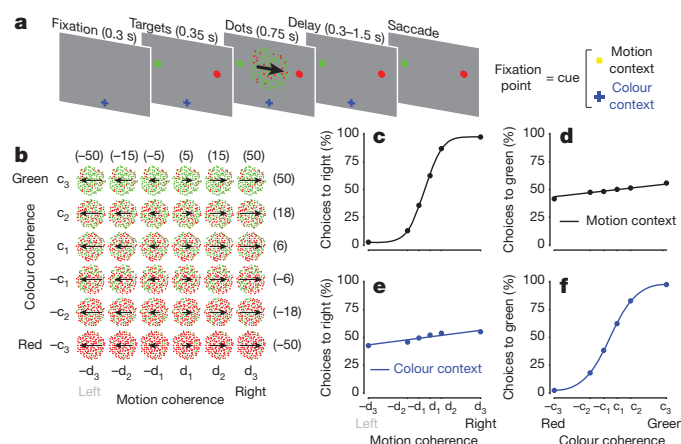


Figure 1 | Behavioural task and psychophysical performance. **a**, Task structure. Monkeys were instructed by a contextual cue to either discriminate the motion or the colour of a random-dot stimulus, and indicate their choice with a saccade to one of two targets. Depending on context, monkeys were rewarded for choosing the target matching the prevalent direction of motion (motion context) or the prevalent colour (colour context) of the random dots. Context was indicated by the shape and colour of the fixation point; offset of the fixation point was the ‘go cue’, signalling the monkey to indicate its choice via the operant saccade. **b**, Stimulus set. The motion and colour coherence of the dots was chosen randomly on each trial. We slightly varied the coherence values on each day, to equate performance across contexts and sessions (numbers in parentheses: average coherences (%) across sessions for monkey A). **c–f**, Psychophysical performance for monkey A in the motion (top) and colour contexts (bottom), averaged over 80 recording sessions (163,187 trials). Performance is shown as a function of motion (left) or colour (right) coherence in each behavioural context. The curves are fits of a behavioural model.

Overall, we analysed 388 single-unit and 1,014 multi-unit responses from the two monkeys.

State space analysis

To study how the PFC population as a whole dynamically encodes the task variables underlying the monkeys’ behaviour, we represent population responses as trajectories in neural state space^{17,19–25}. Each point in state space corresponds to a unique pattern of neural activations across the population. Because activations are dynamic, changing over time, the resulting population responses form trajectories in state space.

We focussed our analyses on responses in a specific low-dimensional subspace that captures across-trial variance due to the choice of the monkey (choice 1 or 2), the strength and direction of the motion evidence, the strength and direction of the colour evidence, and context (motion or colour). We estimated this task-related subspace in two steps (Supplementary Information). First, we used principal component analysis (PCA) to obtain an unbiased estimate of the most prominent features (that is, patterns of activations) in the population response. To ‘de-noise’ the population responses, we restricted subsequent analyses to the subspace spanned by the first 12 principal components. Second, we used linear regression to define the four orthogonal, task-related axes of choice, motion, colour and context. The projection of the population response onto these axes yields de-mixed estimates of the corresponding task variables, which are mixed both at the level of single neurons (Extended Data Fig. 3) and at the level of individual principal components (Extended Data Fig. 4c, g; see also ref. 26).

This population analysis yields highly reliable average response trajectories (Fig. 2 and Extended Data Fig. 4q, r) that capture both the temporal dynamics and the relationships among the task variables represented in PFC. In particular, four properties of the population responses provide fundamental constraints on the mechanisms of selection and integration underlying behaviour in our task.

First, integration of evidence during presentation of the random dots corresponds to a gradual movement of the population response

in state space along the axis of choice (Fig. 2a, f). In both contexts, the trajectories start from a point in state space close to the centre of the plots (‘dots on’, purple point), which corresponds to the pattern of population responses at baseline. During the dots presentation the responses then quickly move away from this baseline level, along the axis of choice (red line; Fig. 2a, f). Overall, the population response moves in opposite directions on trials corresponding to the two different saccade directions (Fig. 2, choice 1 versus choice 2). The projection of the population response onto the choice axis (Extended Data Fig. 5b, f) is largely analogous to the ‘choice-predictive’ signals that have been identified in past studies as approximate integration of evidence during direction discrimination tasks²⁷.

Second, the sensory inputs into PFC produce patterns of population responses that are very different from those corresponding to either choice, meaning that these signals are separable at the level of the population. Indeed, the population response does not follow straight paths along the choice axis, but instead forms prominent arcs away from it (Fig. 2a, f). The magnitude of each arc along the axes of motion or colour reflects the strength of the corresponding sensory evidence (see scale), whereas its direction (up or down) reflects the sign of the evidence (towards choice 1 or 2, filled or empty symbols, respectively). Whereas the integrated evidence continues to be represented along the axis of choice even after the disappearance of the random dots (‘dots off’), the signals along the axes of motion and colour are transient—the arcs return to points near the choice axis by the time of dots offset. These signals thus differ from integrated evidence both in terms of the corresponding patterns of activation and in their temporal profile. For these reasons, we interpret them as ‘momentary evidence’ from the motion and colour inputs in favour of the two choices. This interpretation is also consistent with the observed population responses on error trials, for which the momentary evidence points towards the chosen target, but is weaker than on correct trials (Extended Data Fig. 5c, d; red curves).

Third, context seems to have no substantial effect on the direction of the axes of choice, motion and colour, and only weak effects on the strength of the signals represented along these axes. When estimated separately during the motion and colour contexts, the two resulting sets of axes span largely overlapping subspaces (see Supplementary Table 1); thus, a single set of three axes (the red, black and blue axes in Fig. 2a–f, estimated by combining trials across contexts) is sufficient to capture the effects of choice, motion and colour on the population responses in either context. A comparison of the population responses across contexts (Fig. 2a–c versus d–f) reveals that a single, stable activity pattern is responsible for integrating the relevant evidence in both contexts (the choice axis), while similarly stable activity patterns represent the momentary motion and colour evidence in both contexts (motion and colour axes). Notably, motion and colour inputs result in comparable deflections along the motion and colour axes, respectively, whether they are relevant or not (compare Fig. 2a to d and f to c).

Fourth, although the directions of the axes of choice, motion and colour are largely invariant with context, their location in state space is not. The responses during the motion and colour contexts occupy different parts of state space, and the corresponding trajectories are well separated along the axis of context (Extended Data Fig. 6a, b).

Comparison to models of selection and integration

These properties of the population responses, which are summarized schematically in Fig. 3a, can be compared to the predictions of current models of context-dependent selection and integration (Fig. 3b–d). We first focussed on three fundamentally different mechanisms of selection that could each explain why the motion input, for example, influences choices in the motion context (Fig. 3, top row) but not in the colour context (Fig. 3, bottom row). In the framework of our task the three models predict population responses that differ substantially

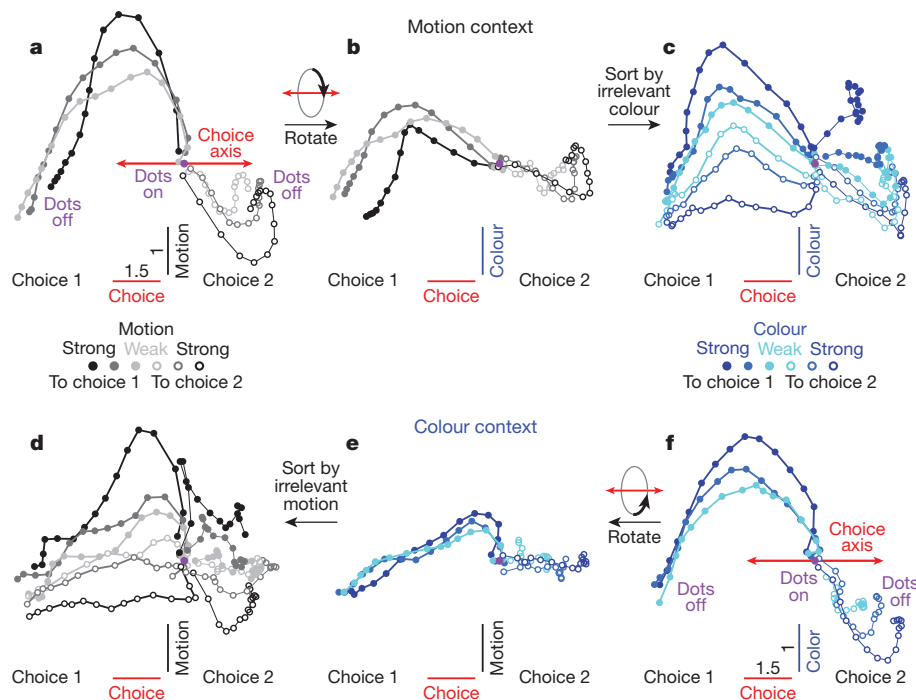


Figure 2 | Dynamics of population responses in PFC. The average population response for a given condition and time is represented as a point in state space. Responses from correct trials only are shown from 100 ms after dots onset (dots on, purple circle) to 100 ms after dots offset (dots off) in 50-ms steps, and are projected into the three-dimensional subspace capturing the variance due to the monkey's choice (along the choice axis), and to the direction and strength of the motion (motion axis) and colour (colour axis) inputs. Units are arbitrary; components along the motion and colour axes are enhanced relative to the choice axis (see scale bars in a, f). Conditions (see colour bars) are defined based on context (motion context, top; colour context, bottom), on the location of the chosen target (choice 1 versus choice 2) and either on the direction and strength of the motion (grey colours) or the colour input (blue colours). Here, choice 1 corresponds to the target in the response field of the recorded neurons. The direction of the colour input does not refer to

the colour of the dots per se (red or green), but to whether the colour points towards choice 1 or choice 2 (see Supplementary Information, section 6.4, for a detailed description of the conditions). **a**, Effect of choice and the relevant motion input in the motion context, projected onto the axes of choice and motion. **b**, Same data as in **a**, but rotated by 90° around the axis of choice to reveal the projection onto the axis of colour. **c**, Same trials as in **b**, but re-sorted according to the direction and strength of the irrelevant colour input. **d–f**, Responses in the colour context, analogous to **a–c**. Responses are averaged to show the effects of the relevant colour input (**e**, **f**) or the irrelevant motion input (**d**). For relevant inputs (**a**, **b** and **e**, **f**), correct choices occur only when the sensory stimulus points towards the chosen target (3 conditions per chosen target); for irrelevant inputs (**c**, **d**), however, the stimulus can point either towards or away from the chosen target on correct trials (6 conditions per chosen target).

from each other (Fig. 3b–d), and can thus be validated or rejected by our PFC recordings (Fig. 3a).

The first model (Fig. 3b) is based on two widely accepted hypotheses about the mechanisms underlying selection and integration of evidence. First, it assumes that inputs are selected early^{3–8}, such that a given input drives PFC responses when relevant (grey arrow in Fig. 3b, top), but is filtered out before reaching PFC when irrelevant (no grey arrow in Fig. 3b, bottom). Second, it assumes that the relevant input directly elicits a pattern of activation in PFC resembling the pattern corresponding to a choice (the grey arrow in Fig. 3b, top, points along the axis of choice), as would be expected by current models of integration^{28,29}.

Both hypotheses are difficult to reconcile with the recorded PFC responses. Whereas the strength of each input is reduced when it is irrelevant compared to when it is relevant, the magnitude of the observed reduction seems too small to account for the behavioural effects. For instance, irrelevant motion of high coherence (Fig. 2d, black) elicits a larger deflection along the motion axis (relative to baseline, purple dot, Fig. 2d) than relevant motion of intermediate coherence (Fig. 2a, dark grey). Yet the former has almost no behavioural effect (Fig. 1e), whereas the latter has a large behavioural effect (Fig. 1c). The analogous observation holds for the colour input (Figs 2c, f and 1d, f), strongly suggesting that the magnitude of the momentary evidence alone does not determine whether the corresponding input is integrated. Furthermore, the actual momentary motion input is represented along a direction that has little overlap

with the choice axis, resulting in curved trajectories (Fig. 3a) that differ markedly from the straight trajectories predicted by the early selection model (Fig. 3b).

The observed PFC responses also rule out two additional models of selection presented in Fig. 3. In the absence of early selection, a motion input might be selected within PFC by modifying the angle between the choice and motion axes (that is, the similarity between patterns of neural activity representing choice and momentary motion evidence) across contexts. This angle could be modified either by changing the direction of the motion axis between contexts while keeping the choice axis fixed (Fig. 3c), or vice versa (Fig. 3d). In both cases, the motion input would elicit movement of the population along the axis of choice in the motion context (top row), but not in the colour context (bottom row), as the motion and choice axes have little or no overlap in the colour context. At the single neuron level, variable axes that change direction across contexts would be reflected as complex, nonlinear interactions between context and the other task variables, which have been proposed in some task-switching models^{30,31}. However, our data (Figs 2 and 3a) lend little support for variable choice (Fig. 3d) or input (Fig. 3c) axes. More generally, the PFC data from monkey A rule out any model of integration for which the degree of overlap between the direction of the momentary evidence and the axis of choice determines how much the corresponding input affects behaviour.

The representation of task variables in PFC of monkey F replicates all but one key feature observed in monkey A. Most importantly, population responses along the choice and motion axes (Extended

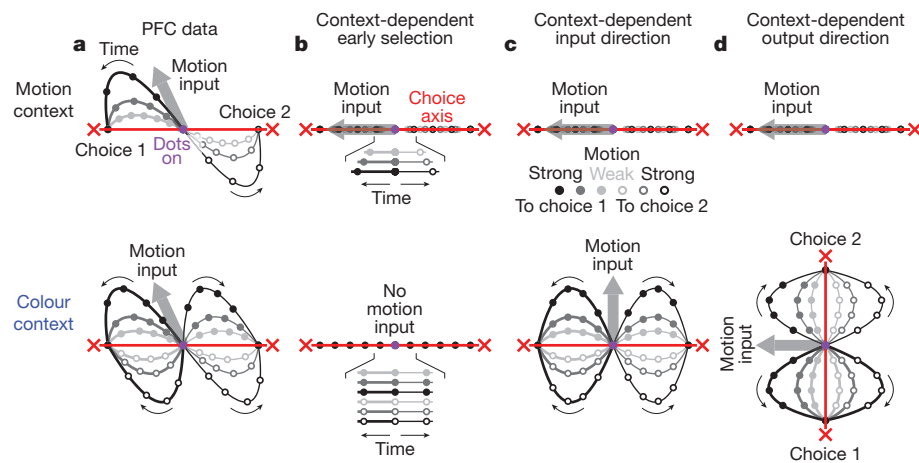


Figure 3 | Models of selective integration inconsistent with PFC responses. Schematic representation of population responses observed in PFC (a) and expected by several models of selective integration (b–d). The models differ from the PFC responses with respect to the relative directions and context dependence of the choice axis (red lines) and the inputs (thick grey arrows; only motion input is shown). The relevant input is integrated as movement along the choice axis towards one of two choices (red crosses). A motion input towards choice 1 ‘pushes’ the responses along the direction of the grey arrow (towards choice 2: opposite direction). Same conditions as in Fig. 2a (motion context, top) and Fig. 2d (colour context, bottom). As in Fig. 2a and d, a single two-dimensional subspace (which contains the choice axis and motion input) is used to represent responses from both contexts. **a**, Idealized schematic of the actual PFC trajectories shown in Fig. 2a, d. Both the choice axis and motion input are stable between contexts. The motion input pushes the population response away from the choice axis. **b**, Early selection model. When relevant

(top), the motion input pushes the population response along the choice axis. When irrelevant (bottom), the motion input is filtered out before reaching PFC (no thick grey arrow) and thus exerts no effect on choice. All trajectories fall on top of each other in both contexts, but the rate of movement along the choice axis increases with motion strength only in the motion context (insets show enlarged trajectories distributed vertically for clarity). **c**, Context-dependent input direction. Motion input direction varies between contexts, whereas the choice axis is stable. Inputs are not filtered out before PFC; rather, they are selected on the basis of their projection onto the choice axis. **d**, Context-dependent output direction. Similar selection mechanism to **c**, except that the choice axis varies between contexts, whereas the motion input is stable. The effects of the motion input on PFC responses in both monkeys (schematized in **a**) and the effects of the colour input in monkey A are inconsistent with predictions of the three models in **b–d** (respectively, Fig. 2a, d; Extended Data Fig. 7a,d; Fig. 2f, c).

Data Fig. 7a, d) closely match those observed in monkey A (Fig. 2a, d); thus, physiological data from both monkeys are consistent in rejecting current models of selection and integration of motion inputs (Fig. 3b–d). The colour signal in monkey F, however, is equivocal. On the one hand, the representation of the colour input closely resembles that of a choice (Extended Data Fig. 1g, i), as expected from the early selection model described above (Fig. 3b). On the other hand, the colour input is also weakly represented along the colour axis in both contexts (vertical displacement of trajectories, Extended Data Fig. 7c, f). For the colour input in monkey F, therefore, we cannot with confidence accept or reject the early selection model. Finally, as in monkey A, context is represented in monkey F along a separate axis of context (Extended Data Fig. 6c, d).

In summary, the population responses in both monkeys are difficult to reconcile with current models of selection and integration (see also Extended Data Fig. 8). Rather, the selective integration of the motion input in monkeys A and F, and of the colour input in monkey A, must rely on a mechanism for which the very same input into PFC leads to movement along a fixed axis of choice in one context but not another.

Recurrent network model of selection and integration

To identify such a mechanism, we trained a network of recurrently connected, nonlinear neurons³² to solve a task analogous to the one solved by the monkeys (Fig. 4). Notably, we only defined ‘what’ the network should do, with minimal constraints on ‘how’ it should do it^{32–34}. Thus, the solution achieved by the network is not hand-built into the network architecture. On each trial, neurons in the network receive two independent sensory inputs that mimic the momentary evidence for motion and colour in a single random dot stimulus. The network also receives a contextual input that mimics the contextual signal provided to the monkeys, instructing the network to discriminate either the motion or the colour input. The network activity is read out by a single linear read-out, corresponding to a weighted sum

over the responses of all neurons in the network (see Supplementary Information). As in PFC, the contextual input does not affect the strength of the sensory inputs—selection occurs within the same network that integrates evidence towards a decision.

We trained the network³⁵ to make a binary choice on each trial—an output of +1 at the end of the stimulus presentation if the relevant evidence pointed leftward, or a –1 if it pointed rightward. After training, the model qualitatively reproduces the monkeys’ behaviour,

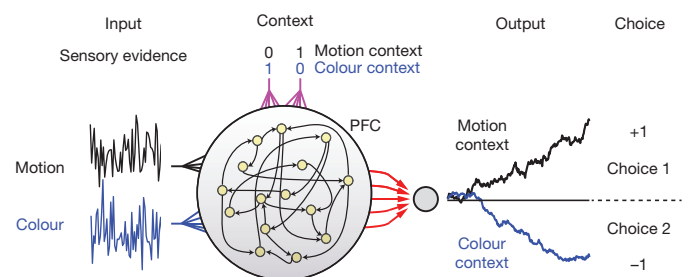


Figure 4 | A neural network model of input selection and integration. PFC is modelled as a network of recurrently connected, nonlinear, rate neurons that receive independent motion, colour and contextual inputs. The network is fully recurrently connected, and each unit receives both motion and colour inputs as well as two inputs that indicate context. At each time step, the sensory inputs are drawn from two normal distributions, the means of which correspond to the average strengths of the motion and colour evidence on a given trial. The contextual inputs take one of two values (0 or 1), which instruct the network to discriminate either the motion or the colour input. The network is read out by a single linear read-out, corresponding to a weighted sum over the responses of all neurons (red arrows). We trained the network (with back-propagation³⁵) to make a binary choice, that is, to generate an output of +1 at the end of the stimulus presentation if the relevant evidence pointed towards choice 1, or a –1 if it pointed towards choice 2. Before training, all synaptic strengths were randomly initialized.

confirming that the model solves the selection problem at the ‘behavioural’ level (Extended Data Fig. 2e–h).

We first analysed model population trajectories in the subspace spanned by the axes of choice, motion and colour, and found that they reproduce the four main features of the PFC population responses discussed above (Fig. 5 and Extended Data Fig. 9a–g). First, integration of evidence corresponds to gradual movement of the population response along the choice axis. Second, momentary motion and colour evidence ‘push’ the population away from the choice axis, resulting in trajectories that are parametrically ordered along the motion and colour axes. Third, the direction of the axes of choice, motion and colour are largely invariant with context, as are the strength of the motion and colour inputs, as these are not gated before entering the network. Fourth, the trajectories during motion and colour contexts are separated along the axis of context (Extended Data Fig. 9f, g). Model and physiological dynamics differ markedly in one respect—signals along the input axes are transient in the physiology, but not in the model, yielding PFC trajectories that curve back to the choice axis before the end of the viewing interval (compare Figs 5a, f to 2a, f). This difference suggests that the sensory inputs to PFC are attenuated after a decision is reached. Additional differences between the model and the physiological dynamics can be readily explained by previously proposed imperfections in the evidence integration process, such as ‘urgency’ signals^{36,37} or instability in the integrator³⁸ (Extended Data Fig. 10).

A novel mechanism of selective integration

We then ‘reverse engineered’ the model³³ to discover its mechanism of selective integration. The global features of the model activity are easily explained by the overall arrangement of fixed points of the dynamics³³ (Fig. 5), which result from the synaptic connectivity learned during training. Fixed points (small red crosses) correspond to patterns of neuronal activations (that is, locations in state space) that are stable when the sensory inputs are turned off. First, we found that the model generates a multitude of fixed points, which are approximately arranged to form two lines along the choice axis. The two sets of fixed points are separated along the axis of context (Extended Data Fig. 9f, g) and never exist together—one exists in the motion context (Fig. 5a–c), the other in the colour context (Fig. 5d–f).

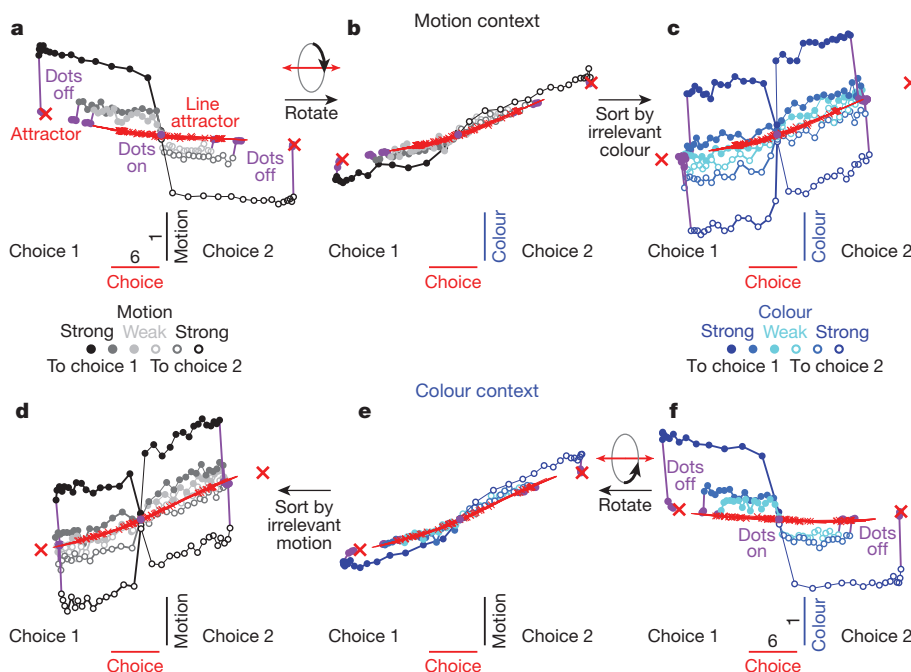


Figure 5 | Model dynamics and fixed points analysis. a–f, Dynamics of model population responses, same conventions as in Fig. 2. Responses are projected into the three-dimensional subspace spanned by the axes of choice, motion and colour (defined here based on the model synaptic weights, see Supplementary Information, section 7.6). Movement along the choice axis corresponds to integration of evidence, and the motion and colour inputs deflect the trajectories along the corresponding input axes. Fixed points of the dynamics (red crosses) were computed separately for motion (a–c) and colour contexts (d–f) in the absence of sensory inputs (see Supplementary Information, section 7.5). The fixed points are ‘marginally stable’ (that is, one eigenvalue of the linearized dynamics is close to zero, whereas all others have strongly negative real parts; see Supplementary Information). The locally computed right zero-eigenvectors (red lines) point to the neighbouring fixed points, which thus approximate a line attractor in each context. After the inputs are turned off (dots off, purple data points and lines) the responses relax back towards the line attractor. Each line attractor ends in two ‘stable’ attractors (that is, all eigenvalues have strongly negative real parts, large crosses) corresponding to model outputs of +1 and –1 (that is, choice 1 or 2).

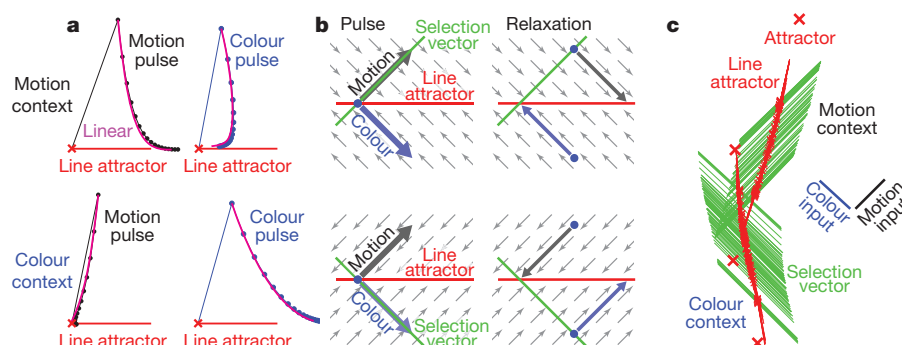


Figure 6 | Selection and integration by recurrent dynamics. **a**, Average model population response to short (1-ms) pulses of motion (left) and colour inputs (right) during motion (top) and colour contexts (bottom). Motion or colour inputs (solid lines) are initiated when the system is steady at one of the identified fixed points (red crosses), and subsequent relaxation back to the line attractor is simulated (dots: 3-ms intervals) and averaged across fixed points. The size of the pulses approximately corresponds to the length of the scale bars in Fig. 5. Selection of the relevant input results from the context-dependent relaxation of the recurrent dynamics after the pulse, and is well approximated by the linearized dynamics around the fixed points (magenta lines). Responses

are projected into the two-dimensional subspace spanned by the direction of the pulse and the locally computed line attractor (the right zero-eigenvector of the linearized dynamics). **b**, Explanation of how the same input pulse (left) leads to evidence integration in one context, but is ignored in the other (right). Relaxation towards the line attractor (small arrows) is always orthogonal to the context-dependent selection vector, and reverses the effects of the irrelevant pulse. **c**, Global arrangement of the line attractor (red) and selection vector (green) at each fixed point. Inputs are selected by the selection vector, which is orthogonal to the contextually irrelevant input (note input axes, right), and integrated along the line attractor.

dynamics, although counterintuitive, nevertheless follow a very simple rule. For a given context, the relaxation always occurs on a path that is orthogonal to a specific direction in state space, which we call the 'selection vector' (Fig. 6b). The direction of the selection vector, like the direction of the line attractor, is a property of the recurrent synaptic weights learned by the model during training (see Supplementary Information). Unlike the line attractor, however, the orientation of the selection vector changes with context—it projects strongly onto the relevant input, but is orthogonal to the irrelevant one (Fig. 6b). As a consequence, the relaxation dynamics around the line attractor are context dependent. This mechanism explains how the same sensory input can result in movement along the line attractor in one context but not the other (Fig. 6b).

The line attractor and the selection vector are sufficient to explain the linearized dynamics around each fixed point (see Supplementary Information), and approximate well the responses of the full model (magenta curves, Fig. 6a). Mathematically, the line attractor and the selection vector correspond to the right and left zero-eigenvector of the underlying linear system. Within a context, these locally defined eigenvectors point in a remarkably consistent direction across different fixed points—the selection vector, in particular, is always aligned with the relevant input and orthogonal to the irrelevant input (Fig. 6c and Extended Data Fig. 10q–s). As a result, the two line attractors (Fig. 6c) show relaxation dynamics appropriate for selecting the relevant input along their entire length.

Discussion

We describe a novel mechanism underlying flexible, context-dependent selection of sensory inputs and their integration towards a choice (see refs 39–41 for related concepts). This mechanism is sufficient to explain the selection and integration of motion inputs in both monkeys, and of colour inputs in monkey A, which are not filtered out by context before they reach PFC.

A randomly initialized, recurrent neural network trained to solve a task analogous to the monkeys' task reproduces the main features of the data, and analysis of the trained network elucidates the novel selection mechanism. Integration along line attractors, and its relation to the selection vector, has been described before³⁹. However, our model demonstrates how a single nonlinear model can implement flexible computations by reconfiguring the selection vector and the corresponding recurrent dynamics based on a contextual input. Counterintuitively, in the model the projection of an input onto the line attractor does

not determine the extent to which it is integrated, a manifestation of 'non-normal' dynamics^{40,42,43} (see Supplementary Information).

Our results show that the modulation of sensory responses is not necessary to select among sensory inputs (see also refs 44–46). Consistent with this conclusion, two studies using tasks similar to ours^{47,48}, as well as our own recordings in the middle temporal visual area (MT) of monkey A (data not shown), have found no evidence for consistent firing rate modulations in the relevant sensory areas. The dynamical process outlined in this paper is fully sufficient for context-dependent selection in a variety of behavioural models^{3–8}, but it need not be exclusive. Multiple selection mechanisms may exist within the brain.

Our results indicate that computations in prefrontal cortex emerge from the concerted dynamics of large populations of neurons, and are well studied in the framework of dynamical systems^{17,19–23,24,39,49}. Notably, the rich dynamics of PFC responses during selection and integration of inputs can be characterized and understood with just two features of a dynamical system—the line attractor and the selection vector, which are defined only at the level of the neural population. This parsimonious account of cortical dynamics contrasts markedly with the complexity of single neuron responses typically observed in PFC and other integrative structures, which reveal multiplexed representation of many task-relevant and choice-related signals^{1,2,15,16,25,26,50}. In light of our results, these mixtures of signals can be interpreted as separable representations at the level of the neural population^{15,17,25,26}. A fundamental function of PFC may be to generate such separable representations, and to flexibly link them through appropriate recurrent dynamics to generate the desired behavioural outputs.

METHODS SUMMARY

Two adult male rhesus monkeys (14 and 12 kg) were trained on a two-alternative, forced-choice, visual discrimination task. While the monkeys were engaged in the behavioural task, we recorded single- and multiunit responses in the arcuate sulcus and the prearcuate gyrus, and in cortex near and lateral to the principal sulcus. The great majority of neurons were not recorded simultaneously, but rather in separate behavioural sessions. All surgical and behavioural procedures conformed to the guidelines established by the National Institutes of Health and were approved by the Institutional Animal Care and Use Committee of Stanford University. We pooled data from single- and multiunit recordings to construct population responses, and used state space analysis to study the effect of task conditions and time on the population responses. We developed a dimensionality reduction technique ('targeted dimensionality reduction') to identify a low-dimensional subspace capturing variance due to the task variables of interest. We compared the recorded responses to the responses of units in a nonlinear, recurrent neural network model. We trained the model (that is, optimized its

synaptic weights with a 'back-propagation' algorithm) to perform a task analogous to the one performed by the monkeys. We then reverse-engineered the model to discover its mechanism of selective integration. We identified fixed points of the model dynamics, linearized the dynamics around the fixed points, and used linear systems analysis to understand the linearized dynamics. Full methods are provided in the Supplementary Information.

Online Content Any additional Methods, Extended Data display items and Source Data are available in the online version of the paper; references unique to these sections appear only in the online paper.

Received 27 September 2012; accepted 8 October 2013.

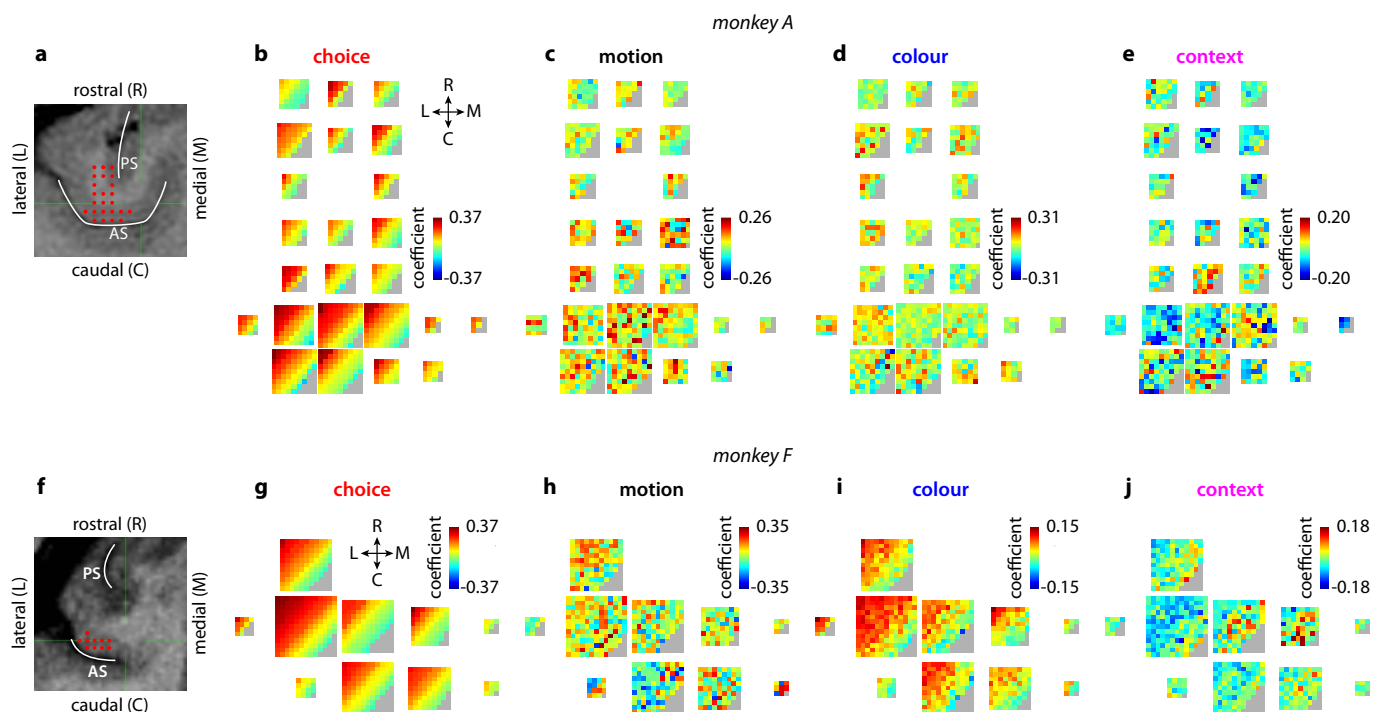
- Fuster, J. M. *The Prefrontal Cortex* 4th edn (Academic, 2008).
- Miller, E. K. & Cohen, J. D. An integrative theory of prefrontal cortex function. *Annu. Rev. Neurosci.* **24**, 167–202 (2001).
- Desimone, R. & Duncan, J. Neural mechanisms of selective visual attention. *Annu. Rev. Neurosci.* **18**, 193–222 (1995).
- Schroeder, C. E. & Lakatos, P. Low-frequency neuronal oscillations as instruments of sensory selection. *Trends Neurosci.* **32**, 9–18 (2009).
- Noudoost, B., Chang, M. H., Steinmetz, N. A. & Moore, T. Top-down control of visual attention. *Curr. Opin. Neurobiol.* **20**, 183–190 (2010).
- Reynolds, J. H. & Chelazzi, L. Attentional modulation of visual processing. *Annu. Rev. Neurosci.* **27**, 611–647 (2004).
- Maunsell, J. H. & Treue, S. Feature-based attention in visual cortex. *Trends Neurosci.* **29**, 317–322 (2006).
- Fries, P. Neuronal gamma-band synchronization as a fundamental process in cortical computation. *Annu. Rev. Neurosci.* **32**, 209–224 (2009).
- Mansouri, F. A., Tanaka, K. & Buckley, M. J. Conflict-induced behavioural adjustment: a clue to the executive functions of the prefrontal cortex. *Nature Rev. Neurosci.* **10**, 141–152 (2009).
- Tanji, J. & Hoshi, E. Role of the lateral prefrontal cortex in executive behavioral control. *Physiol. Rev.* **88**, 37–57 (2008).
- Bruce, C. J. & Goldberg, M. E. Primate frontal eye fields. I. Single neurons discharging before saccades. *J. Neurophysiol.* **53**, 603–635 (1985).
- Schall, J. D. The neural selection and control of saccades by the frontal eye field. *Phil. Trans. R. Soc. Lond. B* **357**, 1073–1082 (2002).
- Moore, T. The neurobiology of visual attention: finding sources. *Curr. Opin. Neurobiol.* **16**, 159–165 (2006).
- Kim, J. N. & Shadlen, M. N. Neural correlates of a decision in the dorsolateral prefrontal cortex of the macaque. *Nature Neurosci.* **2**, 176–185 (1999).
- Machens, C. K., Romo, R. & Brody, C. D. Functional, but not anatomical, separation of "what" and "when" in prefrontal cortex. *J. Neurosci.* **30**, 350–360 (2010).
- Rigotti, M. *et al.* The importance of mixed selectivity in complex cognitive tasks. *Nature* **497**, 585–590 (2013).
- Stokes, M. G. *et al.* Dynamic coding for cognitive control in prefrontal cortex. *Neuron* **78**, 364–375 (2013).
- Hernández, A. *et al.* Decoding a perceptual decision process across cortex. *Neuron* **66**, 300–314 (2010).
- Churchland, M. M. *et al.* Neural population dynamics during reaching. *Nature* **487**, 51–56 (2012).
- Shenoy, K. V., Sahani, M. & Churchland, M. M. Cortical control of arm movements: a dynamical systems perspective. *Annu. Rev. Neurosci.* **36**, 337–359 (2013).
- Stopfer, M., Jayaraman, V. & Laurent, G. Intensity versus identity coding in an olfactory system. *Neuron* **39**, 991–1004 (2003).
- Briggman, K. L., Abarbanel, H. D. & Kristan, W. B. Jr. Optical imaging of neuronal populations during decision-making. *Science* **307**, 896–901 (2005).
- Harvey, C. D., Coen, P. & Tank, D. W. Choice-specific sequences in parietal cortex during a virtual-navigation decision task. *Nature* **484**, 62–68 (2012).
- Afshar, A. *et al.* Single-trial neural correlates of arm movement preparation. *Neuron* **71**, 555–564 (2011).
- Sigala, N., Kusunoki, M., Nimmo-Smith, I., Gaffan, D. & Duncan, J. Hierarchical coding for sequential task events in the monkey prefrontal cortex. *Proc. Natl Acad. Sci. USA* **105**, 11969–11974 (2008).
- Machens, C. K. Demixing population activity in higher cortical areas. *Front. Comput. Neurosci.* **4**, 126 (2010).
- Shadlen, M. N. & Newsome, W. T. Neural basis of a perceptual decision in the parietal cortex (area LIP) of the rhesus monkey. *J. Neurophysiol.* **86**, 1916–1936 (2001).
- Mazurek, M. E., Roitman, J. D., Ditterich, J. & Shadlen, M. N. A role for neural integrators in perceptual decision making. *Cereb. Cortex* **13**, 1257–1269 (2003).
- Wang, X. J. Probabilistic decision making by slow reverberation in cortical circuits. *Neuron* **36**, 955–968 (2002).
- Cohen, J. D., Dunbar, K. & McClelland, J. L. On the control of automatic processes: a parallel distributed processing account of the Stroop effect. *Psychol. Rev.* **97**, 332–361 (1990).
- Deco, G. & Rolls, E. T. Attention and working memory: a dynamical model of neuronal activity in the prefrontal cortex. *Eur. J. Neurosci.* **18**, 2374–2390 (2003).
- Sussillo, D. & Abbott, L. F. Generating coherent patterns of activity from chaotic neural networks. *Neuron* **63**, 544–557 (2009).
- Sussillo, D. & Barak, O. Opening the black box: low-dimensional dynamics in high-dimensional recurrent neural networks. *Neural Comput.* **25**, 626–649 (2013).
- Zipser, D. & Andersen, R. A. A back-propagation programmed network that simulates response properties of a subset of posterior parietal neurons. *Nature* **331**, 679–684 (1988).
- Martens, J. & Sutskever, I. Learning recurrent neural networks with hessian-free optimization. *Proc. 28th Int. Conf. Machine Learn. (ICML)*, 2011).
- Churchland, A. K., Kiani, R. & Shadlen, M. N. Decision-making with multiple alternatives. *Nature Neurosci.* **11**, 693–702 (2008).
- Reddi, B. A. & Carpenter, R. H. The influence of urgency on decision time. *Nature Neurosci.* **3**, 827–830 (2000).
- Brunton, B. W., Botvinick, M. M. & Brody, C. D. Rats and humans can optimally accumulate evidence for decision-making. *Science* **340**, 95–98 (2013).
- Seung, H. S. How the brain keeps the eyes still. *Proc. Natl Acad. Sci. USA* **93**, 13339–13344 (1996).
- Goldman, M. S. Memory without feedback in a neural network. *Neuron* **61**, 621–634 (2009).
- Sejnowski, T. J. On the stochastic dynamics of neuronal interaction. *Biol. Cybern.* **22**, 203–211 (1976).
- Murphy, B. K. & Miller, K. D. Balanced amplification: a new mechanism of selective amplification of neural activity patterns. *Neuron* **61**, 635–648 (2009).
- Ganguli, S., Huh, D. & Sompolinsky, H. Memory traces in dynamical systems. *Proc. Natl Acad. Sci. USA* **105**, 18970–18975 (2008).
- Salinas, E. Context-dependent selection of visuomotor maps. *BMC Neurosci.* **5**, 47 (2004).
- Zénon, A. & Krauzlis, R. J. Attention deficits without cortical neuronal deficits. *Nature* **489**, 434–437 (2012).
- Roy, J. E., Riesenhuber, M., Poggio, T. & Miller, E. K. Prefrontal cortex activity during flexible categorization. *J. Neurosci.* **30**, 8519–8528 (2010).
- Sasaki, R. & Uka, T. Dynamic readout of behaviorally relevant signals from area MT during task switching. *Neuron* **62**, 147–157 (2009).
- Katzner, S., Busse, L. & Treue, S. Attention to the color of a moving stimulus modulates motion-signal processing in macaque area MT: evidence for a unified attentional system. *Front. Syst. Neurosci.* **3**, 12 (2009).
- Machens, C. K., Romo, R. & Brody, C. D. Flexible control of mutual inhibition: a neural model of two-interval discrimination. *Science* **307**, 1121–1124 (2005).
- Huk, A. C. & Meister, M. L. Neural correlates and neural computations in posterior parietal cortex during perceptual decision-making. *Front. Integr. Neurosci.* **6**, 86 (2012).

Supplementary Information is available in the online version of the paper.

Acknowledgements We thank J. Powell, S. Fong and J. Brown for technical assistance, L. Abbott, for conversations on non-normal dynamics, and L. Stryer, S. Hohl, S. Ganguli, M. Sahani, R. Kiani, C. Moore and T. Bhattacharya for discussions. V.M. and W.T.N. were supported by HHMI and the Air Force Research Laboratory (FA9550-07-1-0537); D.S. and K.V.S. by an NIH Director's Pioneer Award (1DP10D006409) and DARPA REPAIR (N66001-10-C-2010).

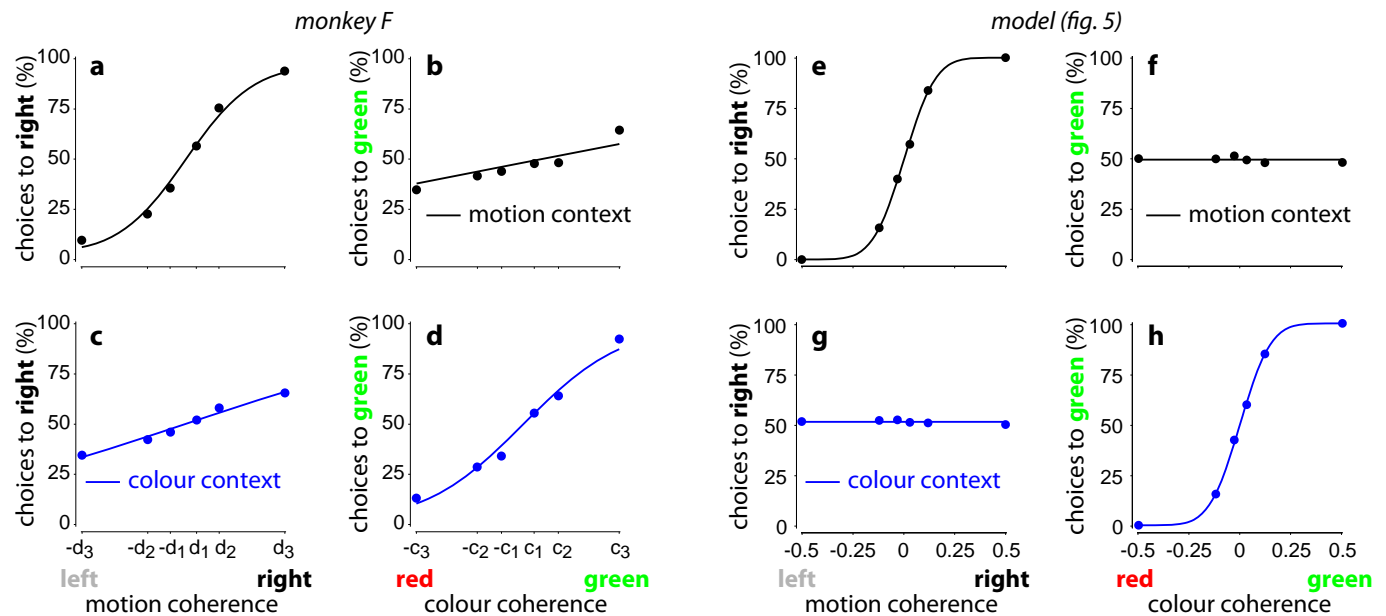
Author Contributions V.M. and W.T.N. designed the study. V.M. collected the data. D.S. implemented the recurrent network. V.M. and D.S. analysed and modelled the data. V.M., D.S., K.V.S. and W.T.N. discussed the findings and wrote the paper.

Author Information Reprints and permissions information is available at www.nature.com/reprints. The authors declare no competing financial interests. Readers are welcome to comment on the online version of the paper. Correspondence and requests for materials should be addressed to V.M. (valerio@ini.phys.ethz.ch) or D.S. (sussillo@stanford.edu).



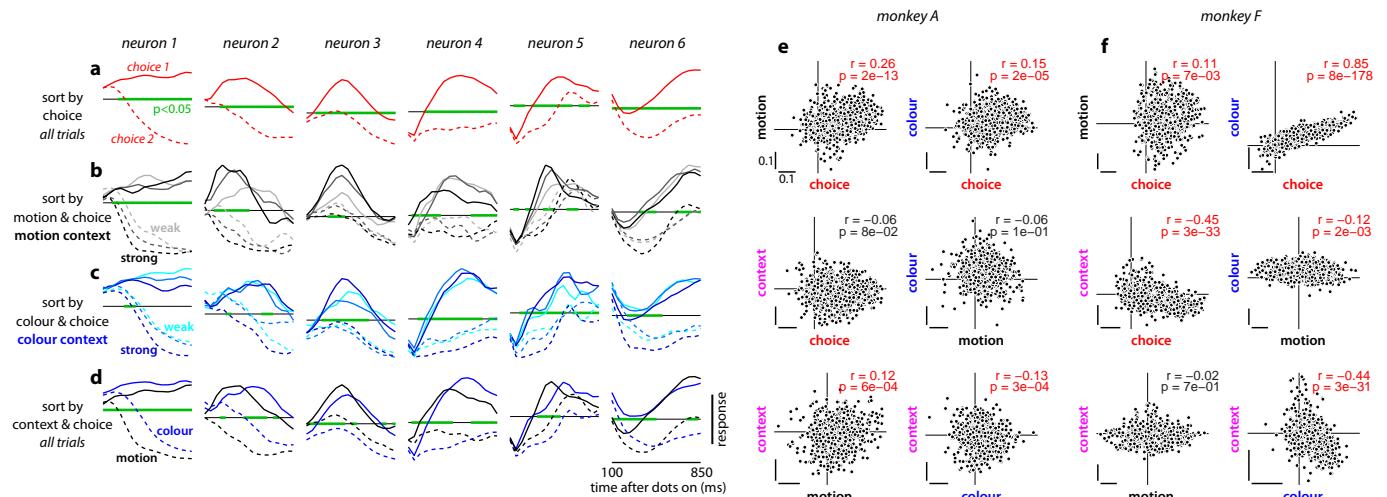
Extended Data Figure 1 | Recording locations and task-related patterns of population activity in PFC. **a**, Recording locations (red dots) in monkey A are shown on anatomical magnetic resonance images in imaging planes that were oriented perpendicularly to the direction of electrode penetrations. Electrodes were lowered through a grid (1-mm spacing) positioned over the arcuate sulcus (AS). Recordings covered the entire depth of the AS and extended rostrally onto the prearcuate gyrus and cortex near and lateral to the principal sulcus (PS). **b–e**, Representation of four task variables in the population response. Each multi-coloured square corresponds to a recording location (red dots) in **a**. Within each square, each pixel corresponds to a unit recorded from that grid position, such that each square represents all the units recorded at the corresponding location. The colour of a pixel indicates the de-noised regression coefficient of choice (**b**), motion coherence (**c**), colour coherence (**d**) and context (**e**) for a given unit (colour bars; grey: no units). These coefficients describe how much the trial-by-trial firing rate of a given unit depends on the task variables in **b–e**. The position of each unit within a square is arbitrary; we therefore sorted them according to the amplitude of the coefficient of choice, which accounts for the diagonal bands of colour in **b** (top-left to bottom-right,

high to low choice coefficient). The positions of the pixels established in **b** are maintained in **c–e**, so that one can compare the amplitude of the coefficient for each task variable for every unit recorded from monkey A. Each of the four panels can be interpreted as the pattern of population activity elicited by the corresponding task variable. The four task variables elicit very distinct patterns of activity and are separable at the level of the population. Importantly, the coefficients were de-noised with principal component analysis (see Supplementary Information, section 6.7) and can be estimated reliably from noisy neural responses (Extended Data Fig. 4i–l). Differences between activation patterns therefore reflect differences in the properties of the underlying units, not noise. **f–j**, Recording locations and task-related patterns of population activity for monkey F. Same conventions as in **a–e**. Recordings (**f**) covered the entire depth of the AS. The patterns of population activity elicited by a choice (**g**), by the motion evidence (**h**) and by context (**j**) are distinct, meaning that the representations of these task variables are separable at the level of the population. The representations of choice (**g**) and colour (**i**), however, are not separable in monkey F, indicating that colour inputs are processed differently in the two monkeys (see main text).



Extended Data Figure 2 | Psychophysical performance for monkey F and for the model. **a–d**, Psychophysical performance for monkey F, for motion (top) and colour contexts (bottom), averaged over 60 recording sessions (123,550 trials). Performance is shown as a function of motion (left) or colour (right) coherence in each behavioural context. As in Fig. 1c–f, coherence values along the horizontal axis correspond to the average low, intermediate and high motion coherence (**a**, **c**) and colour coherence (**b**, **d**) computed over all behavioural trials. The curves are fits of a behavioural model (see Supplementary Information, section 4). **e–h**, ‘Psychophysical’ performance for the trained neural-network model (Figs 4–6) averaged over a total of 14,400 trials (200 repetitions per condition). Choices were generated based on the output of the model at the end of the stimulus presentation—an output larger than zero corresponds to a choice to the left target (choice 1), and an output

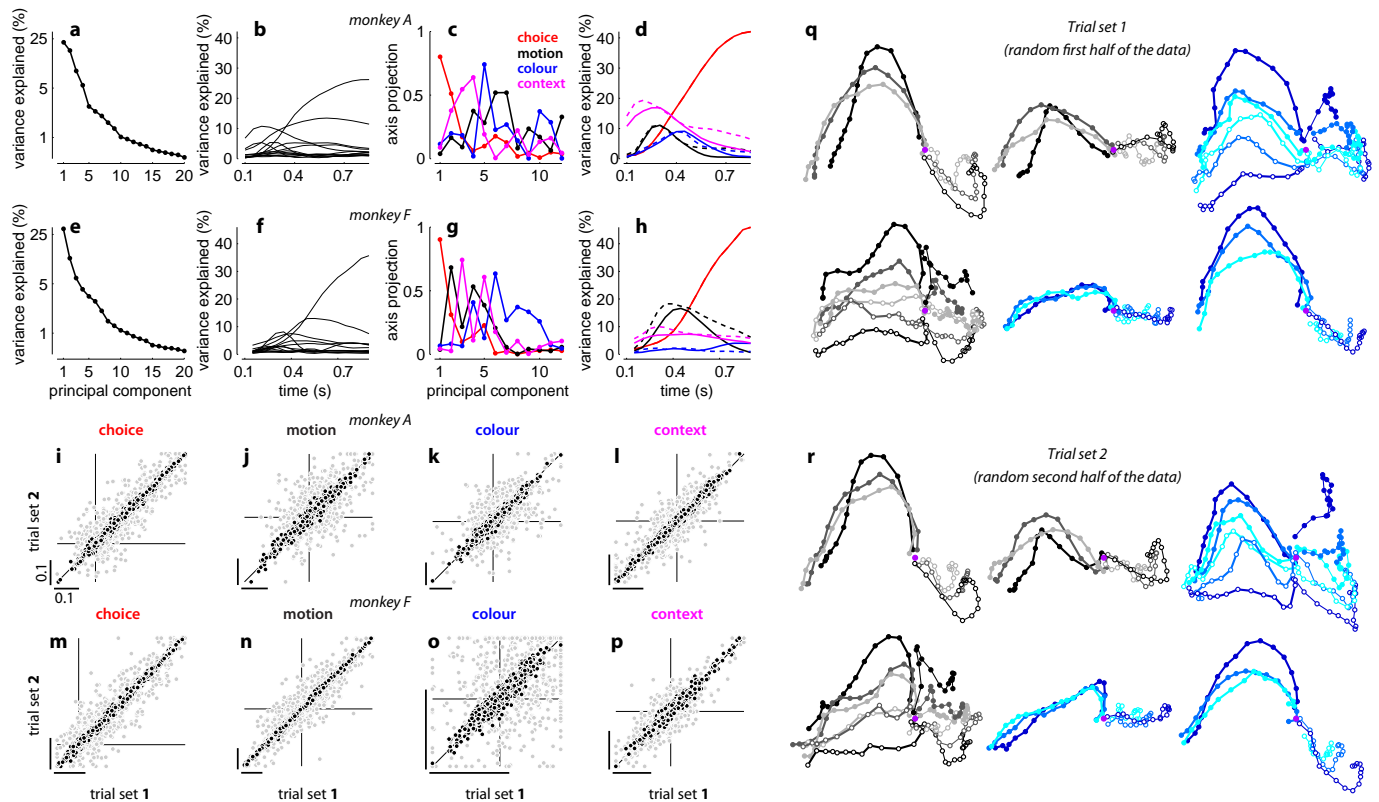
smaller than zero corresponds to a choice to the right target (choice 2). We simulated model responses to inputs with motion and colour coherences of 0.03, 0.12 and 0.50. The variability in the input (that is, the variance of the underlying Gaussian distribution) was chosen such that the performance of the model for the relevant sensory signal qualitatively matches the performance of the monkeys. As in Fig. 1c–f, performance is shown as a function of motion (left) or colour (right) coherence in the motion (top) and colour contexts (bottom). Curves are fits of a behavioural model (as in **a–d** and in Fig. 1c–f). In each behavioural context, the relevant sensory input affects the model’s choices (**e**, **h**), but the irrelevant input does not (**f**, **g**), reflecting successful context-dependent integration. The model output essentially corresponds to the bounded temporal integral of the relevant input (not shown) and is completely unaffected by the irrelevant input.



Extended Data Figure 3 | Mixed representation of task variables in PFC.

a–d, Example responses from six well-isolated single units in monkey A. Each column shows average normalized responses on correct trials for one of the single units. Responses are aligned to the onset of the random-dot stimulus, averaged with a 50-ms sliding window, and sorted by one or more task-related variables (choice, motion coherence, colour coherence, context). The green lines mark time intervals with significant effects of choice (**a**), motion coherence (**b**), colour coherence (**c**), or context (**d**) as assessed by multi-variable, linear regression (regression coefficient different from zero, $P < 0.05$). Linear regression and coefficient significance are computed over all trials (correct and incorrect, motion and colour context; Supplementary Information, section 6.3). The horizontal grey line corresponds to a normalized response equal to zero. **a**, Responses sorted by choice (solid, choice 1; dashed, choice 2) averaged over both contexts. **b**, Responses during motion context, sorted by choice and motion coherence (black to light-grey, high to low motion coherence). **c**, Responses during colour context, sorted by choice and colour coherence (blue to cyan, high to low colour coherence). **d**, Responses sorted by

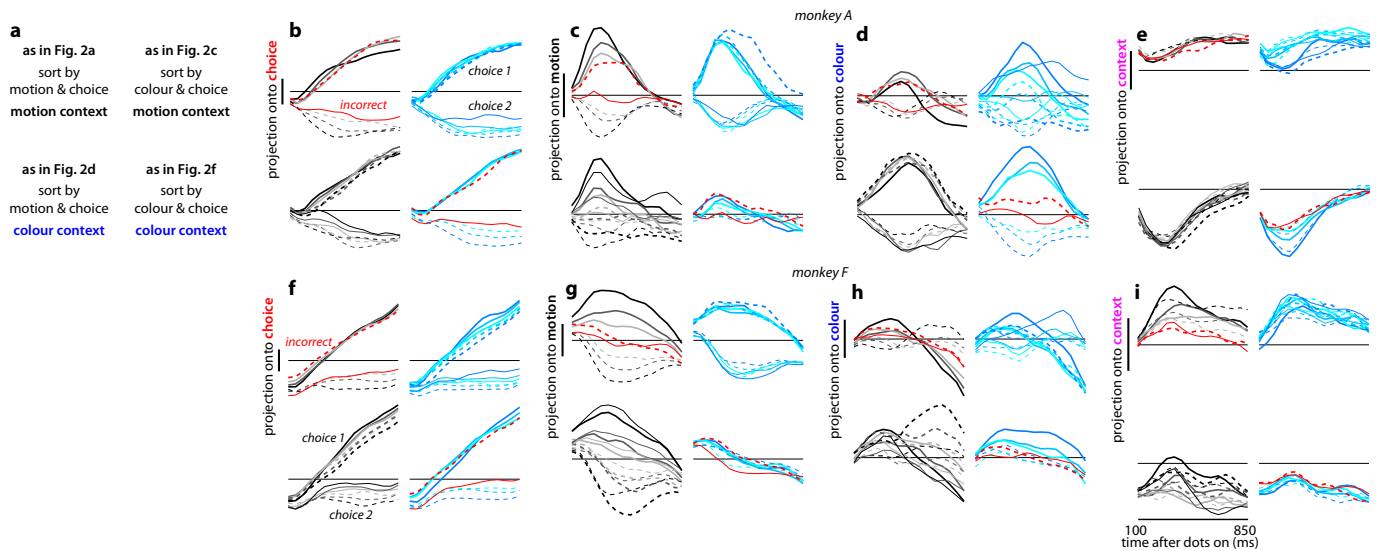
choice and context (black, motion context; blue, colour context). As is typical for PFC, the activity of the example units depends on many task variables, indicating that they represent mixtures of the underlying task variables. **e, f**, De-noised regression coefficients for all units in monkey A (**e**) and monkey F (**f**). The data in Extended Data Fig. 1 are re-plotted here to directly compare the effects of different task variables (choice, motion, colour, context) to each other. Each data point corresponds to a unit, and the position along the horizontal and vertical axes is the de-noised regression coefficient for the corresponding task variable. The horizontal and vertical lines in each panel intersect at the origin (0,0). Scale bars span the same range (0.1) in each panel. The different task variables are mixed at the level of individual units. Although units modulated by only one of the task variables do occur in the population, they do not form distinct clusters but rather are part of a continuum that typically includes all possible combinations of selectivities. Significant correlations between coefficients are shown in red ($P < 0.05$, Pearson's correlation coefficient r).



Extended Data Figure 4 | Targeted dimensionality reduction of population responses, and reliability of task-related axes and population trajectories.

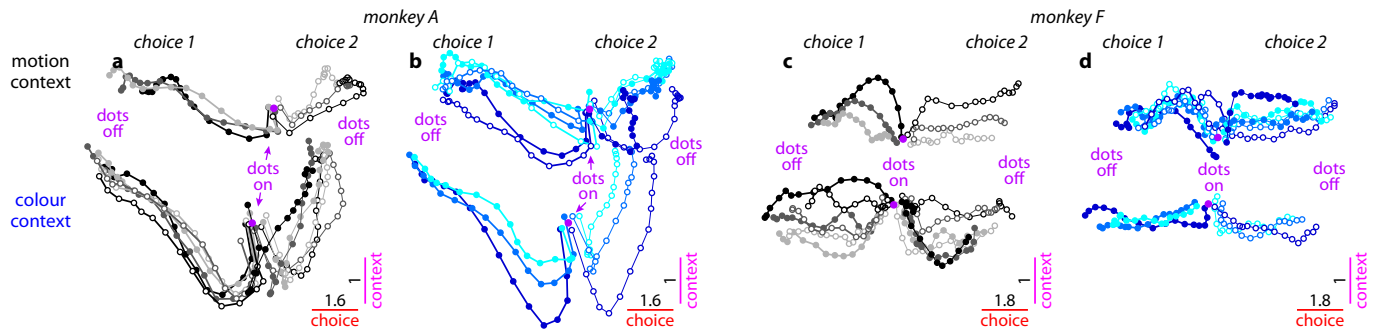
a, Fraction of variance explained by the first 20 principal components of the responses in monkey A. Principal components are computed on correct trials only, on condition-averaged responses. Conditions are defined on the basis of choice, motion coherence, colour coherence and context. Each time point of the average response for a given condition contributes an 'independent' sample for the principal components analysis, and variance is computed over conditions and times. **b**, Fraction of variance explained by the first 12 principal components. The total explainable variance (100%) is computed separately at each time, and reflects response differences across conditions. **c**, The four 'task-related axes' of choice, motion, colour and context expressed as linear combinations of the first 12 principal components. The four axes span a subspace containing the task-related variance in the population response (for example, Fig. 2 and Extended Data Fig. 6) and are obtained by orthogonalizing the de-noised regression vectors for the corresponding task variables (see Supplementary Information, section 6.7; de-noised regression coefficients are shown in Extended Data Figs 1 and 3e, f). The vertical axis in **c** corresponds to the projection of each axis onto a given principal component (that is, the contribution of that principal component to each axis). All four axes project onto multiple principal components and thus the corresponding task variables are mixed at the level of single principal components. **d**, Fraction of variance explained by the task-related axes of choice, motion, colour and context (solid lines), as in **b**. The four axes explain a larger fraction of the variance than the principal components at many times but, unlike the principal components, they do not explain the variance common to all conditions that is due to the passage of time (not shown). A possible concern with our analysis is that the time courses of variance explained in **d** could be misleading if the task-related axes, which we estimated only at a single time for each variable, are changing over time during the presentation of the random dots. Under this scenario, for example, the 'humped' shape of the motion input (solid black trace) might reflect a changing ensemble code for motion rather than actual changes in the strength of the motion signal in the neural population. To control for this possibility, we also computed time-varying 'task-related axes' by estimating the axes of motion, colour and context separately at each time throughout the 750-ms dots presentation. The fractions of variance explained by the time-varying axes (dashed lines) and by the fixed axes (solid lines) have similar amplitudes and time courses. Thus, the effects of the corresponding task variables (during the presentation of the random dots) are adequately captured by the subspace spanned by the fixed axes (see Supplementary Information,

section 6.8). **e–h**, Same as **a–d**, for monkey F. As shown in Extended Data Figs 1g, i and 3f (top-right panel) the de-noised regression coefficients of colour and choice are strongly correlated. As a consequence, the axis of colour explains only a small fraction of the variance in the population responses (**h**, blue; see main text). **i–l**, Reliability of task-related axes in monkey A. To determine to what extent variability (that is, noise) in single unit responses affects the task-related axes of choice, motion, colour and context (for example, Fig. 2 and Extended Data Fig. 6), we estimated each axis twice from two separate sets of trials (trial sets 1 and 2 in **i–l**). For each unit, we first assigned each trial to one of two subsets, and estimated de-noised regression coefficients for the task variables separately for the two subsets. We then obtained task-related axes by orthogonalizing the corresponding de-noised coefficients (see Supplementary Information, section 6.9). Here, the orthogonalized coefficients are computed both with (black) and without (grey) PCA-based de-noising. The horizontal and vertical lines in each panel intersect at the origin (0,0). Scale bars span the same range (0.1) in each panel. Data points lying outside the specified horizontal or vertical plotting ranges are shown on the corresponding edges in each panel. **i**, Coefficients of choice. Each data point corresponds to the orthogonalized coefficient of choice for a given unit, computed from trials in set 1 (horizontal axis) or in set 2 (vertical axis). **j–l**, Same as **i** for the orthogonalized coefficients of motion (**j**), colour (**k**) and context (**l**). **m–p**, Orthogonalized regression coefficients for monkey F, as in **i–l**. Overall, after de-noising the orthogonalized coefficients are highly consistent across the two sets of trials. Therefore, the observed differences in the activation pattern elicited by different task variables (Extended Data Fig. 1) are not due to the noisiness of neural responses, but rather reflect differences in the properties of the underlying units. **q, r**, Reliability of population trajectories. To assess the reliability of the trajectories in Fig. 2, we estimated the task-related axes and the resulting population trajectories (same conventions as Fig. 2) twice from two separate sets of trials (as **i–l**, see Supplementary Information, section 6.9). As in the example trajectories shown in **q** (trial set 1) and **r** (trial set 2), we consistently obtained very similar trajectories across the two sets of trials. To quantify the similarity between the trajectories from the two sets, we used trajectories obtained from one set to predict the trajectories obtained from the other set (see Supplementary Information, section 6.9). On average across 20 randomly defined pairs of trial sets, in both monkeys the population responses from one set explain 94% of the total variance in the responses of the other set (95% for the example in **q** and **r**). These numbers provide a lower bound on the true reliability of trajectories in Fig. 2, which are based on twice as many trials as those in **q** and **r**.



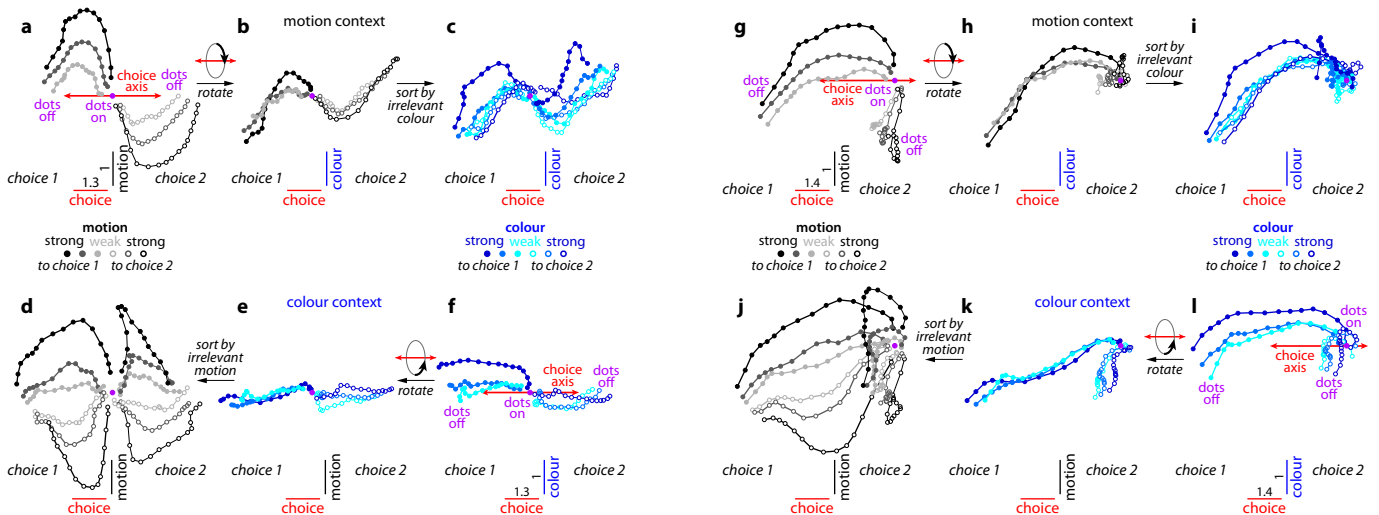
Extended Data Figure 5 | Population responses along individual task-related axes. **a–e**, Responses for monkey A. The average population responses on correct trials are re-plotted from Fig. 2, together with responses on a subset of incorrect trials (red curves). Here the responses are represented explicitly as a function of time (horizontal axis) and projected separately (vertical axes) onto the axes of choice (**b**), motion (**c**), colour (**d**) and context (**e**). As in Fig. 2, correct trials are sorted on the basis of context (motion: top sub-panels; colour: bottom sub-panels; see key in **a**), on the direction of the sensory evidence (filled, towards choice 1; dashed, towards choice 2) and strength of the sensory evidence (black to light-grey, strongest to weakest motion; blue to cyan, strongest to weakest colour), and based on choice (thick, choice 1; thin, choice 2). Incorrect trials (red curves) are shown for the lowest motion coherence (during motion context, top left in **b–e**) and the lowest colour coherence (during colour context, bottom right in **b–e**). Vertical scale bars correspond to 1 unit of normalized response, and the horizontal lines are drawn at the same level in all four sub-panels within **b–e**. **a**, Key to the condition averages shown in each panel of **b–e**, as well as to the corresponding state-space

panels in Fig. 2. **b**, Projections of the population response onto the choice axis. Responses along the choice axis represent integration of evidence in both contexts. **c**, Projection onto the motion axis. Responses along the motion axis represent the momentary motion evidence during both motion (top left) and colour contexts (bottom left) (curves are parametrically ordered based on motion strength in both contexts), but not the colour evidence (right, curves are not ordered based on colour strength). **d**, Projection onto the colour axis. Responses along the colour axis represent the momentary colour evidence in the motion (top right) and colour contexts (bottom right) (ordered), but not the motion evidence (left, not ordered). **e**, Projection onto the context axis. Responses in the motion context (top, all curves above the horizontal line) and colour context (bottom, all curves below the horizontal line) are separated along the context axis, which maintains a representation of context. **f–i**, Responses for monkey F, same conventions as in **b–e**. The responses in **f–i** are also shown as trajectories in Extended Data Fig. 7g–l. The drift along the choice axis in Extended Data Fig. 7g–l is reflected in the overall positive slopes in **f**.



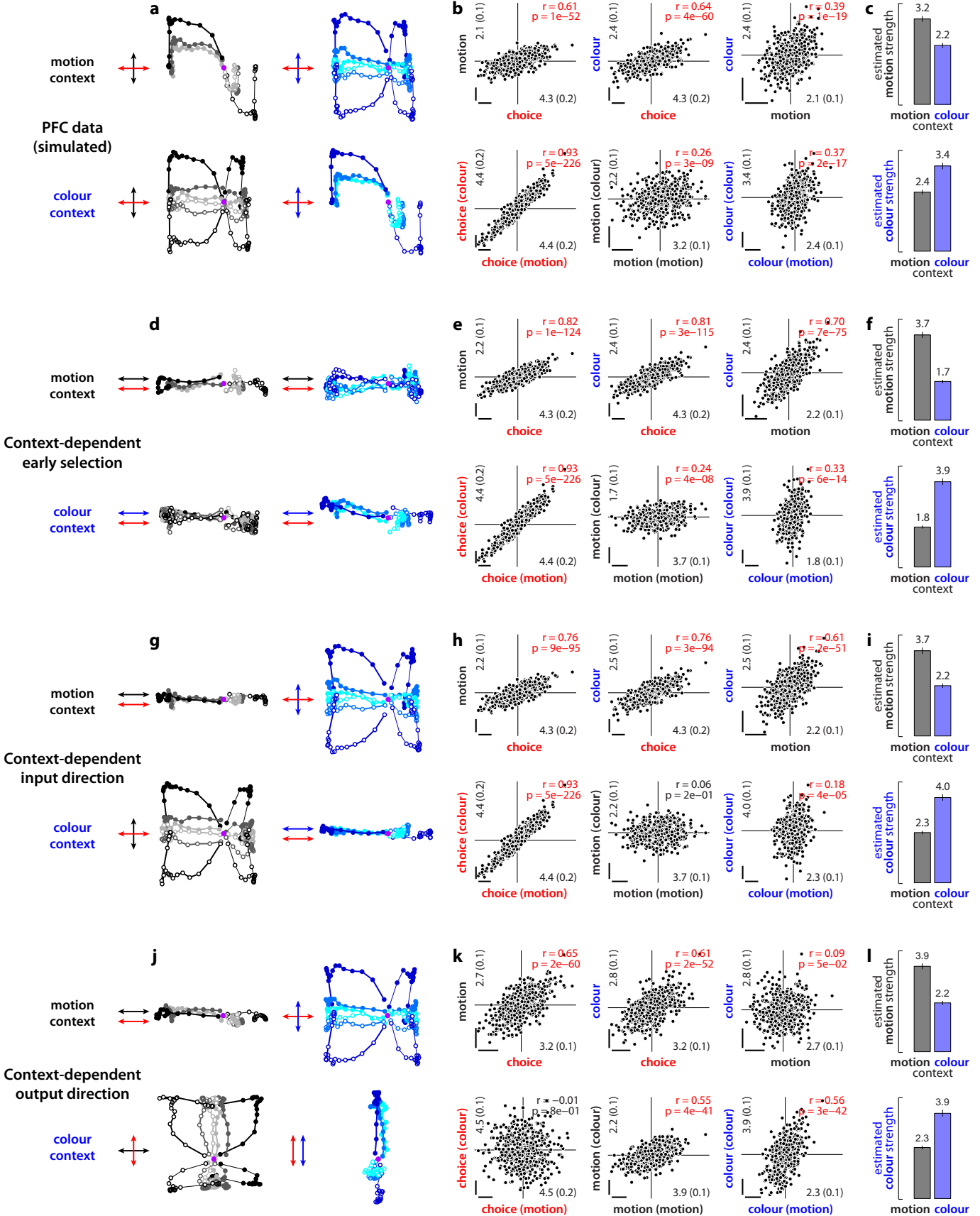
Extended Data Figure 6 | Effect of context on PFC dynamics. **a, b,** Responses from monkey A. Same conditions and conventions as in Fig. 2, but for activity projected into the two-dimensional subspace capturing the variance due to choice (along the choice axis) and context (context axis). Components along the choice axis are enhanced relative to the context axis (see scale bars). The population response contains a representation of context, which is reflected in the separation between trajectories in the motion and colour contexts along the axis of context. The contextual signal is strongest early during the dots presentation. **a,** Effects of context (motion context versus colour context),

choice (choice 1 versus choice 2), and motion input (direction and coherence, grey colours). **b,** Same trials as in **a**, but averaged to show the effect of the colour input (blue colours). **c, d,** Responses from monkey F, same conventions as in **a, b**. As in Extended Data Fig. 7a–f, we subtracted the across-condition average trajectory from each individual, raw trajectory (see Supplementary Information, section 6.10). The underlying raw population responses are shown in Extended Data Fig. 5f–i, and confirm that the representation of context is stable throughout the dots presentation time (Extended Data Fig. 5i).



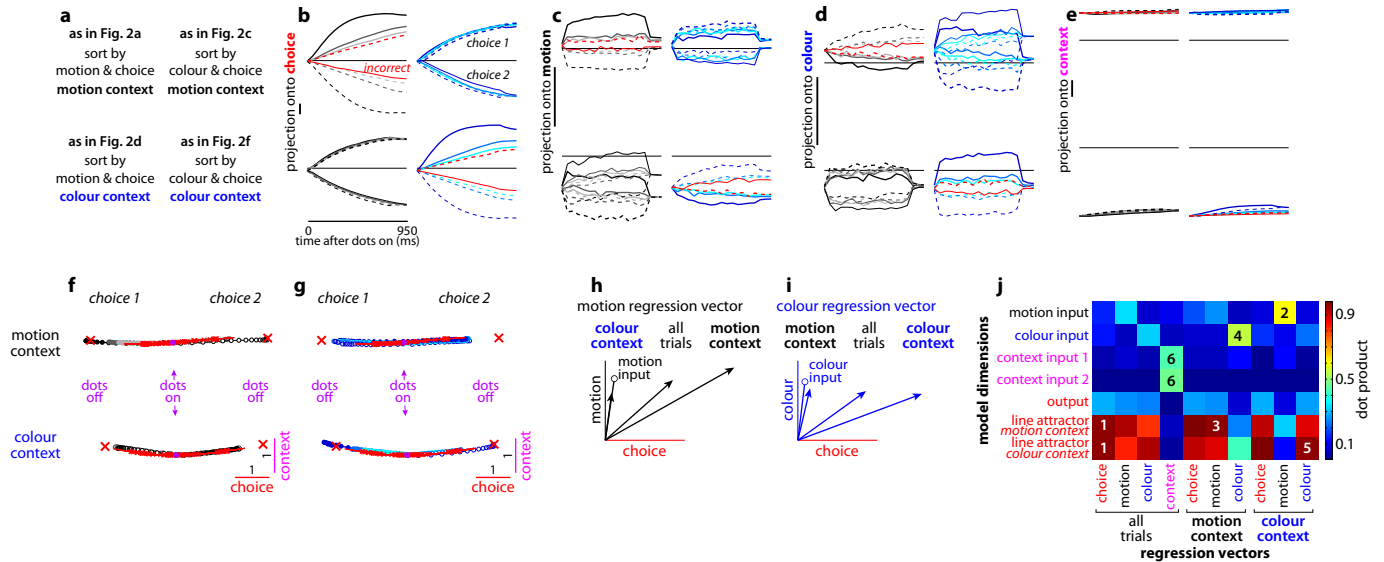
Extended Data Figure 7 | Dynamics of population responses in monkey F. **a–f,** Response trajectories in the subspace spanned by the task-related axes of choice, motion and colour. Same conventions as in Fig. 2. Unlike in Fig. 2, here we subtracted the across-condition average trajectory from each individual, raw trajectory (see Supplementary Information, section 6.10). The raw trajectories are shown in **g–l** and the corresponding projections onto individual axes in Extended Data Fig. 5f–i. Three key features of the population responses are shared in monkey A (Fig. 2) and monkey F. First, movement along a single choice axis (**a** and **f**, red arrows) corresponds to integration of the relevant evidence in both contexts. Second, in both contexts the momentary motion evidence elicits responses along the axis of motion, which is substantially different from the axis of choice (**a** and **d**). Third, the motion evidence is strongly represented whether it is relevant (**a**) or irrelevant (**d**). Thus, the processing of motion inputs in both monkeys is inconsistent with current models of selection and integration (Fig. 3b–d). Unlike in monkey A, responses along the colour axis in monkey F (**f** and **c**) reflect the momentary colour evidence only weakly. The effects of colour on the trajectories in monkey F

resemble the responses expected by the early selection model (Fig. 3b). **g–l,** Raw population responses. Population trajectories were computed and are represented as in Fig. 2. The trajectories in **a–f** were obtained by subtracting the across-condition average from each individual trajectory shown above. Overall, the responses have a tendency to move towards the left along the choice axis. An analogous, although weaker, overall drift can also be observed in monkey A, and contributes to the asymmetry between trajectories on choice 1 and choice 2 trials (Fig. 2). Because choice 1 corresponds to the target in the response field of the recorded neurons (see Supplementary Information, section 6.2), the drift reflects a tendency of individual firing rates to increase throughout the stimulus presentation time. By the definition of choice 1 and choice 2, a similar but opposite drift has to occur in neurons whose response field overlaps with choice 2 (the responses of which we did not record). In the framework of diffusion-to-bound models, such a drift can be interpreted as an urgency signal, which guarantees that the decision boundary is reached before the offset of the dots (refs 36, 37).



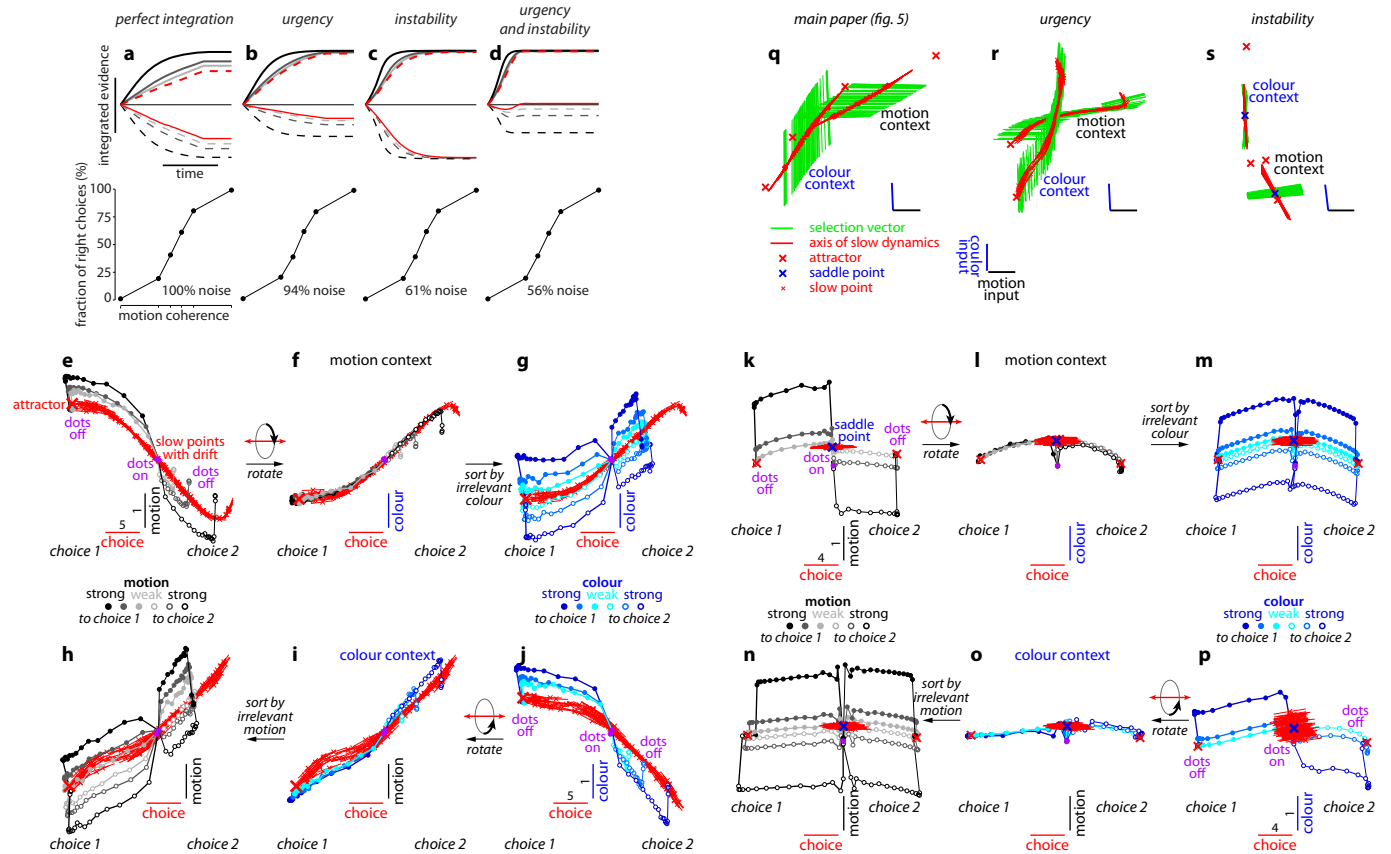
Extended Data Figure 8 | Simulations of models of selective integration inconsistent with PFC responses. We simulated population responses mimicking the observed PFC responses (a–c) and alternative responses expected based on the three models of context-dependent selection described in Fig. 3b–d (d–l) (see Supplementary Information, section 8). These simulations are based on a diffusion-to-bound model, unlike the simulations of the recurrent neural network models in Figs 5 and 6 and in Extended Data Figs 9 and 10e–s. Here, single neurons represent mixtures of three time-dependent task variables of a diffusion-to-bound model, namely the momentary motion and colour evidence and the integrated relevant evidence. At the level of the population, these three task variables are represented along specific directions in state space (arrows in a, d, g, j; red, integrated evidence; black, momentary motion evidence; blue, momentary colour evidence). The four simulations differ only with respect to the direction and context dependence of the three task variables. We computed state space trajectories from the population responses using the targeted dimensionality reduction techniques discussed in the main text and in Supplementary Information. The resulting simulated population responses reproduce the schematic population responses in Fig. 3. a–c, Simulated population responses mimicking the observed PFC responses (Fig. 2). a, Response trajectories in the two-dimensional subspace capturing the effects of choice and motion (left) or choice and colour (right) in the motion (top) and colour (bottom) contexts. Same conditions and conventions as in Fig. 2a, c and Fig. 2d, f. The three task variables are represented along three orthogonal directions in state space (arrows). b, Regression coefficients of choice, motion and colour for all simulated units in the population. For each

unit, coefficients were computed with linear regression on all simulated trials (top) or separately on trials from the motion or colour context (bottom, context in parentheses). Scale bars represent arbitrary units. Numbers in the inset along each axis represent averages of the absolute value of the corresponding coefficients (\pm s.e.m., in parentheses). Significant correlations between coefficients are shown in red ($P < 0.05$, Pearson's correlation coefficient r). c, Estimated strengths of the motion (top) and colour (bottom) inputs during motion (black) and colour (blue) contexts. Input strength is defined as the average of the absolute value of the corresponding regression coefficients. d–f, same as a–c, for simulated population responses expected from context-dependent early selection (Fig. 3b). When relevant, momentary motion (top) and colour (bottom) evidence are represented along the same direction as integrated evidence (arrows in d). g–i, same as a–c, for simulated population responses expected from context-dependent input directions (Fig. 3c). Integrated evidence is represented along the same direction in both contexts (red arrows in g). The relevant momentary evidence (motion in the motion context, top; colour in the colour context, bottom) is aligned with the direction of integration, whereas the irrelevant momentary evidence is orthogonal to it (black and blue arrows in g). j–l, same as a–c, for simulated population responses expected from context-dependent output directions (Fig. 3d). The momentary motion and colour evidence are represented along the same directions in both contexts (black and blue arrows in j). The direction of integration (red arrows in j) is aligned with the motion evidence in the motion context (top), and with the colour evidence in the colour context (bottom).



Extended Data Figure 9 | Model population responses and validation of targeted dimensionality reduction. **a–e**, Model population responses along individual task-related axes, same conventions as in Extended Data Fig. 5. Here we defined the task-related axes directly based on the synaptic connectivity in the model (see Supplementary Information, section 7.6; and panels **h–j**), rather than using the approximate estimates based on the population response (as for the PFC data, for example, Fig. 2). The same axes and the resulting projections underlie the trajectories in Fig. 5. The model integrates the contextually relevant evidence almost perfectly, and the responses along the choice axis (**b**) closely match the output of an appropriately tuned diffusion-to-bound model (not shown). Notably, near-perfect integration is not a core feature of the proposed mechanism of context-dependent selection (see main text, and Extended Data Fig. 10). **f, g**, Effect of context on model dynamics, same conditions and conventions as in Extended Data Fig. 6. Network activity is projected onto the two-dimensional subspace capturing the variance due to choice (along the choice axis) and context (context axis). Same units on both axes (see scale bars). As in Fig. 5, fixed points of the dynamics (red crosses) and the associated right zero-eigenvectors (that is, the local direction of the line attractor, red lines) were computed separately for motion (top) and colour contexts (bottom) in the absence of sensory inputs. The line attractors computed in the two contexts, and the corresponding population trajectories, are separated along the context axis. **f**, Effects of context (motion context, colour context), choice (choice 1, choice 2) and motion input (direction and coherence, grey colours) on the population trajectories. **g**, Same trials as in **f**, but re-sorted and averaged to show the effect of the colour input (blue colours). The context axis is approximately orthogonal to the motion and colour inputs, and thus the effects of motion and colour on the population response (Fig. 5) are not revealed in the subspace spanned by the choice and context axes (**f** and **g**). **h–j**, Validation of targeted dimensionality reduction. To validate the dimensionality reduction approach used to analyse population responses in PFC (see Supplementary Information, sections 6.5–6.7), we estimated the regression vectors of choice, motion, colour and context from the simulated population responses (Fig. 5 and panels **b–g**) and compared them to the exactly known model dimensions that underlie the model dynamics (see definitions below). We estimated the regression vectors in three ways: by pooling responses from all model units and all trials (as in the PFC data, for example, Fig. 2 and Extended Data Fig. 6), or separately

from the motion- and colour-relevant trials (contexts). Orthogonalization of the regression vectors yields the task-related axes of the subspace of interest (for example, axes in Fig. 2). Most model dimensions (motion, colour and context inputs, and output) were defined by the corresponding synaptic weights after training. The line attractor, on the other hand, is the average direction of the right zero-eigenvector of the linearized dynamics around a fixed point, and was computed separately for the motion and colour contexts. **h**, The three regression vectors of motion (black arrows), plotted in the subspace spanned by the choice axis (that is, the regression vector of choice) and the motion axis (that is, the component of the regression vector of motion orthogonal to the choice axis). In the colour context, the motion regression vector closely approximates the actual motion input (black circle—the model dimension defined by synaptic weights). During the motion context, however, the motion regression vector has a strong component along the choice axis, reflecting the integration of motion evidence along that axis. The motion regression vector estimated from all trials corresponds to the average of the vectors from the two contexts; thus all three motion regression vectors lie in the same plane. **i**, The three regression vectors of colour (blue arrows) plotted in the subspace spanned by the choice and colour axes, analogous to **h**. The colour regression vector closely approximates the actual colour input (blue circle) in the motion context, but has a strong component along the choice axis in the colour context. Components along the motion (**h**) and colour (**i**) axes are scaled by a factor of 2 relative to those along the choice axis. **j**, Dot products (colour bar) between the regression vectors (horizontal axis) and the actual model dimensions (vertical axis), computed after setting all norms to 1. The choice regression vector closely approximates the direction of the line attractor in both contexts (squares labelled '1'). As shown also in **h** and **i**, the input regression vectors approximate the model inputs (defined by their synaptic weights) when the corresponding inputs are irrelevant (squares 2 and 4, motion and colour), whereas they approximate the line attractor when relevant (squares 3 and 5). Thus, the motion input is mostly contained in the plane spanned by the choice and motion axes (**h**), and the colour input is mostly contained in the plane spanned by the choice and colour axes (**i**). Finally, the single context regression vector is aligned with both context inputs (squares labelled 6), and closely approximates the difference between the two (not shown).



Extended Data Figure 10 | Urgency and instability in the integration process.

a–d, Choice predictive neural activity (top) and psychometric curves (bottom) predicted by several variants of the standard diffusion-to-bound model (see Supplementary Information, section 7.7). **a**, Standard diffusion-to-bound model. Noisy momentary evidence is integrated over time until one of two bounds (+1 or −1; choice 1 or choice 2) is reached. The momentary evidence at each time point is drawn from a Gaussian distribution whose mean corresponds to the coherence of the input, and whose fixed variance is adjusted in each model to achieve the same overall performance (that is, similar psychometric curves, bottom panels). Coherences are 6%, 18% and 50% (the average colour coherences in monkey A, Fig. 1b). Average integrated evidence (neural firing rates, arbitrary units) is shown on choice 1 and choice 2 trials (thick versus thin) for evidence pointing towards choice 1 or choice 2 (solid versus dashed), on correct trials for all coherences (light grey to black, low to high coherence), and incorrect trials for the lowest coherence (red). The integrated evidence is analogous to the projection of the population response onto the choice axis (for example, Extended Data Fig. 5b, top left and bottom right). **b**, Urgency model. Here the choice is determined by a race between two diffusion processes (typically corresponding to two hemispheres), one with bound at +1, the other with bound at −1. The diffusion in each process is subject to a constant drift towards the corresponding bound, in addition to the drift provided by the momentary evidence. The input-independent drift implements an ‘urgency’ signal, which guarantees that one of the bounds is reached within a short time. Only the integrated evidence from one of the diffusion processes is shown. The three ‘choice 1’ curves are compressed (in contrast to **a**) because the urgency signal causes the bound to be reached, and integration towards choice 1 to cease, more quickly than in **a**. In contrast, the ‘choice 2’ curves are not compressed as the diffusion process that accumulates evidence towards choice 1 never approaches a bound on these trials. **c**, Same as **a**, but here the diffusion process is subject to a drift away from the starting point (0) towards the closest bound (+1 or −1). The strength of the drift is proportional to the distance from the starting point, and creates an ‘instability’ at the starting point. **d**, Same as **b**, with an instability in the integration as in **c** for both diffusion processes. The asymmetry between choice 1 and choice 2 curves in **b** and **d** resembles the asymmetry in the corresponding PFC curves (Extended Data Figs 5b, f, upper left). **e–j**, Neural network model with urgency. This model is based on a similar architecture as the model in Fig. 4. Unlike the neural network in Fig. 4, which was trained solely based on the model output on the last time bin of the trial, here the network is trained based on the output it produces throughout the entire input presentation. The network was trained to reproduce the integrated evidence (that is, the decision variable) for one of the two diffusion processes (that is, one of the two ‘hemispheres’) in a diffusion-to-bound model with urgency (**b**, see Supplementary Information, section 7.7). Similar conventions as in Fig. 5. The urgency signal is controlled by an additional binary input into the network.

Here, the urgency and sensory inputs are turned off as soon as a bound is reached. The network generates only a single, stable fixed point in each context, corresponding to the decision boundary (large red cross). The model also implements a series of points of relatively slow dynamics (small red crosses) approximately lying on a single curve. The axes of slow dynamics at these slow points (red lines) are locally aligned. Notably, responses at these slow points have a strong tendency to drift towards the single, stable fixed point (the decision boundary), and thus the curve of slow points does not correspond to an approximate line attractor. This drift implements the urgency signal and causes an asymmetry in the trajectories, which converge on a single point for choice 1, but have endpoints that are parametrically ordered by coherence along the choice axis for choice 2. As discussed below (panel **r**), this model relies on the same mechanism of selection as the original model (Fig. 5, see main text). **k–p**, Neural network model with instability. Trajectories show simulated population responses for a model (same architecture as in Fig. 4) that was trained to solve the context-dependent task (Fig. 1) only on high-coherence stimuli and in the absence of internal noise (see Supplementary Information, section 7.7). Same conventions as in Fig. 5. In the absence of noise, prolonged integration of evidence is not necessary for accurate performance on the task. As a consequence, the model implements a saddle point (blue cross) instead of an approximate line attractor. Points of slow dynamics (small red crosses, obscured by the red lines) occur only close to the saddle point. The right zero-eigenvectors of the linearized dynamics around these slow points (red lines) correspond to the directions of slowest dynamics, and determine the direction of the axis of choice. When displaced from the saddle point, the responses quickly drift towards one of the two stable attractors (large red crosses) corresponding to the choices. For a given choice, trajectories for all coherences therefore end in the same location along the choice axis, in contrast to the responses in the original model (Fig. 5). Despite these differences, the original model (Fig. 5) and the network model with instability (**k–p**) rely on a common mechanism of context-dependent selection (see panel **s**). **q–s**, Dynamical features (key, bottom) underlying input selection and choice in three related neural network models. All models are based on a common architecture (Fig. 4) but are the result of different training procedures. **q**, Dynamical features of the model described in the main paper (Figs 5 and 6), re-plotted from Fig. 6c. **r**, The urgency model (**e–j**). **s**, The instability model (**k–p**). In all models, the developing choice is implemented as more or less gradual movement along an axis of slow dynamics (specified by the locally computed right eigenvectors associated with the near-zero eigenvalue of the linearized dynamics, red lines). The inputs are selected, that is, result in movement along the axis of slow dynamics, depending on their projection onto the selection vector (the locally computed left eigenvectors associated with the near-zero eigenvalue). In this sense, the three models implement the same mechanisms of context-dependent selection and choice.

X-ray structure of dopamine transporter elucidates antidepressant mechanism

Aravind Penmatsa^{1*}, Kevin H. Wang^{1*} & Eric Gouaux^{1,2}

Antidepressants targeting Na^+/Cl^- -coupled neurotransmitter uptake define a key therapeutic strategy to treat clinical depression and neuropathic pain. However, identifying the molecular interactions that underlie the pharmacological activity of these transport inhibitors, and thus the mechanism by which the inhibitors lead to increased synaptic neurotransmitter levels, has proven elusive. Here we present the crystal structure of the *Drosophila melanogaster* dopamine transporter at 3.0 Å resolution bound to the tricyclic antidepressant nortriptyline. The transporter is locked in an outward-open conformation with nortriptyline wedged between transmembrane helices 1, 3, 6 and 8, blocking the transporter from binding substrate and from isomerizing to an inward-facing conformation. Although the overall structure of the dopamine transporter is similar to that of its prokaryotic relative LeuT, there are multiple distinctions, including a kink in transmembrane helix 12 halfway across the membrane bilayer, a latch-like carboxy-terminal helix that caps the cytoplasmic gate, and a cholesterol molecule wedged within a groove formed by transmembrane helices 1a, 5 and 7. Taken together, the dopamine transporter structure reveals the molecular basis for antidepressant action on sodium-coupled neurotransmitter symporters and elucidates critical elements of eukaryotic transporter structure and modulation by lipids, thus expanding our understanding of the mechanism and regulation of neurotransmitter uptake at chemical synapses.

Chemical neurotransmission is initiated by Ca^{2+} -induced release of neurotransmitters into the synaptic cleft¹. Upon release into the synaptic cleft, neurotransmitters such as glutamate, dopamine, noradrenaline, serotonin, glycine and GABA (γ -aminobutyric acid) activate G-protein-coupled receptors and ligand-gated ion channels, resulting in excitatory or inhibitory postsynaptic signalling cascades and currents^{1–3}. The widespread and critical roles of neurotransmitters in both central and peripheral nervous systems necessitate a requirement for strict spatiotemporal control of their levels at neural synapses. The primary mode of neurotransmitter clearance from the synaptic cleft is through secondary active transporters localized in presynaptic cells and glial cells that harness ionic gradients, across the cell membrane, to drive the uphill transport of neurotransmitters⁴. This symport process requires both Na^+ and Cl^- ions⁵, which has led to the solute carrier 6 (SLC6) family of secondary transporters³ being referred to as neurotransmitter sodium symporters (NSSs)².

Dysregulation of NSS function is associated with several debilitating disorders that include depression², attention deficit hyperactivity disorder⁶, orthostatic intolerance⁷, epilepsy⁸, Parkinson's disease² and infantile parkinsonism dystonia⁹. NSSs are also the primary targets of antidepressants, drugs to treat neuropathic pain, attention deficit hyperactivity disorder, anxiety and of habit-forming substances of abuse such as cocaine and amphetamines³. Development of antidepressants had a serendipitous beginning in the 1950s¹⁰, followed by the discovery that the tricyclic antidepressant (TCA) imipramine inhibits noradrenaline reuptake in tissues¹¹. Numerous variants of imipramine, and the subsequent discovery of selective serotonin reuptake inhibitors, have revolutionized antidepressant treatment^{12,13}. To date, inhibition of neurotransmitter uptake remains the most widely used strategy for antidepressant therapy¹², despite numerous side effects¹⁴.

Gains in our understanding of the molecular mechanisms underlying sodium-coupled transport have benefited from the structures of

multiple conformations of LeuT^{15–17}, a bacterial sodium-coupled amino acid transporter with ~20% sequence identity to the eukaryotic NSSs. Models of eukaryotic NSSs based on LeuT have provided valuable insights into substrate and ion specificities, pharmacology and transport mechanisms in NSS members^{18,19}. However, bacterial NSS models fall short of answering questions concerning the elements of NSS structure and function, including the local structure of NSSs in regions that are unrelated to LeuT in amino acid sequence, the determinants of substrate selectivity and the atomic-level details of transport inhibition by antidepressants and addictive compounds. Moreover, there is no understanding, at the level of three-dimensional structure, of the role of lipids and post-translational modifications in NSS structure and mechanism.

Here we present a 3.0 Å X-ray crystal structure of the *Drosophila melanogaster* dopamine transporter (DAT)²⁰ in complex with the TCA nortriptyline. The *Drosophila* DAT has greater than 50% sequence identity with its mammalian counterparts and harbours a pharmacological profile that is a hybrid of the mammalian DATs, noradrenaline transporters (NETs) and serotonin transporters (SERTs), making it a powerful vehicle to study NSS pharmacology and substrate specificity²⁰. The DAT structure reveals atomic details of TCA recognition, novel structural elements of NSS protein architecture and suggests a role for cholesterol in the allosteric control of transport in eukaryotic NSS members.

Thermostabilization and crystallization

Wild-type *Drosophila* DAT is labile, loses ligand-binding activity upon detergent extraction from the cellular membranes and is refractory to crystallization. To stabilize DAT for functional characterization, antibody generation and crystallization, we screened single point mutants for ligand-binding activity at increased temperatures²¹, ultimately combining five mutations into the construct used for crystallization and structure determination (DAT_{cryst}; Supplementary Fig. 1). Purified DAT_{cryst} binds to the high-affinity inhibitor nisoxetine with a dissociation constant

¹Vollum Institute, Oregon Health & Science University, 3181 South West Sam Jackson Park Road, Portland, Oregon 97239, USA. ²Howard Hughes Medical Institute, Oregon Health & Science University, 3181 South West Sam Jackson Park Road, Portland, Oregon 97239, USA.

*These authors contributed equally to this work.

(K_d) of 29 nM (Supplementary Fig. 2a), and the TCA nortriptyline exhibits an inhibition constant (K_i) of 156 nM (Supplementary Fig. 2b). Unfortunately we were unable to measure the binding of nortriptyline to wild-type DAT because of its instability. Nortriptyline has a K_i of 18 nM at human SERT and 4.4 nM at human NET²², values that are ~9-fold and ~35-fold lower than that for *Drosophila* DAT_{cryst}. In dopamine-uptake measurements with the wild-type DAT and amitriptyline, a precursor of nortriptyline, transport is inhibited with a K_i of 30 nM²⁰, whereas the DAT_{cryst} construct is inactive in transport (Supplementary Fig. 2c, d). Crystallization was further enhanced by the use of a complex with a Fab, resulting in crystals of a DAT_{cryst}-Fab complex that diffract X-rays to 3.0 Å resolution.

Architecture of DAT

The structure of *Drosophila* DAT_{cryst} bound to nortriptyline exhibits an outward-open conformation whereby the antidepressant is bound in a cavity halfway across the membrane bilayer and accessible to solvent from only the extracellular side of the membrane (Fig. 1). The transporter displays an overall LeuT-like fold with 12 transmembrane helices (TMs) in which helices 1–5 and 6–10 are related by inherent pseudosymmetry, akin to LeuT¹⁵ (Supplementary Fig. 3). Residues in TM1 and TM6 make numerous interactions with the ligand and ions via non helical, hinge-like regions at the approximate mid-points of these TMs, connecting the bonding networks of all three ions with the inhibitor. Residues at the bend in TM3 contribute to the hydrophobic pocket that cradles the tricyclic moiety of the ligand, which lays approximately perpendicular to the TMs, mimicking a wedge separating the jaws of a vice. One cholesterol molecule is located in a groove between TM5 and TM7 and poised to modulate the movement of TM1a that occurs during the transport cycle (Fig. 1a)¹⁷.

The primary binding site accommodates nortriptyline but cannot adopt the subsequent helical movements of TMs 1b and 6a required to form the occluded state. Using LeuT for comparison, the occluded state of LeuT is formed in the presence of sodium and leucine substrate, but not in the presence of tryptophan, which binds to the primary site, comparable to the TCA in the context of DAT_{cryst}. We propose that both tryptophan and TCA stabilize the outward-open conformations of LeuT and DAT_{cryst}, respectively, by targeting the primary binding site and sterically blocking the extracellular domains of the transporter, preventing the extracellular gate from closing and thus acting by way of a foot-in-the-door mechanism (Supplementary Fig. 4a, b and Supplementary Table 2).

Whereas the core of DAT_{cryst} closely resembles that of LeuT, the periphery of DAT_{cryst} exhibits several features distinct from LeuT and important for neurotransmitter transport and cellular localization. In TM12, a kink in the centre at Pro 572 causes the second half of the helix to turn away from the transporter, indicating that the dimerization interface of LeuT is not the same as potential oligomerization interfaces of eukaryotic NSSs (Fig. 1a, b and Supplementary Fig. 5). Although previous studies indicate that NSSs oligomerize^{23,24}, DAT_{cryst} is monomeric in detergent micelles and in the crystal lattice (Supplementary Fig. 6), thus suggesting that a membrane bilayer or additional molecules may be required for NSS assembly. The variable extracellular loop 2 (EL2) region has numerous predicted *N*-linked glycosylation sites²⁵ and one disulphide bond²⁶, modifications that have critical roles in proper trafficking of NSSs to the plasma membrane³. The strictly conserved disulphide linkage²⁶ was observed in the structure between two conserved cysteines, Cys 148 and Cys 157 (Supplementary Fig. 7). In the crystal, EL2 has a central role in lattice contacts, packing against a neighbouring Fab with an 870 Å² interface (Supplementary Fig. 6). Because 43 residues were deleted from EL2 in the DAT_{cryst} construct, further studies are required to determine the role of the full-length EL2 in transporter structure and function (Supplementary Fig. 8a). Together with EL2, EL4 harbours a Zn²⁺-binding site in mammalian DATs that modulates transport²⁷. The equivalent residues in *Drosophila* DAT_{cryst} are within a Cα–Cα distance of 10 Å, but because their identities are Glu 161, Leu 374 and Ala 395, they do not form a high-affinity Zn²⁺-binding site in DAT_{cryst}.

TCA-binding site

Unambiguous density for nortriptyline in DAT_{cryst} was observed in the primary site, approximately halfway across the membrane bilayer (Fig. 2a). In accordance with previous chimaeric studies, swapping TM regions between NET and DAT²⁸, the drug-binding site is surrounded primarily by helices 1, 3, 6 and 8 in a region equivalent to the substrate-binding pocket of LeuT¹⁵, and in close proximity to the densities for sodium and chloride ions (Fig. 2a). The dibenzocycloheptene ring of nortriptyline is oriented as a saddle, curving around the central region of TM3 and engaging in hydrophobic interactions with Val 120, Tyr 124 and Ala 117 (Fig. 2b). Val 120 is extensively conserved and faces the cycloheptene ring (Supplementary Fig. 4a), and replacement of the corresponding Ile 172 in human SERT with larger substitutions such as methionine markedly reduce affinity towards most NSS inhibitors¹⁹. This location was previously found in human SERT

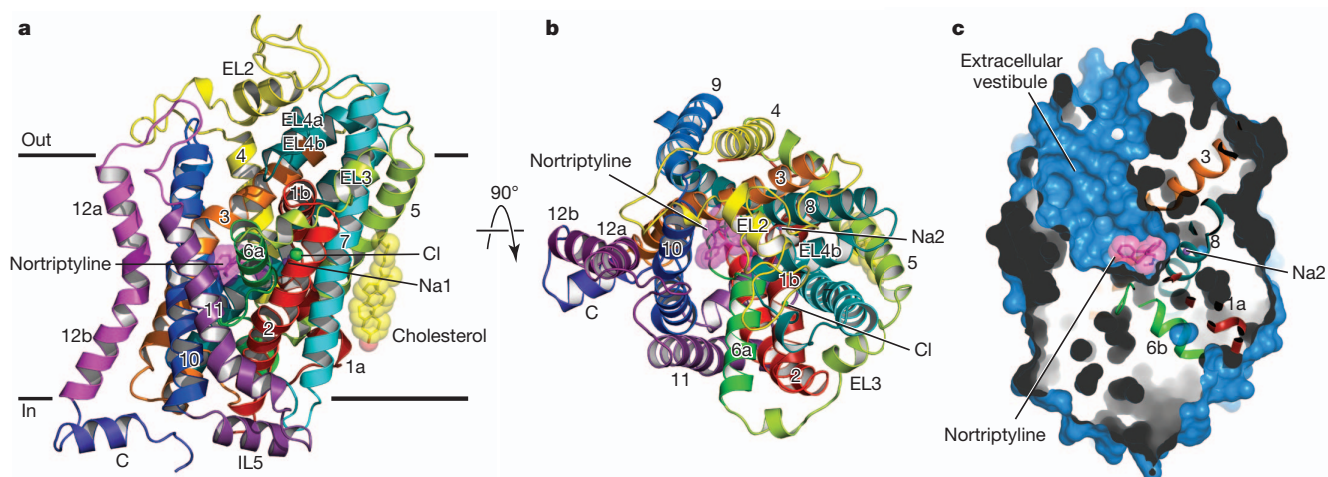


Figure 1 | Architecture of *Drosophila* DAT_{cryst}. **a**, Structure of DAT_{cryst} viewed parallel to membrane. Nortriptyline, sodium ions, a chloride ion and a cholesterol molecule are shown in sphere representation in magenta, purple, green and yellow, respectively. **b**, View of DAT_{cryst} from the extracellular face.

c, Surface representation showing that ligand and ion binding sites are accessible from the extracellular vestibule. Nortriptyline and TMs 1, 3, 6 and 8 are coloured as in **a**.

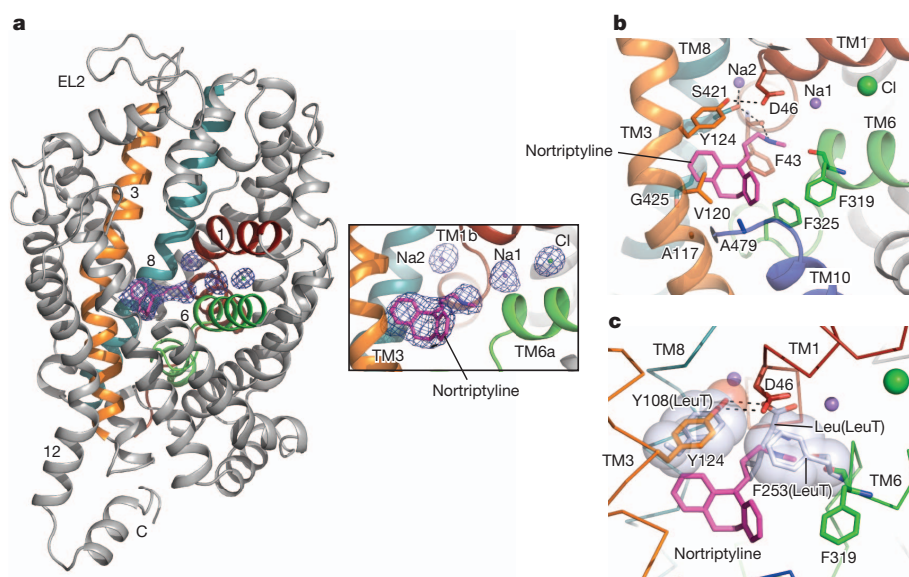


Figure 2 | Antidepressant-binding site.

a, Overall view of the nortriptyline-bound DAT_{cryst}. $F_o - F_c$ densities (blue mesh) for drug and ions are contoured at σ levels of 2.5 and 3.0, respectively. **b**, Close-up view of the drug binding pocket. Na⁺ and Cl⁻ ions are shown as spheres. Nortriptyline is represented as sticks (magenta). The amino group of nortriptyline is 2.7 Å from the carbonyl oxygen of Phe 43 (TM1a) and the N-methyl group of nortriptyline is 3.1 Å from the carbonyl oxygen of Phe 319. Residues lining the drug-binding pocket with interfacial areas greater than 10 Å² are represented as sticks. **c**, Comparison of the drug or substrate binding pocket of DAT_{cryst} with that of LeuT (PDB code 2A65). The distance between the carboxylate group of leucine and Tyr 108 (spheres) is 2.7 Å in the occluded state (2A65) and 5.1 Å in the inhibitor-bound state (3F3A) of LeuT, whereas the equivalent interaction in DAT_{cryst} between Asp 46 and Tyr 124 is 3.1 Å.

to be protected from crosslinking agents in the presence of inhibitor or substrate²⁹. Phe 325 in TM6b forms an edge-to-face aromatic interaction with one of the benzyl groups of nortriptyline. Residues Gly 425 (TM8) and Ala 479 (TM10) also interact with the tricyclic group of the drug. The N-methylpropylamine group of the drug extends across the width of the drug-binding site and prevents TMs 1b and 6a from closing the extracellular gate 'above' the drug. The amine group forms a hydrogen bond with the main-chain carbonyl of Phe 43 and a cation- π interaction with the side chain of Phe 43 (Fig. 2b). Interestingly, residues equivalent to Val 120 and Phe 43 (Ile 172 and Tyr 95) in SERT are necessary for interactions with antidepressants³⁰.

The biogenic amine transporters harbour a crucial aspartate residue in TM1 and in the DAT_{cryst} structure we see how Asp 46 substitutes for the absence of the carboxylate group in biogenic amines as compared to amino acid substrates transported by LeuT and the GABA and glycine transporters (Supplementary Fig. 8b)¹⁵. The side chain of Asp 46 forms a hydrogen bond with the hydroxyl of Tyr 124, which is equivalent to the Tyr 108 residue in LeuT that has a role in substrate recognition (Fig. 2c)³¹. Mutations at this aspartate result in substantial losses in transport activity and reduced binding affinities for cocaine³². Ser 421 (TM8), which coordinates a sodium ion at site 2 (Na2), is within 3.5 Å of the propylamine group of the TCA and also forms a hydrogen bond with the carbonyl of Phe 43. Ser 421 therefore participates in a network of hydrogen bonds that interconnects nortriptyline with the Na2 site and was also found to be crucial for high-affinity recognition of antidepressants by human SERT³³.

The N-methyl group of nortriptyline is 3.1 Å away from the main-chain carbonyl of Phe 319 and sterically prevents Phe 319 and TM6a from closing the extracellular gate above the drug, thereby stabilizing

the outward-open state of the transporter. Phe 319 is the equivalent of Phe 253 in LeuT, which gates the substrate-binding pocket (Fig. 2c)^{15–17}. The relative position of Phe 319 is markedly different from Phe 253 in the substrate-bound, occluded structure of LeuT, and instead resembles the positions of Phe 253 in the substrate-free and inhibitor-bound structures. To address the question of whether nortriptyline could bind to DAT_{cryst} in a LeuT-like, occluded conformation, we superimposed DAT_{cryst} onto the occluded state of LeuT and found that Phe 319 and Phe 325 would clash with the dibenzocycloheptene ring of the TCA (Fig. 2c and Supplementary Fig. 4c). Identification of nortriptyline bound in the substrate-binding pocket of DAT_{cryst} provides the first structural evidence that TCA antidepressants inhibit neurotransmitter transporters by preventing substrate binding and stabilizing the outward-open conformation^{18,19,34}. The DAT_{cryst}-nortriptyline complex, together with the LeuBAT-antidepressant complexes (Wang, H. *et al.*, unpublished observations), demonstrate conclusively that antidepressants inhibit NSSs by acting at the primary or S1 site, in stark contrast to how TCAs inhibit LeuT via a non-competitive mechanism³⁵ by binding within the extracellular vestibule^{35–37}.

Ion-binding sites

Locations of ions essential for transport could be identified in DAT_{cryst} with electron densities ($>4.0\sigma$) at three locations near the non-helical hinge-like regions of TMs 1 and 6, and close to the TCA. Densities at the two sites coincided exactly with Na1 and Na2 sites identified in LeuT (Fig. 3a, b)¹⁵. A chloride ion was positioned at the third position of high omit density nestled in between TMs 2, 6 and 7 and close to Na1 (Fig. 3a). Placing ions in the omit densities during model building led to a concomitant loss of $F_o - F_c$ density during refinement. The atomic

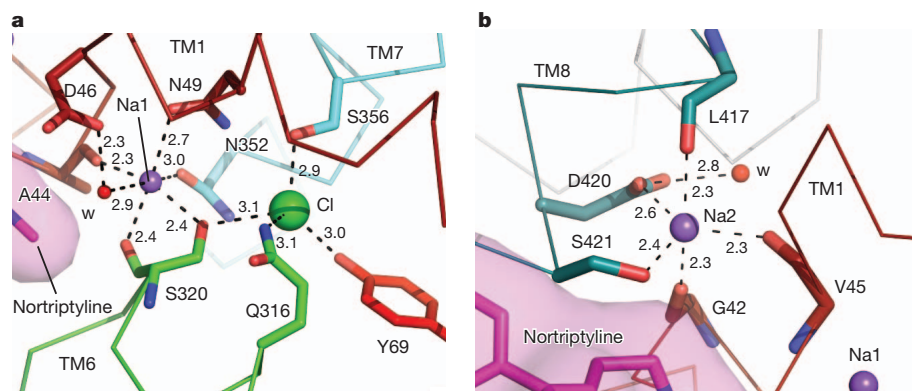


Figure 3 | Ion-binding sites. **a**, Na1 and chloride ion binding sites. Na⁺ is purple and Cl⁻ is green and both are modelled as spheres. **b**, Coordination at the Na2 site is trigonal bipyramidal with the water molecule (w, red sphere) 3.3 Å from the sodium ion. Distances are in Ångströms for residues that are in the coordination sphere and interactions are shown by dashed lines. Residues are coloured according to their respective TMs.

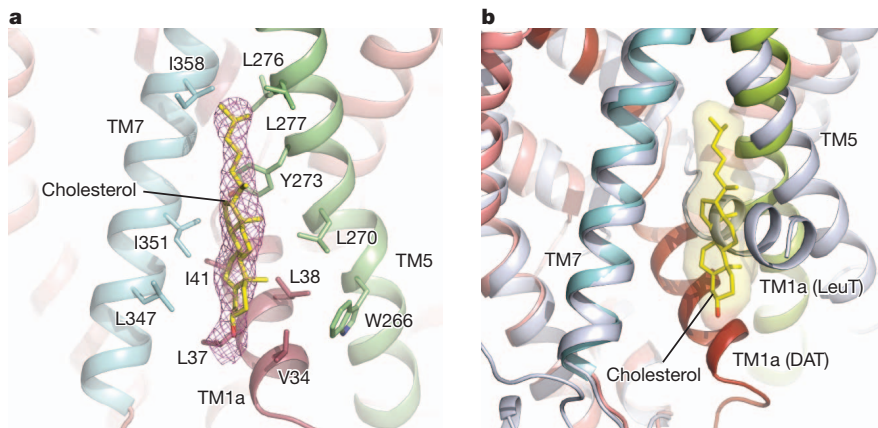


Figure 4 | Cholesterol site. **a**, Cholesterol (yellow sticks) shown with $F_o - F_c$ density (light magenta) contoured at 2.0σ . Residues that interface with the cholesterol group are represented as sticks. **b**, Potential role of cholesterol in maintaining an outward-open state of transporter. Cholesterol (sticks with transparent surface) sterically clashes with the position of TM1a in the inward-open conformation of LeuT (PDB code 3TT3)¹⁷.

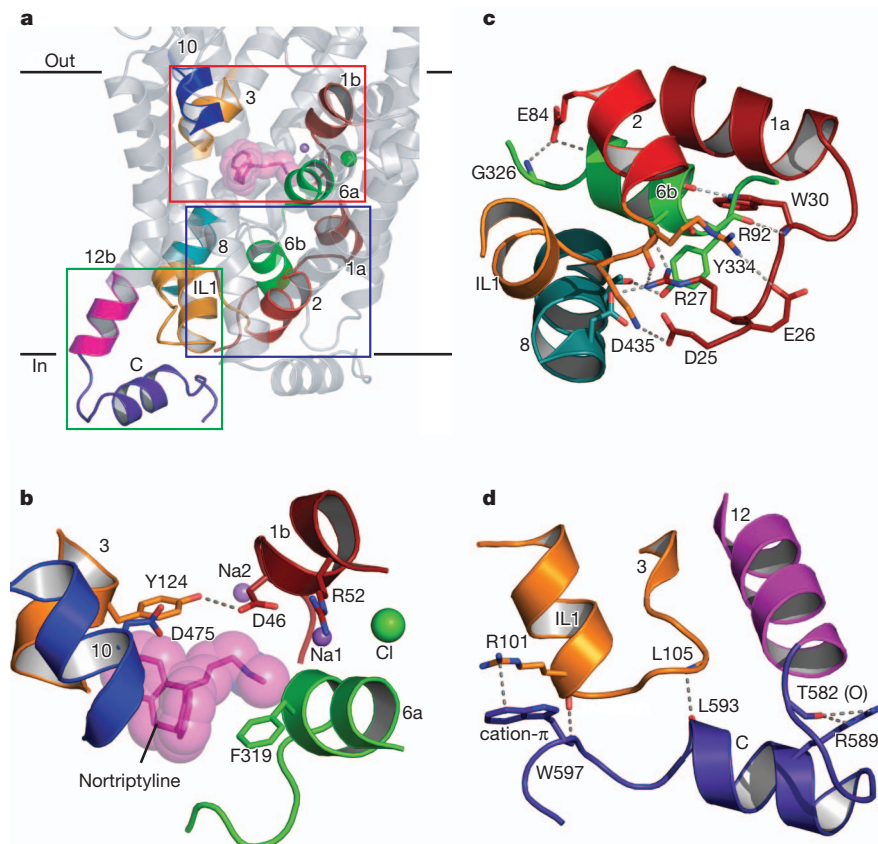
displacement factors of the ions matched the B -values of surrounding atoms. The sodium at site 1 is located ~ 5.2 Å away from the amino group of nortriptyline and is coordinated with an octahedral geometry by side-chain oxygens of Asn 49, Ser 320 and Asn 352, and main-chain carbonyls of Ala 44 and Ser 320 (Fig. 3a and Supplementary Fig. 8b). Interestingly, the sodium at Na1 is also coordinated by one water molecule which in turn is within hydrogen-bonding distance to Asp 46, thus showing that the Asp in TM1 indirectly participates in the sodium ion coordination. The mean ion coordinating distances (2.6 Å) at this site are longer than the distances (2.42 Å) reported for Na^+ ions in solution but shorter than the distances reported for K^+ ions (2.84 Å; Supplementary Table 3)³⁸.

The chloride ion is located 5.0 Å away from the Na1 site at a position previously identified by computational and mutational studies based on LeuT³⁹ and the GABA transporters⁴⁰. A recent structural study of a chloride-dependent E290S mutant of LeuT also identified a chloride ion at this location⁴¹. Chloride is coordinated in a tetrahedral

fashion through residues in TM6 (Ser 320, Gln 316), TM7 (Ser 356) and TM2 (Tyr 69) (Fig. 3a). Interestingly, the hydroxyl group of Ser 320 bridges the Na1 and Cl^- sites and is positioned to interact with both ions. The mean ion–ligand distances at the Cl^- site are 3.0 Å (Supplementary Table 3) and the B -factors of surrounding atoms are similar to that of chloride, supporting the placement of chloride at this site.

The sodium at the Na2 site is located ‘below’ the plane of the drug towards the cytoplasmic face, in between TMs 1 and 8, and is coordinated in a trigonal bipyramidal fashion by main-chain carbonyls from Gly 42 (TM1a), Val 45 (TM1-hinge) and Leu 417 (TM8), and the side-chain oxygens from Ser 421 and Asp 420 (TM8) (Fig. 3b). The mean ion–oxygen distances are 2.4 Å, in line with reported values for sodium coordination in solution (Supplementary Table 3). Although the interconnected network of interactions between TMs 1, 6, nortriptyline, sodium and chloride provides a structure-based mechanism for the coupling of ion and inhibitor binding⁴², we do not have a comprehensive understanding of the ion dependence of inhibitor binding in NSSs.

Figure 5 | Extracellular and cytoplasmic gates and the C-terminal latch. **a**, Relative locations of the open extracellular gate (red box), closed cytoplasmic gate (blue box) and C-terminal latch (green box) in DAT_{cryst}. **b**, The width of the extracellular gate is depicted by the distances between Tyr 124 and Phe 319 (10 Å), and Arg 52 and Asp 475 (10 Å). Nortriptyline, ions and helices are coloured as in Fig. 1. **c**, The cytoplasmic gate is closed by polar and electrostatic interactions between TM1a, TM2, IL1, TM6b and TM8. **d**, The C-terminal helix following TM12 is bound to the cytoplasmic face of the transporter via polar interactions with IL1. Polar and electrostatic bonds are represented as grey dashed lines.



Cholesterol-binding site

A cholesterol molecule is lodged in a trough-shaped cavity bordered by TM5, TM7 and TM1a at a depth equivalent to the inner leaflet of the membrane (Fig. 4a). Branched aliphatic residues are primarily involved in forming the protein–cholesterol interface (359 \AA^2), thus allowing cholesterol to bury $\sim 57\%$ of its solvent-accessible surface area. $F_o - F_c$ density for this site clearly demarcated the orientation of the isooctyl group of cholesterol anchored at the junction of TMs 5 and 7 by residues Leu 276, Leu 277 and Ile 358. The β -face of the sterol ring primarily faces residues Tyr 273, Leu 270 and Trp 266 in TM5 and also interacts with residues Val 34, Leu 37, Leu 38 and Ile 41 on TM1a. The α -face of cholesterol interfaces with residues Leu 347 and Ile 351 in TM7 (Fig. 4a).

Cholesterol has an important role in modulating the function of NSS members^{43,44}, stabilizing an outward-open state of DAT with a concomitant increase in maximum binding or B_{max} for cocaine⁴⁵. In LeuT, TM1a undergoes a large conformational change upon transition from the outward-facing open and occluded states to the inward-open state¹⁷. If a similar conformational change were to occur in DAT, it would entirely disrupt the cholesterol site (Fig. 4b). We propose that one mechanism for the action of cholesterol on DAT is that by occupying its binding site in the outward-open, inhibitor-bound state, cholesterol stabilizes the outward-open conformation of the transporter⁴⁵.

Extracellular and cytoplasmic gates

The ion and ligand binding sites in DAT_{cryst} are accessible to solvent from the extracellular face owing to the open gate above the primary binding pocket. The distance between Tyr 124 of TM3 and Phe 319 in TM6a is 10 \AA , whereas in the substrate-bound, occluded state of LeuT the corresponding distance is half as long (Fig. 5a, b). Similarly, the 10 \AA separation between Arg 52 on TM1b and Asp 475 on TM10 renders the primary binding site accessible to extracellular solution. The steric bulk of the tricyclic moiety combined with the extended *N*-methylpropylamine chain of nortriptyline prevents both TM1b and TM6a from approaching TM3 and TM8 to cap the putative substrate pocket and close the gate.

In contrast to the extracellular gate, extensive polar interactions at the intracellular face of the transporter form a thick barrier of $\sim 24 \text{ \AA}$ between the ligand and ion pockets and solvent to keep the cytoplasmic

gate shut. At the cytoplasmic face of the transporter, the indole nitrogen of Trp 30 caps the carbonyl oxygen of Tyr 331 in TM6b, and Arg 27 forms a salt bridge to Asp 435 of TM8 (Fig. 5c). Arg 27, Trp 30 and Asp 435 are strictly conserved in NSS orthologues and LeuT, suggesting that these intracellular gate interactions are general and important facets of the transport mechanism for this family of sodium symporters^{46,47}. Tyr 334, the residue corresponding to Tyr 335 in human DAT, was previously shown to be responsible for shifting the conformational equilibrium of the DAT towards an inward-open state⁴⁸.

C-terminal latch

Two novel attributes at the C terminus of DAT_{cryst} were immediately evident from the structure. Helix 12 is shifted by 22° in comparison to its position in LeuT, resulting in the exposure of TM3 to solvent and lipid (Supplementary Fig. 5). Pro 572, conserved in most eukaryotic NSS members, is probably at the root of the kink between TMs 12a and 12b, and thus has an important role orienting the second half of the helix away from the rest of the transporter. The hairpin between TM12b and the intracellular C terminus of DAT_{cryst} is stabilized by hydrogen bonding between the ϵ -nitrogen of Arg 589 and carbonyl oxygen of Thr 582 (Fig. 5d). The second feature is the C-terminal helix, which contains 2.5 turns from residues 586 to 595, where several hydrogen bonds and a cation- π interaction between Trp 597 and Arg 101 restrain this C-terminal helix near intracellular loop 1 (IL1) at the cytoplasmic face of DAT_{cryst}. Although sequence conservation within TM12 and the C terminus is rather low across NSS orthologues, Gly 584 is located at the hairpin hinge and strictly conserved, and only Lys or Arg is present at the position equivalent to Arg 589 of DAT_{cryst}, suggesting that the conformation of the C terminus in the structure is a conserved feature among NSS orthologues. Studies of human DAT have identified the region following TM12 to contain sites for protein kinase C-mediated endocytic trafficking^{3,49}, and it is plausible that phosphorylation may alter the conformation or accessibility of the C terminus, allowing it to interact with cellular machinery for internalization. We also note that the latch participates in interactions with IL1, which in turn interacts with TM1a, thus suggesting that the C-terminal latch may modulate transporter activity.

Conclusion

The structure of DAT_{cryst} captures the transporter in an inhibitor-bound, outward-open conformation. The TCA nortriptyline targets the primary substrate site and stabilizes the open conformation by sterically preventing closure of the extracellular gate (Fig. 6a). One chloride and two sodium ions are located adjacent to the ligand, suggesting that the binding of ions and inhibitor are directly coupled. A cholesterol molecule bound to a crevice flanking TM1a probably stabilizes the outward-open, inhibitor-bound conformation (Fig. 6b). The structure reveals a C-terminal latch that makes extensive interactions with the cytoplasmic face of the transporter, proximal to the cytoplasmic gate, and thus in a position to modulate transport activity. Taken together, the structure of a eukaryotic DAT reveals novel insights into antidepressant recognition and structural elements implicated in the regulation of neurotransmitter transport, providing a foundation for drug design strategies.

METHODS SUMMARY

The *Drosophila* DAT_{cryst} construct (Supplementary Fig. 1) was expressed in virus-infected mammalian cells and purified by affinity and size-exclusion chromatography. Fab 9D5 was added before crystallization along with nortriptyline (1 mM) at a DAT:Fab molar ratio of 1:1.1 and concentrated down to 3 mg ml^{-1} . Crystals of the complex were obtained in the presence of 100 mM glycine, pH 9, and 38% polyethylene glycol (PEG) 350 monomethyl ether (MME). The structure was solved by molecular replacement using a polyalanine model of LeuT (PDB code 3F3A) and an ensemble of Fab variable and constant domains. Data

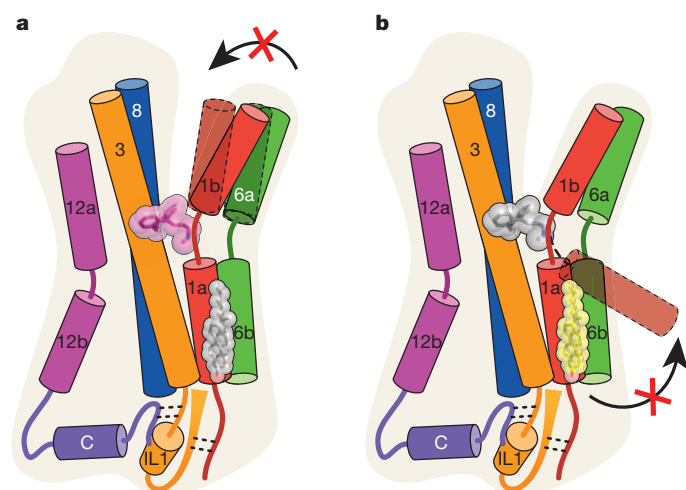


Figure 6 | Mechanisms of antidepressants and cholesterol. **a**, The TCA nortriptyline (magenta) wedges between scaffold helices 3 and 8 and the core helices 1 and 6, preventing the movement of TMs 1b and 6a from closing the extracellular vestibule. **b**, Cholesterol (yellow) is bound in an intracellular pocket and hinders the movement of TM1a, thereby stabilizing the outward-open conformation of DAT. The C-terminal latch interacts with IL1 as part of the cytoplasmic gate.

processing, model building and refinement were performed using standard crystallographic software (Supplementary Table 1).

Full Methods and any associated references are available in the online version of the paper.

Received 2 June; accepted 7 August 2013.

Published online 15 September 2013.

- Jessell, T. M. & Kandel, E. R. Synaptic transmission: a bidirectional and self-modifiable form of cell-cell communication. *Cell* **72**, (Suppl), 1–30 (1993).
- Masson, J., Sagne, C., Hamon, M. & El Mestikawy, S. Neurotransmitter transporters in the central nervous system. *Pharmacol. Rev.* **51**, 439–464 (1999).
- Kristensen, A. S. *et al.* SLC6 neurotransmitter transporters: structure, function, and regulation. *Pharmacol. Rev.* **63**, 585–640 (2011).
- Rudnick, G. Ion-coupled neurotransmitter transport: thermodynamic vs. kinetic determinations of stoichiometry. *Methods Enzymol.* **296**, 233–247 (1998).
- Radian, R., Bendahan, A. & Kanner, B. I. Purification and identification of the functional sodium- and chloride-coupled γ -aminobutyric acid transport glycoprotein from rat brain. *J. Biol. Chem.* **261**, 15437–15441 (1986).
- Waldman, I. D. *et al.* Association and linkage of the dopamine transporter gene and attention-deficit hyperactivity disorder in children: heterogeneity owing to diagnostic subtype and severity. *Am. J. Hum. Genet.* **63**, 1767–1776 (1998).
- Shannon, J. R. *et al.* Orthostatic intolerance and tachycardia associated with norepinephrine-transporter deficiency. *N. Engl. J. Med.* **342**, 541–549 (2000).
- Meldrum, B. S. Neurotransmission in epilepsy. *Epilepsia* **36** (suppl. 1), 30–35 (1995).
- Kurian, M. A. *et al.* Homozygous loss-of-function mutations in the gene encoding the dopamine transporter are associated with infantile parkinsonism-dystonia. *J. Clin. Invest.* **119**, 1595–1603 (2009).
- Kuhn, R. The treatment of depressive states with G 22355 (imipramine hydrochloride). *Am. J. Psychiatry* **115**, 459–464 (1958).
- Axelrod, J., Whitby, L. G. & Hertting, G. Effect of psychotropic drugs on the uptake of H^+ -norepinephrine by tissues. *Science* **133**, 383–384 (1961).
- Berton, O. & Nestler, E. J. New approaches to antidepressant drug discovery: beyond monoamines. *Nature Rev. Neurosci.* **7**, 137–151 (2006).
- Pletscher, A. The discovery of antidepressants: a winding path. *Experientia* **47**, 4–8 (1991).
- Anderson, I. M. Selective serotonin reuptake inhibitors versus tricyclic antidepressants: a meta-analysis of efficacy and tolerability. *J. Affect. Disord.* **58**, 19–36 (2000).
- Yamashita, A., Singh, S. K., Kawate, T., Jin, Y. & Gouaux, E. Crystal structure of a bacterial homologue of Na^+/Cl^- -dependent neurotransmitter transporters. *Nature* **437**, 215–223 (2005).
- Singh, S. K., Piscitelli, C. L., Yamashita, A. & Gouaux, E. A competitive inhibitor traps LeuT in an open-to-out conformation. *Science* **322**, 1655–1661 (2008).
- Krishnamurthy, H. & Gouaux, E. X-ray structures of LeuT in substrate-free outward-open and apo inward-open states. *Nature* **481**, 469–474 (2012).
- Beuming, T. *et al.* The binding sites for cocaine and dopamine in the dopamine transporter overlap. *Nature Neurosci.* **11**, 780–789 (2008).
- Sørensen, L. *et al.* Interaction of antidepressants with the serotonin and norepinephrine transporters: mutational studies of the S1 substrate binding pocket. *J. Biol. Chem.* **287**, 43694–43707 (2012).
- Pözzgen, P., Park, S. K., Hirsh, J., Sonders, M. S. & Amara, S. G. The antidepressant-sensitive dopamine transporter in *Drosophila melanogaster*: a primordial carrier for catecholamines. *Mol. Pharmacol.* **59**, 83–95 (2001).
- Serrano-Vega, M. J., Magnani, F., Shibata, Y. & Tate, C. G. Conformational thermostabilization of the β_1 -adrenergic receptor in a detergent-resistant form. *Proc. Natl Acad. Sci. USA* **105**, 877–882 (2008).
- Tatsumi, M., Groshan, K., Blakely, R. D. & Richelson, E. Pharmacological profile of antidepressants and related compounds at human monoamine transporters. *Eur. J. Pharmacol.* **340**, 249–258 (1997).
- Torres, G. E. *et al.* Oligomerization and trafficking of the human dopamine transporter. Mutational analysis identifies critical domains important for the functional expression of the transporter. *J. Biol. Chem.* **278**, 2731–2739 (2003).
- Sitte, H. H., Farhan, H. & Javitch, J. A. Sodium-dependent neurotransmitter transporters: oligomerization as a determinant of transporter function and trafficking. *Mol. Interv.* **4**, 38–47 (2004).
- Li, L. B. *et al.* The role of N-glycosylation in function and surface trafficking of the human dopamine transporter. *J. Biol. Chem.* **279**, 21012–21020 (2004).
- Chen, R. *et al.* Direct evidence that two cysteines in the dopamine transporter form a disulfide bond. *Mol. Cell. Biochem.* **298**, 41–48 (2007).
- Norregaard, L., Frederiksen, D., Nielsen, E. O. & Gether, U. Delineation of an endogenous zinc-binding site in the human dopamine transporter. *EMBO J.* **17**, 4266–4273 (1998).
- Buck, K. J. & Amara, S. G. Structural domains of catecholamine transporter chimeras involved in selective inhibition by antidepressants and psychomotor stimulants. *Mol. Pharmacol.* **48**, 1030–1037 (1995).
- Chen, J. G., Sachpatzidis, A. & Rudnick, G. The third transmembrane domain of the serotonin transporter contains residues associated with substrate and cocaine binding. *J. Biol. Chem.* **272**, 28321–28327 (1997).
- Henry, L. K. *et al.* Tyr-95 and Ile-172 in transmembrane segments 1 and 3 of human serotonin transporters interact to establish high affinity recognition of antidepressants. *J. Biol. Chem.* **281**, 2012–2023 (2006).
- Bismuth, Y., Kavanaugh, M. P. & Kanner, B. I. Tyrosine 140 of the γ -aminobutyric acid transporter GAT-1 plays a critical role in neurotransmitter recognition. *J. Biol. Chem.* **272**, 16096–16102 (1997).
- Kitayama, S. *et al.* Dopamine transporter site-directed mutations differentially alter substrate transport and cocaine binding. *Proc. Natl Acad. Sci. USA* **89**, 7782–7785 (1992).
- Andersen, J. *et al.* Location of the antidepressant binding site in the serotonin transporter: importance of Ser-438 in recognition of citalopram and tricyclic antidepressants. *J. Biol. Chem.* **284**, 10276–10284 (2009).
- Talvenheimo, J., Fishkes, H., Nelson, P. J. & Rudnick, G. The serotonin transporter-imipramine “receptor”. *J. Biol. Chem.* **258**, 6115–6119 (1983).
- Singh, S. K., Yamashita, A. & Gouaux, E. Antidepressant binding site in a bacterial homologue of neurotransmitter transporters. *Nature* **448**, 952–956 (2007).
- Zhou, Z. *et al.* LeuT-desipramine structure reveals how antidepressants block neurotransmitter reuptake. *Science* **317**, 1390–1393 (2007).
- Zhou, Z. *et al.* Antidepressant specificity of serotonin transporter suggested by three LeuT-SSRI structures. *Nature Struct. Mol. Biol.* **16**, 652–657 (2009).
- Harding, M. M. Metal-ligand geometry relevant to proteins and in proteins: sodium and potassium. *Acta Crystallogr. D* **58**, 872–874 (2002).
- Forrest, L. R., Tavoulari, S., Zhang, Y. W., Rudnick, G. & Honig, B. Identification of a chloride ion binding site in Na^+/Cl^- -dependent transporters. *Proc. Natl Acad. Sci. USA* **104**, 12761–12766 (2007).
- Zomot, E. *et al.* Mechanism of chloride interaction with neurotransmitter:sodium symporters. *Nature* **449**, 726–730 (2007).
- Kantcheva, A. K. *et al.* Chloride binding site of neurotransmitter sodium symporters. *Proc. Natl Acad. Sci. USA* **110**, 8489–8494 (2013).
- Tavoulari, S., Forrest, L. R. & Rudnick, G. Fluoxetine (Prozac) binding to serotonin transporter is modulated by chloride and conformational changes. *J. Neurosci.* **29**, 9635–9643 (2009).
- Scanlon, S. M., Williams, D. C. & Schloss, P. Membrane cholesterol modulates serotonin transporter activity. *Biochemistry* **40**, 10507–10513 (2001).
- North, P. & Fleischer, S. Alteration of synaptic membrane cholesterol/phospholipid ratio using a lipid transfer protein. Effect on γ -aminobutyric acid uptake. *J. Biol. Chem.* **258**, 1242–1253 (1983).
- Hong, W. C. & Amara, S. G. Membrane cholesterol modulates the outward facing conformation of the dopamine transporter and alters cocaine binding. *J. Biol. Chem.* **285**, 32616–32626 (2010).
- Bennett, E. R., Su, H. & Kanner, B. I. Mutation of arginine 44 of GAT-1, a $Na^+ + Cl^-$ -coupled γ -aminobutyric acid transporter from rat brain, impairs net flux but not exchange. *J. Biol. Chem.* **275**, 34106–34113 (2000).
- Cao, Y., Li, M., Mager, S. & Lester, H. A. Amino acid residues that control pH modulation of transport-associated current in mammalian serotonin transporters. *J. Neurosci.* **18**, 7739–7749 (1998).
- Loland, C. J., Norregaard, L., Litman, T. & Gether, U. Generation of an activating Zn^{2+} switch in the dopamine transporter: mutation of an intracellular tyrosine constitutively alters the conformational equilibrium of the transport cycle. *Proc. Natl Acad. Sci. USA* **99**, 1683–1688 (2002).
- Holton, K. L., Loder, M. K. & Melikian, H. E. Nonclassical, distinct endocytic signals dictate constitutive and PKC-regulated neurotransmitter transporter internalization. *Nature Neurosci.* **8**, 881–888 (2005).

Supplementary Information is available in the online version of the paper.

Acknowledgements We thank D. Cawley for generating monoclonal antibodies and S. Amara for providing the wild-type *Drosophila* DAT construct. We would like to thank H. Wang and D. Claxton for comments and suggestions along with other Gouaux laboratory members for discussions during manuscript preparation. We thank L. Vaskalis for assistance with figures and H. Owen for help with manuscript preparation. We thank the staff of the Northeastern Collaborative Access Team (NECAT) at the Advanced Photon Source (APS) for assistance with data collection. This work was supported by a postdoctoral fellowship from the American Heart Association (A.P.), a National Institute of Mental Health research award (K.H.W.) and by the National Institutes of Health (E.G.). E.G. is an investigator with the Howard Hughes Medical Institute.

Author Contributions A.P., K.H.W. and E.G. designed the project. A.P. and K.H.W. performed protein purification, crystallography and biochemical assays. A.P., K.H.W. and E.G. wrote the manuscript.

Author Information The coordinates for the structure have been deposited in the Protein Data Bank under the accession code 4M48. Reprints and permissions information is available at www.nature.com/reprints. The authors declare no competing financial interests. Readers are welcome to comment on the online version of the paper. Correspondence and requests for materials should be addressed to E.G. (gouauxe@ohsu.edu).

METHODS

Screening, construct optimization and protein expression. The *Drosophila* DAT was selected as a promising candidate for structural studies after screening multiple orthologues of DATs and NETs by fluorescence-detection size-exclusion chromatography (FSEC)⁵⁰. In addition, FSEC was used to screen other parameters such as detergent efficacy, thermostability, lipid effects, tertiary epitope-specific monoclonal antibodies and sample homogeneity following purification. The DNA encoding the *D. melanogaster* DAT was provided by S. Amara and was modified by removal of the first 20 amino acids ($\Delta 1-20$), by a deletion in EL2 ($\Delta 164-206$) and by point mutations to enhance thermostability (V74A, V275A, V311A, L415A, G538L) by PCR-based methods. This modified DAT sequence, deemed DAT_{cryst}, was fused to a C-terminal GFP–His₈ tag with a thrombin cleavage site (LVPRGS) in place of residues 602–607. DAT_{cryst}–GFP–His₈ was produced by virus-mediated expression in mammalian cells^{51–53}.

Antibody production. Monoclonal antibodies against DAT_{cryst} were raised by D. Cawley using standard methods. Antibodies were screened by FSEC and western blot to select clones that recognized natively folded DAT_{cryst} protein. Sequencing of Fab regions was performed on mouse hybridoma cells (Fusion Antibodies) and on the intact antibody protein by Edman degradation (by M. A. Gawinowicz). Antibody was purified from hybridoma supernatant using 4-mercapto-ethylpyridine resin. Fab protein was generated by papain cleavage of full-length antibody, followed by F_c capture on Protein A resin and cation exchange. Fab was stored in 20 mM sodium acetate, pH 5, 250 mM NaCl and 10% glycerol.

Purification of DAT_{cryst}. Membranes were solubilized in TBS (20 mM Tris, pH 8, 150 mM NaCl) containing *n*-dodecyl- β -D-maltoside (DDM) at a w/w ratio of 0.1 g detergent per 1 g membrane. The detergent-soluble fraction was incubated with cobalt-charged metal ion affinity resin, and DAT_{cryst}–GFP–His₈ was eluted with 100 mM imidazole in 20 mM Tris, pH 8, 300 mM NaCl, 5% glycerol, 14 μ M lipids (1-palmitoyl-2-oleoyl-*sn*-glycero-3-phosphocholine (POPC), 1-palmitoyl-2-oleoyl-*sn*-glycero-3-phosphoethanolamine (POPE) and 1-palmitoyl-2-oleoyl-*sn*-glycero-3-phospho-(1'-rac-glycerol) (POPG) at a weight ratio of 3:1:1), 1 mM DDM and 0.1 mM cholesteryl hemisuccinate. After thrombin digestion to remove the GFP–His₈ tag, DAT_{cryst} was isolated by size-exclusion chromatography in 20 mM Tris, pH 8, 100 mM NaCl, 5% glycerol, 14 μ M POPE, 4 mM decyl-maltoside and 0.1 mM cholesteryl hemisuccinate. The purified DAT_{cryst} protein was mixed with Fab 9D5 at a molar ratio of 1:1.1 and used for crystallization trials at 3 mg ml^{−1} in the presence of 1 mM nortriptyline.

Crystallization. Crystals grew in 100 mM glycine, pH 9 and 38% PEG 350 MME using a drop ratio of 1 μ l protein and 0.5 μ l reservoir solution by hanging drop vapour diffusion. Initial crystals appeared at 4 °C after 2 days, reaching full size after 7 days. Crystals were flash frozen in liquid N₂ directly and used for X-ray diffraction data collection.

Structure determination. X-ray data were collected at the Advanced Photon Source (Argonne National Laboratory, beamline 24-ID-C). Data were indexed, integrated, and scaled using HKL2000 (ref. 54) (Supplementary Table 1). The structure was solved using molecular replacement, with ensembles of constant (constant domains of heavy and light chains as one set) and variable domains (variable domains of heavy and light chains as a second set) of Fab coordinates in the PDB along with a polyalanine model of LeuT (PDB code 3F3A). A multi-model search was done using Phaser⁵⁵. Initial phases were improved by iterative steps of manual model building, refinement and maximum-likelihood density modification using Coot⁵⁶, Phenix Refine⁵⁷ and Phenix Phase and Build⁵⁸, respectively. Multiple rounds of refinement led to the placement of a majority of main-chain and side-chain atoms for both the Fab and DAT_{cryst}. The structure was refined to acceptable R-factors (Supplementary Table 1) with residues 20–24 and 600–605 in DAT_{cryst} and 135–138 in the heavy chain unmodelled owing to poor density. Nortriptyline, ions and cholesterol molecules were placed into $F_o - F_c$ density contoured at 2σ or greater in

the putative substrate pocket, ion sites and at the periphery of the transporter. Stereochemistry was evaluated using MolProbity⁵⁹.

Ligand binding and uptake measurements. Scintillation-proximity assays using transporter solubilized in detergent⁶⁰ were carried out using copper yttrium silicate (Cu–YSi) beads (Perkin Elmer) at 0.5 mg ml^{−1}, 30 nM ³H-labelled nisoxetine (1:9 ³H:1H) and 10 nM DAT_{cryst}–GFP–His₈ protein in the same buffer as that used for size-exclusion chromatography. Unlabelled nortriptyline was used as the competitor ligand. Assay plates were read using a MicroBeta TriLux 1450 LSC & Luminescence counter. Data were fitted using a standard single site competition equation, and K_i values were calculated from the IC₅₀ values using the Cheng–Prusoff equation.

Uptake assays were performed using HEK293 cells expressing respective mutant constructs. Cells were re-suspended in 10 μ M ³H-dopamine (1:49 ³H:1H) containing uptake buffer made with 25 mM HEPES-Tris, pH 7.1, 130 mM NaCl, 1 mM MgSO₄, 5 mM KCl, 1 mM CaCl₂, 5 mM D-glucose and 1 mM L-ascorbic acid⁶¹. Control samples were pre-incubated with 10 μ M cold desipramine before addition of label. Assays were quenched with cold uptake buffer containing 1 μ M desipramine after 10 min, cells were washed twice with cold uptake buffer and activity was measured from solubilized cells by scintillation counting. Data were plotted using Origin 7.0.

Thermostability screening of DAT. Sites for mutagenesis were selected on the basis of a model of *Drosophila* DAT built on the template of LeuT and residues were altered to Ala, Leu or Phe²¹. Individual mutants along with the wild-type construct were transfected into HEK293 cells and kept in culture for 48 h, then tested for binding activity after detergent solubilization. Samples were split and one part was kept at 4 °C, and the other portion of lysate heated at 40 °C for 10 min. ³H-nisoxetine was added before heating to select for mutants that stabilize an inhibitor-bound state of the transporter. Scintillation proximity assay was used to monitor activity in a high-throughput format. Mutants that consistently had an increased melting temperature (T_m) compared to wild-type ($T_m = 35$ °C) were chosen and pooled into one construct, which yielded a five-mutant construct with a T_m of ~60 °C.

50. Kawate, T. & Gouaux, E. Fluorescence-detection size-exclusion chromatography for precrystallization screening of integral membrane proteins. *Structure* **14**, 673–681 (2006).
51. Dukkkipati, A., Park, H. H., Waghay, D., Fischer, S. & Garcia, K. C. BacMam system for high-level expression of recombinant soluble and membrane glycoproteins for structural studies. *Protein Expr. Purif.* **62**, 160–170 (2008).
52. Reeves, P. J., Callewaert, N., Contreras, R. & Khorana, H. G. Structure and function in rhodopsin: high-level expression of rhodopsin with restricted and homogeneous N-glycosylation by a tetracycline-inducible *N*-acetylglucosaminyltransferase I-negative HEK293S stable mammalian cell line. *Proc. Natl Acad. Sci. USA* **99**, 13419–13424 (2002).
53. Bacongus, I. & Gouaux, E. Structural plasticity and dynamic selectivity of acid-sensing ion channel-spider toxin complexes. *Nature* **489**, 400–405 (2012).
54. Otwinowski, Z. & Minor, W. Processing of X-ray diffraction data collected in oscillation mode. *Methods Enzymol.* **276**, 307–326 (1997).
55. McCoy, A. J. *et al.* Phaser crystallographic software. *J. Appl. Crystallogr.* **40**, 658–674 (2007).
56. Emsley, P. & Cowtan, K. Coot: model-building tools for molecular graphics. *Acta Crystallogr. D* **60**, 2126–2132 (2004).
57. Afonine, P. V. *et al.* Towards automated crystallographic structure refinement with phenix.refine. *Acta Crystallogr. D* **68**, 352–367 (2012).
58. Terwilliger, T. C. *et al.* Iterative model building, structure refinement and density modification with the PHENIX AutoBuild wizard. *Acta Crystallogr. D* **64**, 61–69 (2008).
59. Chen, V. B. *et al.* MolProbity: all-atom structure validation for macromolecular crystallography. *Acta Crystallogr. D Biol. Crystallogr.* **66**, 12–21 (2010).
60. Quick, M. & Javitch, J. A. Monitoring the function of membrane transport proteins in detergent-solubilized form. *Proc. Natl Acad. Sci. USA* **104**, 3603–3608 (2007).
61. Giros, B. *et al.* Cloning, pharmacological characterization, and chromosome assignment of the human dopamine transporter. *Mol. Pharmacol.* **42**, 383–390 (1992).

Demonstration of electron acceleration in a laser-driven dielectric microstructure

E. A. Peralta¹, K. Soong¹, R. J. England², E. R. Colby², Z. Wu², B. Montazeri³, C. McGuinness¹, J. McNeur⁴, K. J. Leedle³, D. Walz², E. B. Sozer⁴, B. Cowan⁵, B. Schwartz⁵, G. Travish⁴ & R. L. Byer¹

The enormous size and cost of current state-of-the-art accelerators based on conventional radio-frequency technology has spawned great interest in the development of new acceleration concepts that are more compact and economical. Micro-fabricated dielectric laser accelerators (DLAs) are an attractive approach, because such dielectric microstructures can support accelerating fields one to two orders of magnitude higher than can radio-frequency cavity-based accelerators. DLAs use commercial lasers as a power source, which are smaller and less expensive than the radio-frequency klystrons that power today's accelerators. In addition, DLAs are fabricated via low-cost, lithographic techniques that can be used for mass production. However, despite several DLA structures having been proposed recently^{1–4}, no successful demonstration of acceleration in these structures has so far been shown. Here we report high-gradient (beyond 250 MeV m^{−1}) acceleration of electrons in a DLA. Relativistic (60-MeV) electrons are energy-modulated over 563 ± 104 optical periods of a fused silica grating structure, powered by a 800-nm-wavelength mode-locked Ti:sapphire laser. The observed results are in agreement with analytical models and electrodynamic simulations. By comparison, conventional modern linear accelerators operate at gradients of 10–30 MeV m^{−1}, and the first linear radio-frequency cavity accelerator was ten radio-frequency periods (one metre) long with a gradient of approximately 1.6 MeV m^{−1} (ref. 5). Our results set the stage for the development of future multi-staged DLA devices composed of integrated on-chip systems. This would enable compact table-top accelerators on the MeV–GeV (10⁶–10⁹ eV) scale for security scanners and medical therapy, university-scale X-ray light sources for biological and materials research, and portable medical imaging devices, and would substantially reduce the size and cost of a future collider on the multi-TeV (10¹² eV) scale.

In a dielectric laser accelerator, the large-amplitude fields responsible for the accelerating force are provided by a laser pulse. Of particular interest are lasers that operate in the optical or near-infrared (NIR) portion of the electromagnetic spectrum to take advantage of the low loss and high damage threshold of dielectric materials at these wavelengths. Direct acceleration of electrons using a NIR laser was demonstrated using inverse transition radiation⁶. That approach, however, requires a material boundary in the path of the electron beam and has a limited interaction length. To achieve scalable acceleration, the electric field must have a component parallel to the electron beam trajectory and a (speed-of-light) phase velocity that matches that of the (relativistic) particle beam.

Previous efforts to accelerate particles with lasers have used a variety of techniques to phase-match the electron beam to a co-propagating laser field. The inverse Cerenkov accelerator^{7,8} uses a gas to slow the phase velocity of the laser light. The inverse free electron laser accelerator^{9,10} requires an undulator at its resonance condition¹¹ to give the electron a synchronous velocity component. However, using a gas cell leads to distortions of the electron beam due to multiple scattering, and use of a

permanent magnet undulator limits the compactness of such a structure and introduces deleterious synchrotron radiation effects.

An alternative way to satisfy the phase-velocity condition is by creating tailored longitudinal modes in near-field structures. One such approach, the inverse Smith–Purcell accelerator¹², has been demonstrated using a metallic grating¹³, and more recently, in a dielectric grating with a NIR laser¹⁴. In configurations that minimize the transverse forces, these open structures do not support speed-of-light longitudinal eigenmodes and are therefore useful only at sub-relativistic particle energies. Additionally, they produce an exponentially decaying accelerating field pattern, which distorts the beam. To address these issues, designs using waveguides and photonic crystals have been proposed^{1–3}. These structures present challenging fabrication tolerances, and the required modes are difficult to excite efficiently; as a result, no successful demonstration has been shown. To circumvent these challenges, we use a planar, phase-reset grating accelerator structure⁴, which permits a relatively simple fabrication process and excitation mechanism.

The DLA is fabricated out of fused silica¹⁵ and operates at the wavelength ($\lambda = 800$ nm) of commercially available Ti:sapphire lasers. The structure consists of two opposing binary gratings of period λ_p , separated by a vacuum gap of height g , where the electron beam travels perpendicular to the grating rulings. A scanning electron microscope (SEM) image of the structure's longitudinal cross-section is shown in Fig. 1a. To generate the required accelerating fields, a linearly polarized laser pulse is incident on the structure perpendicular to both the electron beam direction of propagation and the plane of the gratings. The laser pulse generates a series of grating diffraction modes inside the vacuum channel, and by matching the grating period to the laser wavelength ($\lambda_p = \lambda$) we achieve phase synchronicity between the strong first space harmonic and the particle beam¹⁶.

The structure essentially acts as a longitudinally periodic phase mask, where each grating pillar imparts a π -phase shift on the electric field, with respect to the adjacent vacuum space (Fig. 1b inset). As a result, electrons launched at the correct optical phase (laser–electron timing) remain phase-synchronous and experience net energy gain. In our experiment, the electron beam has a duration of 429 ± 31 fs, much longer than the laser optical cycle ($\lambda/c = 2.6$ fs, where c is the velocity of light). Electrons therefore sample all phases of the laser field, causing the laser–electron interaction to manifest as an energy modulation (broadening), with some electrons gaining energy from acceleration while some are decelerated.

Figure 1b depicts a diagram of the experiment performed at the Next Linear Collider Test Accelerator (NLCTA) facility at the SLAC National Accelerator Laboratory. The incident 60-MeV electron beam is focused by a permanent magnetic quadrupole triplet to a root mean square (r.m.s.) spot size of $24 \mu\text{m} \times 8 \mu\text{m}$. The sample contains multiple 550- μm -long (~ 687 optical periods) DLA structures with a period of 800 nm and apertures of both $500 \mu\text{m} \times 400 \text{ nm}$ and $500 \mu\text{m} \times 800 \text{ nm}$. The 400-nm gap structure provides a higher acceleration gradient

¹Department of Applied Physics, Stanford University, Stanford, California 94305, USA. ²SLAC National Accelerator Laboratory, 2575 Sand Hill Road, Menlo Park, California 94025, USA. ³Department of Electrical Engineering, Stanford University, Stanford, California 94305, USA. ⁴Department of Physics and Astronomy, University of California Los Angeles, Los Angeles, California 90024, USA. ⁵Tech-X Corporation, 5621 Arapahoe Avenue, Boulder, Colorado 80303, USA.

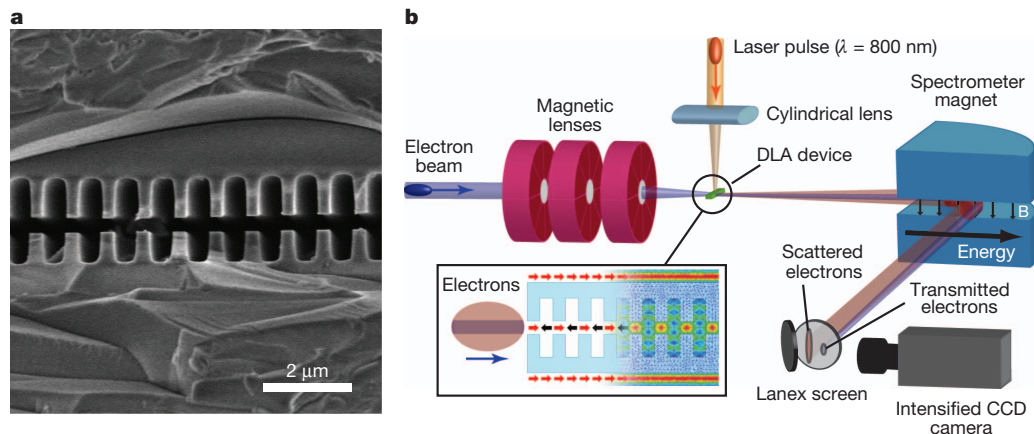


Figure 1 | DLA structure and experimental set-up. **a**, Scanning electron microscope image of the longitudinal cross-section of a DLA structure fabricated as depicted in Extended Data Fig. 1a. Scale bar, 2 μm . **b**, Experimental set-up. Inset, a diagram of the DLA structure indicating the

than an 800-nm gap structure but requires tighter tolerances on the electron beam.

The NIR pulses, 1.24 ± 0.12 ps long, from a regeneratively amplified Ti:sapphire mode-locked laser are focused to an r.m.s. spot size of $30 \mu\text{m} \times 300 \mu\text{m}$ at the interaction point. We use a motorized four-axis stage for precise alignment of the structure with the electron beam. Once aligned, the electron beam leaving the structure goes through a point-to-point focusing spectrometer magnet, which disperses the outgoing electron beam in energy onto a Kodak Lanex phosphor screen that is imaged by an intensified CCD (charge-coupled device) camera. According to particle tracking simulations, 2.2% of the 60-MeV beam is transmitted through the vacuum channel of the 400-nm gap structure (see Methods). A segment of the spectrometer screen focusing on this transmitted distribution is shown in Fig. 2a. The horizontal axis represents beam energy, and the entire image spans 240 keV. The central pixel location of the 60-MeV beam is taken as the reference point, corresponding to zero energy deviation (ΔE).

The spectrometer image in Fig. 2a is a median filtered average of a dozen shots. The least-squares fit to the distribution of electrons scattered by the fused silica substrate and the grating teeth has been removed from this image to emphasize the transmitted distribution (see Methods). A similarly averaged set of laser-on spectrometer images within 0.5 ps of the optimal timing overlap for laser pulses with energy 93 μJ per pulse is shown in Fig. 2b. The white contour in both Fig. 2a and Fig. 2b denotes the location where the spectral charge density is 4.5% of the maximum density (at the peak of the scattered distribution). In the presence of a laser field, there exists a higher charge density on either side of the original peak at $\Delta E = 0$. The white contour shows a sizable fraction of electrons with maximum energy that is ~ 60 keV higher than in the laser-off case.

The laser-induced energy modulation is readily apparent in the energy spectra (Fig. 2c). Using the fits to these spectra, a maximum energy shift of 53.1 keV is calculated from the abscissa of the half-width at half-maximum (HWHM) point in the high-energy tail. We use an analytical interaction model (see Methods and Extended Data Fig. 3) to calculate an accelerating gradient from this measurement. Figure 2c shows the input electron beam distribution used in the model (blue curve), which is a fit to the measured spectrum in the absence of a laser field (light blue crosses). The calculated energy modulation (red curve) agrees with our measurement (pink crosses), and gives a corresponding accelerating gradient of 151.2 MeV m^{-1} for this example. Particle tracking simulations (black dots; see Methods) at this gradient level give an independent confirmation of the observed modulated spectrum.

To determine the maximum gradient at a given laser power level, we measure the energy modulation as the laser pulse is temporally scanned

field polarization direction and the effective periodic phase reset, depicted as alternating red (acceleration) and black (deceleration) arrows. A snapshot of the simulated fields in the structure shows the corresponding spatial modulation in the vacuum channel. See text for details.

across the electron beam, forming a cross-correlation signal. A sample measurement at a laser pulse energy of $91.8 \pm 1.3 \mu\text{J}$ over a laser delay of 6 ps is shown Fig. 3a. The orange circles (laser-off data) show no variation correlated with laser delay, as expected, and have an r.m.s. deviation of 4.5 keV, which is taken as the noise floor level of the measurement. The blue circles (laser-on data) show the expected sech^2 distribution with a full-width at half-maximum (FWHM) of 1.89 ± 0.09 ps,

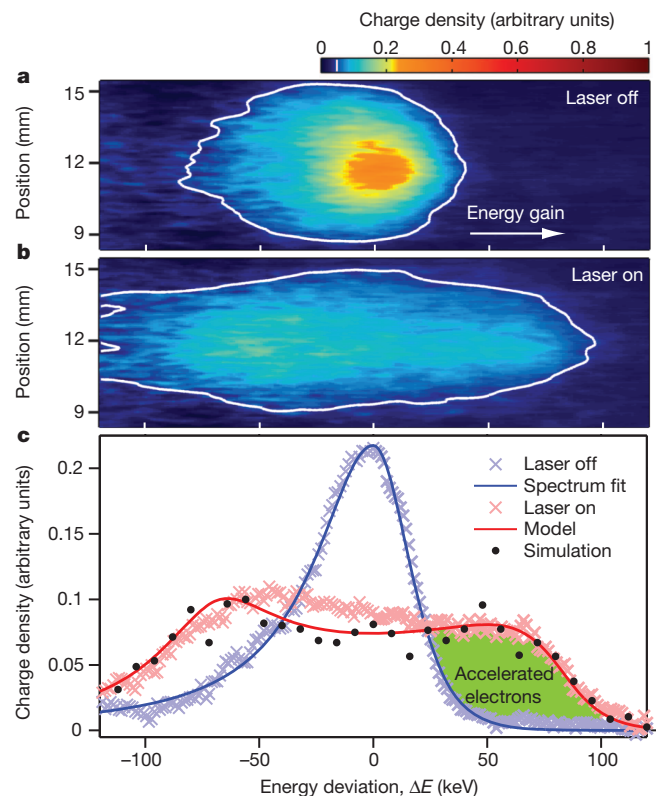


Figure 2 | Demonstration of energy modulation. **a**, Image of the transmitted electron beam on the spectrometer screen, with the laser off. **b**, As **a** but when the laser field is present. **c**, Energy spectra from **a** and **b** showing energy modulation. A fit (blue curve) to the measured laser-off spectrum (light blue crosses) is used as input for the simulations. The calculated energy modulation (red curve) and particle tracking simulations (black dots) agree with our measured spectrum (pink crosses). Images of the entire spectrometer screen are shown in Extended Data Fig. 2.

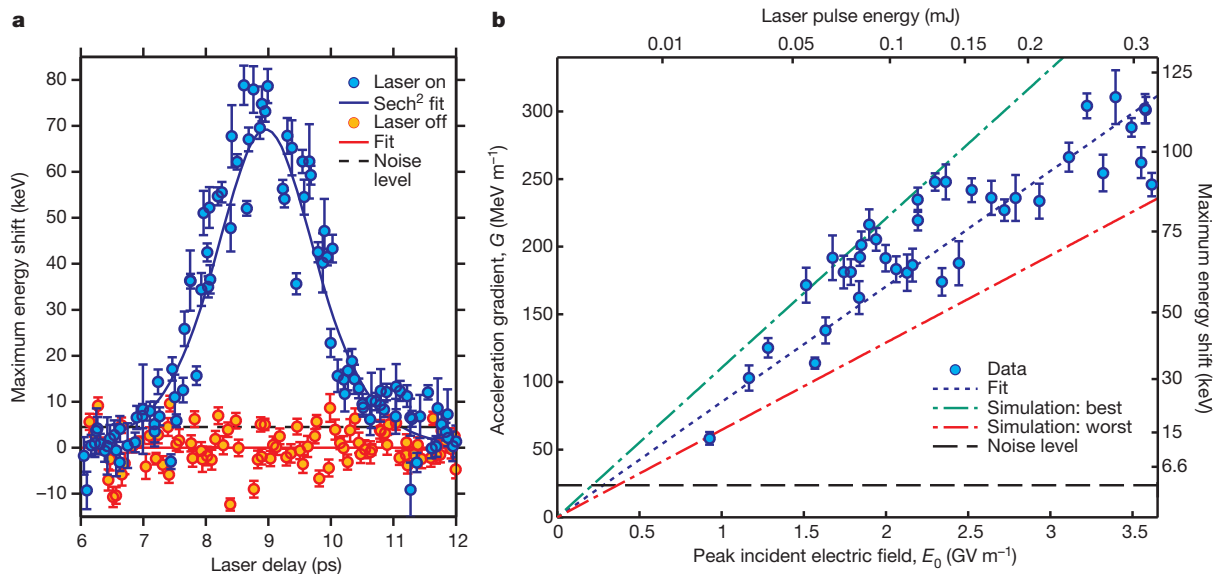


Figure 3 | Measurement of acceleration gradient in the 400-nm gap structure. **a**, Maximum energy shift as a function of laser delay gives a cross-correlation measurement of the laser-electron interaction. The orange filled circles (laser-off data) show no variation with laser delay and have an r.m.s deviation of 4.5 keV which is taken as the noise level (black dashed line). The blue filled circles (laser-on data) show the expected sech^2 distribution (blue curve). **b**, Calculated acceleration gradient (blue filled circles), G , as a function

of peak incident longitudinal electric field, E_0 , showing expected linear dependence (dashed blue line). Gradients in excess of 250 MeV m⁻¹ are observed within the simulated best-case (dashed green line) and worst-case (dashed red line) structure fabrication tolerance limits. Measurements on the 800-nm gap structure are shown in Extended Data Fig. 4. Error bars in **a** and **b**, 68% confidence interval.

which is in agreement with the predicted value of 2.00 ± 0.13 ps (see Methods). For each data set, the magnitude of the electron-laser interaction is determined by the amplitude of the sech^2 fit, which represents the maximum energy gain at an optimal temporal overlap. We use this figure to calculate the accelerating gradient. For the data set shown in Fig. 3a, the observed maximum energy shift is 69.2 ± 2.3 keV and the resulting gradient is 191.1 ± 5.7 MeV m⁻¹, which falls within the expected range (see Supplementary Information).

The cross-correlation measurement was repeated at multiple pulse energies up to 319 μ J, the maximum pulse energy available. Figure 3b shows the acceleration gradient G as a function of peak incident field E_0 , along with analytical gradient calculations (see Methods) for the best case (green line) and worst case (red line) structure fabrication. We find that the measured gradient varies linearly with incident electric field as expected, and the measured values fall within the anticipated range. The highest gradient observed here is 309.8 ± 20.7 MeV m⁻¹; this is twice the highest recorded values in radio-frequency (RF)-based demonstration cavities, and 6–10 times higher than typical operating gradients in RF structures. The deviation of the high-energy data points in Fig. 3b below the predicted linear trend is probably due to structural damage. Further optimization of the fabrication and materials can allow for operation at higher gradients below the laser damage fluence level. Additionally, despite week-long exposure of the structure, no electron-beam-induced charging or radiation damage was observed in the post-examination, demonstrating the robustness of dielectric structures as accelerators¹⁷.

To further verify the linear dependence of the laser-electron interaction on the electric field, the laser polarization and incidence angles were varied at a fixed laser power level. As shown in Extended Data Fig. 5, the measured gradients show good agreement with the expected dependencies and confirm that an intensity-dependent ponderomotive force is not responsible for the observed laser-electron interaction. Additionally, the fit to the data reveals that the laser-electron interaction occurs over $N = 563 \pm 104$ periods of the structure.

We have produced the first demonstration of scalable laser-driven acceleration with gradients exceeding 250 MeV m⁻¹ in an ultra-compact and inexpensive DLA. The results are in agreement with both the

analytical treatment and particle tracking simulations. The pulse duration of the electron beam used in this experiment is longer than the optical cycle of the laser, which results in a modulation of the electron beam in energy. An ideal DLA-matched electron source should not only be sub-femtosecond in duration, but also have a nanometre-scale spot size, to efficiently utilize the maximum acceleration gradients in an optimized sub-wavelength aperture DLA accelerator. To create such a source, a method of bunching the electron beam at optical frequencies has been previously demonstrated¹⁸ and needle cathodes are being developed to create high-brightness low-emittance laser-triggered electron beam sources¹⁹. By bunching the beam, the fraction of captured electrons can jump from a few tens of per cent in a 5% energy window to >80% with an energy spread of <1% (ref. 20).

Integrating these novel electron sources with DLA structures would allow phase-stable net acceleration of synchronous attosecond micro-bunches over many accelerating stages. Additionally, the relatively small operating beam charge in these microstructures can be compensated by the MHz repetition rate of current laser systems to achieve the beam luminosity required for high-energy physics research²¹. Power efficiency estimates for such DLA devices are comparable with conventional RF technology, assuming that similar power efficiency (near 100%) for guided wave systems can be achieved, 40% laser electrical-to-optical conversion efficiencies (feasible with solid state thulium fibre laser systems)²² and 40% laser to electron-beam coupling²³. Continuously tunable radiation is a natural by-product of accelerator technology, so this demonstration supports the viability of DLA for the development of compact sources of coherent, attosecond-scale X-ray pulses²⁴ with applications in medical therapy, biological and materials research, and industrial processing.

METHODS SUMMARY

The DLA structure was fabricated by bonding two fused-silica wafers, which were processed via standard optical lithography and reactive ion etching techniques¹⁵ (Extended Data Fig. 1). We used a conventional linear accelerator to generate a relativistic electron beam, with a 10 μ m spot size. Owing to the dimensional mismatch between the electron beam and the sub-micrometre DLA aperture, many of the electrons experienced collisional straggling energy loss²⁵ as they traversed the fused-silica substrate (rather than the vacuum aperture). This process generated

observable optical transition radiation (OTR) as a by-product, which was subsequently used as a diagnostic to align the laser pulse to the electron beam, both spatially and temporally. The alignment of the electron beam to the aperture of the DLA structure was optimized by maximizing the population of transmitted electrons, as indicated by the electron energy spectrum (Extended Data Fig. 2). Our understanding of the observed spectrum was verified with G4Beamline²⁶ simulations of the beam scattering and radiative losses. To quantify the maximum energy gain in our structure, we developed an analytical model (Extended Data Fig. 3) and performed particle tracking simulations, both of which agreed with our measurements. Damage threshold measurements²⁷ of identical DLA structures yielded a laser damage threshold of $0.85 \pm 0.14 \text{ J cm}^{-2}$.

Online Content Any additional Methods, Extended Data display items and Source Data are available in the online version of the paper; references unique to these sections appear only in the online paper.

Received 28 June; accepted 16 September 2013.

Published online 27 September; corrected online 6 November 2013 (see full-text HTML version for details).

- Lin, X. E. Photonic band gap fiber accelerator. *Phys. Rev. Spec. Top. Accel. Beams* **4**, 051301 (2001).
- Mizrahi, A. & Schachter, L. Optical Bragg accelerators. *Phys. Rev. E* **70**, 016505 (2004).
- Cowan, B. M. Three-dimensional dielectric photonic crystal structures for laser-driven acceleration. *Phys. Rev. Spec. Top. Accel. Beams* **11**, 011301 (2008).
- Plettner, T., Lu, P. P. & Byer, R. L. Proposed few-optical cycle laser-driven particle accelerator structure. *Phys. Rev. Spec. Top. Accel. Beams* **9**, 111301 (2006).
- Ginzton, E. L., Hansen, W. W. & Kennedy, W. R. A linear electron accelerator. *Rev. Sci. Instrum.* **19**, 89–108 (1948).
- Plettner, T. *et al.* Visible-laser acceleration of relativistic electrons in a semi-infinite vacuum. *Phys. Rev. Lett.* **95**, 134801 (2005).
- Shimoda, K. Proposal for an electron accelerator using an optical maser. *Appl. Opt.* **1**, 33–35 (1962).
- Piestrup, M. A., Rothbart, G. B., Fleming, R. N. & Pantell, R. H. Momentum modulation of a free electron beam with a laser. *J. Appl. Phys.* **46**, 132–137 (1975).
- Palmer, R. B. Interaction of relativistic particles and free electromagnetic waves in the presence of a static helical magnet. *J. Appl. Phys.* **43**, 3014–3023 (1972).
- van Steenberg, A., Gallardo, J., Sandweiss, J. & Fang, J.-M. Observation of energy gain at the BNL inverse free-electron-laser accelerator. *Phys. Rev. Lett.* **77**, 2690–2693 (1996).
- Marshall, T. C. *Free-Electron Lasers* 24–26 (McMillan, 1985).
- Takeda, Y. & Matsui, I. Laser linac with grating. *Nucl. Instrum. Methods* **62**, 306–310 (1968).
- Mizuno, K., Pae, J., Nozokido, T. & Furuya, K. Experimental evidence of the inverse Smith-Purcell effect. *Nature* **328**, 45–47 (1987).
- Breuer, J. & Hommelhoff, P. Laser-based acceleration of non-relativistic electrons at a dielectric structure. *Phys. Rev. Lett.* (in the press).
- Peralta, E. A. *et al.* Design, fabrication, and testing of a fused-silica dual-grating structure for direct laser acceleration of electrons. *AIP Conf. Proc.* **1507**, 169–177 (2012).
- Plettner, T., Byer, R. L. & Montazeri, B. Electromagnetic forces in the vacuum region of laser-driven layered grating structures. *J. Mod. Opt.* **58**, 1518–1528 (2011).
- Thompson, M. C. *et al.* Breakdown limits on gigavolt-per-meter electron-beam-driven wakefields in dielectric structures. *Phys. Rev. Lett.* **100**, 214801 (2008).
- Sears, C. M. S. *et al.* Production and characterization of attosecond electron bunch trains. *Phys. Rev. Spec. Top. Accel. Beams* **11**, 061301 (2008).
- Ganter, R. *et al.* Laser-photofield emission from needle cathodes for low-emittance electron beams. *Phys. Rev. Lett.* **100**, 064801 (2008).
- Duris, J. P., Musumeci, P. & Li, R. K. Inverse free electron laser accelerator for advanced light sources. *Phys. Rev. Spec. Top. Accel. Beams* **15**, 061301 (2012).
- Colby, E. R., England, R. J. & Noble, R. J. A laser-driven linear collider: sample machine parameters and configuration. *Proc. 24th Particle Accelerator Conf. C110328* 262–264 (2011).
- Moulton, P. F. *et al.* Tm-doped fiber lasers: fundamentals and power scaling. *IEEE J. Sel. Top. Quant.* **15**, 85–92 (2009).
- Siemman, R. Energy efficiency of laser driven, structure based accelerators. *Phys. Rev. Spec. Top. Accel. Beams* **7**, 061303 (2004).
- Plettner, T. & Byer, R. L. Microstructure-based laser-driven free-electron laser. *Nucl. Instrum. Methods A* **593**, 63–66 (2008).
- Warner, C. & Rohrlach, F. Energy loss and straggling of electrons. *Phys. Rev.* **93**, 406–407 (1954).
- Roberts, T. J. & Kaplan, D. M. G4beamline simulation program for matter-dominated beamlines. *Proc. 22nd Particle Accelerator Conf. C070625* 3468–3470 (2007).
- Soong, K., Byer, R. L., Colby, E., England, R. J. & Peralta, E. A. Laser damage threshold measurements of optical materials for direct laser accelerators. *AIP Conf. Proc.* **1507**, 511–515 (2012).

Supplementary Information is available in the online version of the paper.

Acknowledgements We thank R. Noble, J. Spencer, O. Solgaard and J. Harris for discussions, J. Nelson, D. McCormick and K. Jobe for technical assistance at SLAC, and M. Tang, M. Mansourpour, N. Latta, M. Stevens, J. Conway and U. Thumser for technical assistance at the Stanford Nanofabrication Facility (SNF). This work was supported by the US DoE (grant no. DE-FG03-92ER40693) and DARPA (grant no. N66001-11-1-4199). Device fabrication took place at SNF, which is supported by the NSF under grant ECS-9731293. Work by G.T., J.M. and E.B.S. supported by US Defense Threat Reduction Agency (DTRA) grant HDTRA1-09-1-0043.

Author Contributions E.A.P., K.S., R.J.E., E.R.C. and R.L.B. designed the experiment. E.A.P., K.S., R.J.E., E.R.C., Z.W. and B.M. built the experiment, and with the help of C.McG. and J.McN., carried out the experiment. E.A.P. designed and fabricated the structure. E.A.P. and K.S. wrote the data analysis software and analysed the results, and E.B.S. contributed to that software. K.S. developed the analytical model. K.S., B.M., J.McN, B.C. and B.S. performed supporting simulations. G.T., J.McN, E.B.S. and K.J.L. provided feedback to improve the experiment. K.S. and K.J.L. designed and constructed the vacuum damage threshold measurement set-up, and K.S. carried out such measurements. D.W. performed hardware upgrades and installation. E.A.P. wrote the manuscript with contributions from K.S. and R.J.E. and revisions by all.

Author Information Reprints and permissions information is available at www.nature.com/reprints. The authors declare no competing financial interests. Readers are welcome to comment on the online version of the paper. Correspondence and requests for materials should be addressed to R.L.B. (rlbyer@stanford.edu).

METHODS

Grating structure fabrication. Fabrication of the dual layer grating structures was carried out at the Stanford Nanofabrication Facility (SNF). The gratings are patterned on fused silica wafers via optical lithography using an ASML PAS 5500 i-line stepper and magnetically enhanced reactive ion etching on an Applied Materials P5000 etcher. This is shown schematically in steps 1–3 of Extended Data Fig. 1a.

Four grating structures are included in every sample to facilitate a switch during the experiment, two with a 400-nm gap, and two with an 800-nm gap. Once patterned and etched, alignment channels of decreasing sizes ($250\ \mu\text{m} \times 250\ \mu\text{m} \rightarrow 80\ \mu\text{m} \times 80\ \mu\text{m} \rightarrow 80\ \mu\text{m} \times 20\ \mu\text{m}$) are cut into the wafers to facilitate the alignment of the electron beam with the structure. Two wafers are then bonded directly to each other via fusion bonding and diced into individual samples (steps 4–5 of Extended Data Fig. 1a). The alignment tolerance of the bonding process is $\sim 3\ \mu\text{m}$ so the grating-to-grating longitudinal alignment is not ensured. However, a perfectly aligned structure is not required to generate substantial acceleration gradients¹⁵. As a final step, a section of the sample is metal-coated to serve as a reflector for the NIR laser, and a wedge is cut at 45° to be able to image the infrared laser beam and optical transition radiation (OTR) simultaneously. These two features, along with the alignment channels and the four grating structures, are shown in the schematic in Extended Data Fig. 1c.

Electron beam. Testing of the dielectric accelerator structures is conducted using pre-accelerated electron bunches at the Next Linear Collider Test Accelerator (NLCTA) facility at SLAC National Accelerator Laboratory. The electron bunches are produced by an RF photoinjector and accelerated up to 60 MeV in a travelling wave RF cavity at a repetition rate of 10 Hz. Energy collimation is used to create a stable monoenergetic ‘slice’ of the electron bunch with a FWHM energy spread of 24 keV or 0.04%, an r.m.s. length of $129 \pm 9\ \mu\text{m}$ ($0.43 \pm 0.03\ \text{ps}$), and emittances of $16\ \text{mm mrad} \times 7\ \text{mm mrad}$ in X and Y , respectively. Of the initial 5 pC of charge, 10% is transmitted through the energy collimators, giving an estimated charge of 0.5 pC incident on the grating structure. Based on particle scattering simulations, 2.2% of these particles are transmitted through the 400-nm gap structure’s vacuum channel. Consequently, the population of electrons that pass through the accelerating channel of the 400-nm gap device contains an estimated 11 fC of charge per electron bunch. A sample spectrometer image for the case of the electron beam travelling entirely through vacuum (that is, in the absence of the structure) is shown in Extended Data Fig. 2a. The horizontal axis represents beam energy and the resolution limit of the spectrometer is 1.2 keV per image pixel so the entire image spans 800 keV. The central pixel location of the narrow energy spread 60-MeV beam is taken as the reference point, corresponding to zero energy deviation (ΔE).

Achieving electron transmission. Transmission of electrons through the sub-micrometre grating aperture is achieved with the help of alignment apertures of decreasing size that run parallel to the grating vacuum channels (see Extended Data Fig. 1c). Once transmission on the large channel is observed, the structure’s optimal pitch and yaw are determined by maximizing the transmitted distribution. This is repeated for the smaller apertures until we see transmission through the grating aperture. Once this is achieved, the laser beam incidence angle is adjusted to ensure perpendicularity.

Because the NLCTA beam is significantly larger than the structure aperture, only a small fraction of electrons travels through the vacuum channel when the DLA structure is in place. Extended Data Fig. 2b shows the corresponding spectrometer image for this case, containing two distinct distributions. The prominent broad distribution, centred at $\Delta E = -340\ \text{keV}$, represents the (majority) electron population that travels primarily through the fused-silica substrate. The energy of these electrons is reduced due to collisional straggling loss in the material²⁵. The smaller, more compact distribution at $\Delta E = 0\ \text{keV}$ corresponds to the population of electrons that traverse the grating structure primarily through the vacuum channel. Because the channel has a 1,280:1 aspect ratio (430 nm tall, and 550 μm long), these electrons are collimated with an acceptance angle of 0.04° . This distribution therefore has a reduced vertical spread but retains its original energy spread. Henceforth, we refer to the higher-energy peak as the transmitted population and the lower-energy peak as the scattered population.

The formation of these two distributions is confirmed by simulations of the scattering and radiative losses of the electron beam as it traverses the grating structure. Extended Data Fig. 2c shows a projection of the spectrometer image of Extended Data Fig. 2b onto the energy axis which gives the resulting electron energy spectrum. Also shown is the calculated spectrum from particle scattering simulations, which has peak locations and relative amplitudes in agreement with the observed experimental data. Because the accelerating fields are strongest inside the vacuum channel, we focus on the transmitted distribution when studying the effects of the laser–electron interaction. In our analysis, the resulting spectra are fitted to a curve composed of two distributions (scattered and transmitted), using

the method of least-squares. A sample fit, shown (in orange) in Extended Data Fig. 2c, matches the measured spectra closely.

Particle scattering simulations. We model the scattering and radiative losses of the electron beam as it traverses the grating structure using the Geant4 code G4Beamline²⁶ to calculate the expected electron energy spectrum. In this model, an electron beam with a transverse spot size of $24\ \mu\text{m} \times 8\ \mu\text{m}$ and a transverse vertical emittance of 3 mm mrad is sent through an approximate model of the grating structure with a 400-nm gap. The model structure is made up of five layers. A central, 400-nm tall, vacuum layer surrounded by two 660-nm-thick grating layers in the first 550 μm of the longitudinal dimension. Two 1.1-mm-long, 500- μm -thick layers of fused silica surround the grating layers. Extended Data Fig. 2c shows the results of this simulation in agreement with the experimental data, giving the correct spectrum peak separation of 340 keV and relative peak amplitude.

The simulations give a calculated percentage of 2.2% of the total number of electrons in the transmitted distribution. By comparison, simulations of the 800-nm gap structure yield 5.8% of the electrons in the transmitted distribution.

Energy modulation simulations. The fields in the structure vacuum channel are calculated using the finite-element frequency-domain code HFSS and imported into a MATLAB-based code that computes the resulting relativistic Lorentz force on a test particle as it traverses the structure. In our simulations, we approximate the NLCTA electron beam using 2,500 test particles, whose position and momentum match those of the experiment. Owing to the long computation time required to perform such particle tracking simulations, we elect to model and scale a 100-period structure rather than model the entire 650-period structure. Based on convergence tests, we find that this approach produces accurate results, which is expected from the linearity of the acceleration effect, at a fraction of the computation cost. The final energy distribution of the 2,500-particle ensemble is then calculated from the results of each individual particle trace.

Analytical treatment of energy modulation. The interaction between a NIR laser pulse and a picosecond-scale electron bunch in a grating accelerator structure can be described analytically by partitioning the long electron bunch into a series of short finite slices of length τ , as shown in Extended Data Fig. 3a, where each slice satisfies the relation $\tau \ll \lambda/c$. In the presence of the sinusoidally varying electric fields of the structure, each slice of the electron bunch will experience a net energy shift with a negligible effect on the energy profile. For example, a slice of an electron bunch with an asymmetric energy profile typical of the NLCTA will experience a net energy gain of 50 keV if injected at the optimal phase in a millimetre-long structure capable of $50\ \text{MeV m}^{-1}$ gradients (see green slice in Extended Data Fig. 3b). The net effect of the structure is calculated by superimposing the effect for each individual slice. For a long pulse, we find that the predicted effect on the electron energy spectrum is a transition from a single peaked distribution to a double peaked profile of lower amplitude, as shown in Extended Data Fig. 3c.

Energy spectrum fits. The projected energy spectra are fitted to curves containing the two distinct, scattered and transmitted, electron distributions. Several different profiles including asymmetric Gaussian, Lorentzian, sech^2 and Landau distributions, along with combinations of these were initially employed. These were compared against the measured single-peak data (that is, electron beam incident on the fused-silica sample but away from the grating vacuum channel) to determine a profile that minimized the χ^2 value of the fits. The scattered distribution was ultimately fitted to a half Lorentzian on its low-energy side, and a half sech^2 on its high-energy side. The transmitted distribution was fitted to a double-peak version of the scattered distribution, with the separation of the two peaks as a free parameter and mirrored about its centre. The sum of the two distributions fit the observed spectra very well, as indicated in Extended Data Fig. 2c.

On the basis of comparisons with the particle scattering simulations and the analytical treatment, we find that a partially-straggled population exists, composed of electrons which are scattered (partially) by the grating teeth. This is accurately accounted for by the low-energy side Lorentzian function used to fit the transmitted distribution. To isolate the fully transmitted electrons (as shown in Fig. 2c), we subtract both the straggled distribution and the partially straggled distribution. The difference between the abscissa of the HWHM point in the high-energy tail for a laser-on spectrum and a laser-off spectrum gives a measurement of the laser-induced maximum energy shift.

Spatial overlap. We use a miniature aluminium pellicle mirror and a long working distance Cassegrain telescope to image the back of the grating sample with a resolution limit of $8\ \mu\text{m}$ per image pixel. To perform the spatial alignment, we simultaneously determine the location of the OTR origin on the sample and the laser beam scattering off the fabricated 45° wedge shown in Extended Data Fig. 1c. The laser beam is then steered until the observed scattering lines up with the OTR location to within $\sim 10\ \mu\text{m}$.

Temporal overlap. A fast photodiode (25-GHz bandwidth) is used to detect the OTR signal the electron beam generates at an aluminium pellicle located downstream of the sample. The transmitted NIR pulse is also measured simultaneously,

on the same detector and oscilloscope. We observe the measured arrival time of the two signals and adjust a four-pass optical delay line to achieve sub-nanosecond overlap. A motorized delay line provides gross overlap to within the 50-ps resolution limit of the oscilloscope, and a voice coil actuated retroreflector is scanned during the experiment to achieve picosecond-scale timing.

Cross-correlation measurement. A typical cross-correlation signal in our experiment consist of 300 independent electron–laser interaction events measured at 150 unique temporal overlap positions. The resulting cross-correlation signal follows a hyperbolic secant squared (sech^2) pattern as expected based on the laser pulse profile indicated by autocorrelation measurements.

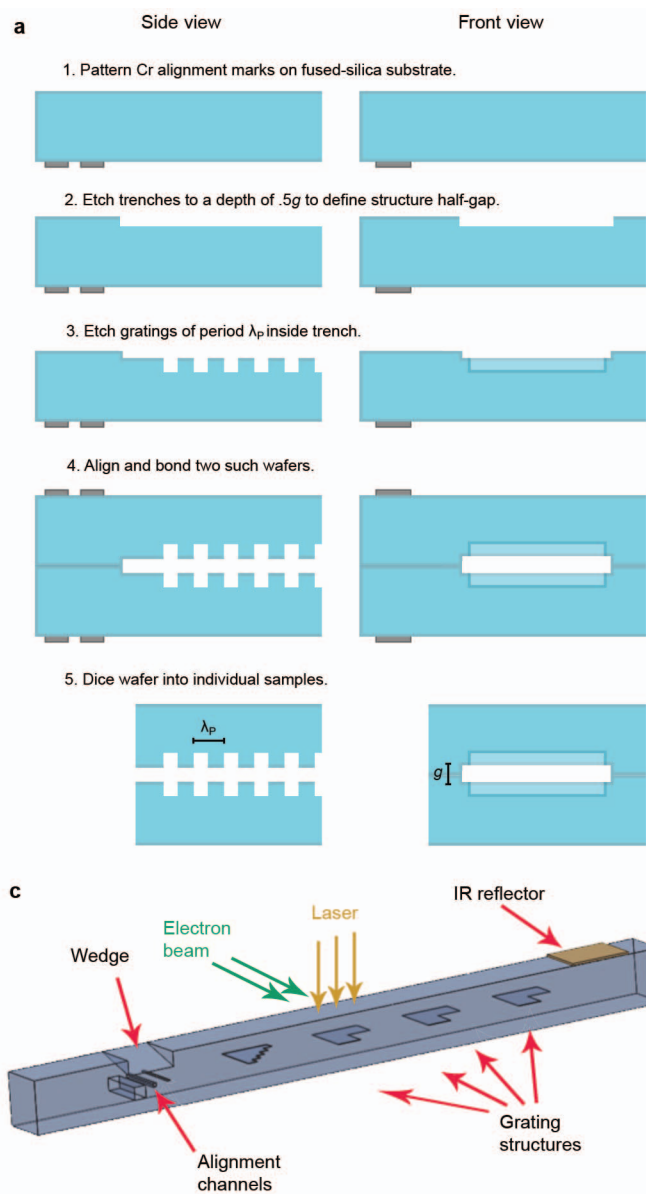
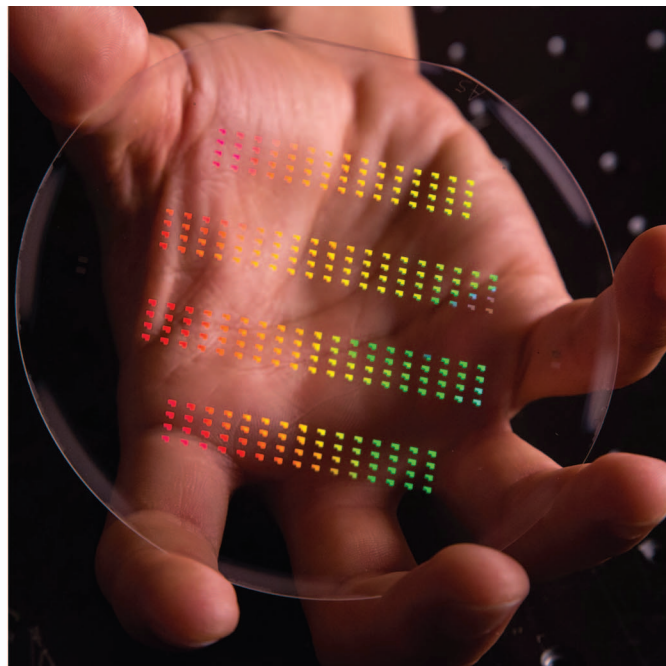
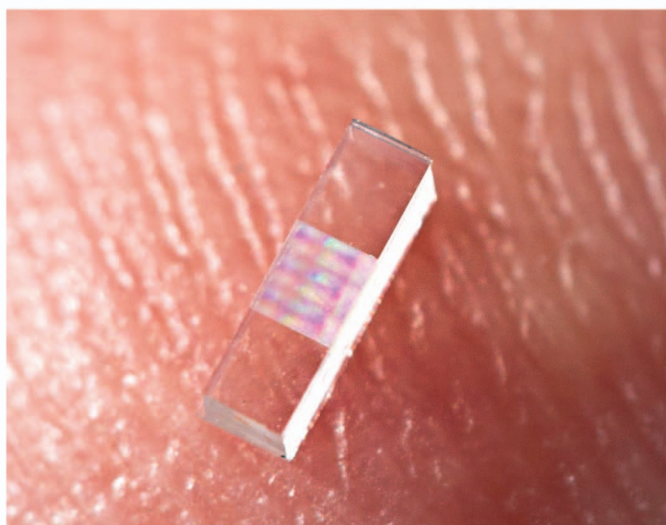
Typical cross-correlation measurements co-propagate two signals through an interacting medium, while varying the temporal overlap. In this case, the cross-correlation signal is solely dependent on the temporal dimension. However, in our cross-correlation measurement, we use two signals incident at perpendicular angles, and as a result, the cross-correlation signal is a function of both the temporal and spatial dimensions of our electron bunch and our laser beam. The expected outcome of this interaction can be calculated by simulating the perpendicular crossing of an electron bunch with a laser beam, with the temporal and spatial dimensions set to match the experimental values. From this calculation, we predict a FWHM of 2.00 ± 0.13 ps for the sech^2 fit to the cross-correlation signal. This is in strong agreement with our experimental findings, where a cross-correlation FWHM equal to 1.89 ± 0.09 ps was observed.

Damage threshold measurement. Damage threshold measurements of DLA structures from the same wafer as the one used in the acceleration experiment were performed using an experimental set-up similar to the one described in ref. 27.

An array of accelerator structures was placed in a vacuum chamber at a pressure of 10^{-5} torr. The NIR pulses from our Ti:sapphire laser system was then focused to a r.m.s. spot size of $27 \mu\text{m} \times 53 \mu\text{m}$ and incident on the structure, in the same manner as in the acceleration experiment. The laser fluence was then gradually increased from an initial value of $2.00 \mu\text{J}$ in increments of $1.85 \mu\text{J}$, while the illuminated site was monitored with a camera. At each energy level, approximately 5,000 laser pulses were applied to the structure. Damage was determined to occur when a visible change in the strength and consistency of the scattered infrared light at the illumination site was observed. A total of 24 independent damage threshold measurements were taken, and each damage site was afterwards inspected under a high powered optical microscope to verify the occurrence of laser damage.

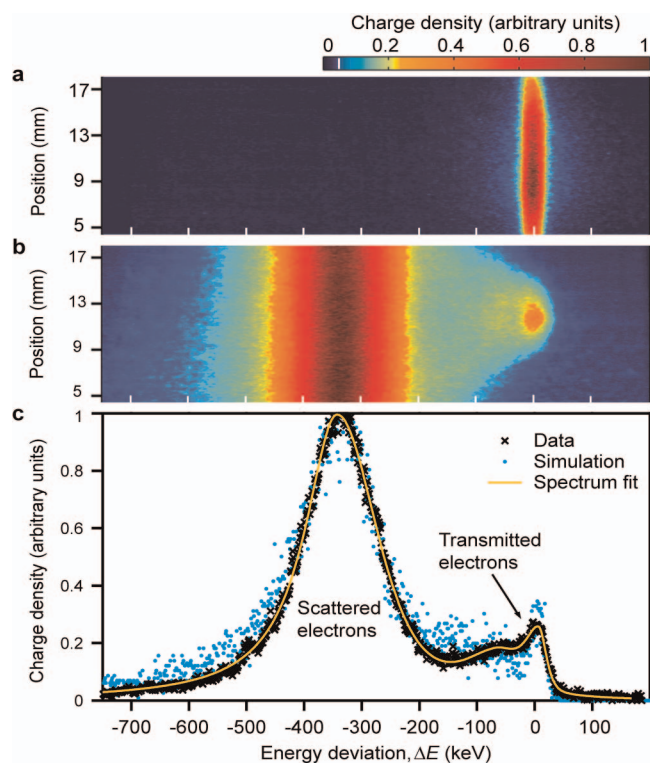
The results of these measurements indicate a laser damage threshold of $0.85 \pm 0.14 \text{ J cm}^{-2}$ for our grating accelerator structures. From post-examination of the structure it is clear that this damage threshold value was exceeded during the course of the experiment. However, we continued to see acceleration up to the maximum available pulse energy. On the basis of post-analysis of a laser damage site, we deduced that our laser r.m.s. spot size during the experiment was actually $76 \mu\text{m} \times 294 \mu\text{m}$, yielding a maximum fluence of 0.85 J cm^{-2} on the gratings.

Error analysis. The corresponding error bar for each data point represents a 68% confidence interval for the plotted fit parameter, as calculated by the Jacobian of the weighted nonlinear least-squares regression. The noise floor in the plots is defined by the laser-off data for each set of measurements. Specifically, we define the gradient of the laser-off data as zero gradient, and used the positive tail of the 68% confidence interval as the noise floor.

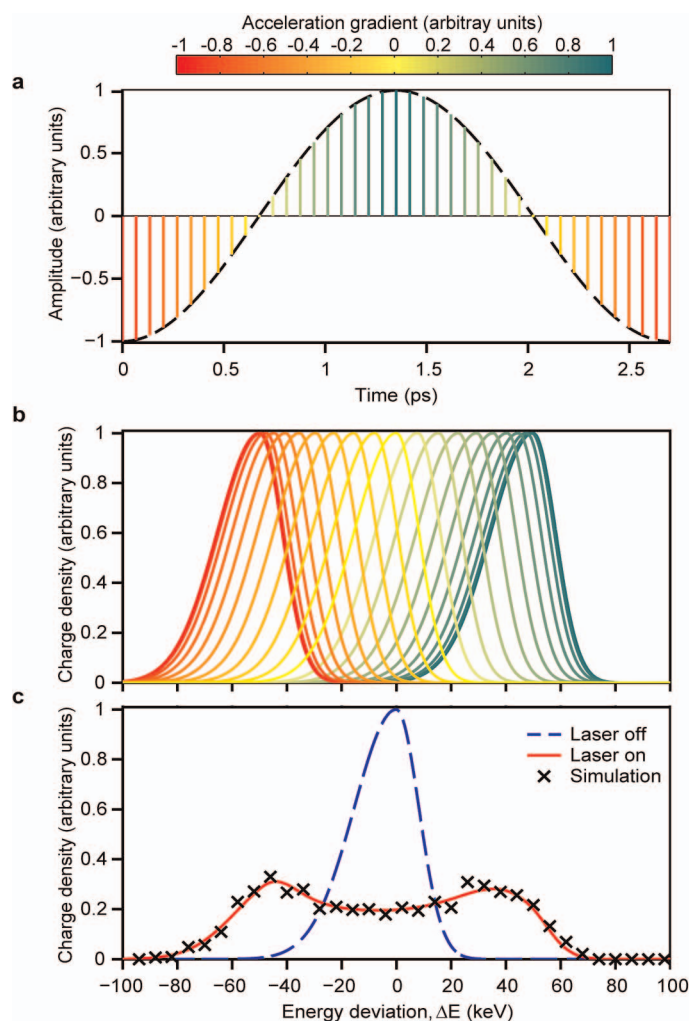
**b****d**

Extended Data Figure 1 | DLA sample preparation. **a**, Diagram of the structure fabrication process. In side view, the electron beam traverses the structure from left to right. In front view, the beam goes into the page. Laser is incident from above. See Methods for details. **b**, Picture of a completed wafer with hundreds of DLA structures. **c**, Diagram of a finished sample ready for

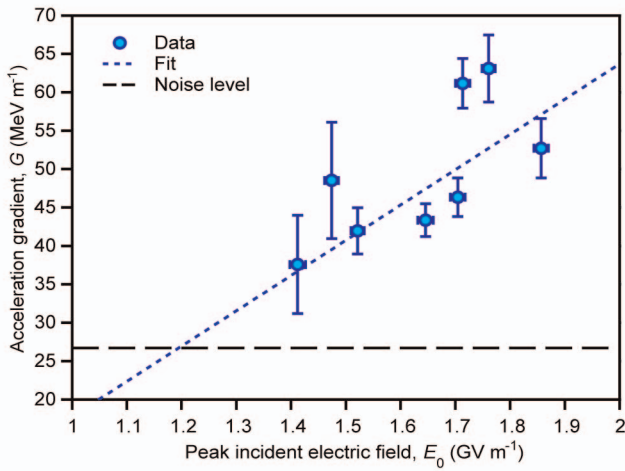
beam tests including four DLA structures, alignment channels, a wedge for spatial alignment of the laser to the electron beam, and a metal coating for perpendicular alignment of the laser. **d**, Picture of a single DLA structure on a fingertip.



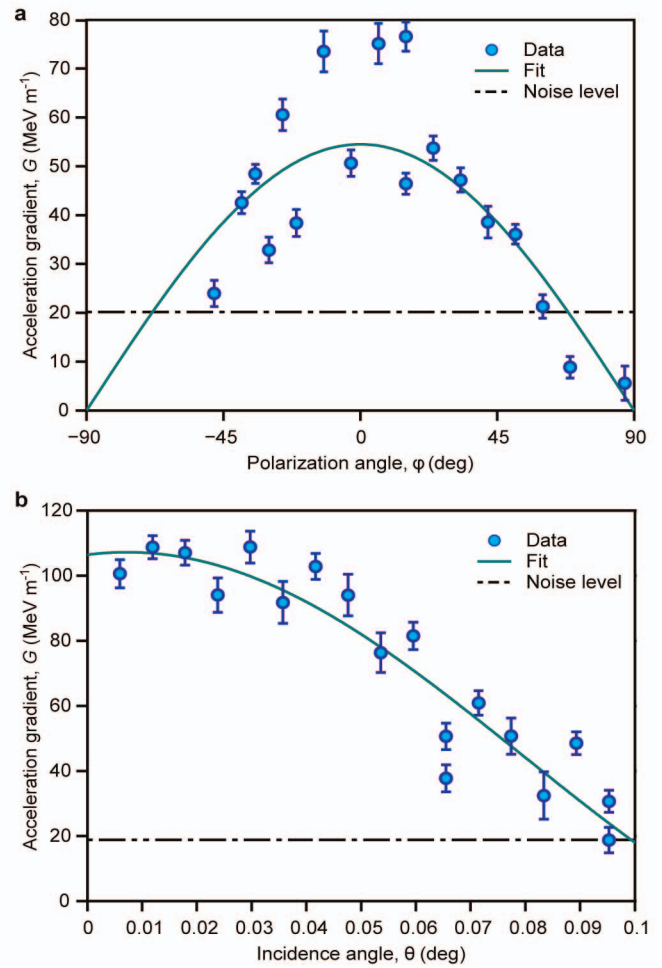
Extended Data Figure 2 | Reference spectrometer screen images and spectrum. **a**, Spectrometer screen image showing the 60-MeV beam with no DLA structure in place. **b**, Spectrometer screen image of the beam after traversing the grating structure. **c**, Projection of **b** onto the energy axis yields the energy spectrum (black crosses) in agreement with particle scattering simulations (blue dots). The corresponding least squares spectrum fit (orange curve) is also shown.



Extended Data Figure 3 | Analytical treatment of laser-driven electron energy modulation. **a**, Picosecond-scale electron beam partitioned into a series of finite slices over one optical cycle of the laser (for example, the green slice is at optimal phase for acceleration). **b**, Each slice samples a different phase of the laser pulse and therefore experiences a corresponding net energy shift with a negligible effect on the energy profile (for example, the green slice experiences net energy gain). **c**, When all contributions are superimposed, the initial single distribution (dashed blue line) becomes a double-peaked profile (red line), in agreement with particle tracking simulations (black crosses).



Extended Data Figure 4 | Gradient measurement on 800-nm gap structure. Calculated gradient (blue filled circles) G as a function of longitudinal electric field E_0 showing expected linear dependence (dashed blue line) and reduced strength when compared to the 400-nm gap structure, as expected for a larger gap. The dashed black line is the measurement noise level. Error bars, 68% confidence interval.



Extended Data Figure 5 | Experimental verification of direct laser acceleration. **a**, Gradient in the 800-nm gap structure for an input pulse energy of $105.2 \pm 3.6 \mu\text{J}$. As the laser polarization is rotated away from the direction of electron propagation by an angle ϕ , the acceleration gradient varies as $G \propto \cos\phi$. Data for $\phi < 0$ were taken last, and beam quality had degraded. **b**, Gradient in the 400-nm gap structure at an input pulse energy of $29.3 \pm 0.4 \mu\text{J}$, averaging the observed modulation over many shots taken at an optimal timing overlap. As the laser incidence angle deviates from perpendicular by an angle θ , the observed gradient decreases according to the expected relationship, equation (2) in Supplementary Information. Data are shown as blue filled circles with the corresponding least squares fit shown as green lines. The dashed black line is the measurement noise level. Error bars, 68% confidence interval.

Emergence of macroscopic directed motion in populations of motile colloids

Antoine Bricard^{1*}, Jean-Baptiste Caussin^{1,2*}, Nicolas Desreumaux¹, Olivier Dauchot³ & Denis Bartolo^{1,2}

From the formation of animal flocks to the emergence of coordinated motion in bacterial swarms, populations of motile organisms at all scales display coherent collective motion. This consistent behaviour strongly contrasts with the difference in communication abilities between the individuals. On the basis of this universal feature, it has been proposed that alignment rules at the individual level could solely account for the emergence of unidirectional motion at the group level^{1–4}. This hypothesis has been supported by agent-based simulations^{1,5,6}. However, more complex collective behaviours have been systematically found in experiments, including the formation of vortices^{7–9}, fluctuating swarms^{7,10}, clustering^{11,12} and swirling^{13–16}. All these (living and man-made) model systems (bacteria^{9,10,16}, biofilaments and molecular motors^{7,8,13}, shaken grains^{14,15} and reactive colloids^{11,12}) predominantly rely on actual collisions to generate collective motion. As a result, the potential local alignment rules are entangled with more complex, and often unknown, interactions. The large-scale behaviour of the populations therefore strongly depends on these uncontrolled microscopic couplings, which are extremely challenging to measure and describe theoretically. Here we report that dilute populations of millions of colloidal rolling particles self-organize to achieve coherent motion in a unique direction, with very few density and velocity fluctuations. Quantitatively identifying the microscopic interactions between the rollers allows a theoretical description of this polar-liquid state. Comparison of the theory with experiment suggests that hydrodynamic interactions promote the emergence of collective motion either in the form of a single macroscopic ‘flock’, at low densities, or in that of a homogenous polar phase, at higher densities. Furthermore, hydrodynamics protects the polar-liquid state from the giant density fluctuations that were hitherto considered the hallmark of populations of self-propelled particles^{2,3,17}. Our experiments demonstrate that genuine physical interactions at the individual level are sufficient to set homogeneous active populations into stable directed motion.

Our system consists of large populations of colloids capable of self-propulsion and of sensing the orientation of their neighbours solely by means of hydrodynamic and electrostatic mechanisms. We take advantage of an overlooked electrohydrodynamic phenomenon known as Quincke rotation^{18,19} (Fig. 1a). When an electric field, E_0 , is applied to an insulating sphere immersed in a conducting fluid, above a critical field amplitude, E_Q , the charge distribution at the sphere’s surface is unstable to infinitesimal fluctuations. This spontaneous symmetry breaking results in a net electrostatic torque, which causes the sphere to rotate at a constant speed around a random direction transverse to E_0 (ref. 18). We exploit this instability to engineer self-propelled colloidal rollers. We use poly(methyl methacrylate) beads of radius $a = 2.4 \mu\text{m}$ diluted in an hexadecane solution filling the gap between two conducting glass slides. Once the particles have sedimented on the bottom electrode, we apply a homogeneous electric field, and indeed observe them to start rolling at high speed (Fig. 1a). Isolated rollers, as

we refer to these particles, travel in random directions (Fig. 1b). Their velocity, v_0 , is set by E_0 and scales as $[(E_0/E_Q)^2 - 1]^{1/2}$ (Fig. 1c and Supplementary Methods).

To study the emergence of collective unidirectional motion, we electrically confine the roller populations in racetracks periodic in the curvilinear coordinate, s , that measures position along the track. Their width is $500 \mu\text{m} < W < 5 \text{ mm}$ (Fig. 2a and Methods). During a typical 10-min-long experiment, millions of rollers travel over distances as large as 10^5 – 10^6 particle radii, which makes it possible to investigate exceptionally large-scale dynamics. At low area fraction, ϕ_0 , the rollers form an isotropic gaseous phase. They all move at the same velocity in random directions, as would an isolated particle (Fig. 2b and Supplementary Video 1). On increasing ϕ_0 above a critical value, ϕ_c , we observe a clear transition to collective motion. A macroscopic fraction of the rollers self-organizes and its constituents cruise coherently in the same direction (Fig. 2c, d and Supplementary Videos 2–4). More quantitatively, we define a polarization order parameter, Π_0 , as the modulus of the time and ensemble average of the particle-velocity orientation. This parameter increases sharply with ϕ_0 and has a slope discontinuity at $\phi_c = 3 \times 10^{-3}$, revealing the strongly collective nature of the transition (Fig. 2e). Remarkably, ϕ_c is a material constant: it is independent of the electric field amplitude.

For area fractions higher than but close to ϕ_c , small density excitations nucleate from an unstable isotropic state and propagate in random directions. After complex collisions and coalescence events, the system phase separates to form a single macroscopic band that propagates at a constant velocity, c_{band} , through an isotropic gaseous phase (Figs 2a, c and 3a and Supplementary Videos 2 and 3). No stationary state involving more than a single band was observed even in the largest systems (10-cm long). The velocity c_{band} is found to be very close to the single-particle velocity, v_0 , at the front of the band. The bands are coupled to a net particle flux: they are colloidal flocks travelling through an isotropic phase. Their density profile is strongly asymmetric, unlike the slender bands observed in dense motility assays⁷. This marked asymmetry is akin to that found in one-dimensional, agent-based models²⁰. It might be promoted by the high aspect ratio of the confinement. The local area fraction at curvilinear coordinate s and time t , $\phi(s, t)$, increases sharply with s and then decays exponentially to a constant value, ϕ_∞ , which is very close to the critical volume fraction, ϕ_c (Fig. 3b). This behaviour is similar to that found in numerical simulations of the celebrated two-dimensional Vicsek model^{21,22}. Remarkably, the bands have no intrinsic scale and their length, L_{band} , is set by particle-number conservation only. This result is readily inferred from Fig. 3c, which shows that the bands span a fraction of the racetrack that merely increases with ϕ_0 regardless of the overall curvilinear length, L .

Looking now at the local polarization, we observe that the colloidal flock loses its internal coherence away from the band front as $\Pi(s, t)$ decays continuously to zero along the band. Quantitatively, $\phi(s, t)$ and $\Pi(s, t)$ are related in a universal manner irrespective of both the particle velocity and the mean volume fraction (Fig. 3d). All our data collapse

¹PMMH, CNRS UMR7636, ESPCI-ParisTech, Université Paris Diderot and Université Pierre et Marie Curie, 10 rue Vauquelin, 75005 Paris, France. ²Laboratoire de Physique, Ecole Normale Supérieure de Lyon, CNRS UMR5672, 46 allée d’Italie, F69007 Lyon, France. ³EC2M, CNRS UMR7083 Gulliver, ESPCI-ParisTech, 10 rue Vauquelin, 75005 Paris, France.

*These authors contributed equally to this work.

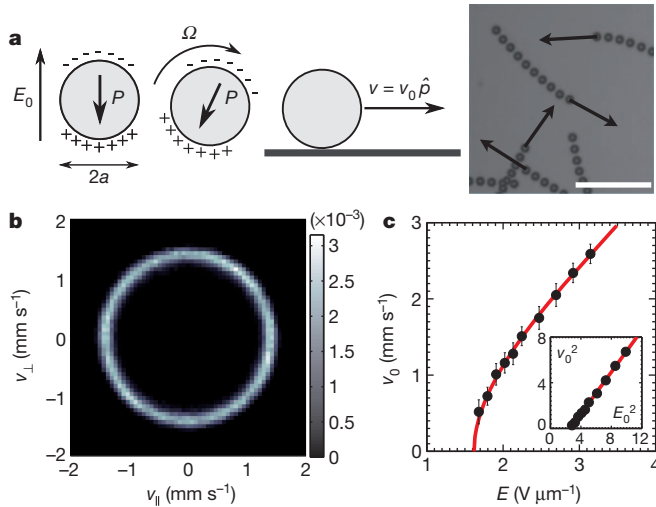


Figure 1 | Single-roller dynamics. **a**, Sketch of the Quincke rotation and of the self-propulsion mechanisms of a colloidal roller characterized by its electric polarization, P , and superposition of ten successive snapshots of colloidal rollers. Time interval, 5.6 ms; scale bar, 50 μm . **b**, Probability distribution of the velocity vector $(v_{\parallel}, v_{\perp})$ for isolated rollers: v_{\parallel} corresponds to the projection of the velocity on the direction tangent to the racetrack (Fig. 2); v_{\perp} is normal to v_{\parallel} . The probability distribution involves more than 1.4×10^5 measurements of instantaneous speed. **c**, Roller velocity, v_0 , plotted versus the field amplitude, E_0 . Inset, v_0^2 versus E_0^2 . The black dots represent the maximum of the probability distribution. Error bars, 1 s.d.

on a single master curve solely parameterized by the particle fraction, ϕ_{∞} , away from the band: $\Pi(s, t) = 1 - \phi_{\infty}/\phi(s, t)$. As it turns out, this relation corresponds to particle-number conservation in a system where density and polarization waves propagate steadily at a velocity v_0 (ref. 22 and Supplementary Methods). This observation unambiguously demonstrates that the band state corresponds to a genuine stationary flocking phase of colloidal active matter.

On further increasing the area fraction to more than $\phi_0 \approx 2 \times 10^{-2}$, transient bands eventually catch up with themselves along the periodic direction and form a homogeneous polar phase (Fig. 2d and Supplementary Video 4) in which the velocity distribution condenses on a single orientation of motion (Fig. 4a, to be contrasted with the perfectly

isotropic distribution for fractions less than ϕ_c in Fig. 1b). Conversely, the roller positions are weakly correlated, as evidenced by the shape of the pair-distribution function, which is similar to that found in low-density molecular liquids (Fig. 4b). We also emphasize that the density fluctuations are normal at all scales (Fig. 4c). This is experimental observation of a polar-liquid phase of active matter. The existence of a polar-liquid phase was theoretically established yet had not been observed in any prior experiment involving active materials. Until now, collective motion has been found to occur in the form of patterns with marked density, orientational heterogeneities or both^{7,10,13,14,16}. Furthermore, in contrast with the present observations, giant density fluctuations are considered to be a generic feature of the uniaxially ordered states of liquids comprising self-propelled particles^{2,3,17}. We resolve this apparent contradiction below and quantitatively explain our experimental observations.

From a theoretical perspective, the main advantage offered by the rollers is that their interactions are clearly identified. We show in Supplementary Methods how to establish the equations of motion of Quincke rollers interacting through electrostatic and far-field hydrodynamic interactions. They take a compact form both for the position r_i and the orientation \hat{p}_i of the i th particle:

$$\dot{r}_i = v_0 \hat{p}_i$$

$$\dot{\theta}_i = \frac{1}{\tau} \sum_{j \neq i} \frac{\partial}{\partial \theta_i} H_{\text{eff}}(r_i - r_j, \hat{p}_i, \hat{p}_j)$$

Here \hat{p}_i makes an angle θ_i with the x axis, and a dot denotes a time derivative. In dilute systems, the particle interactions do not affect their propulsion speed, yet the electric field and flow field compete to align the \hat{p}_i with them. This competition results in an effective potential, H_{eff} for the \hat{p}_i . At leading order in a/r

$$H_{\text{eff}}(r, p_i, p_j) = A(r) \hat{p}_i \cdot \hat{p}_j + B(r) \hat{p}_i \cdot \hat{r} \hat{r} \cdot \hat{p}_j + C(r) \hat{p}_i \cdot (2\hat{r}\hat{r} - I) \cdot \hat{p}_j$$

where $A(r)$ is a positive function and thus promotes the alignment of the neighbouring rollers, I is the identity matrix, $\hat{r}\hat{r}$ is the outer product of \hat{r} with itself, and a dot denotes tensor contraction. Importantly, A is dominated by a hydrodynamic interaction, which arises from a hydrodynamic-rotlet singularity screened over distances of the order of the chamber height²³. The function $B(r)$ is also short ranged and accounts

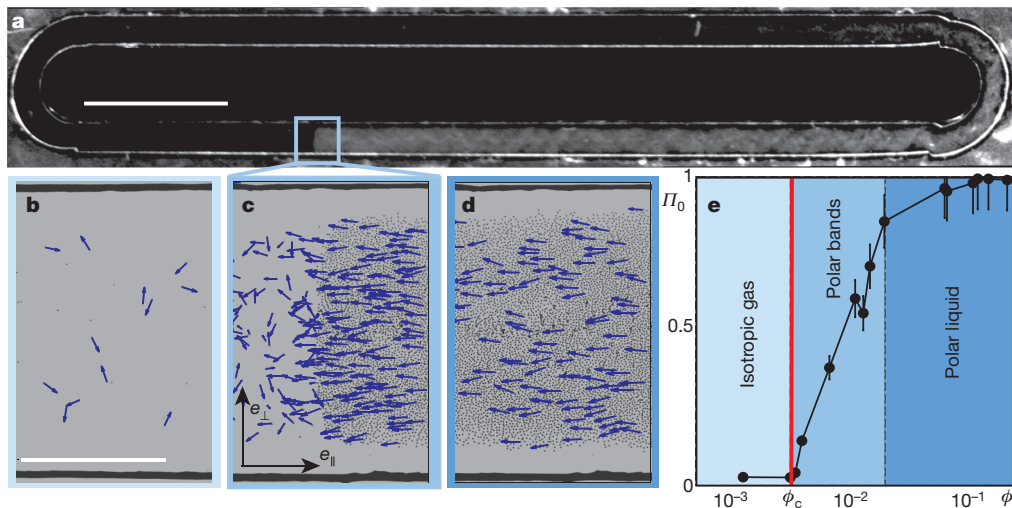


Figure 2 | Transition to directed collective motion. **a**, Dark-field pictures of a roller population that spontaneously forms a macroscopic band propagating along the racetrack. $E_0/E_Q = 1.39$, $\phi_0 = 10^{-2}$. Scale bar, 5 mm. **b–d** Close-up views. The arrows correspond to the roller displacement between two subsequent video frames (180 frames s^{-1}). **b**, Isotropic gas. $\phi_0 = 6 \times 10^{-4}$.

c, Propagating band. $\phi_0 = 10^{-2}$. **d**, Homogeneous polar liquid. $\phi_0 = 1.8 \times 10^{-1}$. Scale bar, 500 μm . **e**, Modulus of the average polarization, Π_0 , plotted versus the area fraction, ϕ_0 . Collective motion occurs as ϕ_0 exceeds $\phi_c = 3 \times 10^{-3}$. ϕ_c is independent of E_0 . Error bars, 1 s.d. e_{\parallel} (or e_{\perp}) is the unit vector oriented along the tangent (or the normal) of the racetrack confinement.

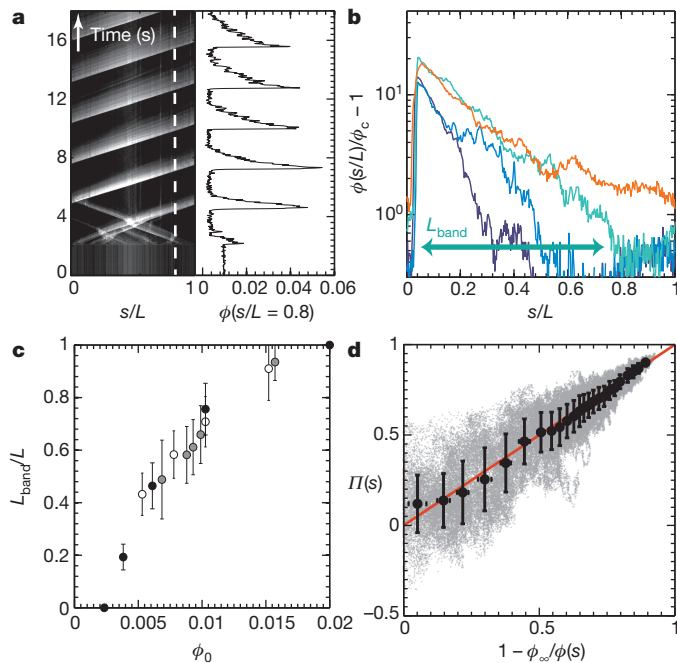


Figure 3 | Propagating-band state. **a**, Spatiotemporal variations of the area fraction measured along the curvilinear coordinate, s , and temporal variations of the area fraction at $s = 0.8L$ (white dashed line), where L is the overall length of the racetrack. **b**, Band shape plotted versus the rescaled curvilinear coordinate, s/L , for $\phi_0 = 5.3 \times 10^{-3}$ (dark blue), 7.8×10^{-3} (blue), 1.0×10^{-2} (cyan) and 1.5×10^{-2} (orange). **c**, The rescaled band length, L_{band}/L , increases with ϕ_0 and is independent of L (white dots, $L = 28$ mm; grey dots, $L = 50$ mm; black dots, $L = 73$ mm). Error bars show the estimated error associated with the measurement of L_{band} . **d**, $\Pi(s)$ plotted versus $1 - \phi_{\infty}/\phi(s)$. The black dots correspond to averages over 5,000 local measurements (grey dots). The red curve is the theoretical prediction. Error bars, 1 s.d.

for a dipolar repulsion. Conversely, $C(r)$ is long ranged and decays algebraically as r^{-2} owing to another hydrodynamic singularity induced by the roller motion in confinement. This singularity is referred to as a source doublet²⁴. Neither B nor C yields any net alignment interaction. If these two terms were neglected, our model built from the actual microscopic interactions would amount to the ‘flying xy model’ introduced on phenomenological grounds in ref. 25. We emphasize that H_{eff} is independent of v_0 and E_0 , and that it is not specific to the Quincke mechanism. Its form could have been deduced from generic arguments based on global rotational invariance.

We then use a conventional Boltzmann-like kinetic-theory framework to derive the large-scale equation of motion for the density, and the polarization fields^{22,25}. In the present case, this approximation was fully supported by the weak positional correlations in all the three phases, as exemplified in Fig. 4b. The resulting hydrodynamic equations are shown in Supplementary Methods. At the onset of collective motion, the magnitudes of the terms arising from the long-range hydrodynamic interactions are negligible. We are therefore left with equations for ϕ and Π akin to those in the model of refs 2, 3. However, we explicitly provide the functional form of the transport coefficients introduced on phenomenological grounds in ref. 2. Accordingly, we find that the competition between the polar ordering (induced by the short-range hydrodynamic interactions) and rotational diffusion yields a mean-field phase transition between an isotropic state and a macroscopically ordered state (Supplementary Methods). The phase transition occurs above a critical fraction, ϕ_c , that does not depend on the particle velocity (that is, on E_0), in agreement with our experiments: collective motion chiefly stems from hydrodynamic interactions between the electrically powered rollers. However, at the onset of collective motion (that is, for $\phi_0 > \phi_c$), the homogeneous polar state is linearly unstable to spatial

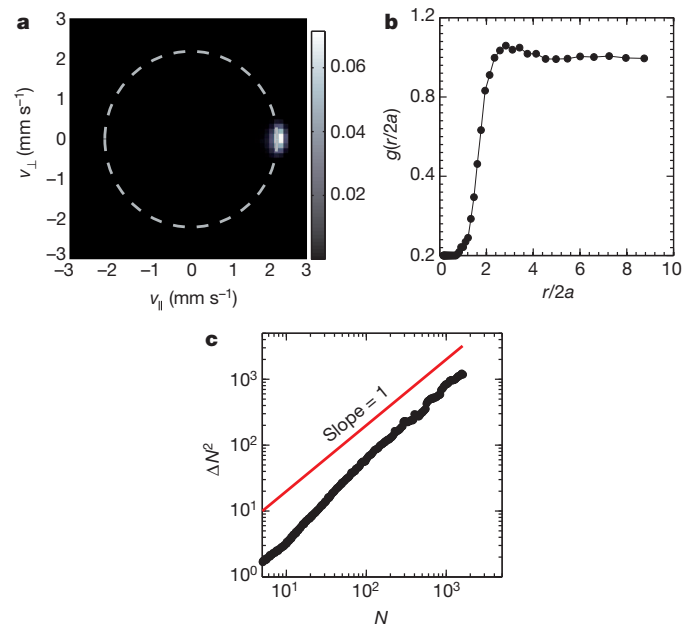


Figure 4 | Polar-liquid state. **a**, Probability distribution of the velocity vector (v_{\parallel} , v_{\perp}) in the polar-liquid state. The probability distribution involves more than 3.2×10^7 measurements of instantaneous speed. **b**, Pair correlation function, g , of the particle position in the polar-liquid state. **c**, The variance of the number of colloids, ΔN^2 , scales linearly with the average number of colloids, N , counted inside boxes of increasing size. $E_0/E_Q = 1.39$, $\phi_0 = 9.5 \times 10^{-2}$.

heterogeneities. Moreover, for $\phi_0 > \phi_c$, the compression modes are unstable eigenmodes of the isotropic state, in agreement with the emergence of density bands observed in the experiments, all starting from a homogeneous state and an isotropic velocity distribution.

We also rigorously establish a kinetic theory for the strongly polarized state reached for $\phi_0 > \phi_c$ (Supplementary Methods). In this regime, the short-range electrostatic repulsion matters, causing the density fluctuations to relax and stabilizing the polar-liquid state. In addition, the long-range hydrodynamic interactions further stabilize the system by damping the modes of Π with non-zero divergence, that is, the splay modes that couple orientation disturbances to density fluctuations²⁴. As a result, the giant density fluctuations²⁶ are suppressed, in agreement with our unanticipated experimental findings (Fig. 4c and Supplementary Methods). We stress here that these long-range hydrodynamic interactions do not depend at all on the propulsion mechanism at the individual level. They solely arise from the confinement of the fluid in the z direction²⁴. They are therefore not specific to the Quincke propulsion mechanism.

The only way to destroy the robust polar-liquid phase is to prevent it geometrically by eliminating the angular periodicity of the confinement in the curvilinear coordinate. In rectangular geometries with large enough aspect ratios, we observe that the bands never relax but rather bounce endlessly against the confining box (Supplementary Video 5). In confinement with an aspect ratio of order one, the band state is replaced by a single macroscopic vortex (Supplementary Video 6).

We have engineered large-scale populations of self-propelled particles from which collective macroscopic polar motion emerges from hydrodynamic interactions at exceptionally small densities. We believe that control over their interactions, and the ease with which they can be confined in custom geometries, will extend the present framework of active matter to include collective motion in more complex environments relevant to biological, robotic and social systems.

METHODS SUMMARY

We use commercial poly(methyl methacrylate) colloids (Thermo Scientific G0500; 2.4- μm radius), dispersed in a 0.15 mol l⁻¹ AOT/hexadecane solution. The suspension is injected into a wide microfluidic chamber made of double-sided Scotch

Tape. The tape is sandwiched between two ITO-coated glass slides (Solems, ITOSOL30; 80-nm thick). To achieve electric confinement, an additional layer of Scotch Tape including a hole with the desired geometry is added to the upper ITO-coated slide. The holes are made with a precision plotting cutter (Graphtec Robo CE 5000). The gap between the two ITO electrodes, $H = 220\ \mu\text{m}$, is constant over the entire chamber. The electric field is applied by means of a voltage amplifier (Trek 606E-6). The colloids are observed with a Nikon AMZ1500 stereomicroscope ($\times 1$ magnification) equipped with a dark-field illuminator, and with a Zeiss Axiovert microscope ($\times 10$ objective) for local measurements. In both case, high-speed videos are taken with CMOS camera (Basler Ace) at frame rates between 70 and 900 frames per second. The particles are detected to a precision of one pixel by locating the intensity maxima on the experimental pictures. The particle trajectories are reconstructed using a conventional tracking code²⁷.

Received 17 May; accepted 12 September 2013.

- Vicsek, T., Czirók, A., Ben-Jacob, E., Cohen, I. & Shochet, O. Novel type of phase transition in a system of self-driven particles. *Phys. Rev. Lett.* **75**, 1226–1229 (1995).
- Toner, J., Tu, Y. & Ramaswamy, S. Hydrodynamics and phases of flocks. *Ann. Phys.* **318**, 170–244 (2005).
- Marchetti, M. C. *et al.* Hydrodynamics of soft active matter. *Rev. Mod. Phys.* **85**, 1143–1189 (2013).
- Vicsek, T. & Zafeiris, A. Collective motion. *Phys. Rep.* **517**, 71–140 (2012).
- Grégoire, G. & Chaté, H. Onset of collective and cohesive motion. *Phys. Rev. Lett.* **92**, 025702 (2004).
- Buhl, J. *et al.* From disorder to order in marching locusts. *Science* **312**, 1402–1406 (2006).
- Schaller, V., Weber, C., Semmrich, C., Frey, E. & Bausch, A. R. Polar patterns of driven filaments. *Nature* **467**, 73–77 (2010).
- Sumino, Y. *et al.* Large-scale vortex lattice emerging from collectively moving microtubules. *Nature* **483**, 448–452 (2012).
- Wioland, H., Woodhouse, F. G., Dunkel, J., Kessler, J. O. & Goldstein, R. E. Confinement stabilizes a bacterial suspension into a spiral vortex. *Phys. Rev. Lett.* **110**, 268102 (2013).
- Zhang, H. P., Be'er, A., Florin, E.-L. & Swinney, H. L. Collective motion and density fluctuations in bacterial colonies. *Proc. Natl Acad. Sci. USA* **107**, 13626–13630 (2010).
- Theurkauff, I., Cottin-Bizonne, C., Palacci, J., Ybert, C. & Bocquet, L. Dynamic clustering in active colloidal suspensions with chemical signaling. *Phys. Rev. Lett.* **108**, 268303 (2012).
- Palacci, J., Sacanna, S., Steinberg, A. P., Pine, D. J. & Chaikin, P. M. Living crystals of light-activated colloidal surfers. *Science* **339**, 936–940 (2013).
- Sanchez, T., Chen, D. T. N., DeCamp, S., Heymann, M. & Dogic, Z. Spontaneous motion in hierarchically assembled active matter. *Nature* **491**, 431–434 (2012).
- Deseigne, J., Dauchot, O. & Chaté, H. Collective motion of vibrated polar disks. *Phys. Rev. Lett.* **105**, 098001 (2010).
- Kudrolli, A., Lumay, G., Volfson, D. & Tsimring, L. Swarming and swirling in self-propelled polar granular rods. *Phys. Rev. Lett.* **100**, 058001 (2008).
- Dombrowski, C., Cisneros, L., Chatkaew, S., Goldstein, R. E. & Kessler, J. O. Self-concentration and large-scale coherence in bacterial dynamics. *Phys. Rev. Lett.* **93**, 098103 (2004).
- Aditi Simha, R. & Ramaswamy, S. Hydrodynamic fluctuations and instabilities in ordered suspensions of self-propelled particles. *Phys. Rev. Lett.* **89**, 058101 (2002).
- Quincke, G. Ueber Rotationen im constanten electrischen Felde. *Ann. Phys. Chem.* **59**, 417–486 (1896).
- Melcher, J. R. & Taylor, G. I. Electrohydrodynamics: a review of the role of interfacial shear stresses. *Annu. Rev. Fluid Mech.* **1**, 111–146 (1969).
- O'Loan, O. J. & Evans, M. R. Alternating steady state in one-dimensional flocking. *J. Phys. A* **32**, L99 (1999).
- Chaté, H., Ginelli, F., Grégoire, G. & Raynaud, F. Collective motion of self-propelled particles interacting without cohesion. *Phys. Rev. E* **77**, 046113 (2008).
- Bertin, E., Droz, M. & Grégoire, G. Hydrodynamic equations for self-propelled particles: microscopic derivation and stability analysis. *J. Phys. A* **42**, 445001 (2009).
- Hackborn, W. W. Asymmetric Stokes flow between parallel planes due to a rotlet. *J. Fluid Mech.* **218**, 531–546 (1990).
- Brotto, T., Caussin, J.-B., Lauga, E. & Bartolo, D. Hydrodynamics of confined active fluids. *Phys. Rev. Lett.* **110**, 038101 (2013).
- Farrell, F. D. C., Marchetti, M. C., Marenduzzo, D. & Tailleur, J. Pattern formation in self-propelled particles with density-dependent motility. *Phys. Rev. Lett.* **108**, 248101 (2012).
- Schaller, V. & Bausch, A. R. Topological defects and density fluctuations in collectively moving systems. *Proc. Natl Acad. Sci. USA* **110**, 4488–4493 (2013).
- Crocker, J. C. & Grier, G. Methods of digital video microscopy for colloidal studies. *J. Colloid Interface Sci.* **179**, 298–310 (1996).

Supplementary Information is available in the online version of the paper.

Acknowledgements We acknowledge support from the Paris Emergence programme (D.B.), C'Nano IdF (D.B.) and the Institut Universitaire de France (D.B.). We thank L. S. Tuckerman and H. Chaté for their useful comments and suggestions.

Author Contributions A.B. and N.D. performed the experiments. A.B., N.D., O.D. and D.B. analysed the experimental results. D.B. conceived the project and designed the experiments. J.-B.C. and D.B. worked out the theory and wrote the Supplementary Methods. J.-B.C., O.D. and D.B. wrote the paper.

Author Information Reprints and permissions information is available at www.nature.com/reprints. The authors declare no competing financial interests. Readers are welcome to comment on the online version of the paper. Correspondence and requests for materials should be addressed to D.B. (denis.bartolo@ens-lyon.fr).

Colloidal assembly directed by virtual magnetic moulds

Ahmet F. Demirörs¹, Pramod P. Pillai¹, Bartłomiej Kowalczyk¹ & Bartosz A. Grzybowski¹

Interest in assemblies of colloidal particles^{1–4} has long been motivated by their applications in photonics^{5,6}, electronics^{7,8}, sensors⁸ and microlenses⁹. Existing assembly schemes^{10–15} can position colloids of one type relatively flexibly into a range of desired structures, but it remains challenging to produce multicomponent lattices, clusters with precisely controlled symmetries and three-dimensional assemblies¹⁶. A few schemes can efficiently produce complex colloidal structures^{2,17,18}, but they require system-specific procedures. Here we show that magnetic field microgradients established in a paramagnetic fluid^{19,20} can serve as ‘virtual moulds’ to act as templates for the assembly of large numbers ($\sim 10^8$) of both non-magnetic and magnetic colloidal particles with micrometre precision and typical yields of 80 to 90 per cent. We illustrate the versatility of this approach by producing single-component and multicomponent colloidal arrays, complex three-dimensional structures and a variety of colloidal molecules from polymeric particles, silica particles and live bacteria and by showing that all of these structures can be made permanent. In addition, although our magnetic moulds currently resemble optical traps in that they are limited to the manipulation of micrometre-sized objects, they are massively parallel and can manipulate non-magnetic and magnetic objects simultaneously in two and three dimensions.

We use magnetic fields to manipulate either paramagnetic or diamagnetic colloids simultaneously. The magnetostatic potential experienced by a particle of radius a in an applied field H at location r is given by

$$U_M(r) = -2\pi a^3 \mu_0 \frac{\chi_{\text{part}} - \chi_{\text{sol}}}{\chi_{\text{part}} + 2\chi_{\text{sol}} + 3} |H(r)|^2$$

where μ_0 is the magnetic permeability of free space, and χ_{part} and χ_{sol} are the magnetic susceptibilities of the particle and of the dispersing medium or solution, respectively. Although magnetic effects on diamagnetic particles are typically small, this limitation can be circumvented by adjusting the magnetic susceptibility contrast between the particles and the solution, $\chi_{\text{part}} - \chi_{\text{sol}}$. In particular, the magnetic susceptibilities of solutions of paramagnetic salts (such as $\text{Ho}(\text{NO}_3)_3$) can be tuned²¹ so that $\chi_{\text{part}}^{\text{dia}} < \chi_{\text{sol}} < \chi_{\text{part}}^{\text{para}}$. In these circumstances, the magnetostatic forces $F_m = -\nabla U_m$ attracting paramagnetic particles to, and expelling diamagnetic particles from, the regions of high field can be made to have comparable magnitudes. We expected that this effect, combined with the patterning of magnetic fields on length scales commensurate with particle sizes, could be used to manipulate or position both paramagnetic and diamagnetic particles.

The magnetic field patterns are produced by using nickel grids of the desired geometry and typical periodicity $L \sim 1\text{--}10\ \mu\text{m}$. These grids were embedded in a layer of poly(dimethyl siloxane) (PDMS) about 300 nm thick and then placed on a permanent magnet of typical strength 0.442 T. (For fabrication details see Supplementary Fig. 1.) The nickel/PDMS composite film (Supplementary Fig. 2) concentrates and modulates the otherwise uniform field of the magnet, with the finite-element calculations in Fig. 1a illustrating how this modulation translates into in-plane forces attracting paramagnetic particles onto the nickel regions and diamagnetic particles onto the voids of the grid.

We first assemble two-dimensional arrays of fluorescently labelled colloidal particles by flowing colloidal suspensions in an index-matched solution (0.2–0.4 M $\text{Ho}(\text{NO}_3)_3$ in DMSO/ H_2O ; see Supplementary

Information for full specifications) over the grid at $\sim 10^6\ \mu\text{s}^{-1}\text{cm}^{-2}$. As expected, magnetic particles localize onto the nickel islands (Fig. 1b) and non-magnetic particles localize to the grid voids (Fig. 1c and Supplementary Figs 5 and 6). The assemblies are highly regular over areas as large as $2\text{ cm} \times 2\text{ cm}$ (see Supplementary Figs 5f and 7a), corresponding to $O(10^8)$ assembled particles. Magnetic and non-magnetic colloids can also be addressed simultaneously to create multicomponent arrays, such as the AB lattice of similarly sized magnetic and non-magnetic particles assembled on a square grid shown in Fig. 1d. When particle sizes differ substantially, steric effects can become important, as in the AB_2 structure in Fig. 1e: the smaller paramagnetic particles only fit onto the threefold junctions of the honeycomb grid, but not onto its edges between proximal larger particles.

In the binary systems discussed so far, particle separation was based predominantly on the differences in their magnetic susceptibilities. The magnetophoretic forces, however, can also discriminate between particles having the same χ_{part} but different sizes (because magnetostatic potential scales with particle volume, $U_M \propto d_{\text{part}}^3$). This makes it possible to assemble structures comprising two types of diamagnetic colloid—when such particles assemble onto the voids of the nickel grid, it is most energetically favourable for the large particle to occupy the void’s centre, leaving only the peripheral region available for the smaller particles (see ‘halo’ structures in the Supplementary Information and Supplementary Fig. 6c, d). This mode of assembly can be also combined with the positioning of paramagnetic colloids to yield ternary structures as shown in Fig. 1f, where the paramagnetic particles (violet) localize onto nickel islands, the larger diamagnetic particles (green) centre in the spaces between four nearby islands, and the small diamagnetic colloids (orange) occupy the rest of the nickel-free surface.

When the magnet is removed, the ‘virtual magnetic mould’ organizing the particles is lost and the assemblies fall apart. But the structures can be made permanent by fixing them to the substrate by means of carbamide bonds, so they can be transferred into polymers such as PDMS to give diffraction elements and photolithographic masks (see Supplementary Information and Supplementary Figs 7–9).

By exploiting the fact that islands larger than the assembling particles will harbour several particles in a configuration that depends on the island’s shape and relative island-to-particle dimensions, we can also use our virtual moulds to drive the assembly of colloidal clusters, also known as colloidal ‘molecules’. The large-area confocal image in Fig. 2a shows an example of an array in which each ‘void’ accumulates four diamagnetic particles. These tetramers A_4 are then attached to the substrate with carbamide bonds, made permanent by silica deposition (see Supplementary Information) and liberated into solution on sonication (Fig. 2b). We have similarly assembled A_6 hexamers in triangular voids (Fig. 2c). The AB dimer in Fig. 2d illustrates the assembly of multicomponent colloidal molecules, which in this example arises because the egg-shaped voids are too small to fit two large ($1.2\ \mu\text{m}$) particles but are able to accommodate one large and one smaller (800 nm) diamagnetic particle. After silica deposition and sonication, these dimers can again be liberated into solution. Voids of other shapes and sizes allow us to assemble particles into AB_2 (Fig. 2e), AB_3 (Fig. 2f) and even A_2B_2 (Fig. 2g) clusters.

The magnetic fields of our virtual moulds extend into the bulk fluid; the plot of magnetic field strength over a nickel grid in Fig. 3a shows

¹Department of Chemistry and Department of Chemical and Biological Engineering, Northwestern University, Evanston, Illinois 60208, USA.

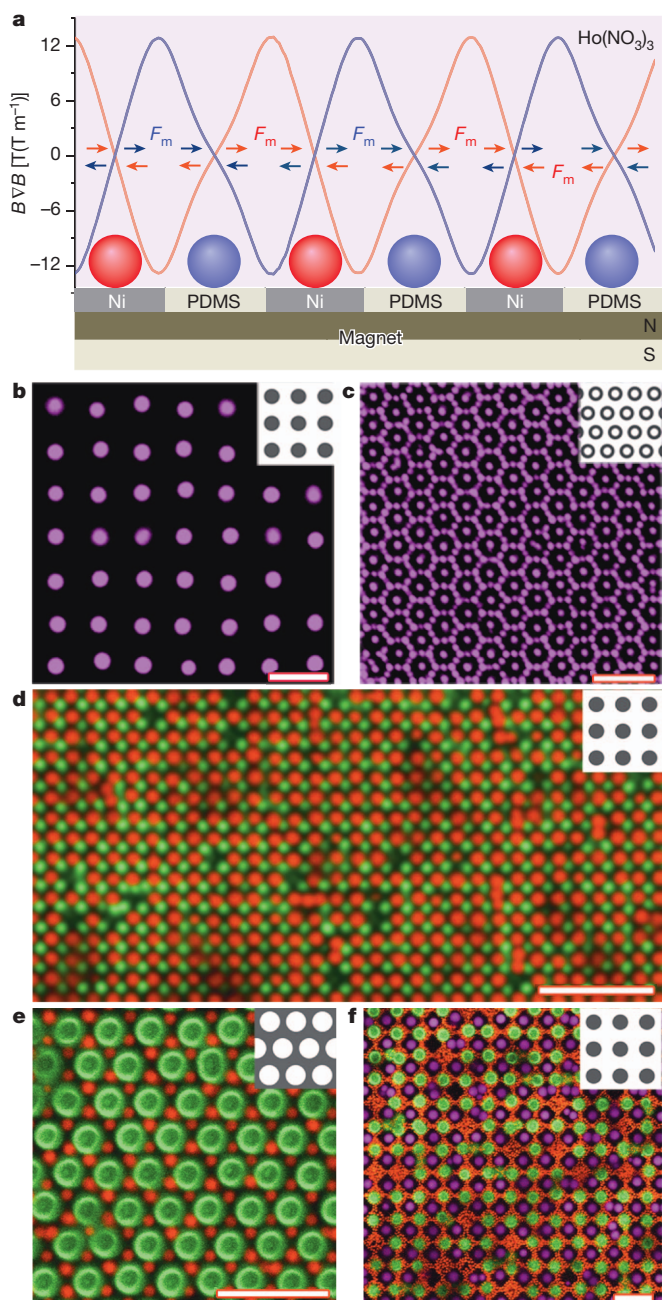


Figure 1 | Micropatterned magnetophoretic forces direct the assembly of single-component and multicomponent colloidal arrays. **a**, Scheme of experimental arrangement and calculated force profiles (see Supplementary Figs 3 and 4). Lateral magnetic forces (arrows labelled F_m) position magnetic particles (red) onto the nickel 'islands' of the grid and non-magnetic particles (blue) onto the 'voids' of the grid. **b**, Magnetic particles $2.85\ \mu\text{m}$ in size assembled on a square grid of nickel islands. Fidelity of the assembly, defined as the percentage of lattice sites without defects, was $f = 97 \pm 2\%$. **c**, Diamagnetic particles $1.2\ \mu\text{m}$ in size arranged in the voids of a hexagonal grid of nickel rings; $f = 95 \pm 3\%$. **d**, Paramagnetic particles (red; $1\ \mu\text{m}$) and diamagnetic particles (green; $1.2\ \mu\text{m}$) organize into an AB lattice on the underlying square grid; $f = 93 \pm 6\%$. **e**, Paramagnetic particles (red; $1.5\ \mu\text{m}$) and non-magnetic particles (green; $2.5\ \mu\text{m}$) on a hexagonal grid form an AB_2 hexagonal lattice; $f = 97 \pm 1\%$. **f**, Tertiary assembly of $2.65\text{-}\mu\text{m}$ magnetic particles (purple) together with $3.2\text{-}\mu\text{m}$ (green) and 800-nm (red) non-magnetic particles on a square nickel grid. The fidelity of the purple particles' assembly was $f = 92 \pm 5\%$; that of green particles was $f = 90 \pm 6\%$ (note that the arrangement of the 800-nm particles is not crystalline). All f values reported for this and subsequent crystalline or cluster assemblies are based on statistics for at least 500 particles and, in most cases, more than 1,000 particles, counted based on at least five (and up to ten) different images from at least three (up to seven) different samples. Scale bars, $10\ \mu\text{m}$. The insets illustrate the underlying nickel grids.

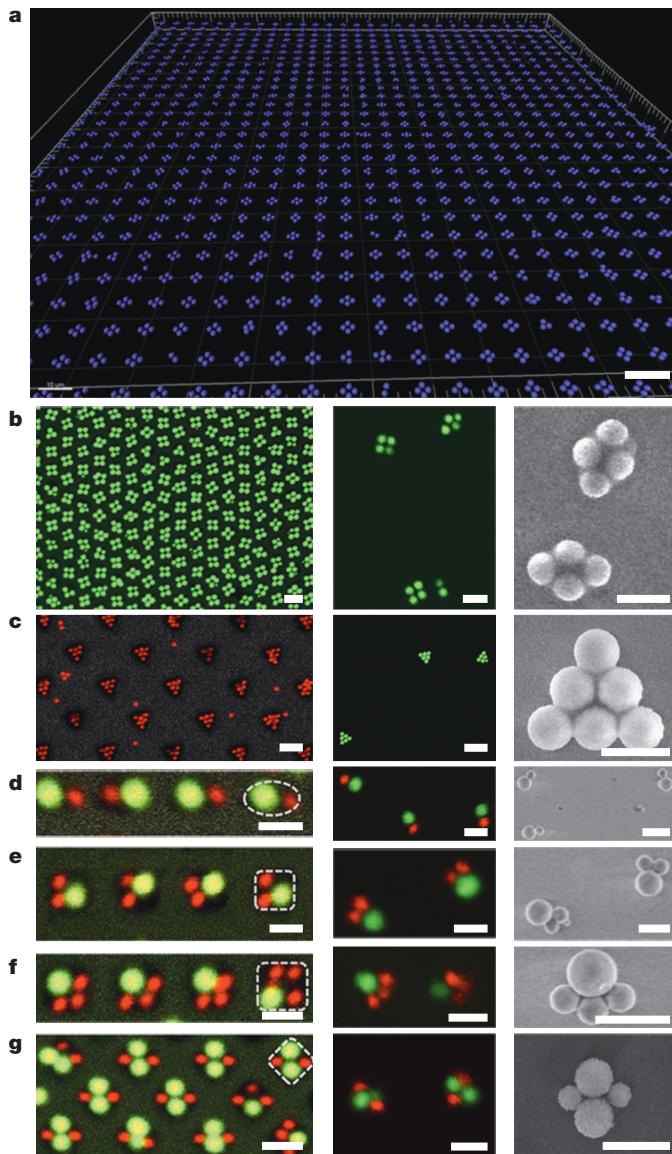


Figure 2 | Planar colloidal molecules. **a**, Large-area confocal image of a monolayer of $1.2\text{-}\mu\text{m}$ diamagnetic particles assembled into tetramers over $2.5\text{-}\mu\text{m}$ round voids of a nickel grid; $f = 84 \pm 5\%$. **b**, Left: the same array fixed to the PDMS substrate by means of isocyanate-amino chemistry and with particles bonded to one another by silica deposition. Middle: confocal image of the bonded particles liberated into solution by sonication. Right: scanning electron microscope (SEM) image of liberated tetramers after drying. **c**, Analogous images of hexamers of $1.2\text{-}\mu\text{m}$ particles assembled on $3\text{-}\mu\text{m}$ triangular voids; $f = 80 \pm 10\%$. **d–g**, Examples of colloidal molecules comprising two types of diamagnetic particles ($1.2\ \mu\text{m}$ (green) and $800\ \text{nm}$ (red)). Fidelities f are $90 \pm 4\%$ in **d**, $70 \pm 6\%$ in **e**, $68 \pm 7\%$ in **f**, and $57 \pm 6\%$ in **g**. Dashed lines outline the contours of the grid voids. Scale bars, $2\ \mu\text{m}$. See also Supplementary Movies 1–4.

that the field is effectively modulated up to a distance above the magnetic islands that is commensurate with their size. We should thus be able to organize colloidal particles into three-dimensional structures. Indeed, small diamagnetic particles introduced above a grid in large quantities pack over the nickel-free voids of the grid and form regular arrays of posts (Fig. 3c). By exploiting the size dependence of magnetic forces acting on non-magnetic particles (see above, Fig. 1f and Supplementary Fig. 6c, d), we can create such posts with complex internal structures. In the example in Fig. 3c, d, the larger particles (green) are expelled from the high-field regions more strongly than the smaller particles; this effect results in pillars with core-and-shell cross-sections. Another

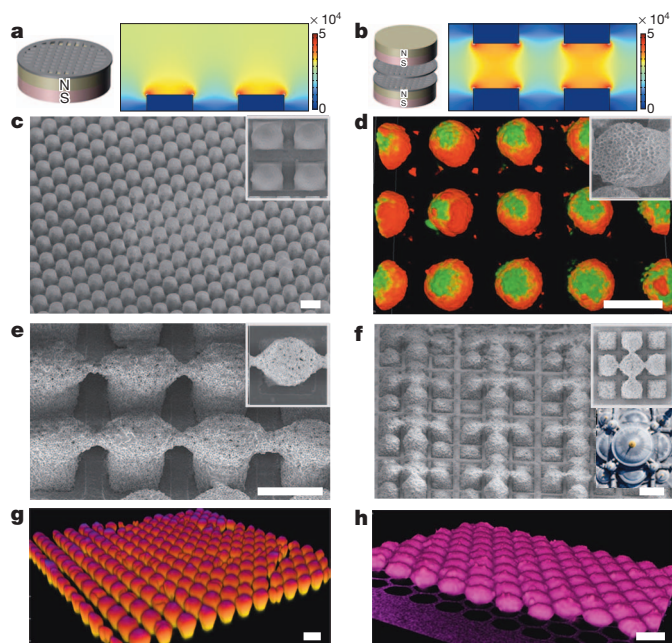


Figure 3 | Magnetic moulds directing the assembly of single-component and multicomponent three-dimensional colloidal structures. **a**, Profile of magnetic field strength above a nickel grid placed on a permanent magnet. **b**, Analogous profile of magnetic field strength but between two aligned nickel grids placed between two permanent magnets. **c**, Large-area SEM image of an array of posts formed by 2.5- μm and 800-nm diamagnetic particles. Inset: magnified top view. **d**, Confocal image of the posts shows that larger particles (green) localize mostly to the core of each post, whereas smaller particles (red) form an outer layer. This core-and-shell arrangement is confirmed by the inset SEM image of a post that was cut with a razor blade at approximately half-height. **e**, Diamagnetic particles 2.5 μm in size assemble into three-dimensional bridges. Inset: top view of one of the pillars. **f**, The same particles assembled into structures inspired by the architecture of the Blue Mosque (lower inset). For the architecture of the underlying nickel grids, see Supplementary Information and Supplementary Fig. 10. **g, h**, 'Fabergé eggs' formed between two nickel grids from 1.2- μm diamagnetic particles. The two structures differ in the amount of particles assembled. All particles used here were $-\text{NH}_2$ functionalized, and before imaging the assembled structures were fixed by the addition of glutaraldehyde (50 μl of 25% solution per 1 ml of $\text{Ho}(\text{NO}_3)_3$ solution). Scale bars, 40 μm .

effect is illustrated in Fig. 3e, where excess non-magnetic particles connect nearby posts along 'arcs' in which magnetic forces are balanced by gravity (that is, these particles are magnetically 'levitated'²² above high-field nickel regions; for calculations see Supplementary Fig. 10). The most sophisticated structure, shown in Fig. 3f, is inspired by the architecture of the famous Blue Mosque in Istanbul and features larger 'domes' connected by arcs and surrounded by four smaller and unconnected satellite 'domes'. The heights of the copulas and the arrangement of arcs reflect the varying widths of different portions of the underlying nickel grid (and thus various field strength and forces acting on the assembling particles at different locations; see Supplementary Fig. 10). These examples illustrate that we can create intricate three-dimensional structures, but they are spatially limited by the decay of the magnetic field away from the grid. This constraint can be overcome by aligning two nickel grids that are each placed on a magnet, thereby modulating the magnetic field through the entire $\text{Ho}(\text{NO}_3)_3$ solution layer between the grids (see Figure 3b). In such fields, non-magnetic particles assemble according to the field profiles into egg-shaped structures that connect the two grids (Fig. 3g, h). The same principles guide the assembly of three-dimensional colloidal molecules when using grids with smaller periodicities that are commensurate with particle sizes. Figure 4 shows examples of such structures, including single-component (for example A_4 – A_7) and binary (for example A_4B and A_5B) clusters of diamagnetic

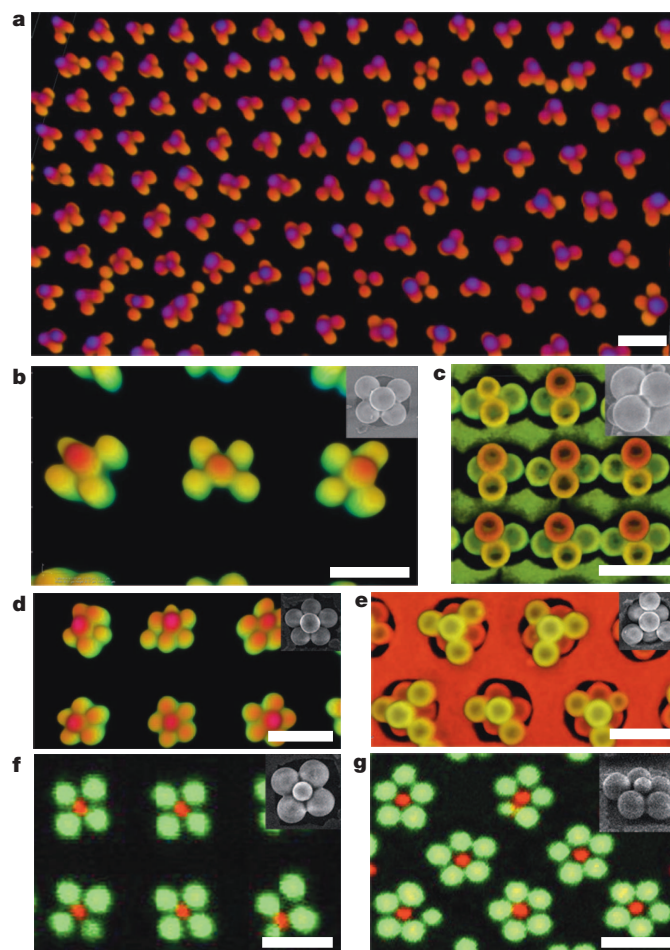


Figure 4 | Assembly of three-dimensional colloidal molecules. **a, b, d**, Single-component 'molecules' of diamagnetic particles: triangular, A_4 (**a**), square, A_5 (**b**) and pentagonal, A_6 (**d**), pyramids made of 1.2- μm particles. **c**, Tetrahedra, A_4 , made of 2.5- μm particles. **e**, Particles 2.5 μm in size assembled into A_7 structures. **f, g**, Multicomponent assemblies of diamagnetic particles: A_4B (**f**) and A_5B pyramids (**g**); A particles (green) are 1.2 μm , and B (red) are 800 nm. Colour coding in the confocal images in (**a**–**e**) corresponds to height; in **f** and **g** different colours represent different types of fluorescently labelled particle. Insets show SEM images. Scale bars, 2 μm . Fidelities for all assemblies were $f > 80\%$. In single-component structures, all particles were functionalized with polyethylenimine (PEI; molecular mass 25 kDa) such that they bound to the isocyanate-functionalized grid surface and also to one another, by chain entanglement²⁷. These polymer–polymer interactions promoted attachment of the top-layer, lower-trapping-stiffness particles (see Supplementary Fig. 3a). For multicomponent structures, planar clusters were first assembled from amine-modified particles forming carbamide bonds with the substrate; they were subsequently modified with isocyanate groups to which the top-layer PEI-functionalized particles of another type then bound. Once made, all structure types were permanently fixed by crosslinking amine functionalities with glutaraldehyde (50 μl of 25% solution per 1 ml of $\text{Ho}(\text{NO}_3)_3$ solution; for further details see Supplementary Information).

particles assembled over micrometre-sized islands. In all cases the assemblies form reliably over large areas with fidelities better than 80%, which significantly exceeds the yield achieved with other recent strategies^{4,18,23} for creating colloidal molecules (see Supplementary Fig. 11).

The magnetic moulds can manipulate objects other than colloids. Perhaps the most striking example is shown in Fig. 5a, in which live *Staphylococcus aureus* bacteria in $\text{Ho}(\text{NO}_3)_3$ at a concentration of less than 0.3 M (see also Supplementary Fig. 12) are positioned onto the voids of a square grid. The hybrid structure in Fig. 5b comprises smaller live bacteria forming halos around larger non-magnetic colloids centring

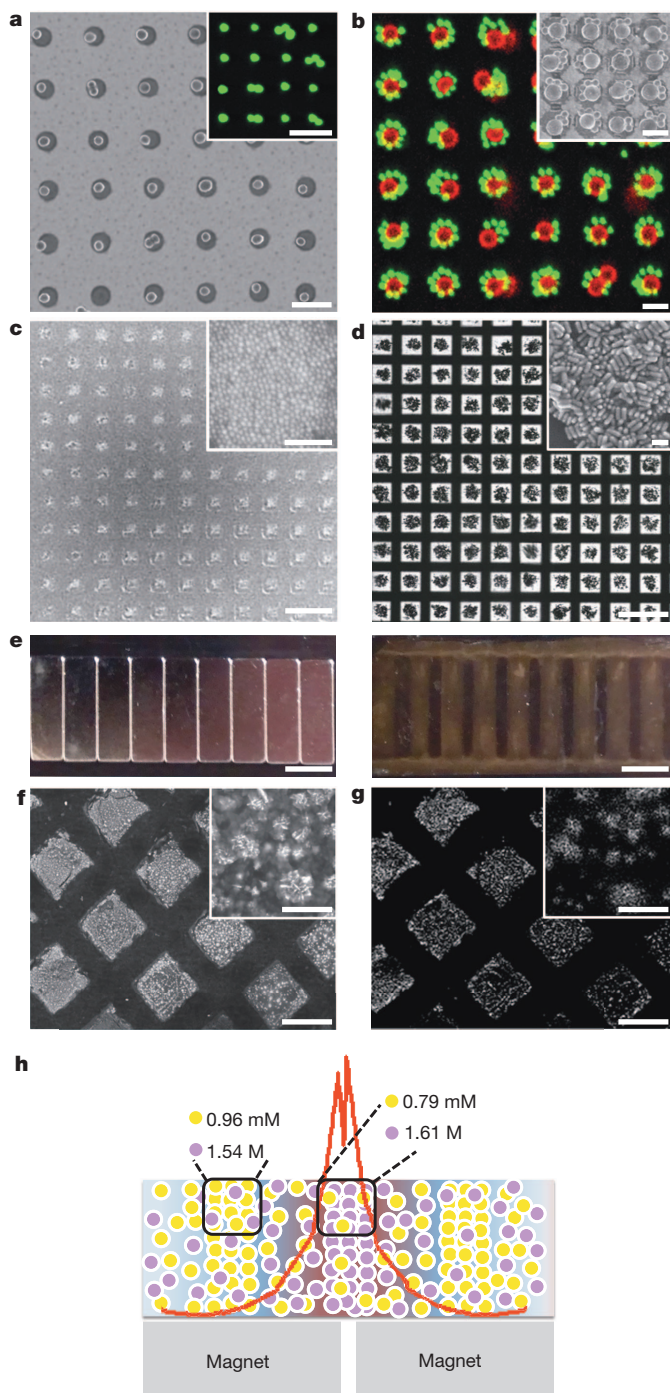


Figure 5 | Magnetic positioning of live bacteria, nanoparticles and ions.

a, SEM image of *S. aureus* ($\sim 0.7 \mu\text{m}$ in diameter) assembled onto $1.5\text{-}\mu\text{m}$ voids of a square nickel/PDMS grid. Inset: corresponding confocal image with bacteria fluorescently labelled (green fluorescence indicates that bacteria are alive; see Supplementary Information). **b**, Confocal and SEM (inset) images of bio-colloidal hybrids comprising *S. aureus* 'halos' around $2.5\text{-}\mu\text{m}$ colloidal SiO_2 particles on a square nickel grid with $4\text{-}\mu\text{m}$ circular voids. Scale bars, $3 \mu\text{m}$ (**a**, **b**). **c**, **d**, SEM image of 5.5-nm gold nanoparticles (**c**) and bright-field microscopy image of gold nanorods 40 nm long (**d**) assembling onto the voids of a square nickel grid. Scale bars, $100 \mu\text{m}$ (50 nm in the insets). **e**, Right: optical image illustrating localized precipitation of Au^{3+} ions onto a glass slide placed above an array of macroscopic permanent magnets (left; see also Supplementary Fig. 14). Scale bar, 4 mm . **f**, SEM image illustrating localized precipitation of Au^{3+} ions onto the voids of a square nickel/PDMS microgrid. **g**, Corresponding elemental map for gold recorded by energy-dispersive X-ray spectroscopy (on SEM SU8030). Scale bars, $50 \mu\text{m}$ (50 nm in the insets). **h**, Illustration of ionic concentration gradients leading to the localized precipitation of diamagnetic ions. The paramagnetic Ho^{3+} ions (purple) are concentrated in the centre area between the two magnets (at the maximum of the magnetic field), and the diamagnetic Au^{3+} ions (yellow) are expelled from these high-field regions. The specific concentrations of Au^{3+} and Ho^{3+} ions shown were determined experimentally by ICP-AES experiments. The red curve shows the magnetic profile calculated in COMSOL.

of the nickel/PDMS grid (Fig. 5f, g). Small solution aliquots sampled at different locations and analysed by inductively coupled plasma atomic emission spectroscopy (ICP-AES) show that $\text{Ho}(\text{NO}_3)_3$ is concentrated in the high-field regions and HAuCl_4 is concentrated in the low-field regions, where it supersaturates and precipitates (Fig. 5h and Supplementary Fig. 14). These observations contrast with the belief^{24,25} that external magnetic fields change only the field inside the fluid but not the salt concentrations, and also suggest that magnetic moulding might find use in separating metal salts on the basis of their different magnetic susceptibilities (for example the retrieval of uranium from solubilized brannerite, UTi_2O_6 , for which $\chi = 1.21 \times 10^{-3}$ for uranium(IV) oxides, in contrast with $\chi = 3.93 \times 10^{-6}$ for titanium(IV) oxide).

One promising avenue for further development of our method is the miniaturization of the system to nanoscopic dimensions (using, for instance, nanohole²⁶ nickel grids) so that individual nanoobjects can be manipulated, although this will probably require stronger fields to overcome the effects of thermal noise. We also expect that the use of less cytotoxic magnetic fluids (such as the chelated organic gadolinium complexes that are used as MRI contrast agents such as gadoterate meglumine with $\chi = 1.60 \times 10^{-4}$) would permit wider uses of the method for positioning and manipulating cells.

METHODS SUMMARY

Nickel grids were fabricated by standard photolithography, dissolution of the exposed photoresist regions, e-beam evaporation of the 200-nm nickel layer, and lift-off of the masking photoresist by sonication. A layer of PDMS about $300\text{--}1,000 \text{ nm}$ thick was then spin-coated for 45 s at $5,000 \text{ r.p.m.}$ onto the nickel grid to yield a flat composite structure. After curing of the PDMS at 65°C overnight, its surface was functionalized with 3-(triethoxysilyl)propylisocyanate (TPI) by immersion for 1 h in a 10% TPI solution in acetonitrile at 70°C . This functionalization allowed the subsequent covalent attachment of amine functionalized particles. The particles used in this study were either polymeric or silica particles purchased from Bangs Laboratories and were fluorescently labelled with either fluorescein isothiocyanate (FITC) or rhodamine isothiocyanate (RITC). Superparamagnetic particles had magnetic susceptibilities $\chi_{\text{part}}^{\text{para}} \approx 0.170\text{--}0.392$, whereas diamagnetic particles had susceptibilities $\chi_{\text{part}}^{\text{dia}} \approx -1.17 \times 10^{-5}$. These particles were suspended in a $0.2\text{--}0.4 \text{ M}$ solution of the paramagnetic salt $\text{Ho}(\text{NO}_3)_3$ in $\text{DMSO}/\text{H}_2\text{O}$. To prevent aggregation of the particles by van der Waals forces, the suspensions were always refractive-index-matched by the addition of an appropriate amount of $\text{DMSO}/\text{H}_2\text{O}$ (75% DMSO (w/w)). Particles that assembled and attached to the PDMS were bonded to one another in a Stober solution ($50 \mu\text{l}$ of tetraethyl orthosilicate per 1 cm^2 of wafer area); after 2 h they were liberated into solution by sonication for 10 s . Simulations of the magnetic fields above nickel grids were performed using COMSOL Multiphysics software with relative magnetic permeabilities of air ($\mu_{\text{r(air)}} = 1$) and of nickel ($\mu_{\text{r(nickel)}} = 200$), and with magnetization of the permanent magnet equal to $105,000 \text{ A m}^{-1}$.

on the grid's voids (see the size-dependent effect discussed above and also Supplementary Fig. 6c, d). These circular bacterial colonies can be made permanent by means of glutaraldehyde crosslinking and can be liberated intact into solution (with bacteria still alive). The virtual moulds can also manipulate collections of objects with dimensions much smaller than the nickel microgrids: Fig. 5c and Fig. 5d show gold nanoparticles and gold nanorods, respectively, placed onto the voids of larger nickel grids.

We can also exploit the impact of magnetic microgradients on the spatial distribution of ionic species in the paramagnetic liquid: in these experiments we achieve the selective precipitation of gold salt from a solution of $\text{HAuCl}_4 \cdot 3\text{H}_2\text{O}$ in $\text{Ho}(\text{NO}_3)_3$ in the low-field regions, either above an array of macroscopic magnets (Fig. 5e; see also Supplementary Information and Supplementary Fig. 13) or over the microscopic voids

Received 18 October 2012; accepted 23 August 2013.

Published online 20 October 2013.

1. Van Blaaderen, A., Ruel, R. & Wiltzius, P. Template-directed colloidal crystallization. *Nature* **385**, 321–324 (1997).
2. Erb, R. M., Son, H. S., Samanta, B., Rotello, V. M. & Yellen, B. B. Magnetic assembly of colloidal superstructures with multipole symmetry. *Nature* **457**, 999–1002 (2009).
3. Van Blaaderen, A. Colloidal molecules and beyond. *Science* **301**, 470–471 (2003).
4. Manoharan, V. N., Elsesser, M. T. & Pine, D. J. Dense packing and symmetry in small clusters of microspheres. *Science* **301**, 483–487 (2003).
5. Xia, Y., Gates, B. & Li, Z.-Y. Self-assembly approaches to three-dimensional photonic crystals. *Adv. Mater.* **13**, 409–413 (2001).
6. Yethiraj, A., Thijssen, J. H. J., Wouterse, A. & van Blaaderen, A. Large-area electric-field-induced colloidal single crystals for photonic applications. *Adv. Mater.* **16**, 596–600 (2004).
7. Hochbaum, A. I., Fan, R., He, R. & Yang, P. Controlled growth of Si nanowire arrays for device integration. *Nano Lett.* **5**, 457–460 (2005).
8. Shipway, A., Katz, E. & Willner, I. Nanoparticle arrays on surfaces for electronic, optical, and sensor applications. *ChemPhysChem* **1**, 18–52 (2000).
9. Lu, Y., Yin, Y. & Xia, Y. A self-assembly approach to the fabrication of patterned, two-dimensional arrays of microlenses of organic polymers. *Adv. Mater.* **13**, 34–38 (2001).
10. Aizenberg, J., Braun, P. & Wiltzius, P. Patterned colloidal deposition controlled by electrostatic and capillary forces. *Phys. Rev. Lett.* **84**, 2997–3000 (2000).
11. Hoogenboom, J. P. *et al.* Template-induced growth of close-packed and non-close-packed colloidal crystals during solvent evaporation. *Nano Lett.* **4**, 205–208 (2004).
12. Yellen, B. B., Hovorka, O. & Friedman, G. Arranging matter by magnetic nanoparticle assemblers. *Proc. Natl Acad. Sci. USA* **102**, 8860–8864 (2005).
13. Jiang, P., Prasad, T., McFarland, M. J. & Colvin, V. L. Two-dimensional non-close-packed colloidal crystals formed by spincoating. *Appl. Phys. Lett.* **89**, 011908 (2006).
14. Misztal, K. *et al.* Hierarchical self-assembly of suspended branched colloidal nanocrystals into superlattice structures. *Nature Mater.* **10**, 872–876 (2011).
15. Chen, Q., Bae, S. C. & Granick, S. Directed self-assembly of a colloidal kagome lattice. *Nature* **469**, 381–384 (2011).
16. Ahn, B. Y. *et al.* Omnidirectional printing of flexible, stretchable, and spanning silver microelectrodes. *Science* **323**, 1590–1593 (2009).
17. Dong, A., Ye, X., Chen, J. & Murray, C. B. Two-dimensional binary and ternary nanocrystal superlattices: the case of monolayers and bilayers. *Nano Lett.* **11**, 1804–1809 (2011).
18. Wang, Y. *et al.* Colloids with valence and specific directional bonding. *Nature* **491**, 51–55 (2012).
19. Rosensweig, R. E. *Ferrohydrodynamics* (Courier Dover Publications, 1997).
20. Shevkoplyas, S. S., Siegel, A. C., Westervelt, R. M., Prentiss, M. G. & Whitesides, G. M. The force acting on a superparamagnetic bead due to an applied magnetic field. *Lab Chip* **7**, 1294–1302 (2007).
21. Bakker, C. J. G. & de Roos, R. Concerning the preparation and use of substances with a magnetic susceptibility equal to the magnetic susceptibility of air. *Magn. Reson. Med.* **56**, 1107–1113 (2006).
22. Mirica, K. A., Shevkoplyas, S. S., Phillips, S. T., Gupta, M. & Whitesides, G. M. Measuring densities of solids and liquids using magnetic levitation: fundamentals. *J. Am. Chem. Soc.* **131**, 10049–10058 (2009).
23. Perro, A. *et al.* A chemical synthetic route towards ‘colloidal molecules’. *Angew. Chem. Int. Ed.* **48**, 361–365 (2009).
24. Coey, J. M. D., Aogaki, R., Byrne, F. & Stamenov, P. Magnetic stabilization and vorticity in submillimeter paramagnetic liquid tubes. *Proc. Natl Acad. Sci. USA* **106**, 8811–8817 (2009).
25. Sun, Z., Guo, M., Vleugels, J., Blanpain, B. & Van der Biest, O. Induced migration of non-magnetic particles and fabrication of metallic-based graded materials by applying a strong magnetic field. *J. Appl. Phys.* **109**, 084917 (2011).
26. Yang, J.-C. *et al.* Enhanced optical transmission mediated by localized plasmons in anisotropic, three-dimensional nanohole arrays. *Nano Lett.* **10**, 3173–3178 (2010).
27. Bishop, K. J. M., Wilmer, C. E., Soh, S. & Grzybowski, B. A. Nanoscale forces and their uses in self-assembly. *Small* **5**, 1600–1630 (2009).

Supplementary Information is available in the online version of the paper.

Acknowledgements We thank P. E. Fuller for his Matlab scripts. This work was supported by the Non-equilibrium Energy Research Center, which is an Energy Frontier Research Center funded by the US Department of Energy, Office of Science, Office of Basic Energy Sciences under award number DE-SC0000989.

Author Contributions A.F.D. conducted colloid experiments and calculations. P.P.P. and B.K. performed experiments on the bacteria and nanoparticle assemblies. A.F.D., P.P.P. and B.K. prepared the figures. B.A.G. conceived the project, supervised the research, and wrote the paper.

Author Information Reprints and permissions information is available at www.nature.com/reprints. The authors declare no competing financial interests. Readers are welcome to comment on the online version of the paper. Correspondence and requests for materials should be addressed to B.A.G. (grzybor@northwestern.edu).

Structural change in molten basalt at deep mantle conditions

Chrystèle Sanloup^{1,2}, James W. E. Drewitt¹, Zuzana Konôpková³, Philip Dalladay-Simpson¹, Donna M. Morton¹, Nachiketa Rai⁴, Wim van Westrenen⁴ & Wolfgang Morgenroth^{3,5}

Silicate liquids play a key part at all stages of deep Earth evolution, ranging from core and crust formation billions of years ago to present-day volcanic activity. Quantitative models of these processes require knowledge of the structural changes and compression mechanisms that take place in liquid silicates at the high pressures and temperatures in the Earth's interior. However, obtaining such knowledge has long been impeded by the challenging nature of the experiments. In recent years, structural and density information for silica glass was obtained at record pressures of up to 100 GPa (ref. 1), a major step towards obtaining data on the molten state. Here we report the structure of molten basalt up to 60 GPa by means of *in situ* X-ray diffraction. The coordination of silicon increases from four under ambient conditions to six at 35 GPa, similar to what has been reported in silica glass^{1–3}. The compressibility of the melt after the completion of the coordination change is lower than at lower pressure, implying that only a high-order equation of state can accurately describe the density evolution of silicate melts over the pressure range of the whole mantle. The transition pressure coincides with a marked change in the pressure-evolution of nickel partitioning between molten iron and molten silicates, indicating that melt compressibility controls siderophile-element partitioning.

Density measurements of silicate melts are much sought after, because density is the primary factor controlling the evolution of magmas at depth. Pioneering results have been obtained using shock-wave⁴ and *ex situ* sink–float experiments^{5,6} at upper-mantle conditions, demonstrating that basalts are more compressible than their crystalline counterparts, which implies that density inversion must occur at depth. This behaviour can be explained by the different compression mechanisms available in liquid silicates, compared to the crystalline structures, including the collapse of ring structures at low pressure and gradual coordination changes. A key point to be investigated is how and where the transition from fourfold- to sixfold-coordinated Si occurs in magmas at depth and, in turn, how the transition affects melt compressibility. Structural data has been obtained on molten silicates using X-ray diffraction and large-volume presses⁷; but they are limited below 10 GPa, that is, below the expected transition. Only shock-wave experiments have been able to probe the properties of magmas at deep-mantle conditions, with data up to 127 GPa reported for molten 36% anorthite–64% diopside⁸. However, these data are difficult to interpret in terms of an isothermal equation of state⁸.

We collected *in situ* X-ray diffraction data in laser-heated diamond anvil cells at the extreme-conditions beamline P02.2 at the PETRA III synchrotron (the Positron-Electron Tandem Ring Accelerator III Deutsches Elektronen-Synchrotron) in Hamburg, Germany. The choice of the basaltic sample was made for the following reasons: (1) basalt is the most commonly produced magma, (2) its SiO₂ content (50.2 weight per cent) is high enough that the Si–O coordination change can be tracked from structural data, (3) its FeO content (7.81 weight per cent) is sufficient to couple with the infrared laser without the need to add a

metallic coupler, (4) its melting curve and petrological relationships are well documented in our targeted pressure–temperature range^{9–11}. The observation of diffuse rings with the simultaneous absence of any crystalline diffraction peaks apart from those of the SiO₂ pressure-transmitting medium was used as the criterion to determine melting. Apart from the lowest-pressure run, which was quenched as glass, all melts fully recrystallized on quenching at room temperature (20 °C). Their mineralogical composition as identified from X-ray diffraction data agrees with previous petrological studies^{10,11}, and is reported in Table 1 along with experimental pressure–temperature conditions.

The intensity data (Fig. 1a) are converted into the structure factor $S(q)$, where q is the scattering vector, using the Ashcroft–Langreth formalism. The radial distribution function $g(r)$ (Fig. 1b) is obtained by Fourier transforming of $S(q)$. Changes of intensity occur gradually up to 35 GPa, with the first sharp diffraction peak shifting to higher q values and decreasing in intensity, interpreted as a collapse of the SiO₂ tetrahedral network, a second diffuse peak growing at 3.3 \AA^{-1} , and a relative decrease of the intensity of the third diffuse peak at 4.5 \AA^{-1} . These changes are expressed in $g(r)$ through a shift of the first contribution to slightly higher distances, and by a broadening of the second main contribution. These changes are very similar to those observed^{12,3,12} in silica glass, and occur over the same pressure range, that is, between 10 GPa and 35 GPa. The shift of the first contribution in $g(r)$ to higher distances reflects increased coordination of the Si–O contribution. The shouldering of the second contribution at 2.5 \AA has been related to O–O interactions as neighbouring polyhedra participate in edge-sharing³. The radial distribution functions obtained are the sum of all ion–ion contributions. To quantify the increase of Si–O coordination number, we have simulated the experimental $g(r)$ against a sum of Gaussians (see Methods), assuming that the Al–O coordination number is 6 for pressure exceeding 15 GPa, as is shown to be the case in the glassy state¹³. The fitted Si–O interatomic distance $d_{\text{Si-O}}$ and coordination number are reported in Fig. 2. Si–O coordination increases from 4.5(0.2) at 15 GPa to 6.0(0.1) at 35 GPa. Concomitantly, $d_{\text{Si-O}}$ increases from 1.62(0.01) Å to 1.66(0.02) Å. (Note that parentheses indicate 1σ errors.) In the quenched samples, sixfold-coordinated Si-bearing phases appear

Table 1 | Experimental pressure–temperature conditions and results

Run	P (GPa)	T (K)	Measured density (kg m^{-3})	Observed quenched products
1	10.5	2,200	$3,611 \pm 69$	Glass
2	15	2,273	$3,821 \pm 70$	st, cpx, gt
6	23.7	2,473	Not determined	st, gt
5	24.6	2,573	$4,313 \pm 52$	st, gt, pv, NAL, cf
13	35	2,700	$4,523 \pm 53$	st, Ca–pv, Mg–pv, NAL, cf
8	45	2,973	$4,750 \pm 71$	st, Ca–pv, Mg–pv, cf
12	60	3,273	$4,978 \pm 70$	st, Ca–pv, Mg–pv, cf

Quenched products were identified on the X-ray diffraction patterns obtained after quenching laser heating. Mineral phases were stishovite (st), clinopyroxene (cpx), garnet (gt), calcium perovskite (Ca–pv), magnesium perovskite (Mg–pv) and new aluminium-rich phase (NAL). The calcium–ferrite phase (cf) is ascribed to an Al-bearing phase with stoichiometric formula $[\text{Na,Ca,Mg,Fe}]_1[\text{Al,Si,Fe,Mg}]_2\text{O}_4$.

¹Centre for Science at Extreme Conditions and School of Physics and Astronomy, University of Edinburgh, Scottish Universities Physics Alliance, Edinburgh EH9 3JZ, UK. ²Université Pierre et Marie Curie, UMR-CNRS 7193, Institut des Sciences de la Terre Paris, F-75005 Paris, France. ³DESY Photon Science, Notkestrasse 85, D-22607 Hamburg, Germany. ⁴Faculty of Earth and Life Sciences, Vrije Universiteit Amsterdam, 1081 HV, The Netherlands. ⁵Institut für Geowissenschaften, Goethe-Universität Frankfurt, D-60438 Frankfurt am Main, Germany.

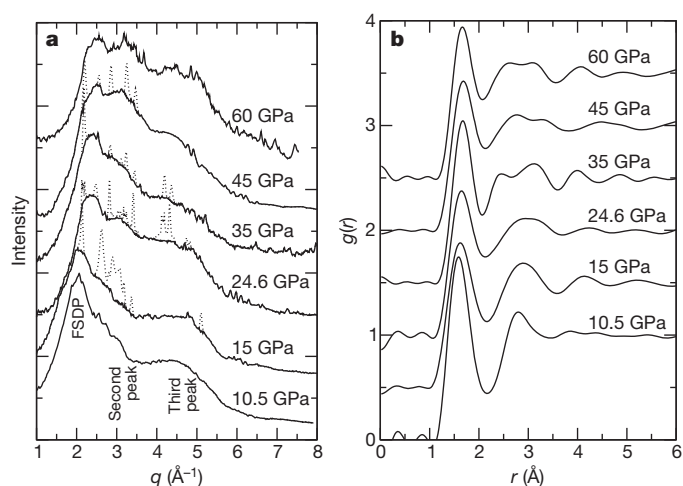


Figure 1 | Structure of molten basalt at high pressures. **a**, Intensity scattered by molten basalt at high pressure. FSDP, first sharp diffraction peak. The dotted lines are the patterns obtained after subtraction of the background signal (see Methods), and contain contribution from the melt and diffraction Bragg peaks from stishovite, the pressure-transmitting medium. These Bragg peaks have been erased in the continuous black data. **b**, Corresponding radial distribution functions.

at 25 GPa (Table 1). Most of the Si-coordination change in the melt thus occurs at lower pressure than in the crystalline phases, but is completed only by 35 GPa. First-principles molecular dynamics calculations predict a more gradual fourfold-to-sixfold coordination increase in molten anorthite and diopside^{14,15}. Instead, Si-coordination changes in the natural basaltic composition are more consistent with calculations on pure silica melt¹⁶. Our data also compare favourably with calculations in that bond lengths initially increase on compression.

In SiO₂ glass, the structural changes are accompanied by a stiffening of the glass^{1,17}. In this work, we measured the density of melts using the X-ray-diffraction-based method first applied to diamond-anvil cell experiments at moderate pressure (ref. 18), and later extended to the megabar range¹⁹. It consists of minimizing the oscillations in $g(r)$ where there should not be any signal, that is, below the minimum

interatomic distance. However, this method requires that the background, essentially the Compton signal from the diamond anvils that dominates the total diffracted intensity, is perfectly subtracted (see Methods). The density values we obtained (Fig. 3) fall within the error bars on the shock-wave isentrope measured for the model 36% anorthite–64% diopside composition and applied to a basaltic composition⁴ at upper-mantle conditions.

At higher pressure, there is a clear deviation from this shock-wave isentrope, with a stiffening of the melt that resembles what has been observed in other shock-wave studies⁸, although the absolute density values are different. This stiffening is related to the fact that Si is the last of the major elements to undergo a coordination increase, so that above 35 GPa, bond-length shortening gradually overtakes coordination change as the dominant compression mechanism. Consequently, our density data can be fitted only with a high-order equation of state. A fourth-order Birch–Murnaghan fit to the data reduced to a common isotherm (2,735 K; see Methods) is obtained for the following values of the isothermal bulk modulus ($K_{T,0}$) and its pressure derivatives (K' and K''): $K_{2,735\text{ K},0} = 24.0 \pm 1.7$ GPa, $K'_{2,735\text{ K},0} = 0.664 \pm 0.032$ and $K''_{2,735\text{ K},0} = -0.057 \pm 0.057$ GPa^{−1}, using $\rho_{2,735\text{ K},0} = 2,480$ kg m^{−3} as a regular point⁶. This equation of state is remarkably close to that obtained theoretically for anorthite melt⁸ (Fig. 3), also a fourth-order finite strain expansion, and slightly different to that of the less polymerized diopside melt¹⁵. The latter was a third-order fit, as for other less polymerized melts²⁰, whereas a fifth-order expansion is necessary to represent pure SiO₂ liquid¹⁶. The presence of Fe in our composition might explain part of the deviation from the shock-wave and theoretical studies that were conducted on Fe-free compositions. Fe-rich melts are expected to have a higher densification rate than their Mg counterparts because the Fe-coordination number starts to increase at lower pressure than the Mg-coordination number does in Mg-rich melts²¹.

Our data provide the first *in situ* experimental insight into the behaviour of a magma ocean of unknown and evolving composition. In the context of the crystallization of a magma ocean, the difference in density between melts and crystals will be at its highest at the bottom of the upper mantle, that is, above the fourfold-to-sixfold Si-coordination transition in crystals. At around 25 GPa, the crystalline silicate phase is denser than the melt because Si is fully converted into sixfold coordination in the former. Silicate melts should also be denser than the solid

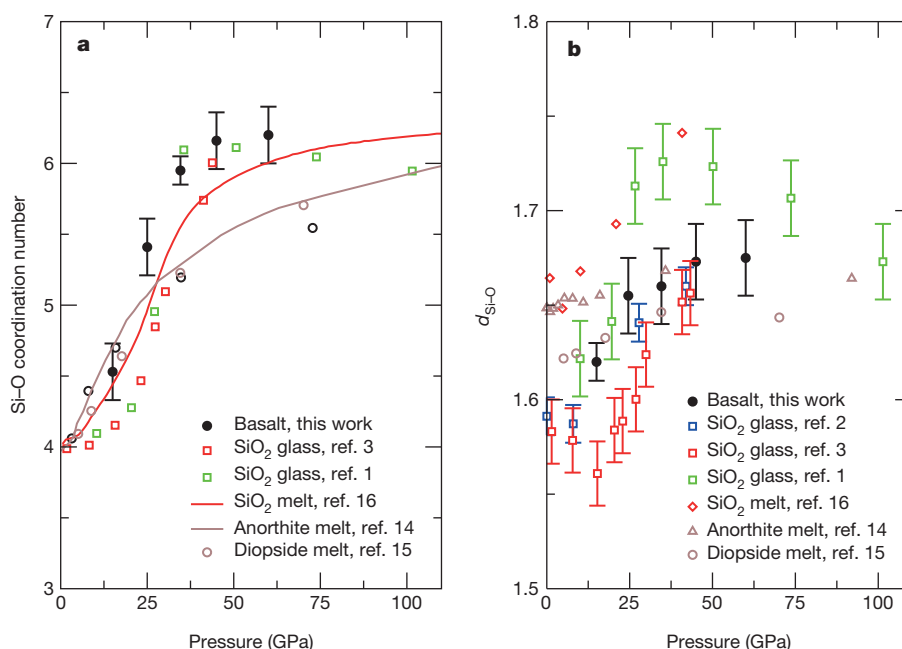


Figure 2 | Pressure evolution of Si–O coordination number and $d_{\text{Si–O}}$ in molten basalt. **a**, Si–O coordination number versus pressure; **b**, $d_{\text{Si–O}}$ versus

pressure. Present data are compared to theoretical calculations on silicate melts^{14–16}, and to experimental data on SiO₂ glass^{2,3,12}. Errors, 1σ .

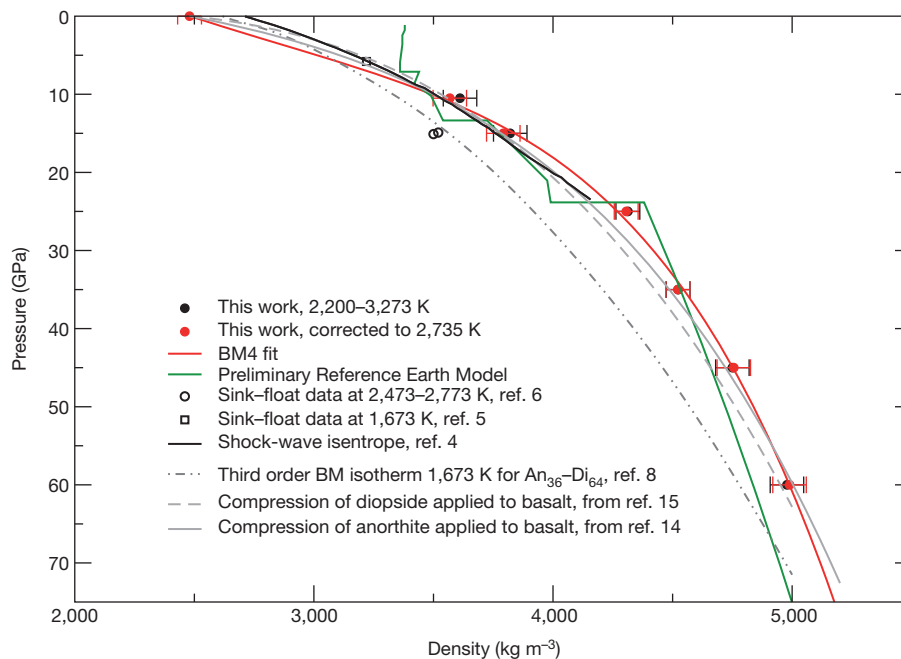


Figure 3 | Density of molten basalt as a function of pressure. Density of molten basalt determined here, and compared to previous sink–float data^{5,6}. Also shown are the seismological density profile for the Earth's mantle³³, the theoretically derived equations of state for molten anorthite¹⁴ and diopside¹⁵ at 3,000 K applied to basalt using its ambient pressure density, the shock-wave

isentrope equation of states measured on a model 36% anorthite–64% diopside composition and applied to basaltic composition⁴, and the shock-wave-derived isothermal equation of state for a 36% anorthite–64% diopside composition⁸. BM, Birch–Murnaghan equation of state; BM4, 4th-order BM. Errors, 1 σ .

phase at the bottom of the lower mantle and will accumulate on top of the core. We should therefore expect a layered magma ocean with a crystalline layer separating an upper magma ocean from a basal one, as posited by thermal evolution models²². On the basis of previous sink–float measurements, it has been proposed that deep melting in the early Archaean Earth generated negatively buoyant melts that would accumulate on top of the 410-km discontinuity²³. These Fe-rich melts would have sunk into the lower mantle as they crystallized to lithologies that are denser than ambient mantle, although that would depend on Fe partitioning at depth. The present measurements extend the negatively buoyant zone for mafic melts down to the 660-km discontinuity (Fig. 3).

Strikingly, the reported structural and compressibility changes coincide with a marked change in the pressure evolution of the distribution

of nickel between metal and silicate melts, as expressed by the nickel partition coefficient D^{Ni} (Fig. 4). The depth of a magma ocean is classically estimated based on the measured pressure-dependence of siderophile elements partitioning between molten silicate and metal. Recent estimates^{24–29} exceed 30 GPa and range up to 60 GPa, with most models relying on extrapolations of experimental data restricted to lower pressures (<25 GPa). The coincidence between the change in silicate melt compressibility and nickel partitioning implies that data obtained below 35 GPa should not be used to constrain partitioning at deeper mantle pressures. We reported a similar coincidence between change in the pressure evolution of siderophile-element partitioning and the compressibility change in molten Fe alloys at 5 GPa (ref. 30). Partitioning of an element between two phases is controlled by its coordination geometry and site compressibility in each phase. At ambient pressure, nickel is in tetrahedral sites³¹, but it may occupy more octahedral sites as pressure increases³². This results in an increased crystal field stabilization energy of these ions in the silicate melt, and stabilizes them in the silicate relative to the metal phase, which explains the initial decrease of D^{Ni} with increasing pressure.

It is unlikely that Ni coordination further increases after completion of the fourfold-to-sixfold coordination transition in Si. The flattening observed around 35 GPa may rather be explained by a change in site compressibility. Silicate melt stiffening implies a convergence of site compressibility between silicate and metal melts, resulting in a weak pressure-dependence of D^{Ni} above 35 GPa. An unfortunate consequence of this weak pressure-dependence is that error bars on magma ocean depths need to be revised upwards, if they can be determined at all. These examples illustrate that models of the magma ocean era, including segregation of the molten Fe core and crystallization of the magma ocean, must incorporate pressure-induced structural changes in melts.

METHODS SUMMARY

We used symmetric diamond-anvil cells equipped with 70°-opening Boehler–Almax seats to access a wider q range up to 9 Å^{−1} and reduce the diamond Compton contribution, given that Boehler–Almax anvils are only 1.5 mm thick. The X-ray monochromatic beam (42 keV) was focused down to a size of 2 $\mu\text{m} \times 4 \mu\text{m}$,

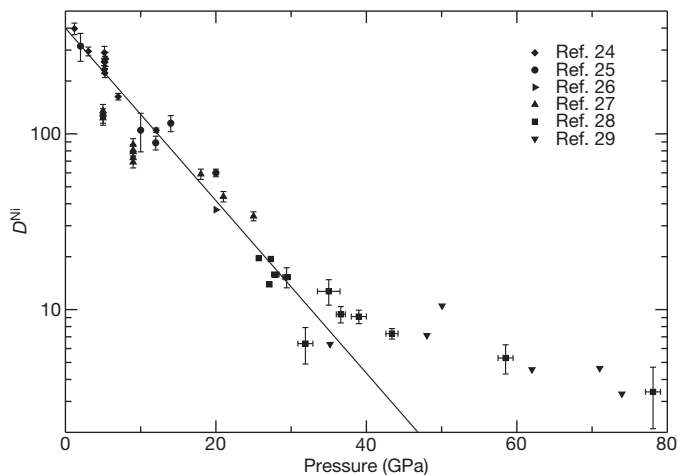


Figure 4 | Pressure evolution of nickel partitioning coefficient between metal and silicate melts. D^{Ni} is defined as the concentration by weight of nickel in molten metal divided by its concentration in a coexisting silicate melt. Data are from refs 24–29. Below 35 GPa, the data plot as a downward-sloping straight line (black) from which they deviate at higher pressures. Errors, 1 σ .

whereas the double-sided infrared laser was focused down to 20 μm . The starting glass sample (Extended Data Table 1) was loaded as a 20- μm -thick platelet between two equally thick platelets of compressed SiO_2 powder. The SiO_2 platelets act as thermal insulators and as the pressure-transmitting medium. To limit iron migration away from the laser heating spot that is due to the Soret effect, the laser shutters were opened only once the targeted power was reached, and held open for 10 s during which ten X-ray diffraction patterns of acquisition time 1 s each were recorded on a Perkin–Elmer 2D detector. Targeted power was increased in 2-W increments from 20 W to 40 W of power on each laser depending on pressure until complete melting of the sample occurred. Only one sample was used per pressure point to avoid repeated laser-heatings and to preserve the chemical integrity of the sample. To isolate the scattered intensity from the molten basalt only, each sample was removed from the gasket, and the gasket put back in place to collect X-ray data on the empty cell. Obtained patterns were then scaled vertically to match the baseline of X-ray patterns collected on the quenched crystalline sample still under pressure. This last step ensures that any pressure effect on the background is corrected for.

Online Content Any additional Methods, Extended Data display items and Source Data are available in the online version of the paper; references unique to these sections appear only in the online paper.

Received 16 May; accepted 13 September 2013.

- Sato, T. & Funamori, N. Sixfold-coordinated amorphous polymorph of SiO_2 under high pressure. *Phys. Rev. Lett.* **101**, 255502 (2008).
- Meade, C., Hemley, R. J. & Mao, H. K. High-pressure x-ray diffraction of SiO_2 glass. *Phys. Rev. Lett.* **69**, 1387–1390 (1992).
- Benmore, C. J. *et al.* Structural and topological changes in silica glass at pressure. *Phys. Rev. B* **81**, 054105 (2010).
- Rigden, S. M., Ahrens, T. J. & Stolper, E. M. Densities of liquid silicate at high pressures. *Science* **226**, 1071–1074 (1984).
- Agee, C. B. Crystal-liquid density inversions in terrestrial and lunar magmas. *Phys. Earth Planet. Inter.* **107**, 63–74 (1998).
- Ohtani, E. & Maeda, M. Density of basaltic melt at high pressure and stability of the melt at the base of the lower mantle. *Earth Planet. Sci. Lett.* **193**, 69–75 (2001).
- Funamori, N., Yamamoto, S., Yagi, T. & Kikegawa, T. Exploratory studies of silicate melt structure at high pressures and temperatures by in situ X-ray diffraction. *J. Geophys. Res.* **109**, B03203 (2004).
- Asimow, P. D. & Ahrens, T. Shock compression of liquid silicates up to 125 GPa: the anorthite–diopside join. *J. Geophys. Res.* **115**, B10209 (2010).
- Hirose, K., Fei, Y., Ma, Y. & Mao, H.-K. The fate of subducted basaltic crust in the Earth's lower mantle. *Nature* **397**, 53–56 (1999).
- Perrillat, J.-P. *et al.* Phase transformations of subducted basaltic crust in the uppermost lower mantle. *Phys. Earth Planet. Inter.* **157**, 139–149 (2006).
- Ricolleau, A. *et al.* Phase relations and equation of state of a natural MORB: implications for the density profile of subducted oceanic crust in the Earth's lower mantle. *J. Geophys. Res.* **115**, B08202 (2010).
- Sato, T. & Funamori, N. High-pressure structural transformation of SiO_2 glass up to 100 GPa. *Phys. Rev. B* **82**, 184102 (2010).
- Yarger, J. L. *et al.* Al coordination changes in high-pressure aluminosilicate liquids. *Science* **270**, 1964–1967 (1995).
- de Koker, N. Structure, thermodynamics, and diffusion in $\text{CaAl}_2\text{Si}_2\text{O}_8$ liquid from first-principles molecular dynamics. *Geochim. Cosmochim. Acta* **74**, 5657–5671 (2010).
- Sun, N., Stixrude, L., de Koker, N. & Karki, B. B. First principles molecular dynamics simulations of diopside ($\text{CaMgSi}_2\text{O}_6$) liquid to high pressure. *Geochim. Cosmochim. Acta* **75**, 3792–3802 (2011).
- Karki, B. B., Bhattarai, D. & Stixrude, L. First-principles simulations of liquid silica: structural and dynamical behavior at high pressure. *Phys. Rev. B* **76**, 104205 (2007).
- Murakami, M. & Bass, J. D. Evidence of denser MgSiO_3 glass above 133 gigapascal (GPa) and implications for remnants of ultradense silicate melt from a deep magma ocean. *Proc. Natl Acad. Sci. USA* **108**, 17286–17289 (2011).
- Eggert, J. H., Weck, G., Loubeyre, P. & Mezouar, M. Quantitative structure factor and density measurements of high-pressure in diamond anvil cells by x-ray diffraction: argon and water. *Phys. Rev. B* **65**, 174105 (2002).
- Sanloup, C., Gregoryanz, E., Degtyareva, O. & Hanfland, M. Structural transition in compressed amorphous sulfur. *Phys. Rev. Lett.* **100**, 075701 (2008).
- Stixrude, L. & Karki, B. Structure and freezing of MgSiO_3 liquid in Earth's lower mantle. *Science* **310**, 297–299 (2005).
- Sanloup, C. *et al.* Structure and density of molten fayalite at high pressure. *Geochim. Cosmochim. Acta* **118**, 118–128 (2013).
- Labrosse, S., Hernlund, J. W. & Coltice, N. A crystallizing dense magma ocean at the base of the Earth's mantle. *Nature* **450**, 866–869 (2007).
- Lee, C.-T. A. *et al.* Upside-down differentiation and generation of a 'primordial' lower mantle. *Nature* **463**, 930–933 (2010).
- Thibault, Y. & Walter, M. J. The influence of pressure and temperature on the metal–silicate partition coefficients of nickel and cobalt in a model C1 chondrite and implications for metal segregation in a deep magma ocean. *Geochim. Cosmochim. Acta* **59**, 991–1002 (1995).
- Li, J. & Agee, C. B. Geochemistry of mantle–core differentiation at high pressure. *Nature* **381**, 686–689 (1996).
- Ohtani, E. & Yurimoto, H. Element partitioning between metallic liquid, magnesiowüstite, and silicate liquid at 20 GPa and 2500°C: a secondary ion mass spectrometric study. *Geophys. Res. Lett.* **23**, 1993–1996 (1996).
- O'Neill, H. S. C., Canil, D. & Rubie, D. C. Oxide–metal equilibria to 2500°C and 25 GPa: implications for core formation and the light component in the Earth's core. *J. Geophys. Res.* **103**, 12239–12260 (1998).
- Tschauner, O. *et al.* Partitioning of nickel and cobalt between silicate perovskite and metal at pressures up to 80 GPa. *Nature* **398**, 604–607 (1999).
- Siebert, J., Badro, J., Antonangeli, D. & Ryerson, F. J. Metal–silicate partitioning of Ni and Co in a deep magma ocean. *Earth Planet. Sci. Lett.* **321–322**, 189–197 (2012).
- Sanloup, C., van Westrenen, W., Dasgupta, R., Maynard-Casely, H. E. & Perrillat, J.-P. Compressibility change in iron-rich melt and implications for core formation models. *Earth Planet. Sci. Lett.* **306**, 118–122 (2011).
- Farges, F., Brown, G. E., Petit, P.-E. & Munoz, M. Transition elements in water-bearing silicate glasses/melts. Part I. A high-resolution and anharmonic analysis of Ni coordination environments in crystals, glasses, and melts. *Geochim. Cosmochim. Acta* **65**, 1665–1678 (2001).
- Keppeler, H. & Rubie, D. C. Pressure-induced coordination changes of transition-metal ions in silicate melts. *Nature* **364**, 54–56 (1993).
- Dziewonski, A. M. & Anderson, D. L. Preliminary reference Earth model. *Phys. Earth Planet. Inter.* **25**, 297–356 (1981).

Acknowledgements The research leading to these results has received funding from the European Community's Seventh Framework Programme (FP7/2007–2013) under grant numbers 312284 and 259649 (European Research Council starting grant to C.S.). The laser heating system on beamline P02.2 is funded by the BMBF (the German Federal Ministry of Education and Research, project number 05K10RFA). We acknowledge G. Prouteau for providing the starting basalt glass, and PETRAIII for provision of synchrotron radiation facilities.

Author Contributions C.S. devised the project, and wrote the paper with input from J.W.E.D., Z.K. and W.v.W. Also, C.S., J.W.E.D., Z.K., P.D.-S., D.M.M., N.R. and W.v.W. participated in data acquisition. Z.K. and W.M. designed the laser-heating system used during the experiments.

Author Information Reprints and permissions information is available at www.nature.com/reprints. The authors declare no competing financial interests. Readers are welcome to comment on the online version of the paper. Correspondence and requests for materials should be addressed to C.S. (chrystele.sanloup@ed.ac.uk).

METHODS

We used symmetric diamond-anvil cells equipped with 70°-opening Boehler-Almax seats to access a wider q range up to 9 \AA^{-1} and reduce the diamond Compton contribution, given that Boehler-Almax anvils are only 1.5 mm thick. The X-ray monochromatic beam (42 keV) was focused down to a size of $2 \text{ \mu m} \times 4 \text{ \mu m}$, whereas the double-sided infrared laser was focused down to 20 \mu m . The starting glass sample, a basalt obtained by grinding and fusing in air a Stromboli pumice³⁴ at 1,400 °C, was loaded as a 20- \mu m -thick platelet between two equally thick platelets of compressed SiO_2 powder. The SiO_2 platelets act as thermal insulators and as the pressure-transmitting medium. To limit the iron migration away from the laser heating spot that is due to the Soret effect, the laser shutters were opened only once the targeted power was reached, and held open for 10 s during which ten X-ray diffraction patterns of acquisition time 1 s each were recorded on a Perkin-Elmer two-dimensional detector. Targeted power was increased in 2-W increments from 20 W to 40 W of power on each laser depending on pressure until complete melting of the sample occurred. Only one sample was used per pressure point to avoid repeated laser-heatings and to preserve the chemical integrity of the sample. To isolate the scattered intensity from the molten basalt only, each sample was removed from the gasket, and the gasket put back in place to collect X-ray data on the empty cell. The patterns obtained were then scaled vertically to match the baseline of X-ray patterns collected on the quenched crystalline sample still under pressure. This last step ensures that any pressure effect on the background is corrected for.

Some samples recovered after the experiments were embedded in epoxy and polished for electron microprobe analysis at the EMMAC centre of the University of Edinburgh (see Extended Data Table 1). We used a defocused beam size of 10 \mu m to get an average composition at the laser-heated spot. Conditions were 15-keV voltage and 2-nA current for the analysis of K, Ca, Na, Mg, Al, Fe and Si, and 15 keV and 80 nA for the analysis of Ti, Mn and P. Electron microprobe analysis shows that no detectable contamination of the sample by the SiO_2 platelets occurred; silica (being Fe-free) is heated only conductively by the laser-heated basalt, and for a short duration (10 s), so potential chemical exchanges are limited.

A ruby sphere was added in the chamber for pressure measurements at room temperature using the ruby fluorescence method³⁵. Two-dimensional patterns were integrated using the Fit2D software³⁶. Because we used the off-axis heating system to avoid using carbon mirrors that would add to the background signal, temperature could not be measured by pyrometric techniques. It was instead assumed that the temperature followed the melting curve of basalt as determined up to 60 GPa (ref. 9). Using these temperature values, pressure at high temperature was calculated using the equation of state of stishovite³⁷.

To determine the Si–O coordination number, the experimental $g(r)$ was simulated against a sum of Gaussians (where each Gaussian corresponds to a particular ion–ion partial distribution function) with the following equation:

$$g(r) = \frac{1}{nS_{\infty}} \sum_i \frac{A_i}{\sigma_i \sqrt{2\pi}} \exp\left(-\frac{(r-d_i)^2}{2\sigma_i^2}\right) \quad (1)$$

where

$$A_i = \frac{\text{CN}_i}{\int \frac{4\pi r^2}{\sigma_i \sqrt{2\pi}} \exp\left(-\frac{(r-d_i)^2}{2\sigma_i^2}\right) dr} \quad (2)$$

where CN_i is the coordination number of the i th ion–ion contribution, d_i is the corresponding interatomic distance and σ_i is a parameter depending on structural disorder³⁸, $\sigma_i = k\sqrt{d_i}$; k is an adjustable parameter (typically 0.15–0.17).

The Al–O coordination number is assumed to be six for pressure exceeding 15 GPa, as has been shown to be the case in the glassy state¹³. First-principles molecular dynamics calculations, however, predict a full conversion to sixfold coordination for the anorthite melt at 3,000 K at 35 GPa only¹⁴, with coordination numbers of 5.47 and 5.8 at 15 GPa and 25 GPa, respectively. If we use these values, then our fitted coordination number for Si–O should be increased by 0.18 at 15 GPa and 0.07 at 25 GPa.

To fit our density data with an equation of state, we first reduced the data to a common isotherm as the data were collected along the melting curve. In the absence of data on the thermal expansion coefficient α for basalt at high pressure, we have calculated α assuming that αK_T is a constant, and chosen the mean experimental temperature T as the appropriate isotherm. The assumption that αK_T is constant is not true, as shown by first-principles calculations³⁹, and so we overestimate α at high pressure. However, this gives a maximum limit on the thermal correction that needs to be applied to our data.

34. Pichavant, M., di Carlo, I., Gac, Y. L., Rotolo, S. G. & Scaillet, B. Experimental constraints on the deep magma feeding system at Stromboli volcano, Italy. *J. Petrol.* **50**, 601–624 (2009).
35. Mao, H. K., Xu, J. & Bell, P. M. Calibration of the ruby pressure gauge to 800 kbar under quasi-hydrostatic conditions. *J. Geophys. Res.* **91**, 4673–4676 (1986).
36. Hammersley, A. P., Svensson, S. O., Hanfland, M., Fitch, A. N. & Hausermann, D. Two-dimensional detector software: from real detector to idealised image or two-theta scan. *High Press. Res.* **14**, 235–248 (1996).
37. Nishihara, Y., Nakayama, K., Takahashi, E., Iguchi, T. & Funakoshi, K.-I. P-V-T equation of state of stishovite to the mantle transition zone conditions. *Phys. Chem. Mineral.* **31**, 660–670 (2005).
38. Hosemann, R. & Bagchi, S. N. *Direct Analysis of Diffraction by Matter* (North-Holland, 1962).
39. de Koker, N. P. & Stixrude, L. Self-consistent thermodynamic description of silicate liquids, with application to shock melting of MgO periclase and MgSiO_3 perovskite. *Geophys. J. Int.* **178**, 162–179 (2009).

Extended Data Table 1 | Chemical composition of the starting sample and recovered samples

Oxide	Starting composition Ref. ¹	Recovered samples (mean of 3 analyses)
K ₂ O	1.86 (0.06)	1.52 (0.42)
CaO	12.4 (0.2)	11.60 (0.29)
Na ₂ O	2.29 (0.05)	1.88 (0.55)
MgO	7.87 (0.12)	8.03 (0.12)
Al ₂ O ₃	15.2 (0.3)	15.06 (0.58)
FeO	7.81 (0.33)	7.23 (0.43)
SiO ₂	50.2 (0.3)	49.97 (0.79)
P ₂ O ₅	0.64 (0.06)	0.41 (0.04)
TiO ₂	0.84 (0.04)	0.76 (0.04)
MnO	0.16 (0.05)	0.12 (0.05)
Total	99.27	96.58

One standard deviations are given in parentheses.

Mating advantage for rare males in wild guppy populations

Kimberly A. Hughes¹, Anne E. Houde², Anna C. Price³ & F. Helen Rodd³

To understand the processes that maintain genetic diversity is a long-standing challenge in evolutionary biology, with implications for predicting disease resistance, response to environmental change, and population persistence^{1–3}. Simple population genetic models are not sufficient to explain the high levels of genetic diversity sometimes observed in ecologically important traits². In guppies (*Poecilia reticulata*), male colour pattern is both diverse and heritable, and is arguably one of the most extreme examples of morphological polymorphism known^{4,5}. Negative frequency-dependent selection (NFDS), a form of selection in which genotypes are favoured when they are rare⁶, can potentially maintain such extensive polymorphism, but few experimental studies have confirmed its operation in nature^{7,8}. Here we use highly replicated experimental manipulations of natural populations to show that males with rare colour patterns have higher reproductive fitness, demonstrating NFDS mediated by sexual selection. Rare males acquired more mates and sired more offspring compared to common males and, as previously reported, had higher rates of survival⁸. Orange colour, implicated in other studies of sexual selection in guppies, did predict male reproductive success, but only in one of three populations. These data support the hypothesis that NFDS maintains diversity in the colour patterns of male guppies through two selective agents, mates and predators. Similar field-based manipulations of genotype frequencies could provide a powerful approach to reveal the underlying ecological and behavioural mechanisms that maintain genetic and phenotypic diversity.

Populations of organisms exhibit enormous genetic diversity. Explaining this diversity has been challenging, particularly when variation occurs in traits under strong natural selection^{1,3}. High genetic variation in ecologically important traits cannot be explained by standard population genetic models that incorporate directional natural selection, genetic drift and mutation². Instead, various kinds of balancing selection, in which genotype fitness varies temporally, spatially, or as a function of genotype frequency, have been proposed to explain this diversity^{2,3}. However, the ecological mechanisms that generate balancing selection are generally unknown³.

The colour patterns displayed by adult male guppies (Fig. 1) are highly heritable, but also highly variable within populations^{5,9}. Female mate choice has been proposed to account for this diversity because laboratory studies indicate a strong preference for rare or novel colour patterns^{10–12}. If this preference occurs in nature, then it would result in NFDS on male colouration and promote variation. However, it can be difficult to detect NFDS in nature because the equilibrium frequencies of different phenotypes under this form of selection are those at which fitnesses are equal¹³. Consequently, a rare-male advantage will be detectable only when phenotype frequencies are perturbed from their equilibrium values.

To determine whether male guppies with rare colour patterns have a reproductive advantage in nature, we conducted 17 separate manipulations in 3 different populations in Trinidad⁸. Over two field seasons, we manipulated frequencies of naturally occurring colour patterns within replicate pools in the Mausica River (5 replicates) and in two

separate tributaries of the Quare River (Quare River 1 (6 replicates); and Quare River 7 (6 replicates)). At each site, we sorted males into groups that were nearly equal in abundance, based on caudal fin colour, as ‘uncoloured’ (>75% of the caudal fin transparent) or ‘coloured’ (>50% of fin coloured); males with intermediate colouration were excluded from the experiment. Males were then re-introduced into pools in a ratio of 3:1 (in which 1 is ‘rare’), with each morph being rare in half of the pools. After 16 to 17 days, depending on the site, all adults were collected, separated by sex, and identified by pool-specific tattoos and pre- and post-release photographs. Adult females ($n = 193$) were taken to the laboratory, where we collected their first two broods (2 to 24 offspring per female, mean = 7.6). We genotyped these females, 166 experimental males, 693 first-brood and 777 second-brood offspring at 9 to 14 variable microsatellite loci^{14,15}. To avoid confounding reproductive success with differential survival, only experimental males that survived to the end of the experiment, and that did not move between pools during the experiment were considered as candidate fathers. Using a conservative 95% confidence level for paternity assignment¹⁶, the number of offspring assigned to candidate fathers ranged from 0 to 12, and mating success (the number of females with which a male produced at least one offspring) ranged from 0 to 8 females (Supplementary Table 1).

Among first-brood offspring, males bearing rare colour patterns had more than twice as many mates and offspring as males bearing common patterns, based on the paternity assignment (Fig. 2a). Other experimental factors such as population, morph (the particular colour pattern chosen to be rare or common within a replicate), and population-by-morph interaction did not significantly affect the number of mates or offspring (Extended Data Table 1). Males with rare colour patterns thus had a reproductive advantage over those with common patterns, and this advantage did not depend on population or on the specific colour pattern that was rare or common in a given replicate (Extended Data Fig. 1). When we relaxed the criterion for paternity

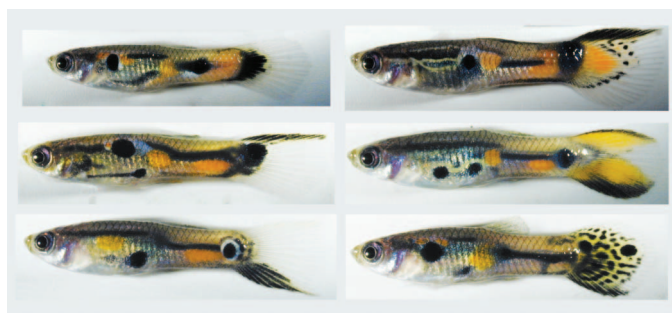


Figure 1 | Colour pattern variation among males from a single population. Male offspring of Quare River 7 tributary fish, reared in a common environment and showing heritable colour-pattern variation. Males on the left have a caudal fin that is representative of the ‘uncoloured’ group, those on right are have a caudal fin that is representative of the ‘coloured’ group. Criteria for classification are described in ref. 9.

¹Department of Biological Science, 319 Stadium Drive, Florida State University, Tallahassee, Florida 32306, USA. ²Department of Biology, Lake Forest College, 555 North Sheridan Road, Lake Forest, Illinois 60045, USA. ³Department of Ecology and Evolutionary Biology, University of Toronto, 25 Harbord Street, Toronto, Ontario M5S 3G5, Canada.

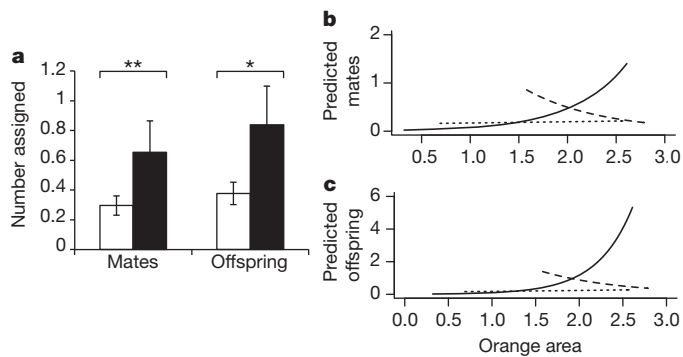


Figure 2 | Rare colour patterns have higher mating and reproductive success. **a**, Number of mates and offspring assigned to common (white, $n = 124$) or rare (dark grey, $n = 42$) males. Centre values are marginal means from the full generalized linear mixed model; bars indicate s.e.m. adjusted for model covariance parameters. $**P < 0.005$ and $*P = 0.01$, respectively; see Extended Data Table 1. **b**, **c**, Association between square-root orange area and reproductive success in Quare River 7 (solid line, $n = 34$), Quare River 1 (dashed line, $n = 72$) and Mausica River (dotted line, $n = 60$), predicted from the full model. **b**, Predicted mates. **c**, Predicted offspring; see Extended Data Table 2. Minimum and maximum values along abscissa indicate range of values recorded.

confidence to $>85\%$, the effects of all experimental factors were similar to the original analysis (Extended Data Table 2). The results are therefore robust to the specific criterion for paternity assignment.

We also examined effects of variation in male size (total body area), and colour (area of orange and black body colouration, Supplementary Table 1) because these traits have been implicated in previous studies of sexual selection in guppies^{4,17}. In generalized linear mixed models (GLMMs, see Methods), main effects of variation in these traits were not significant, but the population-by-orange area interaction was associated with both mate and offspring number (Extended Data Table 1). In both cases, the significant interaction was due to a positive association between reproductive success and orange area that was unique to the Quare River 7 population; the association was negative in Quare River 1, and close to zero in the Mausica River population (Fig. 2b, c and Extended Data Table 3). This population dependence is consistent with laboratory studies that document variation in the existence and strength of female preference for orange among natural guppy populations⁴. Again, these patterns were robust when we relaxed the criterion for paternity assignment (Extended Data Table 2).

Female guppies give birth to live offspring every 27 to 30 days and will fertilize eggs with stored sperm if they have not mated recently^{4,17}. To distinguish the effects of recent insemination from long-term sperm storage, we separately analysed the second broods produced by females following the field experiment. These broods were produced at least 47 days after the end of the field experiment, and a full reproductive cycle after the first broods; they were therefore fertilized by sperm stored for at least 47 days because guppies do not carry embryos at multiple stages of development¹⁸. For these second broods, several aspects of male colouration, but not rarity, significantly influenced male reproductive success (Extended Data Table 4). Males with more highly coloured caudal fins had more assigned mates and offspring than those with little colour, while the number of orange spots on the body was negatively related to mate number (GLMM; $\beta = -1.0 \pm 0.5$, $\chi^2 = 4.83$, d.f. = 1, $P = 0.03$), and non-significantly related to offspring number (GLMM; $\beta = -1.3 \pm 0.6$, $\chi^2 = 3.53$, d.f. = 1, $P = 0.06$). As in first broods, the area of orange body colour interacted significantly with population to predict male reproductive success. Again, the interaction occurred because orange was positively associated with reproductive success in Quare River 7, but not in the other two populations (Extended Data Table 5).

These results for second broods are consistent with laboratory data indicating that male colour can predict sperm competitive ability and/or cryptic female choice¹⁹. Nevertheless, if females mate at least once per reproductive cycle in nature, the first-brood data should better reflect male success because these data capture the effects of recent matings and short-term sperm storage. Two lines of evidence indicate that females do mate at least once per cycle: first, a high proportion of wild females have recently-deposited sperm in their gonoducts^{20,21}; and second, all post-partum females re-mate within 48 h in laboratory studies^{10,22}. These data suggest that nearly all females mate at least once (and probably more than once) per cycle.

Our results support the prediction of the 'rare-male effect' hypothesis that males with phenotypes that are rare in the local environment have a reproductive advantage over males with common phenotypes²³. It is possible that we observed unusually strong NFDS because we perturbed morph frequencies in our experiment, and thereby made it more difficult to detect selection on other aspects of male phenotypes. However, it is precisely this dependence of selection on morph frequency that maintains variation. Our results indicate that if colour pattern frequencies deviate sufficiently from their equilibrium values, NFDS will dominate the evolutionary dynamics.

Although we cannot be certain that the rare-male advantage we observed was caused by female mate preference, abundant evidence from laboratory studies indicates that females prefer males with rare phenotypes^{11,12,24}. Moreover, female preference is more important than male-male competition in determining mating outcomes in this species^{4,17}. These data indicate that rare-male advantage in the field is likely to be mediated by female mate preference. In contrast, male-male competition^{7,25,26} and sexual conflict²⁷ have been implicated in the maintenance of discrete sex-limited polymorphism in other species. In each of those cases, the polymorphism involves two or three discrete morphs, compared to the much larger numbers of morphs found within guppy populations. The relative importance of female preference and other kinds of interactions in driving NFDS and in maintaining polymorphism is an intriguing direction for future research.

Despite strong evidence for the rare-male effect in guppies, the evolutionary processes that account for its prevalence are not known. Mate preference for males with unusual colouration might have evolved as a mechanism for inbreeding avoidance¹⁵, as a consequence of generalized neophilia¹⁰, or because females avoid remating with previous mates and also reject males with colouration similar to that of previous mates¹². It has been previously proposed²⁸ that a survival advantage to rare morphs, as demonstrated in ref. 8, could also drive the evolution of mate preference for rare phenotypes, even though rarity itself is not heritable.

Understanding whether, and when, balancing selection maintains genetic variation in ecologically important traits is a central challenge for modern evolutionary biology, with profound implications for medical, agricultural and ecological genetics³. Manipulative experiments in nature have demonstrated balancing selection in guppies⁸ and other species^{7,29}. In guppies, these experiments have been powerful enough to reveal multiple ecological mechanisms that contribute to balancing selection and to reveal directional and balancing selection that act on the same phenotypes. We suggest that manipulations in natural populations will be useful for discovering the ecological processes that maintain other polymorphisms including those, like the vertebrate major histocompatibility complex, that have been refractory to other approaches³⁰.

METHODS SUMMARY

At each site, we used pools of similar size, structure, substrate and water clarity to form replicate experimental pools⁸. After collecting all adult guppies from each experimental pool, all fish were photographed and given pool-specific elastomer tattoos before being used in the experiment. We also kept density and sex ratio close to natural levels. All procedures complied with animal care standards of the Canadian Council on Animal Care and were approved by University of Toronto's Animal Care Committee.

The candidate fathers were the 166 marked experimental males that survived to the end of the experiment (60 from Mausica River, 72 from Quare River 1, and 34 from Quare River 7). We used CERVUS 3.03 (ref. 16) for paternity assignment. For 135 first-brood offspring, paternity was assigned to an experimental male with >85% confidence; 93 were assigned with >95% confidence (Supplementary Tables 1 and 2). For the rest, the difference in log-likelihoods between the first and second most likely fathers indicated <85% probability that the most likely father was the true father, and these paternity assignments were not used in our analysis. For second broods, 158 offspring were assigned with >85% confidence and 102 with >95% confidence. We fit generalized linear mixed models to counts of assigned mates and offspring, using a negative binomial distribution and Laplace approximation for estimating the marginal likelihood. Pools nested within populations were modelled as random effects. Fixed effects included population, treatment (rare versus common), morph (coloured versus uncoloured caudal fin), body size (area of a two-dimensional image, excluding all fins), body area covered by orange, number of discrete orange and black spots, and all two-way interactions. Area covered by black and three-way interactions were also tested, but never approached significance (all $P > 0.1$) and were not included in the final models.

Online Content Any additional Methods, Extended Data display items and Source Data are available in the online version of the paper; references unique to these sections appear only in the online paper.

Received 10 June; accepted 26 September 2013.

Published online 30 October 2013.

- Lewontin, R. C. *The Genetic Basis of Evolutionary Change* (Columbia Univ. Press, 1974).
- Turelli, M. & Barton, N. H. Polygenic variation maintained by balancing selection: pleiotropy, sex-dependent allelic effects and G×E interactions. *Genetics* **166**, 1053–1079 (2004).
- Mitchell-Olds, T. Willis, J. H. & Goldstein, D. B. Which evolutionary processes influence natural genetic variation for phenotypic traits? *Nature Rev. Genet.* **8**, 845–856 (2007).
- Houde, A. E. *Sex, Color and Mate Choice in Guppies* (Princeton Univ. Press, 1997).
- Brooks, R. & Endler, J. A. Direct and indirect sexual selection and quantitative genetics of male traits in guppies (*Poecilia reticulata*). *Evolution* **55**, 1002–1015 (2001).
- Ayala, F. J. & Campbell, C. A. Frequency-dependent selection. *Annu. Rev. Ecol. Syst.* **5**, 115–138 (1974).
- Bleay, C., Comendant, T. & Sinervo, B. An experimental test of frequency-dependent selection on male mating strategy in the field. *Proc. R. Soc. B* **274**, 2019–2025 (2007).
- Olendorf, R. et al. Frequency-dependent survival in natural guppy populations. *Nature* **441**, 633–636 (2006).
- Hughes, K. A., Rodd, F. H. & Reznick, D. N. Genetic and environmental effects on secondary sex traits in guppies (*Poecilia reticulata*). *J. Evol. Biol.* **18**, 35–45 (2005).
- Hughes, K. A., Du, L., Rodd, F. H. & Reznick, D. N. Familiarity leads to female mate preference for novel males in the guppy, *Poecilia reticulata*. *Anim. Behav.* **58**, 907–916 (1999).
- Zajitschek, S. R. K. & Brooks, R. C. Distinguishing the effects of familiarity, relatedness, and color pattern rarity on attractiveness and measuring their effects on sexual selection in guppies (*Poecilia reticulata*). *Am. Nat.* **172**, 843–854 (2008).
- Hampton, K. J., Hughes, K. A. & Houde, A. E. The allure of the distinctive: reduced sexual responsiveness of female guppies to 'redundant' male colour patterns. *Ethology* **115**, 475–481 (2009).
- Maynard Smith, J. *Evolution and the Theory of Games* (Cambridge Univ. Press, 1982).
- Olendorf, R., Reudi, B. & Hughes, K. A. Primers for 12 polymorphic microsatellite DNA loci from the guppy (*Poecilia reticulata*). *Mol. Ecol. Notes* **4**, 668–671 (2004).
- Johnson, A. M. et al. Inbreeding depression and inbreeding avoidance in a natural population of guppies (*Poecilia reticulata*). *Ethology* **116**, 448–457 (2010).
- Kalinowski, S. T., Taper, M. L. & Marshall, T. C. Revising how the computer program CERVUS accommodates genotyping error increases success in paternity assignment. *Mol. Ecol.* **16**, 1099–1106 (2007).
- Magurran, A. E. *Evolutionary Ecology: The Trinidadian Guppy* (Oxford Univ. Press, 2005).
- Pires, M. N., Arendt, J. & Reznick, D. N. The evolution of placentas and superfetation in the fish genus *Poecilia* (Cyprinodontiformes: Poeciliidae: subgenera *Micropoecilia* and *Acanthophaelus*). *Biol. J. Linn. Soc.* **99**, 784–796 (2010).
- Evans, J. P., Zane, L., Francescato, S. & Pilastro, A. Directional postcopulatory sexual selection revealed by artificial insemination. *Nature* **421**, 360–363 (2003).
- Matthews, I. M. & Magurran, A. E. Evidence for sperm transfer during sneaky mating in wild Trinidadian guppies. *J. Fish Biol.* **56**, 1381–1386 (2000).
- Evans, J. P., Pilastro, A. & Ramnarine, I. W. Sperm transfer through forced matings and its evolutionary implications in natural guppy (*Poecilia reticulata*) populations. *Biol. J. Linn. Soc.* **78**, 605–612 (2003).
- Rosenthal, H. L. Observations on reproduction of the poeciliid *Lebistes reticulatus* (Peters). *Biol. Bull.* **102**, 30–38 (1952).
- Petit, C. & Ehrman, L. in *Evolutionary Biology* Vol. 3 (eds Dobzansky T., Hecht M. K. & Steere W. C.) Sexual Selection in *Drosophila*. (North-Holland, 1969).
- Farr, J. A. Male rarity or novelty, female choice behavior and sexual selection in the guppy *Poecilia reticulata* Peters (Pisces: Poeciliidae). *Evolution* **31**, 162–168 (1977).
- Shuster, S. M. & Wade, M. J. Equal mating success among male reproductive strategies in a marine isopod. *Nature* **350**, 608–610 (1991).
- Dijkstra, P. D., Seehausen, O. & Groothuis, T. G. G. Direct male–male competition can facilitate invasion of new colour types in Lake Victoria cichlids. *Behav. Ecol. Sociobiol.* **58**, 136–143 (2005).
- Takahashi, Y., Yoshimura, J., Morita, S. & Watanabe, M. Negative frequency-dependent selection in female color polymorphism of a damselfly. *Evolution* **64**, 3620–3628 (2010).
- Kokko, H., Jennions, M. D. & Houde, A. Evolution of frequency-dependent mate choice: keeping up with fashion trends. *Proc. R. Soc. B* **274**, 1317–1324 (2007).
- Gigord, L. D. B., Macnair, M. R. & Smithson, A. Negative frequency-dependent selection maintains a dramatic flower color polymorphism in the rewardless orchid *Dactylorhiza sambucina* (L.) Soó. *Proc. Natl Acad. Sci. USA* **98**, 6253–6255 (2001).
- Spurgin, L. G. & Richardson, D. S. How pathogens drive genetic diversity: MHC, mechanisms and misunderstandings. *Proc. R. Soc. B* **277**, 979–988 (2010).

Supplementary Information is available in the online version of the paper.

Acknowledgements We thank R. Olendorf for help with field work and genotyping; D. Punzalan, K. Dixon, M. Bryant, T. Pitcher, C. Baril, A. Inman and C. Hurt for field work; C. Gibson, K. McGhee for photographs in Fig. 1 and for animal rearing; J. Koprivnikar for animal rearing; and A. Vanesyan for collecting morphology data. D. Reznick provided advice on field experiments, and D. Punzalan, K. Dixon and M. Fitzpatrick commented on manuscript drafts. In Trinidad, we thank the Sinanan family for accommodation, and I. Ramnarine and the government of Trinidad for permission to collect guppies and to work in the Quare watershed. This work was supported by grants from the National Science Foundation (to K.A.H. and A.E.H.) and the Natural Sciences and Engineering Research Council (NSERC) of Canada (to F.H.R.).

Author Contributions K.A.H. and F.H.R. conceived and designed the experiment and conducted all data analyses. A.E.H. consulted on experimental design and A.C.P. reared live animals. All authors participated in field experiments and in writing the paper.

Author Information Reprints and permissions information is available at www.nature.com/reprints. The authors declare no competing financial interests. Readers are welcome to comment on the online version of the paper. Correspondence and requests for materials should be addressed to K.A.H. (kahughes@bio.fsu.edu).

METHODS

Field experiment. The sections of the Mautica River, Quare River 1 and Quare River 7 streams that we used had a pool-and-riffle structure that naturally limits migration between pools, particularly during the dry season, which is the time of year when our experiments were conducted³¹. We also built temporary barriers between pools to reduce migration further. At each site, we used five to six pools of similar size, structure, substrate and water clarity to form replicate experimental pools⁸. We collected all adult guppies from each pool and sorted males into two groups that were nearly equal in abundance within sites, based on classification of caudal fin colour morphs as 'uncoloured' (>75% of the caudal fin transparent) and 'coloured' (>50% of fin coloured); males with intermediate amounts of colour were excluded from the experiment. Fish were photographed and given pool-specific marks using a small elastomer injection. Males were reintroduced into pools in a ratio of 3:1 with each morph as the rare type in half the pools. Females that were used in the experiment were always reintroduced into the same pool from which they had been collected. We controlled for the density and size of the pools by maintaining the original, or slightly reducing, the numbers of adults that had been in the pools; we also maintained the natural sex ratio. Detailed methods and the number of males of each type and the number of females reintroduced into each pool are described in ref. 8. All procedures complied with animal care standards of the Canadian Council on Animal Care and were approved by University of Toronto's Animal Care Committee.

Experimental males. We genotyped 166 marked experimental males that survived to the end of the experiment (60 from Mautica River, 72 from Quare River 1, and 34 from Quare River 7); these were the recaptured 'rare' and 'common' males described in ref. 9. Of these, 124 were classified as common (43 in Mautica River, 53 in Quare River 1, and 28 in Quare River 7) and 42 were classified as rare (17 in Mautica River, 19 in Quare River 1, and 6 in Quare River 7). We also genotyped 193 adult females that survived the field experiment (55 from Mautica River, 83 from Quare River 1, and 55 from Quare River 7), 693 first-brood offspring of these females, and 777 second-brood offspring. Animals from Quare River 1 and Mautica River were from the field experiment that was conducted in 2003, and animals from Quare River 7 were from the field experiment that was conducted in 1999. Sixty-one other males caught at the end of the experiment were unmarked and presumed to have matured during the experiment or to have migrated into the study area. Eight marked males migrated between pools during the experiment. We genotyped all mature males that were collected at the end of the experiment so that offspring could be assigned to them, but we did not include the unmarked males or the eight migrant males in subsequent analyses because they were present in the experimental pools or were sexually mature for an unknown period of time. In addition, 58 marked males did not survive to the end of the experiment⁸. These males were not genotyped and therefore not included in the paternity analysis.

Paternity analysis. We genotyped 14, 11, and 9 loci, respectively, from fish of the Quare River 1, Quare River 7 and Mautica River populations, which had a mean number of 11, 16.2 and 11.6 alleles per locus. The individual who scored genotypes was blind to the experimental treatment group of the individuals. For paternity analysis, we used CERVUS 3.0.3 to simulate 100,000 offspring, assuming a mistyping

rate of 0.02, that 80% of candidate fathers were genotyped, a minimum of 5 loci typed, and a strict confidence level of 95%. The combined exclusion probabilities were 3.8×10^{-9} in Quare River 7, 3.9×10^{-5} in Quare River 1, and 4.7×10^{-4} in Mautica River. To assign paternity to a male, the difference in LOD (logarithm of odds) scores between the most likely candidate father and the second most likely candidate father (delta) had to exceed the 95th percentile of values produced from 100,000 simulations.

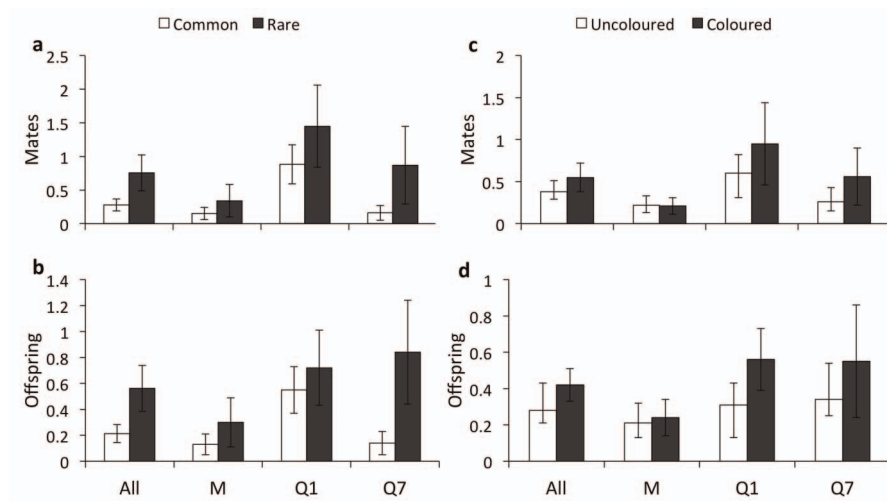
For 424 first-brood offspring, the most likely father was an experimental male; for the remainder the most probable father was a migrant or was unassigned. For 135 offspring, paternity was assigned to an experimental male with >85% confidence; 93 were assigned with >95% confidence. For the rest, the difference in log-likelihoods between the first and second most likely fathers corresponded to <85% probability that the most likely father was the true father, and these paternity assignments were not used in subsequent analyses. For second broods, 435 offspring were assigned to experimental males, 158 of these were assigned with >85% confidence and 102 with >95% confidence (Supplementary Table 2).

Morphological measurements. Images were measured using ImageJ³². Areas were measured by outlining the region with the freehand tool. The area of the entire body, excluding the fins and gonopodium, was measured. Individual coloured spots were each outlined and measured separately. These measures of area were square root transformed before analysis to conform to model assumptions. For three males (two in Quare River 7 and one in Mautica River), pictures taken in the field were of such low quality that reliable morphological measures could not be obtained. These males were excluded from the analyses of quantitative traits, but were included in the analyses that only considered experimental treatment factors.

Statistical analysis. We fit generalized linear mixed models to counts of assigned mates and offspring, using a negative binomial distribution, and Laplace approximation for estimating the marginal likelihood. Replicate experimental pools nested within populations were modelled as random effects. Fixed effects included population, treatment (rare versus common), morph (coloured versus uncoloured caudal fin), body size (area of a two-dimensional image, excluding all fins), body area covered by orange, numbers of discrete orange and black spots, and all two-way interactions. Body area covered by black, and three-way interactions were also tested, but never approached significance (all $P > 0.1$) and were not included in the final models. All analyses were conducted in SAS 9.3 (ref. 33); generalized linear mixed models were implemented in Proc Glimmix.

GPS coordinates of sites. The natural populations used in these experiments were located at: Mautica, PS 685749 1176906; Quare 1, PS 696972 1180687 (called Quare 2 in ref. 34); Quare 7, PS 697407 1179935.

31. Reznick, D. N., Butler, M. J. IV., Rodd, F. H. & Ross, P. Life-history evolution in guppies (*Poecilia reticulata*): 6. Differential mortality as a mechanism for natural selection. *Evolution* **50**, 1651–1660 (1996).
32. Schneider, C. A., Rasband, W. S. & Eliceiri, K. W. NIH Image to ImageJ: 25 years of image analysis. *Nature Methods* **9**, 671–675 (2012).
33. SAS Institute. *SAS/STAT 9.3 User's Guide*. (SAS Institute, 2011).
34. Endler, J. A. A predator's view of animal color patterns. *Evol. Biol.* **11**, 319–364 (1978).



Extended Data Figure 1 | Population means for effects of rarity and morph on reproductive success. Centre values are marginal means from generalized linear mixed models; bars indicate s.e.m. adjusted for model parameters.

* $P < 0.01$ and ** $P < 0.05$, respectively. **a**, Mates assigned to common (white bars) and rare (dark grey bars) males in all populations (All, $n = 124$ common, 42 rare) and by population (M, Mausica, $n = 43$ common, 17 rare; Q1, Quare 1, $n = 53$ common, 19 rare; Q7, Quare 7, $n = 28$ common, 6 rare). **b**, Offspring for

common and rare males. **c**, Mates assigned to males with uncoloured (white bars) or coloured (dark grey bars) tails for all populations (All, $n = 79$ uncoloured, 87 coloured) and by population (M, Mausica, $n = 26$ uncoloured, 34 coloured; Q1, Quare 1, $n = 35$ uncoloured, 37 coloured; Q7, Quare 7, $n = 18$ uncoloured, 16 coloured). **d**, Offspring for males with uncoloured and coloured tails.

Extended Data Table 1 | Effect of experimental factors and quantitative traits on reproductive success in first-brood offspring

Mates	DF	χ^2	P
Population	2	3.82	0.148
Rarity	1	9.09	0.003
Population*rarity	2	4.25	0.120
Morph	1	1.75	0.185
Population*morph	2	0.43	0.805
Body size	1	0.01	0.919
Population*size	2	3.58	0.167
Orange area	1	0.16	0.689
Population*orange area	2	6.15	0.046
Number orange spots	1	1.24	0.266
Population*orange spots	2	0.91	0.634
Number black spots	1	1.31	0.251
Population*black spots	2	5.31	0.070
Offspring			
Population	2	3.10	0.213
Rarity	1	6.69	0.010
Population*rarity	2	1.57	0.457
Morph	1	1.21	0.271
Population*morph	2	0.78	0.677
Body size	1	0.01	0.908
Population*size	2	2.54	0.281
Orange area	1	0.87	0.352
Population*orange area	2	6.52	0.035
Number orange spots	1	2.75	0.098
Population*orange spots	2	1.36	0.506
Number black spots	1	1.18	0.278
Population*black spots	2	3.18	0.204

Significant effects are shown in bold.

Extended Data Table 2 | Effect of experimental factors and quantitative traits on reproductive success

Mates	DF	χ^2	P
Population	2	2.89	0.269
Rarity	1	4.50	0.036
Population*rarity	2	4.68	0.101
Morph	1	0.60	0.440
Population*morph	2	2.83	0.247
Body size	1	0.13	0.721
Population*size	2	2.86	0.244
Orange area	1	0.00	0.986
Population*orange area	2	6.92	0.034
Number orange spots	1	0.62	0.434
Population*orange spots	2	0.65	0.722
Number black spots	1	2.58	0.111
Population*black spots	2	3.38	0.189
Offspring			
Population	2	2.39	0.332
Rarity	1	2.94	0.089
Population*rarity	2	3.03	0.223
Morph	1	0.55	0.462
Population*morph	2	3.26	0.200
Body size	1	0.16	0.689
Population*size	2	2.00	0.370
Orange area	1	0.27	0.602
Population*orange area	2	6.37	0.045
Number orange spots	1	1.43	0.235
Population*orange spots	2	1.23	0.542
Number black spots	1	2.31	0.131
Population*black spots	2	2.37	0.309

First-brood offspring, paternity confidence >85%. Significant effects are shown in bold.

Extended Data Table 3 | Population-specific estimates of the association between area of orange body colour and reproductive success

Mates	Estimate	SE	DF	t	P
Q7	1.8	1.0	128	1.86	0.066
Q1	-1.3	0.8	128	-1.70	0.095
M	0.1	1.0	128	0.14	0.893
Offspring					
Q7	2.5	1.2	128	2.13	0.035
Q1	-1.1	0.8	128	-1.40	0.164
M	0.2	1.1	128	0.24	0.813

First-brood offspring and paternity confidence >95%. Estimates derived from the generalized linear mixed model.

Extended Data Table 5 | Parameter estimates for effects of morph (coloured – uncoloured) and the area of orange body colour, on number of assigned mates and assigned offspring

Mates	Estimate	SE	DF	t	P
Morph	1.5	0.8	128	-2.05	0.043
Q7	3.4	1.3	128	2.60	0.010
Q1	-0.7	0.7	128	-1.01	0.310
M	0.5	1.2	128	0.41	0.682
Offspring					
Morph	2.0	0.9	128	-2.17	0.030
Q7	4.0	1.4	128	2.81	0.006
Q1	-1.2	0.9	128	-1.40	0.165
M	0.3	1.3	128	0.22	0.826

Second-brood offspring, paternity confidence >95%.

Extended Data Table 4 | Effect of experimental factors and quantitative traits on reproductive success

Mates	DF	χ^2	P
Population	2	1.24	0.539
Rarity	1	0.90	0.344
Population*rarity	2	1.38	0.503
Morph	1	7.20	0.007
Population*morph	2	1.34	0.511
Body size	1	1.04	0.308
Population*size	2	1.74	0.418
Orange area	1	2.97	0.085
Population*orange area	2	7.63	0.022
Number orange spots	1	4.83	0.028
Population*orange spots	2	1.44	0.488
Number black spots	1	0.00	0.974
Population*black spots	2	3.68	0.159
Offspring			
Population	2	0.00	0.999
Rarity	1	0.11	0.743
Population*rarity	2	1.00	0.606
Morph	1	7.37	0.007
Population*morph	2	2.12	0.347
Body size	1	1.38	0.241
Population*size	2	0.08	0.960
Orange area	1	2.06	0.152
Population*orange area	2	9.76	0.008
Number orange spots	1	3.53	0.063
Population*orange spots	2	3.96	0.142
Number black spots	1	0.22	0.643
Population*black spots	2	5.10	0.082

Second-brood offspring, paternity confidence 95%. Significant effects are shown in bold.

Genetic identification of a neural circuit that suppresses appetite

Matthew E. Carter^{1,2†}, Marta E. Soden^{3,4}, Larry S. Zweifel^{3,4} & Richard D. Palmiter^{1,2}

Appetite suppression occurs after a meal and in conditions when it is unfavourable to eat, such as during illness or exposure to toxins. A brain region proposed to play a role in appetite suppression is the parabrachial nucleus^{1–3}, a heterogeneous population of neurons surrounding the superior cerebellar peduncle in the brainstem. The parabrachial nucleus is thought to mediate the suppression of appetite induced by the anorectic hormones amylin and cholecystokinin², as well as by lithium chloride and lipopolysaccharide, compounds that mimic the effects of toxic foods and bacterial infections, respectively^{4–6}. Hyperactivity of the parabrachial nucleus is also thought to cause starvation after ablation of orexigenic agouti-related peptide neurons in adult mice^{1,7}. However, the identities of neurons in the parabrachial nucleus that regulate feeding are unknown, as are the functionally relevant downstream projections. Here we identify calcitonin gene-related peptide-expressing neurons in the outer external lateral subdivision of the parabrachial nucleus that project to the latero-capsular division of the central nucleus of the amygdala as forming a functionally important circuit for suppressing appetite. Using genetically encoded anatomical, optogenetic⁸ and pharmacogenetic⁹ tools, we demonstrate that activation of these neurons projecting to the central nucleus of the amygdala suppresses appetite. In contrast, inhibition of these neurons increases food intake in circumstances when mice do not normally eat and prevents starvation in adult mice whose agouti-related peptide neurons are ablated. Taken together, our data demonstrate that this neural circuit from the parabrachial nucleus to the central nucleus of the amygdala mediates appetite suppression in conditions when it is unfavourable to eat. This neural circuit may provide targets for therapeutic intervention to overcome or promote appetite.

The parabrachial nucleus (PBN) contains subpopulations of neurons that regulate taste^{10,11}, sodium intake^{12,13}, respiration¹⁴, pain^{15,16}, thermosensation^{17,18} and appetite suppression^{1–3,7}. To identify a specific genetic marker for PBN neurons that suppress appetite, we analysed expression of Fos, a surrogate marker of neuronal excitation, after genetic ablation of agouti-related peptide (AgRP) neurons or injection of lithium chloride (LiCl). AgRP neurons were ablated in mice expressing the human diphtheria toxin receptor (DTR) specifically in AgRP neurons (*AgRP^{DTR}* mice)¹⁹. Both AgRP neuron ablation (two diphtheria toxin injections at 50 µg kg^{−1}, intramuscular) and LiCl injection (84 mg kg^{−1}, intraperitoneal) induced Fos expression in the outer external lateral subdivision of the PBN (PBelo; Supplementary Fig. 1). To identify a potential genetic marker for these neurons, we consulted the Allen Brain Explorer (<http://mouse.brain-map.org>)²⁰ and searched for genes enriched in the PBelo. The top candidate was *Calca*, the gene that encodes calcitonin gene-related peptide (CGRP) and calcitonin by alternative splicing²¹. Indeed, Fos expression in the PBN after ablation of AgRP neurons strongly overlapped with immunohistochemical detection of CGRP (Supplementary Fig. 2), similar to previous reports of coincident expression of Fos and CGRP after injection of LiCl or lipopolysaccharide (LPS)^{6,22}.

To control gene expression in these neurons, we generated a genetic knock-in mouse expressing Cre recombinase at the *Calca* locus (Supplementary Fig. 3). When these mice were crossed with Cre-dependent TdTomato reporter mice, ubiquitous red fluorescence was detected throughout the brain, probably because of transient Cre expression during development. However, injection of a Cre-dependent adeno-associated virus (AAV) carrying a mCherry reporter directly into the PBN region of adult *Calca^{Cre/+}* mice (Fig. 1a) resulted in specific expression of mCherry in CGRP-positive neurons in the PBelo (Fig. 1b and Supplementary Figs 4 and 5).

To map activity in PBelo CGRP neurons, we compared virally targeted mCherry fluorescence with Fos following an array of environmental conditions that induced appetite suppression (see Supplementary Fig. 6 for specific conditions used). In the lateral PBN, more than 80% of Fos expression co-localized with CGRP neurons after AgRP neuron ablation, intraperitoneal injection of LiCl, injection of LPS (Fig. 1c–h) or injection of the satiety hormones amylin or cholecystokinin (CCK; Supplementary Fig. 7a–d). In contrast, few Fos-positive neurons were observed in animals injected with saline (Fig. 1i, j), fasted for 24 h or after aversive tail pinching (Supplementary Fig. 7e–h). The percentage of CGRP neurons co-expressing Fos significantly correlated with the reduction in food intake relative to baseline conditions (Fig. 1k, l; see figure legends for *P* values and Supplementary Information for detailed statistical analyses). These results indicate that PBelo CGRP neurons are active during conditions in which appetite is suppressed but not in response to general adverse conditions.

To determine whether transient stimulation of PBelo CGRP neurons is sufficient to reduce food intake, we unilaterally injected AAV carrying a Cre-dependent channelrhodopsin-2 transgene (AAV1 DIO ChR2-mCherry)⁸ into the PBN of *Calca^{Cre/+}* mice (Fig. 2a). Photostimulation reliably induced action potentials in mCherry-positive neurons in acute brainstem slices at several frequencies (20–40 Hz; Supplementary Fig. 8a) and *in vivo* photostimulation at 30 Hz was sufficient to induce expression of Fos (Supplementary Fig. 8b, c). Stimulation of CGRP neurons *in vivo* for 5 min at 30 or 40 Hz (10-ms pulses) significantly and reversibly suppressed food intake during both baseline conditions and after a 24-h fast (Fig. 2b, c and Supplementary Fig. 8d), demonstrating that activating these neurons is sufficient to suppress food intake. Suppression of feeding after photostimulation was rapid (within 5–10 s; Supplementary Video 1) and reversible (mice typically resumed feeding in 5–10 min after photostimulation ceased). Stimulation at these frequencies did not impair movement or cause overt signs of distress (Supplementary Video 1).

To determine the effects of longer-term stimulation of PBelo CGRP neurons, we unilaterally transduced these neurons with AAV carrying a Cre-dependent hM₃Dq-mCherry^{9,23} transgene (Fig. 2d). Stimulation of hM₃Dq with clozapine-*N*-oxide (CNO, 1 mg kg^{−1}) induced Fos expression (Supplementary Fig. 9) and suppressed food intake both during baseline conditions and after a 24-h fast (Fig. 2e, f). Chronic stimulation (once every 12 h for 4 d) resulted in a pronounced reduction

¹Howard Hughes Medical Institute, University of Washington, Seattle, Washington 98195, USA. ²Department of Biochemistry, University of Washington, Seattle, Washington 98195, USA. ³Department of Pharmacology, University of Washington, Seattle, Washington 98195, USA. ⁴Department of Psychiatry, University of Washington, Seattle, Washington 98195, USA. [†]Present address: Department of Biology, Williams College, Williamstown, Massachusetts 01267, USA.

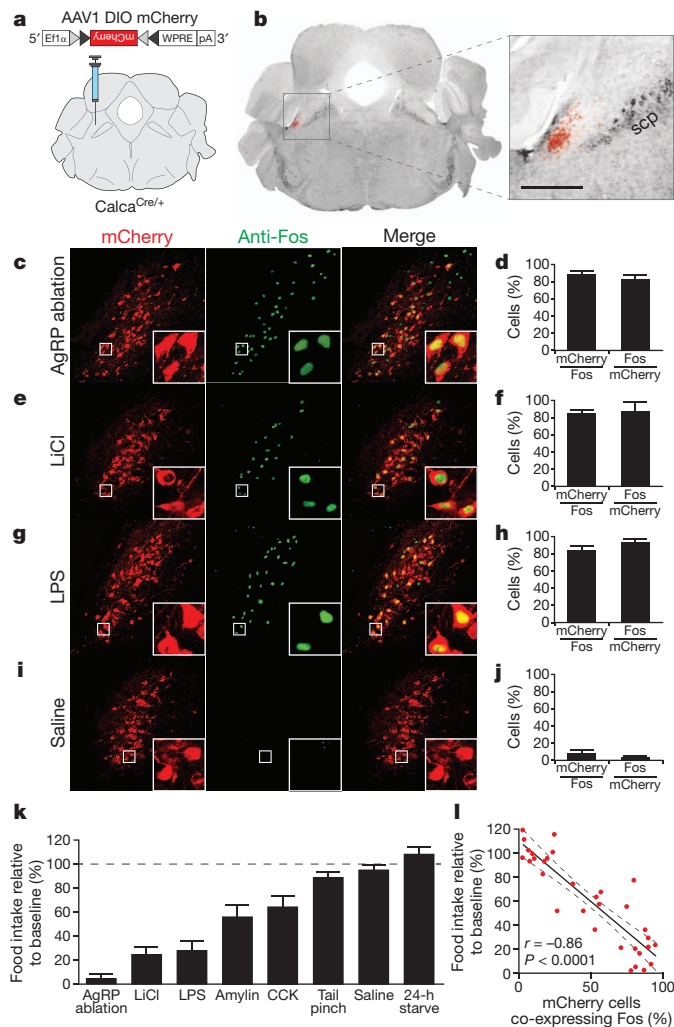


Figure 1 | Co-localization of PBelo CGRP neurons with Fos following conditions that reduce food intake. **a**, AAV carrying a Cre-dependent mCherry reporter injected into the PBN. Grey and black triangles represent loxP and lox2722 sites, respectively. **b**, mCherry expression in the PBelo. scp, superior cerebellar peduncle; scale bar, 500 μ m. **c–j**, Representative histological examples and quantification of coincidence of mCherry and Fos expression ($n = 4$ animals per condition). **k**, Degree to which various conditions reduce food intake ($n = 4$ animals per condition). **l**, Appetite suppression correlates with the percentage of PBelo CGRP neurons expressing Fos. Dashed lines represent 95% confidence intervals. See Supplementary Information for statistical analysis.

in food intake and body weight (Fig. 2g, h), demonstrating that long-term activation of these neurons is sufficient to cause starvation.

To determine the effects of inhibiting PBelo CGRP neurons, we bilaterally transduced these neurons with AAV carrying a Cre-dependent hM₄Di-mCherry^{9,23} transgene (Fig. 3a). In acute brainstem slices, bath infusion of CNO reversibly reduced the firing frequency of hM₄Di-expressing neurons to $24.98 \pm 8.96\%$ of baseline (Supplementary Fig. 10a, b). There was no change in baseline food intake or body weight after intraperitoneal injection of CNO in either acute or chronic (once every 12 h for 4 d) conditions (Supplementary Fig. 11). However, inhibition of CGRP neurons with CNO decreased the suppression of appetite observed after injection of LiCl or LPS (Fig. 3b). Consistent with this observation, inhibition by hM₄Di also blocked the increase of Fos expression in the PBelo under these conditions (Supplementary Fig. 10c–f). Additionally, inhibition of CGRP neurons with CNO ameliorated appetite suppression after injection of amylin and CCK, although not to statistical significance (Fig. 3b). Because genetic ablation of AgRP neurons induces Fos expression in PBelo CGRP neurons

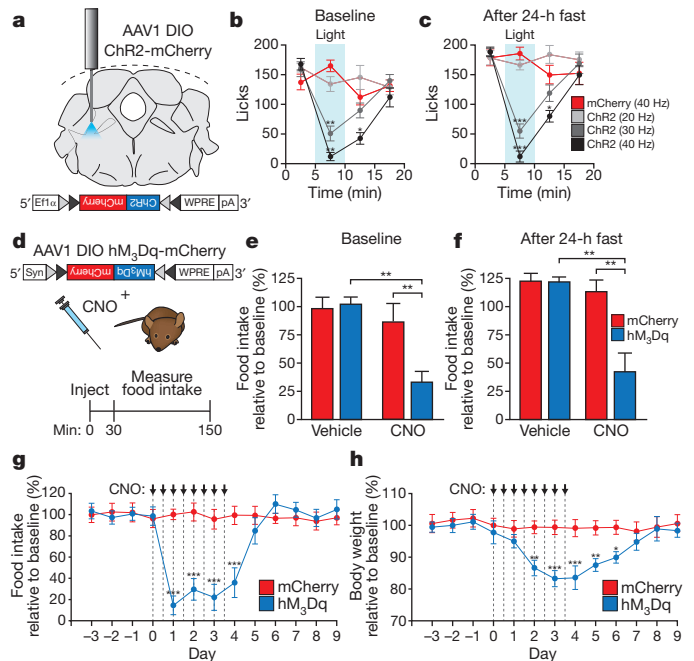


Figure 2 | Stimulation of PBelo CGRP neurons reduces food intake and causes starvation. **a**, Placement of fibre optic implant in the PBN in a *Calca*^{Cre/+} animal injected with AAV DIO ChR2-mCherry. **b**, **c**, Photostimulation of CGRP neurons reversibly inhibits food intake in both baseline (**b**) and fasted (**c**) conditions ($n = 8$ animals per group); experiment replicated at least 20 times per animal in three groups of animals. **d**, Top, diagram showing AAV DIO hM₃Dq-mCherry transgene unilaterally injected into the PBN; bottom, timeline of experiments in **e**, **f**, **e**, **f**, Pharmacogenetic stimulation of CGRP neurons inhibits food intake in both baseline (**e**) and fasted (**f**) conditions ($n = 6$ animals per group); experiment replicated at least 20 times per animal in three groups of animals. **g**, **h**, Chronic administration of CNO (every 12 h for 4 d) suppresses food intake (**g**) and reduces body weight (**h**) ($n = 6$ animals per group; experiment replicated in three groups of animals). * $P < 0.05$, ** $P < 0.01$, *** $P < 0.001$; see Supplementary Information for statistical analyses.

and leads to starvation⁷, we considered that bilateral inhibition of CGRP neurons would prevent starvation in these animals. To test this hypothesis, we bred *AgRP*^{DTR/+} mice with *Calca*^{Cre/+} mice and bilaterally injected *AgRP*^{DTR/+}/*Calca*^{Cre/+} offspring with AAV virus carrying Cre-dependent hM₄Di-mCherry. Indeed, chronic inhibition (injection of CNO every 12 h for 8 d) ameliorated the anorexia and prevented starvation after AgRP neuron ablation (Fig. 3c, d). Taken together, these results demonstrate that inhibition of PBelo CGRP neurons increases food intake under conditions that normally suppress appetite.

To examine the relevant efferent projections of PBelo CGRP neurons, we simultaneously injected two AAV vectors carrying either Cre-dependent mCherry or Cre-dependent synaptophysin-green fluorescent protein (Syn-GFP) transgenes into the PBN of *Calca*^{Cre/+} mice. We observed dense expression of mCherry- and GFP-positive fibres in the laterocapsular division of the central nucleus of the amygdala (CeAlc; Fig. 4a). This expression overlapped with immunohistochemical detection of CGRP in fibre terminals in the CeAlc (Fig. 4a) and is consistent with previous reports describing projections from the PBN to the central amygdala^{16,24,25}. To a lesser degree, we also observed expression of mCherry and Syn-GFP in the bed nucleus of the stria terminalis (BNST; Supplementary Fig. 12). We observed sparse expression of mCherry and Syn-GFP in the lateral hypothalamus, medial thalamus and in the dorsal PBN; expression was notably absent from previously described satiety centres, such as the arcuate nucleus²⁶ or paraventricular hypothalamus²⁷. To confirm the specificity of projections from the PBelo to the CeAlc, we injected green fluorescent retrobeads into the CeAlc and AAV carrying Cre-dependent mCherry in

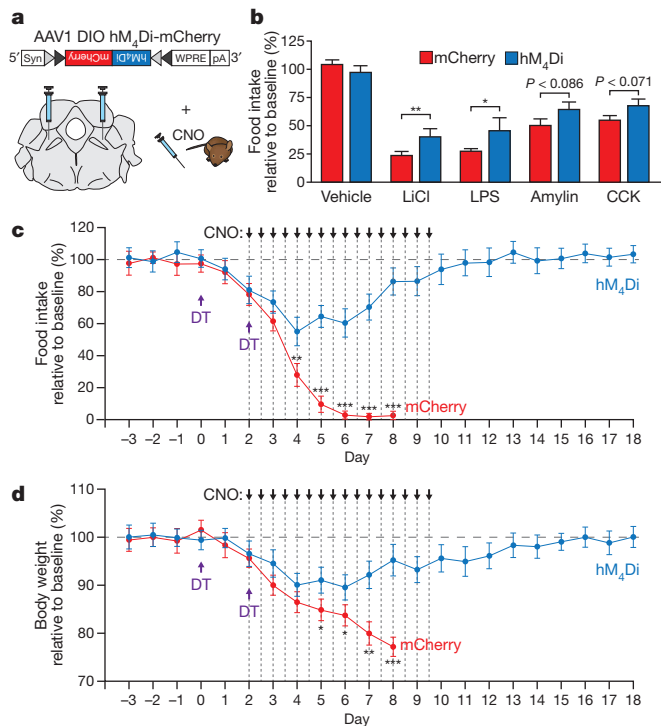


Figure 3 | Inhibition of PBelo CGRP neurons increases food intake during conditions that suppress appetite. **a**, AAV1 DIO hM₄Di-mCherry transgene bilaterally injected into the PBN. **b**, Pharmacogenetic inhibition of CGRP neurons increases food intake after administration of anorexigenic compounds ($n = 6$ animals per group; experiment replicated at least five times per animal in three groups of animals). **c**, **d**, Chronic administration of CNO (every 12 h for 8 d) increases food intake (**c**) and prevents starvation (**d**) in *AgRP^{DTR/+}* mice after two injections of diphtheria toxin. The mCherry animals were killed on day 8 owing to extreme weight loss ($n = 6$ –9 animals per condition; experiment replicated in three groups of animals). * $P < 0.05$, ** $P < 0.01$, *** $P < 0.001$; see Supplementary Information for statistical analyses.

the PBelo of *Calca^{Cre/+}* mice. mCherry was expressed in more than 95% of retrogradely labelled green fluorescent neurons (Supplementary Fig. 13).

To demonstrate functional connectivity between the PBelo and the CeAlc, we transduced PBelo CGRP neurons with Cre-dependent ChR2-mCherry. *In vivo* photostimulation of either the PBelo or downstream projections in the CeAlc resulted in an increase in Fos expression in the CeAlc (Supplementary Fig. 14a–f). In acute brain slices, optical stimulation of ChR2-mCherry-positive fibres in the CeAlc resulted in excitatory postsynaptic currents (EPSCs; Fig. 4b and Supplementary Fig. 14g, h) and an increase in firing rate (Supplementary Fig. 14i) in CeAlc neurons (11 out of 25 cells showed an optically evoked response). The EPSCs and the increase in firing rate were blocked by bath application of the glutamate receptor antagonists 6-cyano-7-nitroquinoxaline-2, 3-dione (CNQX; 10 μ M) and D(-)-2-amino-5-phosphonovaleric acid (AP5; 50 μ M), indicating that PBelo CGRP neurons form an excitatory synaptic connection with neurons of the CeAlc (Fig. 4b and Supplementary Fig. 14g–i). To determine the effect of stimulating PBelo-to-CeAlc projections on food intake, we transduced PBelo CGRP neurons with ChR2-mCherry and implanted fibre optic cannulae above the CeAlc (Fig. 4c). Photostimulation of projections into the CeAlc for 5 min at 20–40 Hz significantly and reversibly suppressed food intake (Fig. 4d and Supplementary Fig. 15). In contrast, stimulation of PBelo projections to the BNST for 5 min had no significant effect on food intake (Supplementary Fig. 16). Taken together, these results indicate that direct projections from PBelo CGRP neurons to the CeAlc are sufficient to reduce food intake.

To determine the necessity of the PBelo-to-CeAlc projection in mediating appetite suppression, we bilaterally injected canine adenovirus

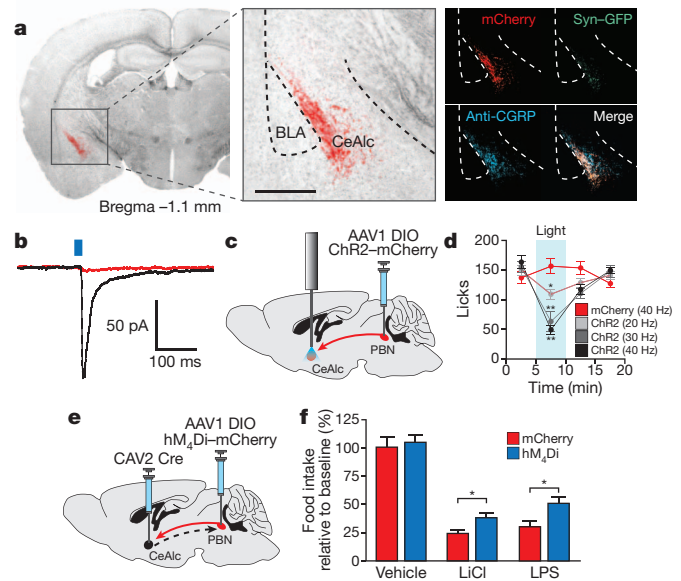


Figure 4 | Efferent projections from PBelo CGRP neurons to the CeAlc mediate appetite suppression. **a**, Left and middle, mCherry-expressing fibres from the PBelo to the CeAlc; scale bar, 500 μ m. Right, PBelo fibres expressing mCherry, synaptophysin-GFP and CGRP. **b**, EPSC from a CeAlc neuron upon photostimulation of PBelo-to-CeAlc fibres before (black) and after (red) bath application of CNQX and AP5. **c**, AAV1 DIO ChR2-mCherry with fibre optic implant above the CeAlc. **d**, Photostimulation of PBelo fibres in the CeAlc reversibly inhibits food intake ($n = 8$ animals for each group; experiment replicated at least 20 times per animal in three groups of animals). **e**, Injection of CAV2 Cre into the CeAlc and AAV1 DIO hM₄Di-mCherry into the PBN. **f**, Inhibition of retrogradely targeted PBelo neurons increases food intake ($n = 6$ animals for each group); experiment replicated at least five times per animal in three groups of animals. * $P < 0.05$, ** $P < 0.01$; see Supplementary Information for statistical analyses.

(CAV2) carrying Cre recombinase into the CeAlc. CAV2 is capable of efficient retrograde transport²⁸ and therefore will express Cre in upstream PBelo neurons. In the same animals, we also bilaterally injected AAV carrying a Cre-dependent hM₄Di transgene into the PBN (Fig. 4e). Inhibition of PBN neurons with CNO decreased the suppression of appetite observed after injection of LiCl or LPS (Fig. 4f), demonstrating that activity in PBelo neurons projecting to the CeAlc is necessary for the normal suppression of appetite observed after injection of LiCl or LPS.

Taken together, these results demonstrate a neural circuit from CGRP-expressing neurons in the PBelo to the CeAlc that mediates appetite suppression. One of our observations was that inhibition of PBN neurons increased food intake when mice did not normally eat (Figs 3b–d and 4f), but did not statistically increase food intake in baseline conditions (Supplementary Fig. 11) or after injection of amylin or CCK (Fig. 3b). These findings are consistent with those of Atasoy *et al.*²⁷, who did not find any effect on food intake after stimulation of inhibitory projections from AgRP neurons to the PBN. Perhaps inhibitory projections from AgRP neurons do not stimulate food intake in baseline conditions but do decrease the suppression of appetite when the PBN is most active. Thus, ablation of AgRP neurons causes starvation in adult mice because of disinhibition in the PBelo⁷. Additionally, PBelo CGRP neurons may not mediate the ordinary, routine satiety experienced after a meal, but may mediate more severe forms of satiety experienced during severe overfeeding (gastric distention), illness or other conditions in which it is unhealthy to eat such as dehydration or vertigo.

Although it is well-established that several hypothalamic and brain-stem nuclei coordinate appetite and satiety^{26,29}, this study demonstrates the involvement of downstream circuitry that may mediate

the 'unpleasant feeling' or discomfort that results from adverse conditions during which it is unfavourable to eat. Indeed, the CeAlc is known to process polymodal information about the internal and external bodily environment including adverse visceral stimuli³⁰. Adding to previous results^{1,7}, we propose that PBelo CGRP neurons integrate visceral and energy balance information and communicate with the CeAlc to mediate extreme satiety and malaise (Supplementary Fig. 17).

METHODS SUMMARY

We generated *Calca*^{Cre/+} mice and *Agrp*^{DTR/+} mice and backcrossed them onto a C57Bl/6 background. AAV1 vectors were stereotactically injected into the PBN; in some experiments, CAV2 Cre was also stereotactically injected into the CeAlc. For photostimulation experiments, mice were implanted with fibre optic cannulae above the PBN, CeAlc or BNST; blue light at 473 nm was delivered in 10-ms pulses at 20 mW intensity through a 1.5-m fibre optic cable. For pharmacogenetic manipulation, CNO was injected at 1 mg kg⁻¹, intraperitoneally. To ablate AgRP neurons, mice carrying the *Agrp*^{DTR/+} allele were injected twice with diphtheria toxin (50 µg kg⁻¹, intramuscularly, 2 days apart). LiCl (84 mg kg⁻¹; 0.2 M, 10 ml kg⁻¹), LPS from *Salmonella typhimurium* (50 µg kg⁻¹), amylin (10 µg kg⁻¹) and CCK (10 µg kg⁻¹) were all injected intraperitoneally as described in Supplementary Fig. 6. Food intake was monitored using lickometer cages supplied with water and liquid diet available *ad libitum*.

Online Content Any additional Methods, Extended Data display items and Source Data are available in the online version of the paper; references unique to these sections appear only in the online paper.

Received 1 May; accepted 20 August 2013.

Published online 13 October 2013.

- Wu, Q., Clark, M. S. & Palmiter, R. D. Deciphering a neuronal circuit that mediates appetite. *Nature* **483**, 594–597 (2012).
- Becskei, C., Grabler, V., Edwards, G. L., Riediger, T. & Lutz, T. A. Lesion of the lateral parabrachial nucleus attenuates the anorectic effect of peripheral amylin and CCK. *Brain Res.* **1162**, 76–84 (2007).
- DiPatrizio, N. V. & Simansky, K. J. Activating parabrachial cannabinoid CB1 receptors selectively stimulates feeding of palatable foods in rats. *J. Neurosci.* **28**, 9702–9709 (2008).
- Yamamoto, T. *et al.* C-fos expression in the rat brain after intraperitoneal injection of lithium chloride. *Neuroreport* **3**, 1049–1052 (1992).
- Elmqvist, J. K., Scammell, T. E., Jacobson, C. D. & Saper, C. B. Distribution of Fos-like immunoreactivity in the rat brain following intravenous lipopolysaccharide administration. *J. Comp. Neurol.* **371**, 85–103 (1996).
- Paues, J., Mackerlova, L. & Blomqvist, A. Expression of melanocortin-4 receptor by rat parabrachial neurons responsive to immune and aversive stimuli. *Neuroscience* **141**, 287–297 (2006).
- Wu, Q., Boyle, M. P. & Palmiter, R. D. Loss of GABAergic signaling by AgRP neurons to the parabrachial nucleus leads to starvation. *Cell* **137**, 1225–1234 (2009).
- Yizhar, O., Fenno, L. E., Davidson, T. J., Mogri, M. & Deisseroth, K. Optogenetics in neural systems. *Neuron* **71**, 9–34 (2011).
- Armbruster, B. N., Li, X., Pausch, M. H., Herlitze, S. & Roth, B. L. Evolving the lock to fit the key to create a family of G protein-coupled receptors potentially activated by an inert ligand. *Proc. Natl Acad. Sci. USA* **104**, 5163–5168 (2007).
- Rosen, A. M., Victor, J. D. & Di Lorenzo, P. M. Temporal coding of taste in the parabrachial nucleus of the pons of the rat. *J. Neurophysiol.* **105**, 1889–1896 (2011).
- Tokita, K. & Boughter, J. D. Jr. Sweet-bitter and umami-bitter taste interactions in single parabrachial neurons in C57BL/6J mice. *J. Neurophysiol.* **108**, 2179–2190 (2012).
- Geerling, J. C. & Loewy, A. D. Sodium deprivation and salt intake activate separate neuronal subpopulations in the nucleus of the solitary tract and the parabrachial complex. *J. Comp. Neurol.* **504**, 379–403 (2007).
- Geerling, J. C. *et al.* FoxP2 expression defines dorsolateral pontine neurons activated by sodium deprivation. *Brain Res.* **1375**, 19–27 (2011).
- Chamberlin, N. L. & Saper, C. B. Topographic organization of respiratory responses to glutamate microstimulation of the parabrachial nucleus in the rat. *J. Neurosci.* **14**, 6500–6510 (1994).
- Hermanson, O. & Blomqvist, A. Subnuclear localization of FOS-like immunoreactivity in the rat parabrachial nucleus after nociceptive stimulation. *J. Comp. Neurol.* **368**, 45–56 (1996).
- Richard, S., Engblom, D., Paues, J., Mackerlova, L. & Blomqvist, A. Activation of the parabrachio-amygdaloid pathway by immune challenge or spinal nociceptive input: a quantitative study in the rat using Fos immunohistochemistry and retrograde tract tracing. *J. Comp. Neurol.* **481**, 210–219 (2005).
- Nakamura, K. & Morrison, S. F. A thermosensory pathway that controls body temperature. *Nature Neurosci.* **11**, 62–71 (2008).
- Nakamura, K. & Morrison, S. F. A thermosensory pathway mediating heat-defense responses. *Proc. Natl Acad. Sci. USA* **107**, 8848–8853 (2010).
- Luquet, S., Perez, F. A., Hnasko, T. S. & Palmiter, R. D. NPY/AgRP neurons are essential for feeding in adult mice but can be ablated in neonates. *Science* **310**, 683–685 (2005).
- Ng, L. *et al.* An anatomic gene expression atlas of the adult mouse brain. *Nature Neurosci.* **12**, 356–362 (2009).
- Jacobs, J. W. *et al.* Calcitonin messenger RNA encodes multiple polypeptides in a single precursor. *Science* **213**, 457–459 (1981).
- Paues, J., Engblom, D., Mackerlova, L., Ericsson-Dahlstrand, A. & Blomqvist, A. Feeding-related immune responsive brain stem neurons: association with CGRP. *Neuroreport* **12**, 2399–2403 (2001).
- Krashes, M. J. *et al.* Rapid, reversible activation of AgRP neurons drives feeding behavior in mice. *J. Clin. Invest.* **121**, 1424–1428 (2011).
- D'Hanis, W., Linke, R. & Yilmazer-Hanke, D. M. Topography of thalamic and parabrachial calcitonin gene-related peptide (CGRP) immunoreactive neurons projecting to subnuclei of the amygdala and extended amygdala. *J. Comp. Neurol.* **505**, 268–291 (2007).
- Schwaber, J. S., Sternini, C., Brecha, N. C., Rogers, W. T. & Card, J. P. Neurons containing calcitonin gene-related peptide in the parabrachial nucleus project to the central nucleus of the amygdala. *J. Comp. Neurol.* **270**, 416–426 (1988).
- Elmqvist, J. K., Coppari, R., Balthasar, N., Ichinose, M. & Lowell, B. B. Identifying hypothalamic pathways controlling food intake, body weight, and glucose homeostasis. *J. Comp. Neurol.* **493**, 63–71 (2005).
- Atasoy, D., Betley, J. N., Su, H. H. & Sternson, S. M. Deconstruction of a neural circuit for hunger. *Nature* **488**, 172–177 (2012).
- Soudais, C., Laplace-Builhe, C., Kissa, K. & Kremer, E. J. Preferential transduction of neurons by canine adenovirus vectors and their efficient retrograde transport *in vivo*. *FASEB J.* **15**, 2283–2285 (2001).
- Gao, Q. & Horvath, T. L. Neurobiology of feeding and energy expenditure. *Annu. Rev. Neurosci.* **30**, 367–398 (2007).
- Neugebauer, V., Li, W., Bird, G. C. & Han, J. S. The amygdala and persistent pain. *Neuroscientist* **10**, 221–234 (2004).

Supplementary Information is available in the online version of the paper.

Acknowledgements We thank B. Roth for hM₃Dq-mCherry and hM₄Di-mCherry constructs, and K. Deisseroth for mCherry and ChR2-mCherry constructs. E. Allen, J. Resnick, M. Soleiman and S. Padilla assisted with histology, E. Allen and A. Rainwater assisted with animal husbandry, and J. Shulkin provided suggestions and advice. We thank members of the Palmiter and Zweifel laboratories for feedback on the manuscript. M.E.C. is financed by a fellowship from the Hilda and Preston Davis Foundation. L.S.Z. is financed by a grant from the National Institutes of Health (R01MH094536). R.D.P. is supported in part by grants from the National Institutes of Health (R01DA024908) and the Klarman Family Foundation.

Author Contributions M.E.C. and R.D.P. conceived and designed the study. M.E.C. performed and analysed histological and behavioural experiments, M.E.S. performed electrophysiology experiments and R.D.P. generated *Calca*^{Cre} knock-in mice. L.S.Z. and R.D.P. provided equipment, reagents and expertise. M.E.C. wrote the manuscript in collaboration with the other authors.

Author Information Reprints and permissions information is available at www.nature.com/reprints. The authors declare no competing financial interests. Readers are welcome to comment on the online version of the paper. Correspondence and requests for materials should be addressed to R.D.P. (palmiter@uw.edu).

METHODS

Mice. All experiments were approved by the University of Washington Institutional Animal Care and Use Committee and were performed in accordance with the guidelines described in the US National Institutes of Health Guide for the Care and Use of Laboratory Animals. We used exclusively heterozygous male *Calca*^{Cre/+} and *Agpr*^{DTR/+} mice backcrossed onto a C57Bl/6 background, aged 7–9 weeks at the start of experimental procedures and no more than 18 weeks at the end of experimental procedures. Before stereotaxic surgery, mice were group housed and maintained with rodent diet (Picolab, number 5053) and water available *ad libitum* with a 12-h light:dark cycle at 22 °C. After surgical procedures, mice were individually housed and maintained with a liquid diet (Vanilla Ensure, Abbot Laboratories) and water available *ad libitum*. We performed experiments on three or four experimental animals (for example, animals transduced with ChR2, hM₃Dq, hM₄Di) and three or four control animals (for example, animals only transduced with mCherry) at the same time to avoid differences in results between experimental sessions. Animals were randomly assigned to either the experimental or control groups in each litter.

Generation of *Calca*^{Cre} mice. A 14-kb BstB1–PacI fragment was isolated from a C57Bl/6 mouse BAC clone. A unique SalI site was introduced at the initiation codon of *Calca* in exon 2 by PCR. Next, a 7-kb SpeI–SalI 5' fragment was cloned into a targeting vector containing a *frt*-flanked *PgkNeo* gene for positive selection and *Pgk-DTA* and *HSV-TK* genes for negative selection. This was followed by insertion of a 3' 7-kb SalI–PacI fragment. The gene encoding the Cre–GFP fusion protein with an amino (N)-terminal myc-tag and nuclear localization signal was cloned into the unique XhoI site adjacent to *frt-PgkNeo*. The targeting construct was linearized with *AscI* and electroporated into G4 hybrid (C57Bl/6 × Sv129) embryonic stem cells. Eighteen correctly targeted clones were identified out of 96 by Southern blot of EcoRV-digested DNA using a unique probe outside the targeting vector. Several of these clones gave good chimaeras when injected into C57Bl/6 hosts. One chimaera was bred with FLPer (Rosa26-Flip recombinase) to remove the *frt-Pgk-Neo* gene.

Virus production. Cre-dependent pAAV mCherry and ChR2–mCherry (driven by the *Eflα* promoter) DNA plasmids were provided by K. Deisseroth, and Cre-dependent pAAV hM₃Dq–mCherry and hM₄Di–mCherry (driven by the human synapsin promoter) DNA plasmids were provided by B. Roth. pAAV synaptophysin–GFP was generated by fusing the 3' end of the mouse *Synaptophysin* coding region with the 5' end of the *GFP* coding region. This sequence was then exchanged with mCherry in the pAAV mCherry plasmid to make the transgene Cre-dependent. Recombination-deficient AAV vectors were prepared in human embryonic kidney (HEK293T) cells with AAV1 coat serotype, purified by sucrose and CsCl gradient centrifugation steps, and re-suspended in 1× Hanks Balanced Saline Solution (HBSS) at a titre of approximately 2×10^9 viral genomes per microlitre. CAV2 Cre was prepared in dog kidney (DK/E1-1) cells, purified by sucrose and CsCl gradient centrifugation steps, and re-suspended in 1× HBSS at a titre of approximately 2.5×10^9 viral genomes per microlitre as described previously³¹. Viral aliquots were stored at –80 °C before stereotaxic injection.

Stereotaxic surgery. At the start of surgical procedures, mice were anaesthetized with isoflurane and placed on a stereotaxic frame (David Kopf Instruments). Stereotaxic coordinates for the anterior–posterior plane were normalized using a correction factor ($F = (\text{Bregma} - \text{Lambda distance})/4.21$) on the basis of the coordinates of Paxinos and Franklin³². Virus was injected unilaterally (on the left side) or bilaterally as described in the text either in the PBN (antero-posterior (AP), –4.9 mm; medio-lateral (ML), 1.4 mm; dorso-ventral (DV), 3.8 mm) or the CeAlc (AP, –1.2 mm; ML, 2.6 mm; DV, 5.4 mm) at a rate of $0.2 \mu\text{l min}^{-1}$ for 2.5 min ($0.5 \mu\text{l}$ total volume). Note that the viral injection coordinates target the most anterior aspect of the PBN but the virus diffuses posteriorly to hit all PBN subnuclei; this injection site improves the accuracy of injecting into the lateral PBN between the superior cerebellar peduncle (scp) and lateral wall of the pons. Also note that the presence of the scp fortuitously limits the spread of virus from the PBN region, thus preventing unintended transduction of other nearby *Calca*-expressing brain regions.

After viral injection, mice used for optogenetic experiments also received unilateral surgical implantation of a Mono Fiberoptic Cannula (Doric Lenses), either above the PBN (AP, –5.2 mm; ML, 1.6 mm; DV, 3.0 mm), CeAlc (AP, –1.2 mm; ML, 2.6 mm; DV, 5.4 mm) or BNST (AP, +0.14 mm; ML, 1.0 mm; DV, 4.0 mm). Cannulae were affixed to the skull with C&B Metabond (Parkell) and dental acrylic.

Slice electrophysiology. Coronal brain slices (250 μm) were prepared in an ice slush solution containing (in mM) 250 sucrose, 3 KCl, 2 MgSO₄, 1.2 NaH₂PO₄, 10 D-glucose, 25 NaHCO₃ and 0.1 CaCl₂. Slices recovered for 1 h at 34 °C in artificial cerebral spinal fluid (ACSF) continually bubbled with O₂/CO₂ and containing (in mM) 126 NaCl, 2.5 KCl, 1.2 NaH₂PO₄, 1.2 MgCl₂, 11 D-glucose, 18 NaHCO₃ and 2 CaCl₂. Whole-cell patch-clamp recordings were made using an

Axopatch 700B amplifier (Molecular Devices) with filtering at 1 kHz using 4–6 M Ω electrodes filled with an internal solution containing (in mM) 120 CsMeSO₃, 20 HEPES, 0.4 EGTA, 2.8 NaCl, 5 Mg-ATP, 0.5 Na-GTP, pH 7.2–7.4, 280 mOsm (for CeAlc single EPSC recordings) or 135 KMeSO₃, 10 KCl, 10 HEPES, 0.1 EGTA, 2.8 NaCl, 5 Mg-ATP, 0.5 Na-GTP, pH 7.2–7.4, 280 mOsm (for PBN recordings and CeAlc high-frequency stimulus recordings). ACSF at 32 °C was continually perfused over slices at a rate of approximately 2 ml min^{-1} during recording.

For photostimulation experiments in the CeAlc, neurons surrounded by mCherry-positive fibres were selected for recording. For light-evoked EPSCs, neurons were held in voltage clamp at –70 mV, and EPSCs were stimulated by 10-ms pulses of blue laser light (single pulse or 300 pulses at 30 Hz) using the same fibre optic as for the *in vivo* experiments, placed in the bath above the slice. Traces are averages of 15–20 sweeps for single EPSCs or averages of three sweeps for 30 Hz trains, collected before and 5 min after bath application of CNQX (10 μM) and AP5 (50 μM). For CeAlc current clamp recordings, most CeAlc neurons had resting membrane potentials between –65 and –80 mV and did not fire action potentials spontaneously unless constant current was injected through the patch pipette to bring the cell closer to threshold. Trains of stimuli at 30 Hz were delivered as above.

For PBN ChR2 recordings, neurons identified by fluorescence were recorded in current-clamp mode and trains of light pulses (1 ms) were delivered at the indicated frequencies for durations of 2 s. For pharmacogenetic experiments, neurons expressing hM₄Di were identified by fluorescence. Cells that did not show spontaneous firing were excluded. Neurons were recorded in current clamp mode in ACSF for a 5-min baseline period, followed by bath application of 3 μM CNO for 3 min, then washout with ACSF. Baseline firing rate was calculated from a 2-min window immediately before CNO application. CNO and washout firing rates were calculated from 2-min windows surrounding the maximum CNO effect and the maximum recovery period, respectively.

Food intake monitoring. For feeding assays, mice were individually housed in lickometer cages (Columbus Instruments) supplied with water and liquid diet (Vanilla Ensure, Abbot Laboratories) available *ad libitum*. Food and water ports were changed daily at the start of the dark cycle. The mice were allowed to acclimate to lickometer cages for 5 days and then baseline food intake was measured for an extra 5 days before experimental procedures. Acute food intake measurements (Figs 2b, c, e, f, 3b and 4d, f) occurred at the onset of the active period (lights off). Long-term measurements (Fig. 2g, h and 3c, d) occurred over a 24-h period with total food-intake and body weight measured approximately 6 h before the onset of the active period. Measurements were performed by an investigator (M.E.C.) with knowledge of the identity of the experimental versus control groups (that is, without blinding).

Photostimulation. After a 14-day recovery period following surgery, mice were individually housed in lickometer cages with open cage tops. Fibre optic cables (1.5 m long, 200 μm diameter; Doric Lenses) coated with opaque heat-shrink tubing were firmly attached to the implanted fibre optic cannulae with zirconia sleeves (Doric Lenses). Mice were allowed at least 5 days to acclimate before experimental sessions. During photostimulation experiments, light pulse trains (10-ms pulses of various frequency; see text) were programmed using a waveform generator (Agilent Technologies, number 33220A) that provided input to a blue light laser (473 nm; LaserGlow). We adjusted the light power of the laser such that the light power exiting the fibre optic cable was 20 mW (160 mW mm^{–2}); using an online light transmission calculator for brain tissue³³ (<http://www.stanford.edu/group/dlab/cgi-bin/graph/chart.php>) we estimated the light power at the PBelo to be 36.2 mW mm^{–2}. Note that this is probably a high estimation because some light was probably lost at the interface between the fibre optic cable and the implanted fibre optic cannula. After the completion of photostimulation experiments, mice were perfused and the approximate locations of fibre tips were identified based on the coordinates of Paxinos and Franklin³².

Pharmacological injections. Pharmacological compounds were prepared in sterile 0.9% saline and stored at –20 °C before use. Diphtheria toxin was injected intramuscularly and all other compounds were administered intraperitoneally as described in Supplementary Fig. 6. Compounds included amylin (10 $\mu\text{g kg}^{-1}$; Bachem, number H-9475), CCK-8 (10 $\mu\text{g kg}^{-1}$; Bachem, number H-2080), CNO (1 mg kg^{–1}; Sigma, number C0832), diphtheria toxin (50 $\mu\text{g kg}^{-1}$; List Biologicals, number 150), LiCl (84 mg kg^{–1}; 0.20 M at 10 ml kg^{–1}; Fisher, number L121) and LPS, *S. typhimurium* (50 $\mu\text{g kg}^{-1}$; Calbiochem, number 437650).

Histology. Mice were anaesthetized with buprenorphine and perfused transcardially with 1× PBS, pH 7.4, followed by 4% paraformaldehyde in PBS. The brains were extracted, allowed to postfix overnight in the same fixative at 4 °C and cryoprotected in 30% sucrose dissolved in 1× PBS for an extra 24 h at 4 °C. Each brain was sectioned at 30 μm on a cryostat (Leica Microsystems) and collected in cold 1× PBS.

For immunohistochemistry experiments, sections were washed three times in PBS with 0.2% Triton X-100 (PBST) for 10 min at room temperature. Sections

were then incubated in a blocking solution composed of PBST with 3% normal donkey serum (Jackson ImmunoResearch, number 017-000-121) for 1 h. For primary antibody exposure, sections were incubated in rabbit anti-c-Fos (1:2000, Calbiochem, number PC38), rabbit anti-GFP (1:1000, Invitrogen, number A11122) and/or goat anti-CGRP (1:500, Abcam, number ab36001) in blocking solution at 4 °C for approximately 20 h. After three 10-min washes in PBST, sections were incubated in Alexa Fluor 594 donkey anti-goat IgG (1:200, Jackson ImmunoResearch, number 705-858-147), Alexa Fluor 488 donkey anti-goat IgG (1:200, Jackson ImmunoResearch, number 705-485-147), DyLight 405 donkey anti-goat (1:200, Jackson ImmunoResearch, number 705-475-147) and/or Alexa Fluor 488 donkey anti-rabbit IgG (1:200 Jackson ImmunoResearch, number 711-545-152) in block solution for 1 h at room temperature. Finally, sections were washed three times in 1× PBS.

Sections were mounted in PBS onto SuperFrost Plus glass slides (VWR, number 48311-703) and coverslipped with Dapi Fluoromount-G (Southern Biotech, number 0100-20). Slides were stored in the dark at 4 °C before microscopy and image acquisition.

Quantification of co-localization of Fos and mCherry in the PBN (Fig. 1c–j and Supplementary Fig. 7) was performed on adjacent sections from approximately Bregma –4.90 to –5.50 (exactly 21 sections per mouse). Quantification of Fos in the CeAlc (Supplementary Fig. 14a–f) was performed on adjacent sections from approximately Bregma –1.14 to –1.26 (exactly five sections per mouse). A Fos-positive cell was considered located in the CeAlc if it was in the field of mCherry fluorescence in that particular section. An investigator (M.E.C.) blinded to the identity of the conditions used to induce Fos performed all quantification.

Microscopy. Fluorescent and brightfield images were collected on either a Nikon upright epifluorescent microscope with a QImaging Camera (Figs 1b and 4a and Supplementary Figs 1 and 4) or a Zeiss LSM 510 Meta confocal microscope.

Images were minimally processed using Photoshop CS5 (Adobe Systems) to enhance brightness and contrast for optimal representation of the data. Low-magnification brightfield images (Figs 1b and 4a and Supplementary Fig. 4) were montaged together to produce a single coronal section. All digital images were processed in the same way between experimental conditions to avoid artificial manipulation between different data sets.

Statistics. We used an online power and sample size calculator to determine an effective sample size for statistical comparisons³⁴ (<http://homepage.cs.uiowa.edu/~rlenth/Power/>). Assuming a standard deviation of 1.0 and a significance level of 0.05, this calculator shows that with eight mice per group we had an 80% confidence level of achieving statistical significance between means of 1.5-fold with a two-tailed Student's *t*-test. We excluded an animal from data analysis if flagged by a University of Washington veterinarian for health reasons during the experimental period or if *post hoc* histological analysis showed no viral transduction as indicated by an absence of mCherry fluorescence.

All data were analysed using Prism 6.0 (GraphPad Software) as described in the text and Supplementary Statistical Analysis. Data were exported into Illustrator CS5 (Adobe Systems) for preparation of figures.

31. Kremer, E. J., Boutin, S., Chillon, M. & Danos, O. Canine adenovirus vectors: an alternative for adenovirus-mediated gene transfer. *J. Virol.* **74**, 505–512 (2000).
32. Paxinos, G. & Franklin, K. B. J. *The Mouse Brain in Stereotaxic Coordinates* 4th edn (Elsevier, 2013).
33. Aravanis, A. *et al.* An optical neural interface: *in vivo* control of rodent motor cortex with integrated fiberoptic and optogenetic technology. *J. Neural Eng.* **4**, S143–S156 (2007).
34. Lenth, R. V. Some practical guidelines for effective sample size determination. *Am. Stat.* **55**, 187–193 (2001).

Dendritic spikes enhance stimulus selectivity in cortical neurons *in vivo*

Spencer L. Smith^{1,2}, Ikuko T. Smith^{1,2}, Tiago Branco^{1,3} & Michael Häusser¹

Neuronal dendrites are electrically excitable: they can generate regenerative events such as dendritic spikes in response to sufficiently strong synaptic input^{1–3}. Although such events have been observed in many neuronal types^{4–9}, it is not well understood how active dendrites contribute to the tuning of neuronal output *in vivo*. Here we show that dendritic spikes increase the selectivity of neuronal responses to the orientation of a visual stimulus (orientation tuning). We performed direct patch-clamp recordings from the dendrites of pyramidal neurons in the primary visual cortex of lightly anaesthetized and awake mice, during sensory processing. Visual stimulation triggered regenerative local dendritic spikes that were distinct from back-propagating action potentials. These events were orientation tuned and were suppressed by either hyperpolarization of membrane potential or intracellular blockade of NMDA (N-methyl-D-aspartate) receptors. Both of these manipulations also decreased the selectivity of subthreshold orientation tuning measured at the soma, thus linking dendritic regenerative events to somatic orientation tuning. Together, our results suggest that dendritic spikes that are triggered by visual input contribute to a fundamental cortical computation: enhancing orientation selectivity in the visual cortex. Thus, dendritic excitability is an essential component of behaviourally relevant computations in neurons.

Neuronal dendrites express voltage-dependent Ca^{2+} and Na^{+} channels that confer electrical excitability, particularly the ability to support the active back-propagation of action potentials and the initiation of local dendritic spikes¹. In addition, the voltage-dependent Mg^{2+} block of synaptic NMDA receptors can also support nonlinear synaptic integration and dendritic spike initiation^{5,10}. These mechanisms of active synaptic integration have been probed extensively *in vitro*². Dendritic spikes have also been observed *in vivo* under certain conditions^{6–8}; however, it remains unclear whether they are involved in behaviourally relevant computations^{11–13}. To investigate whether dendritic non-linearities can contribute to a well-known example of cortical computation, orientation tuning in the visual cortex¹⁴, we made direct dendritic patch-clamp recordings from layer 2/3 neurons in the mouse visual cortex.

To measure dendritic activity *in vivo*, whole-cell patch-clamp recordings were obtained from the thin apical dendrites (diameter, $2.0 \pm 0.4 \mu\text{m}$, mean \pm s.d.; $n = 12$) of layer 2/3 neurons in the mouse primary visual cortex (Fig. 1a) in lightly anaesthetized and awake mice. The patch-clamp pipette was used to fill cells with a fluorescently labelled Ca^{2+} dye (100 μM Oregon Green 488 BAPTA-1), for imaging Ca^{2+} transients, and a red fluorescent dye (25–50 μM Alexa Fluor 594), for imaging the morphology of the dendritic arbor and identifying the precise location of the dendritic recording (Fig. 1b). Dendritic recordings exhibited the expected physiological features, such as a high local input resistance that increased with distance from the soma^{15,16} (Extended Data Fig. 1a–c).

In somatic recordings, visual stimulation with drifting square-wave gratings evoked conventional action potential activity, with the firing rate tuned to the orientation of the stimulus^{14,17} (Fig. 1c). By contrast, recordings from distal dendrites ($>75 \mu\text{m}$ from the soma) showed

orientation-tuned, high-frequency bursts of Na^{+} spikes riding on a depolarization envelope, a finding that is consistent with the activation of voltage-gated Ca^{2+} channels and synaptic NMDA receptor currents (Fig. 1d–g and Extended Data Fig. 1d). The properties of these spikes were in contrast to those of isolated spikes (single spikes separated by at least 50 ms from other spikes), which are presumed to be back-propagating action potentials (bAPs; Fig. 1d, e), although not all bAPs are isolated bAPs. The isolated bAPs exhibited a uniform amplitude and shape within a recording, and they decreased in amplitude and increased in width with increasing distance from the soma¹⁵ (Extended Data Fig. 1e, f). In contrast to dendritic bursts, which can contain both local Na^{+} spikes and bAPs, isolated bAPs provide a read-out of somatic activity that can be compared with local dendritic events. Visually evoked spike bursts that were recorded in distal dendrites were tuned to the orientation of the stimulus, with reliable trial-to-trial tuning (Fig. 1e, f). The preferred orientation of dendritic spike bursts did not differ from that of bAPs recorded in the same cell (difference in preferred orientation, $34.7 \pm 28.8^\circ$; $n = 9$; $P = 0.22$, paired *t*-test; Extended Data Fig. 2).

We next sought to determine whether these dendritic events were local. Given that dendritic Na^{+} spikes, a prominent feature of the dendritic regenerative events we recorded, have fast kinetics, their waveform is likely to be heavily attenuated by the cable-filtering properties of the dendritic arbor and thus not propagated efficiently to the soma (by contrast, the slow depolarization envelope that typically underlies dendritic regenerative events can spread more readily to the soma¹⁵). The maximum instantaneous and mean spike rates, as well as the variance-to-mean ratio, were higher in distal dendritic recordings ($>75 \mu\text{m}$; $n = 9$) than in proximal dendritic recordings ($<50 \mu\text{m}$; $n = 5$) or somatic recordings (Fig. 2a), suggesting that many of the individual spikes in the bursts observed in distal dendritic recordings are indeed local dendritic spikes and not bAPs¹⁵. The spike statistics from somatic recordings and proximal dendritic recordings ($<50 \mu\text{m}$ from the soma; $1.7 \pm 0.3 \mu\text{m}$, mean diameter \pm s.d.; $P = 0.14$, two-sample *t*-test, not different from the diameter of distal dendrites recorded) were indistinguishable ($P > 0.05$, two-sample *t*-test), thus confirming that the dendritic recording configuration itself does not affect spike rates. These measurements were made in lightly anaesthetized mice, and similar spiking patterns were observed in dendritic recordings from awake mice (Fig. 2a, filled symbols, and Extended Data Fig. 3), demonstrating that such spiking is also present in the alert, behaving animal. These data indicate that, at distal dendritic recording sites, spiking occurs at higher rates and with a higher degree of ‘burstiness’ than spiking recorded at the soma, and they provide the first piece of evidence that these dendritic events are local.

A second piece of evidence indicating the dendritic origin of these events is provided by the onset, or foot, of the spike waveform. One signature of propagated spikes is a sharp inflection at the foot of the spike, in contrast to the smooth rise observed near the site of spike initiation¹⁸. Isolated spontaneous spikes exhibited a clear ‘kink’ at their

¹Wolfson Institute for Biomedical Research and Department of Neuroscience, Physiology and Pharmacology, University College London, Gower Street, London WC1E 6BT, UK. ²Department of Cell Biology and Physiology and Neuroscience Center, University of North Carolina School of Medicine, Chapel Hill, North Carolina 27599, USA. ³Laboratory of Molecular Biology, Medical Research Council, Cambridge CB2 0QH, UK.

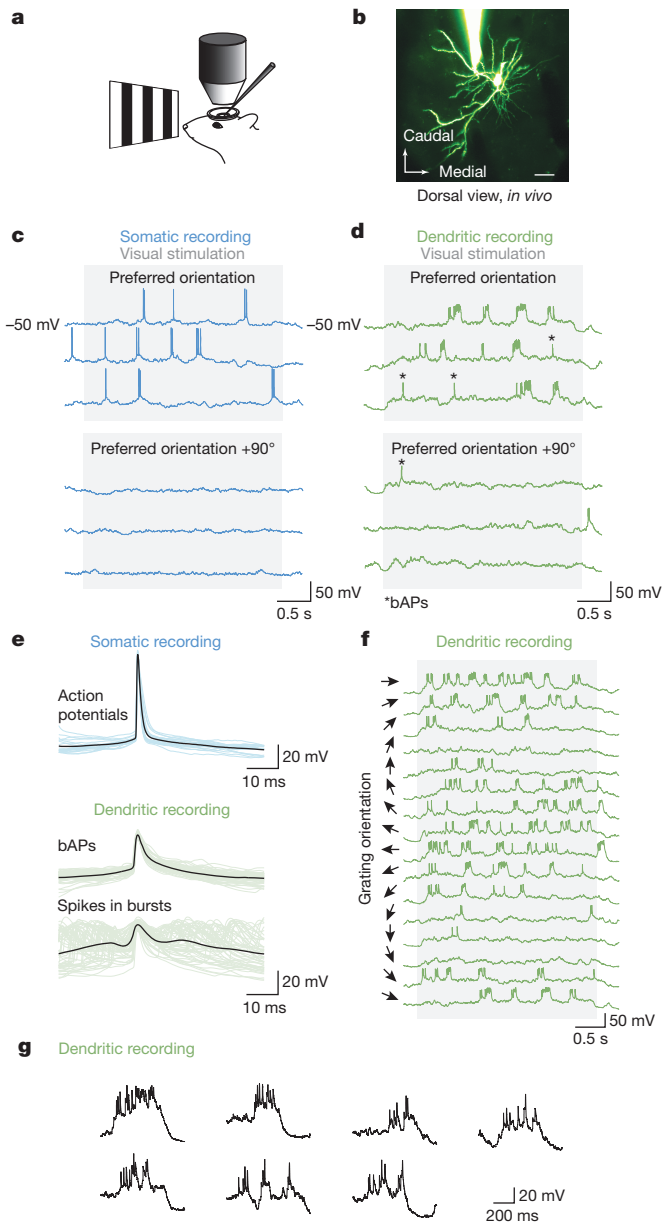


Figure 1 | Dendritic patch-clamp recordings from visual cortex pyramidal neurons *in vivo*. **a**, Schematic of the recording and imaging set-up for *in vivo* dendritic patch-clamp recordings with two-photon microscopy. **b**, A two-photon microscopy image of a layer 2/3 pyramidal neuron in the mouse visual cortex *in vivo*, obtained by filling with Alexa Fluor 594 and dendritic patch-clamp recording at 100 μm from the soma (maximum intensity projection) (scale bar, 20 μm). **c**, **d**, Square-wave grating visual stimuli evoked somatic action potentials (**c**) and dendritic activity (**d**) that exhibited reliable orientation-tuned burst-spiking events. **e**, The spikes within dendritic burst events were highly variable compared with the more stereotyped bAPs and somatically recorded action potentials. **f**, The frequency of dendritic burst events varied with the orientation of the square-wave grating visual stimuli. **g**, Individual burst events were highly variable in amplitude and kinetics (dendritic recording 150 μm from the soma).

onset, as expected for bAPs (Fig. 2b). Spikes within bursts, by contrast, generally exhibited a much slower onset, indicative of local generation (Fig. 2c). The membrane potential at spike initiation did not completely predict the spike onset speed (Extended Data Fig. 4). Thus, the depolarization envelope during dendritic bursts, which can also reduce the speed of spike onset, did not by itself account for the difference in spike shape. Although these spikes were heterogeneous and were probably a mixed population containing some bAPs, spikes within bursts

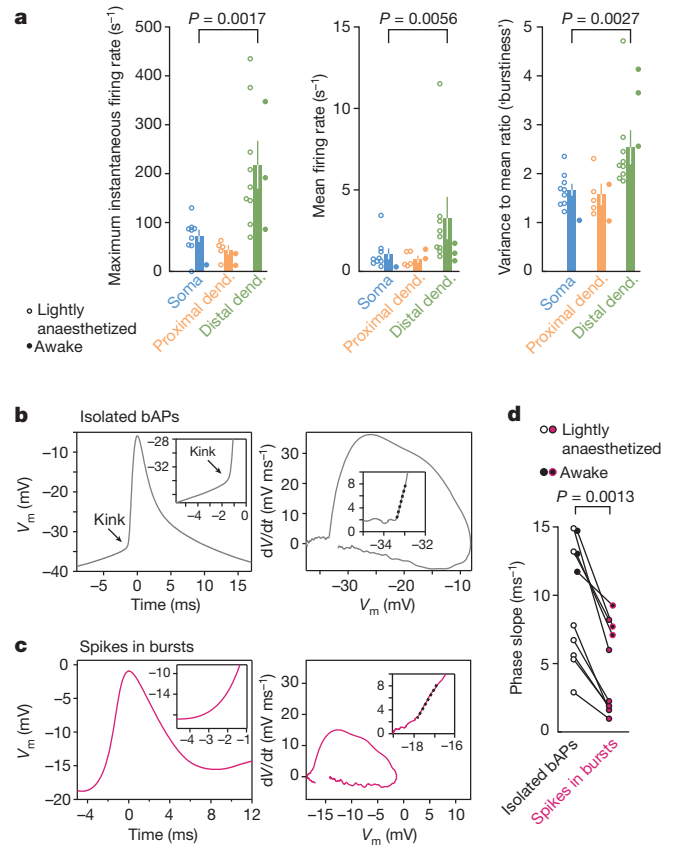


Figure 2 | Visually evoked dendritic burst events are local. **a**, Whole-cell patch-clamp recordings were performed at the soma ($n = 9$), proximal dendritic (proximal dend.) locations (<50 μm from the soma; $n = 5$) or distal dendritic (distal dend.) locations (>75 μm from the soma; $n = 9$). The frequency of stimulus-evoked dendritic burst events at the soma and the proximal dendritic locations were similar; however, the event frequency and burstiness (variance-to-mean ratio of the spike count distribution, or Fano factor) were significantly higher at the distal dendritic locations (P values from the Wilcoxon rank sum test; comparing somatic and distal dendritic recordings). Data from recordings in awake mice ($n = 6$ total) exhibited the same trends as in lightly anaesthetized mice. Error bars indicate s.e.m. **b**, The inflection in membrane potential (V_m) for isolated back-propagated action potentials recorded at distal dendritic locations (>100 μm from the soma) exhibited a sharp kink, consistent with propagated spikes. This is visible both in voltage versus time plots (left) and dV/dt (rate of V_m change, where t is time) versus voltage phase plots (right). The insets show magnifications of the onset at early time points. **c**, By contrast, spikes in bursts exhibited a slower onset, consistent with local generation. **d**, Across the population of dendritic recordings, isolated spikes consistently exhibited sharper inflections at onset (measured as the initial slope in the dV/dt versus voltage phase plots; dashed lines in **b** and **c**) than did spikes in bursts. Distal dendritic recordings from awake mice exhibited the same trend as in lightly anaesthetized mice.

consistently exhibited a slower onset, across the population, than did isolated bAPs ($P = 0.0013$, Wilcoxon rank sum test; $n = 7$ anaesthetized mice; data from awake mice exhibited the same trend; Fig. 2d), consistent with their identity as locally generated dendritic spikes.

To obtain a third piece of evidence, and a more direct read-out of the relationship between dendritic spikes and somatic action potentials, we used two-photon Ca^{2+} imaging to simultaneously measure Ca^{2+} fluctuations at the soma during dendritic patch-clamp recordings, allowing us to infer somatic action potential activity during dendritic patch-clamp recordings. Spike bursts recorded at distal dendritic sites were correlated with somatic Ca^{2+} signals (Fig. 3a). As was the case with the tuning of dendritic bursts and bAPs, the preferred orientation of dendritic bursts (Fig. 3b) was similar to the preferred orientation of the somatic Ca^{2+} signal (Fig. 3c), with qualitative differences in the

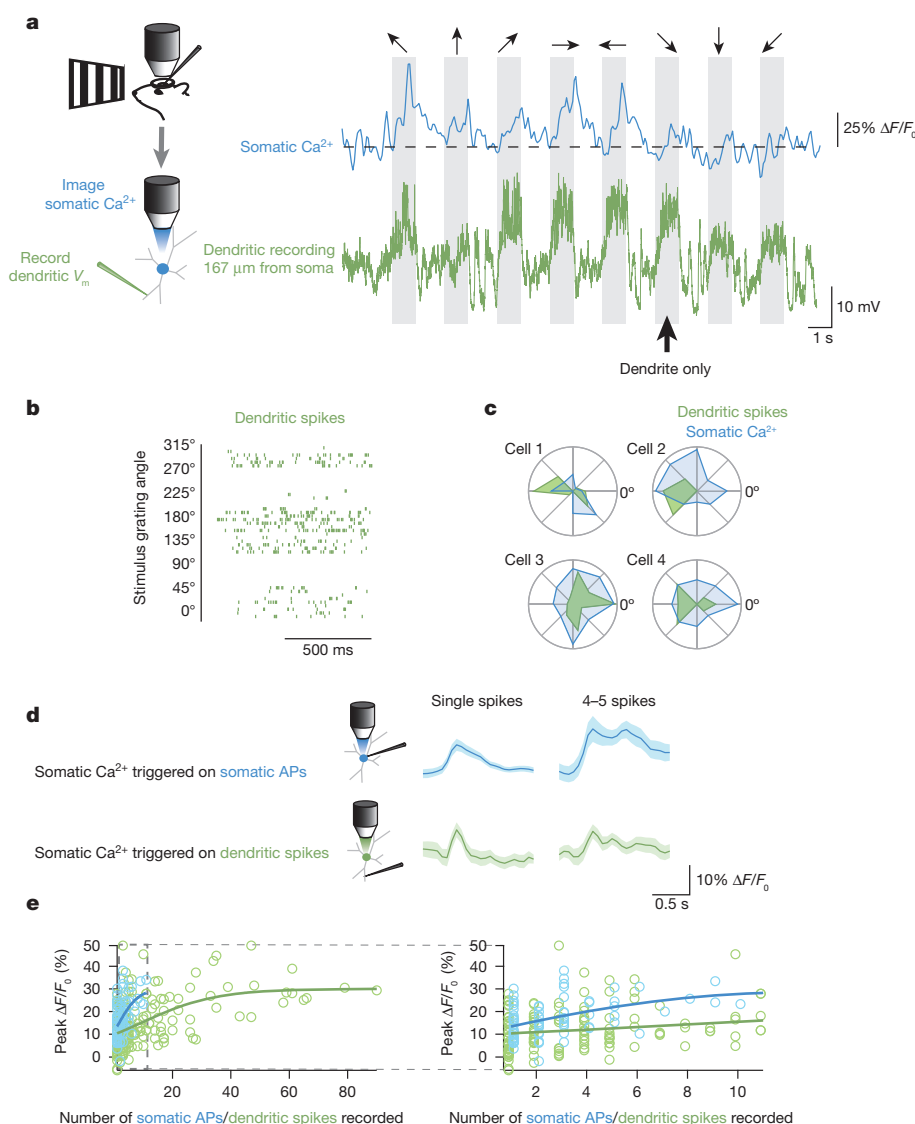


Figure 3 | Simultaneous dendritic recording and Ca^{2+} imaging at the soma shows that dendritic spikes are local. **a**, To infer spiking activity at the soma during dendritic patch-clamp recordings, neurons were filled with a Ca^{2+} indicator and somatic Ca^{2+} signals were imaged. During simultaneous dendritic voltage recordings and somatic Ca^{2+} imaging, dendritic bursts were sometimes not accompanied by robust somatic Ca^{2+} signals (indicated with a heavy arrow). Arrows at the top indicate the orientation of the visual stimulus grating, with shaded boxes indicating the duration of stimulus presentation. **b**, **c**, Dendritic bursting was well tuned (**b**) and overlapped with the orientation tuning at the soma (**c**). (The data for Cell 1 are shown in **a** and **b**.) **d**, To calibrate the Ca^{2+} signals seen at the soma, we calculated spike-triggered averages of the somatic Ca^{2+} signal for well-isolated single spikes and bouts of four to five

spikes (within 640 ms). The somatic Ca^{2+} signal amplitude was similar for single spikes regardless of whether the spikes were recorded at the soma or the dendrite. No difference in Ca^{2+} signal amplitude was found between bouts of four to five spikes recorded at the dendrite and single spikes recorded at the soma, suggesting that some dendritic spikes were local. **e**, Across the population of events, even though the Ca^{2+} signals became saturated at about the same magnitude (fluorescence change over baseline $\Delta F/F_0 \sim 30\%$; not different between the two configurations, $P = 0.99$, two-sample t -test), the somatic Ca^{2+} signal as a function of the number of dendritic spikes rose much more slowly than that for the somatically recorded spikes (left). Data from responses with fewer than ten spikes are presented magnified (right).

tuning curves consistent with the interpretation that a single dendrite contributes only a portion of the input that drives a neuron to fire. To calibrate these measurements, we used separate somatic recordings combined with somatic Ca^{2+} imaging. The somatic Ca^{2+} signal observed during a dendritic burst of four to five spikes was indistinguishable from the Ca^{2+} signal observed during a single action potential recorded at the soma ($P = 0.77$, two-sample t -test; Fig. 3d). Furthermore, although the somatic Ca^{2+} signals became saturated near the same level in both dendritic and somatic recording configurations (fluorescence change over baseline $\Delta F/F_0 \sim 30\%$ for both configurations; not different between the two configurations, $P = 0.99$, two-sample t -test), this saturation level was reached with only 10 spikes recorded at the soma but needed more than 40 spikes in the dendrite ($P < 10^{-8}$, the two distributions are different, multivariate Kolmogorov–Smirnov test; $n = 5$;

Fig. 3e). Thus, many of the individual spikes in bursts recorded at the dendrite were probably locally generated, rather than each reflecting a bAP, and resulted in subthreshold depolarizations at the soma. Measurements of Ca^{2+} signals at the site of distal dendritic recordings (Extended Data Fig. 5a) provided further evidence that individual dendritic spikes were locally generated, by showing that dendritic bursts with Ca^{2+} signals spanning all of the visible dendritic branches (Extended Data Fig. 5b) contained spikes with steeper onsets than did bursts with Ca^{2+} transients that were confined to the local recording site and not observed in adjacent branches¹⁹ ($n = 78$ dendritic bursts; Extended Data Fig. 5c–f). Together, these results demonstrate how dendritic spikes, local Ca^{2+} signals and bAPs interact during visual processing.

A final piece of evidence that dendritic bursts consist of locally generated dendritic spikes is that visually evoked dendritic bursts were

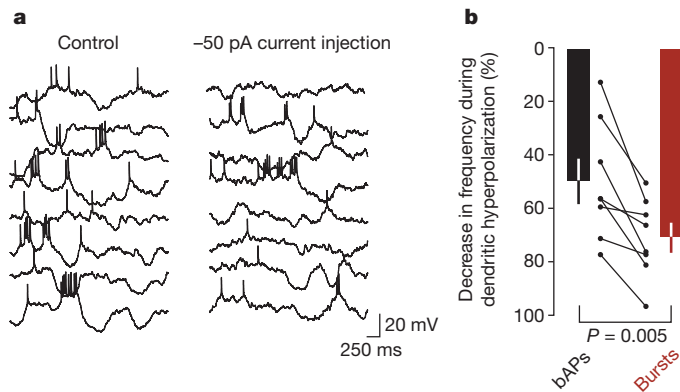


Figure 4 | Hyperpolarization decreases the frequency of dendritic bursts. **a**, An example dendritic recording shows that compared to control conditions (left), hyperpolarization (right) decreased the mean frequency of bursts (from 0.32 Hz to 0.14 Hz; -68%) more than the mean frequency of bAPs (0.51 Hz to 0.36 Hz; -30%). **b**, Population data showing that bursts and bAPs were both suppressed ($P = 3.0 \times 10^{-6}$ and $P = 0.0004$, respectively, *t*-test) and that bursts were suppressed to a greater degree by hyperpolarization than were bAPs ($P = 0.005$, paired *t*-test). Bars indicate population means and error bars indicate s.e.m. for the decrease in mean rates of bAPs and dendritic bursts during hyperpolarization compared with the control condition. Data from individual dendritic recordings are shown between the two bars, with lines connecting data points from the same recording.

more sensitive to local dendritic hyperpolarization than were bAPs. When a steady hyperpolarizing current was delivered through the dendritic patch-clamp pipette, the rate of burst events decreased more than did the rate of isolated bAPs ($P = 0.005$, paired *t*-test; Fig. 4), indicating that the dendritic burst-generating mechanisms were more sensitive to the local membrane potential than were the mechanisms that support back-propagation of somatic action potentials. Taken together, these findings indicate that the spike bursts recorded at the dendrite during visual processing are not a pure population of bAPs but rather consist mainly of locally generated dendritic spikes.

We next sought to uncover how dendritic regenerative events evoked by visual stimulation might influence the orientation tuning of neuronal output. The prolonged depolarization envelope of dendritic bursts can propagate to the soma and influence axonal output. If dendritic bursts, and the somatic depolarizations they cause, are required for normal synaptic integration during visual processing, then blocking them might disrupt an important cortical computation: orientation tuning. Layer 2/3 neurons exhibited spiking that was robustly orientation tuned¹⁷, as well as subthreshold responses (Fig. 5a–d; even when the cells fired few to no spikes, Extended Data Fig. 6). The subthreshold tuning closely matched the spike-based tuning in terms of preferred orientation²⁰ (Pearson's correlation coefficient $R = 0.83$, $P < 10^{-5}$; Extended Data Fig. 7a) and orientation selectivity (as measured by the membrane potential orientation selectivity index, $V_m\text{OSI}$; Pearson's $R = 0.88$, $P = 0.0040$; Extended Data Fig. 7b). This subthreshold tuning provides a way to compare synaptic integration in the control condition and the hyperpolarized condition where dendritic spikes are prevented (Fig. 4). Hyperpolarization degraded this subthreshold orientation tuning both in terms of the modulation amplitude (Fig. 5e, f) and the $V_m\text{OSI}$ (Fig. 5g), without changing the preferred orientation (Pearson's $R = 0.88$, $P = 0.022$; $n = 10$; Extended Data Fig. 7c, d). This effect was not accounted for by changes in the driving force for Cl^- ions (Pearson's $R = 0.34$, $P = 0.15$; Extended Data Fig. 8). These results demonstrate that voltage-gated mechanisms are required for normal synaptic integration and subthreshold orientation tuning during visual processing, which is consistent with the hypothesis that dendritic regenerative events enhance subthreshold orientation tuning.

The synaptic NMDA receptor current, which is subject to voltage-dependent Mg^{2+} block, is a prime candidate for linking synaptic input

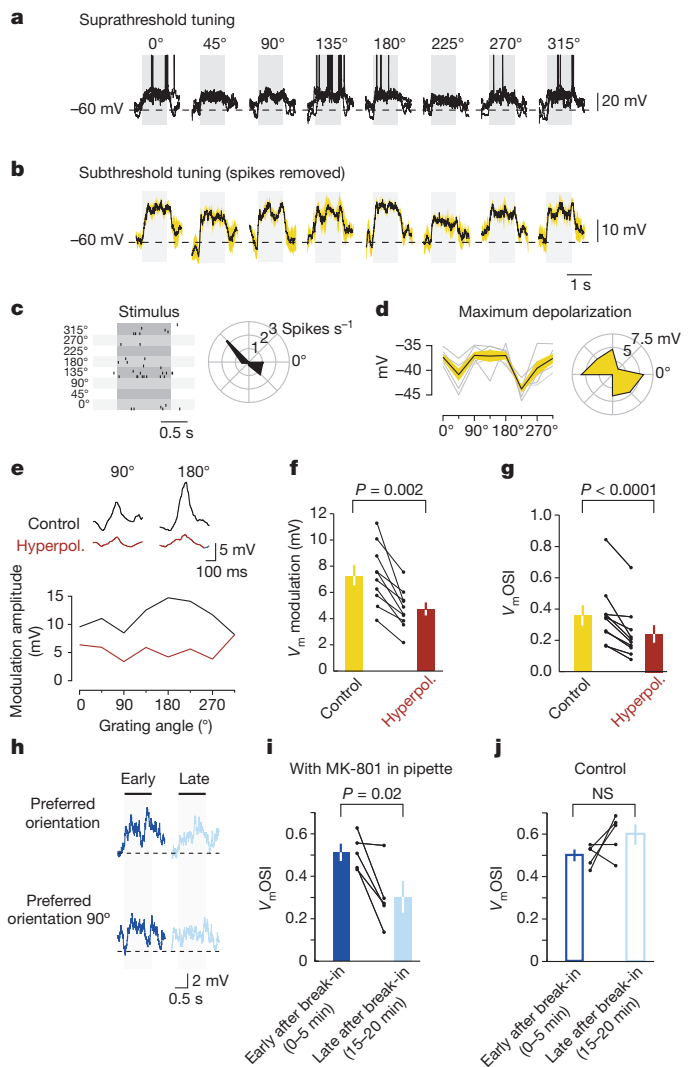


Figure 5 | Dendritic mechanisms contribute to the selectivity of subthreshold orientation tuning. **a**, **b**, Somatic whole-cell recording from a layer 2/3 pyramidal neuron, exhibiting robust visually evoked spiking (three sweeps overlaid; stimulus duration indicated by the grey bars) (**a**) and subthreshold responses (50-ms windows around the spikes were blanked, and the same results were obtained when the blanking window was decreased to 20 ms) (**b**). **c**, **d**, The responses in **a** and **b** were orientation tuned as indicated by spike rasters (**c**) and polar plots of maximal depolarization (**d**). **e**–**g**, Hyperpolarization (hyperpol.) decreased the amplitude of the stimulus-evoked membrane potential modulation and decreased its tuning selectivity (**e**): it decreased V_m modulation amplitude (**f**) and decreased the V_m orientation selectivity index (**g**) across the population. **h**–**j**, To investigate the mechanisms involved in the dendritic spikes contributing to orientation tuning, whole-cell somatic patch-clamp recordings were performed with 1 μM MK-801 in the pipette solution. **h**, The orientation tuning selectivity progressively decreased during the recording as MK-801 diffused into the cell and blocked NMDA channels. In these example traces, the response to the preferred orientation decreased from early in the recording to late in the recording. **i**, Across the population, subthreshold orientation tuning was strongly inhibited at late time points in the recording compared with early time points. **j**, In control recordings, with no blockers in the pipette solution, the orientation tuning selectivity did not significantly change across the recording and was not significantly different from the early period of MK-801 recordings ($P > 0.05$, two-sample *t*-test). Bars in **f**–**i** and **j** represent population means, and error bars indicate s.e.m. Between the bars, the individual data points are shown, and lines connect data taken in the same recording.

to regenerative events in dendrites^{10,15}. Visually driven synaptic input to layer 2/3 pyramidal cells activates synaptic NMDA receptors²¹. To determine whether NMDA receptors form one of the voltage-dependent

mechanisms that contributes to nonlinear synaptic integration *in vivo*, we used whole-cell somatic recordings with a use-dependent, intracellular NMDA receptor blocker, MK-801, included in the pipette solution²². Intracellular MK-801 did not affect up and down state dynamics (Extended Data Fig. 9a, b), confirming that the manipulation was restricted to the recorded cell, and dendritic spiking in the recorded cell was blocked by MK-801 (Extended Data Fig. 9c, d). Early in these recordings, before effective NMDA receptor block, the subthreshold orientation tuning was normal; however, late in these recordings, after MK-801 had diffused through the dendritic tree, V_m OSI decreased markedly (Fig. 5h–j), as did spike-based tuning (OSI early in recording, 0.82 ± 0.12 ; late in recording, 0.45 ± 0.17 ; $P = 0.016$, paired t -test; $n = 5$; Fig. 5i, j). Because the orientation selectivity was degraded despite the remaining, unblocked, receptor pathways (for example, AMPA (α -amino-3-hydroxy-5-methyl-4-isoxazole propionic acid) receptors and metabotropic glutamate receptors), we conclude that NMDA receptor currents are crucial for the tuning of synaptic integration in these neurons and that their depolarization-dependent relief from Mg^{2+} block might be a key mechanism that links synaptic input and dendritic regenerative events, including dendritic spikes^{5,10}.

We have presented multiple lines of evidence, including direct dendritic recordings, showing that visually evoked sensory input triggers local dendritic spikes in cortical pyramidal neurons *in vivo*. Moreover, we have shown that hyperpolarization decreases both the rate of dendritic spiking and V_m OSI, thus demonstrating that voltage-dependent dendritic mechanisms help shape the input–output function of neurons during sensory processing²³. Finally, we have also provided evidence for at least one specific biophysical mechanism that could underlie these dendritic events: NMDA receptor current. Together, these results show that the synaptic integration of sensory input crucially relies on voltage-dependent dendritic mechanisms.

A detailed compartmental model of layer 2/3 pyramidal cells confirmed that a biophysically plausible model can account for our data (Supplementary Note 1, Extended Data Fig. 10 and Supplementary Videos 1–3). This model reproduced the key findings of this study and offers potential mechanistic insight. For example, passively propagated Na^+ spikes can arrive immediately after an actively generated spike on a dendrite and support instantaneous spike rates of several hundred Hertz, as observed in distal dendritic recordings (Fig. 2a). In addition, cooperative recruitment of NMDA receptor current provides a crucial link between synaptic input and fast dendritic spiking. These results show that basic biophysical mechanisms support the electrophysiological phenomena that we observed in direct dendritic recordings *in vivo*.

Our experimental results and compartmental modelling suggest that synaptic input causes a dendritic depolarization that activates voltage-dependent ion channels and relieves the Mg^{2+} block of NMDA receptors^{5,10,15}. This results in a supralinear, local regenerative event that includes dendritic Na^+ spikes. The slow time course of the NMDA receptor current component of the regenerative events causes a prolonged depolarization envelope that propagates to the soma and enhances axonal output. Thus, local computational subunits generated by voltage-dependent mechanisms in dendrites^{22,24} are activated by sensory input *in vivo*, provide an orientation-tuned signal to the soma and thereby help determine stimulus selectivity.

Dendritic regenerative events provide a mechanism by which a relatively small number of inputs can drive spike output^{24,25}, changing the effective connectivity between local functional groups of neurons²⁶ or mitigating the noise in cortical circuits²⁷, by ensuring that variable synaptic input can result in a more reliable postsynaptic response. Our data from experiments on awake mice demonstrate that these dendritic events occur during alert sensory processing²⁸. Because dendrite-targeting inhibitory interneurons are inhibited in awake mice during sensory stimulation²⁹, this circuitry might have a key role in gating sensory input³⁰. Overall, our results demonstrate that dendrites are not passive integrators of sensory-driven input *in vivo*. Rather, sensory input engages dendritic voltage-dependent mechanisms and thereby

generates local regenerative events and dendritic spikes, which have an important role in shaping orientation selectivity, a quintessential cortical computation.

METHODS SUMMARY

Wild-type C57BL/6 mice (24–56 days old, both male and female) were anaesthetized with isoflurane (5% for induction, 1.5–2.5% for surgery and 0–0.5% during recording), augmented with chlorprothixene (0.5–2 mg kg⁻¹). Experiments with awake mice were carried out with head fixation, during which mice could freely move their limbs, groom and drink a sweet liquid reward when offered. Square-wave gratings (0.04 cycles per degree, 2 cycles s⁻¹) were displayed on a liquid crystal display (LCD) screen to map orientation selectivity. The screen was shrouded with a cone up to the eye of the mouse to prevent contamination of the imaging pathway with light from the visual stimulus. For both dendritic and somatic recordings, the pipette solution contained 135 mM or 140 mM K⁺ methylsulphate, 4 mM or 10 mM KCl, 10 mM HEPES, 10 mM Na₂-phosphocreatine, 4 mM Mg-ATP, 0.3 mM Na₂-GTP, 0.1 mM Oregon Green 488 BAPTA-1 and 0.025–0.050 mM Alexa Fluor 594; pH adjusted with KOH to 7.2; 290 mmol kg⁻¹. Pipette resistances ranged from 4.9 M Ω to 11 M Ω (mean, 7.9 M Ω) for dendritic recordings and from 5 M Ω to 8 M Ω (mean, 6.9 M Ω) for somatic recordings. All recordings were from the apical dendrites of superficial layer 2/3 pyramidal neurons. Unlike layer 5 neurons or deeper layer 2/3 neurons, these neurons do not have a prominent apical trunk and tuft; therefore, the recorded dendrites were geometrically similar to basal dendrites. A custom-built two-photon microscope with a 16 \times magnification and 0.8 numerical aperture water immersion objective (Nikon) and a large aperture collection pathway was used to visualize neurons. In dendritic recordings, putative bAPs were automatically identified as single spikes when isolated from other spikes by at least 50 ms. Unless otherwise specified, all measurements are expressed as mean \pm s.e.m.

Online Content Any additional Methods, Extended Data display items and Source Data are available in the online version of the paper; references unique to these sections appear only in the online paper.

Received 16 August 2012; accepted 22 August 2013.

Published online 27 October; corrected online 6 November 2013 (see full-text HTML version for details).

- Johnston, D. & Narayanan, R. Active dendrites: colorful wings of the mysterious butterflies. *Trends Neurosci.* **31**, 309–316 (2008).
- London, M. & Häusser, M. Dendritic computation. *Annu. Rev. Neurosci.* **28**, 503–532 (2005).
- Spruston, N. Pyramidal neurons: dendritic structure and synaptic integration. *Nature Rev. Neurosci.* **9**, 206–221 (2008).
- Larkum, M. E., Zhu, J. J. & Sakmann, B. A new cellular mechanism for coupling inputs arriving at different cortical layers. *Nature* **398**, 338–341 (1999).
- Schiller, J., Major, G., Koester, H. J. & Schiller, Y. NMDA spikes in basal dendrites of cortical pyramidal neurons. *Nature* **404**, 285–289 (2000).
- Helmchen, F., Svoboda, K., Denk, W. & Tank, D. W. *In vivo* dendritic calcium dynamics in deep-layer cortical pyramidal neurons. *Nature Neurosci.* **2**, 989–996 (1999).
- Llinas, R., Nicholson, C., Freeman, J. A. & Hillman, D. E. Dendritic spikes and their inhibition in alligator Purkinje cells. *Science* **160**, 1132–1135 (1968).
- Kamondi, A., Acsády, L. & Buzsáki, G. Dendritic spikes are enhanced by cooperative network activity in the intact hippocampus. *J. Neurosci.* **18**, 3919–3928 (1998).
- Yuste, R., Gutnick, M. J., Saar, D., Delaney, K. R. & Tank, D. W. Ca^{2+} accumulations in dendrites of neocortical pyramidal neurons: an apical band and evidence for two functional compartments. *Neuron* **13**, 23–43 (1994).
- Branco, T., Clark, B. A. & Häusser, M. Dendritic discrimination of temporal input sequences in cortical neurons. *Science* **329**, 1671–1675 (2010).
- Ferster, D. & Jagadeesh, B. EPSP-IPSP interactions in cat visual cortex studied with *in vivo* whole-cell patch recording. *J. Neurosci.* **12**, 1262–1274 (1992).
- Volgushev, M., Pei, X., Vidyasagar, T. R. & Creutzfeldt, O. D. Postsynaptic potentials in cat visual cortex: dependence on polarization. *Neuroreport* **3**, 679–682 (1992).
- Hirsch, J. A., Alonso, J. M. & Reid, R. C. Visually evoked calcium action potentials in cat striate cortex. *Nature* **378**, 612–616 (1995).
- Hubel, D. H. & Wiesel, T. N. Receptive fields of single neurones in the cat's striate cortex. *J. Physiol. (Lond.)* **148**, 574–591 (1959).
- Larkum, M. E., Waters, J., Sakmann, B. & Helmchen, F. Dendritic spikes in apical dendrites of neocortical layer 2/3 pyramidal neurons. *J. Neurosci.* **27**, 8999–9008 (2007).
- Waters, J. & Helmchen, F. Background synaptic activity is sparse in neocortex. *J. Neurosci.* **26**, 8267–8277 (2006).
- Niell, C. M. & Stryker, M. P. Highly selective receptive fields in mouse visual cortex. *J. Neurosci.* **28**, 7520–7536 (2008).
- Yu, Y., Shu, Y. & McCormick, D. A. Cortical action potential backpropagation explains spike threshold variability and rapid-onset kinetics. *J. Neurosci.* **28**, 7260–7272 (2008).

19. Svoboda, K., Helmchen, F., Denk, W. & Tank, D. W. Spread of dendritic excitation in layer 2/3 pyramidal neurons in rat barrel cortex *in vivo*. *Nature Neurosci.* **2**, 65–73 (1999).
20. Tan, A. Y., Brown, B. D., Scholl, B., Mohanty, D. & Priebe, N. J. Orientation selectivity of synaptic input to neurons in mouse and cat primary visual cortex. *J. Neurosci.* **31**, 12339–12350 (2011).
21. Jia, H., Rochefort, N. L., Chen, X. & Konnerth, A. Dendritic organization of sensory input to cortical neurons *in vivo*. *Nature* **464**, 1307–1312 (2010).
22. Polsky, A., Mel, B. W. & Schiller, J. Computational subunits in thin dendrites of pyramidal cells. *Nature Neurosci.* **7**, 621–627 (2004).
23. Lavzin, M., Rapoport, S., Polsky, A., Garion, L. & Schiller, J. Nonlinear dendritic processing determines angular tuning of barrel cortex neurons *in vivo*. *Nature* **490**, 397–401 (2012).
24. Mel, B. W. Synaptic integration in an excitable dendritic tree. *J. Neurophysiol.* **70**, 1086–1101 (1993).
25. Smith, S. L. & Häusser, M. Parallel processing of visual space by neighboring neurons in mouse visual cortex. *Nature Neurosci.* **13**, 1144–1149 (2010).
26. Ohiorhenuan, I. E. *et al.* Sparse coding and high-order correlations in fine-scale cortical networks. *Nature* **466**, 617–621 (2010).
27. London, M., Roth, A., Beeren, L., Häusser, M. & Latham, P. E. Sensitivity to perturbations *in vivo* implies high noise and suggests rate coding in cortex. *Nature* **466**, 123–127 (2010).
28. Xu, N. L. *et al.* Nonlinear dendritic integration of sensory and motor input during an active sensing task. *Nature* **492**, 247–251 (2012).
29. Gentet, L. J. *et al.* Unique functional properties of somatostatin-expressing GABAergic neurons in mouse barrel cortex. *Nature Neurosci.* **15**, 607–612 (2012).
30. Jiang, X., Wang, G., Lee, A. J., Stornetta, R. L. & Zhu, J. J. The organization of two new cortical interneuronal circuits. *Nature Neurosci.* **16**, 210–218 (2013).

Supplementary Information is available in the online version of the paper.

Acknowledgements We are grateful to B. Clark, P. Latham, M. London, D. Ringach, A. Roth, C. Schmidt-Hieber and C. Wilms for discussions and comments on the manuscript. This work was supported by the following: a Long-Term Fellowship and a Career Development Award from the Human Frontier Science Program and a Klingenstein Fellowship (S.L.S.); a Helen Lyng White Fellowship (I.T.S.); a Wellcome Trust and Royal Society Fellowship and MRC Programme Leader Track (T.B.); and by grants from the Wellcome Trust, ERC and Gatsby Charitable Foundation (M.H.).

Author Contributions S.L.S. and M.H. conceived and designed the experiments. S.L.S. and I.T.S. performed the experiments. S.L.S. analysed the data. T.B. designed and carried out the compartmental modelling. S.L.S., I.T.S., T.B. and M.H. interpreted the data and wrote the paper.

Author Information Reprints and permissions information is available at www.nature.com/reprints. The authors declare no competing financial interests. Readers are welcome to comment on the online version of the paper. Correspondence and requests for materials should be addressed to S.L.S. (slab@unc.edu) or M.H. (m.hausser@ucl.ac.uk).

METHODS

Preparation. All experiments were carried out in accordance with the regulations of the UK Home Office or the guidelines and regulations of the US Department of Health and Human Services and the University of North Carolina. Wild-type C57BL/6 mice (24–56 days old, male and female) were anaesthetized with isoflurane (5% for induction, 1.5–2.5% for surgery and 0–0.5% during recording), augmented with chlorprothixene (0.5–2 mg kg⁻¹). During recording, this regime resulted in a sedated state in which the animals did not voluntarily move but responded to a toe pinch. Increased levels of isoflurane (>0.5%) typically suppressed spiking activity, including dendritic bursts. Experiments with awake mice were carried out with head fixation, during which mice could routinely move their limbs, groom and drink a sweet liquid reward when offered.

After gluing a head plate to the skull for head fixation during surgery and recording, a 2–3-mm diameter craniotomy was performed over the monocular visual cortex. A thin layer of agar (1.5%) was dissolved in artificial cerebrospinal fluid (150 mM NaCl, 2.5 mM KCl, 10 mM HEPES, 2 mM CaCl₂ and 1 mM MgCl₂; pH adjusted with NaOH to 7.3; 300 mmol kg⁻¹) and placed on top of the brain to help dampen movement. A homeothermic heat pad was used to maintain the body temperature within the physiological range, and a water-based ophthalmic ointment was used to maintain eye health.

Visual stimulation. Visual stimulus presentation was controlled by routines written in MATLAB (MathWorks) using the Psychophysics Toolbox extensions^{31,32}. Square-wave gratings (0.04 cycles per degree, 2 cycles s⁻¹) of black (2 cd m⁻²) and white (86 cd m⁻²) bars in eight different orientations were displayed on a liquid crystal display (LCD) screen (ESAW 7-inch VGA and composite TFT monitor, set at 1024 × 768 resolution and a 60 Hz refresh rate) to map orientation selectivity. The screen was shrouded with a cone up to the eye of the mouse to prevent contamination of the imaging pathway with light from the visual stimulus. The visual stimulus extended from +20° to +124° in azimuth and from -10° to +42° in elevation. Visual stimuli were presented in a shuffled order: each orientation was presented once per sweep of eight orientations, and the order of the orientations was different in each sweep.

Patch-clamp recordings. For both dendritic and somatic recordings, the pipette solution contained 135 mM or 140 mM K⁺ methylsulphate, 4 mM or 10 mM KCl, 10 mM HEPES, 10 mM Na₂-phosphocreatine, 4 mM Mg-ATP, 0.3 mM Na₂-GTP, 0.1 mM Oregon Green 488 BAPTA-1 and 0.025–0.050 mM Alexa Fluor 594; pH adjusted with KOH to 7.2; 290 mmol kg⁻¹. Pipette resistances ranged from 4.9 MΩ to 11 MΩ (mean, 7.9 MΩ) for dendritic recordings and from 5 MΩ to 8 MΩ (mean, 6.9 MΩ) for somatic recordings. For dendritic recordings, imaging³³ was used to guide the pipette away from blood vessels and somata, and tip resistance measured using a voltage step in voltage-clamp mode was used to detect contact with a dendrite. Shadowpatching techniques³³ were used to directly target the pipette to the soma. In somatic hyperpolarization experiments, cells were hyperpolarized by 21.4 ± 11.4 mV (mean ± s.d.; from a membrane potential of -49.4 ± 6.7 mV to -70.8 ± 9.4 mV, mean ± s.d.; average V_m across all stimuli after removing spikes). All dendritic recordings were from the apical dendrites of superficial layer 2/3 pyramidal neurons. These neurons do not have a large apical trunk and tuft, unlike layer 5 or deeper layer 2/3 neurons; therefore, the recorded dendrites were geometrically similar to basal dendrites. The series resistance was 39 ± 5 MΩ and 34 ± 5 MΩ for dendritic and somatic recordings, respectively. The series resistance did not change as a function of dendritic distance from the soma (Pearson's $R = -0.24$, linear regression, $P = 0.50$; $n = 13$). The bridge was rebalanced as needed during the recording. R_{series} increased less than 2% over the time it took to run a tuning curve. In one case, we obtained two distal dendritic recordings in the same mouse. In all other cases, we obtained at most one distal dendritic recording per mouse.

Compartmental modelling. Simulations were performed with the NEURON simulation environment (version 7.2) using a detailed reconstruction of a biocytin-filled layer 2 pyramidal neuron (NeuroMorpho.org ID Martin, NMO_00904). Passive parameters were $C_m = 1 \mu\text{F cm}^{-2}$, $R_m = 7,000 \Omega \text{ cm}^2$, $R_i = 100 \Omega \text{ cm}$, yielding a somatic input resistance of 110 MΩ, similar to the experimentally measured mean value (Extended Data Fig. 1a). AMPA, NMDA and GABA_A (γ-aminobutyric acid A) synapses had a peak conductance of 1 nS and were modelled as a bi-exponential function, with time constants of AMPA $\tau_1 = 0.1$ ms, AMPA $\tau_2 = 1$ ms, NMDA $\tau_1 = 2$ ms, NMDA $\tau_2 = 20$ ms, GABA_A $\tau_1 = 0.1$ ms and GABA_A $\tau = 4$ ms (the inhibition reversal potential was set to -80 mV). The Mg²⁺ block of NMDA synapses was modelled according to Jahr and Stevens³⁴. Active conductances were introduced in the soma and in all dendritic compartments and included the following: voltage-activated Na⁺ channels (soma 100 mS cm⁻² and dendrite 60 mS cm⁻², distributed as a hot spot in the centre of each branch)³⁵; high-voltage activated Ca²⁺ channels (soma 0.05 mS cm⁻² and dendrite 0.05 mS cm⁻²); low-voltage activated Ca²⁺ channels (soma 0.3 × 10⁻³ mS cm⁻² and dendrite 0.15 × 10⁻³ mS cm⁻²); voltage-activated K⁺ channels (10 mS cm⁻² soma and 0.3 mS cm⁻² dendrite);

M-type K⁺ channels (soma 0.22 mS cm⁻² and dendrite 0.1 mS cm⁻²); and Ca²⁺-activated K⁺ channels (soma 0.3 mS cm⁻² and dendrite 0.3 mS cm⁻²). The time course of dendritic Ca²⁺ was modelled by adding the current carried by voltage-activated Ca²⁺ channels and the calcium fraction of the NMDA current (10%)³⁶ and convolving it with a decaying exponential with a 50 ms time constant. AMPA and NMDA components were colocated and coactivated at each excitatory synapse.

A total of 1,100 synapses were randomly distributed across the dendritic tree: 80% excitatory and 20% inhibitory. The synapses were separated into background and signal synapses (the signal synapses constituted 10% of the total synapse number) and were activated with independent Poisson spike trains delivered to each synapse. The background synapses were continuously activated at a mean rate of 0.5 Hz, and the signal synaptic input was activated at 5–8 Hz after a 200 ms baseline and stayed active for 200 ms. The results did not depend on the total number of synapses but rather the total input rate. For example, 100 synapses activated at 1 Hz yielded the same result as 1,000 synapses activated at 0.1 Hz (the model did not include short-term plasticity).

Imaging. A custom-built two-photon microscope using galvanometer-based scan mirrors (6-mm diameter, Cambridge Technologies) with a 16× magnification, 0.8 numerical aperture water immersion objective (Nikon) and a large aperture collection pathway with low-noise photomultiplier tubes (models 3896 and 7422-40P, Hamamatsu) was used to image neurons. Frame scans (15.6 frames s⁻¹) and line scans (1 ms per line) were acquired using ScanImage³⁷.

Analysis. Custom programs written for MATLAB and IGOR Pro (WaveMetrics), including event detection and analysis routines in IGOR Pro by T. Ishikawa (Jikei University), were used for analysis. Input resistance was measured as the steady-state membrane potential in response to a current step. Maximum instantaneous firing rates were computed as the reciprocal of the smallest interspike interval. In dendritic recordings, putative bAPs were automatically identified as single spikes when isolated from other spikes by at least 50 ms.

Statistics. Unless otherwise specified, all measurements are expressed as mean ± s.e.m. The Shapiro–Wilk test was used, before the application of two-sided parametric tests, to confirm that the deviation of the data from normality was statistically insignificant. For non-normal data, or data with significantly different variances, non-parametric tests were used as noted in the text (for example, the Wilcoxon rank sum test used in Fig. 2). The multivariate Kolmogorov–Smirnov test was computed using the generalization of Fasano and Franceschini³⁸. Experimental manipulations (hyperpolarization and MK-801 block of NMDA receptors) did not involve randomization or blinding because each recorded cell served as its own control (control versus hyperpolarized or early versus late recording, respectively). Sample sizes were designed to reliably measure neurophysiological parameters while remaining in compliance with ethical guidelines to minimize the number of animals used. The results from Fig. 2a remain statistically significant ($P < 0.05$) when the top one or two data points from the distal dendritic recordings are omitted from the analysis. To test the statistical significance of the orientation tuning of dendritic bursts, we first computed the OSI of the measured dendritic burst firing. We then shuffled the responses so that their associated orientation was assigned at random. We then computed the OSI of the new, reshuffled, responses. This procedure was repeated 1,000 times. The P value was taken as the fraction of time for which a randomly shuffled response yielded an OSI equal to or greater than the actual response.

Orientation tuning analysis. The OSI was computed after fitting a sum of two Gaussian curves to the orientation tuning curve (whether based on spiking or membrane potential), with the centres 180° apart:

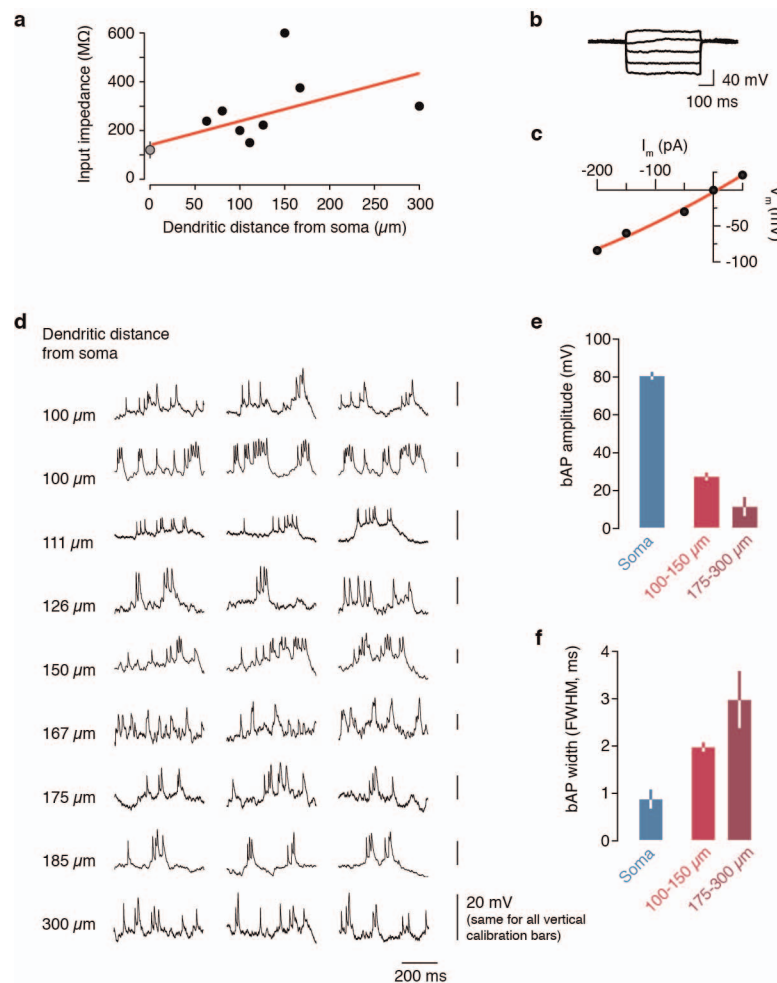
$$\text{OSI} = \frac{R_p - R_o}{R_p + R_o}$$

where R_p is the response to the preferred orientation and R_o is the response at the orthogonal orientation. Cells in which the sum of squared residuals between the Gaussian fit and the observed data was less than 15% of the maximum value of the Gaussian fit were considered to be well described by the Gaussian fit.

Membrane potential (V_m) modulation in response to visual stimuli was computed by taking the peak-to-trough amplitude of the cycle average at 2 Hz (the drift rate of the visual stimulus gratings) (after removing any spikes). This modulation can be seen in the traces in Fig. 5c, particularly at 135° and 315°.

31. Brainard, D. H. The psychophysics toolbox. *Spat. Vis.* **10**, 433–436 (1997).
32. Pelli, D. G. The VideoToolbox software for visual psychophysics: transforming numbers into movies. *Spat. Vis.* **10**, 437–442 (1997).
33. Kitamura, K., Judkewitz, B., Kano, M., Denk, W. & Häusser, M. Targeted patch-clamp recordings and single-cell electroporation of unlabeled neurons *in vivo*. *Nature Methods* **5**, 61–67 (2008).
34. Jahr, C. E. & Stevens, C. F. Voltage dependence of NMDA-activated macroscopic conductances predicted by single-channel kinetics. *J. Neurosci.* **10**, 3178–3182 (1990).

35. Nevian, T., Larkum, M. E., Polsky, A. & Schiller, J. Properties of basal dendrites of layer 5 pyramidal neurons: a direct patch-clamp recording study. *Nature Neurosci.* **10**, 206–214 (2007).
36. Spruston, N., Jonas, P. & Sakmann, B. Dendritic glutamate receptor channels in rat hippocampal CA3 and CA1 pyramidal neurons. *J. Physiol. (Lond.)* **482**, 325–352 (1995).
37. Pologruto, T. A., Sabatini, B. L. & Svoboda, K. ScanImage: flexible software for operating laser scanning microscopes. *Biomed. Eng. Online* **2**, 13 (2003).
38. Fasano, G. & Franceschini, A. A multidimensional version of the Kolomogorov–Smirnov test. *Mon. Not. R. Astron. Soc.* **225**, 155–170 (1987).

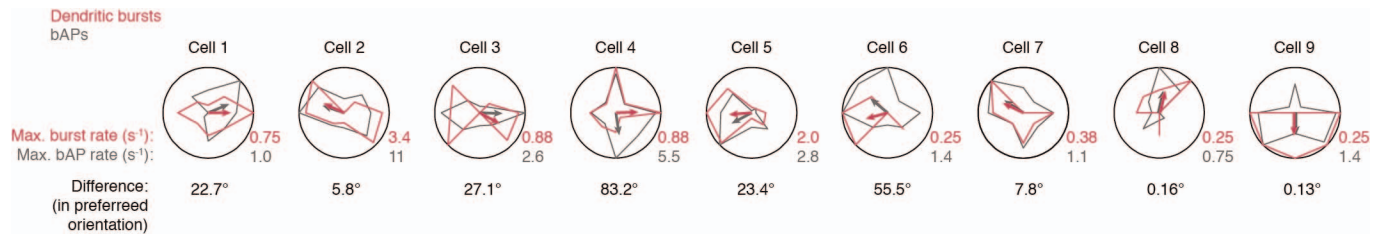


Extended Data Figure 1 | Electrophysiological features of layer 2/3

dendrites *in vivo*. **a**, The input resistance of distal dendrites was typically 100–300 $M\Omega$ but sometimes larger (up to 600 $M\Omega$). The input resistance increased as function of dendritic distance from the soma, approximately doubling every 300 μm . The grey point indicates the input resistance measured in somatic patch-clamp recordings (mean \pm s.e.m.). **b**, During a dendritic recording at 150 μm from the soma, hyperpolarizing current steps did not reveal a voltage sag; thus, there is probably little to no hyperpolarization-activated cation current, I_h , in the dendrites of layer 2/3 pyramidal neurons *in vivo*. **c**, The peak voltage response plotted against the hyperpolarizing current step amplitude in

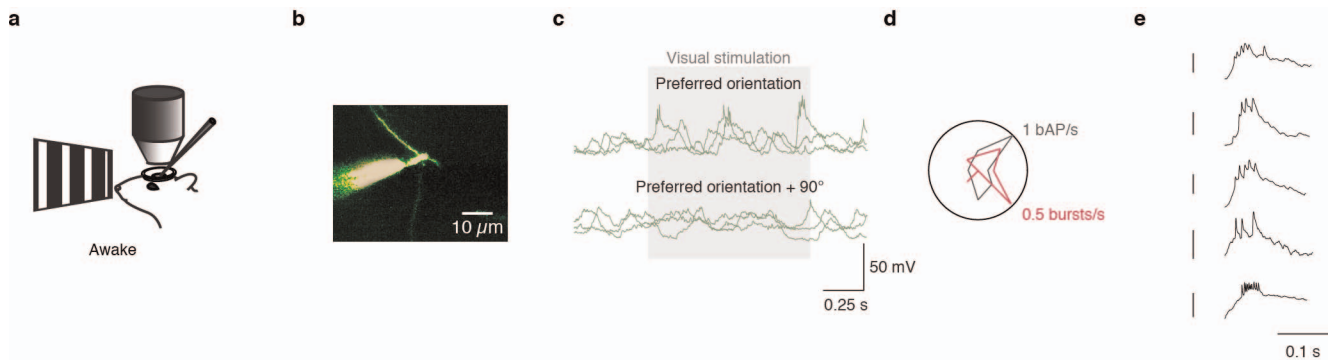
an $I-V$ plot was well fit by a linear function, confirming the lack of I_h .

d, Representative dendritic bursts evoked by visual stimulation at the optimal orientation in nine different dendritic recordings at progressively increasing distances from the soma. All right-hand scale bars are 20 mV. **e**, **f**, Compared with action potentials recorded at the soma, bAPs had a lower amplitude (**e**) and were prolonged in time (**f**), and both of these trends were more pronounced with increasing dendritic distance from the soma (error bars, s.d.). Both the amplitude and width were significantly different among the three groups ($P < 0.01$, unpaired t -tests with the Bonferroni correction for multiple comparisons).



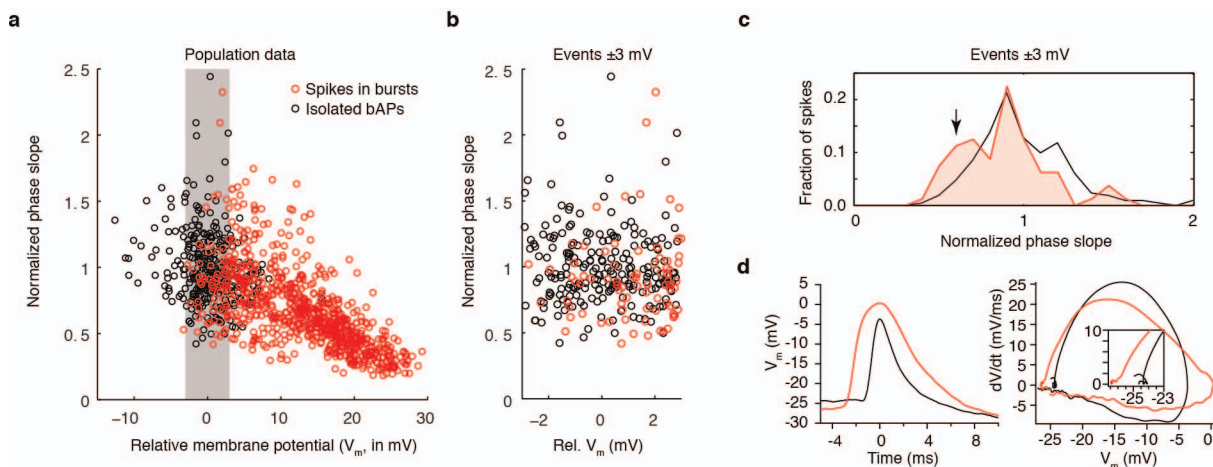
Extended Data Figure 2 | Orientation tuning curves of dendritic bursts compared with bAPs. Tuning curves for dendritic spike bursts and bAPs recorded at distal dendritic locations ($>75 \mu\text{m}$ from soma) are shown. The tuning curves for dendritic bursts match the tuning curves for isolated bAPs. The statistical significance of dendritic burst tuning curves was tested by randomly shuffling responses (details in the Methods) and was found to be significant ($P < 0.05$) for 7 out of 9 cells (dendritic burst tuning in cells 6 and 9 was not significant). The curves were normalized to the maximal values, which are shown at the bottom right of each polar plot. The small qualitative differences may be due to dendrites that are topologically distant from the

dendritic recording site exhibiting slightly different tuning curves. The grating drift direction that elicited the largest response is indicated with an arrow. The difference between these directions is indicated at the bottom of each polar plot. The cross correlation between dendritic bursts and isolated bAPs was highly significant: Pearson's $R = 0.54$, $P = 0.000013$, paired t -test; $n = 9$. When only the spikes in the bursts with rise times in the slowest quartile of the distribution were considered to be dendritic in origin, the preferred orientation of bAPs and the slowest quartile were still matched within individual dendritic recordings (difference in preferred orientation, $41.5 \pm 58.1^\circ$; $P = 0.49$, paired t -test; $n = 9$).



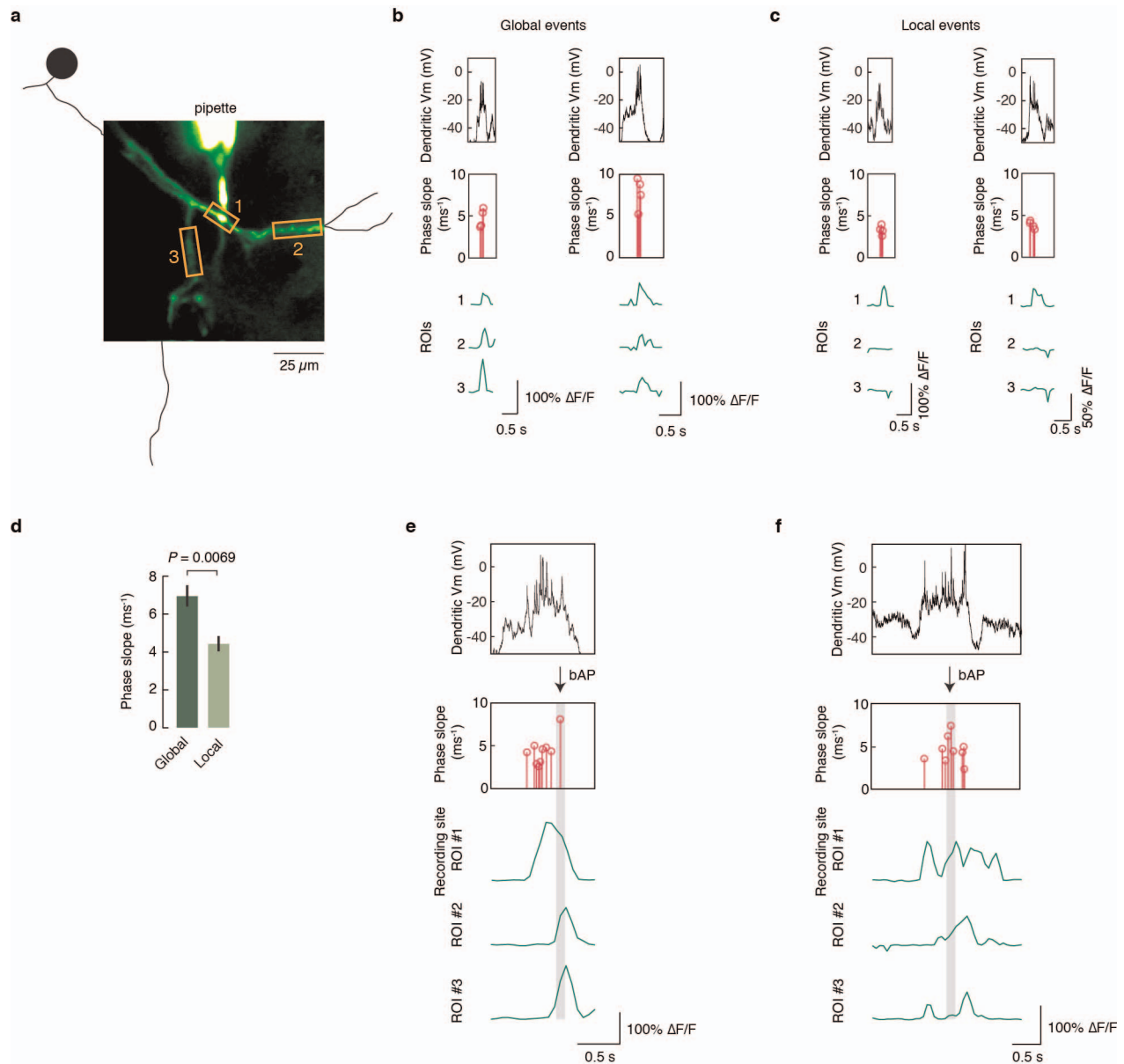
Extended Data Figure 3 | Dendritic recordings in awake mice exhibit dendritic bursts. **a**, Awake, head-fixed mice viewed drifting gratings during electrophysiological recordings. **b**, A two-photon image of the patched dendrite ($117 \mu\text{m}$ from the soma) of a layer 2/3 pyramidal neuron in the mouse visual cortex, after filling with Alexa Fluor 594 with the dendritic patch-clamp pipette.

c, Dendritic bursts were observed when the preferred orientation was presented. **d**, Tuning curves for the isolated bAPs and dendritic bursts. **e**, Example bursts from three different distal dendritic recordings in awake mice. Calibration bars, 25 mV.



Extended Data Figure 4 | The diversity of onset dynamics versus membrane potential. **a**, Spikes from each distal dendritic recording (both isolated bAPs (black) and spikes in dendritic burst events (red)) were normalized such that isolated bAPs had a mean phase slope of 1. The mean baseline membrane potential (V_m) of isolated bAPs was subtracted from the mean baseline V_m of all spikes. Although many spikes in bursts had a depolarized baseline V_m relative to isolated spikes, there was overlap between the two populations around $\pm 3 \text{ mV}$. **b**, Magnification of panel **a** to show spikes at $\pm 3 \text{ mV}$ relative to the

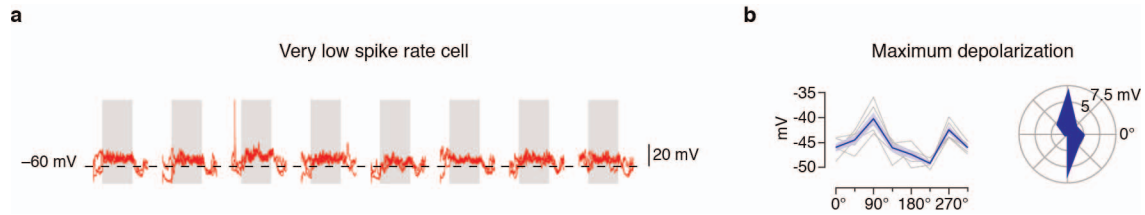
mean baseline V_m of isolated bAPs. **c**, Histograms of the two populations reveal a tendency towards lower phase slope values for spikes in bursts ($P = 0.041$, Kolmogorov–Smirnov test; $n = 211$ bAPs, 80 spikes in bursts). **d**, An example of bAPs and a spike in a burst (both from the same distal dendritic recording): although the bAP has a more depolarized baseline V_m , it still exhibits a steeper phase slope (a kink at the foot of the voltage waveform), indicative of a propagated action potential.



Extended Data Figure 5 | Ca^{2+} imaging at the site of dendritic recording reveals that global Ca^{2+} signals are associated with faster onset spikes.

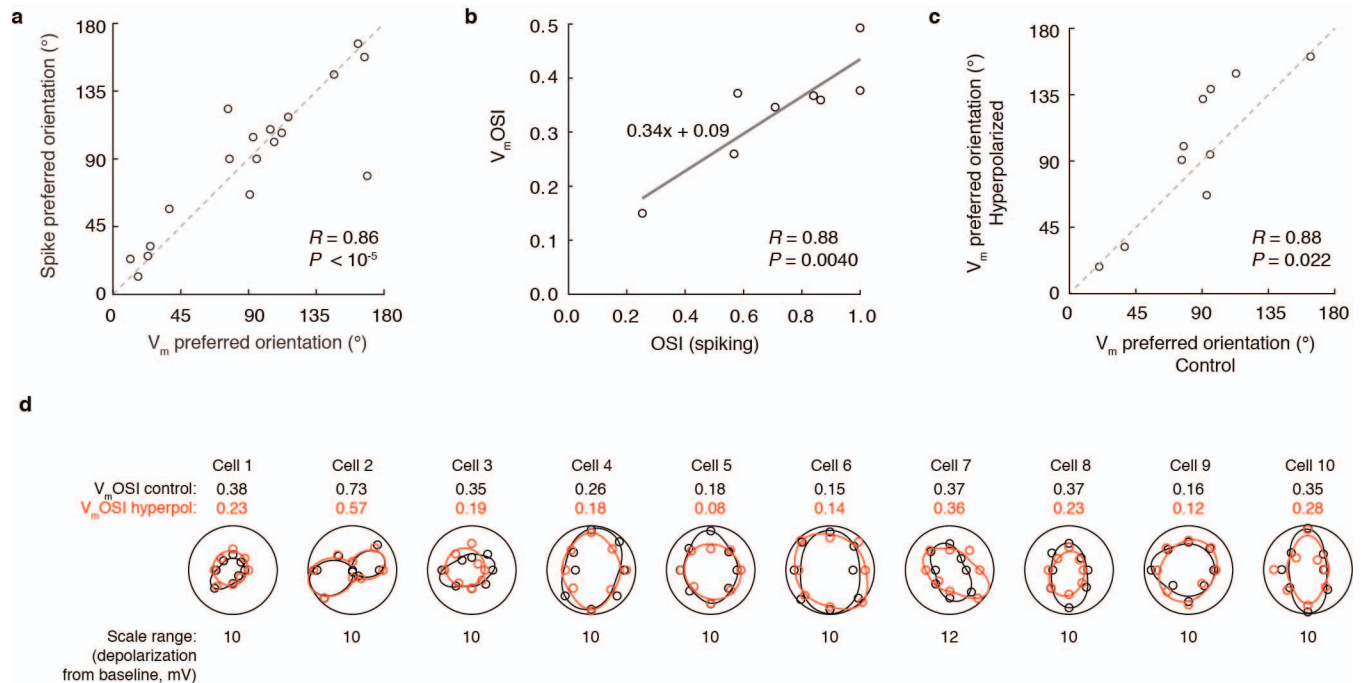
a, During dendritic recordings, Ca^{2+} signals were simultaneously imaged at the site of the recording and at nearby dendrites. **b**, In dendritic bursts with global Ca^{2+} signals that were simultaneously observed in all regions of interest (ROIs), the spikes recorded at the dendrite exhibited steep onsets, indicating that they were probably bAPs. **c**, In local Ca^{2+} signals that were observed only in the ROI

at the site of recording, the dendritic spikes exhibited slower onsets, indicating that they were probably locally generated. **d**, The maximum phase slope of spikes occurring during global Ca^{2+} events was higher than for spikes occurring during local Ca^{2+} events ($P = 0.0069$, t -test). **e**, **f**, When global Ca^{2+} signals occurred during ongoing local Ca^{2+} signals, the initiation was associated with a steep onset spike. Two examples are shown.



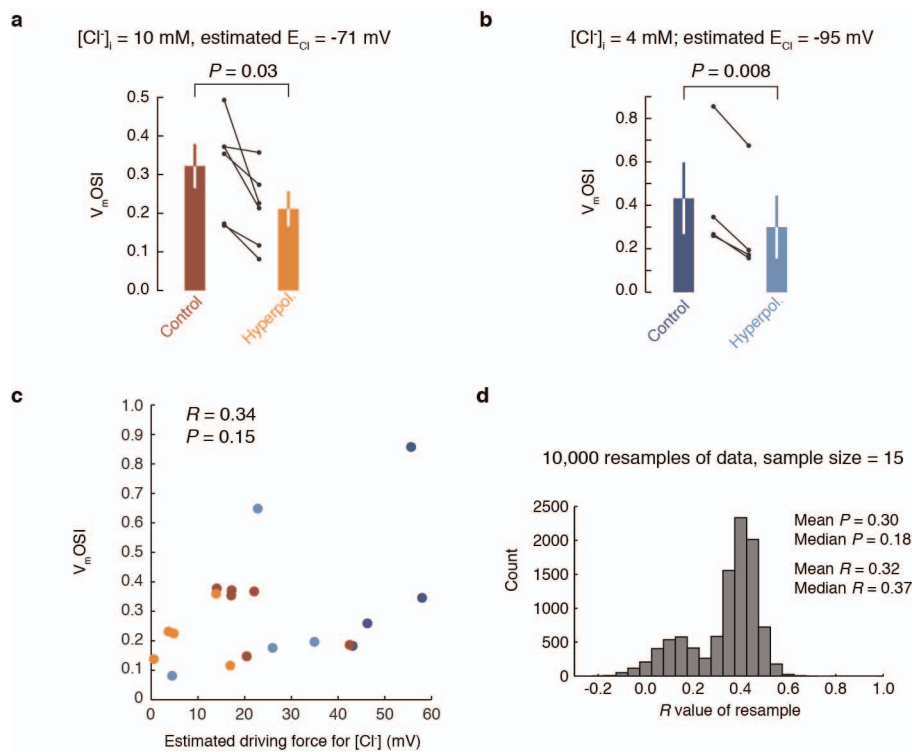
Extended Data Figure 6 | Non-firing cells exhibit subthreshold orientation tuning. **a**, Raw data for an example cell in which subthreshold orientation tuning was observed, although no spikes were fired during stimulus

presentations. **b**, In this case, the tuning width of the subthreshold membrane potential was quite sharp and was confined to two directions.



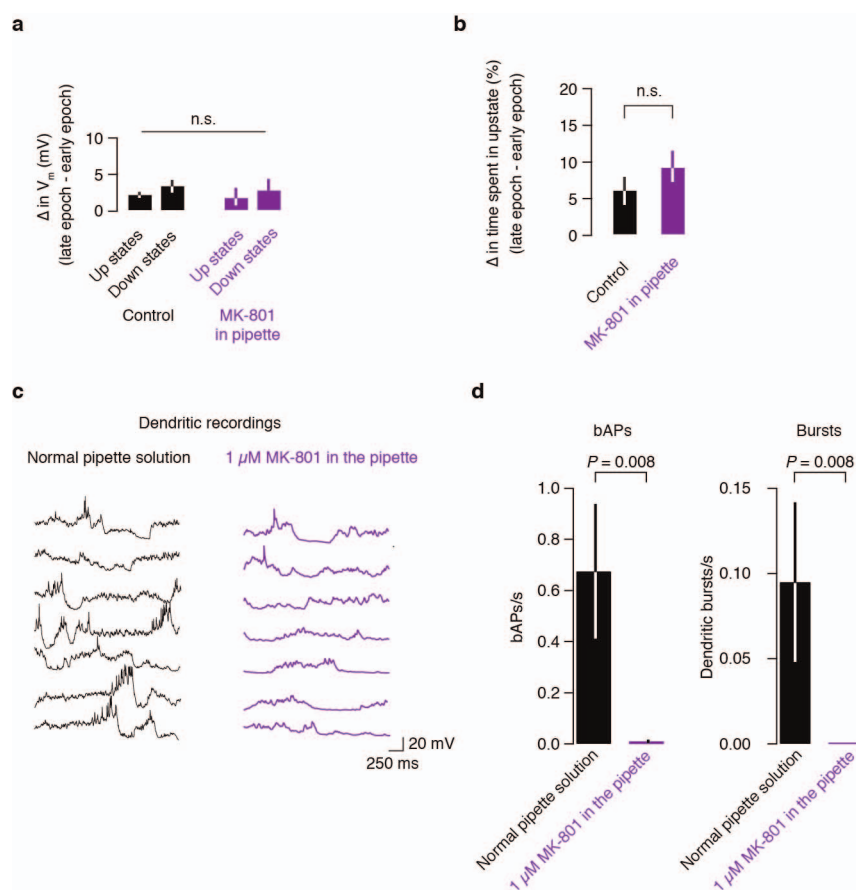
Extended Data Figure 7 | Tuning of action potentials and subthreshold membrane potential. **a**, In individual cells, the orientation tuning of spikes and the membrane potential were highly correlated, indicating that the tuning of the subthreshold responses was not spurious (mean difference in preferred orientation, $14.8 \pm 5.3^\circ$). **b**, In individual cells, the orientation selectivity index based on the membrane potential response (V_m OSI) was highly correlated with the conventional spiking-based OSI. **c**, In individual cells, the preferred orientation of the control subthreshold response was correlated with the

preferred orientation of the subthreshold response during hyperpolarization. **d**, The black curve is the fitted subthreshold orientation tuning curve (the black circles are raw data points), and the red curve is the subthreshold tuning curve during hyperpolarization (the red circles are raw data points). The V_m OSI values for the control and hyperpolarized conditions are shown next to each plot. The radial axes are linear and start at 0. The maximal radial axis range is shown below each polar plot. The differences in V_m OSI are quantified in Fig. 5g.



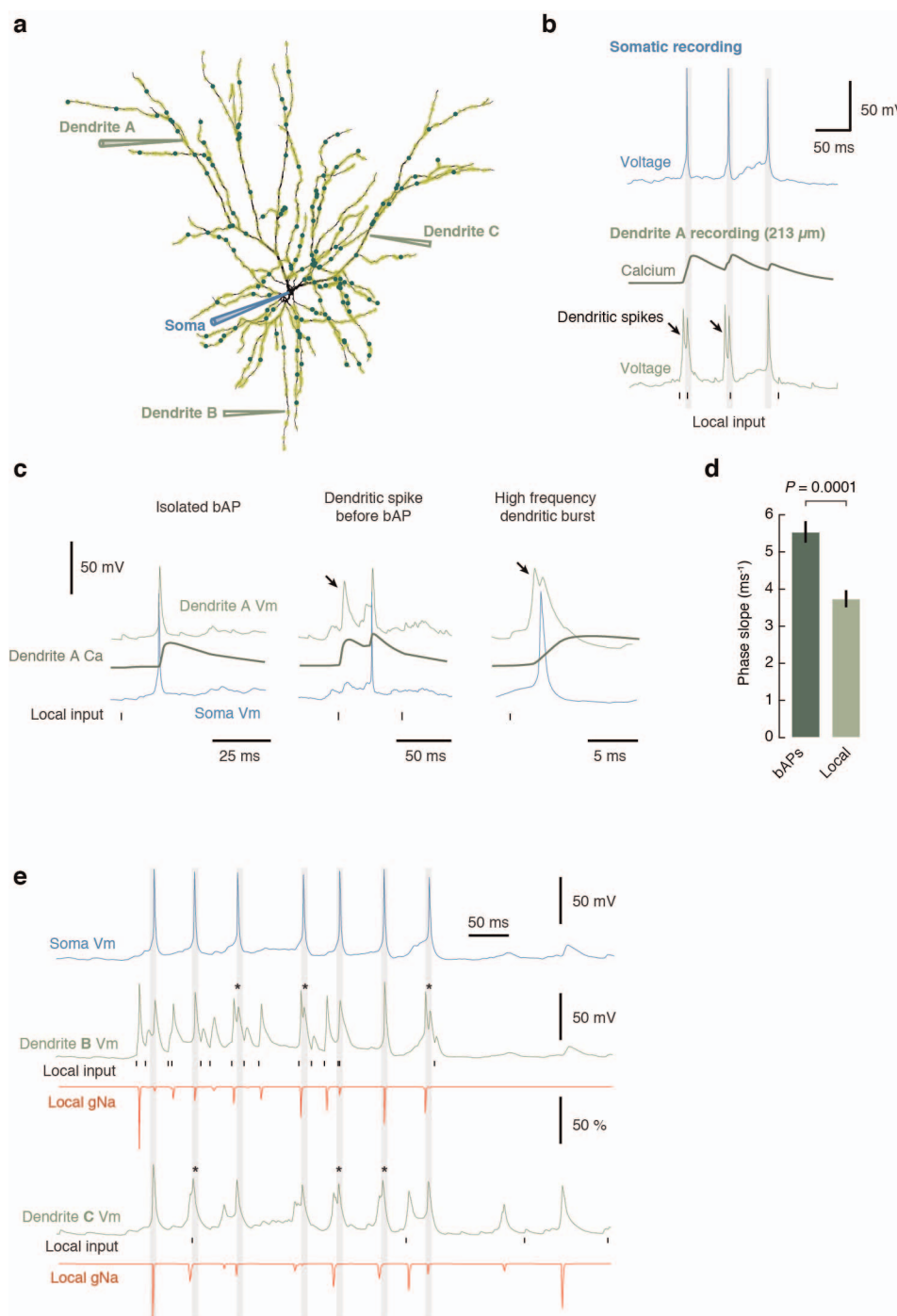
Extended Data Figure 8 | Changes in the driving force for Cl^- do not account for the effects of hyperpolarization on V_mOSI . **a**, When the pipette solution contained $10 \text{ mM } Cl^-$, the reversal potential for chloride, E_{Cl^-} , was estimated to be -71 mV (based on the assumption that natural cerebrospinal fluid contains a similar amount of Cl^- to the artificial cerebrospinal fluid used). In this situation, hyperpolarization decreased the orientation selectivity index. **b**, Even with a low Cl^- concentration (4 mM ; estimated E_{Cl^-} , -95 mV), the

result was the same. **c**, There was no significant correlation between the driving force for Cl^- and V_mOSI . **d**, The data were resampled (15 of the data points in **c** were selected at random, and the R and P values for that set of data points were calculated; this process was repeated 10,000 times), and this process confirmed that the result from the correlational analysis in **c** was not biased by a small subset of the data points (the mean R and P values from the resampling analysis match the values for the full data set in **c** well).



Extended Data Figure 9 | The effect of intracellular MK-801 on up and down states and dendritic spikes. **a**, To determine whether MK-801 that might have leaked out of the pipette during patching affects network circuitry, we examined the dynamics of up and down states in recordings in which MK-801 was in the pipette and in control recordings (no MK-801). **b**, Although, in general, the membrane potential drifted up slightly (<5 mV on average) and the time spent in the up state increased over long recordings (possibly due to the anaesthesia wearing off), these trends were identical with or without MK-801 in the patch pipette. **c**, When 1 μ M MK-801 was included in the recording pipette,

the visually evoked responses contained fewer bAPs and bursts. This trend was clear in individual cells (**a**) and across the population (**d**). This reduction in spiking confirms that dendritic bursts do not occur when NMDA receptors are blocked. Because the low firing rate in MK-801 recordings prevented a reliable measurement of orientation tuning in the MK-801 dendritic patch-clamp recordings, we averaged over all of the stimulus presentations for both conditions, resulting in a lower average firing rate for bAPs and dendritic bursts.



Extended Data Figure 10 | Compartmental modelling of dendritic events.

a, A detailed reconstruction of a layer 2/3 pyramidal cell was used in the simulations. Light green circles over the dendritic tree represent background synapses, and dark green circles represent signal synapses (the model had 1,100 synapses; not all are illustrated). Voltage was recorded at the soma and at all dendritic branches simultaneously. **b**, Activation of signal synapses at 5 Hz produced high-frequency dendritic bursts, composed of local dendritic spikes and bAPs. These bursts were always accompanied by dendritic Ca^{2+} transients. The timing of the activation of excitatory synapses on the recorded dendritic branch is illustrated. Note how the local excitatory postsynaptic potentials (EPSPs) are clearly smaller than the dendritic spikes. **c**, Examples of specific features consistently observed in the model. Isolated bAPs were associated with global Ca^{2+} transients and had kinked onsets. Dendritic spikes often preceded somatic action potentials, had smooth onsets and Ca^{2+} transients that were localized to the branches where the spikes were recorded, and clearly started before the global transients associated with bAPs. Local dendritic spikes initiated in the dendrite could often be recorded in multiple electrotonically close dendritic branches. Pairs of local spikes and bAPs reached very high

frequencies; the example shows a pair at >400 Hz. When NMDA receptors were removed from the simulations, no dendritic spikes were observed, and the soma failed to reach the threshold for action potential firing. This also occurred when there were no dendritic voltage-activated Na^+ channels, indicating that the generation of dendritic spikes is required for producing axonal output.

d, Quantification of spike onset for local dendritic spikes and bAPs in the model reproduced the experimentally observed effect reported in Extended Data Fig. 5d. **e**, Example trial showing the somatic voltage and recordings for two dendrites indicated in **a**. For each dendrite, the local voltage, the Na^+ channel conductance (gNa, expressed as a fraction of the maximum conductance) and the timing of activation of excitatory synapses on the recorded dendrite are shown. The gNa traces show that there is significant local Na^+ channel inactivation after the first spike and that subsequent spikes are associated with varying degrees of Na^+ channel conductance. Asterisks denote extreme cases when a bAP followed a local dendritic spike at very high frequency and did not recruit any local gNa, thereby indicating that the propagation into the recorded branch was passive.

The activity-dependent transcription factor NPAS4 regulates domain-specific inhibition

Brenda L. Bloodgood^{1,2*}, Nikhil Sharma^{1,3*}, Heidi Adlman Browne^{1†}, Alissa Z. Trepman^{1†} & Michael E. Greenberg¹

A heterogeneous population of inhibitory neurons controls the flow of information through a neural circuit^{1–3}. Inhibitory synapses that form on pyramidal neuron dendrites modulate the summation of excitatory synaptic potentials^{4–6} and prevent the generation of dendritic calcium spikes^{7,8}. Precisely timed somatic inhibition limits both the number of action potentials and the time window during which firing can occur^{8,9}. The activity-dependent transcription factor NPAS4 regulates inhibitory synapse number and function in cell culture¹⁰, but how this transcription factor affects the inhibitory inputs that form on distinct domains of a neuron *in vivo* was unclear. Here we show that in the mouse hippocampus behaviourally driven expression of NPAS4 coordinates the redistribution of inhibitory synapses made onto a CA1 pyramidal neuron, simultaneously increasing inhibitory synapse number on the cell body while decreasing the number of inhibitory synapses on the apical dendrites. This rearrangement of inhibition is mediated in part by the NPAS4 target gene brain derived neurotrophic factor (*Bdnf*), which specifically regulates somatic, and not dendritic, inhibition. These findings indicate that sensory stimuli, by inducing NPAS4 and its target genes, differentially control spatial features of neuronal inhibition in a way that restricts the output of the neuron while creating a dendritic environment that is permissive for plasticity.

We assessed NPAS4 expression in the hippocampus by immunofluorescence microscopy. We found that in hippocampi from mice maintained in standard housing, NPAS4 protein is undetectable by immunostaining (Fig. 1a). By contrast, exposure of mice to an enriched environment induces NPAS4 protein expression in neurons in the pyramidal layer, whereas no NPAS4-positive nuclei are observed in the neuropil (Fig. 1b). To obtain more widespread induction of NPAS4, mice were injected intraperitoneally with kainic acid to trigger seizure activity. This treatment led to NPAS4 expression in nearly all excitatory neurons in the pyramidal layer and a minority of inhibitory neurons in the neuropil (Fig. 1c).

We next asked whether the loss of NPAS4 affects inhibitory synapse function *in vivo*. Adeno-associated virus encoding a Cre–GFP fusion protein (AAV-Cre–GFP)¹¹ was injected into the CA1 region of the hippocampus in *Npas4* conditional mice (*Npas4*^{fl/fl}) (Fig. 1d, Extended Data Fig. 1). Post-operative animals were transferred to an enriched environment or maintained in standard housing for 7 to 12 days. Subsequently acute hippocampal slices were prepared, whole-cell voltage clamp recordings were made from neighbouring NPAS4 knockout and wild-type neurons (referred to as NPAS4-KO and NPAS4-WT, respectively) and pharmacologically isolated miniature inhibitory postsynaptic currents (mIPSCs) were recorded (Fig. 1e).

We found that when mice were exposed to an enriched environment significantly less frequent and slightly smaller amplitude mIPSCs were recorded from NPAS4-KO neurons compared to the neighbouring NPAS4-WT neurons (Fig. 1g, Supplementary Table 1). Similar results were obtained from mice injected with kainic acid to induce NPAS4

(Fig. 1h). By contrast, no significant difference in mIPSC frequency or amplitude was observed between neighbouring NPAS4-WT and NPAS4-KO neurons in slices acquired from mice maintained in standard housing (Fig. 1f). Next we measured mIPSCs in wild-type mice and detected no differences between AAV-Cre–GFP infected and uninfected neurons (Extended Data Fig. 2a, b) indicating that the observed changes in mIPSCs in *Npas4*^{fl/fl} neurons are due to *Npas4* excision. Finally, we crossed EMX-Cre and *Npas4*^{fl/fl} mice to generate animals that lack NPAS4 postnatally and specifically in excitatory neurons (Extended Data Fig. 2c, d). Both mIPSC frequency and amplitude were significantly reduced in NPAS4-KO neurons from animals injected with kainic acid compared to mice maintained in standard housing (Extended Data Fig. 2e). From these analyses we conclude that disruption of behaviourally induced NPAS4 expression leads to a decrease in mIPSC frequency recorded from CA1 pyramidal neurons.

This decrease in mIPSC frequency could be a consequence of homeostatic regulation of all inhibitory synapses or the modification of inhibitory synapses that form on discrete regions of the pyramidal neuron. Local inhibitory neuron subtypes have axons that elaborate preferentially in one or more layers of the hippocampus^{2,3}. Thus, stimulation of axons in the different laminar domains of the hippocampus and analysis of the resulting inhibitory currents has the potential to reveal whether the NPAS4-dependent effects on inhibition are due to cell-wide or domain-specific regulation of inhibitory synapses.

We sparsely excised *Npas4* and made direct comparisons of layer-specific, pharmacologically isolated, monosynaptic evoked inhibitory postsynaptic currents (eIPSCs) recorded simultaneously from neighbouring NPAS4-KO and NPAS4-WT CA1 neurons (Fig. 2a). As predicted by cable properties, eIPSC rise times correlated with distance of the stimulating electrode from the recording electrode (Extended Data Fig. 3, Supplementary Table 2) indicating that stimulation of axons within a given layer is predominately activating synapses within that layer.

We found that in slices obtained from mice housed in a standard environment, equivalent eIPSCs were recorded from NPAS4-WT and NPAS4-KO neurons in response to stimulation of axons in any of the hippocampal layers (Fig. 2b–e, Supplementary Table 2). However, in slices obtained from mice exposed to an enriched environment, stimulation of axons in the pyramidal layer generated smaller eIPSCs in NPAS4-KO neurons than in the neighbouring NPAS4-WT neurons (Fig. 2h). By contrast, stimulation of axons in stratum radiatum generated significantly larger eIPSCs in NPAS4-KO neurons than in neighbouring NPAS4-WT neurons (Fig. 2g), whereas no difference was detected between NPAS4-WT and NPAS4-KO neurons upon stimulation of axons in oriens or lacunosum (Fig. 2f, i). Similar results were obtained from mice injected with kainic acid to induce NPAS4 (Extended Data Fig. 4). These findings indicate that NPAS4 expression does not result in uniform, homeostatic regulation of inhibitory synapses. Rather, NPAS4 functions in an unprecedented manner, simultaneously decreasing

¹Department of Neurobiology, Harvard Medical School, Boston, Massachusetts 02115, USA. ²Division of Biological Sciences, University of California San Diego, La Jolla, California 92093, USA. ³Department of Molecular and Cellular Biology, Harvard University, Cambridge, Massachusetts 02138, USA. [†]Present addresses: Icahn School of Medicine at Mount Sinai, New York, New York 10029, USA (H.A.B.); Department of Neuroscience, Brown University, National Institutes of Health Graduate Partnership Program, Providence, Rhode Island 02912, USA (A.T.).

*These authors contributed equally to this work.

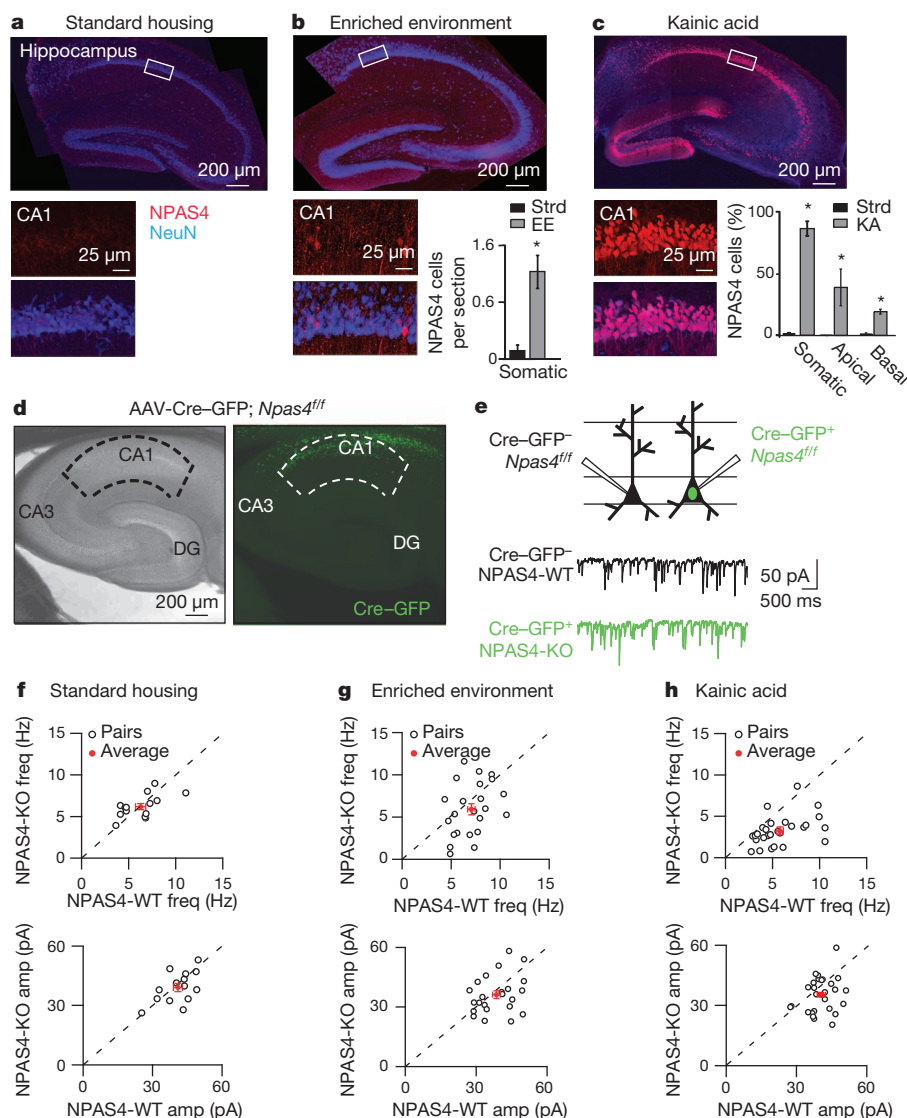


Figure 1 | Exposure of mice to increased circuit activity reveals an NPAS4-dependent regulation of inhibition *in vivo*.

a–c, Hippocampal sections from wild-type mice in standard housing (**a**), enriched environment (EE) (**b**) or after kainic acid (KA) injection (**c**). Sections were immunostained for NPAS4 (red) and NeuN (blue) protein. Quantification is shown in **b** and **c**. Data are shown as mean \pm s.e.m. For each condition $n = 3$ animals with 3–5 sections per animal. $*P < 0.01$. **d**, Wide-field (left) and fluorescence (right) image of hippocampal slice from an *Npas4*^{fl/fl} mouse injected with AAV-Cre-GFP. **e**, Experimental configuration. **f–h**, mIPSC frequency (top) and amplitude (bottom) recorded from neighbouring NPAS4-WT and NPAS4-KO neurons from mice maintained in standard housing (**f**) ($n = 14$ pairs), enriched environment (**g**) ($n = 23$ pairs, freq: $P < 0.05$) or after kainic acid injection (**h**) ($n = 26$ pairs, freq: $P < 0.01$, amp: $P < 0.05$). Open circles represent NPAS4-KO/ NPAS4-WT pairs. Red circles indicate mean \pm s.e.m.

inhibition within the proximal apical dendrites while increasing inhibition at the soma.

Extracellular stimulation of axons could result in the depolarization of axons of passage that preferentially form synapses on NPAS4-WT or NPAS4-KO neurons and in regions other than the intended layer. To address this possibility we compared the rise times of the eIPSCs recorded from NPAS4-WT and NPAS4-KO neurons and found them to be indistinguishable (Extended Data Fig. 3). This indicates that the redistribution of inhibition observed is not due to a bias in synaptic transmission associated with axons of passage onto NPAS4-WT or NPAS4-KO neurons. Additionally, the hippocampus contains several interneuron subtypes that form synapses within multiple layers (that is, bistratified and trilaminar cells). If NPAS4 regulates synapses made by these cell types, it is probable that only boutons that synapse on the apical, and not basal, dendrites are affected by loss of NPAS4.

We next investigated the cellular mechanisms by which NPAS4 differentially regulates inhibition, including possible effects on dendritic growth, changes in the probability of inhibitory synaptic vesicle release or changes in inhibitory synapse number. We first asked whether loss of NPAS4 results in altered dendritic complexity which could indirectly lead to larger eIPSCs in response to stimulation of axons in radiatum. However, this seems unlikely because Sholl analysis revealed that the disruption of NPAS4 function has no effect on dendrite number or length (Fig. 3a, b, Extended Data Fig. 5a, b). In addition, the capacitance of neurons from mice housed under standard conditions, in an enriched

environment or exposed to kainic acid are equivalent (Supplementary Table 3).

We next asked whether disruption of *Npas4* leads to changes in the presynaptic release of neurotransmitter at axons that synapse onto different regions of the pyramidal neuron. We measured the paired pulse ratios (PPRs) upon stimulation of axons in each layer, and compared NPAS4-WT and NPAS4-KO neurons in slices obtained from mice housed under standard conditions, in an enriched environment, or injected with kainic acid. We found no difference between the PPRs of NPAS4-WT and NPAS4-KO neurons under any of these conditions (Fig. 3c–e, Extended Data Fig. 5c–e, Supplementary Table 2) indicating that the NPAS4-dependent changes in eIPSCs are not likely due to changes in the probability of presynaptic vesicle release.

Finally we asked whether NPAS4 differentially regulates the number of inhibitory synapses on the soma or apical dendrites. To quantify inhibitory synapses we co-injected AAVs encoding mCherry-IRES-Cre and Cre-dependent GFP-gephyrin fusion protein into the CA1 region of the hippocampus in wild-type and *Npas4*^{fl/fl} mice. GFP-gephyrin fusion proteins when expressed at low levels localize to inhibitory synapses without significantly altering neurotransmission^{12,13}. Cre was sparsely expressed and GFP-gephyrin puncta quantified on NPAS4-WT and NPAS4-KO neurons. This analysis revealed that when mice were kept in standard housing, NPAS4-WT and NPAS4-KO hippocampal pyramidal neurons have equivalent densities of GFP-gephyrin puncta on the soma and apical dendrites. However, after

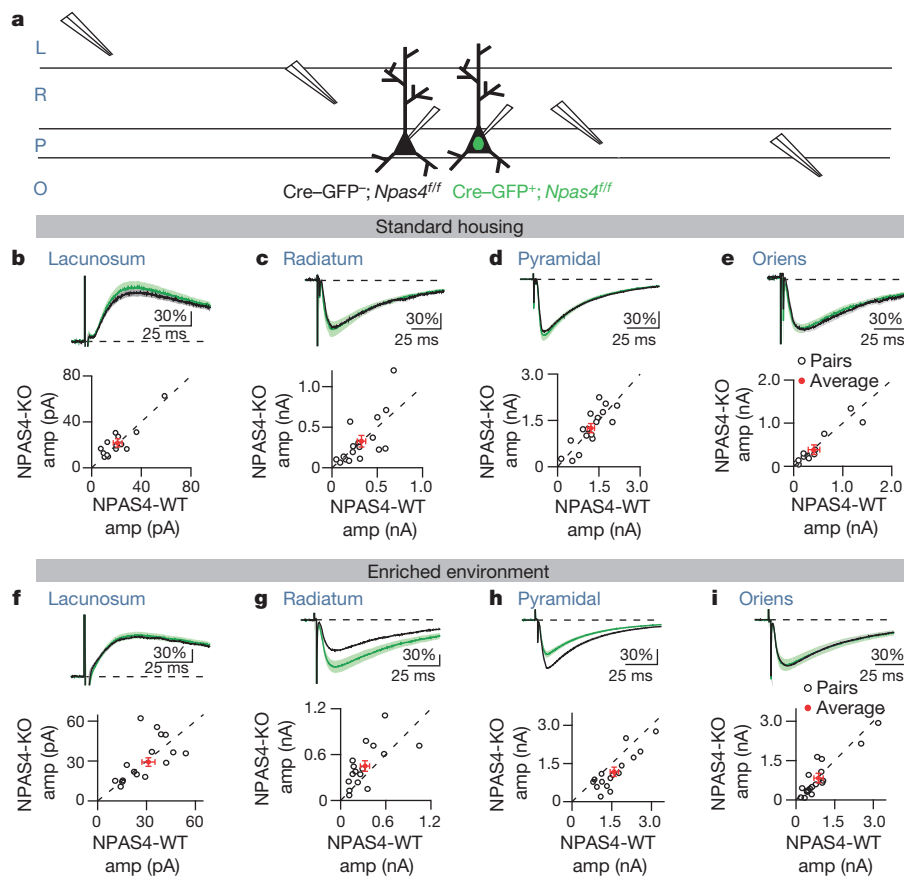


Figure 2 | Behaviourally induced NPAS4 differentially regulates inhibitory synapse function across the somato-dendritic axis of pyramidal neurons. **a**, Experimental configuration. L, lacunosum; R, radiatum; P, pyramidal; O, oriens. **b–e**, eIPSCs measured from mice maintained in standard housing. Top shows average eIPSC, normalized pairwise to the wild-type neuron, measured from NPAS4-WT (black) and NPAS4-KO (green) neurons in response to stimulation in lacunosum (**b**), radiatum (**c**), pyramidal (**d**) or oriens (**e**). Scale bars indicate per cent change from wild type. Bottom shows eIPSC amplitude measured from pairs of neighbouring NPAS4-KO and NPAS4-WT neurons in response to stimulation of axons in lacunosum (**b**) ($n = 14$ pairs), radiatum (**c**) ($n = 13$ pairs), pyramidal (**d**) ($n = 17$ pairs) or oriens (**e**) ($n = 13$ pairs). Open circles represent NPAS4-KO/WT pairs. Red circles indicate mean \pm s.e.m. **f–i**, eIPSCs measured from mice exposed to an enriched environment. Data are displayed as in **b–e**. L, $n = 16$ pairs; R, $n = 16$ pairs, $P < 0.05$; P, $n = 14$ pairs, $P < 0.01$; O, $n = 18$ pairs.

exposure to an enriched environment, NPAS4-KO pyramidal neurons have significantly fewer somatic and more dendritic GFP–gephyrin puncta than NPAS4-WT neurons (Fig. 3f–h) consistent with the electrophysiology data described above. Strikingly, comparison of the number of GFP–gephyrin puncta measured on wild-type neurons revealed that exposure to an enriched environment leads to an increase in the number of somatic and a decrease in the number of dendritic inhibitory synapses. In both domains of the neuron, the behaviourally triggered changes in inhibition are NPAS4 dependent.

NPAS4 is a transcription factor and thus to understand how it mediates sensory-dependent changes in inhibitory synapse number we sought to identify NPAS4 target genes and assess their function. We focused our attention on putative NPAS4 targets that satisfy three criteria: (1) by deep sequencing NPAS4-bound DNA (ChIP-seq), NPAS4 is shown to be bound within 10 kilobases of the putative target gene; (2) by RNA-seq, the mRNA transcribed near the NPAS4 peak is induced greater than fivefold (Extended Data Table 1)¹⁴; (3) upon short hairpin RNA (shRNA)-mediated knockdown of the putative target gene there is a significant change in mIPSC frequency or amplitude. Through this screen we identified 16 putative NPAS4 targets that display a change in mIPSC frequency or amplitude upon knockdown with gene-specific shRNAs in organotypic hippocampal slices, five of which we further validated (Extended Data Figs 6–8).

Of the putative NPAS4 target genes identified by the screen, *Bdnf* seemed a possible candidate to control the number of inhibitory synapses that form on a specific region of an excitatory neuron in response to sensory stimulation. BDNF expression is regulated by neuronal activity *in vivo*^{15–18} and it regulates inhibitory synapse number and function^{19–21}. In addition, *Bdnf* mRNAs can be targeted to discrete regions of the neuron²², and BDNF-containing vesicles are known to be secreted from the axon, soma or dendrites of pyramidal neurons^{23,24}. Furthermore, we confirmed by ChIP and quantitative PCR with reverse transcription (qRT–PCR) that NPAS4 binds to three sites within the *Bdnf* gene

(Fig. 4a, b), and that induction of the transcription of multiple *Bdnf* isoforms is significantly reduced in the hippocampus of *Npas4* knock-out (*Npas4*^{−/−}) compared to wild-type (C57BL/6J) mice (Fig. 4c).

To determine if BDNF is a target of NPAS4 that selectively regulates somatic and/or dendritic inhibition of pyramidal neurons *in vivo*, we injected AAV–Cre–GFP into BDNF conditional knockout mice (*Bdnf*^{fl/fl}) mice and compared eIPSCs between neighbouring *Bdnf* knockout and *Bdnf* wild-type neurons (BDNF-KO and BDNF-WT, respectively) in response to stimulation of axons in the somatic or dendritic layers. In mice housed under standard conditions, we found no differences in eIPSC amplitude measured from neighbouring BDNF-KO and BDNF-WT neurons upon stimulation of axons in any of the layers of the hippocampus (Fig. 4d–f, Supplementary Table 2).

However, when we exposed mice to an enriched environment to induce NPAS4 as well as BDNF expression and secretion, stimulation of axons in the pyramidal layer results in a significantly smaller amplitude eIPSC in BDNF-KO neurons relative to neighbouring BDNF-WT neurons (Fig. 4h). The disruption of *Bdnf* function did not have a significant effect on eIPSC amplitude when axons in radiatum or oriens were stimulated (Fig. 4g, i). Similar results were observed when BDNF expression was induced with kainic acid (Extended Data Fig. 9). Taken together these findings indicate that the differential effects of NPAS4 on pyramidal neuron inhibition are mediated, at least in part, through the induction of BDNF that functions selectively and locally to promote inhibition at the soma. Given that the disruption of BDNF function does not affect eIPSCs in radiatum, the ability of NPAS4 to relieve inhibition on the apical dendrites of CA1 pyramidal neurons is probably mediated by NPAS4 targets other than BDNF.

These findings indicate that when a mouse engages with its environment, the neuronal activity-regulated transcription factor NPAS4 is expressed in pyramidal neurons of the hippocampus where it promotes an increase in the number of inhibitory synapses on the cell soma and a decrease in the number of inhibitory synapses on the apical

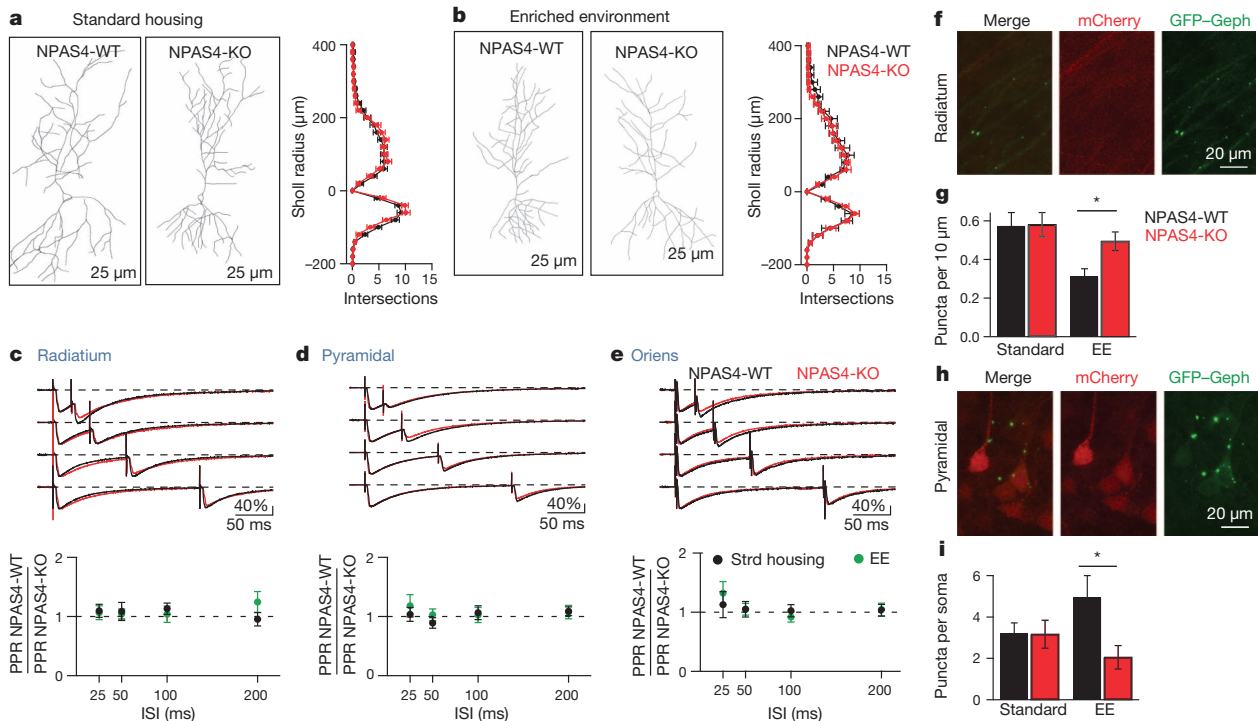
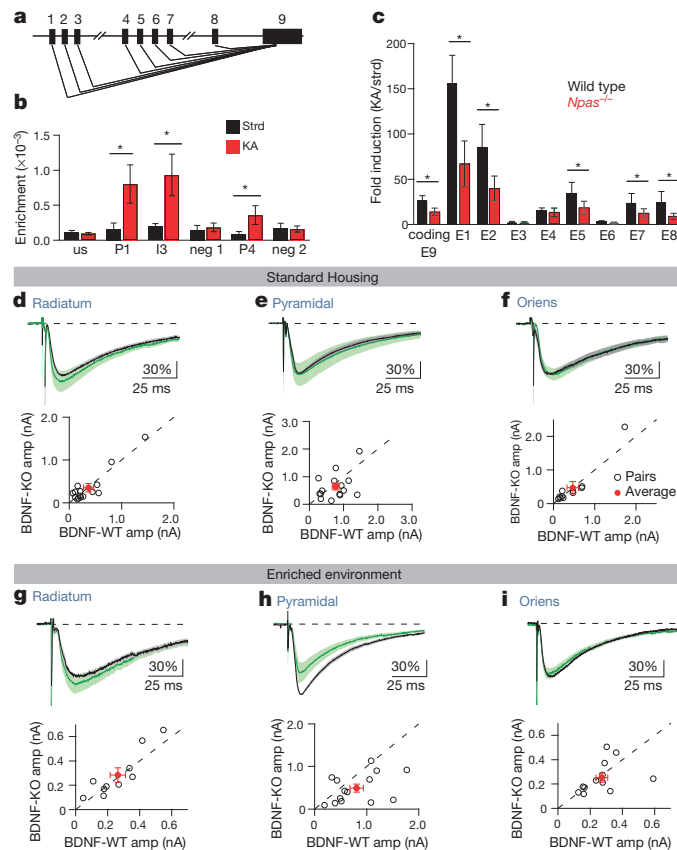


Figure 3 | Behaviourally induced NPAS4 regulates inhibitory synapse number. **a**, Standard housing example NPAS4-WT and NPAS4-KO CA1 pyramidal neurons (left) and quantification of NPAS4-WT (black, $n = 10$ neurons) and NPAS4-KO (red, $n = 10$ neurons) dendrites (right). **b**, Enriched environment example NPAS4-WT and NPAS4-KO CA1 pyramidal neurons (left) and quantification of NPAS4-WT (black, $n = 10$ neurons) and NPAS4-KO (red, $n = 10$ neurons) dendrites (right). **c–e**, PPRs measured from NPAS4-WT and NPAS4-KO neurons in response to stimulation in radiatum (**c**), pyramidal (**d**) or oriens (**e**). Standard housing (black, $R, n = 9$ neurons; $P, n = 10$ neurons; $O, n = 8$ neurons) or enriched environment (green, $R, n = 16$ neurons; $P, n = 11$ neurons; $O, n = 16$ neurons). Examples are from standard housing (top) and are shown normalized to peak current recorded from the NPAS4-WT neuron. Scale bars indicate per cent change from wild type.

ISI, interstimulus interval. **f**, Example image of dendrites in radiatum. **g**, Quantification of dendritic GFP-gephyrin puncta from NPAS4-WT (black, standard housing, $n = 15$ sections/63 dendritic segments; enriched environment, $n = 14$ sections/40 dendritic segments) and NPAS4-KO (red, standard housing, $n = 18$ sections/172 dendritic segments; enriched environment, $n = 18$ sections/167 dendritic segments) neurons. Enriched environment $P < 0.01$. **h**, Example image of somata in pyramidal. **i**, Quantification of somatic GFP-gephyrin puncta from NPAS4-WT (black, standard housing, $n = 14$ sections/32 soma; enriched environment, $n = 11$ sections/20 soma) and NPAS4-KO (red, standard housing, $n = 17$ sections/94 soma, enriched environment, $n = 21$ sections/75 soma) neurons. Enriched environment $P < 0.05$. All data are shown as mean \pm s.e.m.



dendrites. In light of recent reports indicating that inhibition within these cellular domains can have distinct functions^{25–28}, we speculate that this redistribution of inhibition will have significant effects on information processing in the postsynaptic neuron. For example, the opposing regulation of somatic and apical dendritic inhibition may allow integration or plasticity of excitatory events in the apical dendrites while still limiting the generation of somatic action potentials and thus the propagation of information to downstream neurons. This is in contrast to homeostatic scaling of inhibitory synapses—a process whereby the

Figure 4 | Behaviourally induced BDNF regulates somatic but not dendritic inhibition. **a**, Schematic of *Bdnf* gene. Exons 1–9 are indicated. **b**, qPCR of NPAS4 bound DNA. ChIP samples are from wild-type mice in standard conditions (black) or after kainic acid injection (red). us, upstream region; P1, promoter 1; I3, intron 3; neg 1, control region; P4, promoter 4; neg 2, control region. Enrichment relative to input DNA. $n = 3$. $*P < 0.05$. **c**, Induction of *Bdnf* exons in wild-type (black, standard housing, $n = 5$ animals; kainic acid, $n = 6$ animals) or *Npas4*^{-/-} animals (red, standard housing, $n = 5$ animals; kainic acid, $n = 6$ animals) mice as measured by qRT-PCR with exon specific primers, E1–9. $*P < 0.05$. Data in **b** and **c** are shown as mean \pm s.e.m. **d–f**, eIPSCs measured from mice maintained in standard housing. Top shows average eIPSC, normalized pairwise to the wild-type neuron, measured from BDNF-WT (black) and BDNF-KO (green) neurons in response to stimulation in radiatum (**d**), pyramidal (**e**) or oriens (**f**). Scale bars indicate per cent change from wild type. Bottom shows eIPSC amplitude measured from pairs of neighbouring BDNF-KO and BDNF-WT neurons in response to stimulation of axons in radiatum (**d**) ($n = 14$ pairs), pyramidal (**e**) ($n = 15$ pairs) or oriens (**f**) ($n = 11$ pairs). Open circles represent BDNF-KO/BDNF-WT pairs. Red circles indicate mean \pm s.e.m. **g–i**, eIPSC measured from mice housed in an enriched environment. Data are shown as in **d–f**. $R, n = 10$ pairs; $P, n = 14$ pairs; $O, n = 14$ pairs.

action potential output of a neuron is regulated by cell-wide scaling of synaptic strengths that preserves the relative strengths among synapses. The NPAS4-dependent redistribution of inhibitory circuitry may underlie recent findings that associate NPAS4 function with contextual or stimulus dependent fear conditioning^{29,30}.

METHODS SUMMARY

Animals were handled according to protocols approved by the Harvard University Standing Committee on Animal Care and the University of California San Diego Institutional Animal Care and Use Committee, and were in accordance with federal guidelines. Full details of experimental procedures for animal handling, virus injections, acute and organotypic slice preparation, electrophysiology, immunostaining, Sholl analysis, synapse labelling and quantification, ChIP, qRT-PCR and western blots are provided in the Methods.

Online Content Any additional Methods, Extended Data display items and Source Data are available in the online version of the paper; references unique to these sections appear only in the online paper.

Received 13 August; accepted 9 October 2013.

- Somogyi, P. & Klausberger, T. Defined types of cortical interneurone structure space and spike timing in the hippocampus. *J. Physiol. (Lond.)* **562**, 9–26 (2005).
- Danglot, L., Triller, A. & Marty, S. The development of hippocampal interneurons in rodents. *Hippocampus* **16**, 1032–1060 (2006).
- Freund, T. F. & Buzsáki, G. Interneurons of the hippocampus. *Hippocampus* **6**, 347–470 (1996).
- Turner, D. A. Feed-forward inhibitory potentials and excitatory interactions in guinea-pig hippocampal pyramidal cells. *J. Physiol. (Lond.)* **422**, 333–350 (1990).
- Liu, G. Local structural balance and functional interaction of excitatory and inhibitory synapses in hippocampal dendrites. *Nature Neurosci.* **7**, 373–379 (2004).
- Chiu, C. Q. *et al.* Compartmentalization of GABAergic inhibition by dendritic spines. *Science* **340**, 759–762 (2013).
- Larkum, M. E., Zhu, J. J. & Sakmann, B. A new cellular mechanism for coupling inputs arriving at different cortical layers. *Nature* **398**, 338–341 (1999).
- Miles, R., Toth, K., Gulyas, A. I., Hajos, N. & Freund, T. F. Differences between somatic and dendritic inhibition in the hippocampus. *Neuron* **16**, 815–823 (1996).
- Pouille, F. & Scanziani, M. Enforcement of temporal fidelity in pyramidal cells by somatic feed-forward inhibition. *Science* **293**, 1159–1163 (2001).
- Lin, Y. *et al.* Activity-dependent regulation of inhibitory synapse development by Npas4. *Nature* **455**, 1198–1204 (2008).
- Adesnik, H., Li, G., During, M. J., Pleasure, S. J. & Nicoll, R. A. NMDA receptors inhibit synapse unsilencing during brain development. *Proc. Natl Acad. Sci. USA* **105**, 5597–5602 (2008).
- Chen, J. L. *et al.* Clustered dynamics of inhibitory synapses and dendritic spines in the adult neocortex. *Neuron* **74**, 361–373 (2012).
- van Versendaal, D. *et al.* Elimination of inhibitory synapses is a major component of adult ocular dominance plasticity. *Neuron* **74**, 374–383 (2012).
- Kim, T. K. *et al.* Widespread transcription at neuronal activity-regulated enhancers. *Nature* **465**, 182–187 (2010).
- Rocamora, N., Welker, E., Pascual, M. & Soriano, E. Upregulation of BDNF mRNA expression in the barrel cortex of adult mice after sensory stimulation. *J. Neurosci.* **16**, 4411–4419 (1996).
- Castrén, E., Zafra, F., Thoenen, H. & Lindholm, D. Light regulates expression of brain-derived neurotrophic factor mRNA in rat visual cortex. *Proc. Natl Acad. Sci. USA* **89**, 9444–9448 (1992).
- Lein, E. S. & Shatz, C. J. Rapid regulation of brain-derived neurotrophic factor mRNA within eye-specific circuits during ocular dominance column formation. *J. Neurosci.* **20**, 1470–1483 (2000).
- Falkenberg, T. *et al.* Increased expression of brain-derived neurotrophic factor mRNA in rat hippocampus is associated with improved spatial memory and enriched environment. *Neurosci. Lett.* **138**, 153–156 (1992).
- Marty, S., Wehrle, R. & Sotelo, C. Neuronal activity and brain-derived neurotrophic factor regulate the density of inhibitory synapses in organotypic slice cultures of postnatal hippocampus. *J. Neurosci.* **20**, 8087–8095 (2000).
- Kohara, K. *et al.* A local reduction in cortical GABAergic synapses after a loss of endogenous brain-derived neurotrophic factor, as revealed by single-cell gene knock-out method. *J. Neurosci.* **27**, 7234–7244 (2007).
- Baldelli, P., Hernandez-Guido, J.-M., Carabelli, V. & Carbone, E. Brain-derived neurotrophic factor enhances GABA release probability and nonuniform distribution of N- and P/Q-type channels on release sites of hippocampal inhibitory synapses. *J. Neurosci.* **25**, 3358–3368 (2005).
- Pattabiraman, P. P. *et al.* Neuronal activity regulates the developmental expression and subcellular localization of cortical BDNF mRNA isoforms *in vivo*. *Mol. Cell. Neurosci.* **28**, 556–570 (2005).
- Brigadski, T., Hartmann, M. & Lessmann, V. Differential vesicular targeting and time course of synaptic secretion of the mammalian neurotrophins. *J. Neurosci.* **25**, 7601–7614 (2005).
- Dean, C. *et al.* Distinct subsets of Syt-IV/BDNF vesicles are sorted to axons versus dendrites and recruited to synapses by activity. *J. Neurosci.* **32**, 5398–5413 (2012).
- Atallah, B. V., Bruns, W., Carandini, M. & Scanziani, M. Parvalbumin-expressing interneurons linearly transform cortical responses to visual stimuli. *Neuron* **73**, 159–170 (2012).
- Lovett-Barron, M. *et al.* Regulation of neuronal input transformations by tunable dendritic inhibition. *Nature Neurosci.* **15**, 423–430 (2012).
- Royer, S. *et al.* Control of timing, rate and bursts of hippocampal place cells by dendritic and somatic inhibition. *Nature Neurosci.* **15**, 769–775 (2012).
- Lee, S. H. *et al.* Activation of specific interneurons improves V1 feature selectivity and visual perception. *Nature* **488**, 379–383 (2012).
- Ploski, J. E., Monsey, M. S., Nguyen, T., DiLeone, R. J. & Schafe, G. E. The neuronal PAS domain protein 4 (Npas4) is required for new and reactivated fear memories. *PLoS ONE* **6**, e23760 (2011).
- Ramamoorthi, K. *et al.* Npas4 regulates a transcriptional program in CA3 required for contextual memory formation. *Science* **334**, 1669–1675 (2011).

Supplementary Information is available in the online version of the paper.

Acknowledgements We thank members of the Greenberg laboratory for comments, suggestions and critical reading of the manuscript. We thank A. Mardinly for observations and comments on NPAS4 protein induction, P. Greer and S. Flavell for observations and comments on Npas4 mRNA induction in response to enriched environment and B. Cruz Moreno for help with sectioning. We thank M. During for the gift of the AAV-Cre-GFP plasmid. GFP-gephyrin images were collected at the UCSD Neuroscience Microscopy Shared Facility sponsored by grant P30 NS047101. This work was funded by Helen Hay Whitney Foundation, L'Oreal USA Fellowship for Women in Science and The Medical Foundation/Charles A. King Trust Postdoctoral Fellowship (B.L.B.), NSF graduate student research fellowship (N.S.) and National Institutes of Health grant NS028829 (M.E.G.).

Author Contributions Experiments were designed by B.L.B., N.S. and M.E.G. Experiments were conducted and analysed by B.L.B., N.S., H.A.B. and A.Z.T. The manuscript was written by B.L.B., N.S. and M.E.G.

Author Information Reprints and permissions information is available at www.nature.com/reprints. The authors declare no competing financial interests. Readers are welcome to comment on the online version of the paper. Correspondence and requests for materials should be addressed to M.E.G. (Michael_Greenberg@hms.harvard.edu).

METHODS

Animal husbandry and handling. Animals were handled according to protocols approved by the Harvard University Standing Committee on Animal Care and the University of California San Diego Institutional Animal Care and Use Committee, and were in accordance with federal guidelines. The following animal lines were used: *Npas4*^{fl/fl}, NPAS4 knockout (*Npas4*^{-/-}) mice¹⁰, wild type (C57BL/6J, JAX 000664), *Bdnf*^{fl/fl} (*Bdnf* < tm3Jae>/J, JAX 004339) and EMX-Cre (B6.129S2-EMX1^{TM1(cre)Krtj}/J, JAX 005628). Both male and female mice were used. Electrophysiology, Sholl analysis and GFP–gephyrin experiments were performed on animals between postnatal day 21 and 28 (P21–P28). Immunostaining, ChIP and qRT-PCR experiments were done on samples collected from P25–P35 animals.

For experiments in which mice were exposed to an enriched environment, three days after virus injection (P16–P18) animals (dam and pups) were moved to a larger cage that contained a running wheel, hut, tunnel and several other novel objects. To maximize novelty, the objects in the environment were rearranged and new objects introduced every second day. Mice were housed in the enriched environment for 4–10 days. Although we detect a limited number of NPAS4 positive excitatory neurons at a given time point, exploration of a novel environment increases NPAS4 immunoreactivity to an extent similar to that observed for other activity inducible genes such as *Fos* and *Arc*. Moreover, behaviourally triggered NPAS4 induction appears to occur iteratively, and in distinct subpopulations of neurons as the animal engages and explores novel features of the environment, such that the number of NPAS4 immunopositive neurons detected at any given time point significantly underestimates the number of neurons that express NPAS4 over a period of several days.

For experiments in which seizures were induced, kainic acid (2.5–10 mg per kg) was injected intraperitoneally. Mice were euthanized 2 h after the first visible seizure for ChIP, at 3 hours for immunohistochemistry, at 6 h for qRT-PCR or 24 h later for electrophysiology experiments. These time points were selected to allow sufficient time for expression of NPAS4 protein, the execution of an NPAS4-dependent program of gene expression and potential synaptic regulation but before detectable seizure-related cell death.

Stereotactically guided surgery. All surgeries were performed according to protocols approved by the Harvard University Standing Committee on Animal Care and the University of California San Diego Institutional Animal Care and Use Committee, and were in accordance with federal guidelines. Surgeries were performed on mice between P13 and P15. Animals were deeply anaesthetized by inhalation of isoflurane (initially 3–5% in O₂, maintained with 1–2%) and secured in the stereotaxic apparatus (Kopf). Animal temperature was maintained at 37 °C. The fur was shaved and scalp cleaned with betadine and 100% ethanol three times before an incision was made to expose the skull. A small hole was drilled through the skull and the CA1 region of hippocampus was specifically targeted (medial/lateral: ± 2.9 mm; anterior/posterior: −2.5 mm; dorsal/ventral: 2.8 mm below the dura) and virus was injected (250–300 nl; 150 nl min^{−1}). Five minutes post-injection, the needle was retracted, the scalp sutured and the mouse returned to its home cage. All animals were monitored for at least one hour post-surgery and at 12-h intervals for the next 5 days. Post-operatively, analgesic (flunixin, 2.5 mg per kg) was administered at 12-h intervals for 72 h.

Virus production. AAV-Cre-GFP was produced by the Harvard Gene Therapy Initiative or UNC Vector Core with a plasmid provided by M. During (Ohio State University). The plasmids containing the genome for AAV-EF1a-YFP-2A-Cre, AAV-mCherry-IRES-Cre and AAV-FLEX-GFP–gephyrin were generated using standard molecular cloning techniques and were produced by the UNC Vector Core.

Acute slice preparation. Transverse hippocampal slices were prepared from *Npas4*^{fl/fl}, EMX-Cre; *Npas4*^{fl/fl}, *Bdnf*^{fl/fl} or C57BL/6 mice (P21–P28). Animals were anaesthetized by inhalation of isoflurane. The cerebral hemispheres were quickly removed and placed into ice-cold choline-based artificial cerebrospinal fluid (choline-ACSF) consisting of (in mM): 110 choline-Cl, 25 NaHCO₃, 1.25 Na₂HPO₄, 2.5 KCl, 7 MgCl₂, 25 glucose, 0.5 CaCl₂, 11.6 ascorbic acid, 3.1 pyruvic acid and equilibrated with 95% O₂/5% CO₂. Tissue was blocked and transferred to a slicing chamber containing choline-ACSF. Slices (300 µm) were cut with a Leica VT1000 s vibratome (Leica Instruments) and transferred to a holding chamber containing ACSF consisting of (in mM): 127 NaCl, 25 NaHCO₃, 1.25 Na₂HPO₄, 2.5 KCl, 2 CaCl₂, 1 MgCl₂, 25 glucose, and saturated with 95% O₂/5% CO₂. Slices were incubated at 30 °C for 30–40 min and then kept at room temperature for no more than 6 h until recordings were performed. For mice injected with AAV-Cre-GFP, slices showing infection of between 20% to 40% in CA1, as determined by GFP fluorescence, were used for recording. Slices showing greater than ~40% infected neurons or infection outside of CA1 were discarded.

Organotypic slice preparation and transfection. Hippocampi were rapidly dissected from wild-type mice at P7 in ice cold dissection media consisting of (in mM): 1 CaCl₂, 5 MgCl₂, 10 glucose, 4 KCl, 26 NaHCO₃, 218 sucrose, 1.3 NaH₂PO₄·H₂O, 30 HEPES. Tissue was transferred to a tissue chopper (McIlwain Ted Pella) and

400-µm thick sections cut. Sections were transferred to tissue culture plates and grown on PTFE inserts (Millicell Organotypic insert, EMD Millipore) in slice culture media consisting of (in mM or percentage) 1× MEM, 20% horse serum, 1 L-glutamine, 0.125% ascorbic acid, 1 CaCl₂, 2 MgCl₂, 12.8 glucose, 5.25 NaHCO₃, 30 HEPES, pH 7.4, 320 mOsm for 7–10 days. On the second day *in vitro*, cultures were biolistically (Gene Gun, Biorad) co-transfected with 1-µm gold particles coated with GFP and shRNAs targeting the gene of interest (particles prepared with GFP 15 µg, 3–9 µg of shRNA, pcDNA3 to a final DNA mass of 50 µg as per the manufacturer's instructions). The shRNA sequences are indexed in Supplementary Table 4.

Electrophysiology. Whole-cell voltage clamp recordings were obtained from CA1 pyramidal neurons visualized with infrared, differential interference contrast microscopy. Neurons were held at −70 mV except for experiments measuring evoked responses from stimulation of axons in stratum lacunosum, during which neurons were held at 0 mV. Patch pipettes (open pipette resistance 2–4 MΩ) were filled with an internal solution consisting of (in mM) 147 CsCl, 5 Na₂-phosphocreatine, 10 HEPES, 2 MgATP, 0.3 Na₂GTP and 2 EGTA. Osmolarity and pH were adjusted to 300 mOsm and 7.3 with double distilled water and CsOH, respectively. In experiments in which mIPSCs were recorded, currents were pharmacologically isolated with bath application of 0.5 µM tetrodotoxin citrate (Tocris Bioscience), 10 µM (R)-CPP (Tocris Bioscience) and 10 µM NBQX disodium salt (Tocris Bioscience). In experiments in which eIPSCs were recorded, inhibitory currents were pharmacologically isolated with bath application of CPP and NBQX. Additionally, 5 mM QX-314 (Sigma) was added to the internal solution. Extracellular stimulation of local axons within specific lamina of the hippocampus was delivered by current injection through a theta glass stimulating electrode that was placed in the centre of the relevant layer (along the somato-dendritic axis of the CA1 neuron) and within 100–200 µm laterally of the patched pair. The stimulus strength was the minimum required to generate an eIPSC in both NPAS4-KO and NPAS4-WT neurons.

Data acquisition and analysis. Electrophysiology data were acquired using pClamp software, either a Multiclamp 700B or Axoclamp 200B amplifier, and digitized with a DigiData 1440 data acquisition board (Axon Instruments). Data were sampled at 10 kHz and filtered at 4 or 6 kHz except for experiments with stimulation of axons in lacunosum which were filtered at 1 kHz. Off-line data analysis was performed using custom software written in Igor Pro by B.L.B. (Wavemetrics).

Experiments were discarded if the holding current was greater than −500 pA or if the series resistance was greater than 25 MΩ. In experiments in which direct comparisons were made between two neurons, recordings were discarded if the series resistance differed by more than 25% between the two recordings. All recordings were performed at room temperature (~20–22 °C).

Threshold for mIPSC detection was determined independently for each neuron and was based on the average root mean square (r.m.s.) of the first 150 ms of the recording. Amplitude threshold was set to 1.5 times r.m.s. for that cell and recordings were discarded if the r.m.s. was greater than 6 pA. This strategy resulted in fewer missed events and fewer erroneously called events than applying a single amplitude threshold.

The amplitude of eIPSCs was calculated by averaging the amplitude 0.5 ms before to 2 ms after the peak of the current. Data are shown as positive values for clarity. Slopes of the rise times of the eIPSCs were measured by normalizing the eIPSC, then measuring the slope between 10–90% of the peak. Paired pulse ratios (PPR) were calculated by recording a template eIPSC for each cell, subtracting the template wave from the first pulse, and then measuring the corrected amplitude of the second peak.

Immunohistochemistry, Sholl analysis and GFP–gephyrin quantification. Animals were anaesthetized by inhalation of isoflurane. Hippocampi were rapidly dissected in ice-cold dissection media as described above and drop fixed in 4% paraformaldehyde in PBS at 4 °C for 1.5–3 h followed by overnight incubation in 30% sucrose in PBS. Cryoprotected tissue was stored in Tissue-Tec O.C.T. at −80 °C and subsequently sectioned at a thickness of 40–45 µm (Leica CM1950 cryostat) for immunostaining or GFP–gephyrin puncta quantification, or at a thickness of 100 µm for Sholl analysis (Leica Instruments).

For NPAS4 immunostaining, hippocampal sections were blocked in 2% goat serum and 0.2% Triton X-100 in PBS for 1 h at room temperature. Sections were incubated in primary antibody overnight at 4 °C, washed three times in PBS, incubated in species-matched fluorescently conjugated secondary for 1 h at room temperature and washed again in PBS. Finally, sections were mounted on slides with Fluoromount-G (SouthernBiotech). The following antibodies were used: rabbit anti-NPAS4 (1:1,000, made in house), mouse anti-NeuN (1:1,000, Millipore) and rabbit anti-GFP (1:500, Invitrogen). The secondary antibodies were Alexa-488 or Alexa-555 against the appropriate species (1:500, Invitrogen). Sections were imaged on a Zeiss LSM5 Pascal confocal microscope with a ×20 objective. In cases in which the tissue was too large, multiple images were taken and stitched together

post-hoc in Adobe Photoshop. Images for DAPI and NeuN quantification were obtained on an Olympus BX61VS microscope with a $\times 20$ objective and subsequently process and exported into JPEG format with the manufacturer's software. When necessary, nuclei were labelled by adding Hoechst 33582 dye (Invitrogen) to the final PBS (1:5,000). Nuclei positive for the relevant marker were counted and quantified using ImageJ. In *Npas4^{fl/fl}* mice that have been sparsely infected with AAV-Cre-GFP and then administered kainic acid, we see dendritic NPAS4 immunoreactivity in the NPAS4-WT but not in the NPAS4-KO neurons. This indicates to us that the low levels of dendritic staining we observe with our NPAS4 antibody is unlikely due to cross-reactivity with another protein.

The neurons used for Sholl analysis were from animals injected with the AAV-EF1a-YFP-2A-Cre. Tissue was fixed as described above. To maximize signal, GFP signal was amplified by staining with rabbit anti-GFP antibodies (1:1,000, Invitrogen). The secondary antibody was anti-rabbit Alexa-488 (1:500, Invitrogen). Neurons selected for analysis if there were few or no other infected neurons nearby to facilitate reconstruction of dendritic morphology. After imaging, the neurons were traced and skeletonized using the NeuronJ plugin for ImageJ and Sholl intersections were subsequently quantified and significance determined by ANOVA.

The neurons used for GFP–gephyrin puncta quantification were from animals injected with AAV-mCherry-IRES-Cre and AAV-FLEX-GFP–gephyrin. GFP was not amplified by immunostaining. Images were acquired on a Leica SP5 confocal with resonant scanner through a $\times 63$ oil immersion objective. Fluorophores were excited using Argon 488 and HeNe 594 lasers and emitted photons detected through GFP or Alexa 594 filter cubes with Leica hybrid detectors (HyD3). Images were acquired at 16 bit resolution, 1024×1024 pixels and each frame the average of 8 scans. Images were analysed with ImageJ. Maximum intensity projections were made of each channel. A Yen threshold was applied to the green channel and puncta identified using the particle counter. Our reported puncta densities are lower than expected by electron microscopy. This is probably due to detection limitations of our microscope, incomplete or faint labelling of synapses by GFP–gephyrin, and the thickness of our sections.

Chromatin immunoprecipitation. Hippocampi from wild-type mice maintained in standard housing or injected with kainic acid (2.5–10 mg per kg, 2–3 h prior) were rapidly dissected in ice-cold dissection media (as above). The tissue was homogenized and DNA and protein were cross linked for 11 min (in mM: 10 HEPES-NaOH pH 7.5, 100 NaCl, 1 EDTA, 1 EGTA, 1% formaldehyde, in PBS). Formaldehyde was quenched with 2 M glycine in PBS and the sample incubated on a rocker at room temperature for 5 min. Tissue was pelleted (2,000 r.p.m., 5 min, 4 °C), washed with PBS plus PMSF, and re-pelleted (2,000 r.p.m., 5 min, 4 °C). The supernatant was removed and the pellet resuspended in 5 ml L1 buffer (in mM: 50 HEPES-NaOH 7.5, 140 NaCl, 1 EDTA, 1 EGTA, 0.25% Triton X-100, 0.5% NP40, 10% glycerol, 1 M BGP, 0.2 M NaVO₄, 0.5 M NaF, 1× complete protease inhibitor cocktail without EDTA (Roche)). The sample was the further homogenized by ten strokes with a tight pestle in a Dounce homogenizer, pelleted (2,000 r.p.m., 5 min, 4 °C), washed in L1, pelleted and then resuspended in buffer L2 (in mM: 10 Tris-HCl pH 8.0, 100 NaCl, 1 M BGP, 0.2 M NaVO₄, 0.5 M NaF, 1× complete protease inhibitor cocktail without EDTA (Roche)). Samples were placed on a rotator at room temperature for 10 min, pelleted and resuspended in L3 buffer (in mM 10 Tris-HCl pH 8.0, 1 EDTA, 1 EGTA, 1 M BGP, 0.2 M NaVO₄, 0.5 M NaF, 1× complete protease inhibitor cocktail without EDTA (Roche)) to a final concentration of 10 million nuclei per ml. Twenty million nuclei were sonicated using a

Misonix 3000 for a total time of 7 min, power 7.5 and at 4 °C. NPAS4 immunoprecipitation was done using protein G Dyna Beads (Life Technologies) according to the manufacturer's instructions using 4 µg of NPAS4 antibody¹⁰. NPAS4-bound DNA was quantified using qPCR. A list of putative NPAS4 target genes was determined by analysing ChIP and RNA-seq data published under Gene Expression Omnibus accession number GSE21161.

qRT-PCR. qRT-PCR was on cDNA samples made from RNA collected from wild-type of NPAS4-KO hippocampi from mice that been housed in standard conditions or injected with kainic acid. qRT-PCR was carried out with SYBR green (Life Technologies) and primers with the following sequences for NPAS4 ChIP samples probed at the *Bdnf* locus: us 5'-TGGTGAACACACTTGGGCATA-3'; 5'-TGATGAGCTGGGAACCTCTGC-3'; P1 5'-GTCCGCTGGAGACCCCTTAGT-3', 5'-CTGAGCCAGTTACGTGACCA-3'; I3 5'-CTTCCCAGATGGTGCTGT-3', 5'-AATCTCCCAGTTCTGCGTTC-3'; P4 5'-CCCTGGAACGGAATTC TTCT-3', 5'-TGCACGAATTACCAGAATCA-3'; Neg1 5'-CATTACAGCACCTTGGACAGA-3', 5'-GCTTGACAGCGAGGAAAAGA-3'; Neg2 5'-GGCCTGAAGTTCAAGGATGG-3', 5'-GCCTGCCACTGAAGCTTGTA-3'.

In cDNA samples probed for various *Bdnf* isoforms, *Npas4*, *PCSK1*, *Adcyap1* and *Penk1*, the primers used were: *Bdnf* exon1 5'-CACTGAGCAAAGCCGAAC TTCTC-3', 5'-TCACCTGGTGAACATTGTGGC-3'; *Bdnf* exon 2 5'-AGCG GTGTAGGCTGGAATAGACTC-3', 5'-GGTGAACCTTTTTCGGGCTTAC-3'; *Bdnf* exon 3 5'-TACCCCTTCTATCATCCCTCCCG-3', 5'-GAAGCATCCG GCCCGACAGTTCCAC-3'; *Bdnf* exon 4 5'-CGCCATGCAATTTCCACTATC AATAATTTAAAC-3', 5'-CGCCTTCATGCAACCGAAGTATG-3'; *Bdnf* exon 5 5'-CCATAACCCCGCACACTCTGTGTAG-3', 5'-CTTCCCGCACCTTCACA GTTCCAC-3'; *Bdnf* exon 6 5'-GATCCGAGAGCTTTGTGTGGAC-3', 5'-GCC TTCATGCAACCGAAGTATG-3'; *Bdnf* exon 7 5'-GGTCCAAGGTCAACGTT TA-3', 5'-TAAACGTTGACCTTGGACC-3'; *Bdnf* exon8 5'-GAACAACTGA TTGCTGAA-3', 5'-TTCAGCAATCAGTTTGTTC-3'; *Bdnf* exon9/coding exon 5'-GATGCCGCAAACATGTCTATGA-3', 5'-TAATACTGTACACACGCTC AGCTC-3'; *Npas4*: 5'-AGGGTTTGCTGTAGAGTTGC-3', 5'-CCCCCTCCACT TCCATCTTC-3'; *PCSK1*: 5'-TGAGTTGCATATAATTCCAAAGTT-3', 5'-AG CCTCAATGGCATCAGTTAC-3'; *Adcyap1* 5'-GAGAATCTGGGGGCAAGTC T-3', 5'-CACCAGCACCTGATCTGTCA-3'; *Penk* 5'-CCCAGGCGACATCAA TTT-3', 5'-TCTCCCAGATTTTGAAGAAGG-3'.

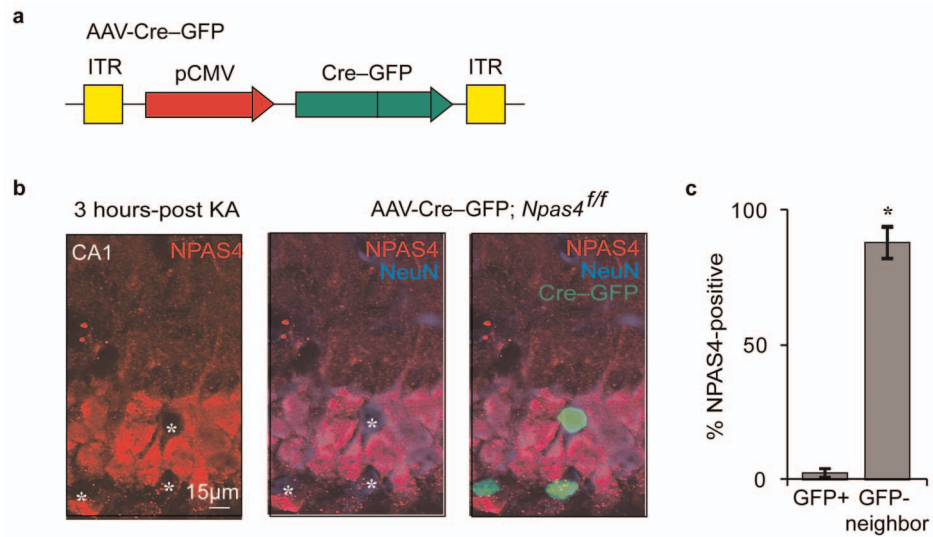
Western blot analysis. Myc-tagged cDNA encoding NPAS4, BDNF, *Pcsk1*, *Adcyap1* or *PENK1* was transfected into 293T cells using Lipofectamine. Twenty-four hours later cells were lysed in 2× Laemmli buffer and boiled for 5 min. Lysates were resolved by SDS-PAGE and immunoblotted with antibodies targeting Myc (1:1,000, Abcam) or actin (1:2,500, Abcam).

Statistics. All data are shown as the mean \pm s.e.m. unless otherwise noted. Data for which a specific *P* value is not indicated are not significant (*P* > 0.05).

For electrophysiology experiments, significance was determined by paired two-tailed *t*-test for direct comparisons of neighbouring neurons, two-tailed *t*-test for comparisons between populations, one-way ANOVA (Dunnett's test) for PPRs, and Wilcoxon for mIPSCs in the screen of putative NPAS4 target genes. All data sets were acquired from at least 3 animals, 2 slices from each animal.

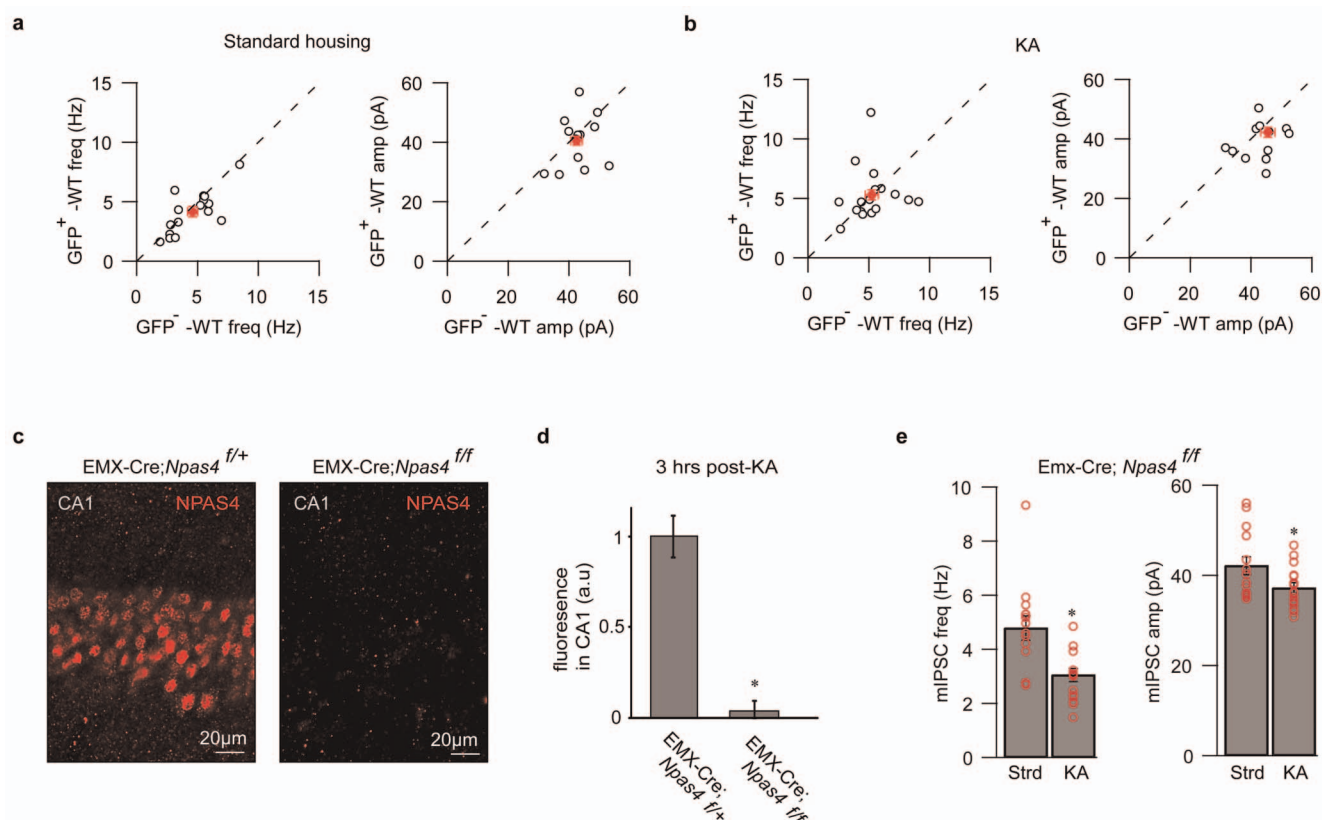
For imaging experiments, significance was determined by ANOVA or two-tailed *t*-test. All data sets were acquired from at least 3 animals, 3–5 images per animal.

For qRT-PCR experiments, significance was determined by two tailed *t*-test.



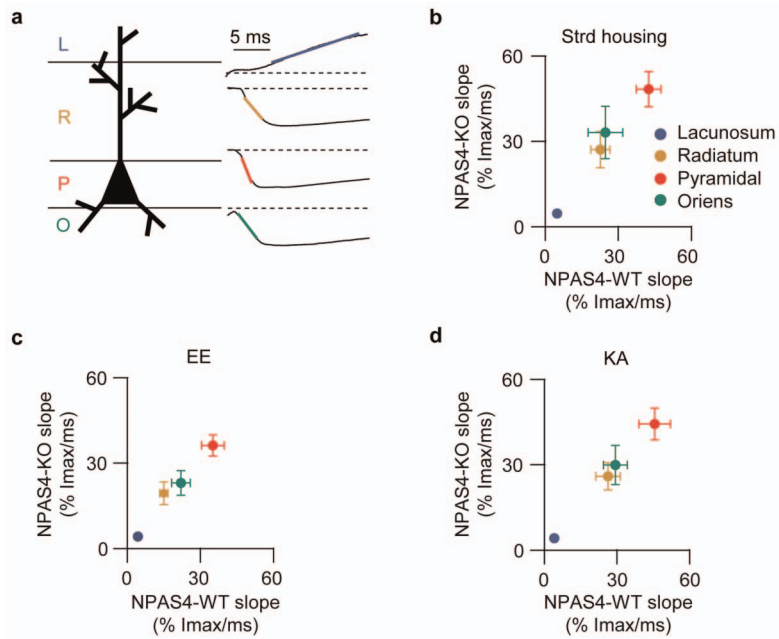
Extended Data Figure 1 | Infection with AAV-Cre-GFP effectively excises *Npas4*. **a**, Schematic of the AAV-Cre-GFP virus genome. **b**, Representative hippocampal section from an AAV-Cre-GFP; *Npas4*^{fl/fl} animal 3 h after kainic acid injection. Sections were imaged for native GFP fluorescence (green) and

immunostained NPAS4 (red) and NeuN (blue) protein. **c**, Quantification of neurons with overlapping GFP and NPAS4 in the sections represented in **b**. $n = 14$ neurons, $*P < 0.01$.



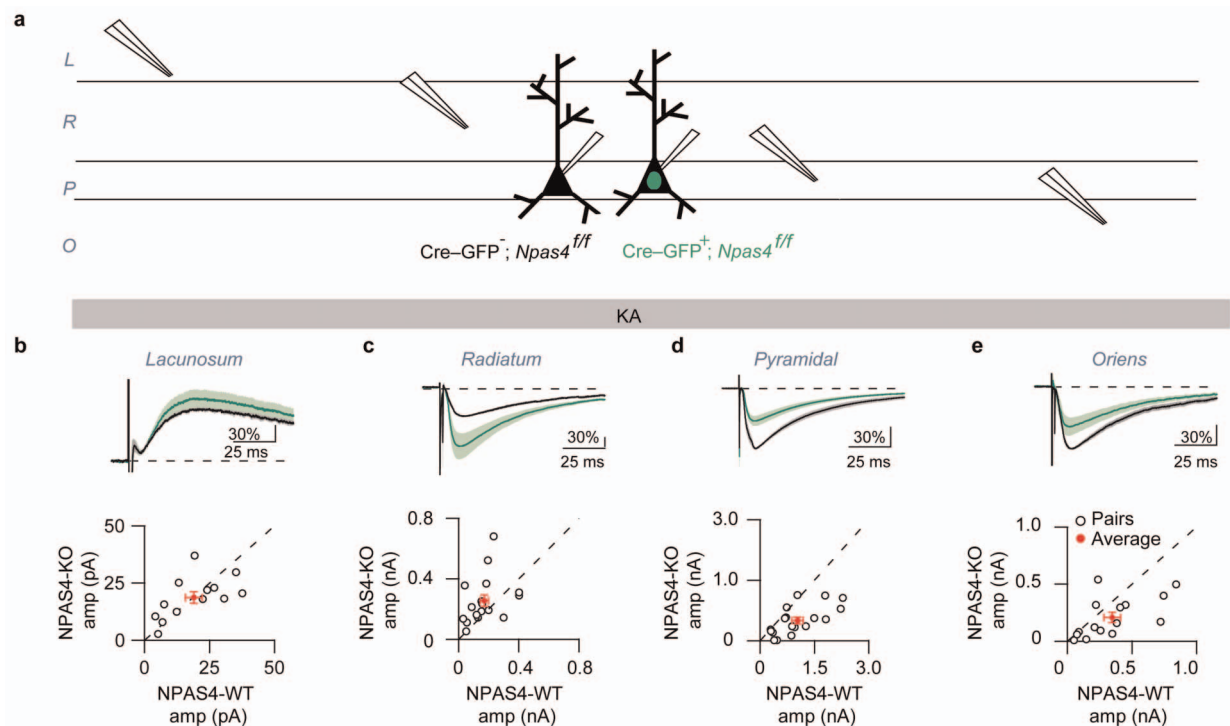
Extended Data Figure 2 | NPAS4-dependent changes in inhibition require loss of NPAS4 in excitatory neurons. **a**, mIPSCs frequency (left) and amplitude (right) were measured from pairs of neighbouring GFP⁺ and GFP[−] neurons from wild-type (C57BL/6) mice maintained in standard housing. $n = 17$ pairs. **b**, mIPSCs frequency (left) and amplitude (right) were measured from pairs of neighbouring GFP⁺ and GFP[−] neurons from wild-type (C57BL/6) mice 24 h after injection of kainic acid. $n = 17$ pairs. Open circles indicate individual GFP⁺/GFP[−] pairs. Red circles indicate mean \pm s.e.m.

c, Representative hippocampal CA1 section from an EMX-Cre;*Npas4*^{f/+} and EMX-Cre;*Npas4*^{f/f} mouse 3 h after kainic acid injection. Sections were immunostained for NPAS4 (red) protein. **d**, Quantification of NPAS4 immunoreactivity. $n = 9$ sections from 3 animals. $*P < 0.05$. **e**, mIPSCs frequency and amplitude measured from neurons in EMX-Cre;*Npas4*^{f/f} mice maintained in standard housing ($n = 14$ neurons) or 24 h after kainic acid injection ($n = 16$ neurons). freq: $P < 0.01$; amp: $P < 0.05$.



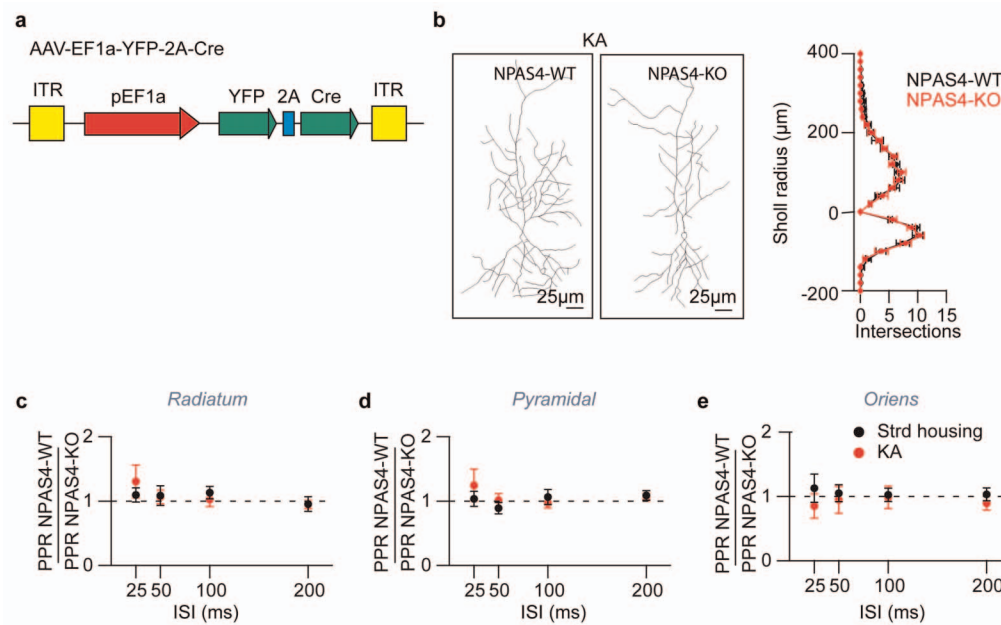
Extended Data Figure 3 | Stimulation of axons in different hippocampal layers generates eIPSCs with distinct rise times. **a**, Cartoon of a CA1 pyramidal neuron and example eIPSCs generated in response to stimulation of axons in lacunosum (L, blue), radiatum (R, yellow), pyramidale (P, red) and oriens (O, green). Slopes (10–90% of the peak eIPSC) are indicated by coloured lines. **b**, Standard housing summary of the slopes of the eIPSC rise times

recorded from neighbouring NPAS4-WT and NPAS4-KO neurons in response to stimulation of axons in each of the four hippocampal layers. Measurements are from eIPSCs in Fig. 2b–e. **c**, Enriched environment summary of the slopes as in **b**. Measurements are from eIPSCs in Fig. 2f–i. **d**, Kainic acid summary of the slopes as in **b**. Measurements are from eIPSCs in Extended Data Fig. 4b–e.



Extended Data Figure 4 | NPAS4 differentially regulates inhibitory synapses across the somato-dendritic axis of pyramidal neurons in response to kainic acid. **a**, Experimental configuration. L, lacunosum; R, radiatum; P, pyramidale; O, oriens. **b–e**, eIPSCs measured from mice injected with kainic acid. Top shows average eIPSC, normalized pairwise to the wild-type neuron, measured from NPAS4-WT (black) and NPAS4-KO (green) neurons in response to stimulation in lacunosum (**b**), radiatum (**c**), pyramidale (**d**) or

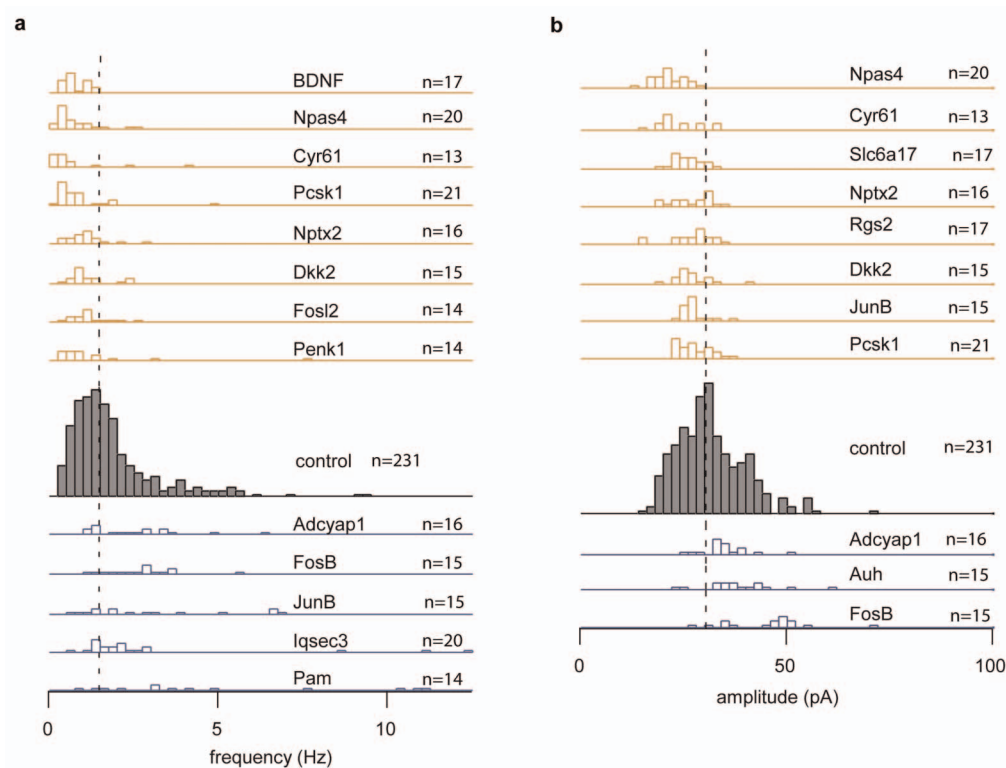
oriens (**e**). Scale bars indicate per cent change from wild type. Bottom shows eIPSC amplitude measured from pairs of neighbouring NPAS4-KO and NPAS4-WT neurons in response to stimulation of axons in lacunosum (**b**) ($n = 13$ pairs); radiatum (**c**) ($n = 17$ pairs, $P < 0.05$); pyramidale (**d**) ($n = 18$ pairs, $P < 0.01$); or oriens (**e**) ($n = 15$ pairs, $P < 0.05$). Open circles represent NPAS4-KO/NPAS4-WT pairs. Red circles indicate mean \pm s.e.m.



Extended Data Figure 5 | Sholl analysis and paired pulse ratios for NPAS4-WT and NPAS4-KO neurons from mice injected with kainic acid.

a, Schematic of the AAV-YFP-2A-Cre virus genome used for Sholl analysis.
b, Kainic acid example NPAS4-WT and NPAS4-KO CA1 pyramidal neurons (left) and quantification of NPAS4-WT (black, $n = 10$ neurons) and NPAS4-

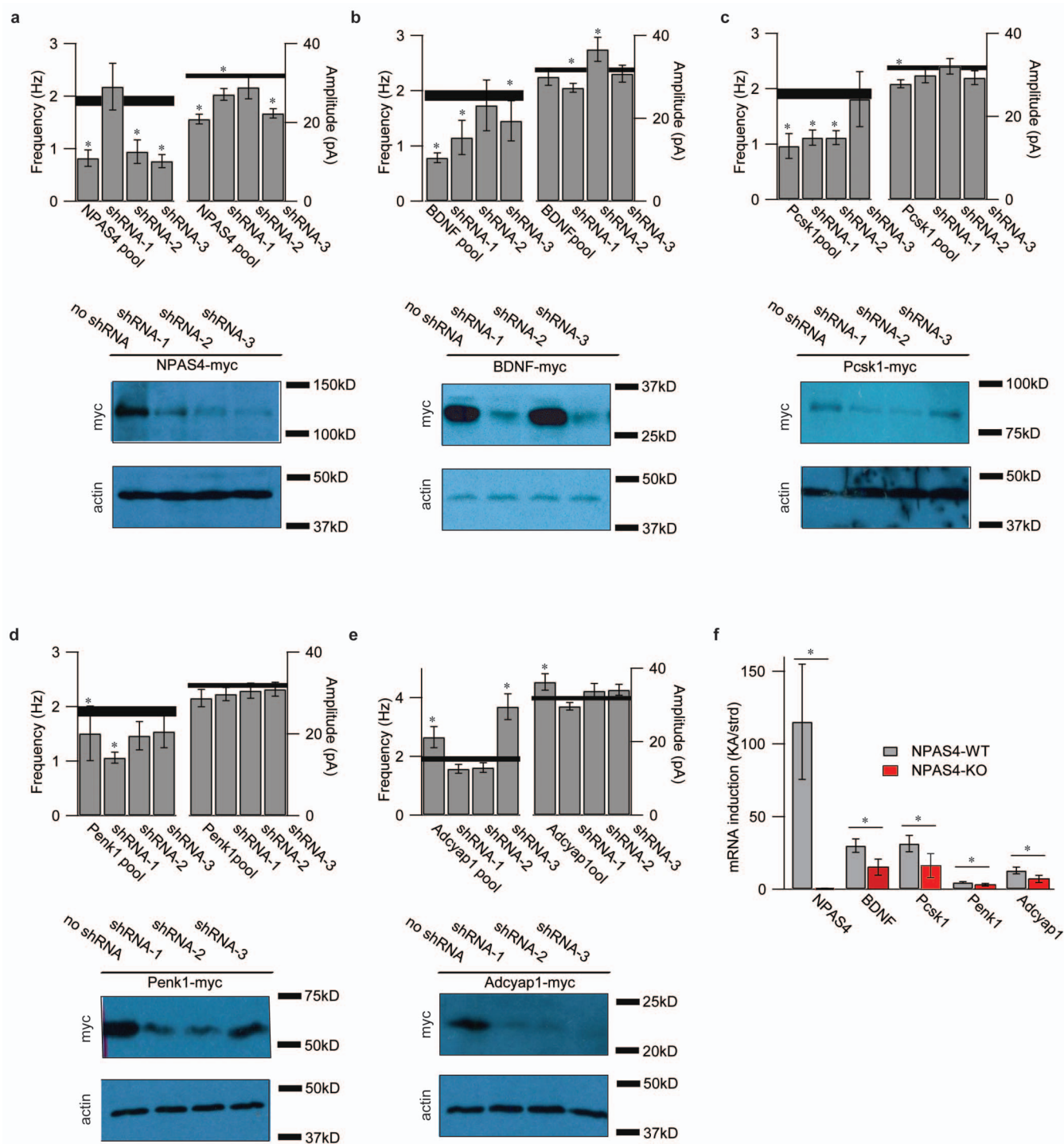
KO (red, $n = 13$ neurons) dendrites (right). **c–e**, PPRs measured from NPAS4-WT and NPAS4-KO neurons in response to stimulation in radiatum (**c**), pyramidal (**d**) or oriens (**e**). Standard housing (black) or kainic acid (red). Standard housing data are re-plotted from Fig. 3c–e. R, $n = 11$ neurons; P, $n = 13$ neurons; O, $n = 8$ neurons. All data are shown as mean \pm s.e.m.



Extended Data Figure 6 | Functional screen of putative NPAS4 target genes identifies many genes that regulate mIPSCs frequency or amplitude.

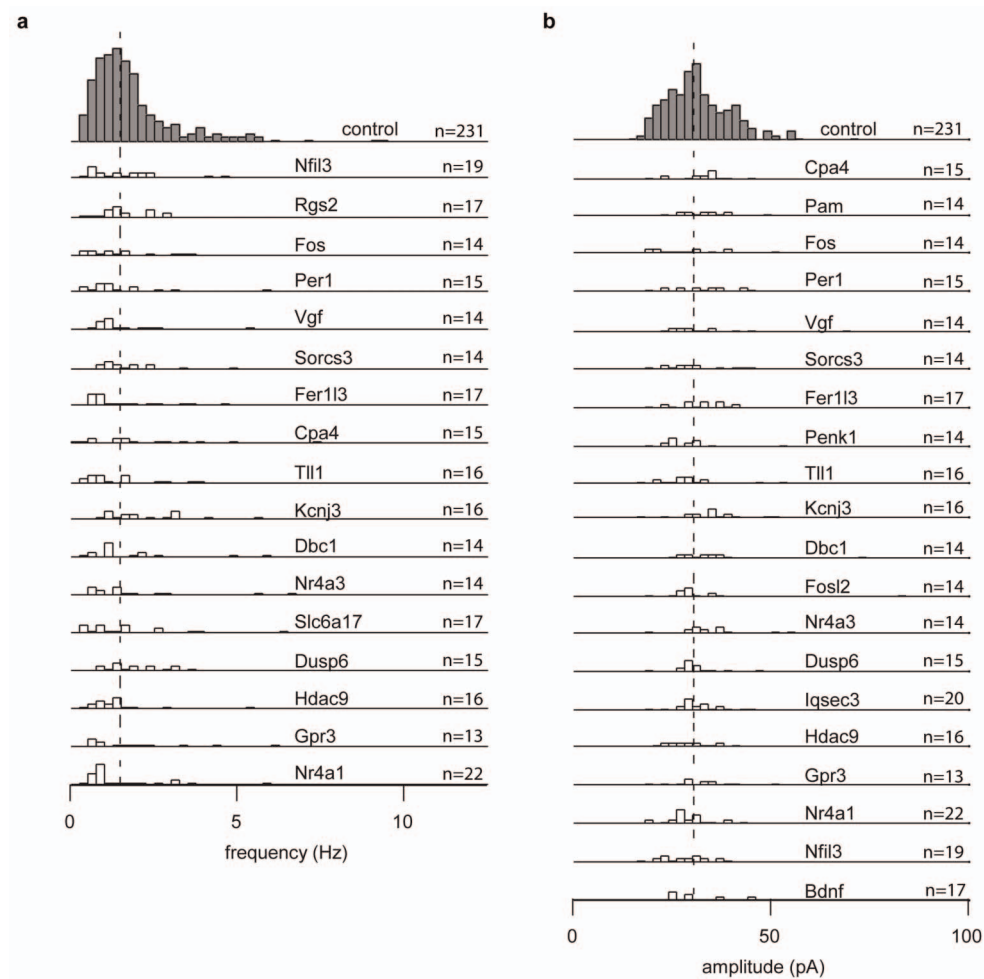
a, b, mIPSCs were recorded from CA1 pyramidal neurons transfected with a pool of three shRNAs targeting a single putative NPAS4 target gene. mIPSC frequency (**a**) and amplitude (**b**) of those significantly different from control are

shown. Knockdown of genes that result in fewer or smaller mIPSCs are shown on top (mustard); knockdown of genes that result in more or larger mIPSCs are shown on the bottom (blue). The dashed line represents the median value from control conditions. $P < 0.05$.



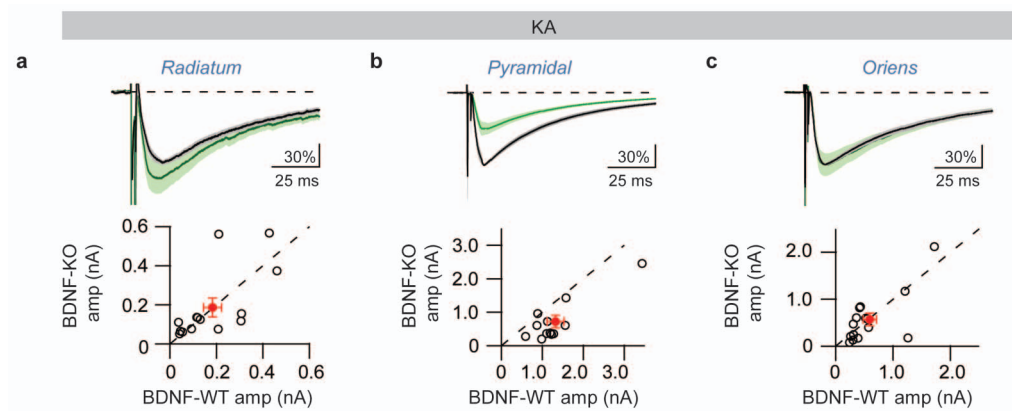
Extended Data Figure 7 | Validation of five putative NPAS4 target genes. **a–e**, Select putative NPAS4 target genes that influence mIPSC frequency and/or amplitude were subjected to additional validation: *Npas4* (**a**), *Bdnf* (**b**), *Pcsk1* (**c**), *Penk1* (**d**) and *Adcyap1* (**e**). Top shows mIPSC frequency and amplitude recorded from CA1 pyramidal neurons that were transfected with individual shRNAs from the pool used in the primary screen. The mean \pm s.e.m. mIPSC frequency and amplitude recorded from control neurons is indicated by the

grey bar. Expression of individual shRNAs phenocopied expression of the pool. Bottom shows expression of target-specific shRNAs reduces expression of the target protein. **f**, qRT-PCR using primers specific to the target gene indicate that all five genes are induced in the hippocampus and their induction is misregulated in NPAS4 knockout neurons. Standard housing, $n = 5$ animals; kainic acid, $n = 6$ animals. All data are shown as mean \pm s.e.m. $*P < 0.05$.



Extended Data Figure 8 | Many putative NPAS4 target genes do not regulate inhibitory synapses. a, b, mIPSCs were recorded from CA1 pyramidal neurons transfected with a pool of three shRNAs targeting a single

putative NPAS4 target gene. mIPSC frequency (a) and amplitude (b) of those not significantly different from control are shown.



Extended Data Figure 9 | BDNF regulates somatic inhibitory synapses in response to kainic acid. **a–c**, eIPSCs were measured simultaneously from neighbouring BDNF4-WT (black) and BDNF-KO (green) neurons from mice injected with kainic acid. Top shows average eIPSC, normalized pairwise to the wild-type neuron, measured from BDNF-WT (black) and BDNF-KO (green) neurons in response to stimulation of axons in radiatum (**a**), pyramidale (**b**) or

oriens (**c**). Scale bars indicate per cent change from wild type. Bottom shows eIPSC amplitude measured from pairs of neighbouring BDNF-KO and BDNF-WT neurons in response to stimulation of axons in radiatum (**a**) ($n = 14$ pairs), pyramidale (**b**) ($n = 12$ pairs, $P < 0.01$), or oriens (**c**) ($n = 15$ pairs). Open circles represent BDNF-KO/BDNF-WT pairs. Red circles indicate mean \pm s.e.m.

Extended Data Table 1 | Putative NPAS4 target genes

gene	chr	pos	induction of gene	induction at peak	gene	chr	pos	induction of gene	induction at peak
4921504E06Rik	2	19476120	8	6.2	Maml3	3	51906195	3.28369	5.75
9530008L14Rik	13	41896890	8.6	21	Maml3	3	51907390	3.28369	11.333
Abcd2	15	90983260	2.48429	5.5	Mest	6	30695130	4.66716	6.274
Adcyap1	17	93602815	4.33656	5.929	Myo3b	2	69952395	2.02105	5
Ankrd56	5	93483350	15.9545	11	Nfil3	13	53078245	4.87197	12.32
Arhgap29	3	121676880	3.56853	5.429	Npas4	19	4989805	73.8489	58.538
Bdnf	2	109532475	35.2919	205.333	Npas4	19	4993095	73.8489	19
Bdnf	2	109518455	35.2919	4.333	Nptx2	5	145308275	7.35033	9.568
Bdnf	2	109514675	35.2919	128	Nr4a1	15	101097330	36.0876	66.4
Cd6	19	10859575	2.11111	7.5	Nr4a2	2	56969220	6.71864	10.25
Cpa4	6	30522930	5.70588	25.5	Nr4a3	4	48057945	12.8444	10.559
Cpxm2	7	139350455	2.56693	6.286	Nr4a3	4	48056410	12.8444	11.375
Crem	18	3281155	5.14777	16.8	Nr4a3	4	48057290	12.8444	12.034
Crem	18	3281830	5.14777	22	Olfml2a	2	38806110	2.34211	17
Cyr61	3	145314740	4.5102	6	Pacsin3	2	91095860	2.12644	15
D16Ertd472e	16	78576220	5.54462	12	Pam	1	99928620	3.52883	11.647
D3Bwg0562e	3	117060470	4.03298	10	Pappa	4	64788065	2.88618	8
Dcb1	4	68615695	4.20687	5.005	Pcdh11x	20	117723835	2.41197	9
Ddx3y	21	622975.5	3.93276	10	Pcsk1	13	75228705	37.6	13.1
Dkk2	3	131749835	9.25532	10.5	Pde4d	13	110612880	2.31523	50
Dusp6	10	98786170	2.54083	9	Penk1	4	4065825	2.1	5.231
E430004N04Rik	10	28532080	8.13043	13	Per1	11	68913080	3.159	7.8
Fer1l3	19	38066355	5.39535	74	Rabggtb	3	153574995	3.08718	6.065
Fer1l3	19	37982665	5.39535	9	Rgs2	1	145852135	8.16283	10.181
Fos	12	86812870	33.5814	14	Rgs2	1	145851380	8.16283	7.207
Fosb	7	19905495	53	5.333	Rgs2	1	145850695	8.16283	8.76
Fosb	7	19894115	53	20	Rspo3	10	29259485	2.27746	6
Fosl2	5	32435940	5.29613	14	Scn1a	2	66246895	2.98474	6.875
Fosl2	5	32438065	5.29613	5.875	Sertad1	7	28271930	9.30631	7.526
Gabra4	5	72008145	3.34333	5.5	Slc6a17	3	107319165	2.54003	5
Gabrb1	5	72460260	2.17759	6	Snx7	3	117526220	2.07258	5.5
Gcnt2	13	41013390	3.71429	6.2	Snx7	3	117529915	2.07258	6.5
Gpr22	12	32394835	5.68515	7.676	Sorcs3	19	48315650	2.76436	11
Gpr3	4	132767740	10.1849	15	Sorcs3	19	48659720	2.76436	5.5
Hcn1	13	118394055	2.98126	5.5	Sorcs3	19	48172075	2.76436	8
Hdac9	12	35213780	8.31166	9.947	Spry2	14	106297475	2.01437	14.75
Hdac9	12	35214265	8.31166	9.915	Stac	9	111591890	3.65815	5.083
Hdac9	12	35182840	8.31166	5	sult2b1	13	96731800	4.05891	9
Hdac9	12	35166755	8.31166	24.75	Sv2c	3	93251570	2	7
Hdac9	12	35183850	8.31166	18	Tchh	8	66685070	6.68364	5.579
Hdac9	12	35173085	8.31166	5.31	Tll1	9	53914130	2.51701	5.75
Hspb3	13	114453860	11.2703	10.947	Tnfaip8l3	1	162079810	11.2174	13
Hunk	16	90387145	2.93033	5	Tnn	9	8544010	8.38462	17
lqsec3	6	121423910	2.03163	7.009	Trpc6	6	30871095	5.66667	6.75
Junb	8	87502555	18.6986	19.684	Tsga13	6	30871525	5.66667	6
Kcna4	2	107257495	3.2902	8.857	Tsga13	6	30858185	5.66667	12
Kcnj3	2	55289600	5.1252	6.675	Tsga13	8	74194390	2.24115	5.667
Klhl4	20	111587385	6.72727	5.889	Unc13a	5	137505265	13.7907	10.625
Maff	15	79177910	10.8679	14	Vgf	5	137506375	13.7907	14.077
Maff	15	79178470	10.8679	6.5	Vgf	9	119920665	13.7907	6.8

Putative NPAS4 target genes were identified by analysing previously published NPAS4 ChIP-seq and RNA-seq data (accession number GSE21161)¹⁴. Inducible genes were selected as putative NPAS4 targets if (1) by ChIP-seq NPAS4 is shown to be bound within 10 kb of the putative target gene and (2) by RNA-seq the mRNA transcribed near the NPAS4 peak is induced greater than fivefold.

Integrin-modulating therapy prevents fibrosis and autoimmunity in mouse models of scleroderma

Elizabeth E. Gerber¹, Elena M. Gallo¹, Stefani C. Fontana¹, Elaine C. Davis², Fredrick M. Wigley³, David L. Huso⁴ & Harry C. Dietz^{1,5}

In systemic sclerosis (SSc), a common and aetiologically mysterious form of scleroderma (defined as pathological fibrosis of the skin), previously healthy adults acquire fibrosis of the skin and viscera in association with autoantibodies¹. Familial recurrence is extremely rare and causal genes have not been identified. Although the onset of fibrosis in SSc typically correlates with the production of autoantibodies, whether they contribute to disease pathogenesis or simply serve as a marker of disease remains controversial and the mechanism for their induction is largely unknown². The study of SSc is hindered by a lack of animal models that recapitulate the aetiology of this complex disease. To gain a foothold in the pathogenesis of pathological skin fibrosis, we studied stiff skin syndrome (SSS), a rare but tractable Mendelian disorder leading to childhood onset of diffuse skin fibrosis with autosomal dominant inheritance and complete penetrance. We showed previously that SSS is caused by heterozygous missense mutations in the gene (*FBN1*) encoding fibrillin-1, the main constituent of extracellular microfibrils³. SSS mutations all localize to the only domain in fibrillin-1 that harbours an Arg-Gly-Asp (RGD) motif needed to mediate cell-matrix interactions by binding to cell-surface integrins³. Here we show that mouse lines harbouring analogous amino acid substitutions in fibrillin-1 recapitulate aggressive skin fibrosis that is prevented by integrin-modulating therapies and reversed by antagonism of the pro-fibrotic cytokine transforming growth factor β (TGF- β). Mutant mice show skin infiltration of pro-inflammatory immune cells including plasmacytoid dendritic cells, T helper cells and plasma cells, and also autoantibody production; these findings are normalized by integrin-modulating therapies or TGF- β antagonism. These results show that alterations in cell-matrix interactions are sufficient to initiate and sustain inflammatory and pro-fibrotic programmes and highlight new therapeutic strategies.

Fibrillin-1 contributes to the regulation of TGF- β , a cytokine that has been descriptively linked to many fibrotic diseases, including both SSS and SSc^{3,4}. TGF- β is secreted from the cell in the context of a large latent complex (LLC) that includes the active cytokine bound to a dimer of its processed amino-terminal propeptide, latency-associated peptide (LAP), which in turn binds to latent TGF- β -binding proteins (LTBPs)⁵. Studies in mouse models and *in vitro* have shown that fibrillin-1 interacts directly with LTBPs, allowing sequestration of the LLC by microfibrils⁵.

Mutations throughout the *FBN1* gene also cause Marfan syndrome (MFS), a disorder characterized by bone overgrowth, ocular lens dislocation and aortic dilatation⁶. Failed matrix sequestration of the LLC in fibrillin-1-deficient patients and mice promotes increased activation of, and signalling by, TGF- β . SSS mutations are specifically localized to the fourth transforming growth factor- β -binding protein-like domain (TB4) of fibrillin-1, which encodes the RGD motif, through which fibrillin-1 binds integrins $\alpha_v\beta_3$, $\alpha_5\beta_1$ and $\alpha_v\beta_6$ (refs 3, 5).

To determine whether failed interaction between integrins and fibrillin-1 is sufficient to initiate skin fibrosis, two *Fbn1*-targeted knock-in mouse

models were generated: one with SSS-associated change W1572C (the mouse equivalent of human W1570C) and the other with an RGD to RGE substitution (D1545E) predicted to cause an obligate loss of integrin binding to fibrillin-1 (Supplementary Fig. 1). Mice heterozygous for either mutation phenocopy SSS with increased deposition of collagen by 1 month of age and a decrease in subcutaneous fat by 3 months of age (Fig. 1 and Supplementary Fig. 2a, b). Whereas homozygosity for D1545E causes embryonic lethality before embryonic day 10.5, mice homozygous for W1572C are viable and show accelerated skin fibrosis when compared with heterozygous littermates (Fig. 1 and Supplementary Fig. 2a, b). As seen in patients with SSS or SSc³, mutant mice show disorganized and excessive microfibrillar aggregates in the dermis, with sparsely distributed elastin (Supplementary Fig. 2c). Freshly isolated cells from mutant dermis show increased surface levels of integrins $\alpha_5\beta_1$ and $\alpha_v\beta_3$ in its active conformation (as assessed using WOW-1 antibody) by flow cytometry (Fig. 2a). There was no corresponding increase in either total β_3 integrin or integrin β_5 , a subtype that can cross-react with WOW-1 (Supplementary Fig. 3). On the basis of these data, we speculated that disrupted cell-matrix interaction in SSS might result in compensatory upregulation of specific integrins at the surface of dermal cells, and that integrins might represent a possible therapeutic target for this disease.

We next investigated whether mimicking integrin-matrix ligand (that is, fibrillin-1) interactions in mutant mice by using a β_1 integrin-activating antibody (β_1 aAb; 9EG7) offered therapeutic potential for the treatment of SSS. Treatment of SSS mouse models with β_1 aAb for 12 weeks normalized integrin expression, skin stiffness and distensibility and skin architecture (Fig. 2a–c and Supplementary Fig. 4). In keeping with a pathogenic role for β_3 integrin, we found that targeted introduction of haploinsufficiency or the complete null state for the β_3 integrin gene (*Itgb3*) in SSS mice normalized skin stiffness, collagen deposition and subcutaneous fat by 3 months of age (Supplementary Fig. 5a, b). By 5 months of age, 8 of 67 (12%) *Itgb3*-targeted animals developed focal dermal and epidermal thickening (irrespective of *Fbn1* genotype) reminiscent of the aberrant wound-healing described previously in β_3 integrin-deficient mice (Supplementary Fig. 5c)⁷.

To assess for a pathogenic contribution for TGF- β , SSS mice were treated for 12 weeks with a panspecific TGF- β -neutralizing antibody (TGF- β NAb; 1D11) or isotype-matched control IgG after establishment of dense fibrosis at 12 weeks of age. Clinical (Fig. 3a) and histological (Fig. 3b) findings confirmed full reversal of skin stiffness and restoration of skin architecture in TGF- β NAb-treated animals. Potential mechanisms for enhanced TGF- β activity include excessive concentration of latent TGF- β by the abnormally abundant microfibrillar aggregates in the dermis, or excessive integrin-mediated activation (release) of TGF- β from its latent complex⁸. To discriminate between these possibilities, we used flow cytometry to monitor mutant mice for increased cell-surface expression of the three integrin subtypes ($\alpha_v\beta_5$, $\alpha_v\beta_6$ and $\alpha_v\beta_8$) known to support potent TGF- β activation⁶; this was not observed (Supplementary Fig. 6a). In addition, immunofluorescence

¹McKusick-Nathans Institute of Genetic Medicine, Johns Hopkins University School of Medicine, Baltimore, Maryland 21205, USA. ²McGill University, Montreal, Quebec H3A 2K6, Canada. ³Department of Medicine, Johns Hopkins University School of Medicine, Baltimore, Maryland 21205, USA. ⁴Department of Molecular and Comparative Pathobiology, Johns Hopkins University School of Medicine, Baltimore, Maryland 21205, USA. ⁵Howard Hughes Medical Institute, Chevy Chase, Maryland 20815, USA.

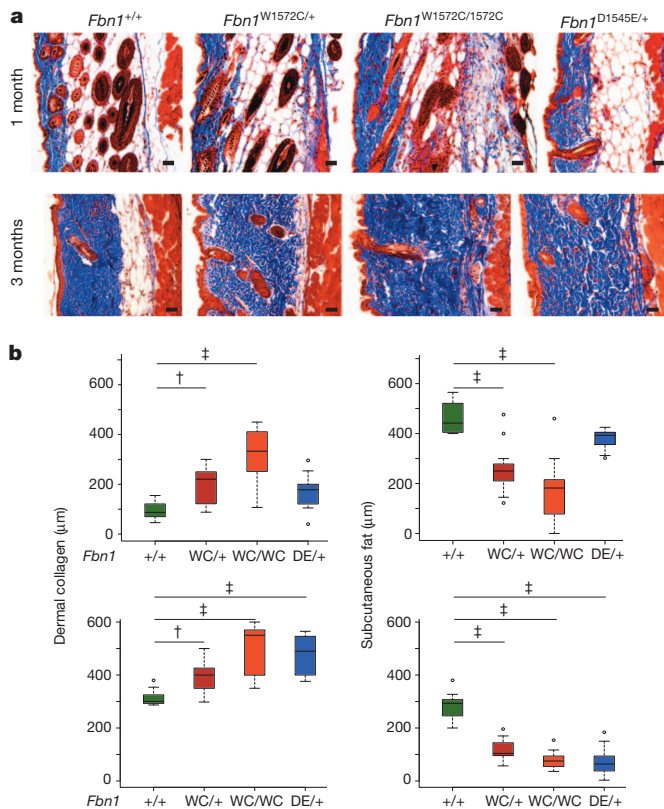


Figure 1 | SSS mouse models show skin fibrosis. **a**, Masson's trichrome staining of back skin sections from male mice (genotypes indicated) at 1 month of age (top panels) and 3 months of age (bottom panels) shows progressive loss of subcutaneous fat and an expanded zone of dense dermal collagen in mutant animals. **b**, Quantification of the thickness of the zones of dermal collagen and subcutaneous fat in wild-type and mutant mice at 1 month of age (top panels) and 3 months of age (bottom panels) is shown. Similar findings were observed in mutant female mice (Supplementary Fig. 2a, b). DE, D1545E; WC, W1572C. For 1-month males, $n = 9$ (+/+), 10 (WC/+), 10 (WC/WC) and 9 (DE/+); for 3-month males: $n = 13$ (+/+), 9 (WC/+), 9 (WC/WC) and 9 (DE/+). Scale bars, 50 μm . $\dagger P < 0.001$; $\ddagger P < 0.0001$. The upper and lower margins of each box define the 75th and 25th centiles, respectively; the internal line defines the median, and the whiskers define the range. Values outside the interquartile range are shown as open circles.

analysis of skin in mutant mice did not reveal increased expression of free TGF- β 1 (Supplementary Fig. 6b), which is known to be activated by integrins through interaction with the RGD sequence in its LAP (LAP1). There was an increase in total (free and active) TGF- β 2 (Supplementary Fig. 6b), which has not been shown to be activated by integrins (presumably as a result of the absence of an RGD sequence in LAP2)⁶. Furthermore, there was excessive concentration of both LAP1 and LAP2 in the dermis of mouse models of SSS, suggesting accumulation of the LLC for TGF- β 1 and TGF- β 2, respectively. Although we cannot exclude a contribution of integrin-mediated TGF- β activation, these data suggest that enhanced TGF- β bioavailability contributes prominently to increased TGF- β activity in mutant mice.

As seen in SSc, SSS mouse models show circulating anti-nuclear and anti-topoisomerase I antibodies (Fig. 4a and Supplementary Fig. 7). The finding that the deep dermal fibrosis seen in early SSS (Fig. 1) colocalizes with high expression of active β_3 integrin and accumulation of CD45⁺ marrow-derived cells (Supplementary Fig. 8a) prompted speculation that an infiltrating class of immune cells might contribute to disease progression. In keeping with this hypothesis, nearly all dermal cells expressing high levels of $\alpha_5\beta_1$ and active β_3 integrins in SSS mice are CD317⁺ plasmacytoid dendritic cells (pDCs) (Fig. 4b). SSS mice show enrichment for cells that are CD11b⁺CD3⁺CD19⁺B220⁺SiglecH⁺Ly6C^{high} in the dermis, further validating this identity (Fig. 4b and Supplementary

Fig. 8b–d)⁹. As is characteristic of mature and active pDCs, these dermal cells express the pro-inflammatory cytokines interleukin (IL)-6 and interferon (IFN)- α (Fig. 4c and Supplementary Fig. 8e)⁹. There is also dermal polarization towards pro-inflammatory T helper (T_H) cell populations, including CD4⁺IL-4⁺ T_H2, CD4⁺IL-17⁺ T_H17 and CD4⁺IL-9⁺ T_H9 cells (Supplementary Fig. 9a, b). In keeping with skewing towards T_H2, T_H9 and/or T_H17 cells, there was also an increased expression of IL-9, IL-13 and IL-22 by CD3⁺ dermal cells (Supplementary Fig. 9a–c). There was no corresponding increase in either IFN- γ ⁺CD4⁺ T_H1 or FoxP3⁺CD4⁺ T-regulatory (T_{reg}) cells in mutant animals (Supplementary Fig. 9d). Last, the dermis of SSS mice also showed infiltration with B220^{high}CD19⁺ activated B cells and CD138⁺B220^{low}CD19⁺ plasma cells (Supplementary Fig. 10). These abnormalities, including circulating autoantibodies and immune cell infiltration and activation, were normalized by treatment of mutant mice with β_1 aAb (Fig. 4 and Supplementary Figs 9 and 10). A similar response was seen in association with reversal of skin fibrosis on treatment with TGF- β NAb (Supplementary Fig. 11).

We speculated that altered presentation of the fibrillin-1 RGD sequence might directly influence the expression of integrins by, and the performance of, pDCs. In keeping with this hypothesis, we found that wild-type spleen-derived pre-pDCs showed increased adherence and activation (expression of IFN- α and IL-6) when plated on the matrix expressed by SSS murine embryonic fibroblasts (MEFs) in comparison with control MEFs (Supplementary Fig. 12).

SSc fibroblasts showed increased cell-surface presentation of total β_1 integrin (Supplementary Fig. 13) and active β_3 integrin (as monitored by WOW-1 staining) in comparison with controls, whereas levels of total β_3 and β_5 integrins were normal (Supplementary Fig. 14a). Treatment with β_1 aAb TS2/16, which promotes and stabilizes integrin β_1 -ligand interactions, normalized cell-surface levels of active β_3 integrin (Supplementary Fig. 14a). Treatment with β_3 integrin-blocking antibody (β_3 bAb) did not significantly decrease the cell-surface presentation of total β_1 integrin (Supplementary Fig. 13). Human SSc cells in culture showed decreased levels of microRNA-29 (miR-29) (Supplementary Fig. 14b), a small regulatory RNA that is repressed by TGF- β and is known to inhibit the expression of multiple matrix elements and to suppress fibrosis in selected disease states^{10,11}. Treatment with β_1 aAb normalized miR-29 expression and dose-dependently attenuated the expression of type I and type III collagen in SSc fibroblasts (Supplementary Fig. 14b). SD208, an antagonist of the kinase activity of the type I TGF- β receptor subunit, also normalized the expression of collagen and miR-29a (Supplementary Fig. 14c).

In addition to canonical (Smad-dependent) signalling, TGF- β can also initiate so-called non-canonical cascades, prominently including extracellular signal-regulated kinase (ERK1/2)⁵. SSc fibroblasts showed normal TGF- β 1-dependent phosphorylation of Smad3 (pSmad3) that was not influenced by integrin-modulating therapies, but uniquely showed TGF- β 1-dependent phosphorylation of ERK1/2 (pERK1/2) in contrast with control fibroblasts that was normalized on treatment with either β_1 aAb or β_3 bAb (Supplementary Fig. 14d, e). The activation of ERK1/2 in SSc fibroblasts was seen within 5 min of stimulation with TGF- β 1 and was inhibited by pretreatment with SD208, suggesting a relatively direct response (Supplementary Fig. 14d, e). In keeping with a pathogenic contribution of pERK1/2, treatment of SSc fibroblasts with U0126, an inhibitor of the mitogen-activated protein kinase/ERK kinase (MEK), increased miR-29a levels and decreased collagen expression in SSc fibroblasts (Supplementary Fig. 14f). Both SSS mouse models showed excessive activation of ERK1/2 in CD317⁺ pDCs and other dermal cells (Supplementary Fig. 14g). Treatment of *Fbn1*^{D1545E/+} mice with the MEK inhibitor RDEA119 prevented skin stiffness, the accumulation of dermal collagen and the loss of subcutaneous fat (Supplementary Fig. 14h, i).

This study shows that point mutations specifically in the sole integrin-binding domain of fibrillin-1 are sufficient to recapitulate the SSS phenotype in mice and to initiate many findings reminiscent of SSc, including

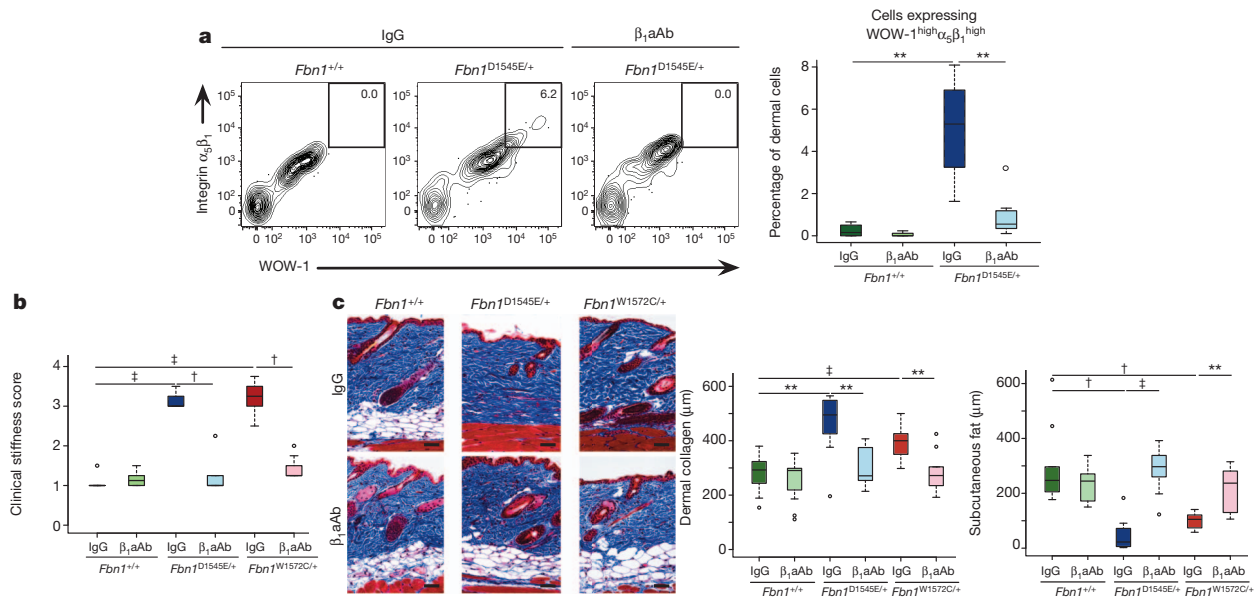


Figure 2 | Integrin-modulating interventions prevent skin fibrosis. **a**, Flow cytometry of cells derived from the dermis reveals a unique population expressing both $\alpha_5\beta_1$ and active β_3 integrins (monitored using WOW-1 antibody) in mutant mice that is eliminated on treatment with β_1 aAb but not an isotype-matched control (IgG). Representative contour plots (left) and quantification (right) are shown. An agonist and antagonist of β_3 integrin activation were used to attest to the specificity of the WOW-1 antibody (Supplementary Fig. 16b). For isotype control-treated animals, $n = 5$ (*Fbn1*^{+/+}) and 7 (*Fbn1*^{D1545E/+}); for β_1 aAb-treated animals, $n = 4$ (*Fbn1*^{+/+}) and 7 (*Fbn1*^{D1545E/+}). **b**, Clinical assessment demonstrated that β_1 aAb prevented skin stiffness in mutant animals when compared with those treated with an

isotype-matched control (IgG). **c**, Masson's trichrome staining reveals decreased skin collagen and preservation of subcutaneous fat in β_1 aAb-treated mutants (left). Quantification of the thickness of the zones of dermal collagen and subcutaneous fat is shown (right). For isotype control-treated animals, $n = 12$ (*Fbn1*^{+/+}), 9 (*Fbn1*^{D1545E/+}) and 8 (*Fbn1*^{D1545E/+}); for β_1 aAb-treated animals, $n = 12$ (*Fbn1*^{+/+}), 10 (*Fbn1*^{D1545E/+}) and 10 (*Fbn1*^{D1545E/+}). Scale bars, 50 μ m. * $P < 0.05$; ** $P < 0.01$; † $P < 0.001$; ‡ $P < 0.0001$. The upper and lower margins of each box define the 75th and 25th centiles, respectively; the internal line defines the median, and the whiskers define the range. Values outside the interquartile range are shown as open circles.

dermal fibrosis, autoantibody production, high IFN- α expression, T_H2 and T_H17 polarization, and accumulation of activated B cells and plasma cells in the skin^{1,2,4,12,13}. Although previous studies have reported autoantibodies and subdermal fibrosis in tight skin (Tsk) mice harbouring a large central duplication in *Fbn1*, there are no direct human correlates, and both the mechanism and pathogenic relevance remain unclear^{14,15}. In SSS, all of these processes can be functionally linked to altered integrin expression and/or function because they are prevented by integrin-modulating therapies. Although skin fibrosis was observed in mice on conditional silencing of β_1 integrin expression in keratinocytes¹⁶, targeting of *Itgb1* in fibroblasts afforded relative protection against bleomycin-induced skin fibrosis¹⁷. This apparent discrepancy has not been explained mechanistically.

A comparison of MFS and SSS highlights the complicated role of the extracellular matrix in cytokine regulation. Unlike MFS, in which a

deficiency of fibrillin-1 is seen, SSS mutations promote the increased deposition of abnormal microfibrillar aggregates that fail to make contact with neighbouring cells but retain the ability to bind to the TGF- β LLC, findings also seen in SSc³. This results in a decreased or increased concentration of latent TGF- β in tissues in MFS or SSS, respectively^{3,5}. It is posited that in MFS a decreased concentration of LLC is offset by increased TGF- β activation but that this may occur in a tissue-specific manner^{5,6}. The relative deficiency of microfibrils and hence latent TGF- β in MFS would mandate continuing TGF- β production to support high signalling, whereas the high dermal concentration of TGF- β in SSS might allow a more sustained enhanced signalling state. Curiously, this does not seem to occur in all tissues in which fibrillin-1 is expressed, perhaps as a result of different repertoires of expressed integrin subtypes that vary in their sensitivity to conformational changes induced by SSS mutations, and/or tissue-specific

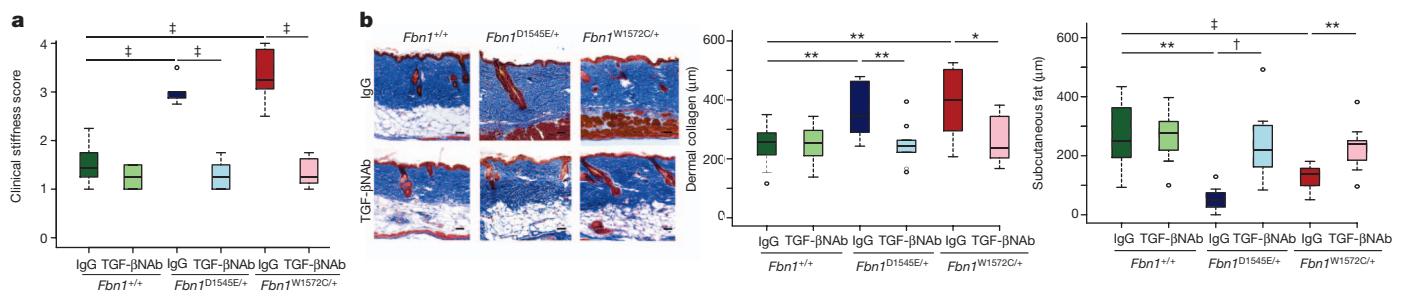


Figure 3 | A panspecific TGF- β -neutralizing antibody reverses established skin fibrosis. **a**, Clinical assessment showing that stiffness was fully normalized by treatment with TGF- β NaB, starting at 3 months of age and continuing for 12 weeks. **b**, Histological and morphometric analyses using Masson's trichrome stain. For isotype control-treated animals, $n = 14$ (*Fbn1*^{+/+}), 9 (*Fbn1*^{D1545E/+}) and 8 (*Fbn1*^{D1545E/+}); for TGF- β NaB-treated animals,

$n = 14$ (*Fbn1*^{+/+}), 10 (*Fbn1*^{D1545E/+}) and 8 (*Fbn1*^{D1545E/+}). Scale bars, 50 μ m. * $P < 0.05$; ** $P < 0.01$; † $P < 0.001$; ‡ $P < 0.0001$. The upper and lower margins of each box define the 75th and 25th centiles, respectively; the internal line defines the median, and the whiskers define the range. Values outside the interquartile range are shown as open circles.

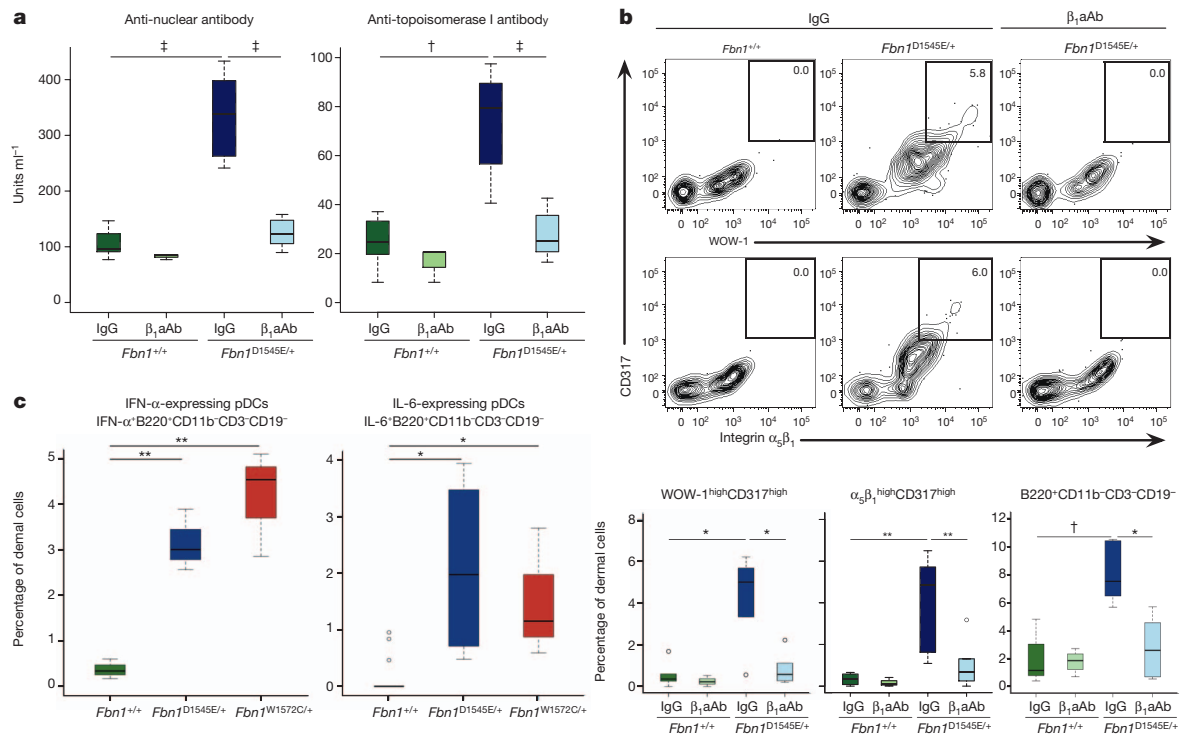


Figure 4 | Immunological abnormalities in SSS mice are prevented by integrin-modulating therapies. **a**, Increased circulating levels of anti-nuclear and anti-topoisomerase I antibodies by enzyme-linked immunosorbent assay in *Fbn1*^{D1545E/+} mice at 3 months of age are normalized on treatment with β_1 aAb but not when treated with an isotype-matched control (IgG). For isotype control-treated animals, $n = 6$ (*Fbn1*^{+/+}), 4 (*Fbn1*^{D1545E/+}); for β_1 aAb-treated animals, $n = 4$ (*Fbn1*^{+/+}), 10 (*Fbn1*^{D1545E/+}). **b**, The cells expressing high $\alpha_5\beta_1$ integrin in the dermis of mutant mice are CD317^{high} cells that fail to accumulate on treatment with β_1 aAb but not with an isotype-matched control (IgG).

b, c, The CD317^{high} cells that accumulate in the dermis of mutant mice are B220⁺CD3⁻CD19⁻ plasmacytoid dendritic cells (**b**) and express both IFN- α and IL-6 (**c**). In **b** and **c**, for isotype control-treated animals, $n = 5$ (*Fbn1*^{+/+}) and 7 (*Fbn1*^{D1545E/+}); for β_1 aAb-treated animals, $n = 4$ (*Fbn1*^{+/+}) and 7 (*Fbn1*^{D1545E/+}). * $P < 0.05$; ** $P < 0.01$; † $P < 0.001$; ‡ $P < 0.0001$. The upper and lower margins of each box define the 75th and 25th centiles, respectively; the internal line defines the median, and the whiskers define the range. Values outside the interquartile range are shown as open circles.

differences in the regulation of microfibrillar assembly. The stiffened ECM in SSS could support mechanical traction-based activation of the excessive amounts of latent TGF- β in the dermis, a plausible feedforward mechanism for the observed fibrosis⁸. Thus the level of TGF- β signalling in a given tissue may, at least in part, be determined by the integration of both positive and negative regulation by microfibrils^{5,6}.

Although the cell type that first detects and responds to aberrant presentation of the RGD sequence in fibrillin-1 remains unknown, it is useful to speculate on the involvement of pre-pDCs that normally perform a surveillance function for viral pathogens at low concentrations in the skin. Previous work has shown that $\alpha_5\beta_1$ integrin influences the adhesion, migration and maturation of DCs and that migration is inhibited by β_1 aAb, at least in part through podosome disassembly¹⁸. Furthermore, a specific role for $\alpha_5\beta_1$ integrin in pre-pDC chemotaxis and trafficking has been demonstrated¹⁹. It is therefore evident that pre-pDCs are informed by and respond to their matrix environment, with fibrillin-1 potentially serving as a prominent informant. In keeping with this, our *in vitro* observations (Supplementary Fig. 12) suggest that an altered matrix environment, devoid of any systemic influence, is sufficient to promote pDC recruitment and activation. It remains to be determined whether this relates to the loss of a physiological inhibitory signal by normal microfibrils or to a pathogenic gain of function by abnormal microfibrillar aggregates seen in SSS and SSc.

pDCs are a major source of IFN- α and are capable of inducing T_H2 and T_H17 skewing, autoreactive B-cell and plasma-cell differentiation, and autoantibody production (Supplementary Fig. 15)^{9,12,20–22}; they have also previously been implicated in multiple autoimmune processes (including SSc)^{9,12,20–22}. Although pDCs can contribute to both tolerogenic T_{reg} or auto-inflammatory T_H17 cell commitment, *in vitro* experiments suggest that TGF- β -treated pDCs favour the latter

through a Smad-dependent mechanism²³. Whereas the altered matrix environment in SSS probably contributes to excessive TGF- β activity early in the course of disease, TGF- β induces its own production and activation by pDCs, as well as IL-6 secretion (known prerequisites for T_H17 polarization)²³. pDCs can also induce either T_H1 or T_H2 skewing through IL-6/IFN- α -dependent or OX40 ligand (OX40L)/IL-4-dependent mechanisms, respectively (Supplementary Fig. 15)⁹. pDCs in a T_H2 environment become activated and show enhanced IL-4 secretion, constituting a potential feedforward mechanism for maintenance of a T_H2 response²⁴. In the context of high TGF- β signalling, this might also allow for T_H9 skewing²⁵. Cytokines related to T_H2, T_H17 and pDCs, including IL-4, IL-6, IL-13, IL-17 and IFN- α , have been prominently implicated in the fibrotic response in various disease states, including SSc^{1,2,4,9,12,13,20–22}. This study implicates TGF- β in pDC recruitment.

Although many studies have highlighted the contribution of integrins to fibrotic disease⁸, their focus has been on the ability of certain integrins to release (activate) TGF- β 1 or TGF- β 3 from the LLC through a direct interaction with RGD sequences in LAP1 and LAP3 (ref. 8). Multiple observations in this study suggest that enhanced bioavailability of TGF- β , rather than its activation, may be the primary determinant of increased TGF- β activity in SSS and perhaps SSc. Our *in vitro* data in SSc fibroblasts suggest that cell-surface integrins can influence the inherent signalling properties of the TGF- β receptor complex in response to free and active TGF- β . Although the initiating pathogenic event in SSc remains unknown, this study provides evidence for a cell autonomous signalling defect that is maintained in culture. In theory, this could relate to primary but poorly penetrant genetic alterations or fixed epigenetic modifications, both of which may require a large environmental trigger.

Activation of ERK1/2 has previously been implicated in the TGF- β -mediated fibrotic response in general, and specifically in SSc fibroblasts^{26–28}. It was previously observed²⁸ that constitutive ERK1/2 signalling in SSc fibroblasts drives the expression of integrin $\alpha_v\beta_3$. Both $\alpha_v\beta_3$ and TGF- β were required for excessive collagen production. Despite overlapping observations and the common conclusion that $\alpha_v\beta_3$ represents an attractive therapeutic target, this study places ERK1/2 activation downstream of both TGF- β and enhanced active $\alpha_v\beta_3$ expression in SSc fibroblasts and shows phenotypic rescue in response to ERK antagonism in an *in vivo* model of scleroderma. Furthermore, we show prominent ERK1/2 signalling in pDCs in SSS mice, a described prerequisite for the stabilization, nuclear export and translation of IFN- α messenger RNA²⁹, and for Toll-like receptor-mediated expression of inflammatory cytokines³⁰. Whereas previous work associated low levels of miR-29, a negative regulator of collagen expression, with fibrotic diseases including post-injury cardiac fibrosis¹⁰ and SSc¹¹, this study offers a pathogenic sequence for scleroderma that integrates structural matrix elements, integrins, TGF- β signalling, ERK activation and miR-29.

SSS mouse models demonstrate the potential to reverse established dermal fibrosis, and they suggest several therapeutic strategies including β_1 integrin activation and blockade of signalling by β_3 integrin, TGF- β or ERK. When paired with the ability to perform preclinical trials in the first described mouse models of a genetically defined human presentation of scleroderma, the potential for therapeutic advancement seems promising.

METHODS SUMMARY

Subjects. Patients were recruited from the Scleroderma Center and Connective Tissue Clinic at Johns Hopkins Hospital. All skin biopsies and protocols were performed in compliance with the Johns Hopkins School of Medicine Institutional Review Board after informed consent.

Mice. All mice were cared for in strict compliance with the Animal Care and Use Committee of the Johns Hopkins University School of Medicine. *Fbn1*^{D1545E/+} and *Fbn1*^{W1572C/+} mice were generated by homologous recombination. *Itgb3*^{+/-} mice were purchased through Jackson Laboratories as heterozygotes. Skin biopsy, sera collection, enzyme-linked immunosorbent assay (ELISA), as well as histological and flow cytometric analysis and *in vivo* trials were performed as described in Methods.

Cell culture. Primary human dermal fibroblasts were derived from skin biopsies from five patients with active diffuse systemic sclerosis and from six healthy controls. All antibodies and *in vitro* drug treatments and dosing, as well as methods for flow cytometric analyses, western blotting, RNA isolation and quantitative PCR are described in Methods. All details regarding co-culture of pDCs and murine embryonic fibroblasts are described in Methods.

Statistics and graphs. All quantitative data are shown as standard boxplots produced in R statistical software. Statistical analysis was performed with a two-tailed *t*-test, assuming equal variance between the compared groups.

Online Content Any additional Methods, Extended Data display items and Source Data are available in the online version of the paper; references unique to these sections appear only in the online paper.

Received 11 March; accepted 28 August 2013.

Published online 9 October; corrected online 6 November 2013 (see full-text HTML version for details).

- Mayes, M. D. *et al.* Prevalence, incidence, survival, and disease characteristics of systemic sclerosis in a large US population. *Arthritis Rheum.* **48**, 2246–2255 (2003).
- Harris, M. L. & Rosen, A. Autoimmunity in scleroderma: the origin, pathogenetic role, and clinical significance of autoantibodies. *Curr. Opin. Rheumatol.* **15**, 778–784 (2003).
- Loeys, B. L. *et al.* Mutations in fibrillin-1 cause congenital scleroderma: stiff skin syndrome. *Sci. Transl. Med.* **2**, 23ra20 (2010).
- Varga, J. & Pasche, B. Transforming growth factor β as a therapeutic target in systemic sclerosis. *Nature Rev. Rheumatol.* **5**, 200–206 (2009).
- Doyle, J. J., Gerber, E. E. & Dietz, H. C. Matrix-dependent perturbation of TGF- β signaling and disease. *FEBS Lett.* **586**, 2003–2015 (2012).
- Lindsay, M. E. & Dietz, H. C. Lessons on the pathogenesis of aneurysm from heritable conditions. *Nature* **473**, 308–316 (2011).

- Reynolds, L. E. *et al.* Accelerated re-epithelialization in β_3 -integrin-deficient mice is associated with enhanced TGF- β 1 signaling. *Nature Med.* **11**, 167–174 (2005).
- Munger, J. S. & Sheppard, D. Cross talk among TGF- β signaling pathways, integrins, and the extracellular matrix. *Cold Spring Harb. Perspect. Biol.* **3**, a005017 (2011).
- Swiecki, M. & Colonna, M. Unraveling the functions of plasmacytoid dendritic cells during viral infections, autoimmunity, and tolerance. *Immunol. Rev.* **234**, 142–162 (2010).
- van Rooij, E. *et al.* Dysregulation of microRNAs after myocardial infarction reveals a role of miR-29 in cardiac fibrosis. *Proc. Natl Acad. Sci. USA* **105**, 13027–13032 (2008).
- Maurer, B. *et al.* MicroRNA-29, a key regulator of collagen expression in systemic sclerosis. *Arthritis Rheum.* **62**, 1733–1743 (2010).
- Hall, J. C. & Rosen, A. Type I interferons: crucial participants in disease amplification in autoimmunity. *Nature Rev. Rheumatol.* **6**, 40–49 (2010).
- Sakkas, L. I., Chikanza, I. C. & Platsoucas, C. D. Mechanisms of disease: the role of immune cells in the pathogenesis of systemic sclerosis. *Nature Clin. Pract. Rheumatol.* **2**, 679–685 (2006).
- Fujimoto, M. *et al.* CD19-dependent B lymphocyte signaling thresholds influence skin fibrosis and autoimmunity in the tight-skin mouse. *J. Clin. Invest.* **109**, 1453–1462 (2002).
- Bona, C. & Rothfield, N. Autoantibodies in scleroderma and tight skin mice. *Curr. Opin. Immunol.* **6**, 931–937 (1994).
- Brakebusch, C. *et al.* Skin and hair follicle integrity is crucially dependent on β 1 integrin expression on keratinocytes. *EMBO J.* **19**, 3990–4003 (2000).
- Liu, S. *et al.* Loss of β 1 integrin in mouse fibroblasts results in resistance to skin scleroderma in a mouse model. *Arthritis Rheum.* **60**, 2817–2821 (2009).
- van Helden, S. F. *et al.* A critical role for prostaglandin E_2 in podosome dissolution and induction of high-speed migration during dendritic cell maturation. *J. Immunol.* **177**, 1567–1574 (2006).
- Zou, W. *et al.* Stromal-derived factor-1 in human tumors recruits and alters the function of plasmacytoid precursor dendritic cells. *Nature Med.* **7**, 1339–1346 (2001).
- Ding, C., Cai, Y., Marroquin, J., Ildstad, S. T. & Yan, J. Plasmacytoid dendritic cells regulate autoreactive B cell activation via soluble factors and in a cell-to-cell contact manner. *J. Immunol.* **183**, 7140–7149 (2009).
- Jego, G. *et al.* Plasmacytoid dendritic cells induce plasma cell differentiation through type I interferon and interleukin 6. *Immunity* **19**, 225–234 (2003).
- Fleming, J. N. *et al.* Capillary regeneration in scleroderma: stem cell therapy reverses phenotype. *PLoS ONE* **3**, e1452 (2008).
- Saas, P. & Perruche, S. Functions of TGF- β -exposed plasmacytoid dendritic cells. *Crit. Rev. Immunol.* **32**, 529–553 (2012).
- Bratke, K., Klein, C., Kuepper, M., Lommatzsch, M. & Virchow, J. C. Differential development of plasmacytoid dendritic cells in Th1- and Th2-like cytokine milieus. *Allergy* **66**, 386–395 (2011).
- Dardalhon, V. *et al.* IL-4 inhibits TGF- β -induced Foxp3⁺ T cells and, together with TGF- β , generates IL-9⁺ IL-10⁺ Foxp3⁺ effector T cells. *Nature Immunol.* **9**, 1347–1355 (2008).
- Nakerakanti, S. S., Bujor, A. M. & Trojanowska, M. CCN2 is required for the TGF- β induced activation of Smad1–Erk1/2 signaling network. *PLoS ONE* **6**, e21911 (2011).
- Chen, Y. *et al.* Heparan sulfate-dependent ERK activation contributes to the overexpression of fibrotic proteins and enhanced contraction by scleroderma fibroblasts. *Arthritis Rheum.* **58**, 577–585 (2008).
- Asano, Y. *et al.* Increased expression of integrin $\alpha_v\beta_3$ contributes to the establishment of autocrine TGF- β signaling in scleroderma fibroblasts. *J. Immunol.* **175**, 7708–7718 (2005).
- Watarai, H. *et al.* PDC-TREM, a plasmacytoid dendritic cell-specific receptor, is responsible for augmented production of type I interferon. *Proc. Natl Acad. Sci. USA* **105**, 2993–2998 (2008).
- Kawai, T. & Akira, S. TLR signaling. *Cell Death Differ.* **13**, 816–825 (2006).

Supplementary Information is available in the online version of the paper.

Acknowledgements We thank those who contributed skin biopsies to this study and those who provided reagents for this study, including S. Shattil, K. Flanders, C. J. Thomas, S. Patnaik and J. J. Maragan. This work was supported by grants to H.C.D. from the Scleroderma Research Foundation, the National Institutes of Health (R01-AR41135 and P01-AR049698), the National Marfan Foundation, the Smilow Center for Marfan Syndrome Research, and the Howard Hughes Medical Institute.

Author Contributions E.E.G., E.M.G. and H.C.D. designed experiments and interpreted the data. E.M.G. performed enzyme-linked immunosorbent assays. F.M.W. obtained skin samples from patients (the Scleroderma Center of Johns Hopkins University School of Medicine) and provided guidance and clinical expertise. S.C.F. assisted in drug trials *in vivo* and in the collection of mouse sera. E.C.D. performed electron microscopy. E.E.G. generated mouse models and performed all other experiments. D.L.H. aided in complete blood count analysis, mouse surgery, and histopathology. E.E.G. and H.C.D. wrote the paper.

Author Information Reprints and permissions information is available at www.nature.com/reprints. The authors declare no competing financial interests. Readers are welcome to comment on the online version of the paper. Correspondence should be addressed to H.C.D. (hdietz@jhmi.edu).

METHODS

Participants. Patients were recruited from the Scleroderma Center and Connective Tissue Clinic at Johns Hopkins Hospital (F.M.W. and H.C.D.). All skin biopsies and research protocols were performed in compliance with the Johns Hopkins School of Medicine Institutional Review Board and after informed consent.

Mice. All mice were cared for in strict compliance with the Animal Care and Use Committee of the Johns Hopkins University School of Medicine. *Fbn1*^{D1545E/+} and *Fbn1*^{W1572C/+} mice were generated by homologous recombination as described in the next section. *Itgb3*^{+/-} mice were purchased through Jackson Laboratories as heterozygotes. All experimental mice were on a mixed C57BL/6J and 129/SvEv background. To minimize potentially confounding background effects, all comparisons between genotypes and between treatment arms within a genotype were made between sex-matched littermates; no other randomization procedures were applied. Sample size estimates for the assessment of therapeutic responses were based on the penetrance and severity of the specific parameter under consideration in untreated cohorts.

Generation of *Fbn1*^{D1545E/+} and *Fbn1*^{W1572C/+} mice. *Fbn1*^{D1545E/+} and *Fbn1*^{W1572C/+} mice were generated by homologous recombination (Supplementary Fig. 1a). A 10-kilobase *Fbn1* fragment was generated by PCR from mouse genomic tail DNA, digested with *Acc65* and *NheI* restriction enzymes (NEB), and ligated into pSL301 (Invitrogen Corp.). Site-directed mutagenesis was performed with the QuikChange mutagenesis kit (Stratagene Inc.), creating either the D1545E or W1572C mutation. The targeting vector was assessed by sequence analysis. Site-directed mutagenesis was again performed to remove the *AatII* restriction site from pSL301. The NeoR cassette was amplified from pEGFP-C1 (Invitrogen Corp.) and the amplicon was subcloned into pCR2.1-TOPO (Invitrogen Corp.). A fragment containing the *AatII* restriction site and NeoR, with flanking *loxP* sequences, was subcloned into a unique *AatII* site in the *Fbn1* intron before exon 38. The sequences of the *loxP* sites and site-directed mutagenesis-created mutations were confirmed by direct sequencing. The vector was linearized using a unique (*NruI*) site and electroporated into R1 embryonic stem cells. Positive clones were identified by Southern blot analysis (Supplementary Fig. 1b) as described previously³¹. Positive clones were injected into 129/SvEv blastocysts at embryonic day 3.5 and transferred into pseudopregnant females. Chimeric offspring were mated to C57BL/6J mice, and germline transmission was observed for at least three independent targeting events for each genotype. All exons encompassed by and immediately flanking the targeting vector were analysed by sequencing of PCR-amplified genomic DNA derived from mutant animals to demonstrate the fidelity of targeting. Complete concordance of phenotype for three or two independent lines for mutations W1572C or D1545E, respectively, excluded any major off-target effect. Mice were genotyped on the basis of creation of a new *AclI* site (W1572C) or destruction of a *BsmAI* site (D1545E) in correctly targeted mice (Supplementary Fig. 1c). Primers used for amplification were 5'-GATCCCACCACCTGCATC-3' (sense) and 5'-CATGTGTTACAGAGAAGGACAC-3' (antisense). The *loxP*-flanked NeoR was removed by breeding *Fbn1*^{D1545E/+} and *Fbn1*^{W1572C/+} mice with transgenic mice that ubiquitously expressed Cre recombinase using a E1a promoter, purchased through Jackson Laboratories. More than 85 embryos were genotyped at embryonic day 10.5 for *Fbn1*^{D1545E/+} homozygosity.

In vivo drug treatment. All antibodies used to treat mice or cells were azide-free. Male mice were treated with β_1 integrin-activating antibody (β_1 aAb, Rat Clone 9EG7; special-ordered more than 98% pure and azide-free from BD Biosciences) or an isotype-matched control (Rat IgG2a, κ ; special-ordered more than 98% pure and azide-free from BD Biosciences) by intraperitoneal injection at 2 mg kg⁻¹ every 5 days for 12 weeks, beginning at 1 month of age. Complete blood cell counts were performed to exclude pancytopenia in β_1 aAb-treated animals (Supplementary Fig. 16a). For the TGF- β -neutralizing trial, 3-month-old male mice were treated with pan-specific TGF- β -neutralizing antibody (Mouse Clone 1D11, catalogue no. MAB1835; R&D) or an isotype control (Mouse IgG1, clone 11711, catalogue no. MAB002; R&D) by intraperitoneal injection at 10 mg kg⁻¹ on alternate days for 12 weeks. RDEA119 was provided by C. J. Thomas, S. Patnaik and J. J. Marugan (National Institutes of Health Chemical Genomics Center). RDEA119 was reconstituted in 10% 2-hydroxypropyl- β -cyclodextrin (Sigma-Aldrich) dissolved in PBS, and was administered twice daily by oral gavage at a dose of 25 mg kg⁻¹. Treatment was initiated at 1 month of age and continued for 8 weeks. 2-Hydroxypropyl- β -cyclodextrin (10% in PBS) was administered as a control. Given the absolute concordance regarding pathology and therapeutic responses for *Fbn1*^{D1545E/+} and *Fbn1*^{W1572C/+} mice seen early in this study, later studies focused on *Fbn1*^{D1545E/+} mice to limit the expense associated with *in vivo* antibody (TGF- β NaB and β_1 aAb) and drug (RDEA119) trials.

Stiffness scoring. A clinical stiffness score was assigned by five observers blinded to genotype and treatment status. Mice were assessed in random order. A score of 1 indicates no stiffness (that is, identical to wild-type mice). A score of 4 indicates extreme stiffness based on previous experience with untreated SSS mice; 2 and 3

indicate a subjective assessment of an intermediate level of stiffness. Early in the course of studies, the same mice were assessed by the same observer on a different day. This pilot demonstrated excellent intra-observer concordance. To measure stretched skin area and total surface area, mice were anaesthetized with isoflurane, and the back skin was shaved and treated briefly with Nair cream. Area measurements were performed with NIH image J software (National Institutes of Health). Mice were then suspended briefly with forceps secured to the back skin by a clamp and photographed in profile in a uniform manner (Supplementary Fig. 4a,b). There were no differences in body weight between all experimental groups (Supplementary Fig. 4c).

Histology. For tissue analysis, animals were killed with inhalational halothane (Sigma) or anaesthetized with isoflurane. Back skin was shaved and treated briefly with Nair cream before biopsy. Fixed skin was paraffin-embedded, sectioned, and stained with a standard Masson's trichrome stain. Dermal and subcutaneous fat thicknesses were measured under high-power fields as described previously³². Immunofluorescent staining was performed on frozen sections as described previously³³. Active $\alpha_v\beta_3$ was detected with the WOW-1 antibody (gift from S. Shattil) and an anti-mouse Alexa Fluor-594 F(ab')₂ fragment secondary antibody (catalogue no. A11020, Invitrogen). Other antibodies used included anti-CD45 antibody (catalogue no. 550539, BD), anti-Siglec H (catalogue no. 14-0333-81, ebiosciences) and antibodies against LAP1 (catalogue no. 141402, BioLegend), LAP2 (catalogue no. LS-C137100, Lifespan BioSciences), active TGF- β 1 (Clone LC(1-30), gift from K. Flanders), and total TGF- β 2 (catalogue no. ab66045, abcam). With the exception of WOW-1, all other antibodies were conjugated by means of an amine-based Alexa Fluor antibody labelling kit (catalogue nos A-20181, A20187, A-20185 and A-20186, Invitrogen).

Electron microscopy. Electron microscopy was performed as described previously³⁴.

Enzyme-linked immunosorbent assay. Mouse sera were collected and enzyme-linked immunosorbent assays (ELISAs) were performed with the Mouse Anti-Nuclear Antigens and Mouse Anti-Scl70 kits (catalogue nos 5210 and 6110, AlphaDiagnostic) in accordance with the manufacturer's instructions.

Cell culture. Primary human dermal fibroblasts were derived from skin biopsies from five patients with active diffuse systemic sclerosis and from six healthy controls. Biopsies were taken from the forearm and cultured as described previously³. All experiments were performed in cell lines at low (less than 5) passage. Primary MEFs were derived from embryonic day 13.5 embryos as described previously³⁵. Murine pDCs were isolated from the spleens of wild-type C57BL/6J mice by using the Plasmacytoid Dendritic Cell Isolation Kit II (catalogue no. 130-092-786, Miltenyi Biotec) and a midiMACS Separator (catalogue no. 130-042-302, Miltenyi Biotec) in accordance with the manufacturer's instructions. The pDC-containing cell suspensions routinely had more than 95% purity, as detected by flow cytometry. For MEF/pDC co-culture experiments, MEFs were cultured to complete confluence in culture medium containing RPMI 1640, 100 μ g ml⁻¹ streptomycin, 100 U ml⁻¹ penicillin, 2 mM L-glutamine (Gibco) and 10% heat-inactivated fetal calf serum. At 72 h after confluence, 5 \times 10⁴ murine splenic pDCs ml⁻¹ were plated onto MEF monolayers. After 72 h of co-culture, both adherent and non-adherent cellular fractions were harvested, counted, and analysed by flow cytometry.

Flow cytometric analysis. Mouse skin was digested for flow cytometric analysis as described previously³⁶. On average, 4 \times 10⁶ cells were obtained from a 1 \times 2 cm² piece of skin for wild-type mice, and 8 \times 10⁶ cells were obtained from either SSS mouse model. Murine Fc receptors were blocked using antibodies against mouse CD16/32 antigens (catalogue no. 553141, BD Biosciences). Murine plasmacytoid dendritic cells were isolated as reported previously³⁷. All isolated cells (including murine dermal cells, cultured MEFs, splenic murine pDCs or human dermal fibroblasts) were stained and fixed using the BD Cytofix/Cytoperm system (catalogue no. 554722, BD Biosciences). Data were acquired using CellQuest-Pro software on a FACSCalibur flow cytometer or BD FACSuite software on a FACSVerse flow cytometer (BD Biosciences). Data were analysed and all flow cytometry plots were contour plots (with outliers) that were generated with FlowJo software (TreeStar). For histograms, FlowJo software divides all events into 256 'bins', which are numerical ranges for the parameter on the x axis. The percentage of maximum (y axis) is the number of cells in each bin divided by the number of cells in the bin that contains the largest number of cells. Gating for live cells was based on staining with the LIVE/DEAD Fixable Dead Cell Stain Kit (catalogue no. L34955, Invitrogen). All staining was performed with fluorophore-conjugated primary and isotype control antibodies. All antibodies were either purchased as fluorochrome conjugates or conjugated by means of amine-based Alexa Fluor antibody labelling kits (catalogue nos A-20181, A20187, A-20185 and A-20186, Invitrogen). Mouse and human active $\alpha_v\beta_3$ was detected with fluorophore-conjugated WOW-1 antibody (gift from S. Shattil). EDTA (10 mM) and 2 mM MnCl₂ were used as negative and positive controls, respectively, for $\alpha_v\beta_3$ activation in flow cytometry experiments (Supplementary Fig. 16b)^{38,39}. Integrin $\alpha_v\beta_5$, a subtype known to react with the WOW-1 antibody³⁹, was monitored in mouse and human

cells with a specific antibody (catalogue no. LS-C36943, Lifespan Biosciences). Other antibodies used on mouse cells were: integrin β_1 (Clone eBioHMB1-1, catalogue no. 17-0291-80, eBiosciences), integrin β_3 (Clone 2C9.G3, catalogue no. 12-0611, eBiosciences), integrin α_5 (catalogue no. 11-0493-83, eBiosciences), integrin β_6 (catalogue no. LS-C152915, Lifespan BioSciences), integrin β_8 (Clone H-160, catalogue no. sc-25714, Santa Cruz Biotechnology) and pERK1/2 (catalogue no. 4370, Cell Signaling). Antibodies used for the immunological characterization of mouse cells included (from eBiosciences) IL-13 (catalogue no. 53-7133-82) and IL-22 (catalogue no. 12-7221-82); (from BD Biosciences) Ly6C (catalogue no. 560593), CD11b (catalogue no. 562127), CD4 (catalogue no. 560783), CD8 (catalogue no. 560469), CD19 (catalogue no. 550992), CD138 (catalogue no. 553714), IL-9 (catalogue no. 561492), IL-17 (catalogue no. 560522), IL-4 (catalogue no. 557739), IL-6 (catalogue no. 561376), IFN- γ (catalogue no. 560660), Foxp3 (catalogue no. 560047) and B220 (catalogue no. 561226); and (from Biolegend) CD3 (catalogue no. 100227) and Siglec H (catalogue no. 129611). The antibody against IFN- α was from PBL interferon source (catalogue no. 22100-3). The antibody against CD317 was from eBiosciences (catalogue no. 46-3172-82). Antibodies used with human fibroblasts were integrin β_1 (Clone MAR4, catalogue no. 557332, BD Biosciences) and integrin β_3 (Clone VI-PL2, catalogue no. 17-0619-42, eBiosciences).

Stimulation of human dermal fibroblasts with TGF- β 1 *in vitro*. All cells were counted at splitting and all treatments were performed at 70% confluence. Cells were serum-starved for 48 h before stimulation with 2 ng ml⁻¹ recombinant TGF- β 1 (catalogue no. 240-B-010, R&D). When TGF- β 1 or vehicle was added, cell culture dishes were immediately rocked on the same rocker three times in air/CO₂ (19:1) at 37 °C, to control for mechanical activation of mitogen-activated protein kinase. Before lysate harvest, cells were washed with prewarmed (42 °C) 1 × PBS (Gibco). All antibody treatments of human fibroblasts were added during starvation for 48 h before stimulation with TGF- β 1, whereas inhibitors SD208 (1 μ M) and UO126 (10 μ M) (catalogue nos 616456 and 662005, EMD Millipore) were added 6 h before stimulation. Antibodies used *in vitro* were mouse IgG1 (0.2 mg ml⁻¹, Clone P3.6.2.8.1, catalogue no. 16-4714-81, eBiosciences), IgG2a (0.2 mg ml⁻¹, Clone eBM2a, catalogue no. 16-4724, eBiosciences), α , β ₃-blocking (30 μ g ml⁻¹, Clone LM609, catalogue no. MAB1976Z, Millipore), β ₁-activating (7 μ g ml⁻¹, Clone TS2/16, catalogue no. 14-0299, eBiosciences) and β ₁-blocking (0.2 mg ml⁻¹, Clone P4C10, catalogue no. MAB1987Z, Millipore) antibodies.

Western blotting. Before lysate harvest, cells were washed with prewarmed (42 °C) 1 × PBS (Gibco). Total protein was isolated from cells with ice-cold RIPA buffer (25 mM Tris/HCl pH 7.6, 150 mM NaCl, 1% Nonidet P40, 1% sodium deoxycholate, 0.1% SDS) with phosphatase and protease inhibitors (catalogue nos

04906837001 and 11836170001, Roche). Western blotting was performed using the Bio-Rad and LiCor Odyssey detection systems as described previously³. The relative intensities were measured using LiCor Odyssey software. The following antibodies were used: phosphorylated and total ERK (Clone D13.14.4E, catalogue no. 4370, and Clone 3A7, catalogue no. 9107, Cell Signaling), vinculin (Clone hVIN-1, catalogue no. V9131, Sigma), and phosphorylated and total Smad3 (catalogue nos 1880-1 and 1735-1, Epitomics).

RNA isolation and qPCR. Total RNA was isolated from cultured cells or tissue by using Trizol (Invitrogen) in accordance with the manufacturer's protocol. Quantitative PCR for miR-29a and 18S ribosomal RNA was performed with pre-designed Taqman primers and probes (ABI) in accordance with the manufacturer's instructions. Relative quantification for each transcript was obtained by normalizing against 18S transcript abundance according to the formula $2^{-C_t}/2^{-C_t(18S)}$.

Statistics and graphs. All quantitative data are shown as standard boxplots produced in R statistical software. The upper and lower margins of each box define the 75th and 25th centiles, respectively; the internal line defines the median, and the whiskers define the range. Statistical analysis was performed with a two-tailed *t*-test, assuming equal variance between the compared groups (asterisk, $P < 0.05$; two asterisks, $P < 0.01$; dagger, $P < 0.001$; double dagger, $P < 0.0001$). Values outside the interquartile range are shown as open circles (R software default), but were not excluded from or treated differently in statistical analyses.

31. Judge, D. P. *et al.* Evidence for a critical contribution of haploinsufficiency in the complex pathogenesis of Marfan syndrome. *J. Clin. Invest.* **114**, 172–181 (2004).
32. Castellino, F. V. *et al.* Amelioration of dermal fibrosis by genetic deletion or pharmacologic antagonism of lysophosphatidic acid receptor 1 in a mouse model of scleroderma. *Arthritis Rheum.* **63**, 1405–1415 (2011).
33. HogenEsch, H. *et al.* Expression of chitinase-like proteins in the skin of chronic proliferative dermatitis (*cpdm/cpdm*) mice. *Exp. Dermatol.* **15**, 808–814 (2006).
34. Davis, E. C. *et al.* Remodeling of elastic fiber components in scleroderma skin. *Connect. Tissue Res.* **40**, 113–121 (1999).
35. Garfield, A. S. Derivation of primary mouse embryonic fibroblast (PMEF) cultures. *Methods Mol. Biol.* **633**, 19–27 (2010).
36. Lakos, G. *et al.* Animal models of scleroderma. *Methods Mol. Med.* **102**, 377–393 (2004).
37. Gehrie, E. *et al.* Plasmacytoid dendritic cells in tolerance. *Methods Mol. Biol.* **677**, 127–147 (2011).
38. Pampori, N. *et al.* Mechanisms and consequences of affinity modulation of integrin $\alpha_v\beta_3$ detected with a novel patch-engineered monovalent ligand. *J. Biol. Chem.* **274**, 21609–21616 (1999).
39. Kiosses, W. B. *et al.* Rac recruits high-affinity integrin $\alpha_v\beta_3$ to lamellipodia in endothelial cell migration. *Nature Cell Biol.* **3**, 316–320 (2001).

A directional switch of integrin signalling and a new anti-thrombotic strategy

Bo Shen¹, Xiaojuan Zhao¹, Kelly A. O'Brien¹, Aleksandra Stojanovic-Terpo¹, M. Keegan Delaney¹, Kyungho Kim¹, Jaehyung Cho¹, Stephen C.-T. Lam¹ & Xiaoping Du¹

Integrins have a critical role in thrombosis and haemostasis¹. Antagonists of the platelet integrin $\alpha_{IIb}\beta_3$ are potent anti-thrombotic drugs, but also have the life-threatening adverse effect of causing bleeding^{2,3}. It is therefore desirable to develop new antagonists that do not cause bleeding. Integrins transmit signals bidirectionally^{4,5}. Inside-out signalling activates integrins through a talin-dependent mechanism^{6,7}. Integrin ligation mediates thrombus formation and outside-in signalling^{8,9}, which requires $G_{\alpha_{13}}$ and greatly expands thrombi. Here we show that $G_{\alpha_{13}}$ and talin bind to mutually exclusive but distinct sites within the integrin β_3 cytoplasmic domain in opposing waves. The first talin-binding wave mediates inside-out signalling and also ligand-induced integrin activation, but is not required for outside-in signalling. Integrin ligation induces transient talin dissociation and $G_{\alpha_{13}}$ binding to an EXE motif (in which X denotes any residue), which selectively mediates outside-in signalling and platelet spreading. The second talin-binding wave is associated with clot retraction. An EXE-motif-based inhibitor of $G_{\alpha_{13}}$ -integrin interaction selectively abolishes outside-in signalling without affecting integrin ligation, and suppresses occlusive arterial thrombosis without affecting bleeding time. Thus, we have discovered a new mechanism for the directional switch of integrin signalling and, on the basis of this mechanism, designed a potent new anti-thrombotic drug that does not cause bleeding.

Integrin signalling involves the binding of several molecules to the cytoplasmic domain of integrin β -subunits including talin^{6,7}, kindlins^{10,11}, SRC^{12,13} and $G_{\alpha_{13}}$ ⁸ (Fig. 1a). Co-immunoprecipitation of $G_{\alpha_{13}}$ with various β_3 carboxy-terminal truncation mutants suggests that $G_{\alpha_{13}}$ binding involves the β_3 sequence between Lys 729 and Thr 741 (Fig. 1b and Extended Data Fig. 2a), but not the kindlin- or SRC-binding sequences (Fig. 1a, b). Alignment of different β cytoplasmic domains reveals an EXE motif in this region, in which the first and third Glu residues are conserved among most β subunits, but not β_8 (Fig. 1a). The EXE-motif-containing β_1 , β_2 and β_3 all bound $G_{\alpha_{13}}$, but not β_8 (Fig. 1c and Extended Data Fig. 2f). Wild-type and E732A mutant β_3 bound to $G_{\alpha_{13}}$, but the E731A, E733A, AAA (E731–733A) (Fig. 1d and Extended Data Fig. 2b), DED (E731D/E733D) and QSE (E731Q/E732S) (Extended Data Fig. 2e) mutants did not, indicating that the first and third Glu within the EXE motif are important for $G_{\alpha_{13}}$ binding. Synthetic peptides containing the EEERA sequence inhibited $G_{\alpha_{13}}$ - β_3 interaction (see below), verifying this EXE-motif-containing $G_{\alpha_{13}}$ -binding site.

The EXE motif is located in a talin-binding region (Fig. 1a)^{14,15}. Overexpression of the integrin-binding talin head domain (THD) in $\alpha_{IIb}\beta_3$ -expressing cells inhibited $G_{\alpha_{13}}$ co-immunoprecipitation with β_3 (Fig. 1e). Purified recombinant THD and $G_{\alpha_{13}}$ competed directly for binding to purified glutathione S-transferase (GST)- β_3 cytoplasmic domain fusion protein (GST- β_3 CD) (Fig. 1f, g and Extended Data

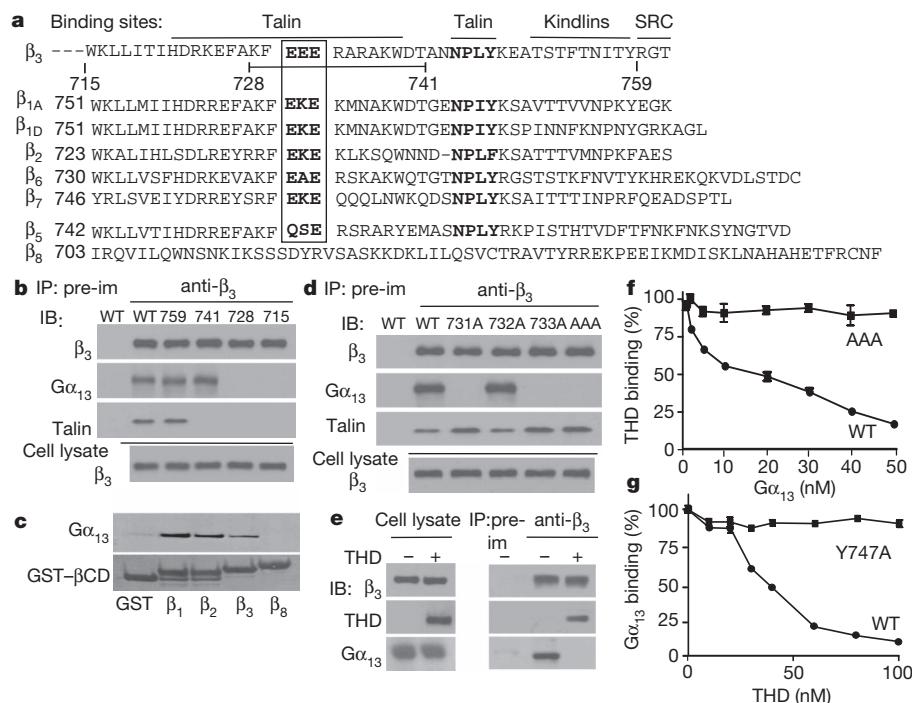


Figure 1 | Mutually exclusive binding of talin and $G_{\alpha_{13}}$ to β_3 . **a**, The sequence of the human β_3 cytoplasmic domain and its alignment with other β subunits, showing conserved EXE motifs and binding sites for talin, kindlins and SRC. **b**, Co-immunoprecipitation of wild-type (WT) and truncated mutant β_3 with $G_{\alpha_{13}}$ and talin using anti- β_3 or control pre-immune (pre-im) rabbit serum. Immunoprecipitates (IP) and CHO cell lysates (10% of that used in immunoprecipitation) were immunoblotted (IB) with indicated antibodies. **c**, Binding of purified recombinant $G_{\alpha_{13}}$ to glutathione-bead-bound GST, and cytoplasmic domain fusion proteins GST- β_1 CD, GST- β_2 CD, GST- β_3 CD or GST- β_8 CD. **d**, Co-immunoprecipitation of CHO-cell-expressed wild-type or EXE-motif-mutated β_3 with $G_{\alpha_{13}}$ and talin using anti- β_3 or pre-immune rabbit serum. **e**, Co-immunoprecipitation of CHO-cell-expressed integrin $\alpha_{IIb}\beta_3$ with $G_{\alpha_{13}}$ and THD after transfection with cDNA encoding THD. **f**, **g**, Inhibition of the binding of THD (20 nM) (**f**) or $G_{\alpha_{13}}$ (40 nM) (**g**) to immobilized GST- β_3 CD proteins (wild-type and negative control mutants) by increasing concentrations of $G_{\alpha_{13}}$ (**f**) or THD (**g**). Bound $G_{\alpha_{13}}$ or THD was detected using anti- $G_{\alpha_{13}}$ or anti-talin. Error bars represent mean \pm s.d.

¹Department of Pharmacology, University of Illinois at Chicago, 835 South Wolcott Avenue, Chicago, Illinois 60612, USA.

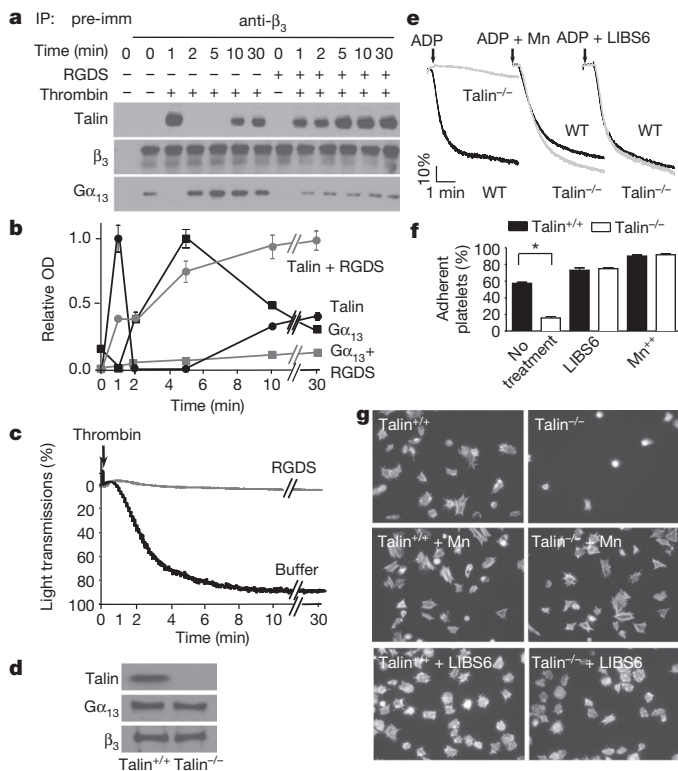


Figure 2 | Dynamics of talin and $G\alpha_{13}$ binding to β_3 and the role of talin in integrin signalling. **a–c**, Human platelets were stimulated with 0.025 U ml^{-1} α -thrombin (in an aggregometer) with or without 2 mM integrin inhibitor RGDS, solubilized at various time points, immunoprecipitated with anti- β_3 or pre-immune rabbit serum, and immunoblotted for $G\alpha_{13}$, talin and β_3 (additional controls in Extended Data Fig. 3d). **a**, Typical immunoblots. **b**, Quantification of immunoblots (mean \pm s.d., three experiments). OD, optical density. **c**, Turbidity changes indicating integrin-dependent platelet aggregation. **d**, Immunoblotting of talin 1 in wild-type and *Tln1*^{-/-} (talin 1^{-/-}) mouse platelets. **e**, Aggregation of wild-type and talin 1^{-/-} platelets stimulated with $5 \mu\text{M}$ ADP in the presence of $20 \mu\text{g ml}^{-1}$ fibrinogen, with or without 1 mM MnCl_2 or $0.3 \mu\text{g ml}^{-1}$ LIBS6. **f**, Adhesion of unstimulated mouse platelets to immobilized fibrinogen for 1 h, with or without 1 mM MnCl_2 or $0.18 \mu\text{g ml}^{-1}$ LIBS6 (quantified as percentage of loaded platelets, mean \pm s.d., $n = 4$, $*P < 0.001$). **g**, Images of phalloidin-stained mouse platelets spreading on fibrinogen for 1 h, with or without 1 mM MnCl_2 or $0.18 \mu\text{g ml}^{-1}$ LIBS6 (quantification in Extended Data Fig. 4e).

Fig. 2c, d), indicating that $G\alpha_{13}$ and talin are mutually exclusive in binding to β_3 . Interestingly, the binding of talin and $G\alpha_{13}$ is regulated temporally during integrin signalling (Fig. 2). The first wave of talin association with $\alpha_{\text{IIb}}\beta_3$ occurred after thrombin-stimulated inside-out signalling (Fig. 2a, b) and before the onset of integrin ligation (as indicated by platelet aggregation (Fig. 2c)). However, after integrin ligation, talin association with $\alpha_{\text{IIb}}\beta_3$ was diminished (Fig. 2a, b). The second wave of talin- β_3 association occurred after full platelet aggregation (Fig. 2a–c), the timing of which correlates with clot retraction. Opposite to the waves of talin binding, the $G\alpha_{13}$ - β_3 association was even lower than the basal level during inside-out signalling when the first talin-binding wave occurred (Fig. 2a, b), but peaked after integrin ligation when the first talin-binding wave subsided, and then decreased again during the second talin-binding wave (Fig. 2a, b). Thus, inside-out and various phases of outside-in signalling are associated with coordinated and opposing waves of $G\alpha_{13}$ and talin binding to β_3 .

Importantly, an increase in $G\alpha_{13}$ binding to integrin can only be induced when integrin is activated in the presence of fibrinogen, but not by integrin activation alone (Extended Data Fig. 3a). Conversely, the integrin inhibitors RGDS (Arg-Gly-Asp-Ser, Fig. 2a, b) or EDTA (ethylenediaminetetraacetic acid, Extended Data Fig. 3b, c) prevented

dissociation of talin from β_3 and inhibited $G\alpha_{13}$ - β_3 interaction in thrombin-stimulated platelets. Thus, the switch from a talin-bound to a $G\alpha_{13}$ -bound state of $\alpha_{\text{IIb}}\beta_3$ is initiated by the binding of macro-molecular ligands.

The opposing waves of talin and $G\alpha_{13}$ binding to β_3 suggest that the interaction of these two proteins with β_3 selectively mediates inside-out and outside-in signalling, respectively. This hypothesis was tested using talin knockout¹⁶ and shRNA-induced talin knockdown platelets, which are defective in adenosine diphosphate (ADP)/fibrinogen-induced, integrin-dependent aggregation (Fig. 2d, e and Extended Data Fig. 4a, c). Their defective aggregation was fully corrected with manganese or an integrin-activating antibody (LIBS6) (Fig. 2e and Extended Data Fig. 4c), which activate integrins independently of inside-out signalling. These data confirm a role for talin in inside-out signalling^{6,15,17}. It is established that inside-out signalling is not the only pathway of $\alpha_{\text{IIb}}\beta_3$ activation. Integrin-fibrinogen interaction may occur independently of inside-out signalling when fibrinogen changes conformation, either by immobilization or conversion to fibrin^{18,19}. This is because the initial contact of the exposed ligand recognition sequence, RGD, with resting integrins triggers ligand-induced integrin activation²⁰. Interestingly, adhesion of resting talin-knockout or -knockdown platelets to immobilized fibrinogen was defective (Fig. 2f and Extended Data Fig. 4b), indicating the importance of talin in platelet adhesion to immobilized fibrinogen in the absence of inside-out signalling. However, addition of manganese or integrin-activating antibody fully corrected talin-knockout and -knockdown platelet adhesion and spreading (and also the spreading of talin-binding-defective mutant β_3 -expressing Chinese hamster ovary (CHO) cells²¹) on immobilized fibrinogen (Fig. 2f, g and Extended Data Fig. 4b, d, e). Thus, the role of talin in resting platelet adhesion to fibrinogen is solely due to its importance in ligand-induced integrin activation. Because cell spreading requires the early phase of outside-in signalling, these data further demonstrate that talin is not required for the early phase of outside-in signalling leading to cell spreading once its role in integrin activation is bypassed.

To assess whether $G\alpha_{13}$ binding to the EXE motif selectively mediates outside-in signalling without perturbing talin-dependent integrin function, wild-type and AAA mutant β_3 -transfected *ITGB3* (β_3)^{-/-} bone marrow stem cells (from β_3 ^{-/-} mice) were transplanted into irradiated β_3 ^{-/-} mice. The platelets from the recipient mice expressed similar levels of wild-type or AAA mutant β_3 (Fig. 3a and Extended Data Fig. 5a). The AAA mutation inhibited β_3 interaction with $G\alpha_{13}$, but not talin (or SRC) (Fig. 3b and Extended Data Fig. 5b), during integrin signalling. The AAA mutation also had no effect on agonist-induced soluble fibrinogen binding (Fig. 3c). Thus, the EXE motif is not required for talin-dependent inside-out signalling. By contrast, the AAA mutant β_3 -expressing platelets were defective in spreading on immobilized fibrinogen (Fig. 3d and Extended Data Fig. 5c, d). Thus, $G\alpha_{13}$ -binding deficiency in β_3 causes a selective defect in integrin outside-in signalling and platelet spreading. Similarly, AAA and more conserved DED or QSE β_3 mutants expressed in CHO cells, all defective in $G\alpha_{13}$ binding (Extended Data Fig. 2e), and were also defective in spreading on fibrinogen (Fig. 3e, f and Extended Data Fig. 6a–c). However, AAA mutant β_3 expressed in CHO cells had no negative effect on THD binding, in contrast to the Y74A mutant (Extended Data Fig. 6d, e). In addition, AAA-expressing cells showed defects in integrin-dependent activation of SRC (as shown by phosphorylation at Tyr416) and transient inhibition of RHOA during cell spreading (Fig. 3g and Extended Data Fig. 6f), both of which are important elements of outside-in signalling. Together with previous studies that identified β_3 sequences mediating talin binding (Fig. 1a)^{6,15,17,22}, our data suggest that talin and $G\alpha_{13}$ dynamically interact with distinct recognition sequences in the same region of β_3 to serve as a molecular switch controlling the direction of integrin signalling.

The specific role of the EXE motif in outside-in signalling prompted us to design selective inhibitors of outside-in signalling. We synthesized several myristoylated (Myr) EXE-motif-containing β_3 peptides: mP₅

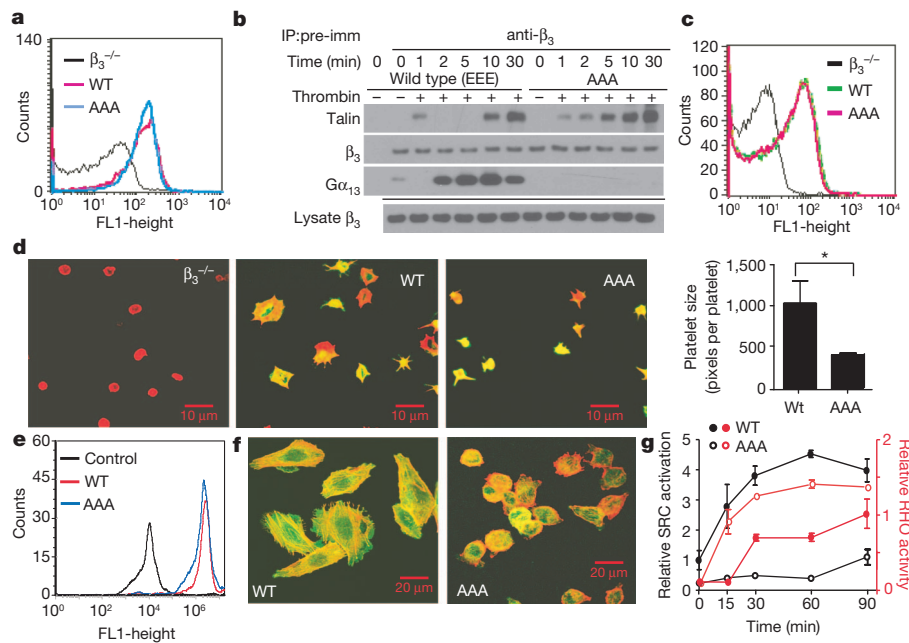


Figure 3 | The selective role of $G\alpha_{13}$ EXE binding in integrin outside-in signalling. **a**, Flow cytometric analysis of β_3 expression in platelets from $\beta_3^{-/-}$ mice transplanted with wild-type or AAA mutant β_3 -transfected bone marrow stem cells. $\beta_3^{-/-}$ platelets served as negative control. Picture shows relative fluorescence (FL1) on the x axis and number of events (count) on the y axis. **b**, Mouse platelets expressing wild-type (EEE) or AAA mutant β_3 were stimulated with 0.025 U ml^{-1} α -thrombin, solubilized at various time points, immunoprecipitated with anti- β_3 or pre-immune rabbit serum and immunoblotted for $G\alpha_{13}$, talin and β_3 . **c**, PAR4 agonist peptide (PAR4-AP)-induced binding of Oregon Green-labelled fibrinogen to wild-type or AAA mutant $\alpha_{IIb}\beta_3$ -expressing platelets with $\beta_3^{-/-}$ platelets as a negative control. **d**, Confocal images of $\beta_3^{-/-}$ platelets and $\beta_3^{-/-}$ platelets expressing wild-type or AAA-mutant β_3 spreading on fibrinogen and surface area quantification (mean \pm s.e.m.). Merged anti- β_3 (green) and Alexa Fluor 546-conjugated phalloidin (red) fluorescence. **e**, Flow cytometric analysis of wild-type or β_3 AAA mutant $\alpha_{IIb}\beta_3$ expression in CHO-1b9 cells. **f**, Confocal images of phalloidin (red)/anti- β_3 (green)-double stained wild-type and AAA-mutant $\alpha_{IIb}\beta_3$ -expressing CHO cell spreading on fibrinogen (45 min). **g**, RHOA activation and SRC Tyr 416 phosphorylation in wild-type or AAA mutant $\alpha_{IIb}\beta_3$ -expressing CHO-1b9 cells adherent to fibrinogen (mean \pm s.d., $n = 3$).

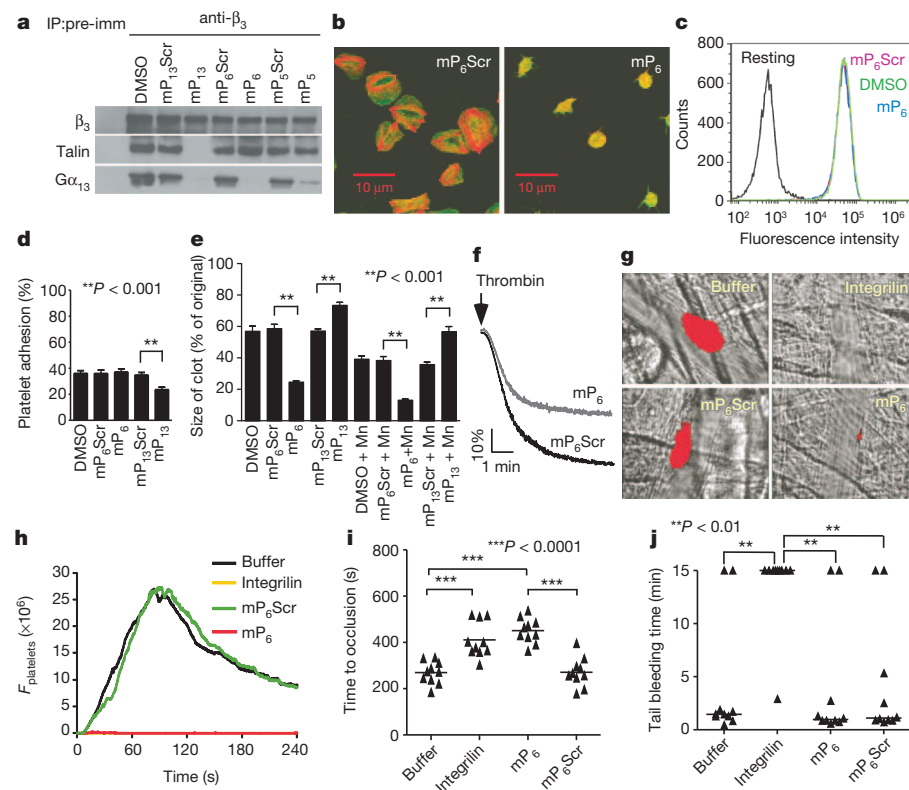


Figure 4 | A new anti-thrombotic that does not cause bleeding. **a**, The effects of $500 \mu\text{M}$ mP_{13} , mP_6 or mP_5 on co-immunoprecipitation of β_3 with $G\alpha_{13}$ or talin in thrombin-stimulated platelets in comparison with scrambled (Scr) controls (also see Extended Data Fig. 7). **b**, Confocal images of phalloidin (red)/anti- β_3 (green)-double-stained human platelets treated with $100 \mu\text{M}$ mP_6 or $mP_6\text{Scr}$ spreading on immobilized fibrinogen (1 h). **c**, PAR4-AP-induced Oregon Green-labelled fibrinogen binding to human platelets pre-treated with DMSO or $100 \mu\text{M}$ $mP_6\text{Scr}$ or mP_6 . **d**, Effect of mP_6 and mP_{13} ($250 \mu\text{M}$) on resting platelet adhesion to immobilized fibrinogen as compared with scrambled peptides (mean \pm s.d., $n = 4$). **e**, Effect of mP_6 or mP_{13} ($250 \mu\text{M}$) on clot retraction of human platelet-rich plasma, with or without 1 mM manganese (Mn) (mean \pm s.d., $n = 3$). **f**, Effects of $10 \mu\text{M}$ mP_6 or $mP_6\text{Scr}$ micelles on platelet aggregation induced by 0.03 U ml^{-1} thrombin. **g**, Comparison of mP_6 micelle ($5 \mu\text{mol kg}^{-1}$) with Integrilin ($12 \mu\text{mol kg}^{-1}$) and their respective controls in inhibiting laser-induced arteriolar thrombosis in mice. Representative images at 60 s after injury are shown. Platelet thrombi were indicated by DyLight 649-labelled nonblocking rat anti-mouse GPIIb/IIIa (red). **h**, Quantification of **g**. The median integrated platelet fluorescence ($F_{\text{platelets}}$) during thrombosis at 30 s injury sites in three mice. **i**, Comparison of mP_6 ($5 \mu\text{mol kg}^{-1}$) with Integrilin ($5 \mu\text{mol kg}^{-1}$) and their respective controls in inhibiting FeCl_3 -induced carotid artery thrombosis in mice. **j**, Comparison of mP_6 ($5 \mu\text{mol kg}^{-1}$) with Integrilin ($5 \mu\text{mol kg}^{-1}$) and controls in mouse tail bleeding time analysis.

(Myr-EEERA), mP₆ (Myr-FEEERA) and mP₁₃ (Myr-KFEEERARAKWDT). These peptides inhibited co-immunoprecipitation between α_{13} and β_3 (Fig. 4a and Extended Data Fig. 7a–d), indicating that the minimal sequence of EEERA is sufficient to bind α_{13} . By contrast, only mP₁₃, but not mP₆ (or mP₅), inhibited talin association with β_3 (Fig. 4a), indicating that mP₆ does not interact with talin. mP₆ inhibited platelet spreading on fibrinogen (Fig. 4b and Extended Data Fig. 7e), but had no effect on either agonist-induced fibrinogen/PAC1 (an ligand-mimetic antibody recognizing activated $\alpha_{IIb}\beta_3$) binding to platelets (Fig. 4c and Extended Data Fig. 7f, g) or platelet adhesion to immobilized fibrinogen (Fig. 4d). Interestingly, mP₆ did not inhibit, but rather accelerated, platelet-dependent clot retraction (Fig. 4e). These data indicate that the EXE-based inhibitor mP₆ selectively inhibits the early phase of outside-in signalling without affecting talin-dependent inside-out signalling, ligand-induced integrin activation, or the late phase of outside-in signalling associated with the second wave of talin binding. By contrast, mP₁₃ inhibited inside-out and outside-in signalling, as it inhibited fibrinogen binding (Extended Data Fig. 7h), platelet adhesion (Fig. 4d) and clot retraction (Fig. 4e) (not reversed by manganese, as previously shown using talin^{-/-} platelets¹⁶). Thus, mP₆ selectively interferes with the early phase of outside-in signalling, but mP₁₃ affects all phases of integrin signalling. Importantly, mP₆ inhibited the second wave of thrombin-induced platelet aggregation *in vitro* (Fig. 4f), and when injected into mice as micelles, was as potent as the currently used integrin antagonist Integrilin in inhibiting laser-induced arteriolar thrombosis (Fig. 4g, h, Extended Data Fig. 8a, b and Supplementary Videos 1–4) and FeCl₃-induced occlusive carotid artery thrombosis (Fig. 4i and Extended Data Fig. 8c). Notably, at the concentration at which both Integrilin and mP₆ similarly inhibited occlusive thrombosis, Integrilin considerably prolonged tail bleeding and increased blood loss, whereas mP₆ had no such adverse effect (Fig. 4j and Extended Data Fig. 8d). Thus, we have discovered a novel anti-thrombotic that prevents thrombosis without causing bleeding.

Together, our study provides a conceptual advance by revealing a molecular switch controlling the directions and consequences of integrin signalling. We show that the switch between inside-out and outside-in signalling is mediated by coordinated but opposing waves of talin and α_{13} binding to distinct yet adjacent sequences within the β_3 cytoplasmic domain. The discovery of this signalling switch forms a conceptual basis for selectively inhibiting outside-in signalling without perturbing the ligand-binding function of integrins. Importantly, we translated this new concept into a potent novel anti-thrombotic, which, unlike currently available integrin antagonists or other anti-thrombotics, potentially inhibits arterial thrombosis without the adverse effect of causing bleeding (Fig. 4g–j), a potentially life-threatening problem that limits the clinical use of current anti-integrin and anti-thrombotic therapies.

METHODS SUMMARY

Co-immunoprecipitation. Co-immunoprecipitation was performed as described previously⁸ using platelets or $\alpha_{IIb}\beta_3$ -expressing CHO-1b9 cells²³.

Myristoylated peptide inhibitors. Myristoylated peptide inhibitors were synthesized and purified at the Research Resource Center at University of Illinois at Chicago. These include mP₅, mP₆ and mP₁₃, as well as their respective scrambled controls: mP₁₃Scr (Myr-EEERERKDWAKFT), mP₅Scr (Myr-EEARE) and mP₆Scr (Myr-ERAFEE). The peptides were prepared in DMSO for *in vitro* and in micellar formulation for *in vivo* (and *in vitro*) uses. The micellar formulation has a molar ratio of PEG₂₀₀₀-DSPE, 1- α -phosphatidylcholine, and peptides of 45:5:2, and was prepared as described previously²⁴. mP₆ is similar to mP₆Scr in uptake by platelets (Extended Data Fig. 9a) and does not cause significant changes in haemogram *in vivo* (Extended Data Fig. 9b).

Bone marrow stem cells. Bone marrow stem cells from 6–8-week-old integrin $\beta_3^{-/-}$ or C57BL/6 mice were infected twice with concentrated lentivirus containing shRNA or complementary DNA constructs, then retro-orbitally injected into irradiated recipient mice (5Gy for integrin $\beta_3^{-/-}$ mice and 9.6Gy for C57BL/6 mice) 1 day after irradiation⁸. Platelet functional analyses^{13,25}, flow cytometry²⁶, laser-induced cremaster muscle arterial thrombosis²⁷ and FeCl₃-induced carotid

arterial thrombosis²⁸ were performed as described previously. Data were analysed using *t*-test or one-way analysis of variance.

Tail bleeding time. Analysis was performed as described previously²⁹. Time to stable cessation of the bleeding is defined as no re-bleeding for 60 s. Bleeding exceeding 15 min was immediately stopped. Data were analysed using the Mann–Whitney test.

Online Content Any additional Methods, Extended Data display items and Source Data are available in the online version of the paper; references unique to these sections appear only in the online paper.

Received 8 November 2012; accepted 28 August 2013.

Published online 27 October 2013.

- Shattil, S. J. & Newman, P. J. Integrins: dynamic scaffolds for adhesion and signaling in platelets. *Blood* **104**, 1606–1615 (2004).
- Coller, B. S. Anti-GPIIb/IIIa drugs: current strategies and future directions. *Thromb. Haemost.* **86**, 427–443 (2001).
- Serebruany, V. L., Malinin, A. I., Eisert, R. M. & Sane, D. C. Risk of bleeding complications with antiplatelet agents: meta-analysis of 338,191 patients enrolled in 50 randomized controlled trials. *Am. J. Hematol.* **75**, 40–47 (2004).
- Hynes, R. O. Integrins: bidirectional, allosteric signaling machines. *Cell* **110**, 673–687 (2002).
- Moissoglu, K. & Schwartz, M. A. Integrin signalling in directed cell migration. *Biol. Cell* **98**, 547–555 (2006).
- Tadokoro, S. *et al.* Talin binding to integrin beta tails: a final common step in integrin activation. *Science* **302**, 103–106 (2003).
- Ye, F., Kim, C. & Ginsberg, M. H. Molecular mechanism of inside-out integrin regulation. *J. Thromb. Haemost.* **9** (Suppl. 1), 20–25 (2011).
- Gong, H. *et al.* G protein subunit G α_{13} binds to integrin $\alpha_{IIb}\beta_3$ and mediates integrin “outside-in” signaling. *Science* **327**, 340–343 (2010).
- Shen, B., Delaney, M. K. & Du, X. Inside-out, outside-in, and inside-outside-in: G protein signaling in integrin-mediated cell adhesion, spreading, and retraction. *Curr. Opin. Cell Biol.* **24**, 600–606 (2012).
- Moser, M., Nieswandt, B., Ussar, S., Pozgajova, M. & Fassler, R. Kindlin-3 is essential for integrin activation and platelet aggregation. *Nature Med.* **14**, 325–330 (2008).
- Ma, Y. Q., Qin, J., Wu, C. & Plow, E. F. Kindlin-2 (Mig-2): a co-activator of β_3 integrins. *J. Cell Biol.* **181**, 439–446 (2008).
- Obergfell, A. *et al.* Coordinate interactions of Csk, Src, and Syk kinases with $\alpha_{IIb}\beta_3$ initiate integrin signaling to the cytoskeleton. *J. Cell Biol.* **157**, 265–275 (2002).
- Flevaris, P. *et al.* A molecular switch that controls cell spreading and retraction. *J. Cell Biol.* **179**, 553–565 (2007).
- Patil, S. *et al.* Identification of a talin-binding site in the integrin β_3 subunit distinct from the NPLY regulatory motif of post-ligand binding functions. The talin N-terminal head domain interacts with the membrane-proximal region of the β_3 cytoplasmic tail. *J. Biol. Chem.* **274**, 28575–28583 (1999).
- Wegener, K. L. *et al.* Structural basis of integrin activation by talin. *Cell* **128**, 171–182 (2007).
- Haling, J. R., Monkley, S. J., Critchley, D. R. & Petrich, B. G. Talin-dependent integrin activation is required for fibrin clot retraction by platelets. *Blood* **117**, 1719–1722 (2011).
- Petrich, B. G. *et al.* Talin is required for integrin-mediated platelet function in hemostasis and thrombosis. *J. Exp. Med.* **204**, 3103–3111 (2007).
- Coller, B. S. Interaction of normal, thrombasthenic, and Bernard-Soulier platelets with immobilized fibrinogen: defective platelet-fibrinogen interaction in thrombasthenia. *Blood* **55**, 169–178 (1980).
- Ugarova, T. P. *et al.* Conformational changes in fibrinogen elicited by its interaction with platelet membrane glycoprotein GPIIb-IIIa. *J. Biol. Chem.* **268**, 21080–21087 (1993).
- Du, X. *et al.* Ligands “activate” integrin $\alpha_{IIb}\beta_3$ (platelet GPIIb-IIIa). *Cell* **65**, 409–416 (1991).
- Arias-Salgado, E. G., Lizano, S., Shattil, S. J. & Ginsberg, M. H. Specification of the direction of adhesive signaling by the integrin β cytoplasmic domain. *J. Biol. Chem.* **280**, 29699–29707 (2005).
- Goksoy, E. *et al.* Structural basis for the autoinhibition of talin in regulating integrin activation. *Mol. Cell* **31**, 124–133 (2008).
- Xi, X., Bodnar, R. J., Li, Z. Y., Lam, S. C. T. & Du, X. P. Critical roles for the COOH-terminal NITY and RGT sequences of the integrin β_3 cytoplasmic domain in inside-out and outside-in signaling. *J. Cell Biol.* **162**, 329–339 (2003).
- Krishnasdas, A., Rubinstein, I. & Onyuksel, H. Sterically stabilized phospholipid mixed micelles: *in vitro* evaluation as a novel carrier for water-insoluble drugs. *Pharm. Res.* **20**, 297–302 (2003).
- O'Brien, K. A., Gartner, T. K., Hay, N. & Du, X. ADP-stimulated activation of Akt during integrin outside-in signaling promotes platelet spreading by inhibiting glycogen synthase kinase-3 β . *Arterioscler. Thromb. Vasc. Biol.* **32**, 2232–2240 (2012).
- Delaney, M. K., Liu, J., Zheng, Y., Berndt, M. C. & Du, X. The role of Rac1 in glycoprotein Ib-IX-mediated signal transduction and integrin activation. *Arterioscler. Thromb. Vasc. Biol.* **32**, 2761–2768 (2012).
- Cho, J. *et al.* Protein disulfide isomerase capture during thrombus formation *in vivo* depends on the presence of β_3 integrins. *Blood* **120**, 647–655 (2012).
- O'Brien, K. A., Stojanovic-Terpo, A., Hay, N. & Du, X. An important role for Akt3 in platelet activation and thrombosis. *Blood* **118**, 4215–4223 (2011).
- Marjanovic, J. A., Li, Z., Stojanovic, A. & Du, X. Stimulatory roles of nitric-oxide synthase 3 and guanylyl cyclase in platelet activation. *J. Biol. Chem.* **280**, 37430–37438 (2005).

Supplementary Information is available in the online version of the paper.

Acknowledgements We thank T. Kozasa, B. Kreutz and C. Chow for providing purified recombinant $G\alpha_{13}$ protein; and B. Petrich and D. Critchley for providing talin^{-/-} mice. We acknowledge that H. Gong performed experiments for this project. This work is supported by grants from National Heart, Lung, and Blood Institute (HL080264, HL062350 (X.D.) and HL109439 (J.C.)).

Author Contributions B.S. performed most of the experiments and participated in experimental design, data analysis and manuscript writing. X.Z., K.A.O., A.S.-T. and M.K.D. each performed parts of the experiments and participated in aspects of data

analyses and manuscript writing. K.K. and J.C. performed laser-induced thrombosis experiments and data analysis; S.C.-T.L. provided talin constructs and purified proteins, and participated in discussions and data analyses; X.D. designed and directed the research, analysed data and wrote the paper.

Author Information Reprints and permissions information is available at www.nature.com/reprints. The authors declare competing financial interests: details accompany the full-text HTML version of the paper at www.nature.com/nature. Readers are welcome to comment on the online version of the paper. Correspondence and requests for materials should be addressed to X.D. (xdu@uic.edu).

METHODS

Animals and reagents. Integrin $\beta_3^{-/-}$ mice were obtained from the Jackson Laboratory. *Tln1^{fl/fl}*, PF4-Cre mice were provided by B. Petrich and D. Critchley¹⁶. Animal usage and protocol were approved by the institutional animal care committee of the University of Illinois at Chicago. For all animal experiments, mice with similar age, weight and sex ratios (1:1, except for laser-induced thrombosis) were used for control and specific treatment. The individual mice chosen for specific treatment were decided randomly. Human integrin β_3 cDNA was cloned into pcDNA3.1 vector following digestion with HindIII and Xho I, or pLenti6-V5/Dest vector following digestion with EcoRI, Mfe I and Xho I. Truncation mutants and integrin Glu to Ala mutants were either reported previously²³ or generated using PCR and cloned into pcDNA3.1 vector by BamHI and Xho I. The upstream (UP) and downstream (DN) primer sequences used are: (1) *ITGB3*-UP: 5'-GCG AAGCTTGCCGCGCATGGACCGAGCGCGCGCGCGCGCGCGCGCTCT-3'; (2) *ITGB3*-728DN: 5'-GCGCTCGAGTCAAGCGAATTTCTTTTCGGTCTGGA TGGTGATGAG-3'; (3) *ITGB3*-715DN: 5'-GCGCTCGAGTCCACAGATGAGC AGGGCGGCAAGGCCAATGAGCAG-3'; (4) *Itgb3*-E731A-UP: 5'-AAGAATT CGCTAAATTTGCAGAAGAACGCGCCAGAGCAA-3'; (5) *Itgb3*-E732A-up: 5'-AAGAATTCGCTAAATTTGAGGCAGAACGCGCCAGAGCAA-3'; (6) *Itgb3*-E733A-UP: 5'-AAGAATTCGCTAAATTTGAGGAAGCACGCGCCAGAGCAA-3'; (7) *Itgb3*-E731-733A-UP: 5'-AAGAATTCGCTAAATTTGCAGCAGCACGCG CAGAGCAA-3'; (8) Mfe-*ITGB3*-UP: 5'-CCGCAATTGGCCGCGCATGGACC GAGCGCGGCGCGCGCGCGCGCTCT-3'; (9) Xho I-*ITGB3*-DN: 5'-GCG CTCGAGTTAAGTGCCTCCCGGTACGCTGATATTG-3'. Human integrin β_8 CD cDNA was cloned into pGEX4T-1 vector following digestion with BamHI and Xho I. Primer sequences used are: (1) *ITGB8*-UP: 5'-CGTGGATCCATTAGACA GGTGATACTACAATGG-3'; (2) *ITGB8*-DN: 5'-GCGCTCGAGTTAGAAGT TGCACCTGAAAGTTTC-3'. GST- β_3 CD and recombinant α_{13} purification was previously described⁸. Human THD cDNA, corresponding to N-terminal talin amino acid residues 1–433, was cloned into pcDNA3.1 vector and pMal-C2 vector between EcoRI and Xho I sites. Anti-RHOA antibody was purchased from Cytoskeleton; anti- α_{13} (sc410), anti-c-Src (sc18), anti-talin (sc7534) and anti-integrin β_3 (sc6627) antibodies were from Santa Cruz Biotechnology; anti- α_{13} (26004) was from NewEast; anti-phospho-Src Y⁴¹⁶ antibody was obtained from Cell Signaling; anti-talin (TA205) was from Millipore; anti-talin antibody 8d4 (T3287) was obtained from Sigma; PAC1 antibody (340507) and anti-mouse α_{11b} antibody MWReg3 (14-0411) were obtained from BD Biosciences; anti-human integrin β_3 antibody Mab15, LIBS6 and 8053 rabbit serum were kindly provided by M. Ginsberg (University of California, San Diego); Lipofectamine 2000, viraPower lentivirus expression system, Alexa Fluor 546-conjugated phalloidin, Alexa Fluor 488-conjugated anti-mouse secondary antibody, talin 1 shRNA plasmids (NM-011602), and non-specific shRNA control vector were from Invitrogen; Y-27632 is from Calbiochem; Fibrinogen from Enzyme Research Laboratories.

Purified α_{13} and THD binding to integrin cytoplasmic domains. GST-tagged integrin cytoplasmic domain proteins were coated onto Pierce Glutathione-coated plates overnight at 4 °C. After washing twice with NP40 buffer (50 mM Tris, pH 7.4, 10 mM MgCl₂, 150 mM NaCl, 1% NP-40, 1 mM sodium orthovanadate, 1 mM NaF) with complete protease inhibitor cocktail tablets (1 tablet per 5 ml buffer, Roche), purified THD or α_{13} proteins were added onto the plate in NP40 buffer (for α_{13} binding, buffer contained 30 μ M AlF₄⁻). Bound THD or α_{13} was estimated with anti-talin or anti- α_{13} antibody, horse radish peroxidase (HRP)-conjugated secondary antibody, and 3,3',5,5'-tetramethylbenzidine Substrates (Pierce). The wells were washed three times with NP40 buffer between each of these steps. The reactions were terminated with 1 M sulphuric acid and measured for OD_{450 nm}. For the competitive inhibition assay, increasing concentrations of THD or α_{13} was added to the reactions.

Platelet preparation. Studies using human blood were approved by the institutional review board at the University of Illinois at Chicago, and informed consent was obtained from all donors. Washed human platelets from healthy donors who have not taken medication within 2 weeks before donation and platelets from 8–12-week-old mice were prepared as described previously and re-suspended in modified Tyrode's buffer¹³.

Platelet aggregation assay. Platelet aggregation and secretion were measured in a turbidimetric platelet aggregometer (Chronolog) at 37 °C with stirring (1,000 r.p.m.). Washed platelets (3 × 10⁸ ml⁻¹) in modified Tyrode's buffer were stimulated with thrombin (Enzyme Research Laboratories). Aggregation traces shown are representative of at least three independent experiments.

Fibrinogen and PAC1 binding assay. For the fibrinogen binding assay, washed human or mouse platelets resuspended in modified Tyrode's buffer were incubated with 10 μ g ml⁻¹ Oregon Green-conjugated fibrinogen (Molecular Probes) and PAR4AP as described previously²³. The reaction was diluted with PBS and analysed by flow cytometry using an Accuri C6 flow cytometry (BD Biosciences). PAC1 binding was measured with FITC-labelled PAC1 antibody (Molecular Probe).

Co-immunoprecipitation. As described previously⁸, platelets or CHO cells expressing recombinant integrin $\alpha_{11b}\beta_3$ were solubilized in NP40 lysis buffer (50 mM Tris, pH 7.4, 10 mM MgCl₂, 150 mM NaCl, 1% NP-40, 1 mM sodium orthovanadate, 1 mM NaF), with complete protease inhibitor cocktail tablets (1 tablet per 5 ml buffer, Roche). Lysis debris was cleared after centrifugation at 14,000g for 10 min. Lysates were then immunoprecipitated with rabbit anti- α_{13} IgG, anti-integrin β_3 rabbit serum or an equal amount of rabbit IgG or pre-immune serum for 2 h before Protein A/G sepharose beads were added. After incubation of Protein A/G sepharose beads for 45 min at 4 °C, beads were centrifuged down and washed for six times with NP40 lysis buffer. Immunoprecipitates were analysed by immunoblotting.

RHOA activity assay. Platelets or $\alpha_{11b}\beta_3$ -expressing CHO cells in modified Tyrode's buffer or adherent on immobilized fibrinogen were solubilized in cold NP40 lysis buffer at 4 °C, and debris-cleared lysates were incubated for 1 h with purified GST-RBD beads, washed, and then immunoblotted with an anti-RHOA monoclonal antibody, as described previously⁸.

Bone marrow transplantation. As described previously⁸, bone marrow stem cells were isolated from femur and tibias of 6–8-week-old integrin $\beta_3^{-/-}$ or C57/BL6 mice using the MACS lineage cell depletion kit (Miltenyi Biotec). Stem cells were subsequently infected twice with concentrated lenti-virus containing shRNA or cDNA constructs, as described in Animals and Reagents section, using a Lenti-X concentrator (Clontech). The cells were then retro-orbitally injected into irradiated recipient mice (5Gy for integrin $\beta_3^{-/-}$ mice and 9.6Gy for C57/BL6 mice, one million cells per recipient mice) one day after irradiation.

Platelet adhesion assay. As described previously²³, washed platelets were pre-incubated with vehicle or peptides, or with either 1 mM MnCl₂ or 0.18 μ g ml⁻¹ LIBS6 before plating. After 1 h incubation at 37 °C, adherent platelets were estimated by measuring platelet phosphatase activity with 0.3% p-nitrophenyl phosphate in 1% Triton X-100, 50 mM sodium acetate, pH 5.0, for 1 h at 37 °C. The reaction was stopped with 1 M NaOH. Results were determined by reading OD_{405 nm}. Statistical significance was determined using t-test ($n = 3$).

Cell spreading, immunofluorescence and confocal microscopy. Washed platelets or $\alpha_{11b}\beta_3$ -expressing CHO cells suspended in modified Tyrode's buffer were added to 100 μ g ml⁻¹ fibrinogen (Enzyme Research Laboratories)-coated cover slides and incubated at 37 °C for various lengths of time. Cells were fixed, permeabilized, blocked with 0.5% BSA in modified Tyrode's buffer, stained with mAb15 (followed by Fluor 488-conjugated anti-mouse secondary antibody) and/or Alexa Fluor 546-conjugated phalloidin, and viewed with a Zeiss LSM510 META confocal microscope, as described previously⁸, or with Leica DM IRB fluorescence microscope, Photometrics CoolSNAP HQ camera and μ Manager software. Cell surface area was measured by NIH ImageJ analysis of 5–10 random images. Statistical significance was determined using t-test.

Clot retraction assay. As previously described⁸, human PRP was incubated with vehicle or peptides for 5 min at room temperature (22 °C) before stimulation with thrombin. The two-dimensional size of retracted clots was quantified using Image J software, and statistical significance was determined using t-test ($n = 3$).

Peptide inhibitors. Myristoylated peptides were synthesized and purified at the Research Resource Center at the University of Illinois at Chicago. These peptides include: mP₁₃ (Myr-KFEERARAKWDT), mP₅ (Myr-EEERA), mP₆ (Myr-FEEERA) and the corresponding control peptides mP₁₃Scr (Myr-EEARERKDWAKFT), mP₅Scr (Myr-EEARE), and mP₆Scr (Myr-ERAFEE). The peptides were prepared in DMSO for use *in vitro*, and in micellar formulation for *in vivo* (and *in vitro*) use. For micellar formulation, PEG₂₀₀₀-DSPE, 1- α -phosphatidylcholine, and peptides were mixed at a molar ratio of 45:5:2. The micelles were suspended to form micelle colloid in HEPES-saline buffer ((10 mM HEPES, 150 mM NaCl, pH 7.4), peptide concentration 1 mM) as described previously²⁴. mP₆ is similar to mP₆Scr in uptake by platelets (Extended Data Fig. 9a) and does not cause significant changes in hemogram *in vivo* (Extended Data Fig. 9b).

Estimation of peptide concentration in platelets. mP₆ and mP₆Scr peptides were dissolved and conjugated with PDAM overnight in the dark in DMSO, or conjugated in methanol and incorporated into the micelle as described above. Platelets were incubated with the PDAM-conjugated peptides for 5 min at room temperature, pelleted via centrifugation, washed and lysed with NP40 lysis buffer, and the concentration of PDAM-conjugated peptide was estimated by measuring fluorescence intensity (absorption 340 nm/emission 395 nm) as described previously³⁰. Platelet lysates (without peptide incubation) were used as a blank control. Standard curve was obtained using known concentrations of peptides added to platelet lysates.

In vivo FeCl₃-induced thrombosis and tail bleeding time. 7–8-week-old C57BL/6 mice were anaesthetized by isoflurane inhalation. Retro-orbital injection of peptide micelle or integrilin (5 μ mol kg⁻¹ mouse weight) were performed 15 min before experimentation. Carotid arterial thrombosis was induced with a filter paper disc (diameter = 2 mm) soaked with 1.2 μ l of 7.5% FeCl₃²⁸. Blood flow was

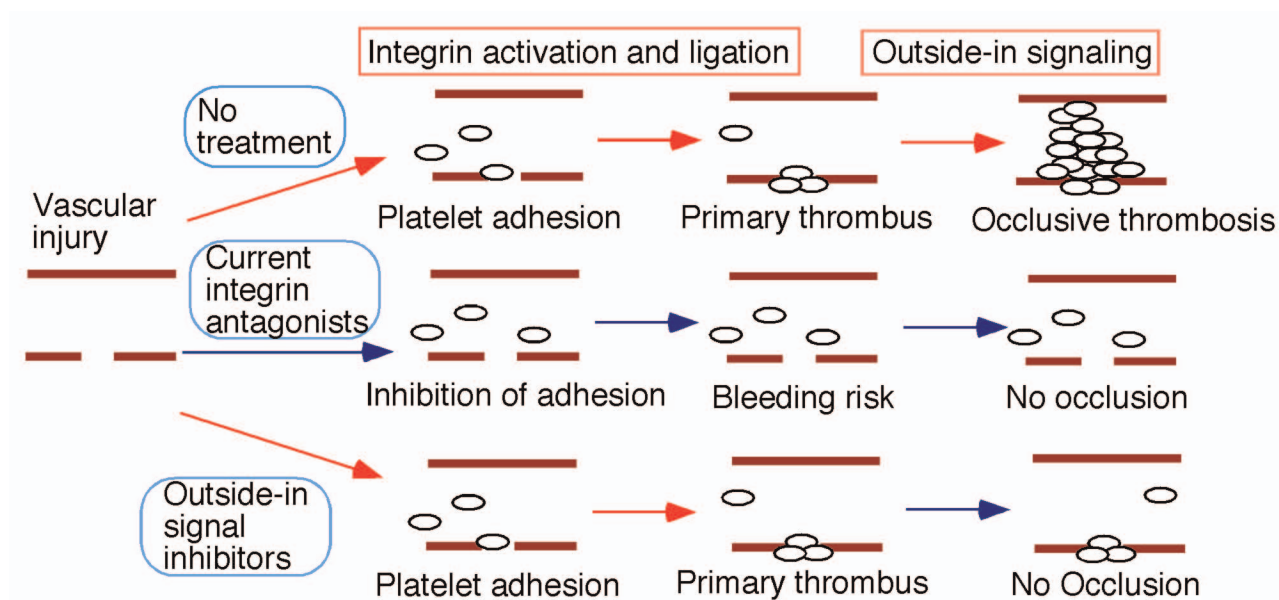
monitored with a TS420 flow meter using a MA-0.5SB dopler probe (Transonic Systems). Data were analysed using one-way ANOVA. Tail bleeding time analysis were performed as described previously²⁹. Time to stable cessation of bleeding was defined as no evidence of rebleeding for 60 s. Bleeding exceeding 15 min was immediately stopped by applying pressure. Statistical significance was determined using the Mann–Whitney test. Similar results were also obtained with a nonparametric ANOVA. For bleeding assays measuring total blood loss, cut mouse tails were immersed in microcentrifuge tubes with 1.5 ml of 0.15 M NaCl at 37 °C for 15 min. The haemoglobin concentration in the tube was determined using a HemoCue photometer. Data were analysed using one-way ANOVA. The experiments were performed in double-blinded fashion.

Intravital microscopy and laser-induced thrombosis. Similar to the methods described previously²⁷, wild-type male mice (6–8 weeks old) were anaesthetized via intraperitoneal injection of ketamine and xylazine and placed on a thermo-controlled blanket (37 °C). The cremaster muscle was exteriorized and superfused with thermo-controlled (37 °C) bicarbonate-buffered saline for the duration of experiments. Fluorescence and bright-field images were recorded using an Olympus BX61W microscope with a 60×/1.0 NA water immersion objective and a high-speed camera (Hamamatsu C9300) through an intensifier (Video Scope International). Fluorescence images were captured at 20 frames per second, and data were analysed using Slidebook v5.5 (Intelligent Imaging Innovations). Arteriolar

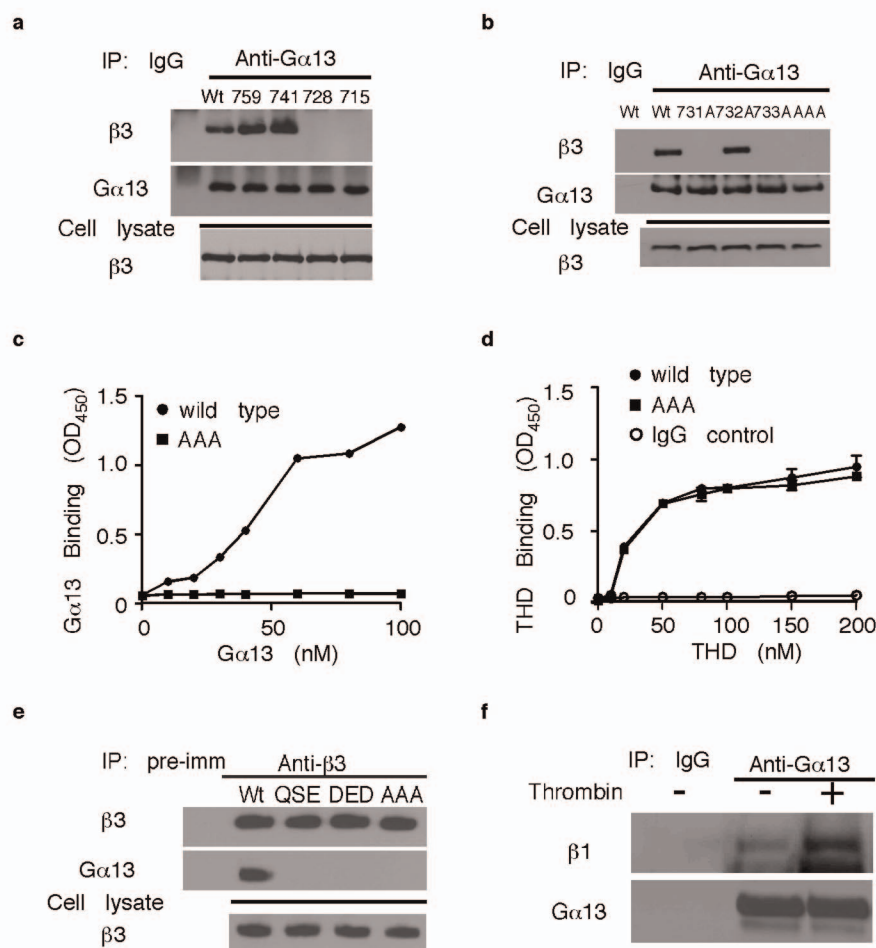
wall injury was induced with a micropoint laser ablation system (Photonics Instruments). Platelet accumulation was visualized by infusion of Dylight 649-labelled anti-mouse CD42c (Emfret, 0.05 µg g⁻¹ body weight) into mice. Vehicle control, Integrilin, scrambled peptide or mP₆ were infused 3 min before laser injury. Laser-induced thrombi were generated at different sites in the blood vessel, with new sites upstream of earlier thrombi. Data were collected for 5 min following laser injury. The kinetics of platelet accumulation was analysed by median fluorescence values of the antibodies as a function of time in approximately 30 thrombi in three mice per group. Statistical difference of fluorescence intensity (mean ± s.d.) at selected time points was also determined using Welch's *t*-test. The experiments were performed in double-blinded fashion.

Statistics. For parametric data, statistical significance was analysed using Student's *t*-test (or Welch *t*-test for samples with nonequal variances) or ANOVA following determination of normal distribution and equal variances. For nonparametric data (bleeding time analysis), Mann–Whitney test was applied. Analyses were performed with GraphPad Prism 4 software. Sample size estimation was performed with Fisher's exact test using GraphPad InStat 3.

30. Nimura, N., Kinoshita, T., Yoshida, T., Uetake, A. & Nakai, C. 1-Pyrenyldiazomethane as a fluorescent labeling reagent for liquid chromatographic determination of carboxylic acids. *Anal. Chem.* **60**, 2067–2070 (1988).

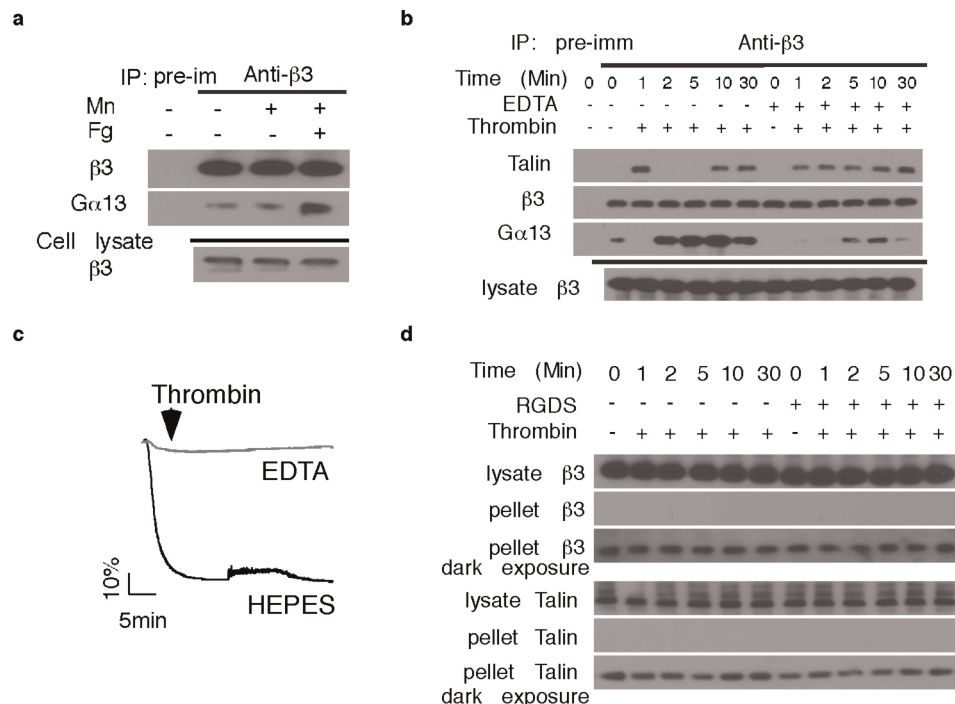


Extended Data Figure 1 | A schematic showing how selective inhibitors of integrin outside-in signalling work as anti-thrombotics. Blue arrows indicate steps that are inhibited.



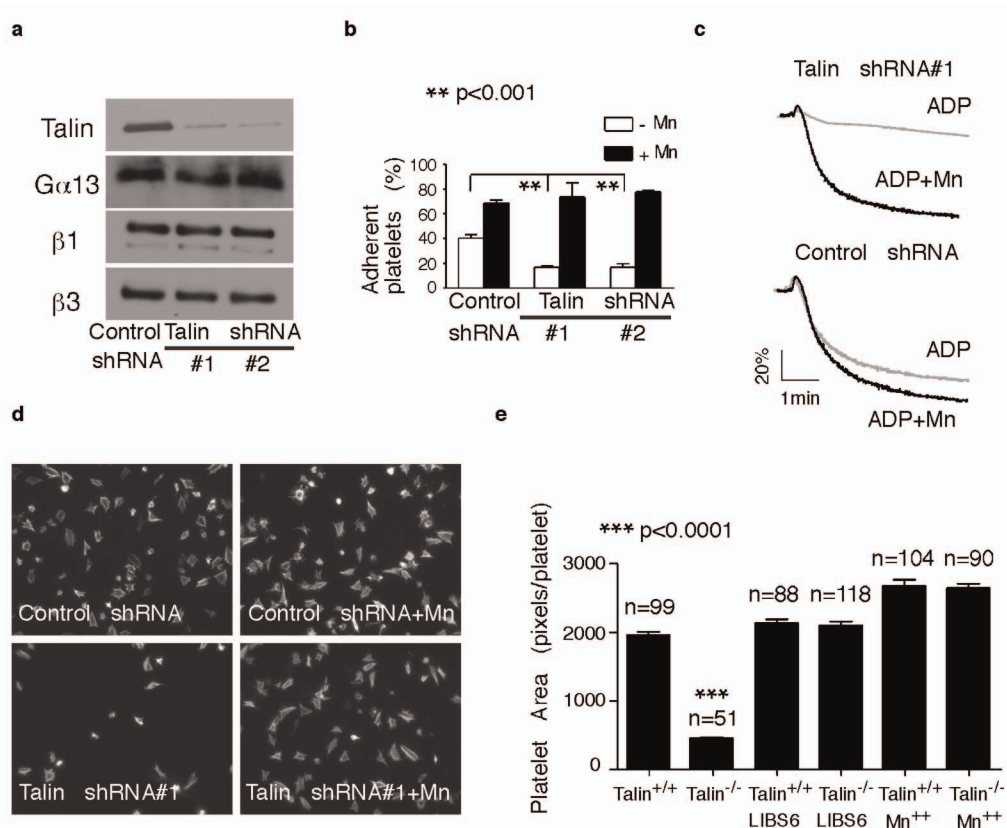
Extended Data Figure 2 | The importance of the conserved EXE motif in integrin- α_{13} interactions. **a, b,** Lysates from CHO cells expressing similar levels of wild-type (WT) $\alpha_{13}\beta_3$, β_3 C-terminal truncation mutants ($\Delta 759$, $\Delta 741$, $\Delta 728$ and $\Delta 715$) complexed with wild-type α_{13} (**a**), and β_3 EXE motif mutants (E731A, E732A, E733A and EEE to AAA) complexed with wild-type α_{13} (**b**) were immunoprecipitated with anti- α_{13} antibody or equal amount of control rabbit IgG. Immunoprecipitates and lysates (equivalent of 10% used for immunoprecipitation) were immunoblotted with anti- α_{13} and anti- β_3 antibodies. **c, d,** GST- β_3 CD (WT) or GST- β_3 (AAA)CD (AAA mutant) proteins immobilized in glutathione-coated microtitre wells were incubated with increasing concentrations of α_{13} (**c**), or increasing concentrations of THD (**d**). After washing, bound α_{13} and THD were respectively detected using anti- α_{13} or anti-talin (mouse IgG was used as a specificity control)

followed by secondary horseradish peroxidase-labelled anti-IgG antibody. **e,** In addition to the AAA mutation, conserved mutations of EEE to DED and EEE to QSE (as found in β_5) were introduced to the β_3 cytoplasmic domain. These mutants were co-transfected with wild-type α_{13} into CHO cells, which were sorted to achieve comparable expression levels with wild-type- $\alpha_{13}\beta_3$ -expressing cells (as shown in Extended Data Fig. 4e). Lysates from these cells were immunoprecipitated with anti- β_3 or equal amount of pre-immune rabbit serum. Lysates (10%) and immunoprecipitates were immunoblotted with anti- α_{13} or anti- β_3 . **f,** Lysates from human platelets (with or without stimulation with 0.025 U ml^{-1} thrombin) were immunoprecipitated with anti- α_{13} antibody or equal amount of control rabbit IgG. Immunoprecipitates were immunoblotted with anti- α_{13} and anti- β_1 antibodies. α_{13} is associated with β_1 , which is increased after thrombin stimulation.



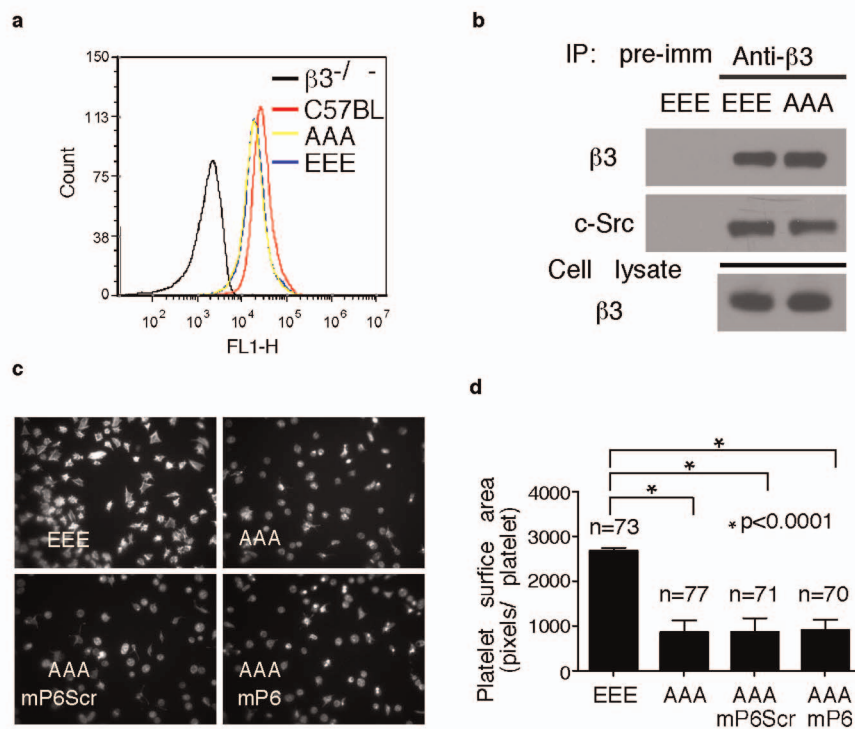
Extended Data Figure 3 | Ligand occupancy induces switch of integrin $\alpha_{IIb}\beta_3$ from the talin-bound to the G α_{13} -bound state. **a**, To determine the effect of integrin activation and ligand occupancy on G α_{13} - β_3 association, human platelets were incubated with or without 1 mM MnCl₂ and 30 μ g ml⁻¹ fibrinogen for 5 min at 22 °C. Platelet lysates were then immunoprecipitated with anti- β_3 or pre-immune rabbit serum. Lysates (10%) and immunoprecipitates were immunoblotted with anti- β_3 or anti-G α_{13} . **b**, **c**, Washed human platelets were stimulated with 0.025 U ml⁻¹ α -thrombin with or without adding 2 mM EDTA (an inhibitor of the ligand binding function of integrins), stirred (1,000 r.p.m.) at 37 °C, solubilized at various time points, and immunoprecipitated with anti- β_3 or equal amounts of pre-immune rabbit serum. Lysates (10%) and immunoprecipitates were immunoblotted with anti-G α_{13} , anti-talin or anti- β_3 antibodies. **b**, Western blot results. **c**, Turbidity changes in platelet suspension indicating integrin-dependent platelet aggregation. Note the inhibitory effect of EDTA on talin dissociation

and G α_{13} binding to β_3 . **d**, As additional controls for Fig. 2a to exclude the possibility of loss of talin and β_3 in platelet lysates to insoluble fraction during integrin signalling, washed human platelets were stimulated with 0.025 U ml⁻¹ α -thrombin in the absence or presence of 2 mM integrin inhibitor RGDS, stirred (1,000 r.p.m.) at 37 °C, and then solubilized at various time points as in Fig. 2a. Solubilized platelets were centrifuged at 14,000g for 10 min to separate lysates from insoluble pellets. Pellets were dissolved in SDS sample buffer to the same volume as the lysates after diluting them 1:1 with 2 \times SDS sample buffer, and both were immunoblotted with anti- β_3 and anti-talin antibodies. Note that the levels of talin and β_3 in platelet lysates kept essentially constant during the course of platelet aggregation and, with low concentrations of thrombin used to stimulate platelets, very little insoluble β_3 and talin were present in the pellet, which were detectable only after prolonged exposure (5-min exposure compared to 10 s of normal exposure time) and with no obvious variation during the course of platelet aggregation.



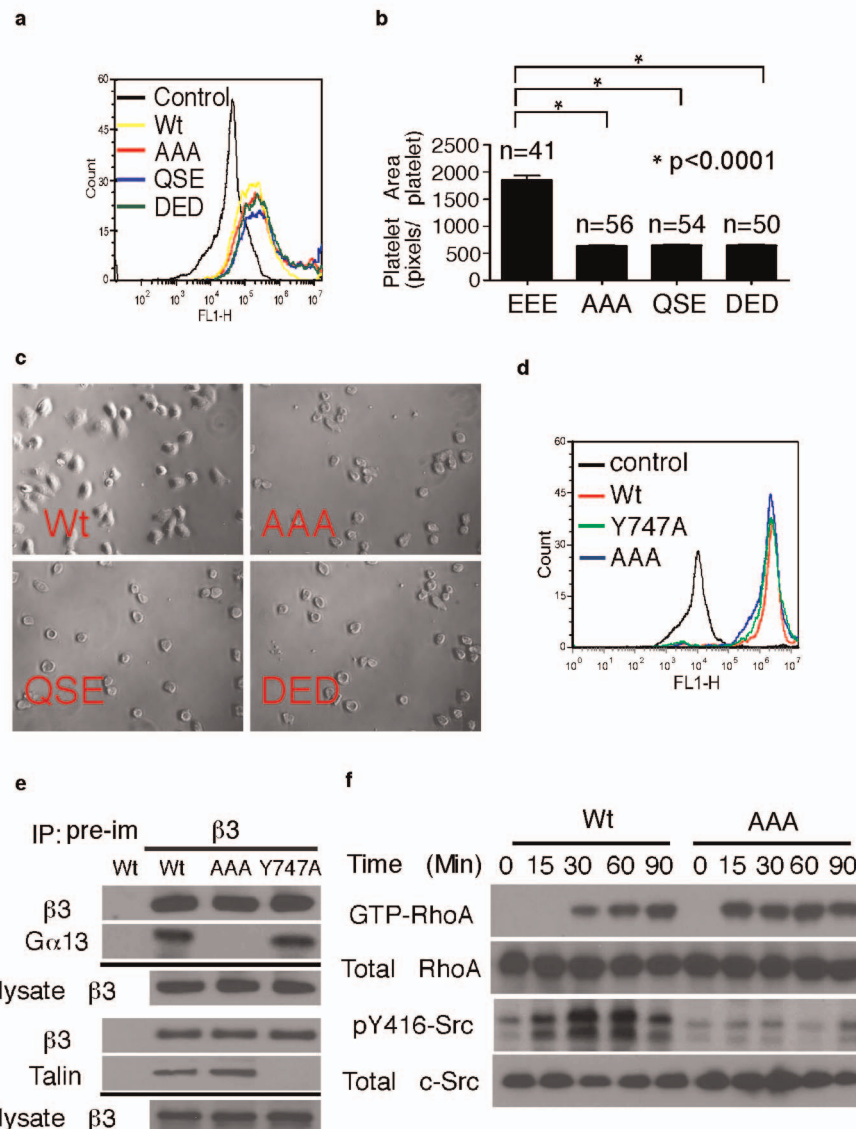
Extended Data Figure 4 | Effects of shRNA-induced talin knockdown and talin knockout on integrin signalling. **a**, Western blot comparison of talin 1 expression levels in mouse platelets derived from control shRNA- or talin-shRNA-transfected bone marrow stem cells. Western blots of Gα₁₃, and integrin β₁ and β₃ are also shown. **b**, Adhesion of unstimulated mouse platelets to immobilized fibrinogen for 1 h. Adherent platelets were quantified as percentage of total platelets loaded (mean ± s.d., *n* = 4). **c**, Turbidity changes in

mouse platelet suspension stimulated with 5 μM ADP in the presence of 20 μg ml⁻¹ fibrinogen, with or without 1 mM MnCl₂, as detected using an aggregometer. **d**, Fluorescence microscopy images of phalloidin-stained mouse platelet spreading on fibrinogen for 1 h, with or without 1 mM MnCl₂. **e**, Quantification of surface areas of individual adherent platelets as shown in Fig. 2g (mean ± s.e.m.).



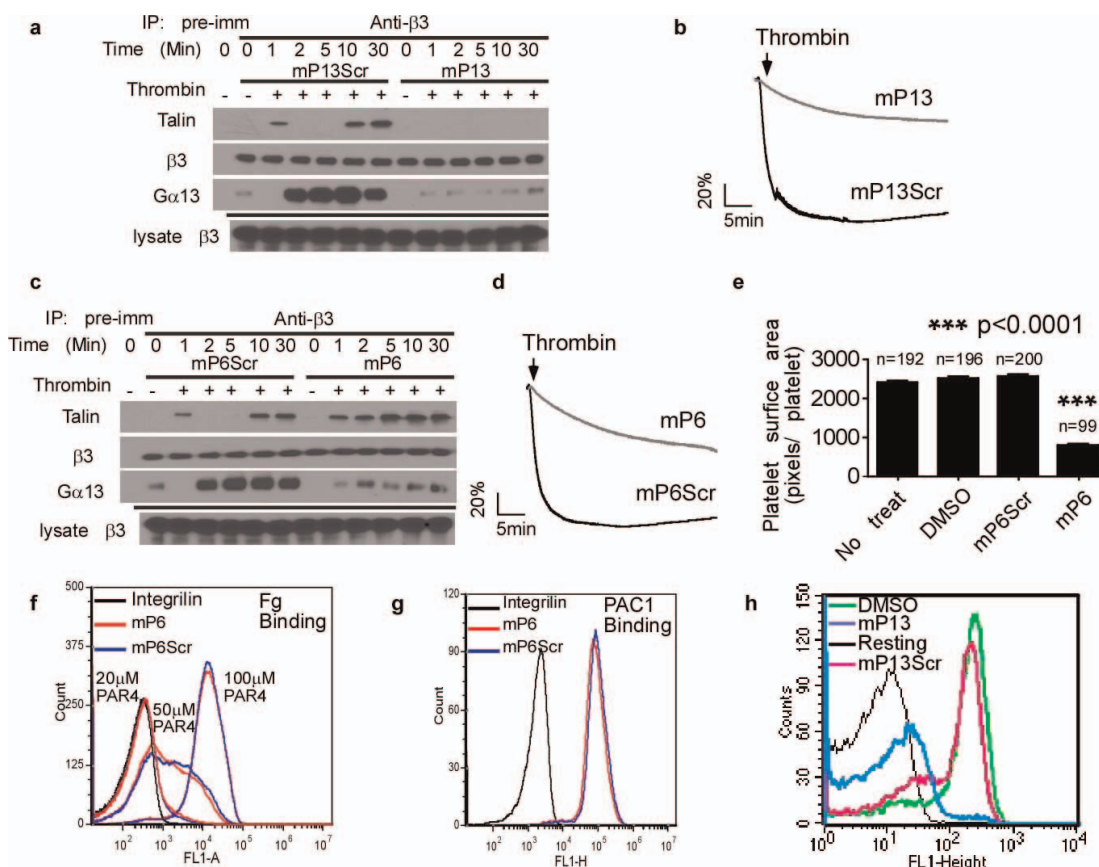
Extended Data Figure 5 | Effects of AAA mutation on integrin outside-in signalling in platelets. **a**, Flow cytometric analysis of integrin $\alpha_{IIb}\beta_3$ expression levels in $\beta_3^{-/-}$ mouse platelets transfected with wild-type or AAA mutant β_3 using bone marrow stem cell transplantation technology in comparison with C57BL/6 mouse platelets. $\beta_3^{-/-}$ platelets were used as a negative control. $\alpha_{IIb}\beta_3$ complex was detected using an anti-mouse α_{IIb} antibody. **b**, Mouse platelets expressing recombinant wild-type or AAA mutant β_3 as in **a** were lysed and

immunoprecipitated with anti- β_3 or equal amounts of pre-immune rabbit serum. Lysates (10%) and immunoprecipitates were immunoblotted with anti-SRC or anti- β_3 antibodies. **c**, **d**, Spreading of phalloidin-stained wild-type platelets (EEE), AAA mutant platelets and AAA mutant platelets incubated with mP6Scr or mP6 on immobilized fibrinogen for 1 h. **c**, Typical fluorescence microscopy images. **d**, Quantification of surface areas of individual platelets (mean \pm s.e.m.).



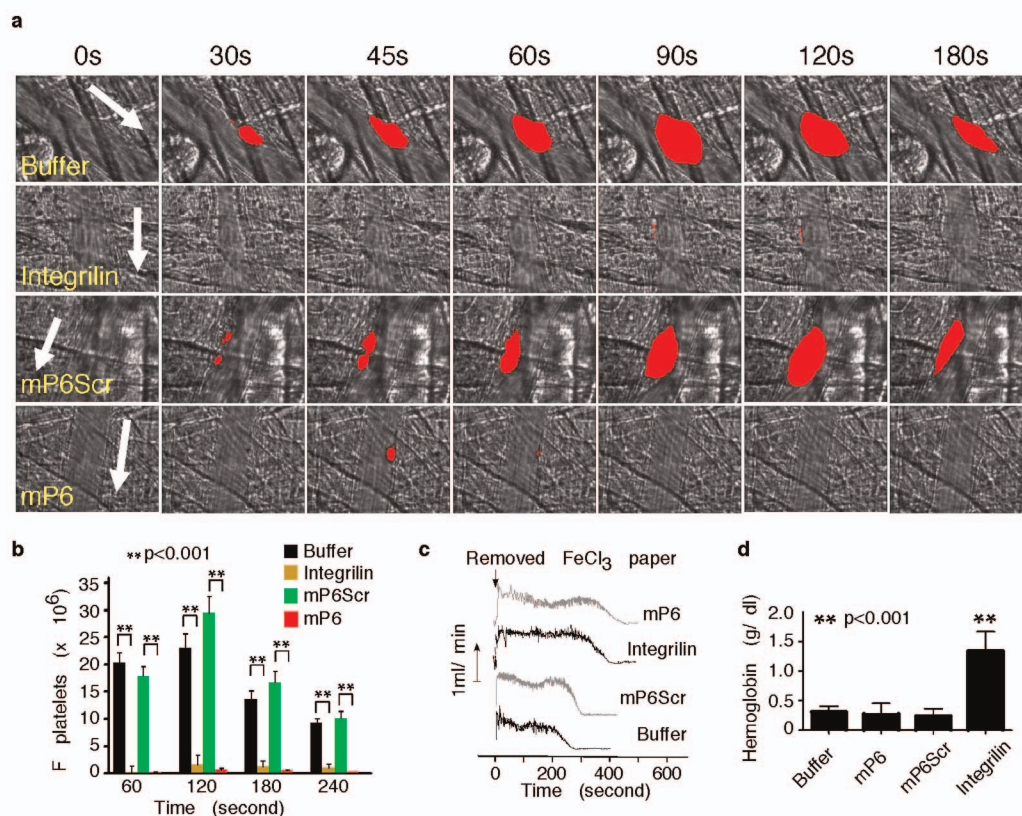
Extended Data Figure 6 | Effects of mutational disruption of the EXE motif on integrin outside-in signalling. **a**, Expression levels of wild-type or the EXE motif (QSE, DED or AAA) mutants of β_3 in complex with wild-type α_{IIb} in CHO cells, as determined by flow cytometry. Mouse IgG was used as a negative control. **b**, **c**, Spreading of CHO-1b9 cells expressing wild-type $\alpha_{IIb}\beta_3$, and QSE, DED or AAA mutant $\alpha_{IIb}\beta_3$ on fibrinogen for 1 h. **b**, Quantification of surface areas of individual cells (mean \pm s.e.m.). **c**, Typical microscopy images. **d**, Flow cytometric analysis of wild-type $\alpha_{IIb}\beta_3$, AAA or Y747A mutant $\alpha_{IIb}\beta_3$ expression in CHO cells. Mouse IgG was used as a control. **e**, CHO cells

expressing wild-type, AAA or Y747A β_3 without (top panels) or with (bottom panels) co-expression of recombinant THD were solubilized and immunoprecipitated with anti- β_3 or pre-immune serum. 10% lysates and immunoprecipitates were immunoblotted with anti-talin, anti-G α_{13} or anti- β_3 antibodies. **f**, Typical western blots for Fig. 3g. Wild-type or AAA-mutant- $\alpha_{IIb}\beta_3$ -expressing CHO-1b9 cells were allowed to adhere to immobilized fibrinogen, solubilized at various time points, and analysed for RHOA activation and SRC Tyr 416 phosphorylation.



Extended Data Figure 7 | mP₆ selectively inhibits integrin outside-in signalling without affecting inside-out signalling. **a–d**, Washed human platelets were stimulated with 0.025 U ml^{-1} α -thrombin in the absence or presence of $250 \text{ }\mu\text{M}$ myristoylated peptides, mP₁₃ (**a**, **b**) and mP₆ (**c**, **d**) with stirring (1,000 r.p.m.) at 37°C , and then solubilized at various time points. Lysates were immunoprecipitated with anti- β_3 rabbit serum or equal amounts of pre-immune serum. Lysates (10%) and immunoprecipitates were immunoblotted with anti- $G\alpha_{13}$, anti-talin or anti- β_3 antibodies. **a**, **c**, Typical western blot results. **b**, **d**, Typical turbidity changes in platelet suspension indicating integrin-dependent platelet aggregation. **e**, Quantification of human platelet spreading on immobilized fibrinogen for 1 h, without or with treatment

with DMSO, mP₆Scr, or mP₆ as shown in Fig. 4b (mean surface area \pm s.e.m.). **f**, Flow cytometric analysis of PAR4-AP-induced Oregon Green-labelled soluble fibrinogen binding to human platelets pre-treated with $100 \text{ }\mu\text{M}$ mP₆Scr or $100 \text{ }\mu\text{M}$ mP₆ stimulated with increasing concentrations of PAR4-AP. Integrilin-treated platelets were used as a negative control. **g**, Flow cytometric analysis of $100 \text{ }\mu\text{M}$ PAR4-AP-induced PAC1 binding to human platelets pre-treated with $100 \text{ }\mu\text{M}$ mP₆Scr or mP₆. Integrilin-treated platelets were used as negative control. **h**, Flow cytometric analysis of PAR4-AP-induced Oregon Green-labelled soluble fibrinogen binding to human platelets pre-treated with solvent DMSO, mP₁₃Scr or mP₁₃. Resting platelets were used as a negative control.



Extended Data Figure 8 | The *in vivo* effect of mP₆: selective inhibition of thrombosis but not haemostasis. **a**, Representative images of laser-induced mouse cremaster arteriolar thrombosis (red) in the context of the bright-field microvascular histology, visualized by infusion of nonblocking rat anti-mouse GPIIb/IIIa antibody conjugated to DyLight 649. The C57BL/6 mice were injected with 5 $\mu\text{mol kg}^{-1}$ micellar formulated mP₆ or mP₆Scr (negative control), 12 $\mu\text{mol kg}^{-1}$ Integrilin or buffer, 3 min before laser-induced arteriolar wall injury. White arrows indicate the directions of the blood flow. **b**, The mean platelet fluorescence intensity for 30 thrombi (performed in three mice) for

each treatment at selected time points (mean \pm s.e.m., $n = 30$, t -test). Fluorescence in mP₆- and Integrilin-treated mice is minimal. **c**, Comparison of mP₆ (5 $\mu\text{mol kg}^{-1}$) with the same dose of Integrilin and their respective controls in occlusion time of FeCl₃-induced carotid artery thrombosis in mice. Typical arterial blood flow charts of FeCl₃-induced occlusive thrombosis are shown. **d**, Comparison of mP₆ (5 $\mu\text{mol kg}^{-1}$) with the same dose of Integrilin and controls in mouse tail bleeding analysis. Released haemoglobin levels were used as a parameter to assess blood loss (mean \pm s.d., $n = 10$).

a

Peptide Conc. (μ M)	nmol mP6 per 10^8 Platelets	nmol mP6Scr per 10^8 Platelets
500 (DMSO)	9.68 \pm 0.52	9.28 \pm 0.44
250 (DMSO)	4.02 \pm 0.27	4.45 \pm 0.14
100 (DMSO)	2.19 \pm 0.23	2.79 \pm 0.36
10 (Micelle)	1.63 \pm 0.08	1.69 \pm 0.10
20 (Micelle)	3.05 \pm 0.08	3.01 \pm 0.09

b

	mP6 t=0	mP6 t=1hr	mP6Scr t=0	mP6Scr t=1hr
WBC (K/ ml)	9.90 \pm 3.54	9.90 \pm 2.22	9.20 \pm 1.53	9.08 \pm 1.47
NE (K/ ml)	0.48 \pm 0.30	0.53 \pm 0.26	0.50 \pm 0.14	0.53 \pm 0.15
RBC (M/ ml)	9.13 \pm 1.16	9.63 \pm 0.81	9.23 \pm 2.11	9.13 \pm 0.54
Hemoglobin (g/ dL)	11.75 \pm 2.63	12.25 \pm 0.96	12.25 \pm 2.06	12.00 \pm 1.41
Platelets (M/ mL)	1.38 \pm 0.36	1.35 \pm 0.17	1.35 \pm 0.14	1.35 \pm 0.20

Extended Data Figure 9 | Platelet uptake of mP₆ and mP₆Scr, and no effect of mP₆ on hemogram. **a**, Estimation of intracellular levels of 1-pyrenyldiazomethane (PDAM)-conjugated mP₆ and mP₆Scr following incubation with platelets for 5 min. Platelets were pelleted by centrifugation, and the amounts of PDAM-conjugated peptides in platelet lysates were estimated (mean \pm s.d., $n = 3$). **b**, Haemogram of mouse whole blood before or 1 h after injection of mP₆ or mP₆Scr ($5 \mu\text{mol kg}^{-1}$), showing no significant differences.

LARGE glycans on dystroglycan function as a tunable matrix scaffold to prevent dystrophy

Matthew M. Goddeeris^{1,2}, Biming Wu^{1,2†}, David Venzke^{1,2}, Takako Yoshida-Moriguchi^{1,2}, Fumiaki Saito³, Kiichiro Matsumura³, Steven A. Moore⁴ & Kevin P. Campbell^{1,2,5,6}

The dense glycan coat that surrounds every cell is essential for cellular development and physiological function¹, and it is becoming appreciated that its composition is highly dynamic. Post-translational addition of the polysaccharide repeating unit [-3-xylose- α 1,3-glucuronic acid- β 1-]_n by like-acetylglucosaminyltransferase (LARGE) is required for the glycoprotein dystroglycan to function as a receptor for proteins in the extracellular matrix^{2,3}. Reductions in the amount of [-3-xylose- α 1,3-glucuronic acid- β 1-]_n (hereafter referred to as LARGE-glycan) on dystroglycan result in heterogeneous forms of muscular dystrophy⁴. However, neither patient nor mouse studies has revealed a clear correlation between glycosylation status and phenotype^{5,6}. This disparity can be attributed to our lack of knowledge of the cellular function of the LARGE-glycan repeat. Here we show that coordinated upregulation of *Large* and dystroglycan in differentiating mouse muscle facilitates rapid extension of LARGE-glycan repeat chains. Using synthesized LARGE-glycan repeats we show a direct correlation between LARGE-glycan extension and its binding capacity for extracellular matrix ligands. Blocking *Large* upregulation during muscle regeneration results in the synthesis of dystroglycan with minimal LARGE-glycan repeats in association with a less compact basement membrane, immature neuromuscular junctions and dysfunctional muscle predisposed to dystrophy. This was consistent with the finding that patients with increased clinical severity of disease have fewer LARGE-glycan repeats. Our results reveal that the LARGE-glycan of dystroglycan serves as a tunable extracellular matrix protein scaffold, the extension of which is required for normal skeletal muscle function.

LARGE is a dual-function glycosyltransferase that adds a glycan repeat to the basement membrane receptor dystroglycan (DG). DG is comprised of a transmembrane β -subunit and a cell-surface-associated α -subunit—the LARGE-glycan is bound to the latter through a rare structure at the amino terminus of its mucin-like domain, a phosphorylated O-mannosyl glycan^{7,8}. The LARGE-glycan binds, with high affinity, to laminin-G-domain-containing matrix proteins (including laminin, agrin, perlecan and neurexin^{9–12}). These interactions can be directly competed by the antibody IIH6, which specifically recognizes the LARGE-glycan. The amount of LARGE-glycan repeat present on α -DG has remarkable variability—both developmental^{13,14} and tissue-specific¹⁵, as shown by marked differences in α -DG apparent molecular mass. Mutations in *LARGE*, the DG-encoding gene (*DAG1*), and several other genes involved in synthesizing the O-mannosyl glycan^{16–22} result in a group of muscular dystrophies termed dystroglycanopathies. These disorders encompass a broad spectrum of severity, ranging from late adult onset with predominant weakness of proximal muscle groups to more severe forms that present at birth and sometimes include defects in brain and eye development. Features common to these disorders are reduced ligand binding by α -DG and reduced to absent IIH6 immunoreactivity. However, when a cohort of dystroglycanopathy biopsies

was assessed for IIH6 immunoreactivity by microscopy a correlation between staining intensity and clinical severity was not found⁵.

It has been proposed that α -DG has separable, currently unknown roles in developing and fully differentiated skeletal muscle^{23,24}; this could explain some of the observed clinical heterogeneity among dystroglycanopathy patients. To address this possibility without interfering with α -DG during embryogenesis, we developed the *GT(ROSA)26Sor^{tm407(H1/tetO-RNAi:Large)}* (hereafter called *Large^{KD}*) inducible mouse model, in which *Large* is knocked down systemically through RNA interference (RNAi) (Extended Data Fig. 1a, b). On a standard diet, heterozygotes are phenotypically indistinguishable from littermates and α -DG glycosylation is normal (Extended Data Fig. 1c, d). When doxycycline is introduced through the diet, however, *Large* transcription is downregulated and IIH6 immunoreactivity in skeletal muscle and elsewhere is lost (Fig. 1a, b). Skeletal muscle has an extraordinary capacity for regeneration, a process that involves triggering satellite cell differentiation into myoblasts, which then proliferate and undergo myogenesis. We designed an experiment to test the impact of disrupted α -DG on regeneration, comparing muscle formed with normal versus defective α -DG. Specifically, we used *Naja nigricollis* cardiotoxin snake venom (CTX) to induce regeneration in select muscles of otherwise healthy adult *Large^{KD}* mice, and simultaneously began *Large* knockdown (Fig. 1c). Although β -DG was preserved in *Large^{KD}* muscle through 3 months after induction, LARGE-glycan was nearly eliminated (Fig. 1d). Gross analysis and quantification of multiple parameters in muscle from CTX-injected *Large^{KD}* mice and uninjected *Large^{KD}* and littermate controls (both CTX and uninjected) revealed that the test mice were profoundly dystrophic (Fig. 1d–g). Some uninjected *Large^{KD}* muscle myofibres featured centrally localized nuclei, indicating that the myofibre had previously regenerated, but evidence of active necrosis or regeneration (eMHC+ myofibres) was minimal despite the absence of LARGE-glycosylated α -DG. From these results we proposed that the degree to which a patient mutation affects α -DG LARGE glycosylation during muscle formation is a major determinant of disease severity.

Physiological assessment at earlier time points confirmed that LARGE-glycan is critical for muscle regeneration. Bilaterally CTX-injected *Large^{KD}* mice had significant deficits in downhill running within 3 weeks (Fig. 2a), whereas uninjected mice maintained running capacity in spite of a significant reduction in normally glycosylated α -DG (Extended Data Fig. 2a). Notably, *Large^{KD}* muscles recovering from CTX injury had abundant IIH6-positive α -DG, although of a reduced molecular mass (Fig. 2b and Extended Data Fig. 2a, b). Despite its low molecular mass, this α -DG was competent to bind laminin (Fig. 2b) and localized to the sarcolemma correctly (Fig. 2c). These results indicated that the number of α -DG LARGE-glycan repeats is critical to the cellular function of α -DG during muscle regeneration.

Histological examination of regenerating *Large^{KD}* muscles early after CTX treatment revealed that myofibres regenerate without a delay, but

¹Howard Hughes Medical Institute, Roy J. and Lucille A. Carver College of Medicine, The University of Iowa, Iowa City, Iowa 52242, USA. ²Department of Molecular Physiology and Biophysics, Roy J. and Lucille A. Carver College of Medicine, The University of Iowa, Iowa City, Iowa 52242, USA. ³Department of Neurology and Neuroscience, Teikyo University School of Medicine, 2-11-1 Kaga, Itabashi-ku, Tokyo 173-8605, Japan. ⁴Department of Pathology, Roy J. and Lucille A. Carver College of Medicine, The University of Iowa, Iowa City, Iowa 52242, USA. ⁵Department of Neurology, Roy J. and Lucille A. Carver College of Medicine, The University of Iowa, Iowa City, Iowa 52242, USA. ⁶Department of Internal Medicine, Roy J. and Lucille A. Carver College of Medicine, The University of Iowa, Iowa City, Iowa 52242, USA. [†]Present address: Department of Biomedical Engineering, University of Michigan, Ann Arbor, Michigan 48109, USA.

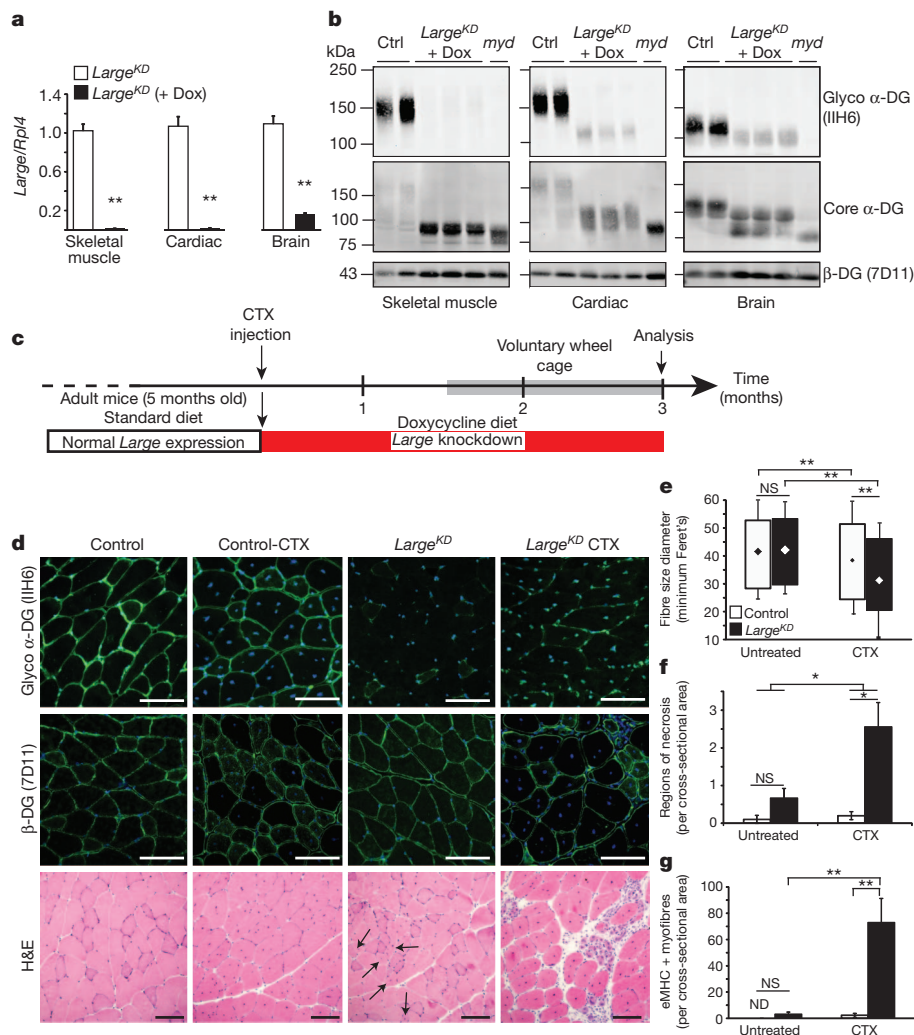


Figure 1 | Muscle generated during *Large* knockdown is predisposed to aggressive dystrophy. **a, b**, Quantification of *Large* mRNA expression in *Large^{KD}* mice on doxycycline (dox) induction (*n* = 3 animals per group, 2 experimental replicates) (**a**), and western blot-based determination of LARGE glycosylation 3 months after shRNA induction, and in littermate controls (ctrl) and LARGE-null negative control (*myd*) (**b**). Each lane is a sample from an individual animal. **c**, Experimental outline. Six weeks after CTX injury and simultaneous induction of *Large* knockdown, the mice were housed in cages with exercise wheels to circumvent the typical sedentary behaviour of laboratory mice (grey bar). Two experimental replicates for all analysis. **d**, Representative images of IIH6 and β -DG reactivity in immunofluorescence- and haematoxylin-and-eosin (H&E)-stained sections (black arrows, centrally nucleated myofibres). **e–g**, Tibialis anterior muscle sections (4 sections/muscle) of control and *Large^{KD}* mice (white and black bars, respectively, *Large^{KD}* mouse, *n* = 3; control, *n* = 4 biological replicates) were assessed for: **e**, fibre diameter (interaction *P* < 0.001, ~2,000 fibres per group; diamonds represent mean fibre diameter); **f**, average regions of necrosis (interaction *P* = 0.057); and **g**, average number of recently regenerated, embryonic myosin-positive fibres (interaction *P* = 0.007). Error bars represent s.d. in **e**, and s.e.m. elsewhere. Post-hoc comparisons **P* < 0.05, ***P* < 0.0001; NS, not significant; ND, not detected. Scale bars, 100 μ m.

adipose cells, a feature commonly seen in severe muscular dystrophies, were observed (Extended Data Fig. 2c, d). Staining for perlecan, which normally co-localizes with laminin in the basement membrane, was reduced in intensity at the basement membrane but was also found mislocalized to the collagen-rich, extracellular matrix layer known as the endomysium (Extended Data Fig. 3a–e). Laminin α 2 was similarly mislocalized to the endomysium (Extended Data Fig. 3f). Given that these findings were indicative of basement membrane abnormalities, we used transmission electron microscopy to probe for defects at the ultrastructural level. The presence of centrally localized nuclei, an increase in the presence of fibroblasts and macrophages, and an increase in the number of mitochondria at the myofibre periphery confirmed that the regions imaged had been damaged by CTX. In CTX-injected *Large^{KD}* muscle, the basement membrane was significantly thickened and, unlike that in CTX control muscles, was often composed of multiple layers (Fig. 2d and Extended Data Fig. 3g). In addition to these abnormalities, collagen fibrils in the endomysial space were unusually abundant and often abnormally oriented with respect to the myofibres, consistent with the fibrous appearance of collagen structures by immunofluorescence (Extended Data Fig. 3a). The expression of collagen VI, perlecan and agrin was unaltered in CTX-injected *Large^{KD}* muscles, although laminin isoforms were found to be elevated at both the mRNA and protein levels (Extended Data Fig. 4 and Fig. 2b). The observed layering of the basement membrane and the increase in thickness is consistent with reduced compaction of laminin and the collagen superstructures during basement membrane formation.

We next assessed the mechanism that underlies the variability in the molecular mass of α -DG. In regenerating control mice, α -DG shifts from approximately 100 kDa to 156 kDa (mode value) within 10 days of injury (Fig. 3a). This shift is closely paralleled by increases in the expression of basement membrane components laminin and collagen VI (Extended Data Fig. 5a), and by other biochemical hallmarks of regeneration such as a gradual loss of embryonic myosin and restoration of dihydropyridine receptor expression (Fig. 3a). To investigate such changes in greater detail we used the C2C12 mouse myoblast cell line, a classical model of myogenesis, which shows a marked increase in DG protein levels upon serum restriction²⁵. The transition to larger glycoforms occurred rapidly after myoblasts are induced to differentiate, preceding myoblast fusion into myotubes on differentiation day (DD) 2 by 24 h (Fig. 3b and Extended Data Fig. 5b). The modal α -DG glycoform increased by 18 kDa over the course of the experiment (Extended Data Fig. 5c). This change correlated with rapid and sustained increases in *Large* and *Dag1* expression (Fig. 3c). Other modifiers of α -DG also showed increased expression levels but later and/or less acutely (Extended Data Fig. 6). We confirmed that other forms of α -DG glycosylation were not responsible for the increase in molecular mass, through enzymatic de-glycosylation removing the *N*-glycans, certain α -DG mucin *O*-glycans and terminal trisaccharides of *O*-mannosyl tetrasaccharides (a treatment that spares the phosphorylated *O*-mannosyl linked LARGE-glycan⁷). Notably, although both DD0 and DD4 α -DG migrated faster after de-glycosylation, the difference in molecular mass between the samples remained, as did the glycoform variation (band

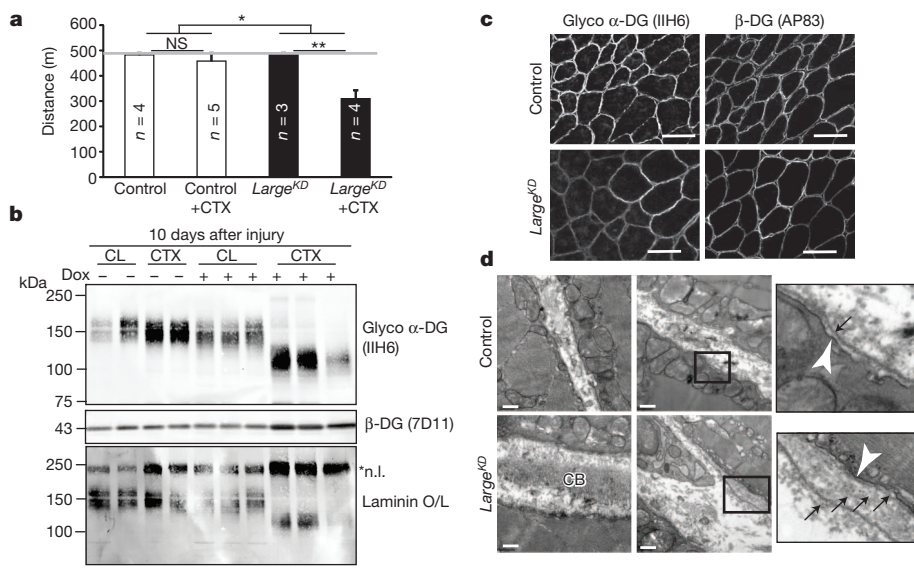


Figure 2 | Regenerating *Large^{KD}* muscle has α -DG of reduced molecular mass and basement membrane defects. **a**, Quantification of muscle performance in downhill treadmill assay. Mice were injected bilaterally in the tibialis anterior and gastrocnemius muscles, and were given a 21-day recovery period. Grey line indicates predetermined assay end point (performance averages, interaction between genotype and CTX injury $P = 0.015$, post-hoc comparisons $*P < 0.05$, $**P < 0.0001$, error bars indicate s.e.m., n = biological replicate number for trial depicted, 3 experimental replicates). **b**, Western blot analysis and laminin overlay assay prepared from regenerating muscle, each lane representing an individual animal. CL, contralateral (un-injured) muscle; *n.l., native laminin. **c**, IIH6 and β -DG immunoreactivity of muscle sections. **d**, Muscle ultrastructure as assessed by transmission electron microscopy. White arrowhead, sarcolemma; black arrows, basement membrane; CB, collagen bundles. Samples in **b–d** were taken 10 days after CTX injury; scale bars, 50 μ m (**c**) and 0.5 μ m (**d**).

smearing) within each sample (Fig. 3d). We conclude that both inter- and intra- α -DG molecular mass variability during myogenesis is due to differences in the quantity of LARGE-glycan repeats. Next we measured inorganic phosphate chemically released from α -DG isolated from C2C12 DD1 (myoblasts) and DD5 (myotubes) after acid hydrolysis in conjunction with the malachite green phosphate assay. We found no significant difference ($6.15 \pm 2.37 \mu\text{M}$ versus $6.83 \pm 2.19 \mu\text{M}$ phosphate released per unit DG for DD1 and DD5, respectively, $n = 3$ trials). Thus, the increase in α -DG LARGE-glycan content during

myogenesis is not attributable to the addition of new LARGE-glycan chains, but rather a consequence of extension of the LARGE-glycan chains present.

We proposed that a reduction in the LARGE-glycan degree of polymerization results in α -DG with reduced ligand-binding capacity. Using synthesized LARGE-glycan chains of either low (up to 13 repeats) or high molecular mass (>13 repeats) immobilized on ELISA assay plates, we performed binding assays for laminin, IIH6 and the perlecan V domain (Fig. 3e, f and Extended Data Fig. 7a–c). Binding to

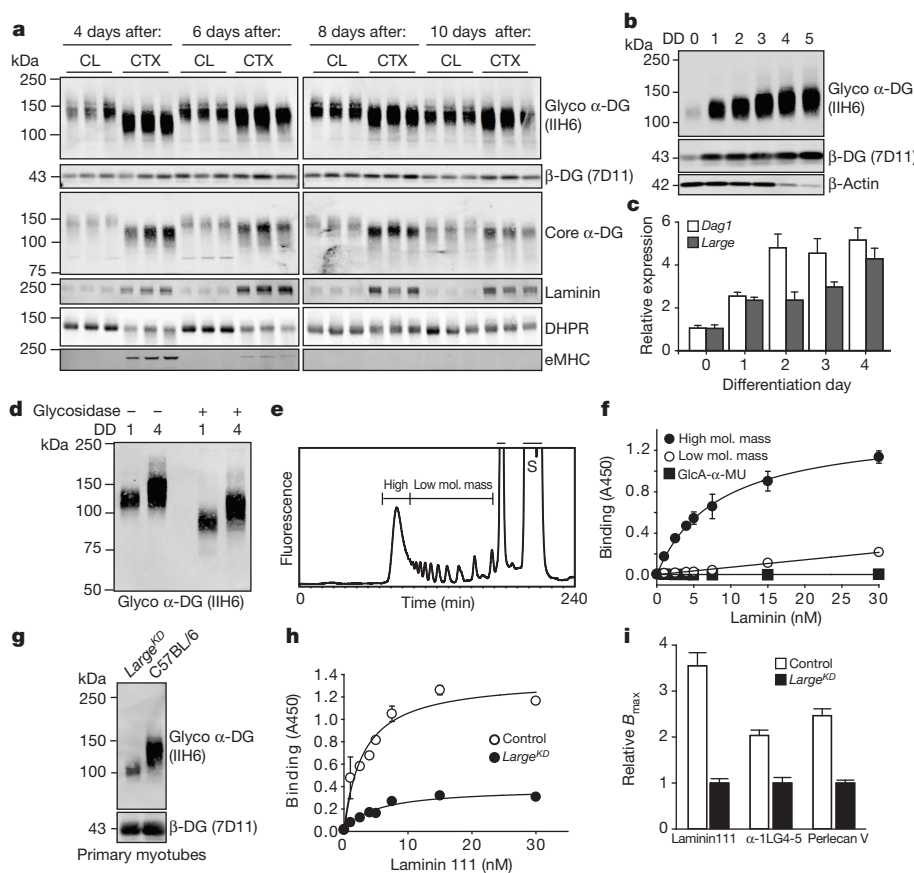


Figure 3 | Increase in α -DG LARGE-glycan chain length during myogenesis enhances ligand-binding capacity. **a**, Western blot analysis of WGA-enriched samples for expression of DG and other proteins at multiple times after CTX-mediated injury to C57BL/6J mice, each lane representing an individual animal. **b**, Western blot analysis of WGA-enriched lysates from C2C12 myoblasts undergoing myogenesis for functional α -DG (DD, differentiation day). At DD4–5 the loading control, β -actin, is downregulated in myotubes. **c**, qPCR analysis of *Dag1* and *Large* during C2C12 myogenesis (averages reported, $P < 0.001$, $n = 3$ biological replicates, $n \geq 7$ technical replicates, relative to *Rpl4* expression, error bars indicate s.e.m.). **d**, Western blot demonstrating effects of enzymatic deglycosylation of DD0 and DD4 C2C12 protein samples. **e**, **f**, Elution profile of LARGE-glycan repeats on a gel filtration column. Bars indicate the fractions that were collected as the high- and low-molecular-mass LARGE-glycan repeats (S, substrate) used for solid-phase laminin 111 (**f**, high molecular mass $K_d = 8.2$) binding. **g**, DG western blot in DD4 myotubes from *Large^{KD}* ($+1 \mu\text{g ml}^{-1}$ doxycycline) and control cultures. **h**, Solid-phase laminin 111 binding demonstrating that binding capacity is dependent on extension of the LARGE-glycan (control $K_d = 2.93 \pm 0.776 \text{ nM}$; *Large^{KD}* $K_d = 4.75 \pm 1.24 \text{ nM}$). **i**, Comparison of solid-phase determined relative B_{max} values for several α -DG ligands (averages represented, B_{max} values for *Large^{KD}* were set to 1 to allow for direct comparisons; error bars indicate s.e.m.). For solid-phase assays (**f** and **h**), error bars indicate s.e.m., $n = 3$ technical replicates, curve fitting to equation $f = B_{\text{max}} \cdot \text{abs}(x) / (K_d + \text{abs}(x))$.

the low-molecular-mass LARGE-glycan was limited compared to that for the high-molecular-mass LARGE-glycan. Next, myotubes generated from primary cultures of isolated control and *Large*^{KD} satellite cells were collected for α -DG solid-phase binding assays (Fig. 3g). The binding capacity (relative B_{\max}) of α -DG from the *Large*^{KD} myotubes was reduced for multiple ligands, including recombinant α 1LG4-5 (2.04-fold), the perlecan V domain (2.47-fold), and laminin 111 (3.55-fold); the latter also displayed a small reduction in dissociation constant (K_d) (Fig. 3h and Extended Data Fig. 7d–f, summarized in Fig. 3i). These data demonstrate that the degree of LARGE-glycan polymerization, and thus the molecular mass of α -DG, correlates directly with the ligand-binding capacity of α -DG.

We reasoned that extension of the LARGE-glycan repeat chain during regeneration increased ligand-binding capacity by providing a larger scaffold for basement membrane components. The neuromuscular junction (NMJ) contains a basement membrane especially rich in α -DG ligands. According to our hypothesis, this structure should be disrupted in *Large*^{KD} mice. Analysis of mice by tail suspension was consistent with such NMJ abnormalities in regenerated muscles; *Large*^{KD} mice subjected to CTX injections into the tibialis anterior and gastrocnemius muscles clasped their hind paws instead of splaying them outward as was typical for control mice (Fig. 4a). Furthermore, analysis of acetylcholine receptor (AChR) labelling in these mice 21 days after CTX damage revealed that the NMJs were fragmented and irregular in shape (Fig. 4b, c), consistent with impaired maturation at the ultrastructural level. Finally, in AChR aggregation assays in primary myotube cultures, the addition of agrin or agrin plus laminin 111 to the medium of control myotubes led to a stepwise increase in AChR aggregate number and size, as previously demonstrated²⁶, but these increases were absent in *Large*^{KD} myotubes (Fig. 4d, e). These findings demonstrate that normal NMJ maturation requires a high degree of LARGE-glycan polymerization, and that in the absence of such extension ligand saturation occurs.

Our data demonstrate that LARGE-glycan extension is required for reformation of both normal NMJs and the basement membrane after injury. Moreover, they indicate that the degree of LARGE-glycan polymerization is temporally coordinated with muscle regeneration. We thus tested whether the presence of excess LARGE-glycan early during regeneration would be detrimental. The overexpression of *Large* (in *CAG-Large* transgenic mice) resulted in hyper-glycosylated muscle α -DG, both at steady state (muscles not subjected to CTX injury) and shortly after CTX-induced muscle injury (Extended Data Fig. 8a, b). Glycosidase treatment of wheat-germ-agglutinin-enriched samples indicated that off-target activity owing to *Large* overexpression was unlikely (Extended Data Fig. 8c, d), although we cannot entirely exclude a small

degree of nonspecific LARGE activity. Regenerated *CAG-Large* myofibres were reduced in diameter and cross-sectional area, and myofibre density was increased, indicative of a defect in myoblast fusion (Extended Data Fig. 8e–i). These data support the notion that the pace of increased LARGE-glycan polymerization is an important aspect of α -DG function during muscle regeneration.

We next assessed human muscle biopsies from several forms of muscular dystrophy. Samples from two broad classes of muscular dystrophy were examined: more severe congenital forms (early-childhood onset, impact on non-muscle organs; congenital muscular dystrophy (CMD)), and a less severe form (adult-onset, impacting proximal muscles to a greater extent; limb girdle muscular dystrophy 2I (LGMD2I)). We observed a reduction in the molecular mass of IIH6-positive α -DG in the congenital muscular dystrophy muscle only (Extended Data Fig. 9a); whereas very little IIH6-positive α -DG was observed in the LGMD2I samples, the residual protein present was of typical molecular mass and restricted (as assessed by immunofluorescence) to muscle regions undergoing regeneration (Extended Data Fig. 9b). These results are in accordance with a previous study¹³. Consistent with our findings from *Large*^{KD} mice, mislocalization of perlecan to the endomysial space was observed only in biopsies where α -DG was of reduced molecular mass (Extended Data Fig. 9c, d). Despite the fact that endomysial fibrosis in the LGMD2I biopsy was extensive, perlecan localization was normal, that is, restricted to the basement membrane. These data suggest that the typical late onset of LGMD2I is caused by loss of functional α -DG in the context of normal basement membrane formation. A previous analysis demonstrated that IIH6-positive α -DG could be recovered with *LARGE* overexpression in dystroglycanopathy cell lines²⁷. In light of our results, we propose that in some dystroglycanopathies the native increase in *LARGE* function during myogenesis provides sufficient LARGE-glycan during muscle regeneration to lessen the impact of certain disease-causing mutations. If true, this would mean that the degree to which LARGE-glycan polymerization is reduced during muscle regeneration is a critical determinant of clinical severity.

Our findings demonstrate that the LARGE-glycan repeat of α -DG is a tunable scaffold for extracellular matrix proteins, the restriction of which through *Large* knockdown during muscle regeneration both reduces muscle physiological function and predisposes it to dystrophy. Whereas the lower molecular mass α -DG retains the ability to bind laminin, our data are consistent with it binding fewer ligands per α -DG protein. In addition to binding the laminin network of the basement membrane, the LARGE-glycan also binds agrin and perlecan, which are capable of binding laminin and collagen concurrently. We speculate that when sufficient LARGE-glycan is available, these collateral linkages facilitate compaction of the basement membrane layers

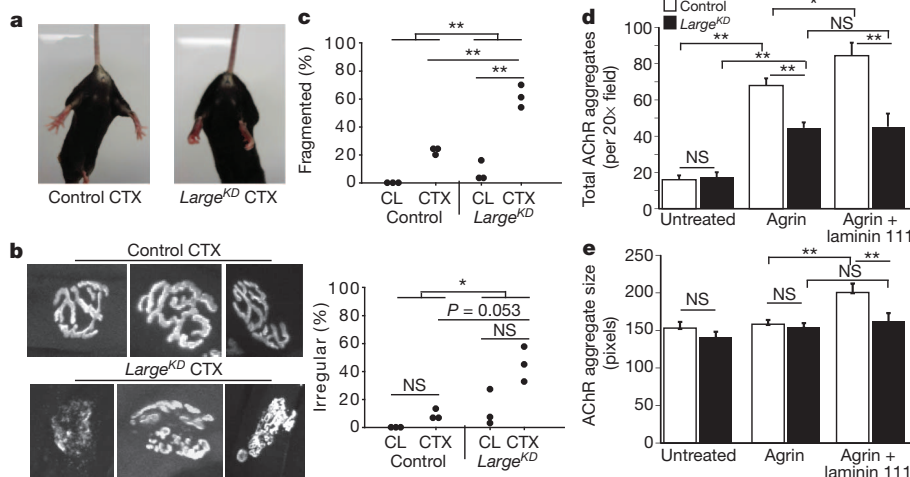


Figure 4 | Reduction in α -DG LARGE-glycan chain length during myogenesis results in NMJ defects. **a**, Hind-paw clasping phenotype during tail suspension in *Large*^{KD} mice, 21 days after injury to the tibialis anterior and gastrocnemius muscles. **b**, Representative confocal images of AChR-labelled NMJs. **c**, Scoring of NMJ defects by blinded observers (scoring criteria in Methods, interaction $P = 0.011$ for fragmentation). **d**, **e**, Average AChR aggregation after ligand addition to control (white) or *Large*^{KD} (black) DD4 myotubes (interaction $P < 0.001$ for total number and $P = 0.007$ for size; error bars indicate s.e.m.; $\times 20$ magnification images, $n = 16$ per group). Post-hoc comparisons for **c–e** * $P < 0.05$, ** $P < 0.0001$.

(Extended Data Fig. 10a, b). We also note that basement membranes from different tissues vary in both thickness and elasticity^{28,29}, and that α -DG is differentially glycosylated in a manner that affects ligand-binding characteristics (due mainly to differences in LARGE-glycan) across many tissues^{15,30} (Extended Data Fig. 10c, d). It is thus possible that the capacity to fine-tune extension of the α -DG LARGE-glycan contributes to diversity in basement membrane structures across mammalian tissues.

METHODS SUMMARY

All mouse studies were performed on adult (8–15-week-old) mice raised on a standard mouse diet. 10 μ M CTX (Accurate Chem & Sci Co in phosphate buffered saline) was used for intramuscular injections, at the following volumes: tibialis anterior, 25 μ l; gastrocnemius, 50 μ l. Injections of phosphate buffered saline alone did not cause observable muscle damage. Injections were unilateral unless otherwise noted. Mouse and human protein samples were processed similarly after 1% Triton X-100 solubilization of physically disrupted tissue. Glycoprotein enrichment via wheat-germ agglutinin (WGA) agarose beads (Vector Labs) was performed as described previously⁹. Induction of *Large* knockdown was achieved by replacing the normal mouse diet with equivalent chow containing 1 g kg⁻¹ doxycycline (Bio-Serv) at the time of CTX injection.

Online Content Any additional Methods, Extended Data display items and Source Data are available in the online version of the paper; references unique to these sections appear only in the online paper.

Received 24 January; accepted 27 August 2013.

Published online 16 October 2013.

- Ohtsubo, K. & Marth, J. D. Glycosylation in cellular mechanisms of health and disease. *Cell* **126**, 855–867 (2006).
- Inamori, K. *et al.* Dystroglycan function requires xylosyl- and glucuronyltransferase activities of LARGE. *Science* **335**, 93–96 (2012).
- Kanagawa, M. *et al.* Molecular recognition by LARGE is essential for expression of functional dystroglycan. *Cell* **117**, 953–964 (2004).
- Muntoni, F., Torelli, S., Wells, D. J. & Brown, S. C. Muscular dystrophies due to glycosylation defects: diagnosis and therapeutic strategies. *Curr. Opin. Neurol.* **24**, 437–442 (2011).
- Jimenez-Mallebrera, C. *et al.* A comparative study of alpha-dystroglycan glycosylation in dystroglycanopathies suggests that the hypoglycosylation of alpha-dystroglycan does not consistently correlate with clinical severity. *Brain Pathol.* **19**, 596–611 (2009).
- Kanagawa, M. *et al.* Residual laminin-binding activity and enhanced dystroglycan glycosylation by LARGE in novel model mice to dystroglycanopathy. *Hum. Mol. Genet.* **18**, 621–631 (2009).
- Yoshida-Moriguchi, T. *et al.* O-mannosyl phosphorylation of alpha-dystroglycan is required for laminin binding. *Science* **327**, 88–92 (2010).
- Hara, Y. *et al.* Like-acetylglucosaminyltransferase (LARGE)-dependent modification of dystroglycan at Thr-317/319 is required for laminin binding and arenavirus infection. *Proc. Natl Acad. Sci. USA* **108**, 17426–17431 (2011).
- Michele, D. E. *et al.* Post-translational disruption of dystroglycan-ligand interactions in congenital muscular dystrophies. *Nature* **418**, 417–422 (2002).
- Willer, T., Valero, M. C., Tanner, W., Cruces, J. & Strahl, S. O-mannosyl glycans: from yeast to novel associations with human disease. *Curr. Opin. Struct. Biol.* **13**, 621–630 (2003).
- Barresi, R. *et al.* LARGE can functionally bypass α -dystroglycan glycosylation defects in distinct congenital muscular dystrophies. *Nature Med.* **10**, 696–703 (2004).
- Sato, S. *et al.* Pikachurin, a dystroglycan ligand, is essential for photoreceptor ribbon synapse formation. *Nature Neurosci.* **11**, 923–931 (2008).
- Brown, S. C. *et al.* Abnormalities in α -dystroglycan expression in MDC1C and LGMD2I muscular dystrophies. *Am. J. Pathol.* **164**, 727–737 (2004).
- Leschziner, A. *et al.* Neural regulation of α -dystroglycan biosynthesis and glycosylation in skeletal muscle. *J. Neurochem.* **74**, 70–80 (2000).
- Ibraghimov-Beskrovnaya, O. *et al.* Primary structure of dystrophin-associated glycoproteins linking dystrophin to the extracellular matrix. *Nature* **355**, 696–702 (1992).
- Kobayashi, K. *et al.* An ancient retrotransposal insertion causes Fukuyama-type congenital muscular dystrophy. *Nature* **394**, 388–392 (1998).
- Jurado, L. A., Coloma, A. & Cruces, J. Identification of a human homolog of the *Drosophila* rotated abdomen gene (POMT1) encoding a putative protein O-mannosyl-transferase, and assignment to human chromosome 9q34.1. *Genomics* **58**, 171–180 (1999).
- Yoshida, A. *et al.* Muscular dystrophy and neuronal migration disorder caused by mutations in a glycosyltransferase, POMGnT1. *Dev. Cell* **1**, 717–724 (2001).
- Brockington, M. *et al.* Mutations in the fukutin-related protein gene (FKRP) cause a form of congenital muscular dystrophy with secondary laminin α 2 deficiency and abnormal glycosylation of α -dystroglycan. *Am. J. Hum. Genet.* **69**, 1198–1209 (2001).
- Willer, T., Amselgruber, W., Deutzmann, R. & Strahl, S. Characterization of POMT2, a novel member of the PMT protein O-mannosyltransferase family specifically localized to the acrosome of mammalian spermatids. *Glycobiology* **12**, 771–783 (2002).
- Longman, C. *et al.* Mutations in the human *LARGE* gene cause MDC1D, a novel form of congenital muscular dystrophy with severe mental retardation and abnormal glycosylation of α -dystroglycan. *Hum. Mol. Genet.* **12**, 2853–2861 (2003).
- Willer, T. *et al.* ISPD loss-of-function mutations disrupt dystroglycan O-mannosylation and cause Walker-Warburg syndrome. *Nature Genet.* **44**, 575–580 (2012).
- Cohn, R. D. *et al.* Disruption of DAG1 in differentiated skeletal muscle reveals a role for dystroglycan in muscle regeneration. *Cell* **110**, 639–648 (2002).
- Beedle, A. M. *et al.* Mouse fukutin deletion impairs dystroglycan processing and recapitulates muscular dystrophy. *J. Clin. Invest.* **122**, 3330–3342 (2012).
- Kostrominova, T. Y. & Tanzer, M. L. Temporal and spatial appearance of α -dystroglycan in differentiated mouse myoblasts in culture. *J. Cell. Biochem.* **58**, 527–534 (1995).
- Montanaro, F. *et al.* Laminin and α -dystroglycan mediate acetylcholine receptor aggregation via a MuSK-independent pathway. *J. Neurosci.* **18**, 1250–1260 (1998).
- Barresi, R. *et al.* LARGE can functionally bypass α -dystroglycan glycosylation defects in distinct congenital muscular dystrophies. *Nature Med.* **10**, 696–703 (2004).
- Osawa, T., Onodera, M., Feng, X. Y. & Nozaka, Y. Comparison of the thickness of basement membranes in various tissues of the rat. *J. Electron Microsc.* **52**, 435–440 (2003).
- Buxboim, A., Ivanovska, I. L. & Discher, D. E. Matrix elasticity, cytoskeletal forces and physics of the nucleus: how deeply do cells 'feel' outside and in? *J. Cell Sci.* **123**, 297–308 (2010).
- Satz, J. S. *et al.* Distinct functions of glial and neuronal dystroglycan in the developing and adult mouse brain. *J. Neurosci.* **30**, 14560–14572 (2010).

Acknowledgements M.M.G. was supported by a NIH/NIAMS Ruth L. Kirschstein National Research Science Award (F32 AR057289-01) and NIH grant (T32-DK07690-16). The work was supported by American Reinvestment and Recovery Act Grant (1RC2NS069521-01), a Muscular Dystrophy Association Research Grant (157538), and a Paul D. Wellstone Muscular Dystrophy Cooperative Research Center Grant (1U54NS053672). F.S. and K.M. were supported by an Intramural Research Grant (23-5) for Neurological and Psychiatric Disorders of NCNP (Ministry of Health and Welfare, Japan) and a MEXT Grant-in-Aid for Scientific Research (C 23591256, 24501357, 25430075). We thank P. Yurchenco for his gift of α 1LG4-5 producing cells; J. Levy for microscopy expertise; M. B. Zimmerman for assisting with statistical analysis; R. Crawford for technical expertise; H. Nguyen for illustrations; J. Hartner for oversight of *Large*^{KO} mouse targeting; J. Shao and R. Nessler of the University of Iowa Central Microscopy Core for their contributions to imaging; and J. Sanes, G. Valdez, D. Glass, C. Blaumueller and Campbell laboratory colleagues for discussions. K.P.C. is an Investigator of the Howard Hughes Medical Institute.

Author Contributions M.M.G. co-designed the project, carried out the experimental work, analysed and interpreted the data and co-wrote the manuscript. B.W. conducted experimental work and analysed the data. D.V. generated essential reagents. T.Y.-M. generated LARGE-glycan repeat chains and performed binding assays thereon. F.S. and K.M. generated the CAG-*Large* transgenic mouse model. S.A.M. compiled patient biopsies and edited the manuscript. K.P.C. co-designed the project, co-wrote the manuscript and supervised the research. All authors discussed the data and the manuscript.

Author Information Reprints and permissions information is available at www.nature.com/reprints. The authors declare no competing financial interests. Readers are welcome to comment on the online version of the paper. Correspondence and requests for materials should be addressed to K.P.C. (kevin-campbell@uowa.edu).

METHODS

Experimental replicates. Unless otherwise stated, all experiments were repeated in the laboratory three times. Data reported are representative.

Animals. Animal care, ethical usage and procedures were approved and performed in accordance with the standards set forth by the National Institutes of Health and the Animal Care Use and Review Committee at the University of Iowa. At the University of Iowa all mice are socially housed (unless single housing is required) under specific pathogen-free conditions in an AAALAC accredited animal facility. Housing conditions are as specified in the Guide for the Care and Use of Laboratory Animals (NRC). Mice are housed on Thoren brand, HEPA filtered ventilated racks, in solid bottom cages with mixed paper bedding. A standard 12/12-h light/dark cycle was used. Standard rodent chow (or special diet if required) and water is available ad libitum. C57BL6/J and *Large^{myd}* mice were obtained from The Jackson Laboratory. *Large^{KD}* mice were generated at TaconicArtemis GmbH. *CAG-Large* transgenics were generated by ligating a 1.7-kb fragment of the *CAG* promoter to a 2.3-kb fragment corresponding to positions +174 through +2444 of the *Large* (NM_010687) cDNA, plus the rabbit β -globin polyadenylation signal. The linearized 4.6-kb Sall-StuI *CAG-Large* construct was injected into pronuclei of fertilized zygotes from C57BL/6NTac mice and transferred to pseudopregnant females. Offspring were screened for genomic integration of this fragment by PCR of tail DNA, using the following *CAG-Large*-specific primers (PCR product size of 2.5 kb): forward 5'-CCTACAGCTCCTGGGCAACGTGCTGGTT-3', reverse 5'-AGAGGGAAAAAGATCTCAGTGGTAT-3'. Mice were generated by breeding F₁ heterozygous transgenic males to wild-type females.

Mice were bred onto a C57BL6/J background (backcross 6 or greater). All mouse studies were performed on adult (8–15-week-old) mice raised on a standard mouse diet. Whereas within each experiment all subjects were sex- and age-matched (littermates where possible), both male and female mice were used and found to respond similarly with the exception of the downhill running assessment (Fig. 2a) wherein only male mice were used as performance variability was noted between the sexes. Previous experience with standard deviation of given techniques and pilot studies using naive animals were used to determine required power for experiments where appropriate with all efforts made to ensure animals for a given experiment were littermates or within 1 week of age. All treatment group designations (randomization) were assigned based on mice identification number and genotype information before experimenter's observation of the animals to exclude any bias based on animal appearance. 10 μ M CTX (Accurate Chem & Sci Co) in phosphate buffered saline (PBS) was used for intramuscular injections, at the following volumes: tibialis anterior, 25 μ l; gastrocnemius, 50 μ l. Injections of PBS alone caused no observable muscle damage. Injections were unilateral unless otherwise noted. Induction of knockdown was achieved by replacing the normal mouse diet with an equivalent chow containing 1 g kg⁻¹ doxycycline (Bio-Serv) at the time of CTX injection (day 0). Animals were exercised by downhill running (15° grade), using a variable speed belt treadmill (OmniPacer, AccuScan Instruments, Inc.) by an experimenter blinded to the genotypes of individual animals. Warm-up: 5 min, 3 metres per min (m.p.m.); running at the following paces; 10 m.p.m., 15 m.p.m., 20 m.p.m. for 5 min each, and 25 m.p.m. for 10 min or to exhaustion. Exhaustion was scored as 10 consecutive seconds of non-performance.

Human subjects and samples. Muscle biopsies were originally collected for diagnostic purposes and were obtained and tested according to the guidelines set out by the Human Subjects Institutional Review Board of the University of Iowa; informed consent was obtained from all subjects or their legal guardians.

Cell culture. C2C12 mouse myoblasts (freshly purchased from ATCC) were maintained in DMEM containing 10% FBS, 1% L-glutamine at 37 °C in 5% CO₂, and kept to a maximum of eight passages. For differentiation, cells were grown to confluence (designated differentiation day 0, DD0) and then switched to DMEM with 2% donor equine serum. AraC (cytosine β -D-arabinofuranoside hydrochloride, 10 nM final, Sigma) was added to differentiating C2C12 cells after myotubes formed, to limit the proliferation of differentiation-incompetent myoblasts. Satellite cell isolation was performed as per ref. 31. Satellite cells were plated on BD Matrigel-coated dishes and activated to differentiate into myoblasts in DMEM-F12, 20% fetal bovine serum (FBS), 40 ng ml⁻¹ basic fibroblast growth factor (R&D Systems, 233-FB/CF), 1 \times non-essential amino acids, 0.14 mM β -mercaptoethanol, 1 \times penicillin/streptomycin and Fungizone. Myoblasts were maintained with 10 ng ml⁻¹ basic fibroblast growth factor and differentiated in DMEM-F12, 2% FBS, 1 \times insulin-transferrin-selenium. For AChR-aggregation assays, primary myoblasts were seeded on BD Matrigel-coated glass coverslips.

Muscle analysis. Immunofluorescence and haematoxylin and eosin staining were carried out as described previously⁹. All images are representative from larger analysis of at least three animals per group, per condition. Fibre size diameter (minimal Feret's diameter) was assessed using ImageJ software (version 1.45s), based on β -DG immunofluorescence. Necrosis was assessed using anti-mouse IgG

fluorescent antibody (detects immune-cell infiltration of degenerating fibres). qRT-PCR for mouse *Dag1* and associated glycosyltransferases was performed using a BioRad MyIQ system, with protocols and primer sets previously described³². The following primer sets were also used: *Ispd1* forward 5'-TGGTGTGGATTA GGGGGTTA-3', reverse 5'-TGGCTGCACTTTGTCCTAAA-3'; *Tmem5* forward 5'-GAGAACAGTGGCAGCCTCA-3', reverse 5'-CAAAGGAGCAGGCCCTCAT AG-3'; *Sgk196* forward 5'-GCTGTCTGTGAAGAGCTGA-3', reverse 5'-GGG AGAGAGCGACTTTGTGT-3'; *Ignt1* forward 5'-ACATTGACGACGCTTC-3', reverse 5'-CCTCCTTTTGGGGATGGAAC-3'; *Itga7* forward 5'-TTGCTGTT AGCCACGATCAG-3', reverse 5'-CGCCAGAGAAGAAGAGTTGC-3'; *Col6a* forward 5'-CTCTCCTGGTTCACCCATGT-3', reverse 5'-CCCAGCTCTACCG AGATTGA-3'; *Lama2* forward 5'-CCAAGAAGGAGGCTGCATAG-3', reverse 5'-CCAGGTGTTGGGAAGACACT-3'; *Lamb1* forward 5'-GTTGAGGGAAC TGCTTCTG-3', reverse 5'-GTTCAGGCCCTTTGGTGTGT-3'; perlecan (*Hspg2*) forward 5'-GAGCGGACTGTACCTTGGTC-3', reverse 5'-ACCAGTTGCACA CAGCTCAC-3'; agrin forward 5'-CAGTGGGGGACCTAGAAACA-3', reverse 5'-ACCTTTCCAATCCACAGCAC-3'.

Fold changes were calculated using the $\Delta\Delta$ Ct method. Failed reactions, those with Ct values within 1 Ct value of water control, were excluded. Mouse and human protein samples were obtained by 1% Triton X-100 solubilization of physically disrupted tissue. Glycoprotein enrichment via WGA agarose beads (Vector Labs) was performed as described previously⁹. Densitometry was performed using LiCor Odyssey Software, V3.0, of triplicate blots. Laminin overlay and solid-phase assays were performed as previously described^{33,9}. For analysis of NMJs, Alexa-488-conjugated α -bungarotoxin was used to stain 4% paraformaldehyde-fixed tibialis anterior muscle cut into thirds longitudinally. Labelled muscle was cleared using glycerol and flattened. Maximal-intensity projections were obtained using an FV1000 Olympus Scanning Confocal laser microscope and z-stack sections compiled with FluoViewer-1.5 (Olympus). Next, individual NMJs from each image were assigned a number, cropped and copied onto a scoring PowerPoint file in a randomized fashion before scoring. Individual NMJs were scored by three blinded observers, using criteria established previously³³. NMJs were scored as 'fragmented' if they were comprised of 5 or more AChR islands, and 'irregular' if they were abnormally shaped (either shallow folds and involutions or none at all). NMJs throughout the muscle were sampled, from 3 animals per group. *CAG-Large* mice were analysed for fibre size diameter (minimal Feret's), fibre cross-sectional area and density from images acquired using a VS120-S5-FL slide scanner microscope (Olympus) with VS-ASW (version 2.6). Analysis was carried out using VS-Desktop software version 2.6.

Statistics. All experimental data are representative of repeated experiments. Statistical analysis was performed using SigmaPlot software which determines if testing assumptions are met (Shapiro–Wilk normality and equal variance testing). Figure 1a used the Student's *t*-test, two sided. Figures 1e, f, 2a and 4c–e were analysed by two-way ANOVA. Post-hoc, pairwise multiple comparison procedures used the Holm–Sidak method with correction for multiple testing. Figure 3c data were analysed by one-way ANOVA on ranks.

Malachite green phosphate assay and sample preparation. C2C12 cells were differentiated on three 15-cm dishes and collected by physical scrapping. Cells were homogenized with 1% Triton X-100 by vortexing for 5 min, and insoluble material was centrifuged and discarded. An initial Lowry protein assay determined that starting protein was equivalent in each sample. DG pull-down was carried out using a β -DG-specific monoclonal antibody (8D5, Developmental Studies Hybridoma Bank) pre-bound to protein-A agarose beads (Santa Cruz Biotechnology). After extensive washing with 0.1% Triton X-100 in Tris-buffered saline, DG and the associated proteins were eluted using 0.1 M β -DG peptide. Samples were then dialysed exhaustively in ddH₂O (6,000–8,000 molecular mass cutoff, 5 days, 12+ 41 changes). Concentrations relative to that of the α -DG core protein were determined by ELISA. Equal starting amounts of α -DG were then treated with 150 units calf intestinal alkaline phosphatase (CIP, New England Biolabs) for 30 min at 37 °C, to remove organic phosphate modifications such as the O-linked *N,N'*-diacetylactosamine modification recently described for α -DG³⁴. To release phosphate associated with the LARGE-glycan, samples were incubated with ice-cold 48% aqueous hydrofluoric acid at 0 °C for 20 h. The reagent was removed under a steady stream of nitrogen gas while on ice. Control samples were prepared by the same procedure, except that ice-cold water was used in place of hydrofluoric acid. Re-suspended samples were then assessed for phosphate content using the Malachite Green Phosphate Detection kit (R&D Systems).

LARGE-glycan preparation for the binding assays. 0.2 mM biotinylated GlcA-MU (custom synthesis by Sussex Research Laboratories Inc.) was incubated with LARGETM 10 mM UDP-glucuronic acid (GlcA), 10 mM UDP-xylose (Xyl), 10 mM MgCl₂ and 10 mM MnCl₂ in 100 mM 2-(*N*-morpholino)ethanesulphonic acid (MES) buffer (pH 6.5) at 37 °C for 18 h. The enzymatic reaction was terminated by boiling in the presence of 50 mM EDTA. After centrifugation (20,000g for

10 min), the supernatant was fractionated using gel-filtration chromatography (Superdex peptide 10/300GL, GE Healthcare) as described previously⁷. The peaks eluted from retention time 75–97 min, and from 97–170 min were pooled as low-molecular-mass and high-molecular-mass LARGE repeats, respectively, and then lyophilized. The LARGE repeats in these two pools were dissolved in water and then analysed using a Bruker UltrafleXtreme MALDI-TOF/TOF mass spectrometer in negative reflection mode. α -Cyano-4-hydroxycinnamic acid (saturated in a mixture of acetonitrile and 0.1% TFA in 1:1 v/v) was used as the matrix as described⁷. To measure the concentration of MU-linked glycan, the glycan samples and known amounts of GlcA-MU were hydrolysed in 1 M of HCl at 95 °C for 20 min. The amounts of 4-methylumbelliferone released by acid hydrolysis were measured using a microplate reader Synergy4 (BioTek) (excitation, 350 nm; emission, 450 nm). GlcA-MU and low- and high-molecular-mass LARGE repeats (0.08 nmol per well) were immobilized on a NeutraAvidin coated 96-well plate (Pierce) according to the manufacturer's protocol. The plates were used for the solid-phase binding assays as described below.

Solid-phase binding assays. Myotube culture samples were collected by scraping and homogenized as described above. Total protein was quantified by Lowry protein assay, and equal amounts of protein were used to enrich for glycoproteins, using WGA agarose beads (Vector Labs) as described previously⁹. The use of equivalent amounts of DG was confirmed by ELISA to α -DG core protein and western blotting for β -DG. Samples were diluted with Tris-buffered saline 1:50, and bound to Costar 96-well, High Bind EIA/RIA plates (50 μ l per well) overnight at 4 °C. Unbound sample was carefully aspirated and the plate blocked with 3% bovine serum albumin in laminin binding buffer (LBB; 746 mM triethanolamine, 140 mM NaCl, 1 mM CaCl₂, 1 mM MgCl₂, pH 7.6) for 2 h at room temperature. A series of ligand dilutions was prepared in LBB with a final concentration of 3% bovine serum albumin and 2 mM CaCl₂. Laminin 111 (Invitrogen), the perlecan V domain³⁵, the α 1LG4-5 domain (isolated from conditioned medium from HEK293 cells secreting Flag-tagged α 1LG4-5 domain, collected and enriched as described³⁶), and AEBF-laminin 111 were used in separate binding assays. To generate AEBF-laminin 111, 10 mM serine protease inhibitor *p*-aminoethylbenzenesulphonyl fluoride AEBF, HCl (Sigma) was incubated overnight on ice with 1 mg mouse laminin protein (Invitrogen) and used to inactivate laminin polymerization. AEBF-treated laminin was dialysed to remove free AEBF with 5 LBB changes of one litre each. Binding solutions were incubated with bound sample for 1 h at room temperature. Mixtures were aspirated completely and washed three times with 200 μ l of 1% bovine serum albumin in LBB (wash solutions were aspirated each time). Primary antibodies to detect ligands were prepared in 3% bovine serum albumin in LBB and incubated for 1 h at room temperature. Antibody solutions were aspirated and washed before adding horseradish peroxidase conjugated secondary antibody (diluted in 3% bovine serum albumin in LBB) and incubating for 30 min at room temperature. After washing as before, sample reactions were developed using 100 μ l pre-warmed 1-Step Ultra TMB-ELISA solution (Thermo Scientific) and stopped with 100 μ l 2 M sulphuric acid. Absorbance was read at 450 nm, using a BioTek Synergy 4 microplate reader. For each ligand concentration, non- α -DG ligand binding was determined by blocking any LARGE-glycan bound to the plate with IIH6 antibody. The absorbance value from IIH6-blocked samples was subtracted from those of non-blocked samples to determine the specific binding activity of α -DG. Data from triplicate samples were assessed and fitted to a ligand-binding curve using SigmaPlot software. IIH6 ELISAs were completed similarly.

Tissue-specific α -DG ligand binding. Brains (cerebrum), hearts and quadriceps were collected from nine C57BL/6J male mice (9–10 weeks of age) and rinsed with ice-cold PBS. Samples were homogenized by Brinkmann Plytron (cardiac and skeletal muscle) or Wheaton Overhead Stirrer (brain) in 7.5 volumes of 20 mM sodium pyrophosphate, 20 mM sodium phosphate monobasic, 1 mM MgCl₂, 0.303 M sucrose, 0.5 M EDTA, pH 7.0. Samples were spun (15 min, 14,000g, 4 °C) and the supernatant was passed through cheesecloth to remove non-homogenized material. Total microsomes were obtained from the supernatant through ultracentrifugation (37 min, 142,000g, 4 °C) and the microsomes were washed twice with 0.303 M sucrose, 0.6 M KCl, 20 mM Tris-maleate, pH 7.0 (recollecting microsomes by repeating ultra-centrifugation each wash) to remove loosely associated proteins. Total KCl washed microsomes were re-suspended in 0.303 M sucrose, 20 mM Tris-maleate, pH 7.0 and solubilized with 1% Triton X-100, 0.1% SDS. Non-solubilized material was removed by centrifugation (30 min, 30,000g, 4 °C) and the solubilized proteins (supernatant) were enriched for glycoproteins by WGA-agarose as described above. Equivalent loading for solid-phase binding assays was determined by preparing dilution curves and performing a β -DG ELISA assay. Solid-phase assays were performed as described above.

Glycosidase treatment. Treatment with glycosidases was as described previously⁷, with sialidase (Prozyme) added to the Enzymatic Protein Deglycosylation kit (Sigma-Aldrich) containing: PNGaseF, O-glycosidase, β -N-acetylglucosaminidase,

β (1-4)-galactosidase. Glycosidase treatment was carried out on WGA-enriched total cell lysates after the native enzymes were heat inactivated (5 min incubation at 94 °C). Control (non-glycosidase treated) samples were treated identically without adding glycosidases.

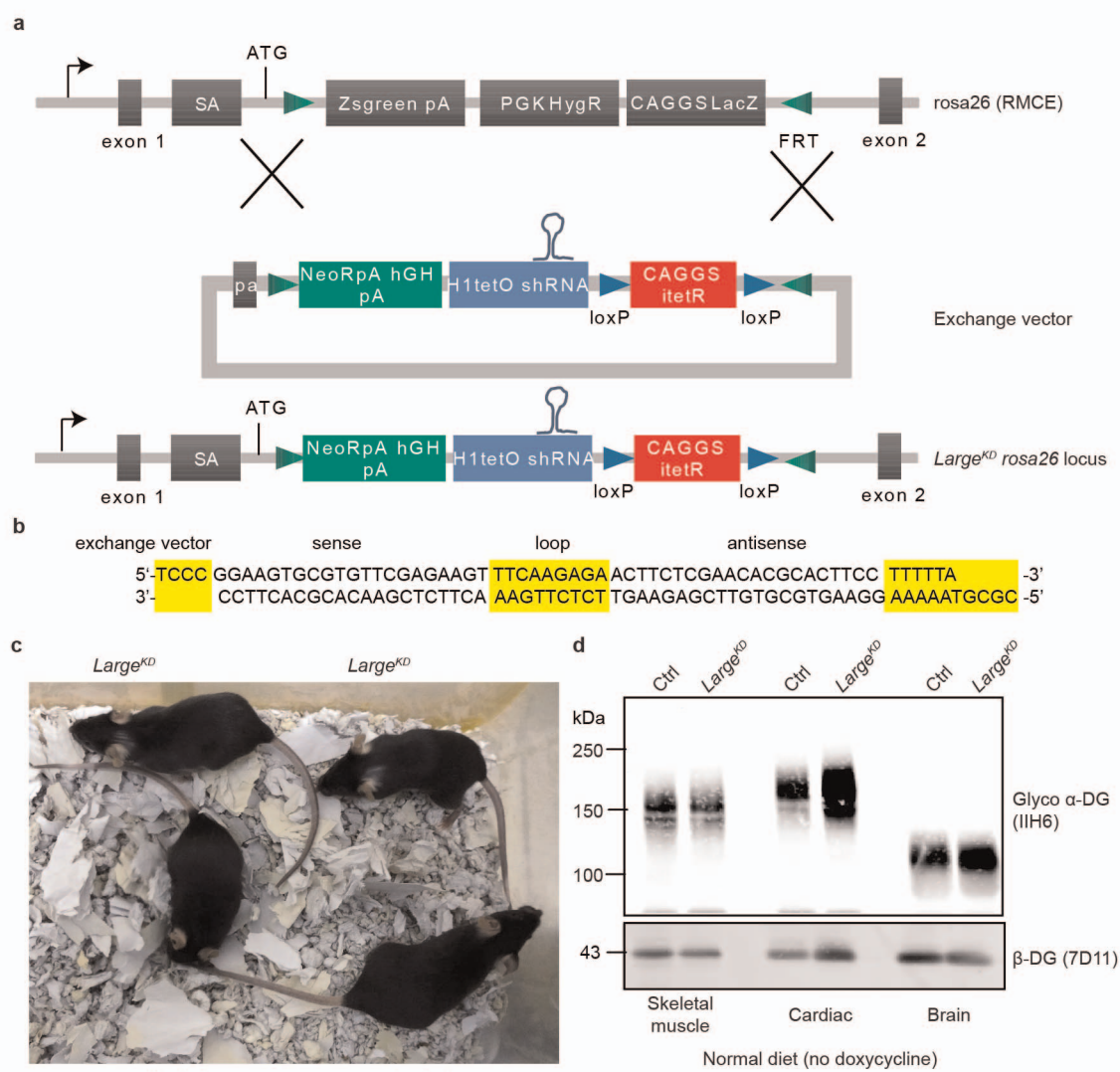
AChR aggregation. The AChR aggregation assay was performed on DD4 myotubes differentiated on Matrigel-coated glass cover slides. Twelve hours before fixation, agrin (R&D Systems, 200 pM) and/or laminin 111 (7.5 nM) was added to the differentiation medium, to stimulate AChR aggregation. Samples were incubated for 30 min with Alexa-488-conjugated α -bungarotoxin (Invitrogen, 1:500), washed twice with cytoskeleton stabilizing buffer³⁷ (CSB) and fixed with 2% paraformaldehyde in CSB for 20 min at room temperature. Samples were blocked with 10% FBS, 0.3% Triton X-100 in PBS for 10 min and incubated overnight with IIH6 (1:50) and additional Alexa-488-conjugated α -bungarotoxin (1:1,000). Samples were imaged by confocal microscopy. Maximal intensity projections were obtained from confocal z-stacks and quantified using ImageJ software (version 1.45s).

Transmission electron microscopy. Tibialis anterior muscles were isolated from mice 10 days after CTX injection, after cardiac perfusion with PBS, and were treated with 4% paraformaldehyde in PBS. Samples were fixed in 2.5% glutaraldehyde, 2% paraformaldehyde, 1% tannic acid in 0.1 M Na cacodylate buffer (pH 7.3) for 1 h at 4 °C. They were then washed in 0.1 M Na cacodylate buffer and post-fixed with 1% osmium tetroxide for 1.5 h at 4 °C. After serial alcohol dehydration (50%, 75%, 95% and 100%), the tissue samples were embedded in Epon 12 (Ted Pella). Ultramicrotomy was performed, and ultrathin sections (65 nm) were post-stained with uranyl acetate and lead citrate. Samples were examined and imaged using a JEOL 1230 transmission electron microscope. Regions of interest, which had undergone regeneration due to CTX damage, were identified based on the presence of centrally localized nuclei and/or an accumulation of mitochondria at the sarcolemma.

Antibodies. The following antibodies have been described previously and were obtained from the listed sources: IIH6³⁸ monoclonal antibody (Campbell laboratory); monoclonal β -DG antibodies 8D5³⁹, MANDA G2 7D11⁴⁰ (Campbell laboratory); polyclonal anti-laminin (L9393) (Sigma-Aldrich); anti-Flag (Sigma-Aldrich); laminin-2 (α 2 chain) 4H8-2 (Enzo Life Sciences); perlecan Ab-1 (NeoMarker); DHPH rabbit polyclonal antibody⁴¹ to α 2 subunit (Campbell laboratory); affinity purified β -DG rabbit polyclonal AP83⁴² (Campbell laboratory); embryonic myosin heavy chain developed by H. Blau (F1.653, obtained from the Developmental Studies Hybridoma Bank under the auspices of the NICHD and maintained by The University of Iowa, Department of Biology); core α -DG antibody, RbtG6317²² (Campbell laboratory); anti-collagen type VI (70R-CR009x, Fitzgerald Industries International); anti- β -actin (clone AC-74, Sigma-Aldrich); and anti-Flag antibody (F7425, Sigma-Aldrich).

- Cerletti, M. *et al.* Highly efficient, functional engraftment of skeletal muscle stem cells in dystrophic muscles. *Cell* **134**, 37–47 (2008).
- Groh, S. *et al.* Sarcoglycan complex: implications for metabolic defects in muscular dystrophies. *J. Biol. Chem.* **284**, 19178–19182 (2009).
- Valdez, G. *et al.* Attenuation of age-related changes in mouse neuromuscular synapses by caloric restriction and exercise. *Proc. Natl Acad. Sci. USA* **107**, 14863–14868 (2010).
- Breloy, I. *et al.* O-linked N,N'-diacetylglucosamine (LacdiNAc)-modified glycans in extracellular matrix glycoproteins are specifically phosphorylated at subterminal N-acetylglucosamine. *J. Biol. Chem.* **287**, 18275–18286 (2012).
- Kanagawa, M. *et al.* Disruption of perlecan binding and matrix assembly by post-translational or genetic disruption of dystroglycan function. *FEBS Lett.* **579**, 4792–4796 (2005).
- Harrison, D. *et al.* Crystal structure and cell surface anchorage sites of laminin α 1LG4-5. *J. Biol. Chem.* **282**, 11573–11581 (2007).
- Trendelenburg, A. U. *et al.* Myostatin reduces Akt/TORC1/p70S6K signaling, inhibiting myoblast differentiation and myotube size. *Am. J. Physiol. Cell Physiol.* **296**, C1258–C1270 (2009).
- Ervasti, J. M., Ohlendieck, K., Kahl, S. D., Gaver, M. G. & Campbell, K. P. Deficiency of a glycoprotein component of the dystrophin complex in dystrophic muscle. *Nature* **345**, 315–319 (1990).
- Masaki, T. *et al.* Expression of dystroglycan complex in satellite cells of dorsal root ganglia. *Acta Neuropathol.* **101**, 174–178 (2001).
- Pereboev, A. V., Ahmed, N., thi Man, N. & Morris, G. E. Epitopes in the interacting regions of beta-dystroglycan (PPXY motif) and dystrophin (WW domain). *Biochim. Biophys. Acta* **1527**, 54–60 (2001).
- Gurnett, C. A., Kahl, S. D., Anderson, R. D. & Campbell, K. P. Absence of the skeletal muscle sarcolemma chloride channel ClC-1 in myotonic mice. *J. Biol. Chem.* **270**, 9035–9038 (1995).
- Williamson, R. A. *et al.* Dystroglycan is essential for early embryonic development: disruption of Reichert's membrane in Dag1-null mice. *Hum. Mol. Genet.* **6**, 831–841 (1997).
- Hsu, N. Y. *et al.* Matrix-assisted laser desorption/ionization mass spectrometry of polysaccharides with 2',4',6'-trihydroxyacetophenone as matrix. *Rapid Commun. Mass Spectrom.* **21**, 2137–2146 (2007).

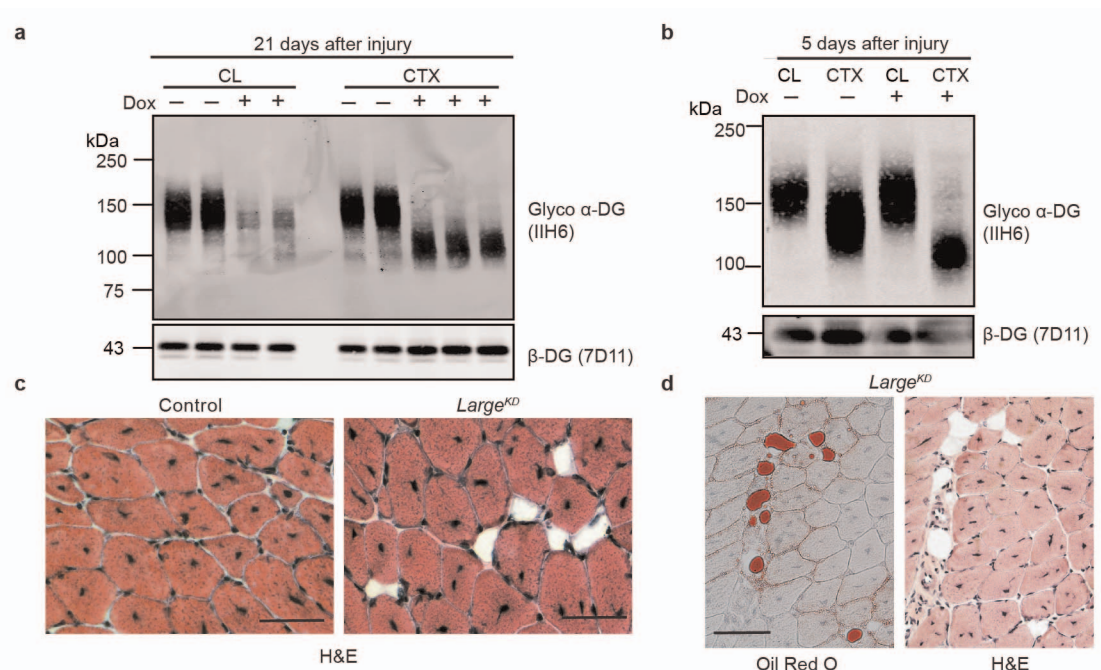
44. Colognato, H., Winkelmann, D. A. & Yurchenco, P. D. Laminin polymerization induces a receptor-cytoskeleton network. *J. Cell Biol.* **145**, 619–631 (1999).
45. Behrens, D. T. *et al.* The epidermal basement membrane is a composite of separate laminin- or collagen IV-containing networks connected by aggregated perlecan, but not by nidogens. *J. Biol. Chem.* **287**, 18700–18709 (2012).
46. Noakes, P. G., Gautam, M., Mudd, J., Sanes, J. R. & Merlie, J. P. Aberrant differentiation of neuromuscular junctions in mice lacking s-laminin/laminin β 2. *Nature* **374**, 258–262 (1995).
47. Han, R. *et al.* Basal lamina strengthens cell membrane integrity via the laminin G domain-binding motif of α -dystroglycan. *Proc. Natl Acad. Sci. USA* **106**, 12573–12579 (2009).



Extended Data Figure 1 | Generation of *Large^{KD}* mice.

a, *GT(ROSA)26Sor^{tm407(H1/tetO-RNAi:Large)}* (*Large^{KD}*)-targeted mice were generated at TaconicArtemis GmbH, using an engineered recombinase-mediated exchange acceptor site in the *Rosa26* gene, and an exchange vector with the following elements: a neomycin resistance marker; an H1-Tet-On promoter-driven shRNA that targets *Large*; and a loxP-flanked CAGGS promoter-driven Tet repressor. Mouse embryonic stem cells with the above-described *Rosa26* gene were exposed to six distinct doxycycline-inducible/conditional shRNA constructs that target *Large*. After validation for correct targeting by Southern blotting, the ES cells were evaluated for efficient *Large*

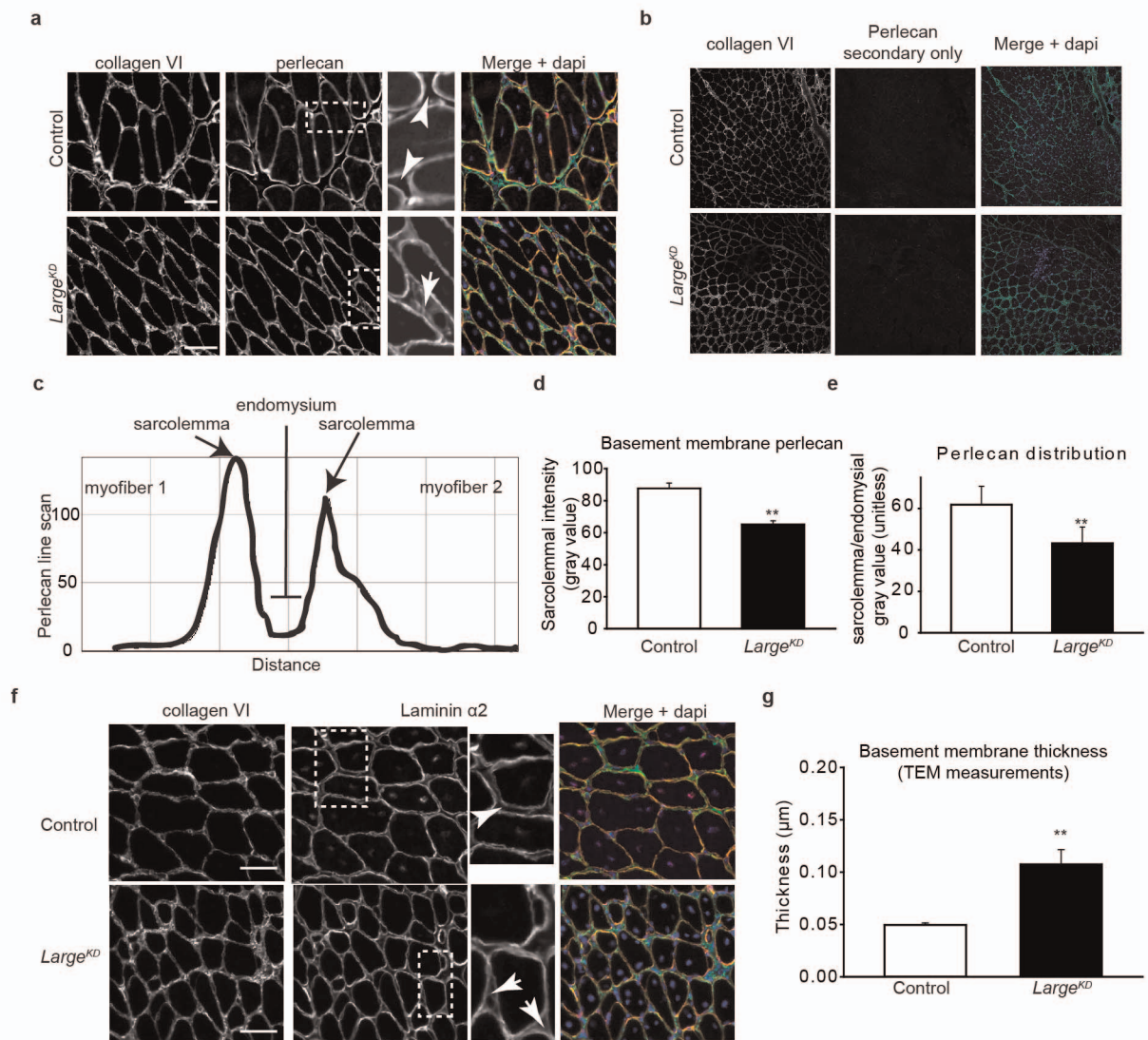
knockdown by qPCR, and for functional loss of IIH6-positive α -DG by western blotting. One knockdown embryonic stem (ES) cell line (targeting the sequence: GGAAGTGC GTGTTTCGAGAAGT) was selected for use in blastocyst injections to generate chimaeric mice, on the basis of the efficiency of *Large* knockdown efficiency therein. Germline animals heterozygous for the knockdown cassette were backcrossed onto a C57BL6/J background. **b**, shRNA sequence used to target *Large*. **c**, **d**, *Large^{KD}* mice and littermate controls. In the absence of doxycycline, the animals are indistinguishable from control littermates both phenotypically (**c**) and biochemically (**d**).



Extended Data Figure 2 | Reduction in molecular mass of α -DG during and after regeneration and increased adipose staining in *Large^{KD}* muscle.

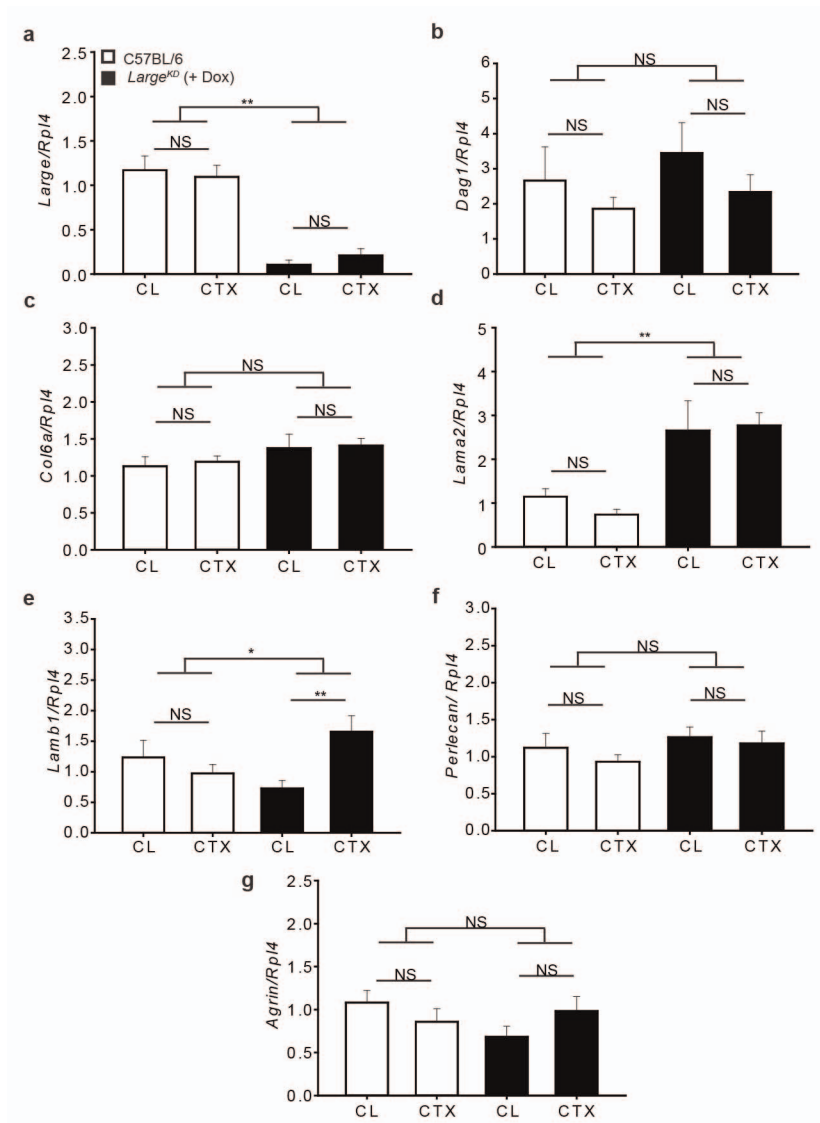
a, b, Western blot analysis of WGA-enriched Triton X-100-soluble homogenates from the tibialis anterior muscles of *Large^{KD}* mice 21 (**a**) and 5 (**b**) days after CTX injury. Glycosylation of α -DG is 're-set' to a lower molecular mass in the *Large^{KD}* (dox+) mice. At 21 days after CTX injury, the contralateral (CL), uninjured *Large^{KD}* (dox+) muscle exhibits reduced IIH6 intensity relative to control (dox-), although the molecular mass in the two samples is

equivalent. In the 5-day samples, this reduction is not observed, a finding that indicates the loss of reactivity in the 21-day samples is attributable to loss of pre-existing α -DG and failure to replace with IIH6-positive α -DG owing to *Large* knockdown. At 5 days after injury, a marked increase in molecular mass variation is observed in CTX control tissue (similar to Fig. 3a). **c**, Haematoxylin and eosin (H&E) analysis reveals evidence of intramuscular adipose cells in *Large^{KD}* gastrocnemius muscle 10 days after CTX. **d**, Staining with the lipophilic dye Oil Red O, confirming that fat is present. Scale bars, 50 μ m.



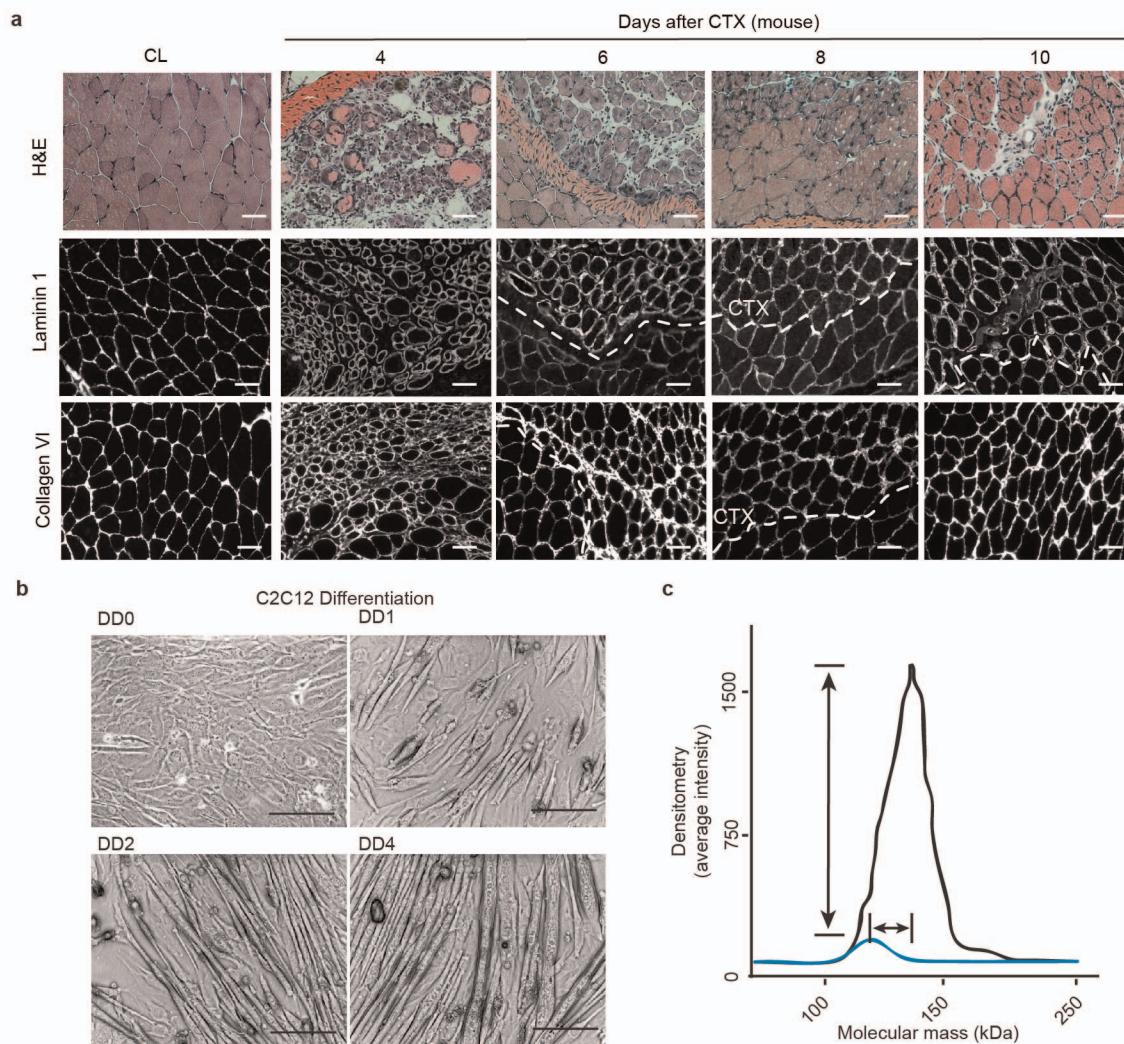
Extended Data Figure 3 | Basement membrane abnormalities in *Large^{KD}* muscle. *Large^{KD}* muscle at 10 days after CTX. **a**, Collagen VI and perlecan co-labelling of muscle sections. Arrowheads, lack of perlecan (normal) in endomysial space; arrow, perlecan in the endomysium. **b**, Secondary only control experiment demonstrating specificity of perlecan signal. **c**, Line scan intensity analysis for perlecan staining across adjacent myofibers, conducted by a blinded third-party. In the example shown (from a control muscle), increased sarcolemmal/basement membrane staining intensity is observed for the two adjacent myofibers, with minimal staining in the intervening endomysial space. Results of this analysis are quantified in **d**, **e**. For perlecan analysis eight line scans were conducted on at least three, $\times 20$ images from 10-day post CTX injury muscles ($n = 4$ CTX injured mice per group). One-way ANOVA on

ranks was used to assess the data. For **d** and **e**, $**P < 0.001$, error bars indicate s.e.m. **f**, Collagen VI, which is expressed during muscle regeneration, localizes to both the basement membrane and the endomysium in control and *Large^{KD}* muscle 10 days after CTX. Laminin $\alpha 2$, which is normally restricted to the basement membrane in control muscle, is also observed in the endomysium of *Large^{KD}* muscle (arrows). Arrowhead points to endomysium in control muscle. All images in **a**, **b** and **f** were collected with confocal microscopy, scale bars, 50 μm . **g**, Quantification of the increase in basement membrane thickness on the basis of transmission electron microscopy of muscle 10 days after CTX injury. Over six images from two *Large^{KD}* and three control animals were assessed by a blinded observer using ImageJ software. One-way ANOVA was used to assess the data; $**P = 0.001$, error bars indicate s.e.m.



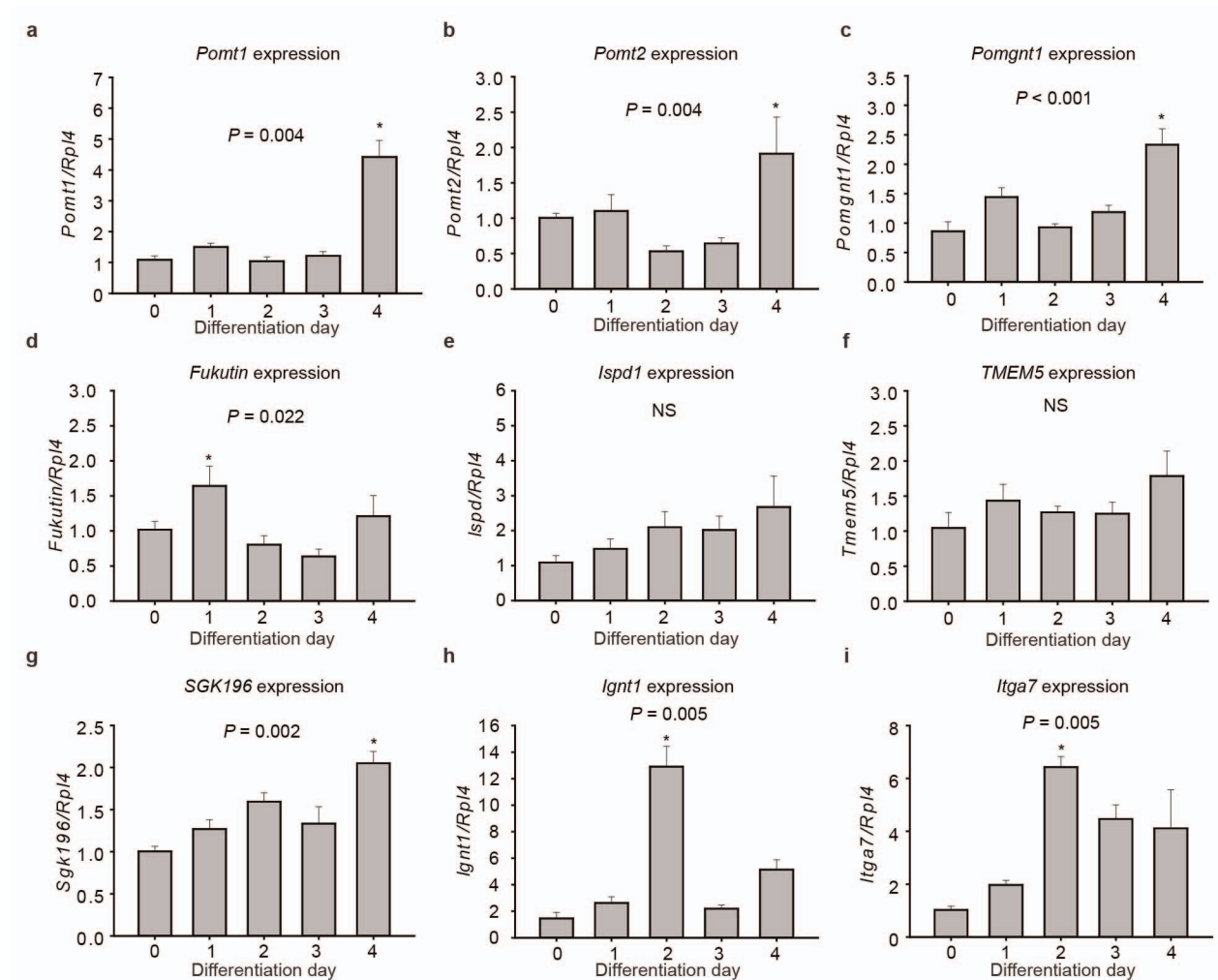
Extended Data Figure 4 | Expression analysis of *Large*^{KD} muscles undergoing regeneration. RT-PCR-based comparisons of gene expression in CTX and CL tibialis anterior muscles 10 days after injury, for *Large* (a), *Dag1* (b), collagen VI α (*Col6a1*) (c), laminin α 2 (*Lama2*) (d), laminin β 1 (*Lamb1*) (e), perlecan (f) and agrin (g). $n \geq 3$ biological repeats and $n \geq 3$ technical

repeats. The expression of all genes was compared to that for the reference gene *Rpl4*. Two-way ANOVA was used to analyse the data, and post-hoc comparisons between relevant groups are depicted; * $P < 0.05$, ** $P < 0.001$, NS, not significantly different; error bars indicate s.e.m.



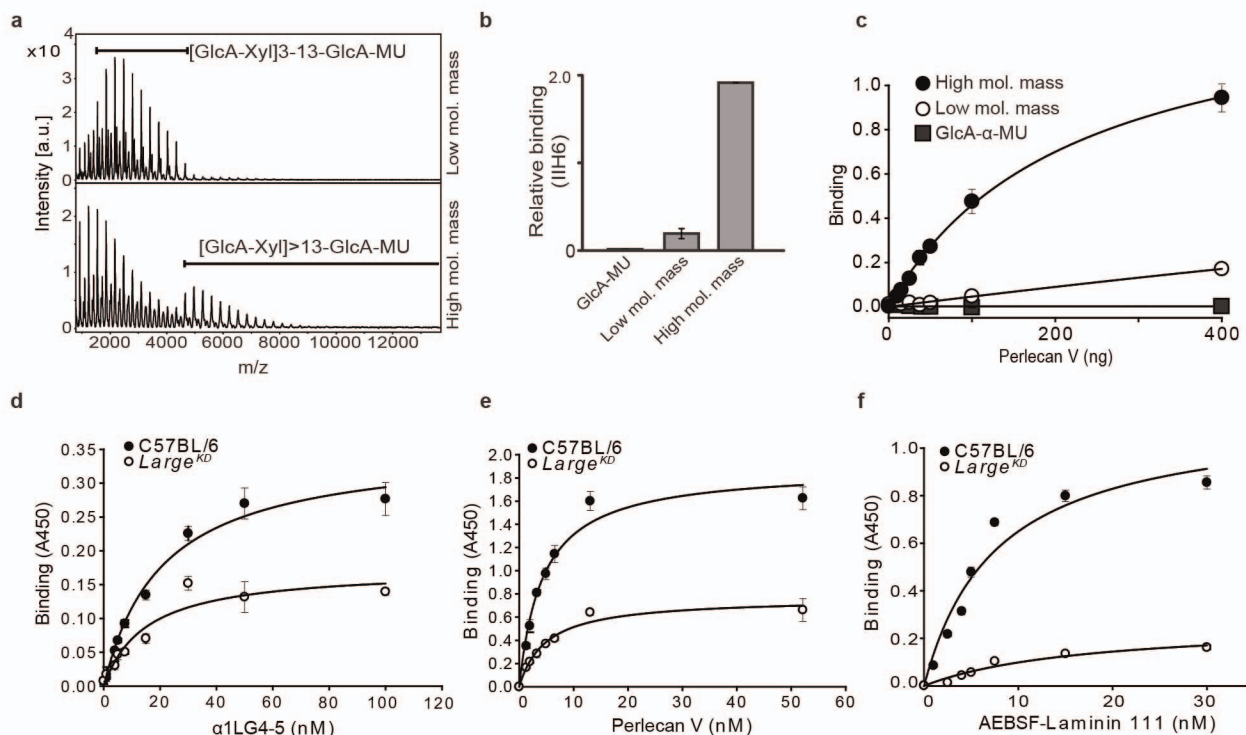
Extended Data Figure 5 | Muscle and basement membrane recovery from CTX injury and cellular hallmarks of C2C12 myogenesis. **a**, Serial sections of CTX-injected gastrocnemius muscle stained with haematoxylin and eosin (H&E) and with laminin and collagen antibodies. Existing laminin-containing basement membranes from degenerated myofibres are observable 4 days after CTX treatment. In areas of injury to myofibres (determined by central nucleation of myofibres), laminin and collagen VI are increased in intensity and appear more diffuse than in nearby uninjured regions. Dotted lines demarcate boundaries of damaged regions. Scale bars, 50 μ m. CL, contralateral.

b, Confluent myoblast cultures stimulated to differentiate by switch to low-serum medium (viewed by phase contrast). Differentiation day (DD) 0 is defined as when C2C12 myoblasts reach confluence in growth medium. 24 h after switching to serum-restricted medium (DD1), the myoblasts are elongated and begin to align with one another. By DD2, myoblast fusion is apparent, and steady myotube growth is observed over the next several days. Scale bars, 100 μ m. **c**, Representative densitometry-based quantification of IIH6-positive α -DG on DD0 (blue line) and DD5 (black).



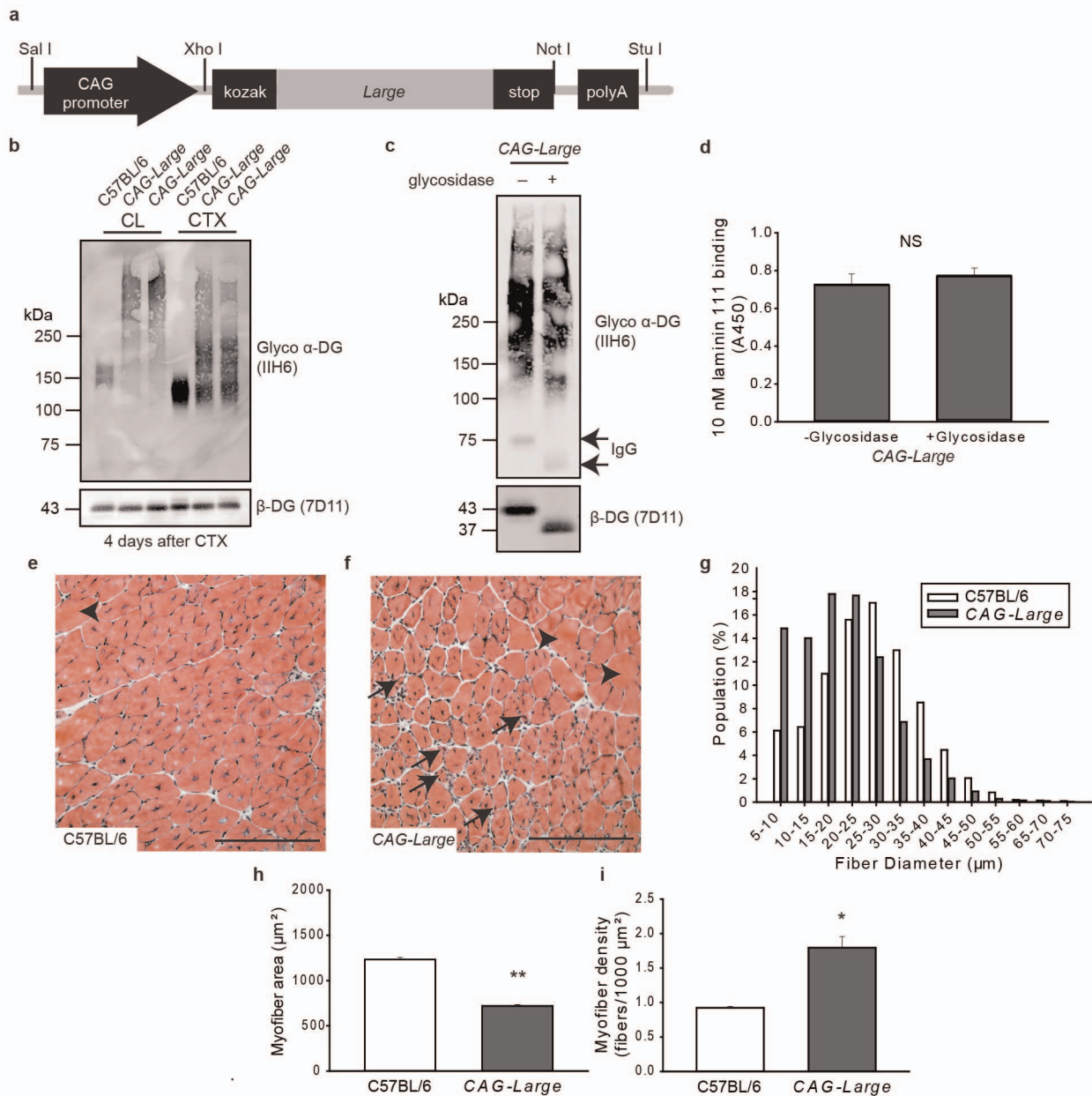
Extended Data Figure 6 | Expression of α -DG-related genes during C2C12 myogenesis. qRT-PCR analysis for *Pomt1* (a), *Pomt2* (b), *Pomgnt1* (c), fukutin (d), *Ispd1* (e), *Tmem5* (f), *Sgk196* (g), *Ignt1* (h) and $\alpha 7$ integrin (*Itga7*, i) over the course of C2C12 myogenesis. Although significant changes in expression were observed for some genes, the pattern of expression did not match the increase in molecular mass observed in α -DG, or the increase observed in the expression of

Large and *Dag1*. Biological and technical samples were assessed in triplicate. One-way ANOVA P values are included where significance was found, and time points with significantly increased expression (as determined by post-hoc analysis) are denoted with asterisks. * $P < 0.05$, NS, not significantly different; error bars indicate s.e.m.



Extended Data Figure 7 | Mass spectrometry and binding characteristics of *in vitro* generated LARGE-glycan repeats and associated binding characteristics of *Large^{KD}* α -DG. **a**, Mass spectrometry analysis of high- and low-molecular-mass LARGE-glycan repeats using MALDI-TOF MS. High-molecular-mass species are under-represented owing to the difficulty in detecting polysaccharides of greater than 10 kDa using this approach⁴³. **b**, IHH6 antibody binding to low- and high-molecular-mass LARGE-glycan repeats (error bars indicate s.e.m.). **c**, Solid-phase binding assay for the perlecan V domain (error bars indicate s.e.m.). **d**, Dystroglycan in DD4 myotubes generated from isolated primary *Large^{KD}* (+ 1 $\mu\text{g ml}^{-1}$ doxycycline) and control satellite cells was assessed for substrate binding. Solid-phase $\alpha 1\text{LG4-5}$ binding demonstrated that binding capacity is dependent on extension of the

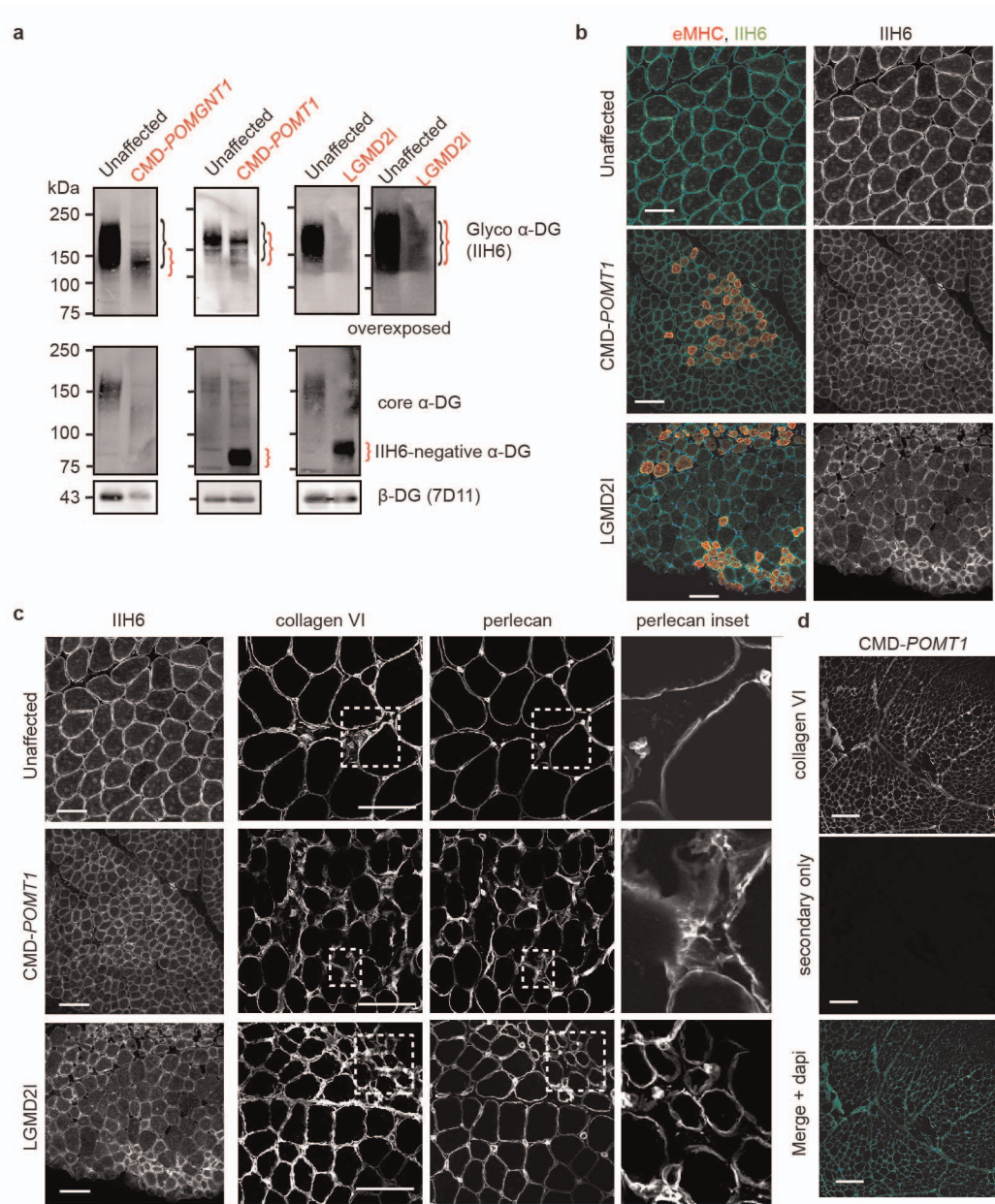
LARGE-glycan (control $K_d = 15.0 \pm 5.20$ nM; *Large^{KD}* $K_d = 20.6 \pm 3.15$ nM). **e**, Findings for the perlecan V domain were similar to those of $\alpha 1\text{LG4-5}$ (control $K_d = 4.37 \pm 0.749$ nM; *Large^{KD}* $K_d = 4.88 \pm 0.846$ nM). **f**, Laminin 111 self assembly, and we wished to test the binding characteristics of a form that is unable to do so. AEBSEF-laminin 111 is unable to polymerize yet retains receptor binding capacity⁴⁴ and when it was tested the differences in binding between *Large^{KD}* and control samples were greater than those for laminin 111. This finding indicates that the polymerization of laminin bound to LARGE-glycan reduces the apparent differences in binding between *Large^{KD}* and control α -DG (AEBSEF-laminin 111 binding control $K_d = 7.61 \pm 2.12$ nM, $B_{\text{max}} = 1.14$; *Large^{KD}* $K_d = 17.1 \pm 7.36$ nM, $B_{\text{max}} = 0.268$). Error bars indicate s.e.m., curve fitting to equation $f = B_{\text{max}} * \text{abs}(x) / (K_d + \text{abs}(x))$.



Extended Data Figure 8 | Overexpression of LARGE in a transgenic mouse results in abnormal muscle regeneration.

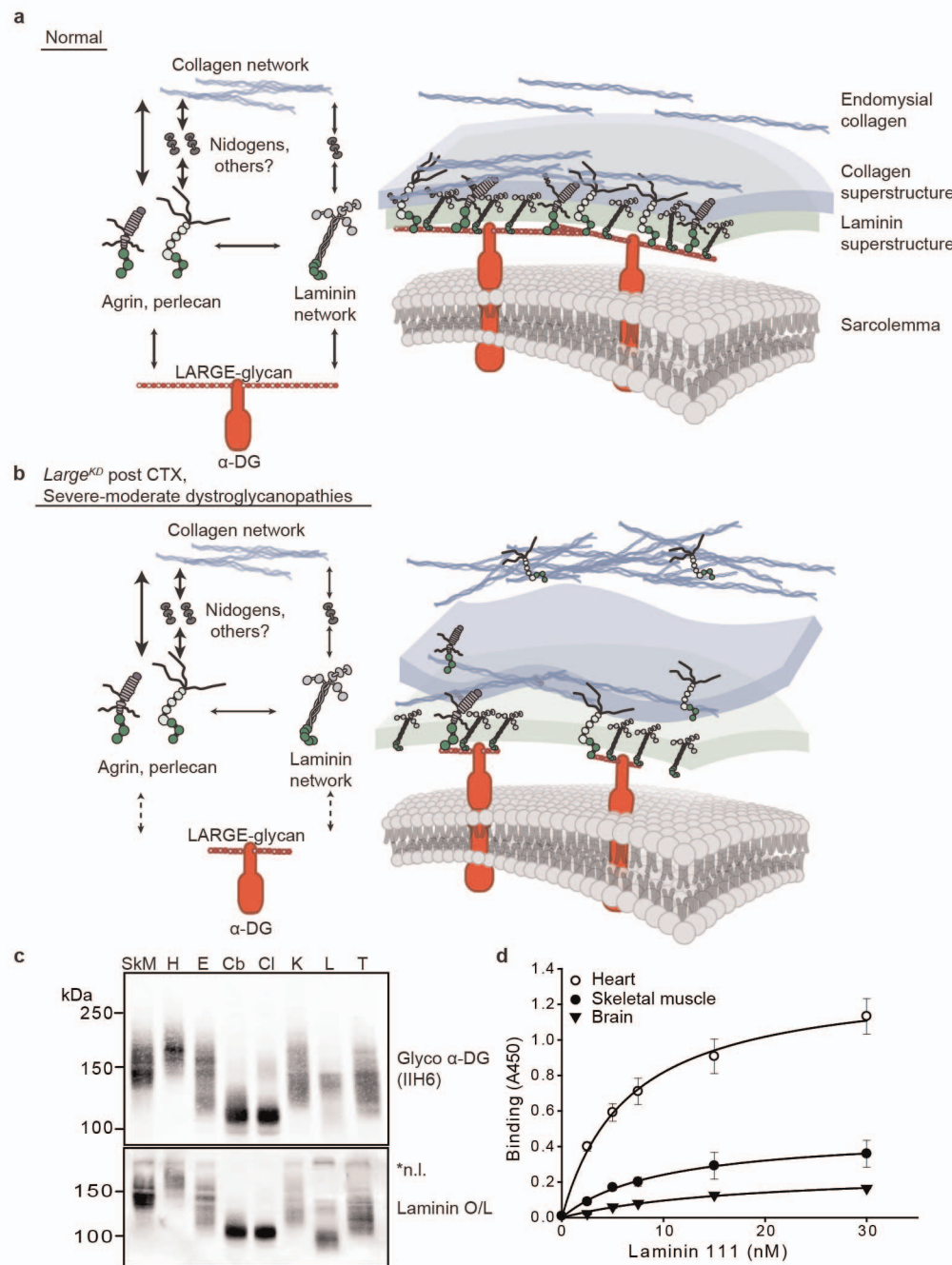
a, Map of transgene used to generate the *CAG-Large* transgenic mouse. **b**, Western blot of α -DG from CL and CTX injured tibialis anterior muscles 4 days after injury, demonstrating that the protein is hyperglycosylated in *CAG-Large* muscles. **c**, WGA-enriched samples from *CAG-Large* muscles 10 days after CTX injury were treated with enzymatic de-glycosylation to remove *N*-glycans, certain α -DG mucin *O*-glycans and terminal trisaccharides of *O*-mannosyl tetrasaccharides while sparing the phosphorylated *O*-mannosyl-linked LARGE-glycan as evidenced by the maintenance of IIH6-positive α -DG and reduction in molecular mass of

β -DG and the IgG present in the samples. **d**, No change in laminin 111 binding, as detected by solid-phase assay, was observed in glycosidase-treated *CAG-Large* samples (error bars indicate s.e.m., $n = 4$ biological replicates) compared to untreated samples indicating that despite *Large* overexpression, nonspecific LARGE modification is minimal in these muscles. **e**, **f**, Haematoxylin-and-eosin-based histological analysis of muscles 10 days after CTX injury revealed an increase in myofibres of small diameter, quantified in **g**–**i**. Scale bars represent 200 μ m. >6,000 fibres per group were measured, $n = 3$ animals per group, * $P = 0.006$, ** $P < 0.001$ by one-way ANOVA; error bars indicate s.e.m.



Extended Data Figure 9 | Increased IIH6 reactivity in regenerating myofibres from patients. **a**, Western blots of WGA-enriched muscle lysates from patient biopsies. CMD, congenital muscular dystrophy; LGMD2I, limb-girdle muscular dystrophy 2I. **b**, Patient biopsies were analysed by immunofluorescence for the presence of the α -DG LARGE-glycan (using antibody IIH6) and for signs of regeneration (using antibody to the embryonic myosin heavy chain, eMHC). Increased IIH6 signal correlates with regions of

muscle regeneration. In the LGMD2I sample, IIH6 signal is nearly exclusively localized to regions of regeneration. **c**, Representative immunofluorescence images from patient muscle biopsies. Insets highlight mislocalized (endomysial) perlecan in CMD sample. Intense, localized capillary staining is also observed with perlecan antibody. **d**, Secondary only staining for perlecan in human dystrophic muscle sample, demonstrating that the signal in **c** is specific. Scale bars, 100 μ m.



Extended Data Figure 10 | Model depicting the role of LARGE-glycan in organizing specialized basement membranes. **a**, In normal skeletal muscle, LARGE-glycan on α-DG is abundant and forms long chains, providing many binding sites for ligands such as laminin, agrin and perlecan. In addition to binding the LARGE-glycan, perlecan and agrin bind (directly, or indirectly via accessory proteins like nidogen) to laminin and collagen networks, providing collateral linkages as was recently suggested in regards to perlecan⁴⁵. Increased collateral linkage probably enables compaction of the basement membrane. **b**, In *Large^{KO}* muscle and some dystroglycanopathies, reduced extension of the LARGE-glycan during muscle formation results in a reduction in the number of binding sites for ligands, and the few collateral linkages between collagen, laminin and the sarcolemma are unable to compress the basement membrane. Also, because the basement membrane anchors less collagen, this protein accumulates in the endomysium where it provides ectopic binding sites for perlecan. Agrin is both a high-affinity ligand for the LARGE-glycan and highly concentrated at the NMJ. When the number of LARGE-glycan binding sites at the NMJ basement membrane is limited, agrin saturation of the NMJ may limit the laminin-mediated maturation of the NMJ⁴⁶. Although DG is depicted as

having only two LARGE-glycan chains in this model, it is likely that between 2 and 5 chains are present per DG molecule in skeletal muscle⁷. Integrins, which are not depicted here, can also bind laminin, and thus could contribute to this network; however, mouse studies indicate that its cellular roles are largely independent of DG⁴⁷. **c**, Representative western blot analysis of α-DG in various mouse tissues, demonstrating extensive heterogeneity in molecular mass. Tissues were collected from C57BL6/J mice and samples from multiple mice were pooled before homogenization and Triton X-100 solubilization. Equal amounts of lysate, enriched for glycoprotein by WGA pull down, were loaded. Laminin 111 overlay assay demonstrated that despite differences in molecular mass, the α-DG glycoforms in various tissues retain the capacity to bind laminin. Cb, cerebrum; Cl, cerebellum; E, eye (globe); H, heart; K, kidney; L, lung; n.l., native laminin; SkM, skeletal muscle; T, thymus. **d**, However, higher molecular mass α-DG species have increased binding capacity for laminin 111, as demonstrated by solid-phase assay, indicating that tissue-specific modification of α-DG LARGE-glycan levels is a possible means to modify cell interactions with the extracellular matrix environment. Error bars indicate s.e.m., curve fitting to equation $f = B_{\max} * \text{abs}(x) / (K_d + \text{abs}(x))$.

Structural basis for action by diverse antidepressants on biogenic amine transporters

Hui Wang¹, April Goehring¹, Kevin H. Wang¹, Aravind Penmatsa¹, Ryan Ressler¹ & Eric Gouaux^{1,2}

The biogenic amine transporters (BATs) regulate endogenous neurotransmitter concentrations and are targets for a broad range of therapeutic agents including selective serotonin reuptake inhibitors (SSRIs), serotonin–noradrenaline reuptake inhibitors (SNRIs) and tricyclic antidepressants (TCAs)^{1,2}. Because eukaryotic BATs are recalcitrant to crystallographic analysis, our understanding of the mechanism of these inhibitors and antidepressants is limited. LeuT is a bacterial homologue of BATs and has proven to be a valuable paradigm for understanding relationships between their structure and function³. However, because only approximately 25% of the amino acid sequence of LeuT is in common with that of BATs, and as LeuT is a promiscuous amino acid transporter⁴, it does not recapitulate the pharmacological properties of BATs. Indeed, SSRIs and TCAs bind in the extracellular vestibule of LeuT^{5–7} and act as non-competitive inhibitors of transport². By contrast, multiple studies demonstrate that both TCAs and SSRIs are competitive inhibitors for eukaryotic BATs and bind to the primary binding pocket^{8–16}. Here we engineered LeuT to harbour human BAT-like pharmacology by mutating key residues around the primary binding pocket. The final LeuBAT mutant binds the SSRI sertraline with a binding constant of 18 nM and displays high-affinity binding to a range of SSRIs, SNRIs and a TCA. We determined 12 crystal structures of LeuBAT in complex with four classes of antidepressants. The chemically diverse inhibitors have a remarkably similar mode of binding in which they straddle transmembrane helix (TM) 3, wedge between TM3/TM8 and TM1/TM6, and lock the transporter in a sodium- and chloride-bound outward-facing open conformation. Together, these studies define common and simple principles for the action of SSRIs, SNRIs and TCAs on BATs.

We used the structure of wild-type LeuT in complex with the competitive inhibitor tryptophan (PDB code 3F3A)⁴ as a template for mutant design (Fig. 1a). We analysed residues within a 10 Å radius of the primary binding pocket of the LeuT–Trp complex (Fig. 1a) together with a LeuT/human serotonin transporter (SERT) amino acid sequence alignment to identify about 20 residues which point towards the primary binding pocket and are divergent from SERT (Supplementary Fig. 1). These residues are located in both bundle and scaffold domains¹⁷, sodium binding sites³, the chloride binding site^{18,19} and the extracellular vestibule. Previous studies have demonstrated the importance of many of these residues in SERT pharmacology^{9–12,15,20,21}. By tracking the binding constant (K_d) of [³H]paroxetine, we introduced these mutations into LeuT, focusing initially on ‘first shell’ residues predicted to interact directly with inhibitors and next on ‘second shell’ residues (Supplementary Table 1). The K_d values for paroxetine and mazindol binding to the final LeuBAT mutant, deemed $\Delta 13$ LeuBAT (Supplementary Table 1), are 431 ± 24 nM and 112 ± 18 nM, respectively (Supplementary Fig. 2). Notably, the K_d of $\Delta 13$ for mazindol is similar to that of SERT (103 ± 4.7 nM)⁹. Because uptake experiments using the $\Delta 6$ or $\Delta 13$ variants reconstituted into liposomes show that the constructs are not active in transporting either serotonin or dopamine (Supplementary Fig. 3), further experiments would be required to engineer a variant

of LeuBAT that possesses both high-affinity inhibitor binding and transport activity.

For the $\Delta 13$ LeuBAT construct we performed competition experiments using [³H]paroxetine and multiple cold SSRIs, SNRIs and a TCA (Fig. 1b–d and Supplementary Table 2). Notably, sertraline possesses the highest affinity ($K_d = 18 \pm 2$ nM; $K_i = 14 \pm 2$ nM; Fig. 1c, d), thus approaching the reported value for sertraline binding to SERT (0.3 nM)²². To demonstrate that the $\Delta 6$ and $\Delta 13$ variants possess increased affinities for inhibitors relative to wild-type LeuT, we determined the K_d values for sertraline and mazindol binding to wild-type LeuT to be 308 ± 63 nM and 22.3 ± 5.4 μ M, respectively, whereas the binding of paroxetine could not be fit to an isotherm because of low affinity (Supplementary Fig. 2). The substrate alanine, which binds to the primary pocket of wild-type LeuT⁴, could not suppress the binding of sertraline to wild-type LeuT (Supplementary Fig. 2h), consistent with the conclusion that these drugs bind within the extracellular vestibule of wild-type LeuT^{5–7}.

We determined crystal structures of LeuBAT in complex with a panel of SSRIs, SNRIs and a TCA using the $\Delta 5$, $\Delta 6$ and $\Delta 13$ variants (Supplementary Table 3). For the $\Delta 5$ and $\Delta 6$ mutants, we determined structures for the $\Delta 5$ –mazindol, $\Delta 6$ –sertraline, $\Delta 6$ –desvenlafaxine, $\Delta 6$ –duloxetine and $\Delta 6$ –mazindol complexes at resolutions of 2.3–2.7 Å. For the $\Delta 13$ variant, we determined seven structures with sertraline, paroxetine, fluoxetine, fluvoxamine, duloxetine, desvenlafaxine and clomipramine (CMI) at resolutions of 2.85–3.31 Å (Supplementary Fig. 4 and Supplementary Table 3). Because the binding positions of inhibitors is similar between the $\Delta 6$ and $\Delta 13$ constructs (Supplementary Fig. 5), we used the higher resolution structures of the $\Delta 6$ complexes for analysis and validation of the drug-binding sites in $\Delta 13$.

All LeuBAT structures adopt an outward-facing open conformation (Figs 2a and 3), similar to that of wild-type LeuT in complex with tryptophan⁴ (root mean squared deviation (r.m.s.d.) of 0.48 Å for C α atoms). All drugs bind to the primary binding pocket², interact with both the bundle (TM1, TM6) and scaffold (TM3, TM8) domains, and are lodged between the extracellular gate residues Arg 30 and Asp 404 (ref. 3). These observations invalidate the notion that SSRIs and TCAs elicit their effects on SERT by binding in the extracellular vestibule^{6,7,23}.

We find two sodium ions, Na1 and Na2, bound to sites similar to those in the LeuT–Trp complex with the following distinction. In the wild-type LeuT structures^{3,4} the α -carboxyl group of Leu or Trp participates in the coordination of Na1, whereas in the LeuBAT structures a water molecule is found at the equivalent position, bridging the carboxylate of Asp 24 and Na1 (Supplementary Fig. 6). We detected electron density for a chloride ion in the LeuBAT–paroxetine structure ~ 4.5 Å from Na1, coordinated by Tyr 47, Ser 254, Asn 286 and Ser 290, as predicted previously (Supplementary Fig. 6)^{18,19,24}.

We solved structures of four LeuBAT–SSRI complexes: sertraline, paroxetine, fluoxetine and fluvoxamine. Sertraline occupies the primary pocket surrounded by TM1, TM3, TM6 and TM8 and buries 438.6 Å², or 93%, of its surface area (Fig. 2). The amine group forms a salt bridge with the carboxyl group of Asp 24 whereas the tetrahydronaphthalene

¹Vollum Institute, Oregon Health & Science University, 3181 SW Sam Jackson Park Road, Portland, Oregon 97239, USA. ²Howard Hughes Medical Institute, Oregon Health & Science University, 3181 SW Sam Jackson Park Road, Portland, Oregon 97239, USA.

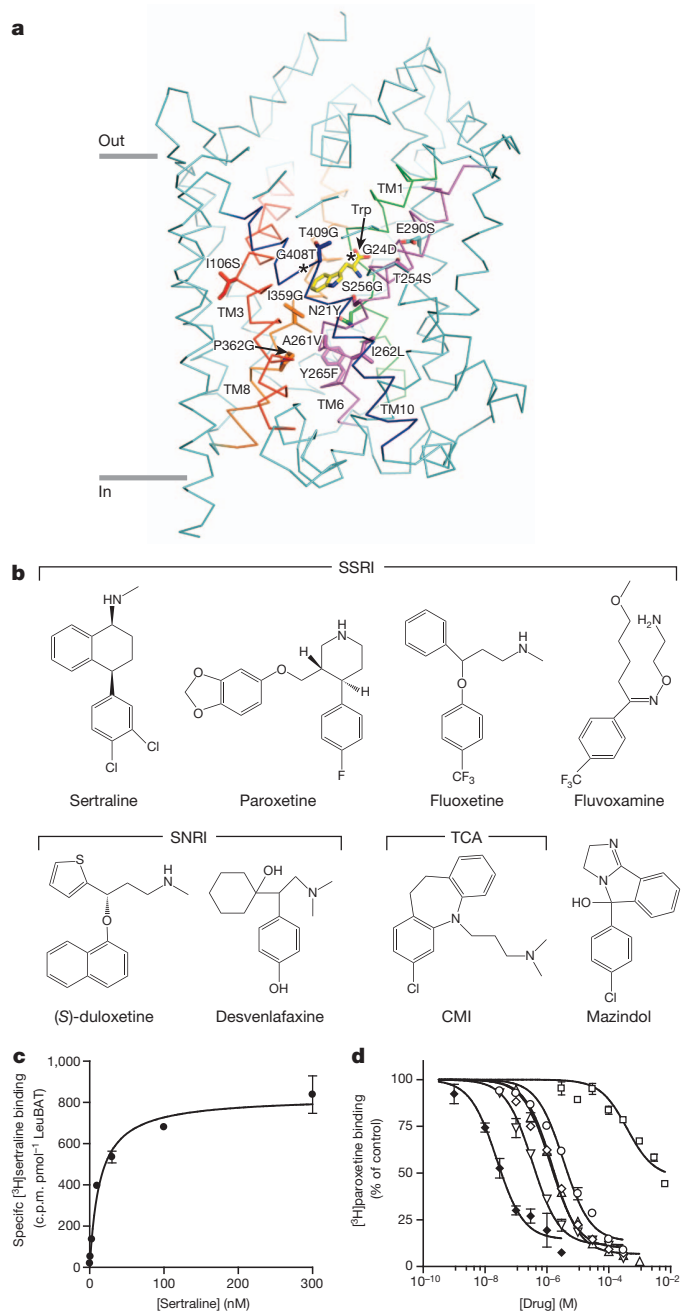


Figure 1 | LeuBAT design and pharmacology. **a**, The representation of mutation positions around the primary binding pocket in the wild-type LeuT–Trp structure (PDB 3F3A). Bound tryptophan (yellow) and the mutated residues are in sticks. The transmembrane helices TM1, TM3, TM6, TM8 and TM10 around the pocket are highlighted as green, red, purple, orange and blue, respectively. Asterisks depict the glycine residue positions. **b**, Chemical structures of four SSRIs, two SNRIs, one TCA (CMI) and one stimulant (mazindol). **c**, Measurement of [3 H]sertraline binding (filled circles) to Δ 13 LeuBAT. **d**, Dose–response curves for inhibition of [3 H]paroxetine binding to Δ 13 LeuBAT by sertraline (filled diamonds), fluvoxamine (empty circles), fluoxetine (empty diamonds), duloxetine (empty inverted triangles), CMI (empty triangles) and desvenlafaxine (empty squares). Error bars, s.e.m., $n = 3$.

ring participates in hydrophobic interactions with Tyr 21 and is sandwiched between Val 104, Tyr 108 and Phe 259 (Fig. 2). The two chlorine atoms on the dichlorophenyl ring insert into a groove formed by Pro 101, Val 104, Ala 105, Ser 356 and Gly 359. We suggest that these extensive hydrophobic and van der Waals interactions contribute to the high affinity of sertraline for LeuBAT and human SERT.

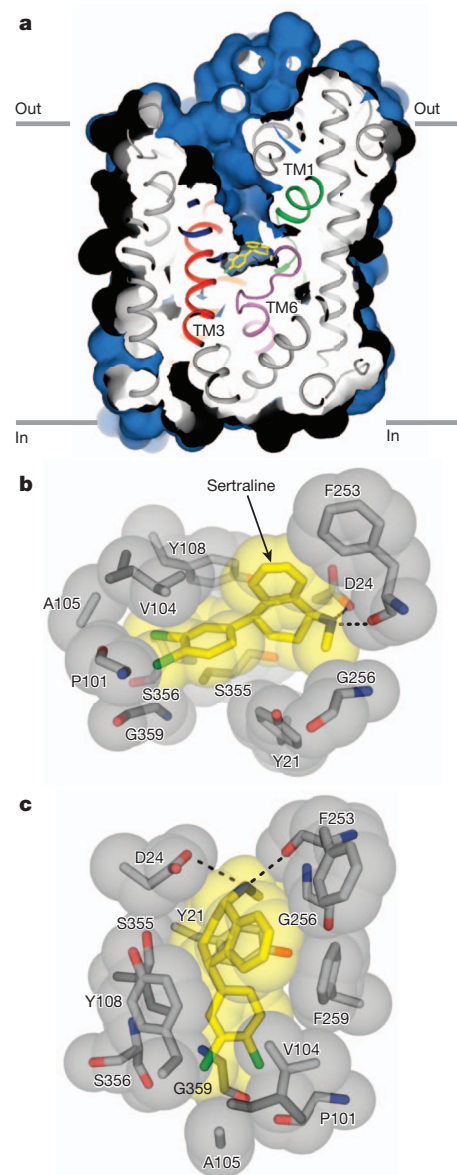


Figure 2 | LeuBAT Δ 13–sertraline complex adopts an outward-facing open conformation. **a**, Cross-sections of the crystal structure of Δ 13–sertraline showing the solvent-accessible surface area (blue). Bound sertraline is shown in yellow sticks. **b**, **c**, Zoom into the sertraline binding pocket viewed within the membrane plane (**b**) and from the extracellular side (**c**). Sertraline and key residues in the pocket are depicted in both sticks and spheres showing the van der Waals radii. Salt bridges and hydrogen bonds are in dashed lines. Phe 259 in **b** is omitted for clarity.

The other SSRIs—paroxetine, fluoxetine and fluvoxamine—also bind to the primary binding pocket in an orientation similar to that of sertraline. Consistent with previous SERT–paroxetine and SERT–fluoxetine models¹³, the amine groups are proximal to the carboxyl group of Asp 24 (Fig. 3a, b). The amine groups of the inhibitors also form direct hydrogen bonds with main-chain carbonyl groups of Tyr 21, Ala 22 and/or Phe 253. The benzodioxol group of paroxetine and trifluoromethylphenyl rings from fluoxetine and fluvoxamine insert to the same groove, as does the chlorophenyl ring of sertraline, forming hydrophobic interactions with Val 104, Tyr 108 and Phe 259, and/or van der Waals interactions with the main-chain carbonyl groups of Pro 101, Ala 105, Ser 356 and Gly 359. In addition, the fluorophenyl ring of paroxetine, the phenyl ring of fluoxetine and the ether chain of fluvoxamine extend into the extracellular vestibule, forming

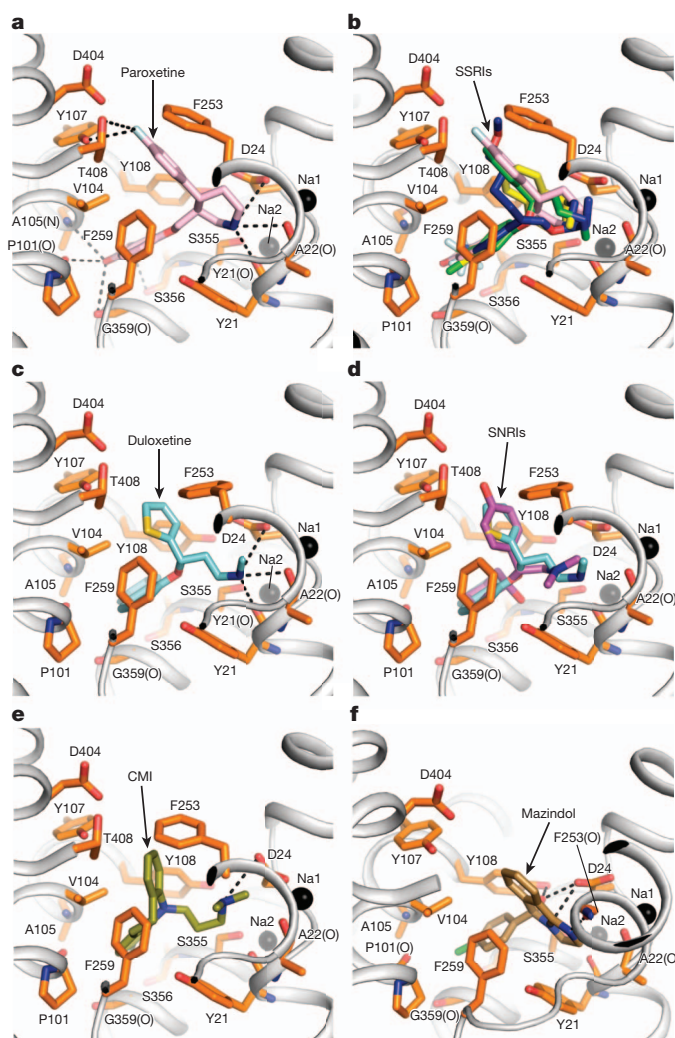


Figure 3 | SSRIs, SNRIs, TCA and mazindol share similar binding features.

a, Paroxetine binding site in the $\Delta 13$ LeuBAT mutant, viewed within the membrane plane with paroxetine shown as pink sticks. Sodium ions and key residues are shown as black spheres and orange sticks, respectively. Hydrogen bonds, salt bridges and polar interactions are in dashed lines. **b**, Superimposition of paroxetine (pink), (*R*)-fluoxetine (green), fluvoxamine (blue) and sertraline (yellow) in the primary binding pocket of the $\Delta 13$ LeuBAT. **c**, (*S*)-duloxetine binding site in the $\Delta 13$ LeuBAT with duloxetine shown as cyan sticks. **d**, Superimposition of (*S*)-duloxetine (cyan) and (*S*)-desvenlafaxine (magenta) in the primary drug-binding pocket. **e**, CMI binding site in $\Delta 13$ LeuBAT with CMI shown as olive sticks. **f**, Mazindol binding site in the LeuBAT $\Delta 6$ variant with mazindol molecule shown as sand-coloured sticks.

hydrophobic interactions, van der Waals contacts and hydrogen-bonding interactions with Tyr 107, Phe 253, Asp 404 and/or Thr 408.

In the SNRI complexes with duloxetine and desvenlafaxine, the inhibitors sit in the primary pocket with the amine groups interacting with the carboxyl group of Asp 24 and, in the case of duloxetine, also with the main-chain carbonyl of Tyr 21 (Fig. 3c, d). The naphthalene ring from duloxetine and the cyclohexanol ring from desvenlafaxine are sandwiched by hydrophobic groups Tyr 21, Val 104, Phe 259 and Tyr 108. The thiophene ring from duloxetine and the phenol ring from desvenlafaxine protrude into the extracellular vestibule and interact with Phe 253 by edge-to-face interactions. For desvenlafaxine, the hydroxyl group in the cyclohexanol moiety makes a hydrogen bond with the main-chain carbonyl group of Ser 355, whereas the phenol hydroxyl interacts with Asp 404 and the phenol group of Tyr 107.

The tricyclic antidepressant CMI binds to the primary binding pocket of $\Delta 13$ LeuBAT (Fig. 3e), in agreement with a human SERT–TCA

model^{11,12} and in contrast to wild-type LeuT–TCA structures^{5,6}. The tricyclic ring is surrounded by hydrophobic residues including Tyr 21, Val 104, Tyr 108, Phe 253 and Phe 259. The chlorine atom in the tricyclic ring extends to the pocket formed by Ala 105, Ser 356 and Gly 359, similar to the chorine positions in sertraline or the trifluoromethyl moiety in fluoxetine. Not only are previously proposed interactions¹² observed in our LeuBAT–CMI structure, such as the salt bridge between Asp 24 (Asp 98 in SERT) and the tertiary aliphatic amine of the TCA, the structure is consistent with interactions between Ala 105 (Ala 173 in SERT) and the TCA 3-position, and with Phe 253 (Phe 335 in SERT) being near the TCA 7-position. Our structure is in harmony with the conclusion that Ser 438 in human SERT (Ser 355 in LeuBAT) is vicinal to the aminopropyl chain of TCA and that the S438T mutation affects the binding affinity because of steric clash¹¹.

The stimulant mazindol binds to the primary site and is surrounded by a hydrophobic pocket formed by Tyr 21, Val 104, Tyr 108 and Phe 259 (Fig. 3f). The amine nitrogen forms a salt bridge with the carboxyl group of Asp 24. The hydroxyl group hydrogen bonds with the carboxyl group of Asp 24 and the phenol group of Tyr 108. The chlorophenyl ring inserts into the pocket formed by Ala 105, Ser 356 and Gly 359, similar to sertraline. The importance of these interactions is supported by the fact that removal of the chlorophenyl ring or changes in the substitution on the phenyl ring decreases the affinity of mazindol to SERT⁹.

By soaking $\Delta 6$ mutant crystals in 20 mM desvenlafaxine, we identified a second desvenlafaxine molecule in the extracellular vestibule (Supplementary Fig. 7). The second molecule occupies a similar position to the positions that TCAs, sertraline and fluoxetine occupy in wild-type LeuT structures reported previously^{5–7} (Supplementary Fig. 7). These results demonstrate that the *n*-octyl- β -D-glucoside molecule bound to the extracellular vestibule of wild-type LeuT^{25,26} is readily substituted by a drug molecule and that the extracellular vestibule is a site for the low-affinity, non-specific binding of small molecules.

Analysis of the sertraline (SSRI), duloxetine (SNRI) and CMI (TCA) complexes with LeuBAT allows us to identify three subsites within the primary binding site to which the pharmacophores of these chemically diverse inhibitors bind (Fig. 4a, b). Subsite A is defined by Asp 24, Tyr 21, Gly 256 and Ser 355 from TM1, TM6 and TM8, and accommodates the polar, amine moiety of the inhibitors²⁷. Asp 24 interacts with the amine groups of most drugs by salt bridge, which echoes the suggestion that Asp 98 in human SERT forms a similar interaction with the amine groups of SSRIs, TCAs and serotonin^{9,12,13,20,21}.

Subsite B includes residues from TM3, TM6 and TM8 and involves two types of interactions. First, nonpolar residues form hydrophobic interactions with the hydrophobic rings of the drugs. Phe 259 (Phe 341 in human SERT) together with Val 104 (Ile 172 in human SERT or Val 148 in the human noradrenaline transporter (NET)) define a non-polar ridge that accommodates the hydrophobic groups of the drugs^{27,28}. Previous studies showed that the F341Y mutation in human SERT reduces the potency of paroxetine and escitalopram²⁷. Here we suggest that the F341Y mutation leads to a clash with the fluorophenyl ring of paroxetine. The second type of interaction in subsite B is the groove delineated by Pro 101, Ala 105, Gly 359 and Ser 356. This groove accommodates the polar groups in the drugs' rings, such as the chloro, dichloro, trifluoromethyl and benzodioxol groups of CMI, sertraline, fluoxetine and paroxetine, respectively, and is capped by Tyr 108. A SERT–imipramine model suggests that the imipramine 3-position is vicinal to Ala 173 (Ala 105 in LeuBAT)¹², and here we show that the chlorine atom in the 3-position of CMI forms a direct contact with this ridge.

Subsite C, distal to the primary, orthosteric binding site, is located in the extracellular vestibule, and is comprised of residues in TM6 and TM10, including Phe 253, Asp 404 and Thr 408. Subsite C interacts with bulky drugs such as paroxetine, desvenlafaxine and fluoxetine, and probably has a role in enhancing inhibitor affinity and specificity.

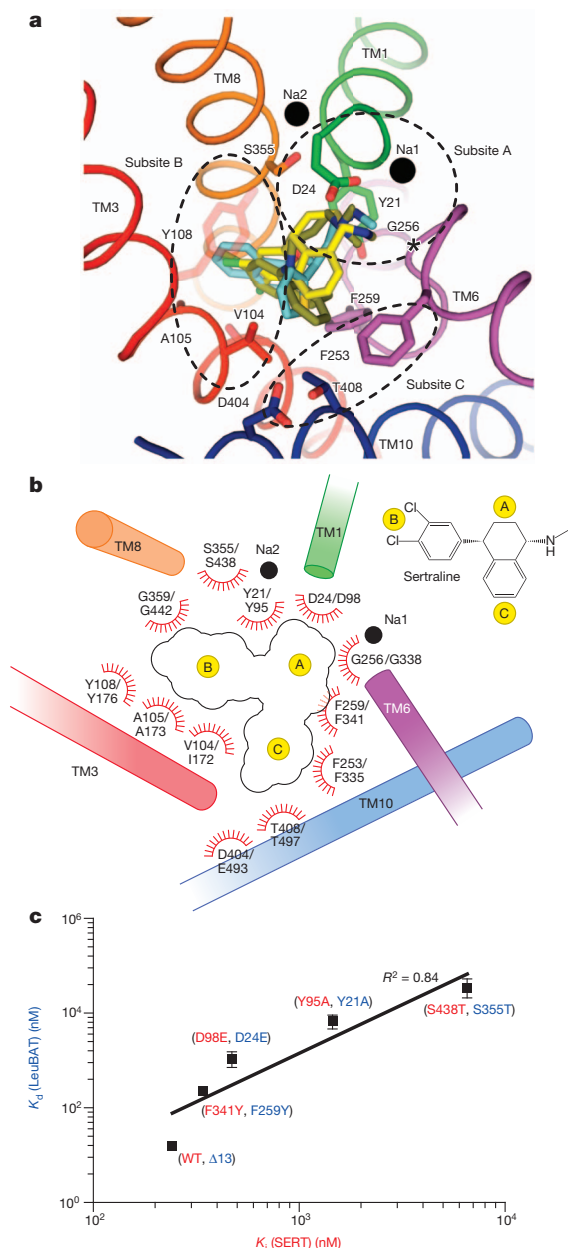


Figure 4 | Implication for drug binding in human SERT and validation by mutational studies. **a**, Superposition of SSRI (sertraline, yellow), SNRI (duloxetine, cyan) and TCA (CMI, olive) in the primary binding pocket of LeuBAT, viewed from extracellular side. The key residues in the pockets and the two sodium ions are shown as sticks and black spheres, respectively. The regions enclosed by dashed lines define subsites A, B and C in the primary drug binding pocket. **b**, Schematic representation of drug interactions in the primary binding pocket of LeuBAT. The transmembrane helices are shown as cylinders. Residue numbering follows LeuBAT and SERT, respectively. **c**, Plot of sertraline binding constants for Y21A, D24E, F259Y and S355T mutants of the $\Delta 13$ LeuBAT against the inhibition constants for the corresponding mutants Y95A, D98E, F341Y and S438T in SERT, respectively. WT, wild type. Error bars, s.e.m., $n = 3$.

Indeed, previous studies determined that mutation of E493Q in human SERT (Asp 404 in LeuBAT) attenuates the potency of fluoxetine⁷.

To support the conclusion that the LeuBAT complexes represent reliable models for BAT–inhibitor complexes, we prepared and analysed the individual Y21A, D24E, F259Y and S355T mutations in the context of the $\Delta 13$ LeuBAT construct. Y21A, D24E and S355T are in subsite A and F259Y is in subsite B. We next measured their [³H]sertraline K_d values and plotted log K_d of the LeuBAT mutants against log K_i of the

homologous human SERT mutants²⁷ (Fig. 4c). The resulting linear relationship suggests that the mutations in LeuBAT have similar effects to those in SERT, and suggests that LeuBAT represents a framework for understanding the pharmacology of human SERT. We further compared the pharmacological selectivity of LeuBAT with all human BATs by plotting log K_i (LeuBAT) versus log K_i (human dopamine transporter (DAT), NET or SERT) (Supplementary Fig. 8). Inspection of these plots suggests that the pharmacological properties of LeuBAT are a hybrid of human BATs. Moreover, we compared the TCA binding site of the LeuBAT–CMI complex with the recently determined structure of the *Drosophila* DAT–nortriptyline complex²⁹ (Supplementary Fig. 9). We note that the overall outward-open conformation and the essential elements of inhibitor binding are shared between the two structures. Finally, we reverted residues Asp 24, Gly 256 and Gly 359 in LeuBAT to their LeuT identities and investigated their effects on the drug binding. These mutations profoundly diminish drug binding (Supplementary Fig. 10), thus supporting the conclusion that the LeuBAT–inhibitor crystal structures represent specifically bound ligand–transporter complexes.

Taken together, the LeuBAT complexes allow us to map crucial subsites within the primary, orthosteric binding site that are responsible for binding the pharmacophores of a chemically diverse group of SSRIs, SNRIs and TCAs (Supplementary Fig. 11); they show that these inhibitors act by binding to the outward-open conformation of the transporter; and, perhaps most importantly, they provide molecular guideposts for the development of new therapeutic agents.

METHODS SUMMARY

The LeuBAT mutants were expressed and purified as previously described³ except that lauryl maltose neopentyl glycol was used for solubilization and purification. After final purification by size-exclusion chromatography in *n*-octyl- β -D-glucoside, LeuBAT was concentrated to 2.5 mg ml^{−1} and supplemented with saturating serotonin or mazindol prior to crystallization. All LeuBAT–drug complexes except mazindol were formed by soaking LeuBAT crystals in crystallization solutions containing 3–20 mM of each drug. The structures were solved by molecular replacement using the LeuT–Trp structure⁴ as a search probe and then subjected to crystallographic refinement. The functional activities of LeuBAT mutants were examined by [³H]paroxetine, [³H]sertraline and [³H]mazindol saturation and competition binding assays.

Online Content Any additional Methods, Extended Data display items and Source Data are available in the online version of the paper; references unique to these sections appear only in the online paper.

Received 2 June; accepted 11 September 2013.

Published online 13 October 2013.

- Bröer, S. & Gether, U. The solute carrier 6 family of transporters. *Br. J. Pharmacol.* **167**, 256–278 (2012).
- Kristensen, A. S. *et al.* SLC6 neurotransmitter transporters: structure, function, and regulation. *Pharmacol. Rev.* **63**, 585–640 (2011).
- Yamashita, A., Singh, S. K., Kawate, T., Jin, Y. & Gouaux, E. Crystal structure of a bacterial homologue of Na⁺/Cl[−]-dependent neurotransmitter transporters. *Nature* **437**, 215–223 (2005).
- Singh, S. K., Piscitelli, C. L., Yamashita, A. & Gouaux, E. A competitive inhibitor traps LeuT in an open-to-out conformation. *Science* **322**, 1655–1661 (2008).
- Singh, S. K., Yamashita, A. & Gouaux, E. Antidepressant binding site in a bacterial homologue of neurotransmitter transporters. *Nature* **448**, 952–956 (2007).
- Zhou, Z. *et al.* LeuT–desipramine structure reveals how antidepressants block neurotransmitter reuptake. *Science* **317**, 1390–1393 (2007).
- Zhou, Z. *et al.* Antidepressant specificity of serotonin transporter suggested by three LeuT–SSRI structures. *Nature Struct. Mol. Biol.* **16**, 652–657 (2009).
- Talvenheimo, J., Nelson, P. J. & Rudnick, G. Mechanism of imipramine inhibition of platelet 5-hydroxytryptamine transport. *J. Biol. Chem.* **254**, 4631–4635 (1979).
- Barker, E. L. *et al.* High affinity recognition of serotonin transporter antagonists defined by species-scanning mutagenesis: an aromatic residue in transmembrane domain I dictates species-selective recognition of citalopram and mazindol. *J. Biol. Chem.* **273**, 19459–19468 (1998).
- Henry, L. K. *et al.* Tyr-95 and Ile-172 in transmembrane segments 1 and 3 of human serotonin transporters interact to establish high affinity recognition of antidepressants. *J. Biol. Chem.* **281**, 2012–2023 (2006).
- Andersen, J. *et al.* Location of the antidepressant binding site in the serotonin transporter: importance of Ser-438 in recognition of citalopram and tricyclic antidepressants. *J. Biol. Chem.* **284**, 10276–10284 (2009).

12. Sinning, S. *et al.* Binding and orientation of tricyclic antidepressants within the central substrate site of the human serotonin transporter. *J. Biol. Chem.* **285**, 8363–8374 (2010).
13. Tavoulari, S., Forrest, L. R. & Rudnick, G. Fluoxetine (Prozac) binding to serotonin transporter is modulated by chloride and conformational changes. *J. Neurosci.* **29**, 9635–9643 (2009).
14. Koldsø, H. *et al.* The two enantiomers of citalopram bind to the human serotonin transporter in reversed orientations. *J. Am. Chem. Soc.* **132**, 1311–1322 (2010).
15. Andersen, J. *et al.* Mutational mapping and modeling of the binding site for (S)-Citalopram in the human serotonin transporter. *J. Biol. Chem.* **285**, 2051–2063 (2010).
16. Jørgensen, A. M. *et al.* Homology modeling of the serotonin transporter: insights into the primary escitalopram-binding site. *ChemMedChem* **2**, 815–826 (2007).
17. Forrest, L. R. & Rudnick, G. The rocking bundle: a mechanism for ion-coupled solute flux by symmetrical transporters. *Physiology* **24**, 377–386 (2009).
18. Zomot, E. *et al.* Mechanism of chloride interaction with neurotransmitter:sodium symporters. *Nature* **449**, 726–730 (2007).
19. Forrest, L. R., Tavoulari, S., Zhang, Y.-W., Rudnick, G. & Honig, B. Identification of a chloride ion binding site in Na⁺/Cl[−] dependent transporters. *Proc. Natl Acad. Sci. USA* **104**, 12761–12766 (2007).
20. Celik, L. *et al.* Binding of serotonin to the human serotonin transporter. Molecular modeling and experimental validation. *J. Am. Chem. Soc.* **130**, 3853–3865 (2008).
21. Kaufmann, K. W. *et al.* Structural determinants of species-selective substrate recognition in human and *Drosophila* serotonin transporters revealed through computational docking studies. *Proteins* **74**, 630–642 (2009).
22. Tatsumi, M., Groshan, K., Blakely, R. D. & Richelson, E. Pharmacological profile of antidepressants and related compounds at human monoamine transporters. *Eur. J. Pharmacol.* **340**, 249–258 (1997).
23. Sarker, S. *et al.* The high-affinity binding site for tricyclic antidepressants resides in the outer vestibule of the serotonin transporter. *Mol. Pharmacol.* **78**, 1026–1035 (2010).
24. Tavoulari, S., Rizwan, A. N., Forrest, L. R. & Rudnick, G. Reconstructing a chloride-binding site in a bacterial neurotransmitter transporter homologue. *J. Biol. Chem.* **286**, 2834–2842 (2011).
25. Wang, H., Elferich, J. & Gouaux, E. Structures of LeuT in bicelles define conformation and substrate binding in a membrane-like context. *Nature Struct. Mol. Biol.* **19**, 212–219 (2012).
26. Quick, M. *et al.* Binding of an octylglucoside detergent molecule in the second substrate (S2) site of LeuT establishes an inhibitor-bound conformation. *Proc. Natl Acad. Sci. USA* **106**, 5563–5568 (2009).
27. Sørensen, L. *et al.* Interaction of antidepressants with the serotonin and norepinephrine transporters: mutational studies of the S1 substrate binding pocket. *J. Biol. Chem.* **287**, 43694–43707 (2012).
28. Andersen, J. *et al.* Molecular determinants for selective recognition of antidepressants in the human serotonin and norepinephrine transporters. *Proc. Natl Acad. Sci. USA* **108**, 12137–12142 (2011).
29. Penmatsa, A., Wang, K. H. & Gouaux, E. X-ray structure of dopamine transporter elucidates antidepressant mechanism. *Nature* <http://dx.doi.org/10.1038/nature12533> (15 September 2013).

Supplementary Information is available in the online version of the paper.

Acknowledgements We thank J. Michel for help in binding experiments, D. Claxton for comments and L. Vaskalis for assistance with illustrations. We also thank the beamline staff at the Advanced Light Source (beamlines 8.2.1 and 5.0.2) and Advanced Photon Source (Argonne National Laboratory, beamlines 24-ID-C and 24-ID-E). H.W. also thanks the presenters at 2012 CCP4/APS summer school for useful lectures and tutorials. This work was supported by the National Institutes of Health. E.G. is an Investigator with the Howard Hughes Medical Institute.

Author Contributions H.W. and E.G. designed the research; H.W., A.G. and R.R. performed protein expression and purification; H.W., A.G., K.H.W. and A.P. carried out ligand-binding and flux experiments; H.W. conducted crystallization and structure determination; H.W. and E.G. wrote the manuscript together with comments from all authors.

Author Information Coordinates and structure factors for the LeuBAT Δ 13-paroxetine, Δ 13-sertraline, Δ 13-duloxetine, Δ 13-desvenlafaxine, Δ 13-fluoxetine, Δ 13-fluvoxamine, Δ 13-clomipramine, Δ 6-sertraline, Δ 6-desvenlafaxine, Δ 6-duloxetine, Δ 6-mazindol and Δ 5-mazindol crystal structures have been deposited in the Protein Data Bank with codes 4MM4, 4MM5, 4MM6, 4MM7, 4MM8, 4MM9, 4MMA, 4MMB, 4MMC, 4MMD, 4MME and 4MMF, respectively. Reprints and permissions information is available at www.nature.com/reprints. The authors declare no competing financial interests. Readers are welcome to comment on the online version of the paper. Correspondence and requests for materials should be addressed to E.G. (gouauxe@ohsu.edu).

METHODS

Protein expression and purification. The LeuBAT mutants were expressed and purified as described previously for wild-type LeuT^{32,25} with two exceptions. First, lauryl maltose neopentyl glycol (MNG-3) instead of *n*-dodecyl- β -D-maltopyranoside (C₁₂M) was used for solubilization and purification. Second, no drugs or substrate were added during purification. Cell membranes were solubilized using a buffer composed of 25 mM Tris-HCl (pH 8.0), 250 mM NaCl and 1% MNG-3 and the protein was then purified by immobilized-metal affinity chromatography (IMAC) in the presence of 0.02% MNG-3. For crystallization, LeuBAT was purified by size-exclusion chromatography in 25 mM Tris-HCl (pH 8.0), 150 mM NaCl and 40 mM *n*-octyl- β -D-glucoside.

Crystallization and crystal soaking. LeuBAT with saturated serotonin or mazindol was crystallized by vapour diffusion at 20 °C with two different precipitating solutions containing: 100 mM NaPi (pH 7.0), 100 mM NaCl, 32–34% PEG300; or 100 mM glycine (pH 9.4), 0.1 M Li₂SO₄, 29–31% PEG400. LeuBAT crystals grown in the presence of serotonin were soaked for 1 h in crystallization solution containing 4 mM paroxetine, 20 mM desvenlafaxine, 3.7 mM sertraline, 3.7 mM fluoxetine, 3 mM duloxetine, 3 mM fluvoxamine or 10 mM CMI. After soaking, crystals were directly flash frozen in liquid nitrogen before X-ray diffraction data collection.

Data collection and structure elucidation. Diffraction data sets were collected at the Advanced Light Source (beamlines 5.0.2 and 8.2.1) and Advanced Photon Source (Argonne National Laboratory, beamlines 24-ID-C and 24-ID-E). Data sets were processed using HKL2000 software³⁰ and iMOSFLM³¹. The LeuBAT-antidepressant structures were determined by molecular replacement using LeuT-Trp (PDB code 3F3A) as a search probe using Phaser³² in CCP4 suite³³. The drugs were built based on the omit maps that were calculated by Phenix³⁴, with the antidepressants omitted from the structure factor calculation. The refinements were carried out using Phenix and Refmac in CCP4 suite³³, and manual adjustments were made using Coot³⁵. The structure quality analysis was carried out using Molprobity³⁶ with 97% of the residues in the most favoured regions and none in disallowed regions based on Ramachandran analysis. All structure figures were generated with PyMOL (DeLano Scientific).

Binding and competition assays. For binding studies, protein from IMAC fractions was desalted by Zeba Desalt Spin Columns in buffer A (150 mM Tris-MES (pH 7.5), 100 mM NaCl, 20% (v/v) glycerol, 0.02% MNG-3). Scintillation proximity assays (SPA) were performed as before³⁷. Sertraline binding was performed by incubating 4 nM protein with 1–2 mg ml⁻¹ copper yttrium silicate (Cu-Ysi) SPA beads in buffer A in the presence of 0.3–300 nM [³H]sertraline (4 Ci mmol⁻¹). For mazindol binding, 25 nM protein was incubated with 1–2 mg ml⁻¹ Cu-Ysi SPA beads in buffer A in the presence of 1–3,000 nM [³H]mazindol (2.5 Ci mmol⁻¹). For paroxetine binding, 50–100 nM protein was incubated with 1–2 mg ml⁻¹ Cu-Ysi SPA beads in buffer A in the presence of 0.01–10 μ M [³H]paroxetine (1.04 Ci mmol⁻¹). Nonspecific binding was measured in the presence of 400 mM imidazole, 0.1 mM

mazindol and/or 0.5 mM CMI. Plate readings were taken using a Wallac Microbeta plate counter. Data after overnight incubation was analysed by GraphPad Prism4 and fit into a single-site binding function. Experiments were performed three times.

Competition assays were performed by using 300 nM [³H]paroxetine (4.16 Ci mmol⁻¹) in buffer A. For half-maximum inhibitory concentration measurements, the concentrations of inhibitors were varied from 3 nM to 6.7 mM. A protein concentration of 100 nM was used for the competition assays, except that 10 nM protein was used for the sertraline competition experiments. The *K_i* values were calculated by using the Cheng-Prusoff equation.

To compare mazindol binding to the Δ 13, Δ 13(D24G), Δ 13(G256S) and Δ 13(G359I) mutants, proteins (50 nM) were incubated with 1 mg ml⁻¹ Cu-Ysi SPA beads in buffer A in the presence of 100 nM [³H]mazindol (27.8 Ci mmol⁻¹). For sertraline binding, proteins (27 nM) were incubated with 1 mg ml⁻¹ Cu-Ysi SPA beads in buffer A in the presence of 15 nM [³H]sertraline (80 Ci mmol⁻¹). Nonspecific binding was measured in the presence of 0.1 mM mazindol and sertraline, respectively.

Fluorescence-detection size-exclusion chromatography. Fluorescence-detection size-exclusion chromatography (FSEC) was performed as described previously³⁸. Before the FSEC experiment, 1.2–4.8 pmol of each variant protein was incubated with 45–90 pmol of the 2B12 monoclonal antibody³⁹ for 1 h and then loaded onto a Superose 6 column pre-equilibrated with 20 mM Tris-HCl (pH 8.0), 150 mM NaCl and 0.02% MNG-3 detergent. The elution was monitored by an in-line fluorescence detector which was set with excitation at 280 nm and emission at 335 nm. The proteins in the absence of 2B12 were used as a control (Supplementary Fig. 10).

30. Otwinowski, Z. & Minor, W. Processing of X-ray diffraction data collected in oscillation mode. *Methods Enzymol.* **276**, 307–326 (1997).
31. Battye, T. G. G., Kontogiannis, L., Johnson, O., Powell, H. R. & Leslie, A. G. W. iMOSFLM: a new graphical interface for diffraction-image processing with MOSFLM. *Acta Crystallogr. D* **67**, 271–281 (2011).
32. McCoy, A. J. et al. Phaser crystallographic software. *J. Appl. Crystallogr.* **40**, 658–674 (2007).
33. Collaborative Computing Project. The CCP4 suite: programs for protein crystallography. *Acta Crystallogr. D* **50**, 760–763 (1994).
34. Adams, P. D. et al. PHENIX: a comprehensive Python-based system for macromolecular structure solution. *Acta Crystallogr. D* **66**, 213–221 (2010).
35. Emsley, P., Lohkamp, B., Scott, W. G. & Cowtan, K. Features and development of Coot. *Acta Crystallogr. D* **66**, 486–501 (2010).
36. Chen, V. B. et al. MolProbity: all-atom structure validation for macromolecular crystallography. *Acta Crystallogr. D* **66**, 12–21 (2010).
37. Wang, H. & Gouaux, E. Substrate binds in the S1 site of the F253A mutant of LeuT, a neurotransmitter sodium symporter homologue. *EMBO Rep.* **13**, 861–866 (2012).
38. Kawate, T. & Gouaux, E. Fluorescence-detection size-exclusion chromatography for precrystallization screening of integral membrane proteins. *Structure* **14**, 673–681 (2006).
39. Krishnamurthy, H. & Gouaux, E. X-ray structures of LeuT in substrate-free outward-open and apo inward-open states. *Nature* **481**, 469–474 (2012).

CORRIGENDUM

doi:10.1038/nature12747

Corrigendum: Exercise-induced BCL2-regulated autophagy is required for muscle glucose homeostasis

Congcong He, Michael C. Bassik, Viviana Moresi, Kai Sun, Yongjie Wei, Zhongju Zou, Zhenyi An, Joy Loh, Jill Fisher, Qihua Sun, Stanley Korsmeyer, Milton Packer, Herman I. May, Joseph A. Hill, Herbert W. Virgin, Christopher Gilpin, Guanghua Xiao, Rhonda Bassel-Duby, Philipp E. Scherer & Beth Levine

Nature **481**, 511–515 (2012); doi:10.1038/nature10758

In this Letter, information was inadvertently omitted that the results in Supplementary Fig. 21 represent the mean + s.e.m. for 4–5 mice per group. We also note that the samples used for Fig. 3f, Supplementary Figs 3 and 13a were derived from the same experiment, and that the gels/blots were processed in parallel. Equal concentrations of protein were loaded on all gels. The same actin loading control gel is shown in Fig. 3f, Supplementary Figs 3 and 13a. Furthermore, owing to a production error at the proof stage, the time point labels were missing from Fig. 1e. After ‘Exercise (min)’, the labels should read 0, 15 and 30. This has now been corrected in the PDF and HTML versions of the paper. None of these changes alters the conclusions of the paper.

RETRACTION

doi:10.1038/nature12727

Retraction: Functional dissection of lysine deacetylases reveals that HDAC1 and p300 regulate AMPK

Yu-yi Lin, Samara Kiihl, Yasir Suhail, Shang-Yun Liu, Yi-hsuan Chou, Zheng Kuang, Jin-ying Lu, Chin Ni Khor, Chi-Long Lin, Joel S. Bader, Rafael Irizarry & Jef D. Boeke

Nature **482**, 251–255 (2012); doi:10.1038/nature10804

In response to a concern raised by a reader about inconsistencies in our Letter between the results from the primary microarray screen and cell growth validation studies (Supplementary Table 2), we reviewed the methods described, and the subsequent analytical and validation work. We conclude that the Methods section in our Letter is inaccurate, and that for 38% of the interactions found by the primary screen there was a discordance in sign when validated (for example, an interaction might be called ‘synthetic lethal’ by the primary screen but ‘synthetic rescue’ in the cell growth validation assay, or vice versa). Although the results from the reanalysis did not contradict our key conclusions, we also re-evaluated the experiments in Figs 2–4 that indicate that p300 acetylates PRKAA1 and HDAC1 deacetylates it. We sequence-verified and spot-checked many of the plasmids and cell lines described, which are available on request. The biological materials were found to be as we described, and certain aspects, such as p300 acetylation of PRKAA1 protein *in vitro*, could be reproduced. However, despite several attempts, we were unable to obtain results definitively supporting the major claims of the Letter, namely that p300 is the acetyltransferase and HDAC1 is the deacetylase for PRKAA1 in cells. The batch of polyclonal antibody against acetyl-lysine originally used is no longer available. More definitive experiments require antibodies that specifically recognize acetylated sites on PRKAA1, which we are developing. Although our inability to reproduce these results does not mean our conclusions are incorrect, we cannot say with confidence that they are correct. Given the time that has elapsed, and our inability to reproduce the main conclusions of the Letter, we feel obliged to retract it. All the authors have signed this retraction with the exception of Y.-Y.L., who is deceased. Correspondence should be addressed to J.D.B. (jboeke@jhmi.edu).

TECHNOLOGY FEATURE

BRAIN MAPPING IN HIGH RESOLUTION

Tools that make it possible to chart every neuron and its connections are helping neuroscientists to realize their dream of whole-brain maps.

KHENG GUAN TOH/SHUTTERSTOCK



BY VIVIEN MARX

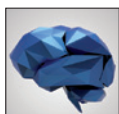
Researchers wanting to understand the workings of the brain need maps on many different scales — to link structure to function, to parse the complexities of memory loss or learning disability, or to find out what is different about the brains of people with neurodegenerative diseases. For instance, programmes such as the Human Connectome Project, funded by the US National Institutes of Health (NIH) in Bethesda, Maryland, and the Consortium of Neuroimagers for the Non-invasive Exploration of Brain Connectivity

and Tracts (CONNECT), funded by the European Commission in Brussels, are producing magnetic resonance imaging (MRI) maps that follow neuronal connections across the entire brain, on a scale of tens of centimetres.

Some research teams are embarking on even more ambitious projects to create maps that reveal structure and connections at the scale of individual neurons. The slender processes

of neurons — the axons and dendrites — are 20 micrometres or less in diameter, but can extend for several millimetres. Mapping the thicket of 86 billion neurons and their connections in the human brain at this scale is still a distant dream, but the goal of mapping the 75 million neurons in the mouse brain could be a little closer. And the second might pave the way for the first.

To achieve this, however, researchers need new tools, starting with refinements to electron microscopy. In conventional electron-microscopy approaches, scientists have to make ultrathin slices of brain tissue and ►



NEW ANGLES ON THE BRAIN

A *Nature* special issue

www.nature.com/neuroscience2013

SOURCE: DIATOME

► laboriously image them slice by slice to build up a three-dimensional (3D) picture. In 1986, the complete nervous system of one model organism was mapped using this approach — the 302 neurons of the nematode *Caenorhabditis elegans*¹ — but the process is too slow and cumbersome to scale up. Now, electron microscopes at many universities are “being mothballed”, says neurobiologist Jeff Lichtman at Harvard University in Cambridge, Massachusetts, because they are deemed a throwback to an era when “all you could do was stain and look”.

Nevertheless, high-resolution, 3D neuronal mapping by electron microscopy is gaining momentum. “It’s not just the old neuro-anatomy gussied up with new machines,” says Lichtman, who studies the neuronal architecture of the mouse brain. “It’s giving us three-dimensional information about structure at the super-resolution of nanometres — and that is invaluable.” These capabilities are spurring the development of new ways to prepare, image and analyse brain tissue from model organisms such as mice, and from people who have donated their brains to science on their death.

Until now, when neuroscientists published cell-level images and analysis, they were looking at a tiny region of brain; for example, a few hundred neurons in the mouse or fruitfly^{2,3}. Efforts to map all the neurons and circuits in the mouse brain are just beginning in several labs. Creating structural maps is a high priority of the NIH-funded Brain Research Through Advancing Innovative Neurotechnologies (BRAIN) Initiative, which US President Barack Obama launched in April⁴. Another large-scale effort is the Human Brain Project, funded by the European Union, which is focused on a different kind of map — a computational model of the brain.

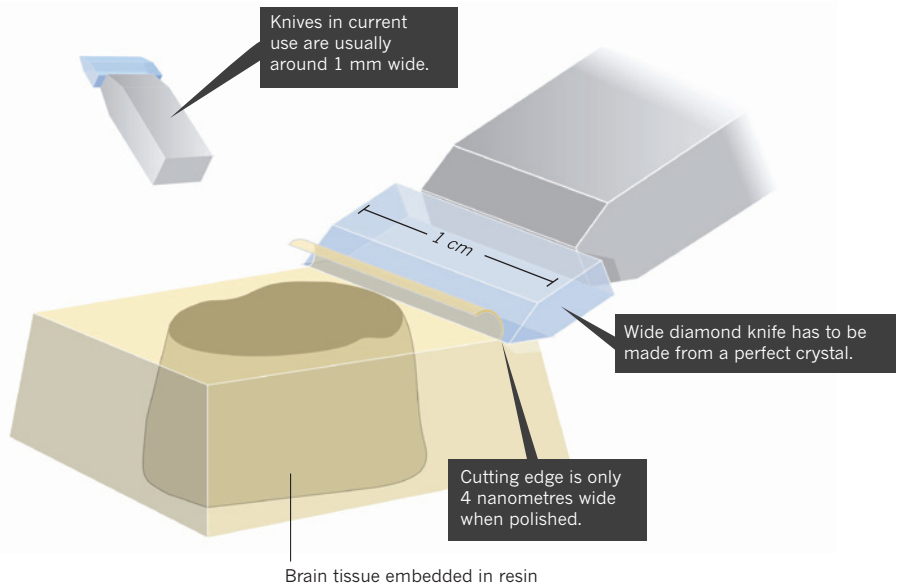
Neurobiologist and microscopist Winfried Denk at the Max Planck Institute for Medical Research in Heidelberg, Germany, thinks that the technology to image an entire mouse brain at cellular resolution is within grasp. Late next year, he and Lichtman are each scheduled to receive a new multi-beam scanning electron microscope (SEM) for their labs, developed by Carl Zeiss Microscopy in Oberkochen, Germany. Now in the prototype stage, this instrument will enable the imaging of brain slices to be accelerated hugely — possibly by as much as 60 times. Such



Winfried Denk estimates that image capture of a whole mouse brain could yield 60 petabytes of data.

SHARP TOOLS

One manufacturer is developing wide diamond knives that can be used to shave off samples containing a slice of the whole mouse brain.



gains could make it feasible to map all the neurons in a mammalian brain. Other microscope manufacturers, such as FEI in Eindhoven, the Netherlands, are also developing tools to enable detailed brain mapping.

PREPARING TO SEE

Before brain tissue can be imaged using electron microscopy, samples must be prepared by slicing and staining. These steps are important for the subsequent process of using the two-dimensional images generated by the electron microscope to reconstruct the three dimensions of the brain and its neuronal connections. Scientists are exploring new ways to prepare samples so that they can obtain higher contrast for electron microscopy and view larger pieces of brain tissue.

When brain tissue is well stained with chemicals, thinly sliced and viewed using electron microscopy, researchers see slices that look like thin plates covered with tiny soap bubbles. Some bubbles represent the cross-section of a neuron, and the soap-bubble boundary shows where one neuron ends and another begins. Contrast is crucial, because scientists need to discern neurons from a wealth of other cell types and organelles in the brain tissue. They can then trace each neuron in each of the imaged slices, by hand and by eye.

But such imaging has its problems: staining often does not show enough structure, the slices might be warped and images can be blurry.

Denk and his team previously developed an approach called serial block-face electron microscopy (SBEM), which obviates the need to prepare slices before imaging them. Instead, successive images are obtained by scanning the face of an unsliced block of tissue placed

in the electron microscope, then cutting off an ultrathin slice using an automated microtome within the instrument. The newly exposed surface of the sliced block is rescanned, and so on until a stack of images has been obtained. The advantage of imaging the unsliced tissue, Denk says, is that it does not matter if the slice itself crumples.

Until now, Denk and his team have cut only from pieces of tissue that measured much less than 1 mm across. But Denk's ultimate aim is to image and cut slices from a whole mouse brain, which will mean dealing with tissue blocks that are some 10 mm across. Denk is now building a whole-brain microtome to incorporate into the microscope. This will require a diamond knife that is 8–10 mm wide instead of the 1-mm knife used at present, he says.

To make these knives, he is collaborating with diamond-knife manufacturer Diatome in Biel, Switzerland. The longer blade width is a challenge, says Diatome engineer Helmut Gnaegi. At 10 mm, it is around ten times wider than a typical diamond knife, and the blade must be made from a large diamond that is free of crystalline imperfections (see ‘Sharp tools’).

The entire 10-mm cutting edge must be polished to perfection, Gnaegi says, because even a single knife mark would interfere with the smooth sample surface that Denk requires. After polishing, the cutting edge must have a maximum thickness of only 4 nm. This is a “formidable challenge” that the company hopes to overcome by the end of this year, says Gnaegi. He and his team have designed special polishing equipment for the task.

Gnaegi's team is also addressing the build-up of electrostatic charge that occurs when the knife tries to cut through tissue that has

W. DENK/MAX PLANCK INST. FOR MED. RES.

been embedded in non-conducting resin. The charge tends to make the sections stick to the sample surface, which makes imaging difficult. “An electrically conductive knife surface with optimized gliding properties leads to a sample surface free of cutting debris,” says Gnaegi.

The SBEM approach helps with precise rendering of tissue in three dimensions, but it is hard to make it high-throughput. Researchers would have to set up many microscopes in a dedicated facility. The alternative is an instrument that is “intrinsically a parallel imaging machine”, Denk says. That is why his lab is so interested in the Zeiss multi-beam machine that is due next year.

Lichtman and his team take a different approach to sample preparation. He has developed an automatic tape-collecting ultramicrotome (ATUM), which slices tissue, places each slice on a tape and delivers the slices to the microscope in a conveyor-belt fashion. Still other labs are working on different tissue-slicing approaches. “One of them will eventually emerge as the way to do things, probably,” says Denk.

Many labs are working on ways to improve the conventional tissue-staining methods used for electron microscopy, which rely on heavy metals such as lead and osmium. For example, Shawn Mikula, a postdoc in Denk’s team, has been experimenting with immersing whole, unsliced mouse brains in various staining chemicals for extended periods to enhance the spread of osmium throughout the tissue and to achieve adequate contrast in the electron microscope. This procedure worked well for imaging axons, Denk says, but was less successful for imaging the finer processes⁵. Given time, he says, “we’re pretty confident that we’ll figure it out.”

BEAM BONANZA

As part of their collaboration with Zeiss, both Lichtman and Denk deliver test samples to the company, which are imaged using the prototype microscope. At present, the number of scientist-testers has to be limited, and the instrument is not available for pre-order.



Dirk Zeidler (left) and Gregor Dellemann are developing the new Zeiss microscope.

Looking at images generated by the device has been “very exciting, because you realize how much faster those images were taken”, says Lichtman. When he and his team run experiments, the lab generates around 1 terabyte of image data a day. With the new microscope, he says, the rate will be more like 3 terabytes per hour.

Using his tape-collecting microtome with the new instrument, Lichtman plans to slice a mouse brain into many tens of thousands of sections, which can be put into the machine in large groups. “It images all of them and then you put the next several hundred or thousand in,” he says.

The Zeiss multiple-beam SEM resembles a standard SEM in many ways, says Dirk Zeidler, the physicist who led its design. It has an electron source, lenses and a scanning unit that moves the beam across the sample surface horizontally, in the same way as a reader’s eye moves over lines of text. It is built to be compatible with the various ways in which neuroscientists prepare tissue for imaging.

But the differences from a conventional SEM are crucial. The machine has been engineered for a wide view of the tissue and for speed, says Gregor Dellemann, who is the business-development manager for the new microscope. The most obvious difference is that the instrument has 61 electron beams scanning across the sample instead of the one beam in a conventional SEM, and an array of 61 secondary electron detectors (see ‘Speed

reading’). It also dispenses with features such as energy-dispersive X-ray spectroscopy detectors or back-scattered electron detectors, both of which are used in standard electron microscopes to map variations in a sample’s chemical composition.

Dellemann explains that including several detector types would mean incorporating three arrays of 61 detectors each, and would require a mechanism to guide the right signal to each one. Although possible, such a configuration would add cost and complexity to the instrument and slow it down.

Some scientists had voiced doubts about the multiple-beam SEM when they first heard about it, says Zeidler, who notes that they even questioned whether it might violate the principles of optics. But they recanted when shown a working instrument as it generated images, he says, adding “that was quite fun”.

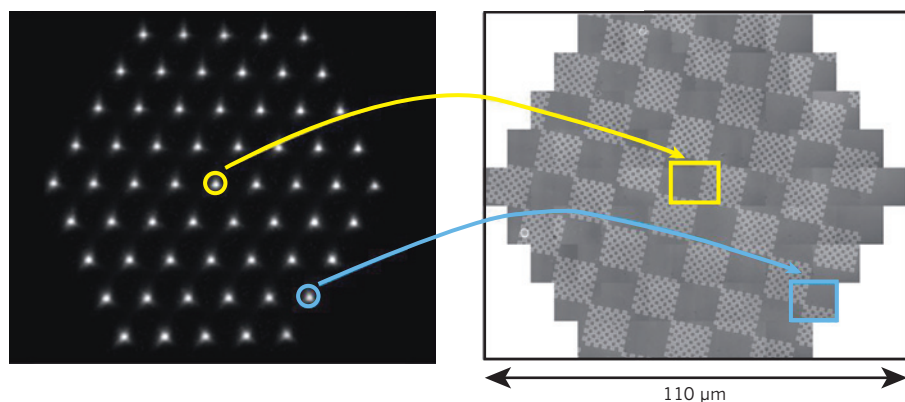
The new instrument addresses the speed limits and blind spots of a standard SEM. When the beam of electrons hits the sample, it emits secondary electrons that give information about, for example, the sample’s surface shape and staining. Detectors record the intensities of the secondary electrons and the instrument analyses these data to give an image of the sample.

To speed up this process, the beam would need to move more quickly and detect secondary electrons in less time. But when detection times fall below about 50 nanoseconds, the images get noisy. Furthermore, in the brief moment when electrons hit the detector, “it goes blind”, Dellemann says. No data can be collected until this ‘dead time’ is over and the detector ‘sees’ again.

Enhancing the abilities of an SEM using multiple electron beams and detectors for wider and quicker imaging requires attention to be paid to basic physics. Image quality suffers if the multiple beams are too close to each other because the electrons repel one another. “It will get blurry, which means you do not see the features you want to see,” says Zeidler.

The solution was to spread the charge over a larger area, minimizing the forces between electrons. More beams cover a larger sample area, and more detectors mean that the temporary blind spots are less of a hindrance. But the team still had to optimize the number of beams and their spacing, Dellemann says. Adding electron beams in a hexagonal configuration turned out to be the best geometry, and 61 beams with 61 detectors turned out to be the optimal number.

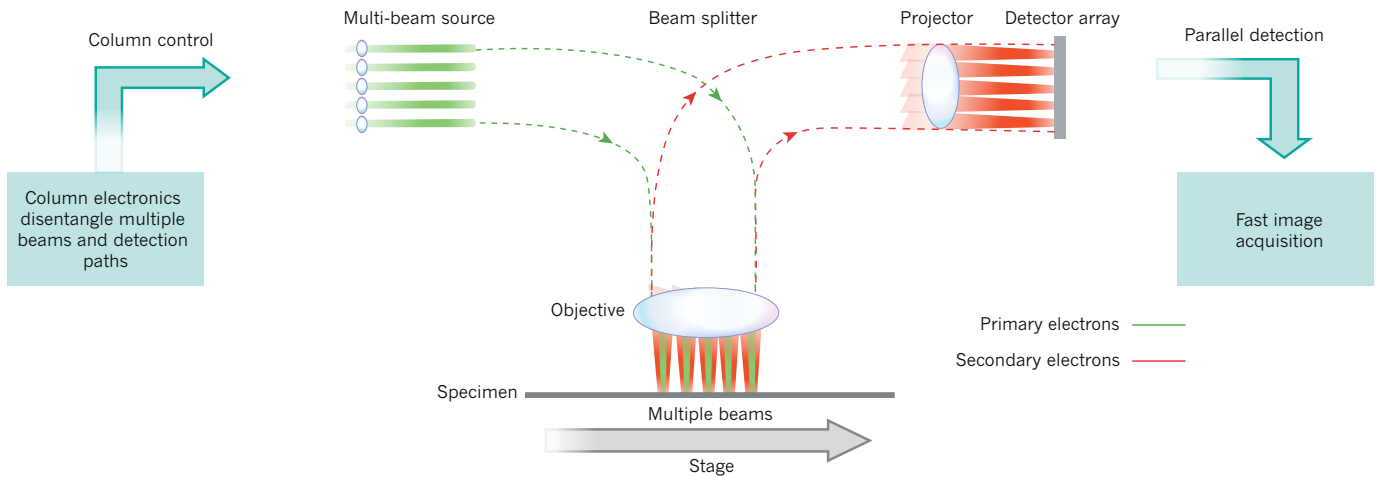
Most SEMs detect electrons for intervals of around 50 nanoseconds, such that the observer can image 20 million pixels per second before any physical limits are reached, Dellemann says. In a multi-beam instrument, each beam has a dedicated detector in the array and the 50-nanosecond detection speed stays the same. So with 61 beams, the images can get bigger. In



Zeiss’s prototype electron microscope uses 61 beams in a hexagonal configuration (left). The beams simultaneously scan sub-images (shown in yellow and blue squares) that merge into a large image (right).

SPEED READING

The prototype multiple-beam electron microscope has 61 beams and detectors to give a wide view of the sample and to enhance imaging speed.



1 second, Dellemann says, the instrument can take images of up to 1.2 billion pixels.

Zeiss started developing the instrument in 2000, when the company began exploring multi-beam SEM for the semiconductor industry in partnership with Applied Materials of Santa Clara, California. The aim was to develop technology that could inspect semiconductors using partially automated, parallel imaging. A few years later, Zeiss realized the potential of this technology for the life sciences, with the most interest coming from neuroscientists who wanted high-resolution brain mapping.

ENERGY BOOST

At microscope company FEI, engineers are souping up SEMs in a different way, using a single electron beam. The prototype of a new multi-energy deconvolution SEM is currently undergoing testing at the company, says Ben Lich, who handles business development for the life sciences at FEI. This instrument, too, is intended to speed up neuronal mapping.

Lich and his team have long worked with neuroscientists to optimize the standard components of SEMs. The US BRAIN Initiative and other ventures are encouraging the company to “do a bit more” for neuroscience, Lich says, so that researchers in the field can extract more information from their samples.

Current technology has a hard time imaging the more slender processes. To see cell bodies and axons, tissue sections need to be 30–40 nm thick, but to see the fine processes, they can be only 10–20 nm thick. Missing thinner branches in the imaging increases the risk of inaccuracies when reconstructing 3D circuits of connected neurons.

To address this challenge, FEI’s new microscope performs ‘sub-surface imaging’. It takes multiple images of the same area of a sample and is able to image below the surface. It can

help scientists to track down finer processes that they may have missed at a different resolution, Lich says.

The instrument sends sequential electron beams into the sample at differing speeds — starting at 1 kilovolt and ramping up to around 2.5 kV. This way, it obtains more information from the sample than a conventional single-scan microscope can, Lich says. After it acquires images, the instrument applies a mathematical technique called deconvolution, which separates the information from the different depths in the sample and produces virtual sections.

The instrument lets researchers scan their samples with varying resolution. A first image at low magnification might reveal cell bodies, which are important for neurobiology but not for understanding neuronal connectivity. An area that is densely forested with finer processes might merit a high-resolution scan.

Microscope manufacturers say that their experience in other fields helps with the challenge of whole-brain mapping, which will involve imaging many samples for months at a time. FEI, for example, has microscope customers who are checking the quality of small structures on semiconductors or determining the association of minerals and precious metals in mining ores. Their instruments run 24 hours a day, seven days a week for many months, says Lich, and they hold up.

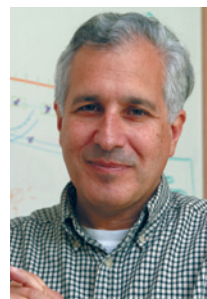
The engineering

of microscopes for neuroscience in particular also means helping to achieve better contrast from all samples, including those that might not be well stained. Lich says that FEI has designed its electron-beam column to optimize detection sensitivity.

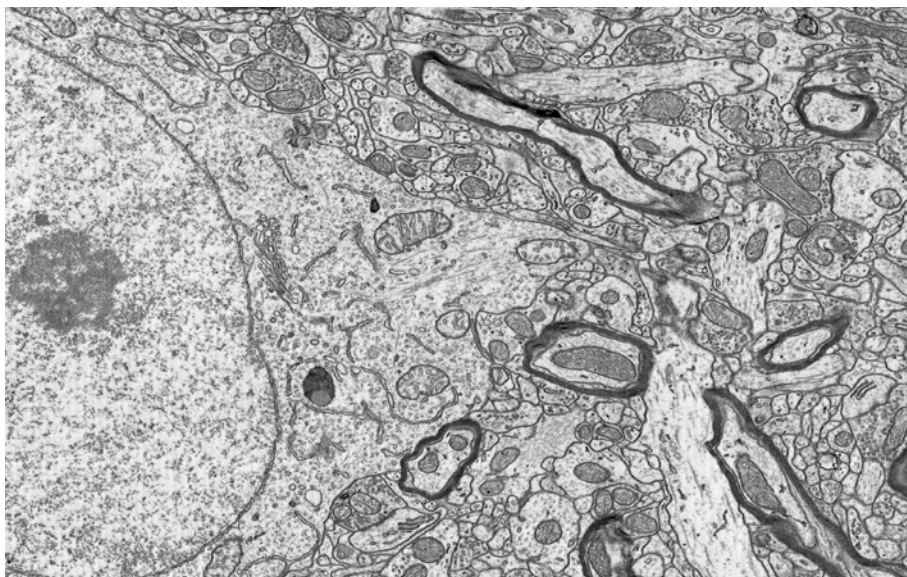
In juggling such factors as data quality, scanning speed and robustness, FEI’s team designed the multi-energy SEM so that its detectors for back-scattered electrons are engineered for speed, particularly at low energies. Using back-scatter signals is a more stable way to create images, Lich says. Secondary electron detectors are more prone to showing sample-charging problems, which is when the interaction between the electron beam and the sample leads to distorted images. In areas where the sample is charged, the acquired data can lead to ambiguous interpretations of neuronal connectivity. Back-scatter images are not as sensitive to this problem, he says.

For neuron mappers, FEI’s method for SEM imaging offers a way to slice a sample virtually before physically cutting it, Lich says. The microscope’s electron beam hits an area multiple times, generating a virtual image stack. Rather than needing to physically slice tissue to much less than 40 nm thickness, the sample can be imaged ten times at 4-nm resolution to create a virtual slice of the desired width. The technique could reduce the need for ultrathin slicing and the consequent risk of sample damage and distortion. Physical slices could remain relatively thicker, and intermediate layers in the slice would still be resolved, says Lich. And for a scientist using Denk’s approach of imaging followed by slicing, the tissue can be virtually imaged several times to different depths before it is physically shaved off.

The new SEM technology quickly creates issues of scalability for those who want to image large brain sections, Lich says. If scientists want data at 5-nm resolution, every voxel



Brain mapping is “not just the old neuroanatomy gussied up with new machines”, says Jeff Lichtman.



Under an electron microscope, mouse brain tissue shows neuronal cells (including myelinated axons; black rings) and organelles such as mitochondria. Careful analysis reveals where neurons end and begin.

— a 3D pixel — must be 5 nm on each side. At this resolution, the FEI microscope can obtain images, but imaging a cube of brain tissue measuring 1 mm on each side would yield 8 petavoxels of data — and those could take years to analyse, says Lichtman.

In his view, the neuroscience community is pushing microscope development with its structural mapping projects. Some, he says, might call the plan to image the whole mouse brain outrageous. “In principle, nothing is impossible — but it is really an extraordinary challenge,” he says.

DATA ANALYSIS

As neuroscience ramps up its mapping efforts, the challenge of big data becomes more apparent. Mapping the human brain is as difficult as creating a 3D map of a city 10,000 times the size of Tokyo, London or New York, and locating every inhabitant in every building, street, stairwell, lift and subway. To establish the same connectivity that neuroscientists are hoping to achieve, the mapping would then have to unearth all lines of communication — personal interactions as well as those by phone, post and e-mail — between all inhabitants of these 10,000 cities, explains Moritz Helmstaedter at the Max Planck Institute of Neurobiology in Munich, Germany.

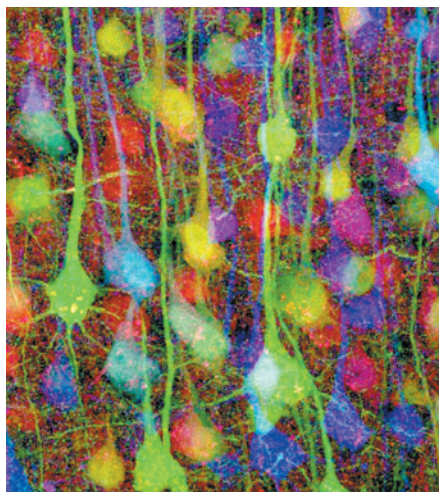
Denk estimates that capturing images of a whole mouse brain with the new Zeiss SEM could deliver 60 petabytes of data. And Lichtman notes that such large amounts of data are going to be even more challenging to share than they are now. At present, he sends his microscopy data sets to the Open Connectome project at Johns Hopkins University in Baltimore, Maryland. The project’s website is an open repository for data accrued from different labs working on the brains of model organisms such as mice and nematodes. It enables

anyone to download information from MRI, electron-microscopy and brain-wiring studies.

Lichtman has one data set that is around 100 terabytes in size. “How do you give that to somebody?” he asks. As data sets get even larger, the community will have to explore ways to make data available to scientists for perusal without download, he says.

The next-generation microscopes can deliver the high-resolution images, but new approaches, including computational tools, are needed to build 3D wiring diagrams of neuronal circuits based on those images.

Denk and colleagues in the United States and Germany have recently used SBEM to map a small section of mouse retina². Even with computer software, tracing the neuronal pathways in the images would have taken vastly more time and more people than are available in a typical lab. The team turned to crowd-sourcing, enlisting the help of a host of



Fluorescence microscopy can show many types of mouse neuron using the ‘Brainbow’ technique.

non-scientists sitting at their home computers.

Software to help researchers with these tasks is being developed, and computer scientists plan to keep pace with the advances in microscope technology, Lichtman says. Image-analysis software under development includes tools with built-in machine learning and other types of algorithm to automate or semi-automate the tasks.

Denk says that he used to think that researchers had to solve data-analysis problems before imaging larger brain volumes and generating huge data sets. But his view has changed. “My current thinking is that we’ll just produce a large volume,” Denk says. “Then, that will embarrass the analysis people into coming up with something.”

Neuroscientist Sebastian Seung at the Massachusetts Institute of Technology in Cambridge, who collaborated on the mouse retina mapping study², leads a group that launched the online game EyeWire. More than 80,000 volunteers worldwide have helped to trace the complete 3D contours of neurons running through the game’s electron-microscopy images. He is undaunted by the large data sets that brain mappers will be sending his way for analysis. “Why would we be frightened?” he says. “It is just an opportunity.” Size in image data sets is a plus when imaging the mammalian nervous system. Imaging too small a section risks missing neuronal connections, he says.

Still, the challenge in mammals is formidable. When scientists image fruitfly brain tissue, a small imaging volume can capture much of a neuronal circuit, because many neurons do not run and branch over long distances, says Seung. In mammals, many researchers trace connections found in the retina, because much of the circuit can be captured with a small tissue volume, he says. But that is already a huge challenge — and it gets worse when tracing connections in the brain, because neuronal circuits are spread out over much larger volumes in mammals than in flies. “You can’t really map out connections and circuits unless the volume you are imaging is reasonably large,” he says.

Lichtman believes that the neurobiology community will ultimately find a way to garner the required knowledge because researchers stand to learn so much about the brain. “Without it, there are lots of mysteries,” he says. “With it, mysteries become just facts.” ■

Vivien Marx is technology editor for *Nature* and *Nature Methods*.

1. White, J. G., Southgate, E., Thomson, J. N. & Brenner, S. *Phil. Trans. R. Soc. Lond. B* **314**, 1–340 (1986).
2. Helmstaedter, M. *et al. Nature* **500**, 168–174 (2013).
3. Takemura, S. Y. *et al. Nature* **500**, 175–181 (2013).
4. Advisory Committee to the NIH Director. *Interim Report: Brain Research through Advancing Innovative Neurotechnologies* (NIH, 2013).
5. Mikula, S., Binding, J. & Denk, W. *Nature Meth.* **9**, 1198–1201 (2012).

CAREERS

COLUMN A love affair with research can break your heart, too **p.155**

NATUREJOBS BLOG Up-to-the-minute careers news and issues go.nature.com/ielkkf

NATUREJOBS For the latest career listings and advice www.naturejobs.com



The neuronal pathways in the brain's white matter are picked out in this magnetic resonance image.

NEUROSCIENCE

A head start for brain imaging

With several big data projects under way, there is growing demand for neuroimaging expertise.

BY VIRGINIA GEWIN

Corey White felt pretty fortunate during his job search late last year. Over the course of 4 months, he found at least 25 posts to apply for — even after he had filtered the possibilities to places where his wife also had job prospects. Competition for the jobs was, as he expected, fierce, but he secured three interviews. In the end, he says, it was his skills in functional magnetic resonance imaging (fMRI) that helped him to clinch a post at Syracuse University in New York, where they were eager to elevate their neuroscience profile.

The human brain is something of an enigma. Much is known about its physical

structure, but quite how it manages to marshal its myriad components into a powerhouse capable of performing so many different tasks remains a mystery. Neuroimaging offers one way to help find out, and universities and government initiatives are betting on it. Already, an increasing number of universities across the United States and Europe are buying scanners dedicated to neuroimaging — a clear signal that the area is set for growth. “Institutions feel an imperative to develop an imaging programme because



NEW ANGLES ON THE BRAIN

A *Nature* special issue

www.nature.com/neuroscience2013

everybody's got to have one to be competitive,” says Mark Cohen, an imaging pioneer at the Semel Institute for Neuroscience and Human Behavior at the University of California, Los Angeles.

At the same time, a slew of major projects focusing on various aspects of the brain is seeking to paint the most comprehensive picture yet of the organ's organizing principles — from genes to high-level cognition. As a result, young scientists with computational expertise, a fluency in multiple imaging techniques and a willingness to engage in interdisciplinary collaborations could readily carve out a career in this dynamic landscape.

INSIDE THE MIND

Several imaging techniques are experiencing fresh demand. The development of tracers that bind to the β -amyloid proteins that form the plaques associated with Alzheimer's disease has reinvigorated the use of positron emission tomography (PET), for example. PET scans can now be used to detect the earliest stages of Alzheimer's disease, which could aid the development of effective treatments. And fMRI, which detects changes in blood flow, is now being used to identify neural networks involved in cognitive function, to recognize and diagnose neurodegenerative diseases and to assess treatments or therapies (see *Nature* **484**, 24–26; 2012). Researchers have also combined fMRI skills with novel optogenetic techniques, which use genetic controls to activate specific neurons in order to track neuronal activity in live animals.

These imaging techniques are being pulled together in a number of big projects that aim to integrate findings on the molecular, cellular and whole-brain scales. In January, the European Commission announced that it would fund the 10-year Human Brain Project at roughly €1 billion (US\$1.4 billion); the project has the ambitious aim of producing realistic computer simulations of the brain, all the way from individual cells to the entire organ (see *Nature* <http://doi.org/phz>; 2013). Some 250 scientists from 80 groups are involved so far, says Richard Frackowiak of the University of Lausanne in Switzerland, who is one of the project's co-leaders. He expects that number to grow in future funding rounds.

In the United States, the US\$110-million Brain Research through Advancing Innovative Neurotechnologies (BRAIN) Initiative, announced in April, will map the brain's activity in exquisite detail, with imaging likely ►

► to be among the funding priorities (see page 26).

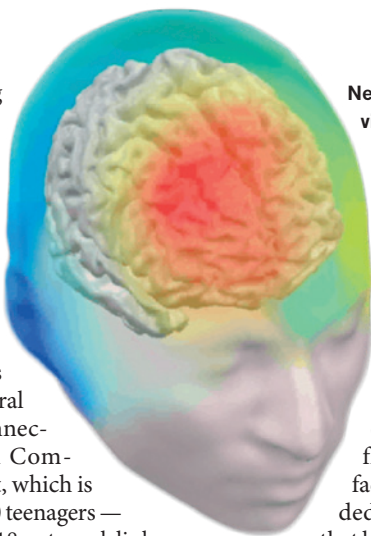
Technological advances in neuroimaging are the foundation of other big, interdisciplinary collaborative efforts, such as the Human Connectome Project, funded by the US National Institutes of Health (NIH), which is mapping the brain's structural and functional neural connections; and the European Commission's IMAGEN project, which is scanning the brains of 2,000 teenagers — at the age of 14 and again at 18 — to seek links between brain structure, risk-taking behaviour and mental health. “Even though studying diseases is a big driver in neuroscience, we’ve put increasing effort into understanding how healthy brains work,” says IMAGEN scientist Christian Büchel, director of the neuroimaging centre at the University Medical Center Hamburg-Eppendorf in Germany.

Although these big projects offer significant career opportunities, there is a potential downside that researchers need to keep in mind, says Ray Dolan, director of the Wellcome Trust Centre for Neuroimaging at University College London. Search committees typically place a premium on independence and individual initiative. “I worry about top-down initiatives creating an army of workers who, when the projects are done, are no longer attractive as potential hires by universities because they haven’t developed the ability to generate their own ideas,” he says. Even so, Dolan believes that neuroimaging skills allow researchers to cross disciplinary boundaries relatively easily.

BEYOND NEUROSCIENCE

The university neuroimaging boom is not confined to neuroscience departments. There is a real hunger for ways to quantify brain and behaviour in psychology and psychiatry, says Graeme Mason, director of the neuroimaging sciences training programme at Yale School of Medicine in New Haven, Connecticut.

Most of the faculty positions in established disciplines, such as cognitive psychology, require neuroimaging skills. And neuroimaging has fuelled the rapid growth of subfields such as neuroeconomics, which looks at human decision-making, and social neuroscience, which studies disorders and the development of human social behaviour. Todd Heatherton, a cognitive neuroscientist at Dartmouth College in Hanover, New Hampshire, and a frequent job-search chair, says that, until recently, social neuroscience had more jobs available than there were truly qualified applicants — those with both the computational skills and an appreciation of social psychology. Competition for the top applicants remains fierce, he says.



Neuroimages explore real-time views into cerebral function.

For many young neuroscientists, the biggest concern is the lack-lustre state of federal funding in some countries, especially given that scanning programmes are costly to get up and running. At Syracuse University, White is one of the few people doing fMRI studies. Given that the facilities he uses are not solely dedicated to research, he fears that he would struggle to meet the criteria for an NIH grant to fund his work on cognitive behaviour. So he is trying to bolster his chances by setting up cross-disciplinary collaborations that take advantage of local expertise in genetics, cardiovascular health or exercise science. Already he has been talking to an exercise scientist about relating the metrics of artery stiffness to cognitive processing.

It is not a bad strategy. Carolyn Asbury, a consultant for the Dana Foundation, a non-profit organization in New York city that is dedicated to neuroscience, says that funding applications have become increasingly interdisciplinary and collaborative during the past decade, often combining different imaging techniques. The foundation allocates at least half of its annual funds of some \$2.8 million to support budding neuroscientists starting careers. It is particularly interested in proposals involving cellular and molecular imaging techniques, such as developing new tracers for use in PET.

Funders are also increasingly interested in applied clinical uses of neuroimaging techniques, which open yet more avenues for collaboration. For example, the European Commission in September put €4.2 million into a €6-million project called METSY. This aims to identify neuroimaging biomarkers of psychosis and to study the links between psychotic disorders, such as schizophrenia, and

other conditions, such as obesity and diabetes.

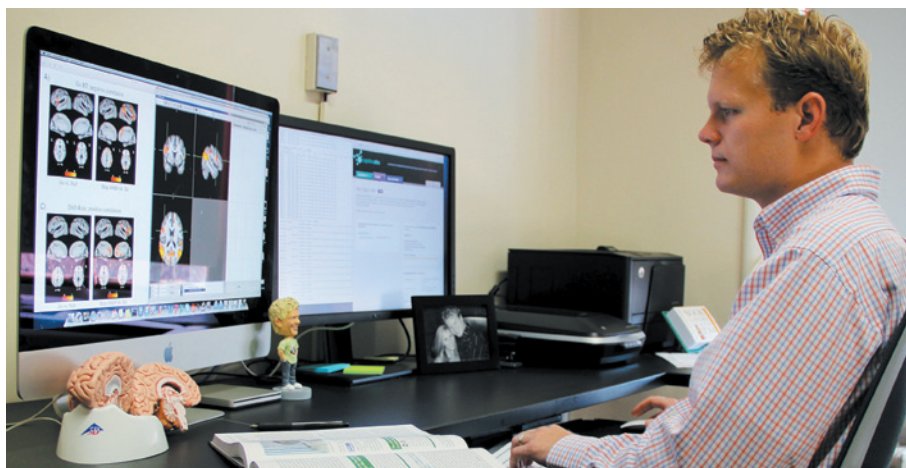
In Switzerland, the Translational Neuro-modeling Unit at the University of Zurich has brought clinicians, neuroimagers and computational analysts together under one roof to develop diagnostic tools based on models to offer treatment recommendations and predict clinical outcomes for psychiatric patients. And in September the Kessler Foundation in West Orange, New Jersey, opened the first independent neuroimaging-focused rehabilitation institute in the United States, where it will conduct research and clinical trials aimed at bolstering recovery from brain trauma.

Companies also see the potential for imaging to become a staple of health care and drug development. Bin He, director of the Center for Neuroengineering at the University of Minnesota in Minneapolis, says that his graduate students sometimes end up working at major imaging companies. Philips recruited one of his students last year, he says, and companies such as Siemens, General Electric and Medtronic are also looking for neuroimaging talent. Russell Schramm, head of talent acquisition for Philips North America, says that imaging systems will be a key area of focus for the company's health-care business over the next five years. Projects such as the Alzheimer's Disease Neuroimaging Initiative — an effort funded in part by the Alzheimer's Association to study changes in cognition, function and brain structure in elderly people — could have an impact in the clinic and spark interest from industry, he says.

SURVIVAL SKILLS

To capitalize on the opportunities for neuroimaging, it is important to gain the appropriate statistical and computational skills. This means taking advanced statistics courses and learning a programming language.

“Neuroimaging is now seen as a quantitative field — built on real data, not clever parlor tricks — that has an impact in a variety of areas of medicine,” says Cohen. Computational skills, including multimodal analyses,



Corey White hopes to build interdisciplinary collaborations that capitalize on his fMRI skills.

ALEXANDRIA WEAVER

signal processing and parametric statistical modelling, are key to successful analyses. "It takes quite a bit of skill to look at data and identify what is artefact versus what is real and important," Cohen says.

Russell Poldrack, director of the Imaging Research Center at the University of Texas at Austin, doesn't even bother to interview applicants who can't write computer code. Data sets are getting so big that trying to analyse them without using automated methods simply takes too long, he says. Off-the-shelf software packages tend not to lend themselves to the most interesting and novel analysis methods, Poldrack notes, so he wants people who can write programs that can do those analyses.

Computational skills have become so important that, in July, Dartmouth College hired Alireza Soltani, a computational neuroscientist with a background in theoretical physics, to model other people's data rather than collect his own. Soltani uses detailed computational modelling at the synaptic, cellular and network levels to look for mechanisms that help to explain behaviour and cognition. This hiring strategy is necessary to ensure that the college has the people "with the skills to advance the field beyond pretty pictures", says Heatherton.

As universities increase their neuroimaging capacity, they are facing a recruitment challenge. "The applicant pool for neuroimaging posts is diversified and of variable quality," says Kamil Ugurbil, director of the Center for Magnetic Resonance Research at the University of Minnesota. It can be difficult to find good people with rigorous computational skills in neuroimaging, he notes. At the same time, physicists, engineers and statisticians can have quantitative skills but lack the psychology or life-sciences background for a neuroimaging-related post.

Even those who can offer the right mix of skills should consider gaining expertise in more than one imaging technique. "We all need to specialize to some extent, but it's more advantageous to be well versed in a range of complementary techniques to avoid being labelled as just the PET guy or just the fMRI guy," says Brian Bacskaï, a neuroscientist at Massachusetts General Hospital in Boston, whose work combines cellular and molecular imaging techniques to study Alzheimer's disease.

Bacskaï reiterates the importance of collaboration for neuroimaging. "Cross-disciplinary studies are the only way to move the field forward," he says. "I think institutions will look at how good applicants are at working with others as a key factor in a CV or tenure package." ■

Virginia Gewin is a freelance writer based in Portland, Oregon.

COLUMN

Postdoc's torch song

A love affair with research can be just as heartbreaking as romantic love, says **Christopher Schmitt**.



Maybe it was never meant to be. Such was my resigned perspective when I was dumped by a boyfriend while conducting my doctoral field research. I had been studying the behaviour of wild spider monkeys and woolly monkeys in the Amazon for six months, and as the data had been slowly coming in, my relationship had been slowly deteriorating. Communication had devolved from lengthy nightly video chats — me providing virtual tours of the field station and images of monkeys, him displaying Manhattan skyscrapers — to a slow fade of curt, non-committal missives that bred a terrible uncertainty. When I saw him smiling with an unfamiliar man on my social-network newsfeed, I knew which way the wind was blowing.

But it was OK. I was getting my data. I was working towards a doctorate and an academic career, something bigger than that relationship. And I knew that once I recovered from being dumped by instant message, I could find another man — a better man! — who would be more supportive of my increasingly demanding relationship with my work. My research seemed to offer the affirmation and validation that my personal relationships had stopped providing. After all, I thought, it could never cut me off the way my now ex-boyfriend had.

I did get my doctoral degree. I got grants. I published. I landed a promising postdoc post across the country from my graduate school; I could check out a new dating pool while leaning on my more gratifying love affair with science.

Now I am three years into a postdoc that has been not quite as productive as promised. The wait for overdue data from collaborators has made me miss my funding deadlines. When I do pitch my research to funders and

foundations, they send me curt summary statements wondering about my lack of post-doctoral publications. Letters to tenure-track university job-search committees come back with polite but deflating responses.

It's the slow fade all over again.

Of course, my challenges are not uncommon. Postdocs in the current market, especially in the life sciences, have little chance of landing the tenure-track posts they had in mind when they started out. The dire situation in the US job market was exacerbated by a massive increase in trainees in the early 2000s with no increase in faculty positions, and may well be amplified by sequestration, that package of deep cuts to US federal agencies that took effect in March and has no end in sight.

So it seems that the most important relationship in my life, the one I have put above all others — my love for academic research — is falling apart, owing in no small measure to circumstances beyond my control. As this happens, I think about all the time I have spent away from family and friends, and all the relationships that have fallen by the wayside as I moved from state to state to build my career.

Academia has been a difficult love. It seems to have made some promises it did not intend to keep, and no amount of torch-song singing will make the potential loss feel any less dire. I need to remember the refrain from Joni Mitchell's *A Case of You*: having drunk my fill of academia, I can still be on my feet. If my career comes to an end now, maybe I can keep my heart intact, and move on.

But until it comes to that, I will hold on to this love. Maybe, despite the chilly job climate and data delays, my career can still flourish. Why else would I have given up so much? I continue to submit papers and grant applications. I'm looking for postdoc posts or teaching positions that will keep me in the game until the tenure track comes courting. I'm throwing away my misgivings, refusing to become resigned to a life outside academia, and hoping beyond hope that this love is the one that will not leave me.

And if it does?

Well, I'll defer again to Joni: "If you want me I'll be in the bar..." ■

Christopher Schmitt is a postdoctoral research fellow in the Center for Neurobehavioral Genetics at the University of California, Los Angeles.

IMMEASURABLE

Off the scale.

BY H.E. ROULO

Students streamed out of Yvonne's geology class, rolling up their flexible displays and shoving them into backpacks. Yvonne lingered outside, dreading what came next: she needed to press the button.

The funeral home had just sent her a microfluidic hot key that would take action with one nail press. The new button rose like a blister on the band of the flesh-coloured Metric that clung to her wrist. Her racing heartbeat and clammy skin revealed her anxiety, casting her Meta-score down with each moment she delayed, but her finger refused to tap — even if it meant losing points.

Peggy careered around the corner of the building, blonde hair brushing the wolf on her airbrushed T-shirt. She grinned at Yvonne. "How'd you do today?"

Yvonne glanced at her Metric as if she hadn't been staring at it. "I scored basic learning and self-actualization points. Just another weekday in class."

Peggy frowned. "No class participation bonus? That's not like you. Hey, let's walk the long way back to the dorms. I'm short on exercise."

Across campus, a student in a college sweatshirt threw a Frisbee to a girl in a tank top. Other students sat beneath a tree, listening to a guitar. They'd all be filling their socializing bars, and it looked like fun. On another day, in another mood, Yvonne might have joined them.

Peggy's touch startled her. "Hello? You're barely here."

"Brian —," Yvonne choked on her brother's name, and watched the Frisbee fly into the bushes. "His ashes are ready to be dispersed."

The girl in the tank top fished in the undergrowth for the Frisbee and stood up with a glad cry, a wrapper flapping in her hand. Her partner groaned, obviously wishing he'd found it. The girl dropped the litter into a bin, Metric dinging.

Peggy pouted. "Damn, the college announced a green initiative, and bonus goals like *community improvement*. She probably got 500 points. I'm behind for the day. I didn't get up with my alarm and I skipped breakfast. I chose pizza Friday night as my reward — doesn't look like I'm going to get it."

"On the other hand, you don't have to deal with your dead brother's remains. Bonus, right?" Yvonne pinched her lips shut. Since



Brian's accident she'd learned she shouldn't resent how the world went on as if nothing had changed. For them, it hadn't. She scuffed the ground with her foot.

Peggy shrugged.

They'd circled round on the asphalt path and the dorms stood a block away. Yvonne wished she was already there, tucked under the blankets. She'd lose points, of course. Since arriving at school she'd focused her Metric on rewarding education and new experiences. Peggy used hers to avoid her freshman fifteen. But their concentration on scoring drew them together. Nothing felt as good as the chime for a new high score.

"Doesn't your Mum want to handle his ashes? That's a major emotional milestone. It's a level-up for sure!"

"Mum wouldn't use the points. She relies on a cell phone. I tried to set a Metric up for her, but she never got into it. She says her MMO is a better game."

"Old-fashioned! They're such a different generation, escaping into TV, video games and movies. Hanging out with friends online. Real-world accomplishments are so much more fulfilling, I mean, as long as you've set your incentives right."

"I've hit my exercise goal. Let's cross the street, it'll be shorter."

Cyclists rode by, their Metrics ticking up health and social responsibility points. "Mum's had a hard time dealing with Brian's death, so I said

I'd do it. I don't know why I'm making a fuss. It's just a button." Yvonne raised her wrist.

Why delay? There were no extra points for doing it in person. Stomach clenching, her index finger hovered but would not descend. Although she'd said goodbye at the memorial — held at a virtual church so friends from all over could mourn together — this would be final. Real.

Peggy halted. "I don't know what it's like to lose a family member, but I know it's tough. You've been strong, and you're helping your family by taking this on."

Tears blurred the bottom of Yvonne's vision. She embraced Peggy.

Peggy squeezed back. She sniffed and wiped a hand across her nose. Her Metric dinged and her eyes brightened.

"Social connection! I was totally there for a friend. Look, I'm ahead for the day." She gave Yvonne's unresisting shoulders another squeeze. "And usually I score low on empathy. See you later. Thanks for making it a great day!"

Peggy bounded towards her dorm, humming.

Yvonne's fingers stroked the bubbled key of her Metric. One press, and she'd complete a mega-life task. She'd level-up. Some people were born rich, and exotic trips set their experiences scores ahead. But with this, she'd be ahead of most of her peers. She could gain something nice from a painful life event. Brian would like that.

But she didn't want to score points for this. "Peggy!" she called.

The girl stopped on the steps.

Yvonne slipped the Metric from her wrist. The thin coil dangled between her fingers, innocent of the weight she'd given it. She tossed the Metric into the bushes and heard a sad chime — lost points.

"OMG, what are you doing?" Peggy yelled.

Vertigo flooded Yvonne and her knees threatened to buckle as she tried to orientate herself towards the mortuary without her Metric to guide her. Once familiar buildings hid the way, their configuration confusing to a sleepwalker who'd awakened. On the second step towards her goal, her stride strengthened. Over her shoulder she called: "There's litter in the bushes if you want it!"

Peggy squealed. A Metric chimed. ■

➔ NATURE.COM

Follow Futures:

🐦 @NatureFutures

📘 go.nature.com/mtoodm

H. E. Roulo is a Pacific Northwest author whose stories have appeared in a dozen podcasts, magazines and anthologies (www.heroulo.com).